SPACE SCIENCE ACTIVITIES IN CHINA
NATIONAL REPORT 2018—2020

CNCOSPAR
2020

Members of the Chinese National Committee for COSPAR

President

XIANGLI Bin	Chinese Academy of Sciences (CAS)

Vice Presidents

HUANG Weidong	Researcher
LI Ming	China Academy of Space Technology (CAST)
HAO Zhaoping	China Academy of Launch Vehicle Technology (CALT)
WANG Qi'an	National Remote Sensing Center, Ministry of Science and Technology (MOST)
YU Qi	Department of System Engineering, China National Space Administration (CNSA)

Members

JIANG Jingshan	National Space Science Center, CAS
AI Guoxiang	National Astronomical Observatories, CAS
HU Wenrui	Institute of Mechanics, CAS
WANG Shui	University of Science and Technology of China (USTC)
OUYANG Ziyuan	National Astronomical Observatories, CAS
GONG Huixing	Shanghai Institute of Technical Physics, CAS
TU Chuanyi	Peking University
LÜ Daren	Institute of Atmospheric Physics, CAS
LI Tipei	Institute of High Energy Physics, CAS
GU Yidong	Technology and Engineering Center for Space Utilization, CAS
WU Yirong	Institute of Electronics, CAS
GUO Huadong	Institute of Remote Sensing and Digital Earth, CAS
WANG Weihua	Institute of Physics, CAS
ZHOU Zhixin	Academician
WANG Jianyu	Chinese Academy of Sciences Shanghai Branch
DOU Xiankang	Wuhan University
CHANG Jin	Purple Mountain Observatory, CAS
WANG Chi	National Space Science Center, CAS
XU Ronglan	National Space Science Center, CAS
XIAO Zuo	Peking University
CAI Zhenbo	China Academy of Space Technology (CAST)
LI Yinghui	Researcher, Astronaut Center of China
GAN Weiqun	Purple Mountain Observatory, CAS
YAN Yihua	National Astronomical Observatories, CAS
ZHANG Xingwang	Institute of Semiconductors, CAS
WANG Jingsong	China Meteorological Administration
CAO Jinbin	Beihang University
FANG Guangyou	Institute of Electronics, CAS
WANG Shijie	Institute of Geochemistry, CAS
FENG Xueshang	National Space Science Center, CAS
DONG Xiaolong	National Space Science Center, CAS
LU Feng	Institute of Geographical Sciences and Natural Resources Research, CAS
JIANG Luhua	Institute of High Energy Physics, CAS
GAO Ming	Technology and Engineering Center for Space Utilization, CAS
LONG Mian	Institute of Mechanics, CAS
CHEN Hongbin	Institute of Atmospheric Physics, CAS
LU Jinying	China Academy of Space Technology (CAST)
SUN Yeqing	Institute of Environmental System Biology, Dalian Maritime University
PAN Mingxiang	Institute of Physics, CAS
WEI Jianyan	National Astronomical Observatories, CAS
ZHANG Tao	Shanghai Institute of Technical Physics, CAS
DING Mingde	Department of Astronomy, Nanjing University
LI Chunlai	National Astronomical Observatories, CAS
HUANG Maohai	National Astronomical Observatories, CAS
XUE Hongwei	Shanghai Institute for Biological Sciences, CAS
LIU Lin	Department of Astronomy, Nanjing University
XU Minqiang	Harbin Institute of Technology
DENG Yulin	Beijing Institute of Technology
LIU Siqing	National Space Science Center, CAS
SUN Yueqiang	National Space Science Center, CAS

Secretary General

WU Ji	National Space Science Center, CAS

Deputy Secretary General

LI Lei	National Space Science Center, CAS
ZHUANG Yan	Bureau of International Cooperation, CAS
YAN Jingye	National Space Science Center, CAS

Secretariat Contact

LI Xiaoyu, XU Yongjian	Tel: 86-10-62586404. Fax: 86-10-62632257. E-mail: xuyongjian@nssc.ac.cn
CNCOSPAR Secretariat	c/o NSSC, No.1 Nanertiao, Zhongguancun, 100190, Beijing, China

Contents

GU Yidong, GAO Ming, ZHAO Guangheng. Science Research and Utilization Planning of China's Space Station in Operation Period 2022–2032. *Chin. J. Space Sci.*, 2020, **40**(5): 001-006. DOI:10.11728/cjss2020.05.001

Science Research and Utilization Planning of China's Space Station in Operation Period 2022–2032

GU Yidong GAO Ming ZHAO Guangheng

(*Key Laboratory of Space Utilization, Technology and Engineering Center for Space Utilization, Chinese Academy of Sciences, Beijing* 100094)

Abstract The core module of China's Space Station (CSS) is scheduled to be launched around the end of 2020, and the experimental module I and II will be launched in the next two years. After on-orbit constructions, CSS will be transferred into an operation period over 10 years (2022–2032 and beyond) to continuously implement space science missions. At present, based on the project selection and research work in the ground development period of CSS, China is systematically making a utilization mission planning for the operation period, which focuses on the fields of aerospace medicine and human research, space life science and biotechnology, microgravity fluid physics, combustion science, materials science, fundamental physics, space astronomy and astrophysics, Earth science, space physics and space environment, space application technology, *etc.* In combination with the latest development trend of space science and technology, China will continue to update planning for science research and technology development, carry out project cultivation, payload R&D, and upgrade onboard and ground experiment supporting systems to achieve greater comprehensive benefits in science, technology, economy, and society.

Key words China's space station, Utilization, Planning, Experiment

Classified index V 476

1 Progress of CSS Development

The core module of China's Space Station (CSS) will be launched by the launcher Long March 5B after 2020, the experimental module I, II will be launched in the next two years and the assembly of three modules is expected to be completed around 2022, and then the CSS will be transferred into an operation period over 10 years (2022–2032 and beyond)[1]. At present, the scientific experimental racks and related supporting systems are in the pressurized module and some exposed facilities are being developed. By 2019, China has issued two large-scale AO (Announcement of Opportunity) to solicit scientific research and application projects, published a number of project guidelines[2], a total of nearly 1000 proposals have been received, which laid a good foundation for the ground research and preparation for the follow-up consecutive projects of CSS. Based on all these works, China is systematically working out a complete scientific research plan on board for CSS operation which will guide to make full use of the experiment facilities and maximize the utilization efficiency.

2 Main Mission of CSS Operation

CSS aims to become a national space laboratory at an international advanced level in the operation period. The main mission of CSS comprehensively focuses on the research fields of space science, aerospace medicine, and new technology for future applications, continuously implement science and other application projects on orbit. At the same time, firstly, it is necessary to continuously update the planning of CSS utilization, carry out project cultivation (ground research), and payloads R&D,

Received May 25, 2020
E-mail: gxd@nssc.ac.cn

make full use of the facilities that have been planned in CSS ground development period. Secondly, it is necessary to further expand the scale of researches and utilizations by making full use of the resources inside and outside three modules, to promote new scientific experimental platforms and facilities. Thirdly, it is necessary to make rational and efficient use of relevant scientific data and research results, systematically and comprehensively popularize technology and achievements, lead international cooperation and expand space educations, to achieve greater benefits in science, technology, economy, and society ultimately.

3 Planning Ideas

The science planning should be based on the principle of combining science and technology to ensure every project with high scientific significance and cutting-edge technologies. At the same time, it must pay attention to the maturity of the technical solutions of the mission and consider the feasibility of the project, and establish project cultivation mechanism to carry out ground research in depth, strengthen the integration of science and engineering, and improve the Technology Readiness Level (TRL), so that engineering development could effectively under the guidance of planning. Firstly, expert teams composed of chief scientists, senior scientists (including experimental system engineers) and young scientists have been organized to continuously specify a systematic, serialized and step-by-step research plan, to optimize the top-level design of key research directions for CSS. The top-level design will contribute to the foundational framework and main content of the planning. Secondly, the planning process will continue to collect new research proposals and ideas through an extensive AO mechanism effectively supplement the planning contents. In addition, based on the planning priorities, targeted project guidance can be conducted for directional AO, so that the science planning can be closely integrated with the specific research projects, which will help to consolidate major projects with scientific significances and influential results.

Before the launch of CSS until the whole operation period, the planning is expected to provide a clear and definite reference for scientific research and utilization, continuously guide to review and select high-quality projects, and to propose a scientific project planning suitable for the project implementation through ground cultivations (ground research funding), so as to maximize the outputs in fundamental science researches, applied basic researches, and related technological innovations.

4 Science Planning for CSS Operation

China's manned spaceflight program has accumulated utilization experiences and achieved fruitful research results in Shenzhou spaceships and Tiangong laboratories. With the ground development of CSS, planning has been carried out for many years. On those earlier bases, at present, the planning is more oriented to the international scientific frontier[3], to original innovations and China's development needs[4], and all work will comply with a more comprehensive science plan with series research fields and directions.

4.1 Aerospace Medicine

The field of aerospace medicine focuses on human science and major medical problems that restrict human long-term spaceflight[5]. It also takes into account the health needs of the general public on the ground. The planning is mainly to research and solve the problems of long-term weightlessness on astronaut's physiological functions and protection mechanisms, impacts of space radiation on astronaut's health and protection mechanisms, new technologies and methods for aerospace medical research, mechanisms of traditional medical aerospace application technology, aerospace nutrition, and metabolic mechanisms, *etc.* Research achievements are expected to provide basic support for the long-term mission health in the space station, provide technical support for improving the operation ability of astronauts, and accumulate experience for longer-term manned flight and manned deep space exploration.

4.2 Space Life Science and Biotechnology

Researching the existence, response, and activities of

life under space radiation, microgravity and weak magnetic could deeply understand the nature of life phenomena and the needs of human long-term space exploration. The objectives of space life science research are to promote the understanding and cognition of the essence of life phenomena and to explore the scientific laws, including the perception and response mechanism of various levels of life to the change of gravity[6]; the mechanism of damage, change and stress under space radiation; the basic issues of the controlled ecological support system, and the exploration of the origin of life. Space biotechnology is focused on obtaining innovative materials, drugs, and medical technologies by using space microgravity and other environments. It is expected to help improve people's health, the development and application of regenerative medicine, biological cell therapy, biological medicine, and environmental biotechnology; carry out research on biomolecular design and its synthetic biology, expand germplasm resources by using space radiation mutagenesis, and promote agriculture and medicine service: develop the controlled ecosystem that can operate stably and adapt to the needs of long-term human space exploration.

4.3 Microgravity Fluid Physics

The planning of microgravity fluid physics focuses on discovering new phenomena and new laws of fluid movement under microgravity conditions, expanding the development of fluid basic theory, realizing new systems that are difficult to construct on the ground, and forming systematic theoretical innovations and technological breakthroughs[7]. The science research focuses on the dynamics of interface and diffusion processes, including multiphase flow and heat transfer problems, and complex fluid behavior. The application research is closely related to fluid management, chemical smelting, biology and medicine, material manufacturing and processing, and is helpful to solve the key technologies of propellant management, optimizing propellant storage and transportation on-orbit. On the ground, it is conductive to the transfer of related technologies, and promoting R&D and manufacturing of new high-efficiency-safe space fluid and thermal equipment.

4.4 Microgravity Combustion Science

The planning of combustion science focuses on combustion characteristics and basic theory research, space fire safety, *etc.* In addition, microgravity combustion science research is closely related to energy saving and emission reduction, improving the characteristics of spacecraft engines, and testing the flammability of related materials. The research achievements are expected to deepen understanding of droplet-phase, gas-phase, and solid combustion phenomena in reduced gravity with longer durations, larger scale. CSS will establish the international leading combustion research platform which can provide advanced diagnostic means, integrate models with experiment and design, and provide other knowledge to terrestrial applications.

4.5 Space Material Science

Space materials science is an integrated field with both science and applications. More discoveries, techniques, and methods of materials research can be obtained under microgravity conditions. The planning focuses on material science and the national strategic needs, will carry out serialized and interdisciplinary researches on the basic theoretical issues of material science and the development of new materials with major national needs. The plan is related to: firstly, revealing the special physical and chemical properties and processing rules of various materials under the conditions of space environment, solving key scientific issues in materials microstructure and defect control, enriching and develop basic theories of materials science, and guiding the research and application of ground materials science; major breakthroughs are expected in the basic principles of material science, materials preparation and processing methods, and development of new materials; secondly, researching and preparing new materials is expected to achieve important results in special structural materials, functional materials, energy materials and biological materials; thirdly, recognizing the special laws and behaviors of materials in the outer space environment, and providing scientific basis for the design and development of advanced materials and components for aerospace engineering and space technology are expected; fourthly, developing new types of space materials science on-orbit experimental facilities, and making important breakthroughs in

terms of guarantee conditions, experimental technology and research capabilities.

4.6 Fundamental Physics

An important advantage of using space conditions to research fundamental physics is that high- precision physical measurements can be performed, many of the essential problems of modern physics are likely to be solved only through space research. The planning of fundamental physics in microgravity is going to make use of the Cold Atom Experimental Rack (CAER) for carrying out a series of ultra-cold atomic physics experiments under extreme conditions to achieve breakthroughs in the theories of modern physics[8]. Utilizing the High-precise Time-Frequency Rack (HTFR) to improve the stability and accuracy for precise fundamental physics research, will promote practical applications, such as leading the quantum sensor technology, and promoting the advanced technologies and science for high precision measurement in space. As for the complex plasma physics research, a world-leading microgravity complex plasma experiment platform will be developed into a series of basic science and applications such as the interaction between dust particles and the spacecraft.

4.7 Space Astronomy and Astrophysics

With the prosperity of international big-science project, the observation of space astronomy entered a new age of multi-messenger with all-weather, all-round, high-resolution, high-sensitivity, and wide-field detection. Space Astronomy and Astrophysics is highly valued in CSS, the 2 m-caliber China Space Station Telescope (CSST, or called Multifunctional Optical Facility)[9], the High Energy Cosmic-Radiation Detection (HERD)[10], POLAR-2[11] and other astronomical observation equipment will be launched after 2022, those will acquire a series of major breakthroughs in international frontier hotspots such as dark matter and dark energy, the origin of cosmic rays, the formations and early evolutions of the universe, the large-scale structure of the universe, galaxies and supermassive black holes, and exoplanet search, *etc.*, it is demonstrated the ultraviolet telescope will open up a new research field and fill in the blank of the observation of the ultraviolet diffuse source. These studies will make outstanding contributions to the development of astronomy, physics, and a series of key technologies such as high-sensitivity particle detection, ultra-low temperature refrigeration, and high-precision polarization detection. These technologies will strengthen engineering development, including optics, high-performance electronic devices, and advanced electromechanical and thermal technologies.

4.8 Earth Science

Using the CSS platform to conduct Earth science project could cross-penetrate with other disciplines and supplement science satellites, with a long term, a more refined, in-depth and more quantitative perspective to detect and understand the Earth, and can provide possibilities for many basic scientific problems on Earth science and acquire many application achievements that were difficult to solve on the ground. The planning of Earth science focuses on developing a new generation of high-precision and quantitative remote sensing technology, to acquire multidimensional information of the Earth system, research global climate change and natural disasters, monitor environmental pollution, and explore resources.

4.9 Space Physics and Environment

The orbit of the CSS is located in the middle chain of the Sun-Earth system, which is involved with different physical properties, various physical phenomena in unique high-vacuum, high-radiation, and high-conductivity environments. It is an important channel for material and energy transfer, such as the mechanism and path of the matter outflow, the energy deposition[12]. The science planning focuses on a comprehensive exploration of near-earth space environment, remote sensing of solar physics, and remote sensing of planetary space environment. Making full use of the advantages of long-term stability in orbit, multiple detectors with long-term observation data, explore the role of the plasmasphere in the coupling process of the ionosphere and the magnetosphere, the influence of the plasmasphere on the near-Earth space environment, to establish a dynamic three-dimensional model of the plasmasphere. To understand the origin

and burst mechanism of the solar activity such as the transmission mechanism of matter and energy in the solar atmosphere, scientific problems such as coronal heating, triggering and acceleration of solar wind, the origin of solar activity will be analyzed in order to improve the forecasting model accuracy of near-earth space weather.

5 Upgrade Planning of Experiment Support Systems

5.1 Onboard Experiment Support Systems

The onboard science experimental systems are mainly composed of experimental racks in-station and exposed experiment facilities extra-station. At present, the experimental racks include experiment rack Life and Ecology Research Rack (LER), Biotechnology Research Rack (BTR), High Microgravity Level Research Rack (HMLR), Fluid Physics Research Rack (FPR), Cold Atom Physics Research Rack (CAPR), High Precision Time-Frequency System (HPTFS), High-Temperature Materials Research Rack (HTMR), Containerless Materials Processing Rack (CMPR), Two-Phase System Research Rack (TPSR), Combustion Sciences Research Rack (CSR), Glovebox and Cold Storage Rack (GCSR), On-orbit Maintenance and Manipulation Workbench (MMW), Varying Gravity Research Rack (VGR)[13]. The exposed experiment facilities include Biology Research Exposed Facility (BREF), Material Research Exposed Facility (MREF), and Components Test Exposed Facility (CTEF). All the experiment capabilities can provide effective support for most of the projects planned in the early operation period.

To ensure the continuous and efficient development of on-orbit science projects, it is necessary to carry out maintenance and capacity improvement of onboard experimental support systems including scientific experimental racks, CSST, payload adapters, exposed experiment facilities, information systems, application fluid circuits. The scientific experiment racks need to be periodically replaced with components, upgraded in the diagnostic methods and scientific experiment modules, replaced by new SDU and SPU, *etc.* The fluid circuit needs to be upgraded and improved in heat dissipation capacity. The level of microgravity environment needs to be improved by developing the active vibration isolation devices and microgravity measurement network. The on-orbit storage and transportation equipment needs to be developed to meet the storage requirements such as active biological samples and special test samples. The CSST needs to reserve key components, cooperate with astronauts and space station systems to conduct maintenance training, prepare maintenance manuals, and update back-end scientific modules.

5.2 Ground Experiment Support Systems

The ground experimental support system mainly consists of the mission development support system, Payloads Operation Management Center, and ground research infrastructures. During the operational period, Firstly, it is needed to ensure the routine operation and maintenance of the facility building in CSS ground development period. Secondly, it is needed to build a full-lifecycle collaborative design system, demonstration support system, project certification test system, *etc.*, for the large-scale and complex characteristics of a science project during the operation period. The upgrading of the ground experiment support system will strengthen the operational support for planning, demonstration, development, and management of space science project, and will improve the capability of integrated test for experimental payloads, and will improve the support capability and intelligence level of the payload operation management system.

The ground experiment base of space laboratory aims to build the world's leading ground experimental base, including experimental research, sample analysis, simulated microgravity experiments, and data processing. In the meantime, the ground mirror platforms of the experiment system are being developed and built, which could solve the problem of the shortage of ground station scientific research facilities and provide support for the continuous research work before launching.

6 International Cooperation, Education and Achievements Transfer

International cooperation in a variety of ways can be carried out during the CSS operation, including scientific experiment, project cooperation, astronaut training, and visits, *etc.* In 2018, China Manned Space Agency and the United Nations Office for Outer Space Affairs jointly issued a cooperation opportunity announcement to the United Nations members, inviting member states to participate in space science and utilizations in the China Space Station. 42 project proposals from 27 countries were received. Through two stages of primary and final selections, 9 projects from 17 countries and 23 entities were successfully selected, which include space astronomy, space life science and biotechnology, space application technology, microgravity fluid physics, combustion science, and Earth science[14]. China will actively use the capabilities of CSS platform to organize international big science project and contribute to the development of space science and technology all over the world.

Manned spaceflight, as a participatory space exploration activity, has a unique advantage as an educational resource and platform. In terms of the science outreach program, an integrated STEM (Science, Technology, Engineering, and Mathematics) education system with unique characteristics of manned spaceflight will be built to carry out various science education activities such as scientific experiment projects, popular science competitions, hardware development, and educational demonstrations. It is expected to strengthen public support for the space industry and stimulate young people's interest in manned spaceflight.

It is an important work to transfer new technologies produced in the CSS operation period into new products, new processes, new materials, and to promote new jobs and industries. Establishing a comprehensive platform for the release of scientific and technological achievements will build an effective bridge between CSS knowledge, technologies, and the market. These scientific and technological achievements could be transferred into biopharmaceuticals, medical health, material manufacturing, advanced energy, disaster relief support, land resource exploration. Improvement in the comprehensive benefits of CSS will drive industrial reform and promote socio-economic development.

References

[1] China Manned Space Agency. China's Manned Space Station Program actively preparing, all research and manufacturing work steadily advancing [EB/OL]. [2020-03-11]. http://www.cmse.gov.cn/art/2019/3/4/art_18_32969.html

[2] China Manned Space Agency. Announcement of opportunity for scientific experiments and technical experiments of china space station [EB/OL]. [2020-03-11]. http://www.cmse.gov.cn/art/2019/4/23/art_810_33072.html

[3] GU Y D, GAO M, ZHAO G. Space research plan of China's Space Station [J]. *Chin. J. Space Sci.*, 2016, **36**(5):595-599

[4] GU Y D. Challenge and Opportunity for promoting space science in China [J]. *Bull. Chin. Acad. Sci.*, 2014, **29**(5):575

[5] WANG L, LI Z, TAN C, *et al.* Physiological effects of weightlessness: countermeasure system development for a long-term Chinese manned spaceflight [J]. *Front. Med.*, 2019, **13**(2):202-212

[6] ZABEL P, BAMSEY M, SCHUBERT D, *et al.* Review and analysis of over 40 years of space plant growth systems [J]. *Life Sci. Space Res.*, 2016, **10**:1-16

[7] JIA Y M, ZHONG H E, ZHANG B C. Requirements analysis for experiment facilities of microgravity fluid science on Chinese Space Station [J]. *Chin. J. Space Sci.*, 2016, **36**(4):584

[8] ELLIOTT E R, KRUTZIK M C, WILLIAMS J R, *et al.* NASA's Cold Atom Lab (CAL): system development and ground test status [J]. *NPJ Microgravity*, 2018, **4**(1):1-7

[9] ZHAN H. An Overview of the Chinese Space Station Optical Survey [C]//42nd COSPAR Scientific Assembly. California: COSPAR, 2018, 42

[10] HUANG X, LAMPERSTORFER A S, TSAI Y L S, *et al.* Perspective of monochromatic gamma-ray line detection with the High Energy cosmic-Radiation Detection (HERD) facility onboard China's space station [J]. *Astropart. Phys.*, 2015, **78**(78):35-42

[11] KOLE M. POLAR-2: The First Large Scale Gamma-ray Polarimeter [C]// 36th International Cosmic Ray Conference (ICRC2019). Madison: International Union of Pure and Appplied Physics, 2019, 36

[12] WEI Y, YUE X A, RONG Z J, *et al.* A planetary perspective on Earth's space environment evolution [J]. *Earth Planet. Phys.*, 2017, **1**(1):63-67

[13] China Manned Space Agency. Scientific Experiment Resource Manual of China's Space Station [R], 2019

[14] China Manned Space Agency. List of Selected Space Science Experiment Projects for the 1st Cycle Concerning UN/China Cooperation on the Utilization of China Space Station [EB/OL]. [2020-03-11]. http://www.cmse.gov.cn/art/2019/6/12/art_22_33158.html

XU Lin, PEI Zhaoyu, ZOU Yongliao, WANG Chi. China's Lunar and Deep Space Exploration Program for the Next Decade (2020–2030). *Chin. J. Space Sci.*, 2020, **40**(5): 007-009. DOI:10.11728/cjss2020.05.007

China's Lunar and Deep Space Exploration Program for the Next Decade (2020–2030)*

XU Lin[1] PEI Zhaoyu[2] ZOU Yongliao[1] WANG Chi[1]

1 (*State Key Laboratory of Space Weather, National Space Science Center, Chinese Academy of Sciences, Beijing* 100190)

2 (*Lunar Exploration and Space Engineer Center, China National Space Administration, Beijing* 100190)

Abstract China has carried out four unmanned missions to the Moon since it launched Chang'E-1, the first lunar orbiter in 2007. With the implementation of the Chang'E-5 mission this year, the three phases of the lunar exploration program, namely orbiting, landing and returning, have been completed. In the plan of follow-up unmanned lunar exploration missions, it is planned to establish an experimental lunar research station at the lunar south pole by 2030 through the implementation of several missions, laying a foundation for the establishment of practical lunar research station in the future. China successfully launched its first Mars probe on 23 July 2020, followed in future by an asteroid mission, second Mars mission, and a mission to explore Jupiter and its moons.

Key words Lunar exploration, Deep space exploration, Lunar research station, Lunar south pole

Classified index V 475

1 Lunar Exploration Mission

According to the plan of China's lunar exploration program, the three phases of orbiting, landing, returning (*i.e.*, lunar exploration phase 1, 2 and 3) will be completed by 2020. At present, the Chang'E-1 to Chang'E-4 missions have been successfully carried out, which means the exploration program for the two stages of "orbiting and landing" has been completed. The Chang'E-5 mission, to be launched at the end of 2020, will collect lunar rock and soil samples and return them to Earth, which means the third phase of returning will also be completed.

With the successful implementation and gradual promotion of China's Lunar Exploration Program (CLEP), China officially launched the demonstration of a new unmanned lunar exploration program, now known as lunar exploration phase 4 since 2017, namely the demonstration of the lunar exploration program from 2021–2030. The plan is to initially build the basic outline of a research station in the South Pole of the Moon around 2030 and carry out scientific exploration and technology experiments, so as to lay the foundation for the future construction of a longer-term lunar research station on the Moon.

The overall scientific goals are: (i) to detect and study the distribution, content, and source of water and volatile components; (ii) to acquire the characteristics of the chemical composition of the deep part of the Moon; (iii) to study the age of the South Pole Aitken basin and the early impact history of the solar system; (iv) to explore the near surface environment of the lunar south pole; (v) to carry out lunar resource in-situ utilization tests; (vi) to carry out bio-scientific experiment and study on the lunar surface; (vii) to carry out observation and research on macro-geological phenomena in the base of the Moon; and (viii) to carry out the Earth-Moon VLBI

* Supported by National Key R & D Program of China (2020YFE0202100) and Beijing Municipal Science and Technology Commission (Z181100002918003)
Received August 28, 2020
E-mail: xulin@nssc.ac.cn

test and observation.

The fourth phase of CLEP consists of several missions, respectively.

The first mission, also named as Chang'E-7, which consists of a telecommunication relay, an orbiter, a lander, a rover and a flying detector, will be launched around 2024. Its main scientific goals are: (i) to investigate the topography and geomorphology, mineral element composition, and the distribution of water (or water ice) in the permanently shadowed area of the Moon, studying the distribution of the Moon's mineral resources; (ii) to perform geological investigation in the landing and patrol area, studying the geological structure and evolution history of the area, especially the composition and structure of the deep lunar interior; (iii) to probe the water ice in-situ on the Moon's permanent shadowed area, learning its source; (iv) to study the magnetic field characteristics of the lunar south pole; (v) to make observations of the Earth's magnetosphere, studying its physical laws and mechanisms; (vi) to construct an Earth-Moon VLBI experimental system and study astrophysics, astrometry and its applications.

The second mission which consists of a mobile lander, an ascender and a returner, will be launched around 2025. Its most important task is to collect soil and rock samples on the Moon's South Pole and return them to Earth, and a series of analyses and studies, including rocks, minerals, elements and isotopes, will be carried out to provide new evidence to the Moon's major scientific questions. It will also explore the topography and geomorphology, the structure of the lunar soil, and the mineral composition of the landing site.

The third mission, which consists of a lander, a rover and a flying detector, is planned to be launched before 2030. It will carry out scientific exploration of the Moon and conduct technical verification of relevant experiments on the lunar surface, laying the foundation for the future practical lunar research station. The main scientific objectives are: (i) to perform in-situ resource utilization experiment, including separation and extraction of rare gases from lunar soil, and verify the key technical problems involved; (ii) to carry out terrestrial mini-ecosystem experiments on lunar surface, revealing the rule of material circulation and energy moving on the terrestrial ecosystem-based bioregenerative life support system; (iii) to perform Moon-based observation on the Earth, so as to provide insight into the mechanism of Earth climate system energy imbalance and the global climate change; (iv) to investigate the topography and geomorphology, mineral composition, and substructure of the landing site; (v) to study the properties of space physics related effects and the coupling mechanisms at the Lunar South Pole.

2 Deep Space Exploration Mission Planning beyond the Moon

China has so far planned four missions in deep space exploration, namely an asteroid mission, second Mars mission, a Jupiter mission (Jupiter and its moons), and interplanetary exploration in addition to the first mission to Mars in July 2020.

China has planned a mission to asteroid. A near-Earth asteroid named 2016HO3 will be detected and returned with samples, and a main belt comet named 133P will be orbited. The main scientific goals are: (i) to determine the relevant physical parameters, physical characteristics of the target small body, further understanding the origin and evolution of the early solar system; (ii) to detect the topography, composition, structure, and water and organic matter of the target body; (iii) to collect samples from the target asteroid and return them to Earth for detailed research.

The most important scientific goal of China's second Mars exploration mission is aimed at collecting the soil and rock samples of the Mars and return them to Earth for detailed research, which will help us further our exploration into the origin and evolution history of Mars. It will also carry out scientific investigations on the landing site.

A mission to Jupiter is also planned. It will detect Jupiter and its moons (Callisto or Ganymede), as well as conduct interplanetary exploration beyond

Jupiter. The main scientific goals are: (i) to detect changes in the composition and structure of Jupiter's atmosphere; (ii) to explore the space environment, surface features, and internal structure of its moon; (iii) to study the interaction between the solar wind and the planetary magnetosphere and compare the responses of different types of planetary magnetosphere to the solar wind.

3 International Cooperation

China has always attached great importance to international cooperation in its lunar exploration. During Chang'E-1 to Chang'E-4 missions, China conducted in-depth and pragmatic cooperations with Russia, ESA, the Netherlands, Germany, Sweden, Saudi Arabia and other countries (agencies), and achieved fruitful results in science and technology.

Especially in Chang'E-4 mission, the lander is equipped with Germany-China Lander Neutrons and Dosimetry (LND), Sweden-China Advanced Small Analyzer for Neutrals (ASAN), and the Chang'E-4 probe's relay satellite is equipped with Netherland-China Low-frequency Explorer (NCLE) and the cubsat which piggybacks the relay satellite is equipped with Saudi Arabia's camera, together to complete the human first mission to the moon's farside. On 18 April 2019, China released a global announcement of opportunity for scientific payloads on the orbiter and lander for the asteroid mission. In addition, Chang'E-7 also has weight reserved for international payload, and the announcement of opportunity will be made. International payloads have become an important part of international cooperation in China's lunar and deep space exploration mission.

Since the launch of the lunar exploration program, China has always adhered to the principle of openness. International cooperation has always been a priority in both project implementation and scientific research, reflecting China's openness in space science exploration. China, providing global carrying platforms and scientific payloads carrying opportunities, as well as the scientific data open to the world, is welcoming more and more countries to participate, especially in strengthening international cooperation and exchanges in sciences in the field of lunar and deep space exploration.

At present, more and more countries or agencies have put forward the lunar exploration plans to build scientific research facilities on the lunar surface, focusing on the Moon's South Pole. China has also put forward plans to build an international lunar research station. It is the first landmark platform built and operated by a number of countries at the Moon's South Pole, initiated by China. It will follow the principle of extensive consultation, joint contribution, and shared benefits. The platform will support not only unmanned lunar exploration but also manned lunar missions, as well as a combination of unmanned and manned modes, paving the way for deep space exploration. Based on the fourth phase of the lunar exploration program, the plan will focus on global strengths and carry out comprehensive cooperation in science, technology, and project tasks. International cooperation will also take many forms and have different contents, including joint scientific research, payload carrying, formation of joint research teams, joint laboratories, joint data centers, and so on.

Through extensive international cooperation, China will work with countries interested in participating, including those along the One Belt One Road route to carry out joint planning, exploration and use of the Moon. China will contribute its efforts to the lunar exploration in accordance with the cooperation mode of openness and mutual benefit.

Acknowledgements We thank the scientists and technical experts in related fields in China.

WANG Chi, SUN Lilin, FAN Quanlin, LI Chao, BAI Qingjiang. Progress and Prospects of the Strategic Priority Program on Space Science. *Chin. J. Space Sci.*, 2020, **40**(5): 010-017. DOI:10.11728/cjss2020.05.010

Progress and Prospects of the Strategic Priority Program on Space Science*

WANG Chi SUN Lilin FAN Quanlin LI Chao BAI Qingjiang

(*National Space Science Center, Chinese Academy of Sciences, Beijing* 100190)

Abstract In May 2018, the second phase of the Strategic Priority Program on Space Science (SPP II) was officially approved by the Chinese Academy of Sciences, in view of the significant scientific achievements of the first phase of the Strategic Priority Program on Space Science (SPP I) which includes 4 space science missions: the Dark Matter Particle Explorer (DAMPE), ShiJian-10 (SJ-10), Quantum Experiments at Space Scale (QUESS) and Hard X-ray Modulation Telescope (HXMT). Aiming to address fundamental scientific questions, SPP II focuses on two major themes: How the universe and life originate and evolve and What is the relationship between the solar system and human beings. In areas that Chinese scientists have advantages, new space science missions including Graviational wave high-energy Electromagnetic Counterpart All-sky Monitor (GECAM), the Advanced space-based Solar Observatory (ASO-S), the Einstein Probe (EP), and Solar wind Magnetosphere Ionosphere Link Explorer (SMILE) have been approved in the framework of SPP II. This paper presents the research highlights of the SPP I, introduces the recent progress of SPP II, and puts forward the prospects for future development.

Key words Space science, Strategic Priority Program, Space science missions

Classified index P 35

In January 2011, the first phase of the Strategic Priority Program on Space Science (hereafter referred to as SPP I) officially kicked off as the first batch of the Strategic Priority Program initiated by the Chinese Academy of Sciences (CAS), which marks the beginning of systematic funding support to space science in China. During the 12th Five-Year Plan period, under the framework of SPP I, four space science missions have been developed and launched, including the Dark Matter Particle Explorer (DAMPE, or Wukong), Shijian-10 (SJ-10), Quantum Experiments at Space Scale (QUESS, or Micius) and Hard X-ray Modulation Telescope (HXMT, or Insight), while an intensive study of the future space science missions and advanced research of space science missions and payloads have been conducted. The implementation of SPP I has enabled the following researches, *e.g.* the properties of black holes and the laws of physics under extreme conditions, the test on completeness of quantum mechanics, dark matter, the laws of the movement of matter and the laws of life activities in space environment, and by far, a number of high impact scientific findings have been achieved.

On 31 May 2018, CAS officially kicked off the second phase of the Strategic Priority Program on Space Science (SPP II). Revolving around two major science themes: how the universe and life originate and evolve and what is the relationship between the solar system and human beings, SPP II will implement a batch of new space science missions, including the Gravitational wave high-energy Electromagnetic Counterpart All-sky Monitor (GECAM), the Advanced space-based Solar Observatory (ASO-S), the Einstein Probe (EP), and Solar wind Magnetosphere Ionosphere Link Explorer (SMILE). Meanwhile, new

* Supported by the Strategic Priority Program on Space Science of the Chinese Academy of Sciences (XDA15000000)
Received May 23, 2020
E-mail: cw@nssc.ac.cn

intensive study of the future space science missions, advanced research of space science missions and payloads, and projects for general support are conducted. SPP II is expected to make original breakthroughs in the following areas, *e.g.* gravitational wave electromagnetic counterpart, the relationship between the solar magnetic field and solar flares/Coronal Mass Ejection (CME), the time-domain astronomy, the interaction between the solar wind with the magnetosphere, *etc.*, which will deepen our understanding of the laws of the universe and nature.

1 Major Achievements of SPP I

By the end of December 2019, the DAMPE mission has finished the all-sky mapping for 8 times and detected 7.3 billion high-energy particles. The observation data in the last three years have provided precise measurements of the cosmic ray proton spectrums from 40 GeV to 100 TeV (see Figure 1). The results were published in *Science Advances* in September 2019[1].

The Shijian-10 mission has made several new scientific and technological achievements with high impact. A total of 252 papers (including 181 SCI papers) have been published. In addition, Springer and China Science Press have jointly published two monographs on microgravity and life science in space based on Shijian-10 data respectively.

The QUESS mission has successfully realized its three scientific objectives: the satellite-ground and ground-satellite quantum entanglement distribution, satellite-ground quantum key distribution, and satellite-ground quantum teleportation over the scale of 1000 km. In collaboration with the California Institute of Technology in the US, the University of Queensland in Australia *etc.*, the QUESS team has also conducted experimental testing on a theoretical model that predicted the quantum decoherence induced by gravitational fields (see Figure 2). The result was published online as First Release in *Nature* on 19 September 2019[2].

The HXMT mission has made important scientific contributions regarding the X-ray observations in the first gravitational wave event caused by binary neutron star merging. The X-ray pulsar navigation experiment has been successfully carried out, with the positioning accuracy within 10 km (3 s), which further demonstrates the feasibility of spacecraft autonomous navigation using pulsars, and paves the way for its future practical application in deep space (see Figure 3). The findings were published in the *Astrophysical* (supplement) on 21 August 2019[3].

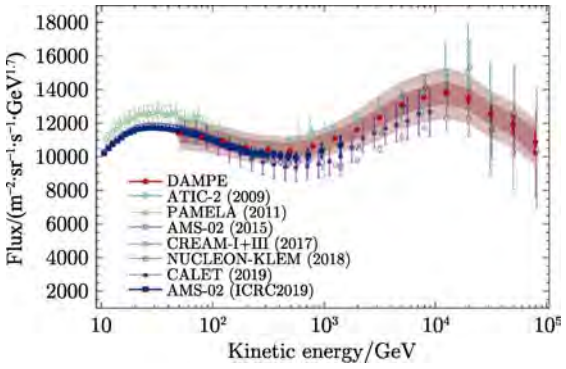

Fig. 1 Comparison of proton spectrum by DAMPE and those by other experiments

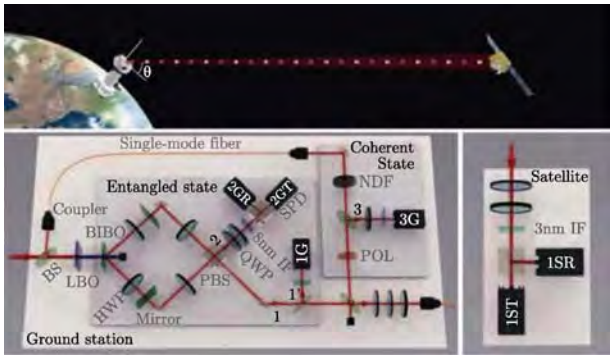

Fig. 2 Experimental test of gravitationally induced quantum decoherence

Fig. 3 HXMT pulsar navigation

2 Recent Progress of SPP II

2.1 Space Science Missions

2.1.1 Gravitational Wave High-energy Electromagnetic Counterpart All-sky Monitor (GECAM)

Making full use of the two-satellite constellation, GECAM (see Figure 4) has the comprehensive advan- tages of all-time and all-sky field of view, high sensitivity and high positioning capability, *etc.* The mission aims to detect as many gravitational wave gamma-ray bursts and new electromagnetic counterparts as possible to unveil the mystery of the violent merger of dense celestial bodies in the universe, and it is expected to obtain important original results. It will also detect high-energy radiation from fast radio bursts, special gamma-ray bursts, magnetar bursts, and high-energy radiation phenomena in space, such as solar flares and earth gamma-ray flashes, to further understand their burst mechanisms.

The GECAM mission was approved in December 2018 and entered into the Flight Model phase in November 2019. It is expected to be launched into space in November 2020. The launcher will carry the two satellites of GECAM mission whose total mass is not exceeding 360 kg, and it will operate in a Sun-synchronous orbit 600 km from the Earth with an inclination of 29°. The designed lifetime of the mission is 3 years.

2.1.2 Advanced Space-based Solar Observatory (ASO-S)

ASO-S (see Figure 5) aims to study the relationship between solar magnetic field, solar flare, and Coronal Mass Ejection (CME), observe the responses of different layers of solar atmosphere to solar eruption, and study the transmission mechanism and dynamic characteristics of solar eruption energy.

The ASO-S mission was approved in December 2017. It entered into the Engineering Model phase in June 2019. It is planned to be launched before the end of 2021. The total mass of the ASO-S spacecraft is about 1000 kg, and it operates in a Sun-synchronous orbit 720 km from the Earth with an inclination of 98.2°. The expected lifetime of the spacecraft is 4 years.

2.1.3 Einstein Probe (EP)

The EP mission (see Figure 6) is a scientific probe in the field of time-domain astronomy and high-energy astrophysics. It will carry out a wide field-of-view time-domain survey in the soft X-ray band (below 4.0 keV), aiming to systematically detect high-energy transients and variable cosmic X-ray sources, and explore their natures and physical processes.

The EP mission was approved in December 2017 and passed the mission Preliminary Design Review (PDR) in December 2019. It is scheduled to be launched before the end of 2022. The total mass of the EP spacecraft is about 1400 kg and it operates in a near-earth orbit of 500 km with an inclination of 29°. The expected lifetime of the mission is 3 years.

Fig. 4 Artist's view of GECAM

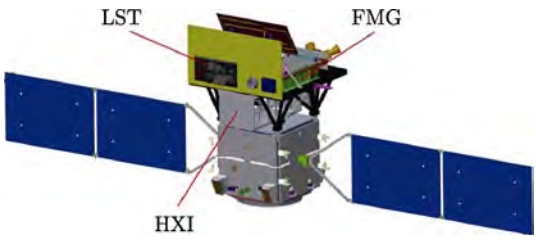

Fig. 5 Configuration diagram of ASO-S satellite

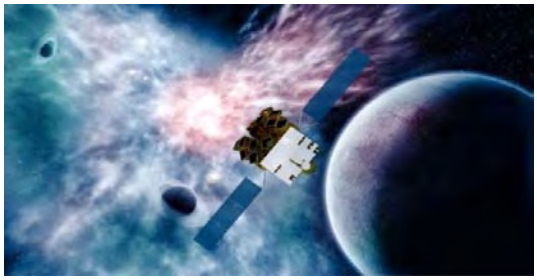

Fig. 6 Artist's view of EP satellite in orbit

2.1.4 Solar Wind Magnetosphere Ionosphere Link Explorer (SMILE)

The SMILE mission (see Figure 7) is a novel self-standing mission dedicated to observing the solar wind-magnetosphere coupling *via* simultaneous X-ray imaging of the magnetosheath and polar cusps, UV imaging of global auroral distributions and in situ solar wind/magnetosheath plasma and magnetic field measurements.

Jointly initiated by CAS and the European Space Agency (ESA), the mission is jointly proposed by the Chinese and European scientists, and has comprehensive and in-depth cooperation between China and ESA after the Geospace Double Star Exploration Program (DSP), making the mission a new model for international cooperation in space science[4, 5].

The SMILE mission was approved by CAS in November 2016 and by ESA in March 2019 respectively. In January 2020, it passed joint Mission Preliminary Design Review (M-PDR) and is scheduled to be launched from the Kourou launch site in 2023–2024. The total mass of SMILE spacecraft (including the propulsion module) is about 2000 kg, with the operation perigee >5000 km, the apogee around 20 R_e, and the inclination of 70°~98°. The spacecraft follows the large elliptical orbit and the lifetime of SMILE satellite is expected to be 3 years.

2.2 Intensive Study of the Future Space Science Missions

The intensive study of the future space science missions is dedicated to selecting from the submitted space science mission proposals, which have finished the mission concept study, a few missions with high impact, strong innovation and with Technology Readiness Level (TRL) enabling the launch in the next Five Years Plan period. For the missions selected for intensive study, the following work will be conducted accordingly, including an in-depth study of the mission's scientific objectives, optimization of detection methods, key technologies development, and test. For the time being, the following five missions have been selected for intensive study.

2.2.1 Enhanced X-ray Timing and Polarimetry Mission (eXTP)

Through the exploration of one singularity (black hole), two stars (neutron star and quark star), and three extremes (extreme conditions of gravity, magnetism, and density) in the waveband of 0.5~30 keV, the mission (see Figure 8), with unprecedented capabilities, aims to reveal the laws under extreme conditions. The mission entered into the definition phase in November 2019.

2.2.2 Taiji Program: Chinese Space-based Gravitational Wave Detection Missions

Aiming for the orbiting and merging system of intermediate-mass binary black holes whose total mass is within the range of a few hundred to a hundred thousand solar mass, the mission strives to detect the gravitational waves for the first time in space and to further understand the universe. The program adopts the space laser interferometry in the middle and low frequency band (0.1 mHz~1.0 Hz). A three-step development strategy has been established for the program: single satellite mission, double satellites mission, and triple satellites mission. As the first step

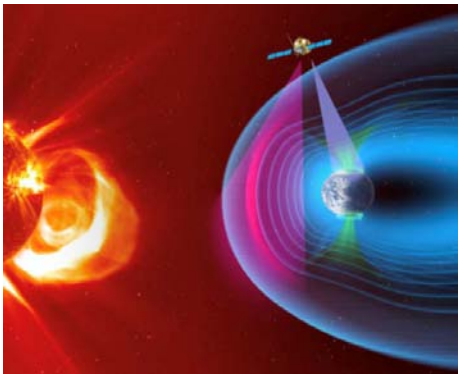

Fig. 7 Artist's view of SMILE in operation

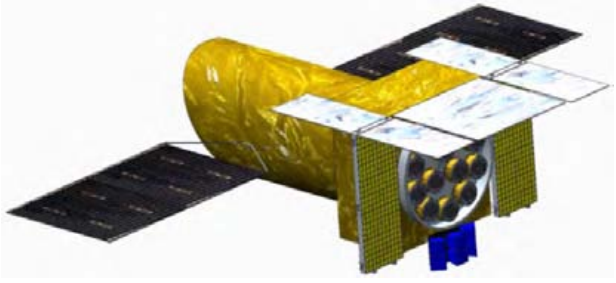

Fig. 8 eXTP space observatory

of the Taiji program, Taiji-1, also known as the Microgravity Technology Experimental Satellite, was successfully launched into orbit on 31 August 2019 (see Figure 9). By December 2019, Taiji-1 has successfully completed in-orbit tests, marking the first step of Chinese gravitational wave detection in space.

2.2.3 MEO-to-GEO Quantum Satellite

On the basis of the successful low earth orbit experiments by the QUESS mission, the key technology development for MEO-to-GEO quantum satellite (see Figure 10) is in full swing and the ground verification test of all-day quantum key distribution over a long distance is conducted to explore the application of space quantum communication technology in the global all-day quantum communication network. At present, the key technology development and the satellite prototype development are underway.

2.2.4 Ultra-long Wavelength Astronomical Observation Array

The interferometry array (see Figure 11) is composed of satellites formation flying around the moon to make observations of the sky at frequencies less than 30 MHz which are difficult to observe on Earth, opening a new window to electromagnetic spectrum to explore the dark ages and the cosmic dawn. At present, the intensive study of the mission scientific objectives and the payload prototypes development are underway.

Fig. 9 Taiji-1 successfully launched on 31 August 2019

Fig. 10 MEO-to-GEO quantum satellite

2.2.5 Small Bodies Sample Return Mission

The mission (see Figure 12) will explore the most primordial asteroids and comets, collect samples and return them to Earth for laboratory investigation. The mission aims at revealing the formation of the solar system, surveying the space resources, and providing science knowledge for defending the Earth against the impact of small objects. The candidate asteroid of the mission is the one which was formed closest to the Sun and is associated with the birth of the Earth. At present, the intensive study of the mission scientific objectives and the key technology development are underway.

2.3 Pre-study of Space Science Missions and Payloads

The pre-study of space science missions and payloads aims for the planning of future space science missions

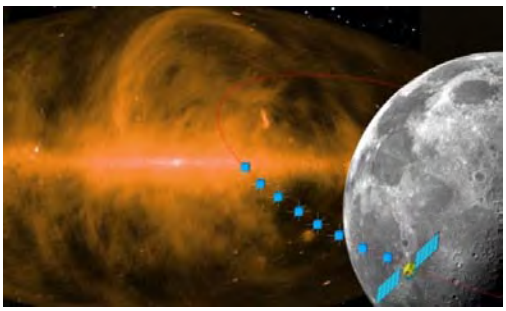

Fig. 11 Ultra-long wavelength astronomical observation array

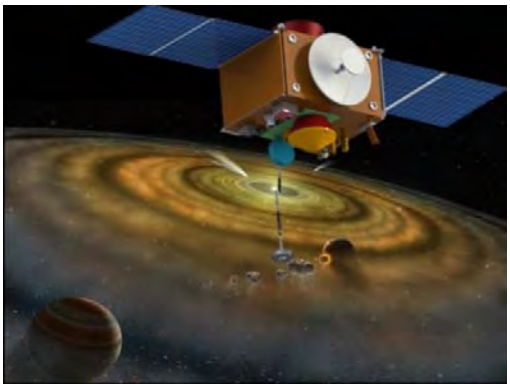

Fig. 12 Small bodies sample return mission

and the pre-study of the necessary key technologies by establishing a cluster of projects, covering the strategic study of space science development, mission concept research, cutting-edge technologies, key technology development, and ground test and demonstrations, which will lay a solid foundation for the sustainable development of space science.

2.3.1 Space Science Mission Concept Study

Focusing on the mission concepts with major innovative ideas, Space Science Mission Concept Study is dedicated to providing initial impetus and lay a solid foundation for the optimization of scientific objectives for future space science missions and future implementation. At present, 80 mission concepts have been selected to proceed with half-year study, and 11 mission concepts have entered the phase 0 of space science missions and payloads.

2.3.2 Pre-study of Space Science Missions and Payloads

The pre-study of Space Science Missions and Payloads is targeted for developing key technologies for future space science missions by planning a cluster of research subjects, including innovative concepts of space science missions, key technologies of payloads, ground calibrations as well as short-time flight demonstrations. Until now, two batches of research projects, 82 in total, have been selected.

2.3.3 Space Science Mission Planning and Data Analysis Study

Supports are given to approve missions to conduct mission in-orbit planning, calibration analysis, systematic simulation, algorithm optimization and team building, which will pave the way for the scientific data analysis after launch, and provide a guarantee for the realization of scientific objectives of space science missions and the achievement of major scientific breakthroughs. 9 projects have been approved by far.

3 International Cooperation in SPP II

In-depth and extensive international cooperation has been conducted in the missions under SPP II.

The SMILE mission is jointly initiated and implemented by CAS and ESA, and both sides are committed to the joint mission plan, the joint call for proposals, the joint selection, as well as joint mission design, implementation, and data analysis and application within the mission life cycle. Following the principle of no funding exchange, the SMILE mission is another example of the in-depth cooperation between China and ESA after DSP.

For the EP mission, China and ESA are jointly carrying out the payload development and calibration. Follow-up X-ray Telescope (FXT), as one of the two payloads on board, is jointly developed by CAS, ESA, and the Max Planck Institute for Extraterrestrial physics (MPE).

For ASO-S mission, CAS will jointly calibrate the Lyman-alpha Solar Telescope (LST) with the Turin Observatory in Italy.

The eXTP mission is an ultra-large X-ray observatory led by China with participation from a couple of European countries. International cooperation has been carried out in the following areas, *e.g.* study of scientific objective, payloads development and calibration *etc.*

4 Management of SPP II

National Space Science Center is entrusted for the management of SPP and is responsible for the implementation of the space science missions. Under the leadership of CAS, a complete chain has been established covering strategic planning, mission concept research, advanced research of space science missions and payloads, intensive study of the future space science missions, implementation of space science missions, launching and in-orbit operation, science output and evaluation. The "Principal Investigator + Mission Commander + Chief Engineer" mechanism has been set up for the mission management. The Mission Commander and the Chief Engineer are responsible for the implementation of space science missions, while the Principal Investigator is responsible for the realization of the mission scientific

objectives. SPP has attracted the major space science communities and related institutions in China to participate in the research and mission implementation. In the meantime, scientists from UK, Germany, France, Italy, Switzerland, Canada *etc.*, to some degree, have taken part in the mission implementation under SPP, as well as the intensive study of the future space science missions.

5 Prospects by 2035

A new chapter of Chinese space science endeavor has been opened with the implementation of SPP. China puts a high value on space science and will continuously push forward the space science endeavor.

Since the study of Space Science Mid- and Long-term Plan by 2035 led by Ministry of Science and Technology of the People's Republic of China from April 2019, the Chinese Space Science community has proposed a new National Science and Technology Major Program (see Figure 13), of which missions fall into 4 categories, with 3 science themes to be studied. It should be considered as a reasonable extension and enlargement of SPP.

The program addresses 3 science themes, *i.e.* the origin and evolution of the universe, the origin and evolution of the solar system, and the solar activity and its impact on humans. To be specific, for the theme concerning the origin and evolution of the universe, it focuses on space-based detection of the medium and low-frequency gravitational wave and the electromagnetic counterpart, the physical property and rule of black hole in extreme conditions, the superfine structure of compact objects, and the nature of dark matter and dark energy. For the theme concerning the origin and evolution of solar system, it focuses on the property, origin, and evolution of planets like the Moon and the Mars, asteroids and comets, the habitability of Planet Earth, the origin and evolution of life, and the search of terrestrial exoplanets. For the theme concerning the solar activity and its impact on human, it aims to unveil the fundamental rule of solar activity, understand the propagation and evolution of solar activities in interplanetary space, study the impact of solar activities on the geospace environment and human's

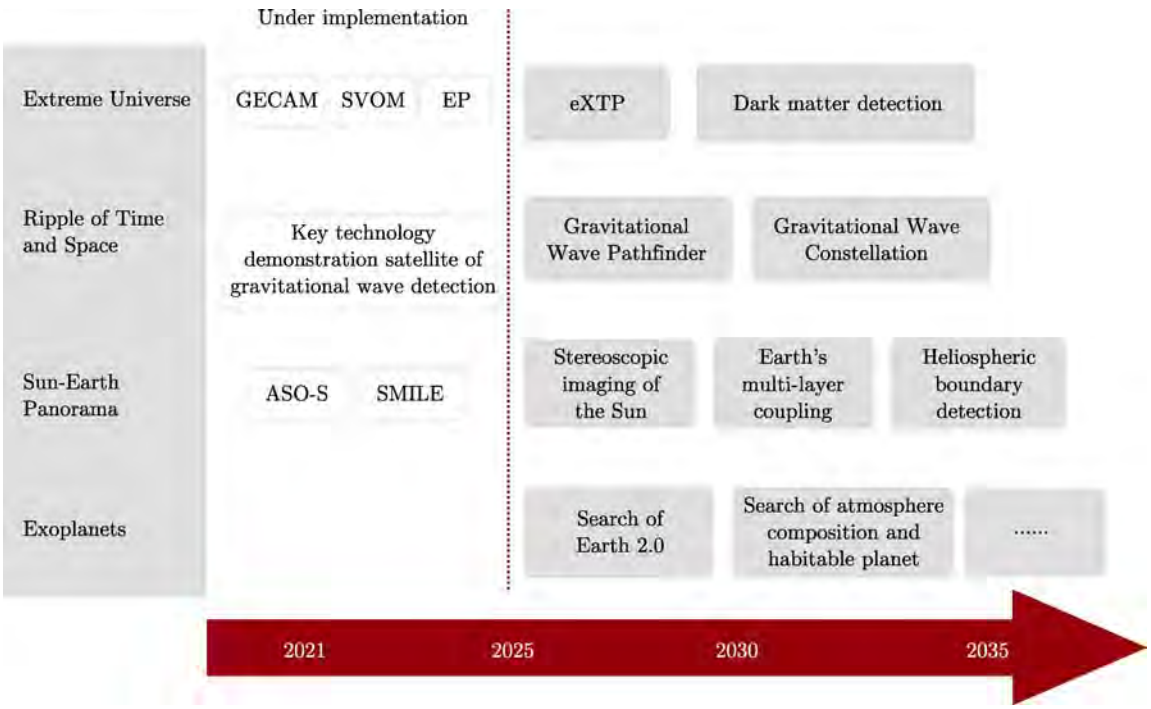

Fig. 13 Roadmap of Chinese space science

high-tech systems, unveil the kinetic properties of matter and the rule of life activity in the space environment, and study and predict the interaction evolution of Earth multi-layer system.

In the program, the missions fall into 4 categories, including Extreme Universe, Space-Time Ripples, Sun-Earth Panorama, and Habitable Planets. Open for international cooperation, the program plans 12 launches, for 7 flagship science missions, *e.g.* eXTP, Gravitational wave constellation, Heliospheric boundary exploration, and Search for Earth 2.0.

Among them, eXTP is expected to get ready for launch by 2025, to unveil the physical rule under extreme conditions, and answer the core science questions about black hole and neutron star; by 2030, missions including gravitational wave pathfinder, Stereoscopic imaging of the Sun, Earth's multi-layer coupling detection, and Search for Earth 2.0, will be implemented to achieve great breakthroughs in space-based gravitational wave detection, heliophysics, earth science, and terrestrial exoplanets search. By 2035, high-resolution gamma-ray dark matter mission, gravitational wave constellation, heliospheric boundary detection, search for atmospheric composition and the habitable planet will be implemented, to achieve promising results in dark matter detection, space-based gravitational wave detection, heliophysics, and terrestrial exoplanets search.

To support the mission implementation, a new National Key Research and Development Project is also proposed to carry out the development of the key technologies. Up to now, around 30 technologies have been included in the program, covering solar system exploration technologies like mission system design, launcher, propulsion, measurement and control; cutting-edge payload technologies and platforms; and common technologies like intelligent landing, in-situ analysis on the surface of planets and sample return.

The Chinese space science community is eager to see the above-mentioned projects to be adopted by the government, to realize the scientists' dream and push forward China's space science endeavor.

6 Conclusion Remarks

The implementation of SPP II has progressed smoothly after getting approved. At the same time, technology preparations and pre-study are underway to pave the way for future space science development in the next five years and the distant future.

In order to continuously produce high impact scientific achievements, SPP will keep abreast to the scientific frontiers, continue to strengthen the science-driven principal, stick to the high impact scientific objectives and strengthening of space science disciplines as the most important criteria for mission selection, adhere to the "Principle Investigator + Mission Commander + Chief Engineer" mechanism in the implementation of space science missions, and continue the open policy to support multi-level international cooperations.

Great undertakings begin with dreams, based on innovation, and succeed in solid work[6]. Chinese space scientists will forge ahead to deepen humans' understanding of the universe and the laws of nature, contributing more to the advance of human civilization.

References

[1] AN Q, ASFANDIYAROV R, AZZARELLO P, *et al.* Measurement of the cosmic ray proton spectrum from 40 GeV to 100 TeV with the DAMPE satellite [J]. *Sci. Adv.,* 2019, **5**(9):eaax3793

[2] XU Ping, MA Yiqiu, REN Jigang, *et al.* Satellite testing of a gravitationally induced quantum decoherence model [J]. *Science*, 2019, **366**(6461):132-135

[3] ZHENG S J, ZHANG S N, LU F J, *et al.* In-orbit demonstration of X-ray pulsar navigation with the Insight-HXMT satellite [J]. *Astrophys. J. Ser.*, 2019, **244**(Supp.):1

[4] ESA. ESA Gives Go-ahead for SMILE Mission with China [EB/OL] (2019-03-05) [2019-7-19]. https://phys.org/news/2019-03-esa-go-ahead-mission-china.html

[5] WANG Chi, BRANDUARDI-RAYMOND Graziella. Progress of Solar Wind Magnetosphere Ionosphere Link Explorer (SMILE) Mission [J]. *Chin. J. Space Sci.*, 2018, **38**(5):657-661

[6] Speech by President XI Jinping upon meeting representatives of space scientists and engineers who participated in the research and development of the Chang'E-4 mission [EB/OL]. [2019-12-01]. http://china.cnr.cn/news/20190221/t20190221_524517116.shtml?from=groupmessage&isappinstalled=0

Chang Jin. Progresses of the Dark Matter Particle Explorer. *Chin. J. Space Sci.*, 2020, 40(5): 018-024. DOI:10.11728/cjss2020.05.018

Progresses of the Dark Matter Particle Explorer *

CHANG Jin

1(*Key Laboratory of Dark Matter and Space Astronomy, Purple Mountain Observatory, Chinese Academy of Sciences, Nanjing* 210033)

2(*School of Astronomy and Space Science, University of Science and Technology of China, Hefei* 230026)

Abstract The Dark Matter Particle Explorer (DAMPE) is a space high-energy particle andg-ray detector whose major scientific goals are the indirect detection of dark matter particles, the origin of cosmic rays and high-energyg-ray astronomy. Since its successful launch in December, 2015, the DAMPE has been operated smoothly in orbit for more than 4 years, and has recorded over 8 billion cosmic ray events. Very precise measurements of the electron plus positron spectrum and the proton spectrum have been obtained, with interesting new spectral features revealed for the first time. The DAMPE's results are expected to significantly advance our understanding of the fundamental problems in astroparticle physics.

Key words Dark matter, Indirect detection, Cosmic rays

Classified index P 35

1 Introduction

It has been well established that our universe is made up of about 4.9% baryonic matter, 26.8% Dark Matter (DM), and 68.3% dark energy[1] (Figure 1). The physical nature of DM is one of the most important fundamental questions of modern physics. Many types of candidate DM models have been proposed, among which the leading one is a kind of Weakly Interacting Massive Particles (WIMPs) beyond the standard model of particle physics, as motivated by the relic abundance of DM and the bottom-up evolution pattern of the large scale structures of the universe[2,3]. Many efforts have been paid to search for the WIMP DM in laboratories, including the direct detection of the WIMP-nucleon scattering by underground detectors, the indirect detection of the annihilation or decay products in the cosmic radiation, and the collider detection of WIMP pairs produced in high-energy particle colliders[4]. After several decades of efforts, no convincing evidence has been found yet. Particularly, the direct detection experiments push the WIMP-nucleon scattering strength to a very low level[5], which has already severely constrained a series of WIMP models.

In recent years, some interesting anomalies have been found in cosmic ray (CR) and γ-ray observations, such as the positron excess discovered by

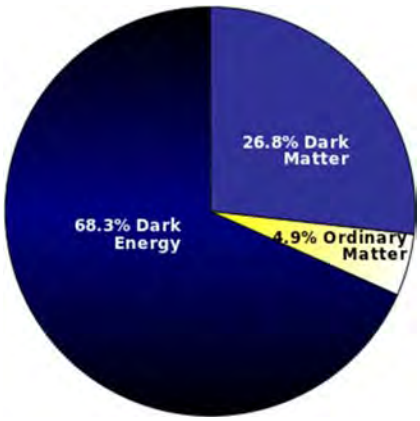

Fig. 1 Composition of the universe inferred from the PLANCK observations of the cosmic microwave background

* Supported by the National Key Research and Development Program of China (2016YFA0400200), and the National Natural Science Foundation of China (U1738205, U1738206)

Received May 26, 2020

E-mail: chang@pmo.ac.cn

PAMELA[6], Fermi-LAT[7], and AMS-02[8], and the associated total Cosmic Ray Electron plus positron (CRE) excess by ATIC[9], Fermi-LAT[10], and AMS-02[11]. The excesses of positrons and CREs can be explained by either the astrophysical sources such as pulsars and the DM annihilation or decay[12-17]. There are still debates on the astrophysical or DM origin of the positron and/or CRE excesses, in particular that the most recent HAWC observations of two nearby pulsars tend to disfavor the pulsar interpretation[18]. Higher precision measurements in a wider energy band are crucial to identifying their physical origin. Other anomalies include the γ-ray excess in the Galactic center[19], and potential excess of CR antiprotons[20,21].

The purpose of the Dark Matter Particle Explorer (DAMPE) is to search for possible annihilation/decay relics of DM in CREs, with unprecedentedly high energy resolution and low background[22,23]. DAMPE is also a general purpose high-energy particle detector for observations of γ-rays and CR nuclei, which can be particularly helpful in the study of high-energy astrophysical phenomena and CR physics[23]. The DAMPE mission was launched into a 500 km Sun synchronous orbit on 17 December 2015, with an inclination angle of 97°. It orbits the Earth every 95 minutes. All the detectors perform excellently in space. The daily event rate of DAMPE is about 5 million. It has recorded in total over 8 billion CR events as of May, 2020, most of which are CR nuclei. There are about 1% CREs and 3×10^{-5} γ-ray photons in the DAMPE data.

2 DAMPE Detector

DAMPE is made of 4 sub-detectors, which are, from top to bottom, the Plastic Scintillator strip Detector (PSD[24]), the Silicon-Tungsten tracKer-converter (STK[25]), the BGO imaging calorimeter[26], and the NeUtron Detector (NUD[27]). A schematic plot of the DAMPE detector is shown in Figure 2[23]. The total weight of the payload (satellite) is about 1.5 (1.9) tons, and the power consumption is 300 (500) W. The size of the satellite is about 1.2 m×1.2 m×1.0 m.

The PSD is to measure the (absolute) charge of incident particles up to Z=30 *via* the ionization effect ($\mathrm{d}E/\mathrm{d}x$). It also serves as an anticoincidence detector for γ-rays. The PSD consists of two layers of orthogonally placed plastic scintillator bars. For each layer, 41 plastic scintillator bars are further placed in two sub-layers with a shift of 0.8 cm between them to reduce the gaps. The effective area of the PSD is 82.5 cm×82.5 cm[23]. The weight of the PSD is about 103 kg, and the power is 8.5 W.

The main function of STK is to measure the trajectory of a particle. The charge of light nuclei

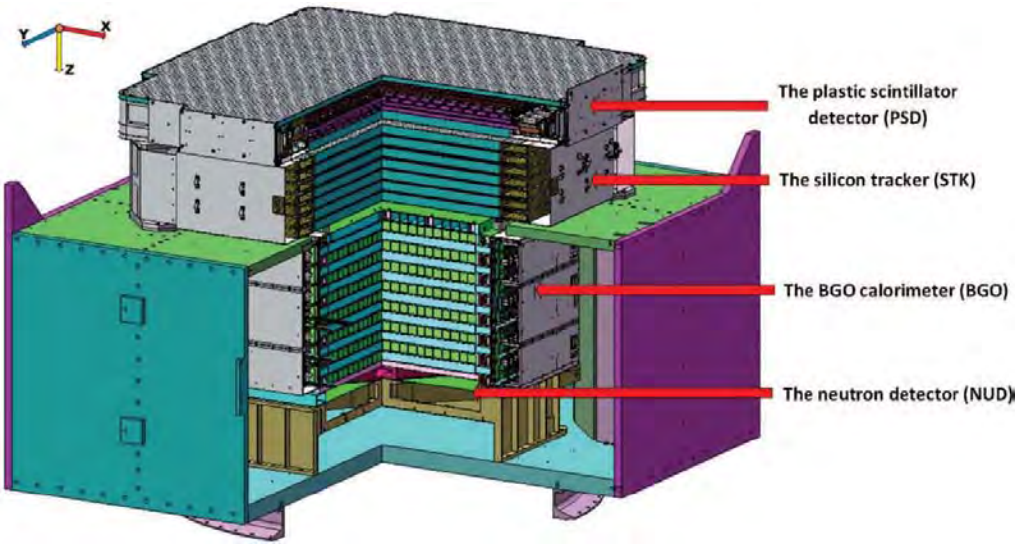

Fig. 2 Schematic plot of the DAMPE detectors

(Z<8) can also be measured by the STK. The STK consists of 12 layers (6 for x direction and 6 for y direction) of silicon trackers, each with two sub-layers arranged orthogonally to measure the x and y positions of a track. The STK is also a γ-ray converter by means of three 1 mm thick tungsten plates inserted in the second, third, and fourth planes. Each silicon layer is made of 16 ladders, each formed by 4 Silicon micro-Strip Detectors (SSD). Every ladder is segmented into 768 strips, half of which are readout strips and the other half are floating strips. In total there are 384×16×12=73728 readout channels of the STK. The effective detection area of STK is 76 cm× 76 cm. The STK has a weight of 154 kg and a power consumption of 82 W.

The BGO calorimeter is the major instrument of DAMPE. It has three functions: (i) measuring the energy deposition of incident particles, (ii) imaging the 3D profile of the shower development, and providing electron/hadron discrimination, and (iii) providing the level 0 trigger for the DAMPE data acquisition system. The BGO calorimeter is made of 308 BGO bars, each is read out at two ends by Photomultiplier Tubes (PMTs). The BGO crystals are placed orthogonally in 14 layers, with a total depth of about 32 radiation lengths and about 1.6 nuclear interaction lengths. The length of the BGO crystal is 60 cm, which is the longest in the world. The calorimeter has an effective area of 60 cm×60 cm, a total weight of 1052 kg, and a power consumption of 42 W.

The NUD is at the bottom of the detector. The main purpose of the NUD is to perform electron/hadron discrimination by means of the fact that neutrons are much more abundant in hadronic showers than in electromagnetic ones. Once the neutrons are created, they are quickly thermalized in the BGO calorimeter, and then get captured by Boron-doped plastic scintillators. The NUD is made of four 30 cm×30 cm× 1 cm plastic scintillators with 5% (weight) Boron element. The NUD has an effective area of 61 cm× 61 cm, a mass of 12 kg, and a power of 0.5 W.

Table 1 summarizes the expected detector performance of DAMPE, for observations of electrons, γ-rays, and protons[23]. With good measurements of the charge, direction, energy of various types of particles, DAMPE is expected to play a significant role in exploring the high-energy universe.

Table 1 Expected performance of DAMPE

Parameter	Value
Energy range (e/γ)	5 GeV to 10 TeV
Energy resolution (e/γ)	1.5% at 800 GeV
Energy range (p)	50 GeV to 500 TeV
Energy resolution (p)	40% at 800 GeV
Effective area (vertical γ)	1100 cm^2 at 100 GeV
Geometry factor (e)	0.3 m^2·sr above 30 GeV
Angular resolution (γ)	0.1° at 100 GeV
Field of view	1.0 sr

3 On-orbit Performance

Dedicated calibration of each unit of the detector has been done using the on-orbit data, which enables precise measurements of the physical quantities of each event[28]. Figure 3 gives the charge measurements by the PSD[29]. The absolute charge resolution is about 0.20e for Z=8 (Oxygen) and 0.30e for Z=26 (Iron). Such a good charge resolution is the basis of precise spectral measurements of each species. Using the bright γ-ray sources we can calibrate the angular resolution of the STK, which results in about 0.5° for energies higher than 5 GeV.

The very thick BGO calorimeter enables that

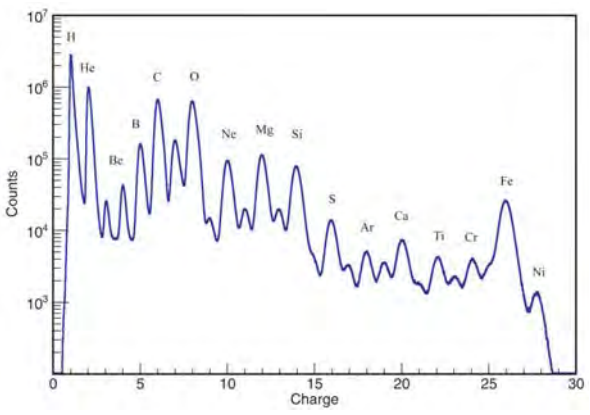

Fig. 3 Charge spectrum obtained using two years of on-orbit data

there is no significant leakage of electromagnetic showers from the bottom for energies as high as TeV. There are, however, a few percents of energy loss due to the dead materials of the calorimeter. An event level energy correction method was developed and verified by MC simulations and the beam test data[30]. The beam test data and the MC simulations show that the energy resolution for CREs is better than 1.2% for energies above 100 GeV. DAMPE also has P- and N-side readouts for each BGO crystal, which have different gains. These two-side readouts give a consistency check of the energy measurement. We find that the energies measured by both sides agree with each other very well. Figure 4 presents the ratios of energies measured by the two sides, together with a Gaussian fit that gives a mean of 1.005±0.005 and a width of 0.016±0.001[31]. Such a result further supports the quoted energy resolution of about 1%.

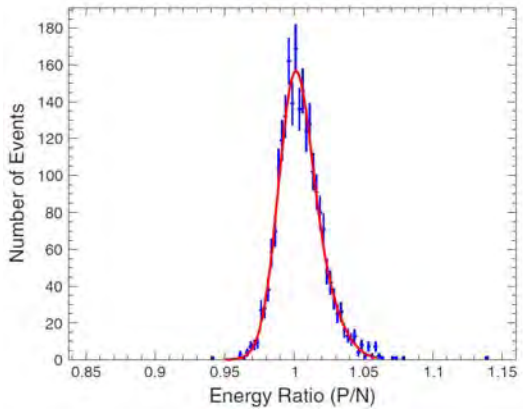

Fig. 4 Ratios of energies reconstructed with P- and N-side data

Particle identification is one of the most challenging things for the observations of CREs. The background of CREs is CR protons (heavier nuclei can be effectively rejected *via* the charge measurement in PSD). The fluxes of CREs are about three orders of magnitude lower than that of protons. Therefore, a high rejection power of protons is essential for reliable measurements of the CRE fluxes. DAMPE uses the morphology difference between CREs and protons in the calorimeter to distinguish them[32,33]. This is basically due to different developments of hadronic and electromagnetic showers in the calorimeter. A simple two-parameter method was adopted to describe the longitude and latitude developments of the showers. They are: (i) an energy-weighted root-mean-square (RMS) value of hit positions in the calorimeter (shower spread), and (ii) the deposited energy fraction of the last BGO layer ($F_{\rm last}$). The left panel of Figure 5 shows the distributions of these two parameters for the flight data with BGO energies between 500 GeV and 1 TeV[31]. We can see clearly two populations of events in this plot, with the upper population being proton candidates and the lower one being CRE candidates. To better quantify the separation between these two populations, we further define a shape parameter, $\zeta = F_{\rm last} \times (\text{shower spread/mm})^4/(8\times10^6)$, which projects these two parameters into one dimension. The distributions of the ζ parameter for the flight data and Monte Carlo (MC) simulations for CREs and protons are shown in the right panel of Figure 5. We select CREs with $\zeta \leqslant$

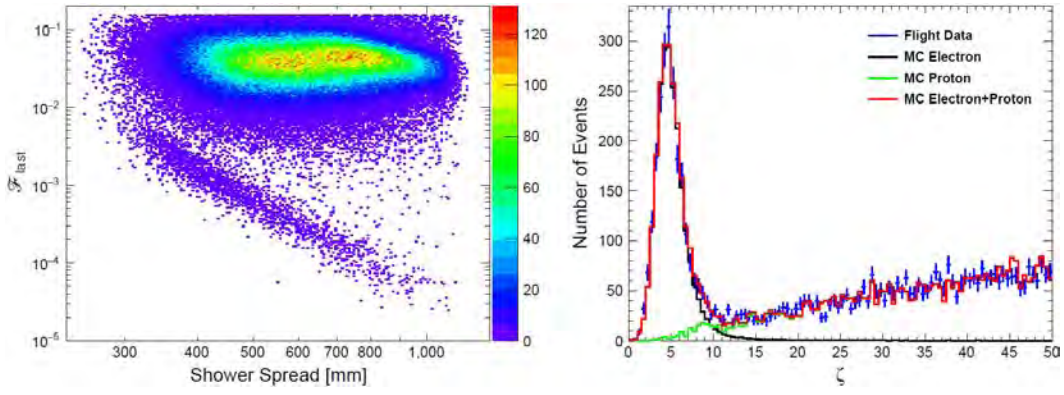

(a) (b)

Fig. 5 (a) Shower spread versus the last layer energy fraction for selected events with BGO energies between 500 GeV and 1 TeV. (b) One-dimensional distributions of the shape parameter ζ, compared with MC simulations

8.5, which gives only about 2% proton background in this energy range[31]. For energies below TeV, the proton background is lower than 3%. The highest background in the energy range from 25 GeV to 4.6 TeV is estimated to be about 18%[31].

The NUD provides additional help of the electron-proton discrimination, since the neutron yields for hadronic showers are much higher than that of the electromagnetic showers. Simulations show that using the NUD alone the proton background can be suppressed by a factor of about 25 when keeping a CRE efficiency of 95%, for 1~5 TeV deposited energies[34]. Together with the calorimeter, the total suppression power improves by a factor of about 2[34]. The NUD capability is expected to be more important at higher energies.

4 Scientific Results

The derived CRE spectrum from 25 GeV to 4.6 TeV, obtained by the first 530 days of DAMPE data is shown in Figure 6[31]. Compared with other measurements[11,35-37], the DAMPE data are more precise with smaller uncertainties and lower background for energies higher than about 500 GeV. For the first time, the CRE spectrum has been directly measured to about 5 TeV. The previous indirect measurements to such high energies by ground-based experiments suffer from quite large systematic uncertainties. A spectral break at about 0.9 TeV, with the spectral index changing from –3.1 to –3.9 is clearly revealed by the DAMPE data. The significance of this break is estimated to be about 6.6σ. This result confirms the previous weak evidence found by H.E.S.S.[36,37]. The spectral index below the break is consistent with that observed by Fermi-LAT[35], and above the break, it is consistent with the result by H.E.S.S.[36]. The CALET measurements are also consistent with the existence of such a break, but with relatively large uncertainties[38]. The DAMPE spectrum also shows a tentative narrow peak at about 1.4 TeV. This peak structure is not statistically significant enough, and more data are needed for confirmation.

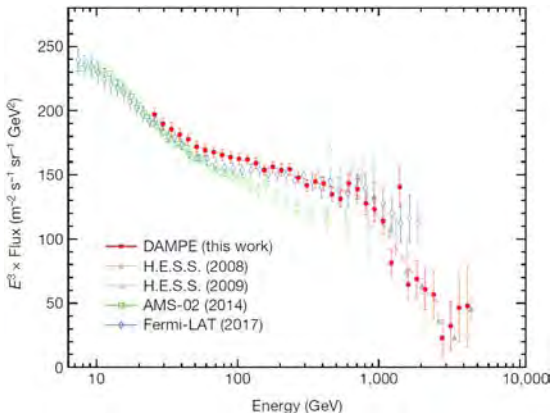

Fig. 6 CRE spectrum measured by DAMPE (red: Ref.[31]), compared with that by Fermi-LAT (blue: Ref. [35]), AMS-02 (green: Ref. [11]), and the indirect measurement by H.E.S.S. (gray: Ref. [36,37])

Figure 7 shows the proton spectrum measured by DAMPE using its 2.5 years of data[39], compared with that by other experiments[40-45]. The DAMPE result improves the precision significantly for energies above 1 TeV. The spectral hardening feature around several hundred GeV discovered previously by other experiments is confirmed. Furthermore, a softening structure around 14 TeV has been revealed with a high significance for the first time. Previous measurements by CREAM and NUCLEON gave some hints of the softening structure[43,44], which is inconclusive due to quite large statistical and/or systematic uncertainties. The spectral softening feature is possibly the imprint of a nearby CR accelerator[46].

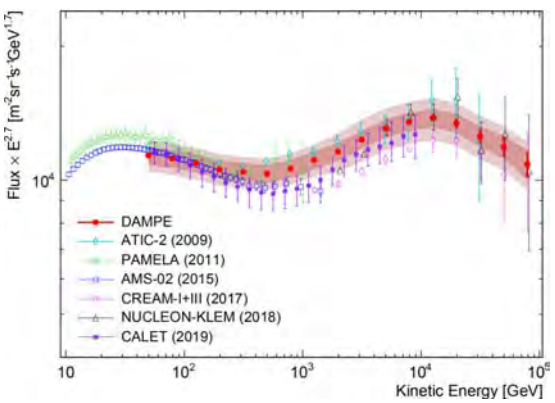

Fig. 7 CR proton spectrum measured by DAMPE (red: Ref.[39]), compared with that by ATIC [40], PAMELA [41], AMS-02 [42], CREAM [43], NUCLEON [44], and CALET [45]

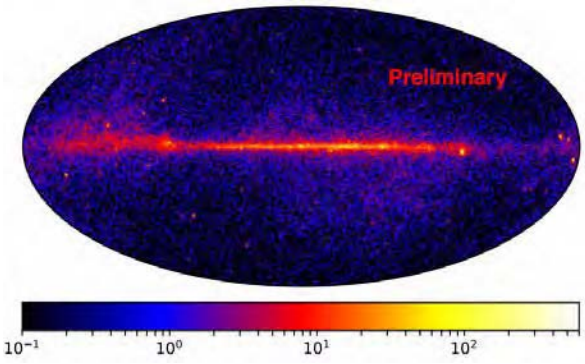

Fig. 8 Three-year skymap of γ-ray counts above 2 GeV

Figure 8 shows the all-sky γ-ray map above 2 GeV obtained using 3 years of the DAMPE data[47]. The luminous Galactic plane and some bright sources can be clearly seen. One unique capability of DAMPE is its excellent energy resolution, which makes it well suitable for the search for monochromatic γ-ray emission. The preliminary analysis gives a comparable sensitivity on the DM annihilation cross section into monochromatic photons compared with that of 5.8 years of Fermi-LAT data[48]. Variable emission from a population of active galactic nuclei has also been observed[47].

5 Summary

DAMPE has been operating smoothly in orbit for more than four years. Using the high-quality data recorded by DAMPE, precise measurements of the CRE and proton spectra have been obtained. Spectral breaks around 0.9 TeV for CREs and 14 TeV for protons are firmly detected by DAMPE, which provide important implications in understanding the origin of such particles in the Milky Way. The DAMPE results also give useful constraints on the DM models. DAMPE keeps on operating and collecting data. More data from DAMPE are expected to shed new light on our understandings about DM and the high-energy universe.

Acknowledgements The DAMPE mission was funded by the strategic priority Science and technology projects in space Science of the Chinese Academy of Sciences.

References

[1] ADE P, AGHANIM N, ARNAUD M, *et al.* (PLANCK collaboration), Planck 2015 results. XIII. Cosmological parameters [J]. *Astron. Astrophys.*, 2016, **594**:A13

[2] JUNGMAN G, KAMIONKOWSKI M, GRIEST K. Supersymmetric dark matter [J]. *Phys. Rept.*, 1996, **267**:195-373

[3] BERTONE G, HOOPER D, SILK J. Particle dark matter: evidence, candidates and constraints [J]. *Phys. Rept.*, 2005, **405**:279-390

[4] BI X J, YIN P F, YUAN Q. Status of dark matter detection [J]. *Front. Phys.*, 2013, **8**:794-827

[5] LI Z, LIU J. Experimental search for dark matter in China [J]. *Front. Phys.*, 2020, **15**:44301

[6] ADRINAN O,BARBARINO G, BAZILEVSKAYA G, *et al.* (PAMELA collaboration). An anomalous positron abundance in cosmic rays with energies 1.5~100 GeV [J]. *Nature*, 2009, **458**:607-609

[7] ACKERMANN M, AJELLO M, ALLAFORT A, *et al.* (Fermi-LAT collaboration). Measurement of separate cosmic ray electron and positron spectra with the Fermi Large Area Telescope [J]. *Phys. Rev. Lett.*, 2012, **108**:011103

[8] AGUILAR M, ALBERTI G, ALPAT B *et al.* (AMS collaboration). First result from the Alpha Magnetic Spectrometer on the International Space Station: precision measurement of the positron fraction in primary cosmic rays of 0.5~350 GeV [J]. *Phys. Rev. Lett.*, 2013, **110**:141102

[9] CHANG J, ADAMS J, AHN H S, *et al.* (ATIC collaboration). An excess of cosmic ray electrons at energies of 300~800 GeV [J]. *Nature*, 2008, **456**:362-365

[10] ABDO A A, ACKERMANN M, AJELLO M, *et al.* (Fermi-LAT collaboration). Measurement of the cosmic ray e++e- spectrum from 20 GeV to 1 TeV with the Fermi Large Area Telescope [J]. *Phys. Rev. Lett.*, 2009, **102**:181101

[11] AGUILAR M, ALBERTI G, ALPAT B, *et al.* (AMS collaboration). Precision measurements of the e++e- flux of the primary cosmic rays from 0.5 GeV to 1 TeV with the Alpha Magnetic Spectrometer on the International Space Station [J]. *Phys. Rev. Lett.*, 2014, **113**:221102

[12] SHEN C S. Pulsars and Very High-Energy Cosmic-Ray Electrons [J]. *Astrophys. J. Acad. Sci. Phys. Lett.*, 1970, **162**:L181

[13] HOOPER D, BLASI P, SERPICO P D. Pulsars as the sources of high energy cosmic ray positrons [J]. *J. Cosmol. Astropart. Phys.*, 2009, **1**:25

[14] YUKSEL H, KISTLER M D, STANEV T. TeV gamma rays from Geminga and the origin of the GeV positron excess [J]. *Phys. Rev. Lett.*, 2009, **103**:051101

[15] BERGSTROM L, BRINGMANN T, EDSJO J. New positron spectral features from supersymmetric dark matter - a way to explain the PAMELA data? [J]. *Phys. Rev. D*, 2008, **78**:103520

[16] CIRELLI M, KADASTIK M, RAIDAL M, *et al.* Model-independent implications of the e+/-, pbar cosmic ray spectra on properties of dark matter [J]. *Nucl. Phys. B*, 2009, **813**:1-21

[17] YIN P F, YUAN Q, LIU J, *et al.* PAMELA data and lep-

tonically decaying dark matter [J]. *Phys. Rev. D*, 2009, **79**:023512

[18] ABEYSEKARA A U, ALBERT A, ALFARO R, *et al.* (HAWC collaboration). Extended gamma-ray sources around pulsars constrain the origin of the positron flux at Earth [J]. *Science*, 2017, **358**:911-914

[19] HOOPER D, GOODENOUGH L. Dark matter annihilation in the Galactic center as seen by the Fermi gamma ray telescope [J]. *Phys. Lett. B*, 2011, **697**:412-428

[20] CUI M Y, YUAN Q, TSAI Y L S, *et al.* Possible dark matter annihilation signal in the AMS-02 antiproton data [J]. *Phys. Rev. Lett.*, 2017, **118**:191101

[21] CUOCO A, KRAMER M, KORSMEIER M. Novel dark matter constraints from antiprotons in light of AMS-02 [J]. *Phys. Rev. Lett.*, 2017, **118**:191102

[22] CHANG J. Dark Matter Particle Explorer: The First Chinese Cosmic Ray and Hard γ -ray Detector in Space [J]. *Chin. J. Space Sci.*, 2014, **34**:550-557

[23] CHANG J, AMBROSI G, AN Q, *et al.* (DAMPE collaboration). The dark matter particle explorer mission [J]. *Astropart. Phys.*, 2017, **95**:6-24

[24] YU Y, SUN Z, SU H, *et al.* The plastic scintillator detector for DAMPE [J]. *Astropart. Phys.*, 2017, **94**:1-10

[25] AZZZARELLO P, AMBROSI G, ASFANDIYAROV R, *et al.* The DAMPE silicon-tungsten tracker [J]. *Nucl. Instrum. Method. Phys. Res. A*, 2016, **831**:378-384

[26] ZHANG Z, ZHANG Y, DONG J, *et al.* Design of a high dynamic range photomultiplier base board for the BGO ECAL of DAMPE [J]. *Nucl. Instrum. Method. Phys. Res. A*, 2015, **780**:21-26

[27] HE M, MA T, CHANG J, *et al.* GEANT4 simulation of neutron detector for DAMPE [J]. *Acta Astron. Sin.*, 2016, **57**:1-8

[28] AMBROSI G, AN Q, ASFANDIYAROV R, *et al.* (DAMPE collaboration). The on-orbit calibration of dark matter particle explorer [J]. *Astropart. Phys.*, 2019, **106**:18-34

[29] DONG T K, ZHANG Y, MA P, *et al.* Charge measurement of cosmic ray nuclei with the plastic scintillator detector of DAMPE [J]. *Astropart. Phys.*, 2019, **105**:31-36

[30] YUE C, ZANG J, DONG T, *et al.* A parameterized energy correction method for electromagnetic showers in BGO-ECAL of DAMPE [J]. *Nucl. Instrum. Method. Phys. Res. A*, 2017, **856**:11-16

[31] AMBROSI G, AN Q, ASFANDIYAROV R, *et al.* (DAMPE collaboration). Direct detection of a break in the teraelectronvolt cosmic-ray spectrum of electrons and positrons [J]. *Nature*, 2017, **552**:63-66

[32] CHANG J. On the detection and identification of cosmic gamma-rays in a cosmic ray detector [J]. *Int. Cosmic Ray Conf.*, 1999, 5:37

[33] CHANG J, ADAMS J, AHN H, *et al.* Resolving electrons from protons in ATIC [J]. Advances in Space Research, 2008, **42**:431-436

[34] HUANG Y Y, MA T, YUE C, *et al.* Calibration and performance of the neutron detector onboard of the DAMPE mission [J]. arXiv:2005.07828

[35] ABDOLLAHI S, ACKERMANN M, AJELLO M, *et al.* Cosmic-ray electron-positron spectrum from 7 GeV to 2 TeV with the Fermi Large Area Telescope [J]. *Phys. Rev. D*, 2017, **95**:082007

[36] AHARONIAN F, AKHPERJANIAN A, BARRES DE ALMEIDA U, *et al.* Energy spectrum of cosmic ray electrons at TeV energies [J]. *Phys. Rev. Lett.*, 2008, **101**:261104

[37] AHARONIAN F, AKHPERJANIAN A, ANTON G, *et al.* Probing the ATIC peak in the cosmic-ray electron spectrum with H.E.S.S. [J]. *Astron. Astrophys.*, 2009, 508:561-564

[38] ADRIANI O, AKAIKE Y, ASANO K, *et al.* Extended measurement of the cosmic ray electron and positron spectrum from 11 GeV to 4.8 TeV with the Calorimetric Electron Telescope on the International Space Station [J]. *Phys. Rev. Lett.*, 2018, **120**:261102

[39] AN Q, ASFANDIYAROV R, AZZARELLO P, *et al.* (DAMPE collaboration). Measurement of the cosmic ray proton spectrum from 40 GeV to 100 TeV with the DAMPE satellite [J]. *Science Adv.*, 2019, **5,** eaax3793

[40] PANOV A D, ADAMS J, AHN H, *et al.* Energy spectra of abundant nuclei of primary cosmic rays from the data of ATIC-2 experiment: Final results [J]. *Bull. Russ. Acad. Sci. Phys.*, 2009, **73**:564-567

[41] ADRIANI O, BARBARINO G C, BAZILEVSKAYA G A, *et al.* PAMELA measurements of cosmic ray proton and helium spectra [J]. *Science*, 2011, **332**:69

[42] AGUILAR M, AISA D, ALPAT B, *et al.* Precision measurement of the proton flux in primary cosmic rays from rigidity 1 GV to 1.8 TV with the Alpha Magnetic Spectrometer on the International Space Station [J]. *Phys. Rev. Lett.*, 2015, **114**:171103

[43] YOON Y S, ANDERSON T, BARRAU A, *et al.* Proton and helium spectra from the CREAM-III flight [J]. *Astrophys. J. Acad. Sci. Phys.*, 2017, **839**:5

[44] ATKIN E, BULATOV V, DOROKHOV V, *et al.* New universal cosmic ray knee near a magnetic rigidity of 10 TV with the NUCLEON space observatory [J]. *JETP Lett.*, 2018, **108**:5-12

[45] ADRIANI O, AKAIKE Y, ASANO K, *et al.* Direct measurement of the cosmic ray proton spectrum from 50 GeV to 10 TeV with the Calorimetric Electron Telescope on the International Space Station [J]. *Phys. Rev. Lett.*, 2019, **122**:181102

[46] YUE C, MA P, YUAN Q, *et al.* Implications on the origin of cosmic rays in light of 10 TV spectral softenings [J]. *Front. Phys.*, 2020, **15**:24601

[47] LI X, DUAN K K, JIANG W, *et al.* Recent gamma-ray results from DAMPE [J]. *Proc. ICRC*, 2019, **36**:576

[48] ACKERMANN M, AJELLO M, ALBERT A, *et al.* Updated search for spectral lines from Galactic dark matter interactions with pass 8 data from the Fermi Large Area Telescope [J]. *Phys. Rev. D*, 2015, **91**:122002

CHEN Yuesong, HAN Juanjuan, FAN Yu, ZOU Yongliao, WANG Chi. Overview of the Latest Scientific Results of China's Lunar Exploration Program. *Chin. J. Space Sci.*, 2020, **40**(5): 25-41. DOI:10.11728/cjss2020.05.25

Overview of the Latest Scientific Results of China's Lunar Exploration Program

CHEN Yuesong[1] HAN Juanjuan[1] FAN Yu[1]

ZOU Yongliao[1,2] WANG Chi[1,2]

1(*National Space Science Center, Chinese Academy of Sciences, Beijing* 100190)

2(*State Key Laboratory of Space Weather, National Space Science Center, Chinese Academy of Sciences, Beijing* 100190)

Abstract China's Chang'E-4 probe successfully landed on 3 January 2019 in Von Kármán crater within the South Pole-Aitken (SPA) basin on the lunar far side. Based on the data acquired by the scientific payloads onboard the lander and the rover, the researchers obtained the related information such as the geologic and tectonic setting of the landing area, compositional characteristics of the landing surface materials, dielectric permittivity and density of the lunar soil. The experiments confirmed the existence of materials dominated by olivine and low-calcium pyroxene in the SPA basin on the lunar far side, which preliminary revealed the geological evolution history of the SPA basin and even that of the early time lunar crust, as well as the tectonic setting and formation mechanism of the materials in the lunar interior. The researchers also investigated the particle radiation, Linear Energy Transaction (LET) spectrum, and so forth on the lunar surface. The low-frequency radio observations were carried out on the lunar far side for the first time as well. This article summarizes the latest scientific results in the past years, focusing on the Chang'E-4 mission.

Key words CLEP, Chang'E-4, Scientific objectives, Scientific payloads, Scientific results

Classified index V 475

1 Overview of China's Lunar Exploration Program

China's Lunar Exploration Program (CLEP) has been divided into three main operational phases: lunar orbiting, soft-landing, and sample return. Lunar orbiting means remote sensing exploration around the Moon, which was successfully implemented by Chang'E-1 mission in October 2007 (http://www.gov.cn/jrzg/2007-10/24/content_785388.htm). The global and comprehensive observations were carried out including the topographic and geomorphologic characteristics of the lunar, material compositions of the lunar surface, the characteristics of the lunar soil and the Earth-Moon space environment.

After the successful implementation of Chang'E-1 mission, as the backup spacecraft of Chang'E-1 and the precursor mission of the soft-landing phase of CLEP, Chang'E-2 underwent an adaptive transformation, with the mandate to collect remote sensing data with higher precision and to image the candidate landing site of Chang'E-3. Chang'E-2 launched successfully in October 2010 and acquired the global lunar map with a resolution of 7 m. It flew by and explored the asteroid 4179 Toutatis in December 2012 (http://www.gov.cn/jrzg/2012-12/15/content_2290992.htm).

The second phase of CLEP refers to soft-landing and roving exploration on the lunar surface. As one of the missions scheduled in this phase, Chang'E-3

* Supported by National Key R&D Program of China (2020YFE0202100) and Beijing Municipal Science and Technology Commission (Z181100002918003)

Received September 11, 2020

E-mail: chenyuesong@nssc.ac.cn. Correspondence auther: zouyongliao@nssc.ac.cn

was successfully launched in December 2013 (http://www.gov.cn/jrzg/2013-12/14/content_2547901.htm). As of now, it has carried out the activities to explore topography, geomorphology, tectonic geomorphology and sub-surface geotectonic of the Moon and to conduct research on the Earth's plasmasphere and astronomy by use of the Moon-based observation.

Chang'E-4 spacecraft was initially built as the backup of Chang'E-3. After the successful implementation of Chang'E-3, according to the worldwide development route of lunar exploration and China's overall thinking on future scientific researches on the Moon, the expert group made a very careful evaluation of Chang'E-4 mission based on the techniques of Chang'E-3 and finally selected the SPA Basin of the lunar far side as the landing and roving area, which gave Chang'E-4 a new scientific value.

After the relay communication satellite and Chang'E-4 probe were launched respectively in May 2018 and December 2018, Chang'E-4 probe made a successful landing on 3 January 2019 in the Von Kármán crater within the SPA basin on the Moon far side (177.6° east longitude and 45.5° south latitude), realizing the first soft-landing on the Moon's far side and the first relay communication between the lunar far side and the Earth in the human history (http://www.gov.cn/xinwen/2019-01/03/content_5354498.htm).

On 3 January 2020 (Beijing Time), Chang'E-4 completed work on its 13th lunar day and the rover traveled a total of 357.695 m. More than 210 GB of scientific data at all levels has been released publicly (http://www.clep.org.cn/n5982341/c6808601/content.html). A large number of scientific results has been published by China's Lunar Exploration Program[1]. The paper mainly focuses on the latest major scientific results achieved by Chang'E-4 mission.

2 Scientific Objectives and Payloads of Chang'E-4

2.1 Scientific Objectives of Chang'E-4

The Chang'E-4 mission consists of three platforms: lander, rover and relay satellite. Four scientific goals were chosen in the Moon science, the lunar space environment and low-frequency radio astronomy: (i) low-frequency radio astronomical study on the lunar surface; (ii) shallow structure investigation of the roving area on the lunar far side; (iii) the topographic and the mineralogical composition investigation of the roving area on the lunar far side; (iv) neutron radiation dose and neutral atom study on the lunar environment.

The chosen landing site for Chang'E-4 is the South Pole-Aitken Basin, which has been revealed to be a basin 2500 km in diameter with an average depth of more than 13 km, and recognized as the largest, oldest and deepest impact crater yet discovered in the solar system. It faithfully records the primary differentiation of the Moon, is a hot spot of lunar science[2-4].

The SPA basin is thought to be formed from an impact that penetrated through the Moon's distinctive plagioclase rich crust, exposing the lunar lower crust and probably upper mantle material[5-7]. It also contains some of the relatively few far side maria. Therefore, exploration of this region may address some fundamental questions, such as the nature of the lunar mantle, the cause of the greater crustal thickness on the far side, and how far side maria differ from their nearside counterparts. Furthermore, better constraints of the age of this basin may inform our understanding of the early impact flux on the Moon, and therefore also on the Earth[6].

The SPA basin has been studied with spectral observations and recently been subdivided into four distinct compositional zones based on Moon Mineralogy Mapper (M3) data: (i) a central about 700-km-wide SPA Compositional Anomaly (SPACA), which exhibits a strong Ca-pyroxene signature, which is different from typical mare basalts; (ii) an Mg-Pyroxene Annulus, which is characterized by Mg-rich pyroxenes; (iii) a Heterogeneous Annulus, which exhibits mixing of localized pyroxene-rich units and feldspathic materials; and (iv) the SPA Exterior, which is mafic-free and dominated by feldspathic materials[7]. The Chang'E-4 landing site is located at the eastern edge of the mare-containing Von Kármán crater, within the ejecta field of the nearby Finsen crater[6]. The Von Kármán crater

(diameter $D = 186$ km; central coordinates as 44.4°S, 176.2°E) lies within the Mg-Pyroxene Annulus, just northwest of the SPACA terrain. Finsen crater (diameter $D = 73$ km; central coordinates as 42.3°S, 182.3°E)[7]. This location was selected to optimize the likelihood of being able to investigate the crustal stratigraphy and regolith development, and to access material from farside maria, the deep crust, and possibly the mantle[6].

Chang'E-4 lander and Yutu-2 rover carried a landing camera, a terrain camera, two panoramic cameras, an infrared imaging spectrometer, and a lunar penetrating radar[2, 6]. These instruments enable an analysis of the topography, regolith, shallow structure, and rock and mineral compositions of the landing and roving sites[6]. In situ exploration within the Von Kármán landing region brings unprecedented imaging, spectral, radar, and low-frequency radio spectral data for the landing region, and it greatly improves our understanding about the compositions of farside mare basalt, SPA compositional zones including SPA compositional anomaly and Mg-pyroxene annulus, regolith evolution, and the lunar space environment[7].

Low-frequency radio astronomy in the frequency band below about 10 MHz cannot be done on the ground or be well done from space due to the Earth's ionosphere cut-off, man-made Radio Frequency Interference (RFI), and the Auroral Kilometric Radiation (AKR) noise[2]. The lunar farside is shielded from radio interference from the Earth, blocks the RFI, the AKR noise from the Earth, as well as from solar emissions during the lunar night, so it is expected to be an excellent location for low-frequency radio astronomy[2, 6]. The experiment uses the Low-frequency Radio Spectrometer on the lander, and the Netherlands-China Low-frequency Explorer on the relay satellite, to do joint low frequency radio astronomical observation. Its specific exploration goals include, to obtain the map of radio sky at 2 frequencies in the band of 1~80 MHz, to investigate the AKR in the band of 0.1~1 MHz, to observe the Jovian radio emission in the band of 1~40 MHz, to observe and study the disastrous space weather events and the Type II and III solar burst in the band above 0.1 MHz[2].

Based on the lunar surface platform, the researchers conducted the measurement of the comprehensive particle radiation and LET spectrum so as to carry out a study on the lunar space environment, as well as to reveal the physical process and characteristics of the interaction between the solar wind and lunar soil, and to understand the high-energy particle radiation environment on the Moon surface and its relation to solar activity by measuring fast neutron energy spectra and thermal neutrons flux on the Moon surface.

2.2 Chang'E-4 Payloads and Their Tasks

Totally there are 9 payloads mounted on the Chang'E-4 probe, as shown in Table 1.

3 Latest Scientific Results of Chang'E-4

3.1 Topographic and Geological Characteristics of the Chang'E-4 Landing Area

Liu *et al.*[8]. reconstructed the powered descent trajectory of Chang'E-4 using photogrammetrically processed images of the Chang'E-4 landing camera, navigation camera, and terrain data acquired by Chang'E-2. The study confirmed that the precise location of the Chang'E-4 landing site is 177.5991°E, 45.4446°S with an elevation of -5935 m. The landing site was accurately identified with lunar imagery and terrain data with spatial resolutions of 7 m, 5 m, 1 m, 10 cm and 5 cm per pixel. As shown in Figure 1.

Fu *et al.*[9] proposed that both of the lander and the rover locate on the basalt impact sputtering in the Von Kármán crater by the analysis results of multi-source high-resolution remote sensing and hyperspectral image data. Li *et al.*[3] proposed that the geologic setting of the landing site is a region of impact craters superposed on the floor of the SPA basin (the 225-km-diameter Von Kármán crater and the 245-km-diameter Leibnitz crater). Chang'E-4 landing site is about 138 km away from the center of Finsen crater.

Di *et al.*[5] proposed that the terrain of the landing area is high in the northeast and low in the southwest, and there are undulating waves from the

Table 1 Chang'E-4 payloads and their tasks

Scientific objectives	Tasks	Scientific payloads		
		Lander	Rover	Relay
Low-frequency radio astronomical study on the lunar surface	Characterize low-frequency radio emissions from the Sun, the Solar system and the Milky Way galaxy	Low-frequency Radio Spectrometer		Netherlands-China Low-frequency Explorer
Exploring morphology and mineral constituents of patrol area in Moon's far side	Acquire optical images related to topography and geomorphology of the landing and roving sites; Acquire infrared images of the landing site	Landing Camera Terrain Camera	Panoramic Camera Infrared Imaging Spectrometer	
Probing shallow structures of patrol area on Moon's far side	Acquire data related to Lunar soil and sub-surface structure of the lunar crust		Lunar Penetrating Radar	
Study on lunar space environments such as neutrons radiation dose and neutral atoms	Measure neutrons and dose rate on the lunar surface, including the energy spectrum, the flux of these particles, and Linear Energy Transfer (LET); Measure energetic neutral atoms and positive ions on the lunar surface, including the energy, mass and flux of these particles	Lunar Lander Neutrons and Dosimetry	Advanced Small Analyzer for Neutrals	

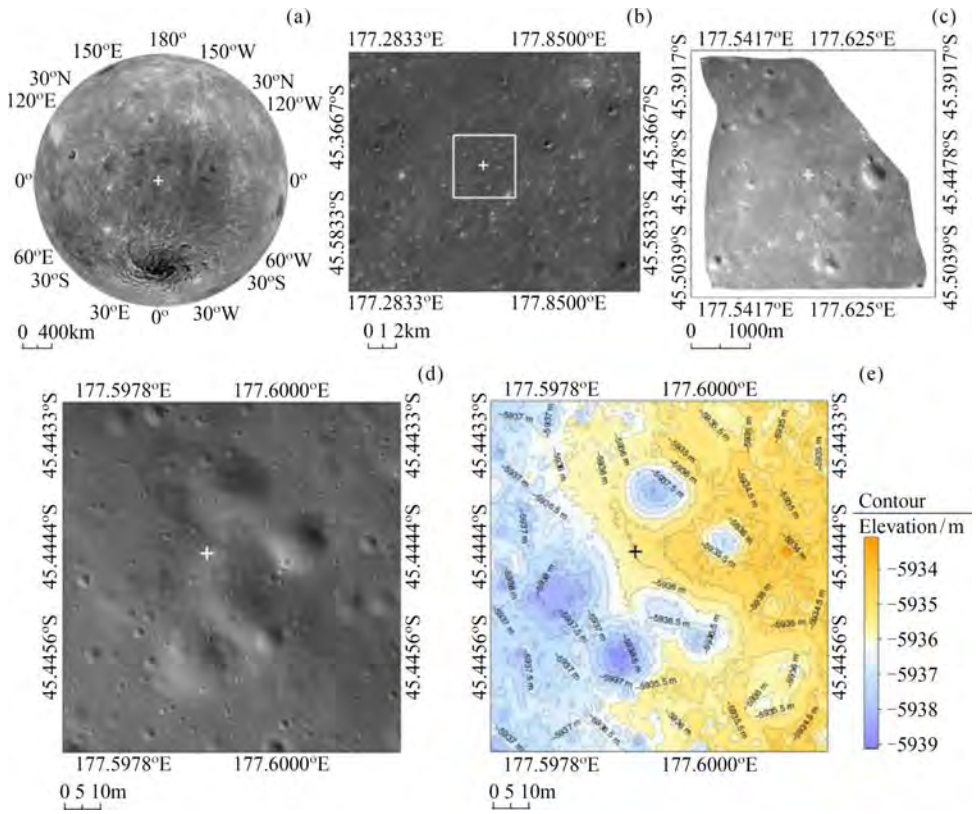

Fig. 1 Location of the Chang'E-4 landing site. The "+" is the identified landing location. (a) (b) Chang'E-2 DOMs, using the Chang'E-4 landing site as the projection center of the azimuth projection. (c) LCAM DOM with a resolution of 5 m per pixel. (d) LCAM DOM generated by the LCAM images with resolutions from 21.4 cm to 0.2 cm per pixel and is uniformly resampled at 5 cm per pixel during mapping. (e) shaded-relief map with a contour line produced by the LCAM DEM, which area and resolution are the same as that in (d)

southeast to northwest. Qiao *et al.*[10] proposed that the overall terrain around the landing site presents relatively flat, of which the slope of more than 90% of the area is less than 5° (30 m baseline), and few rocks on the Moon surface are exposed. The main geomorphological characteristics of the landing area are represented as a large number of circular craters with a diameter of less than 1 km and secondary craters with cluster-shape or chain-shape, as well generally there are no rocks are exposed near these craters. Other nearby craters are likely to deliver SPA-basin-subfloor material to the landing site. The youngest of these is the 72-km-diameter crater Finsen, which is located to the northeast of the landing site crater. The results are shown in Figure 2[3]. The Finsen crater is considered to be formed when small bodies impact the surface within the SPA basin. The deep-seated materials below the surface of the SPA basin are excavated, whose ejecta scattered on the plain of the Von Kármán crater[9].

Di *et al.*[5] proposed that the ejecta covered over the landing area are 60~70 m thick, at least comprised of two sets of ejecta with approximately perpendicular directions. They further interpreted the superimposition of NE-SW ejecta from Finsen crater on the underlying SE-NW dome-like surface relief from Alder crater. Numerical simulations predict about 30 and 35 m ejecta deposited at the landing site from Finsen and Alder craters, respectively. Numerical simulations show that the thicknesses of the sputters from Finsen and Alder pits at the landing points are about 30 m and 35 m (Figure 3), respectively.

The study of Fu *et al.* indicated that the boundary between Finsen ejecta and underlying mare basalt at the Chang'E-4 landing site is constrained to a depth of 18 m, shown as in Figure 4. Furthermore, Based on the derived permittivity, Lai *et al.*[16] gave an estimate for the thickness of fine-grained lunar regolith at the Chang'E-4 location of 11.1±0.4 m.

3.2 Constitution of Deep-seated Materials of the Moon

The Visible and Near-Infrared Imaging Spectrometer (VNIS) on board the Chang'E-4 rover enabled the first in situ reflectance measurements of the far side of the Moon. The route of the rover experienced 14 lunar days as of January 2020, as shown in Figure 5.

The geological characteristics of the Chang'E-4 landing site indicated that the surface materials

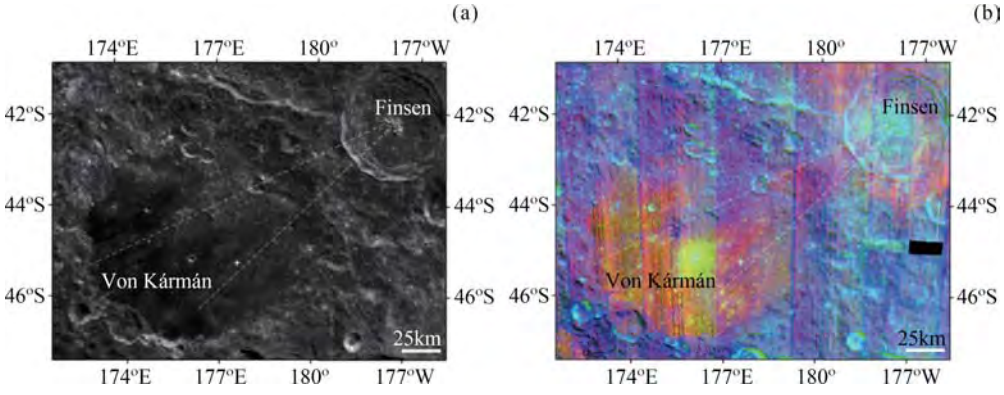

Fig. 2 Distribution of Finsen ejecta in the Von Kármán crater. (a) Chang'E-1 Digital Orthophoto Map; spatial resolution, 120 m. (b) M3 color composite. R, 2-μm-band center; G, 2-μm-band depth; B, reflectance at 1580 nm. White dashed lines represent two major northeast–southwest ejecta rays of the Finsen crater converging towards its central peak. The white cross is the Chang'E-4 landing site, which is located on the ejecta material of the Finsen crater. The 2-μm-band center can be used to distinguish between LCP and HCP. As the content of Fe and Ca in the pyroxene increases, the 2-μm-band center shifts towards longer wavelengths (redder). The 2-μm-band depth indicates the relative amounts of mafic minerals. The 1580 nm reflectance represents the brightness of the lunar soils (which can be affected by plagioclase content). LCP-bearing materials appear light blue, and HCP-bearing materials appear green

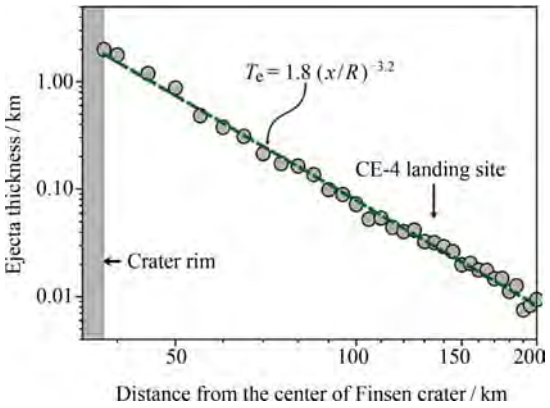

Fig. 3 Ejecta thickness simulation for Finsen crater. The thickness of ejecta at the Chang'E-4 landing site from Finsen crater is about 32 m. A similar simulation was also carried out for ejecta from Alder crater with a result of about 35 m

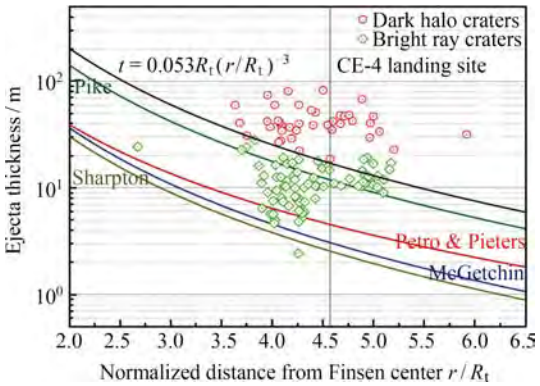

Fig. 4 Thickness estimates for the Finsen ejecta plotted as a function of the distance from Finsen center. The red circles and green diamonds represent the DHCs and BRCs identified in the study area. Their distance from Finsen crater center have been normalized to the transient radius of Finsen crater (R=30.66 km). The solid curves present the thickness of Finsen ejecta calculated using the different models. The vertical gray line represents the Chang'E-4 landing site (r=140.15 km, r/R=4.57)

explored by the lunar rover were delivered mostly from Finsen[3,5,9-15]. Li *et al.*[3] provided the evidence that the deep-seated materials mainly exist as olivine and low calcium pyroxene within the SPA basin, which are the mantle material that exposed the lunar surface. The study of Gou *et al.*[11] and Yan *et al.*[14] drew a similar conclusion. However, Hu *et al.*[15] proposed that the materials may originate from the

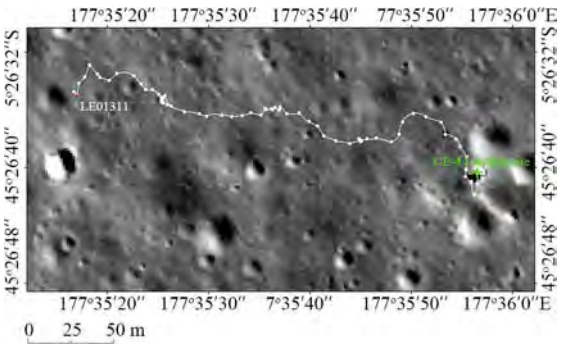

Fig. 5 Route of the Yutu-2 rover drove (as of the 14th lunar days)

ejecta of neighboring carter.

Li *et al.*[3] studied the radiance spectra of two sites (point S1: CE4_0016 and point A: CE4_0015) adjacent to the lander were collected during the first lunar day, shown in Figure 6. By analysis of VNIS spectra, as shown in Figure 7. the research team find that the absorption characteristics of spectra of soil within the Chang'E-4 landing area are obviously different from those of spectra of mare soil in Mare Imbrium where Chang'E-3 landed in and it presents apparent spectral features of Low-Calcium Pyroxene (LCP) and olivine. The analysis suggests that the materials at the Chang'E-4 landing site exhibit an LCP signature with the existence of rich olivine.

Their results imply that the Chang'E-4 landing site is characterized by mafic components that are dominated by LCP and olivine, with a very small amount of High-Calcium Pyroxene (HCP), suggesting the presence of deep-seated material from the upper mantle. Alternatively, these mafic components might originate from the base of a differentiated melt sheet. Several studies indicate that the impact event that formed the SPA basin might not have excavated through the lunar crust and exposed the mantle material on the surface of the Moon. The study interprets to present the presence of LCP and olivine may originate from the lunar mantle.

Di *et al.*[5] conducted an analysis using the in-situ spectra of the eleven sites and a rock within the Chang'E-4 landing area. Their study reveals that the surface materials are lunar deep interior material excavated from Finsen crater with possible contributions from Alder crater rather than the underlying

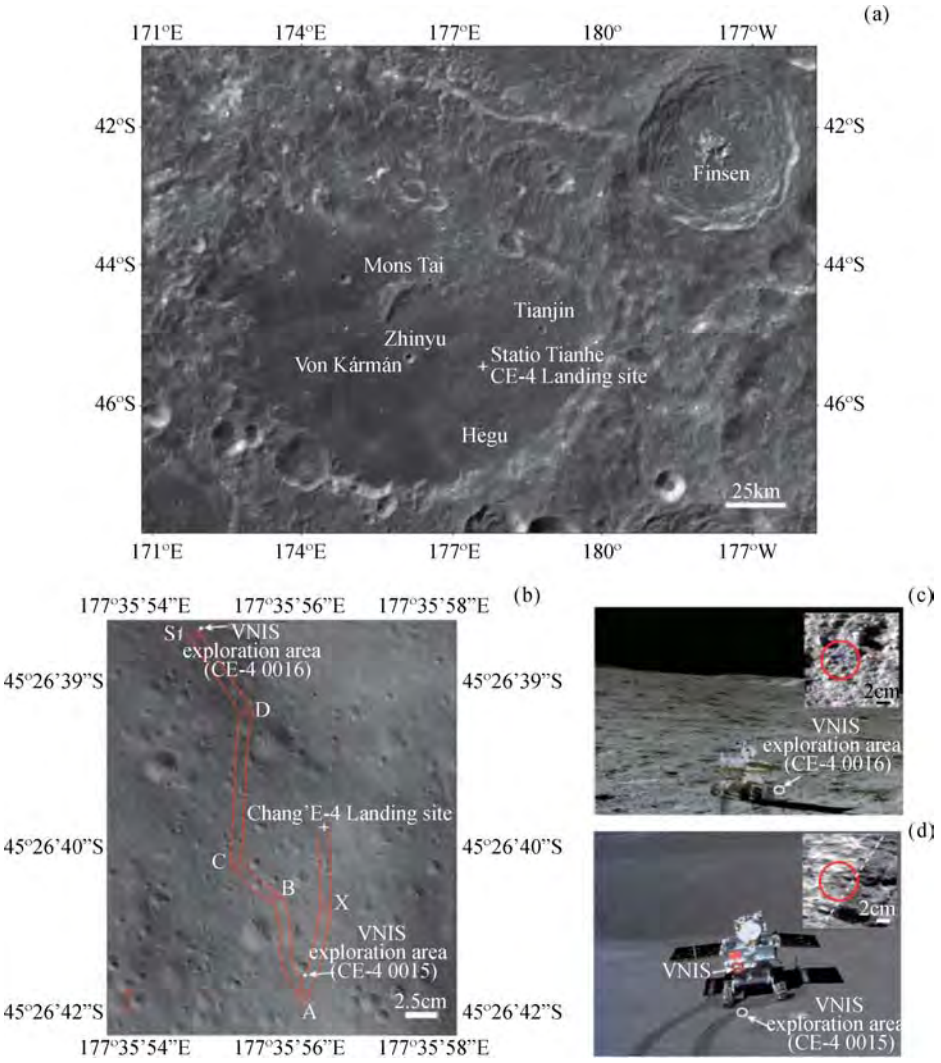

Fig.6 Locations of the Chang'E-4 landing site and the VNIS measurements. (a) The Chang'E-4 landing site on a 7-m-resolution Chang'E-2 Digital Orthophoto map. (b) Yutu-2 rover traverse map and location of VNIS detection points S1 (CE4_0016) and A (CE4_0015) during the first lunar day; red lines are Yutu-2 wheel tracks. (c)(d) Images of the VNIS conducting spectral detection at points of the VNIS conducting spectral detection at points S1 and A on the lunar surface. The images were acquired by the Terrain Camera 5. Insets, 600-nm-band images of points S1 and A, obtained by the VNIS. The red circles show the field view of the SWIR detector, and the white dashed line is the boundary between the rover wheel track and the lunar surface

mare basalt. The constituents of the lunar regolith in the Chang'E-4 landing area are relatively uniform, mainly consist of pyroxene, feldspar and agglutinates, and a small amount of olivine. The ratio of olivine/pyroxene is relatively high. Pyroxene is mainly LCP enriched in magnesium. Their results are shown in Figure 8 and 9[11, 12]. The composition is likely representative of the materials of the SPA basin floor excavated by the Finsen crater[5,11,12]. Gou *et al.*[11] proposed that although it cannot be ruled out that it originated from impacting molten foreign bodies, the regolith and rock fragments observed by the probe are likely to be lunar mantle material excavated in the neighboring Finsen crater.

Lin *et al.*[12] conducted an in-situ spectrum analysis of a rock with size larger than 20 cm along the driving route of the rover. The results as shown in Figure 10, indicate that the spectrum of the rock is

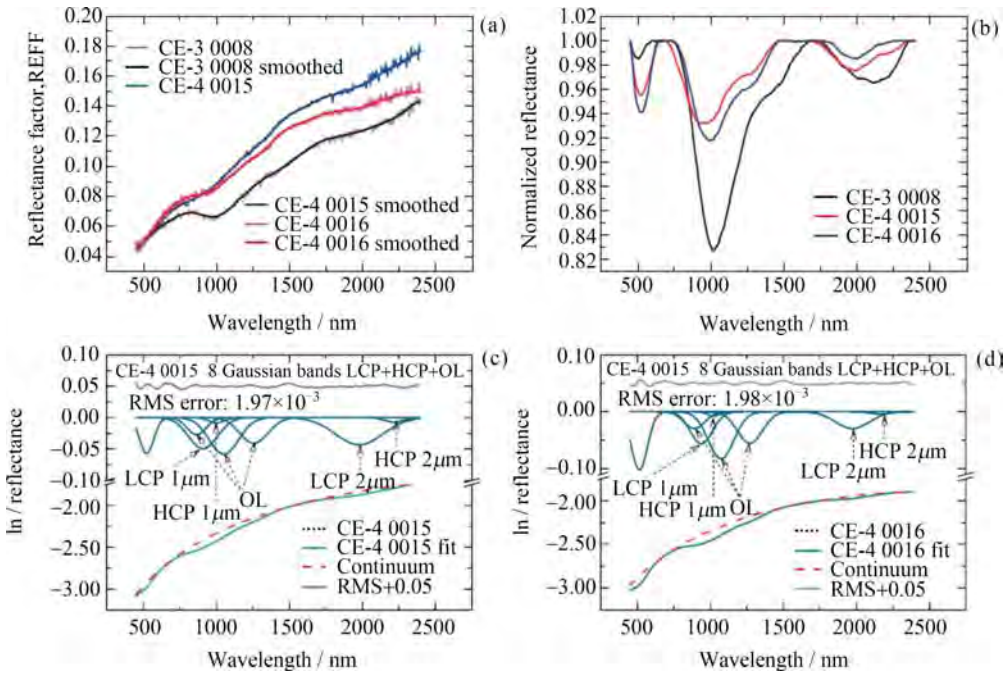

Fig. 7 Chang'E-4 reflectance spectra acquired by the VNIS during the first lunar day. (a) Reflectance (REFF) spectra obtained by Chang'E-4 VNIS (CE4_0015 and CE_0016) and the Chang'E-3 VNIS detection point (CE3_0008). (b) Continuum-removed spectra of (a). (c) (d) MGM-fitting results for CE4_0015 and CE4_0016 using endmember LCP, HCP and olivine

Fig. 8 Scatter plots of spectral parameters. (a) BAR–BC1000; (b) BC2000–BC1000. Reference compositional groups are from Cloutis *et al.* (1986) and Adams (1974), respectively. The error bars in each plot represent a first-order approximation for the uncertainty determined by the law of propagation of uncertainty. Here OC represents ordinary chondrites and BA represents pyroxene dominated basaltic achondrites

similar with that of the lunar regolith and both of them may be the homologous substances. The composition of the rock consists of 38.1%±5.4% low-Ca pyroxene, 13.9%±5.1% olivine and 48.0%±3.1% plagioclase, referred to as olivine-norite. According to the analysis, it is inferred that the rock may be crystallized from the impact-derived melt pool formed by the SPA impact event *via* mixing the lunar crust and mantle materials, the related results are indicated in Figure 10.

Mare basalts at the landing site are dominated by low-titanium basalts, and appear to be less mafic and iron-depleted than all typical kinds of retuned lunar basalt samples and may represent a new kind of

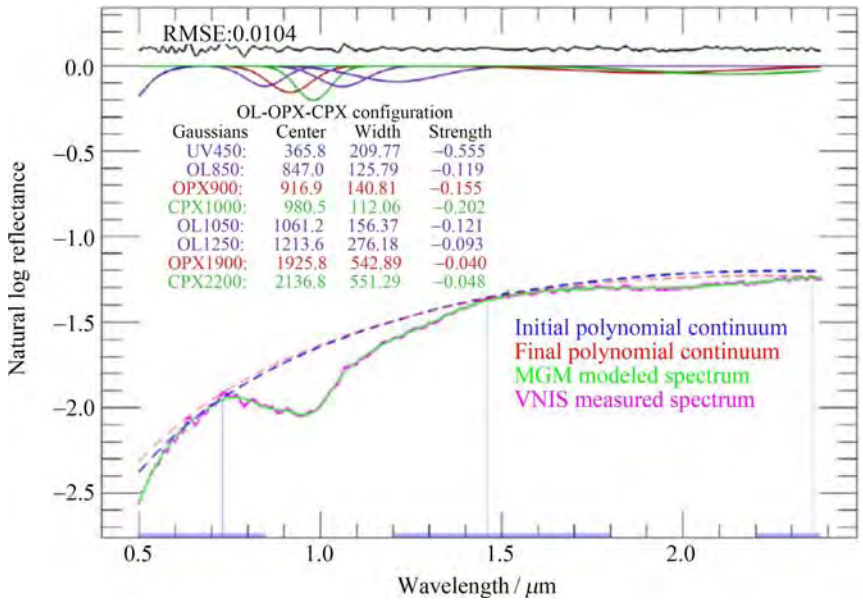

Fig. 9 Rock spectrum modeled with OL-OPX-CPX configuration by MGM

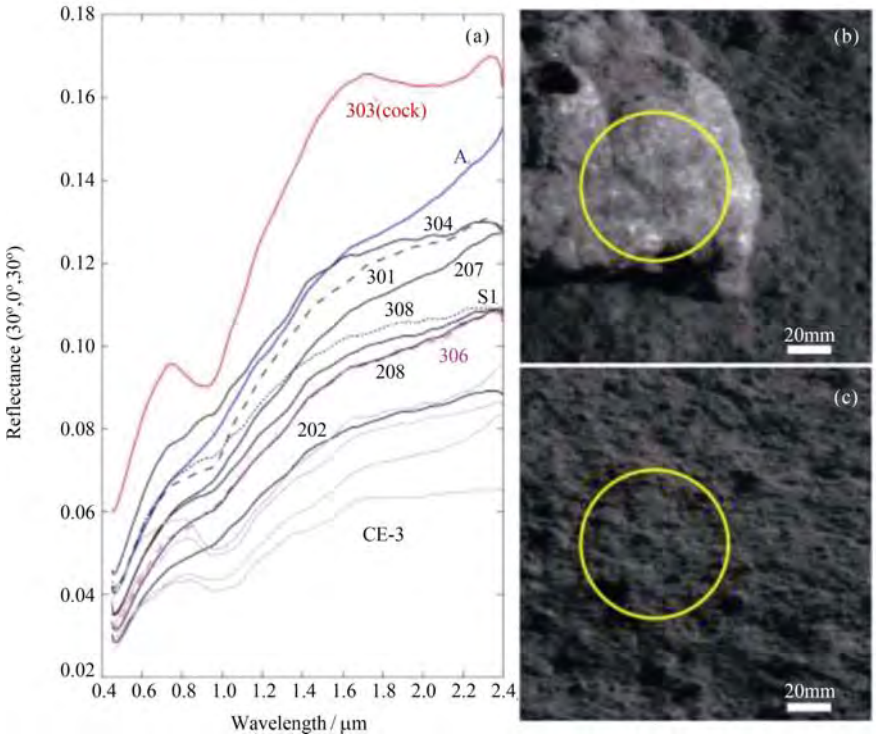

Fig. 10 (a) VNIS spectra of the rock and lunar regolith measured by Chang'E-4. (b) (c) CMOS images of the rock (labeled as 303) and the lunar soil (labeled as 207) at 0.75 μm observed by VNIS imaging spectrometer, respectively. The yellow circle is SWIR field, and the scale bar is 20 mm

mare basalt, as shown in Figure 11 and 12. The landing site mare is heavily sculptured by a set of linear parallel ridged and furrowed textures formed by ballistic ejecta from the Finsen crater, which is characterized by a more feldspathic composition, while with elevated orthopyroxene abundance, and may

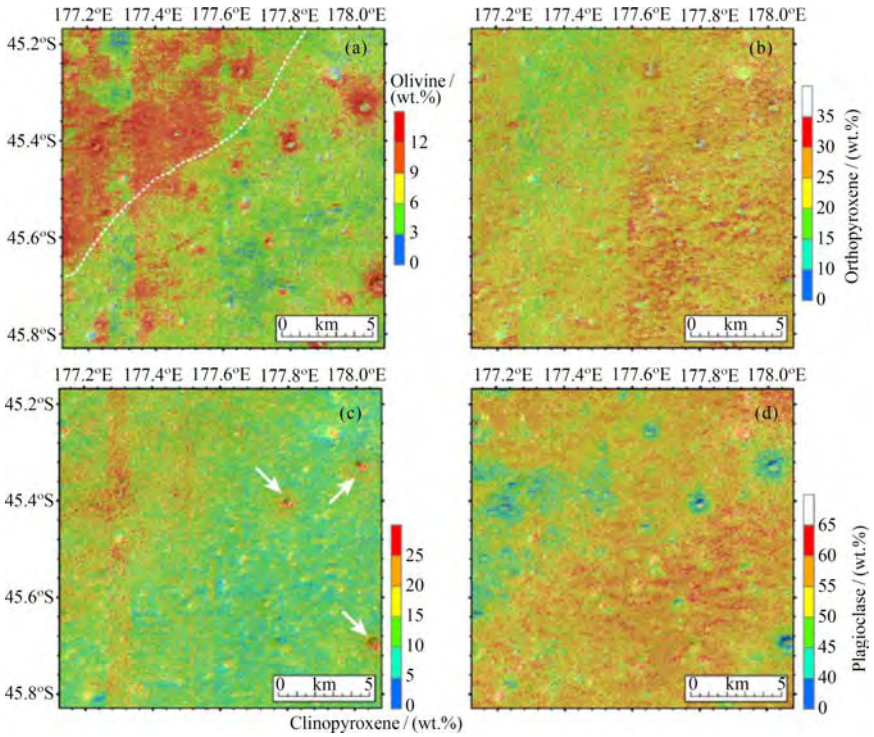

Fig. 11 Major rock-forming minerals of the studied landing area: (a) olivine, (b) orthopyroxene, (c) clinopyroxene, (d) plagioclase, (e) mafic minerals

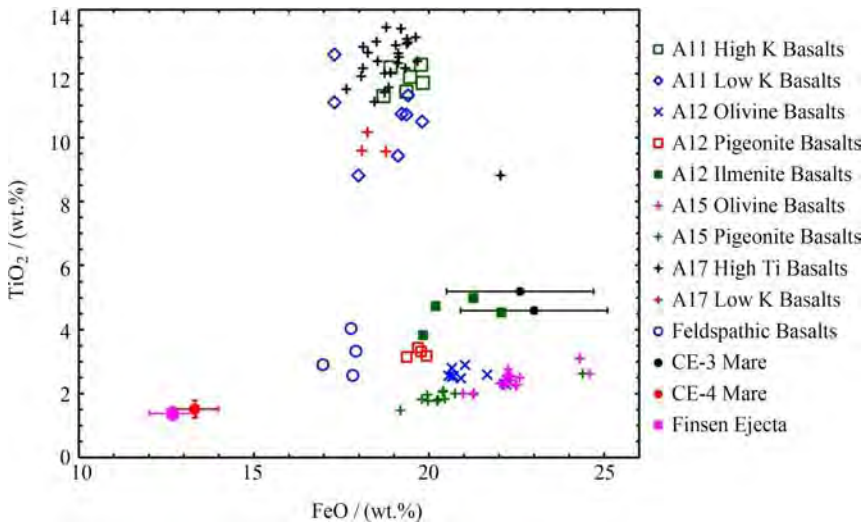

Fig. 12 Comparison of iron and titanium contents for mare basalts and Finsen crater ejecta materials at Chang'E-4 landing site (average values $\pm 1\,\delta$) with all typical kinds of lunar basalts and Chang'E-3 surface in-situ measurements

represent compositional properties of the primitive SPA basin floor materials[10].

Chisenga *et al.*[14] performed a 3D inversion of the GRAIL gravity data to produce a density model of the Von Kármán Crater. The results reveal that the region is underlain by a mass excess anomaly beneath the Von Kármán M Crater with a density of about 3200 kg·m^{-3}, on the southern rim of the Von Kármán basin. A relatively high-density mass excess anomaly with a density value of up to 3100 kg·m^{-3} connects to the first anomaly in the northern part. The study suggests that this was the result of the

buried mare basalts that created a buried impact basin in the Von Kármán M Crater. The occurrence of high-density materials that extend to the lower crust correlates with excavated mantle materials observed on the floor of the Von Kármán basin, suggesting that the impact cratering could have brought upper mantle materials to the surface. The study infers that the evolution of the Von Kármán basin was due to multiple episodes of impact cratering that resulted in crustal reworking and secondary excavation of mantle materials.

Hu *et al.*[15] conducted an analysis of the main constituents of a large area covering the Finsen crater. Their study proposed that the results indicate a strong correlation between the materials at the landing site and the Finsen crater, and the relevant results are shown in Figure 13. The ejecta of Finsen crater is the major contributor to the surficial materials at the Chang'E-4 landing site. They proposed that the high plagioclase abundance at the landing site may indicate the associated olivine is inherent of anorthosites, rather than the Mg-suite troctolites erupted from the interior of the Moon. The expected mantle materials are not observed at the Chang'E-4 landing site, indicating that the materials of the present-day crust (at least the upper crust) at the landing area is not the breccia deposits derived from the ejecta of the SPA basin. The relevant results are shown in Figure 13.

3.3 Mineral Abundance and Soil Maturity of the Lunar Surface

Li *et al.*[3] used four different groups of mineral combinations in the Modified Gaussian Model (MGM) deconvolution: (i) LCP, HCP and olivine (OL); (ii) LCP, HCP and plagioclase (Plag);(iii) LCP and Plag; (iv) LCP and OL. Further analysis on the deconvolved 1-μm-band depth of LCP, HCP and OL suggests that for CE4_0015 the abundances for LCP:HCP:OL are 42%:10%:48%, with the highest abundance for OL, followed by LCP and the lowest abundance for HCP. MGM deconvolution of CE4_0016 (Figure 2d) indicates that LCP:HCP:OL 38%:7%:55%. CE4_0016 is dominated by LCP and OL and has a greater abundance of OL than CE4_0015 and a very small amount of HCP.

Hu *et al.*[15] utilized a synthesized lunar spectral

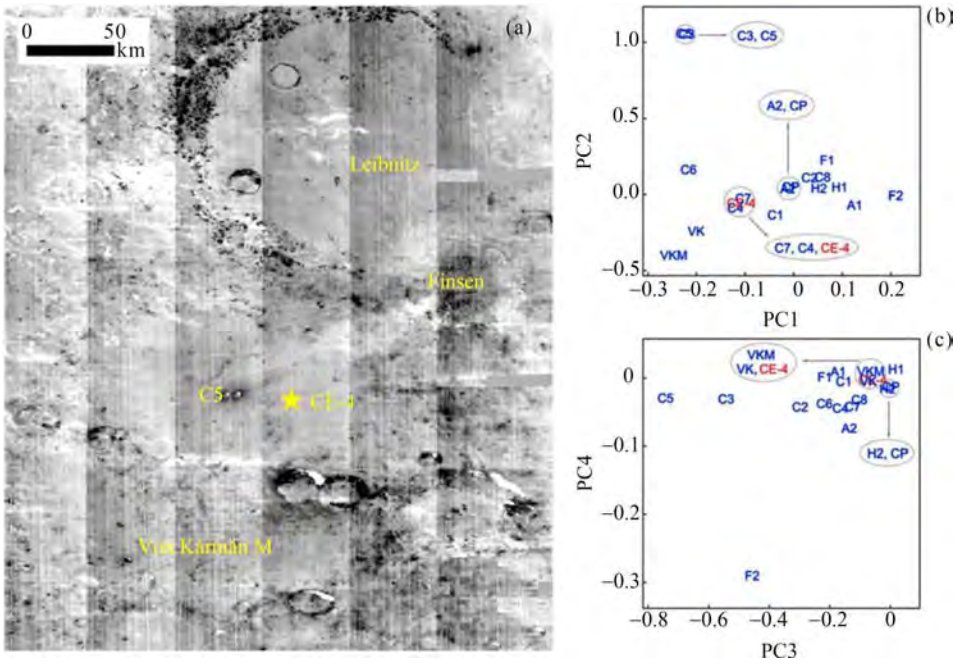

Fig. 13 Principal component analysis results of Chang'E-4 landing site. (a) The image of the fourth principal component (PC4) of the M3 data. (b) PC2 *vs.* PC1 and (c) PC4 *vs.* PC3 are distributions of the typical PC values of selected regions of interest calculated from the M3 spectra in the PC space

mineral Lookup Table (LUT) based on radiative transfer models, considered spectra of olivine (OLV), clinopyroxene (CPX), orthopyroxene (OPX), and plagioclase (PLG). The results indicate that the landing site is dominated by PLG (56%~72%), followed by OPX (9%~28%), CPX (4%~19%), and OLV (2%~12%), in relative abundance, in agreement with the results from Kaguya Multiband Imager mineral mapping. The mineral abundances with uncertainties, obtained by averaging the four results, are summarized in Figure 14 and Table 2.

Qiao *et al.*[10] studied a detailed geologic context, topographical, morphological, geochemical and mineralogical characterization of a 20 km×20 km area centered at the Chang'E-4 landing area. The result indicated that the majority (> 80%) of the landing area has calculated FeO content between 11% and 13%wt. and > 95% of the regional surface has TiO_2 content between 1% and 2%wt. The result is shown in Figure 15. The studied landing area surface was divided into two major units with slightly different iron contents: a northern belt region with relatively elevated FeO abundance (about 13%~14% wt., the mean value of 13.3%wt. with 1 δ = 0.7) and a broader

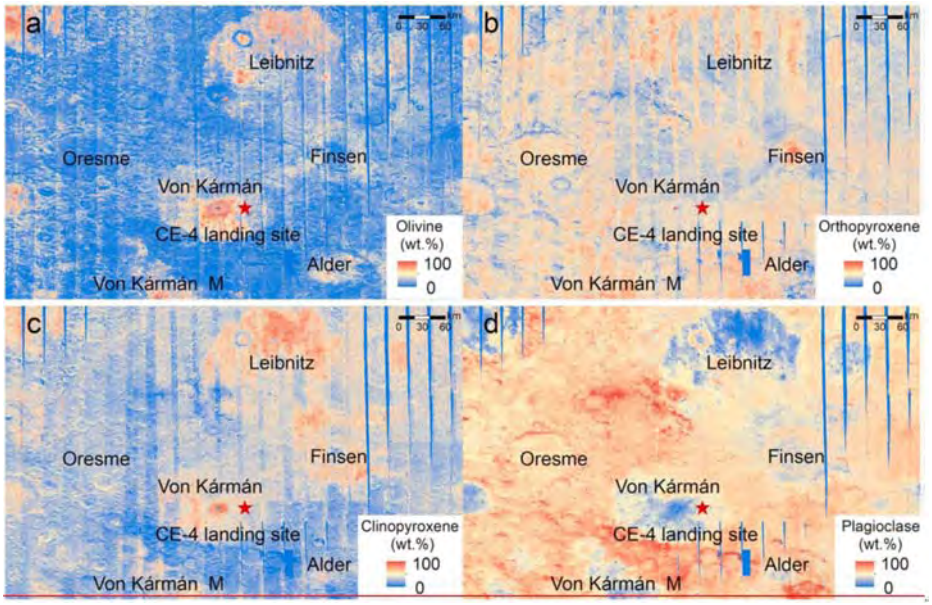

Fig. 14 Mineral mapping results. (a) Olivine mineral abundance, (b) orthopyroxene mineral abundance, (c) clinopyroxene mineral abundance, and (d) plagioclase mineral abundance

Table 2 Mineral abundance (%wt.) obtained by comparing the CE-4 data and the LUT spectra, and the errors were obtained by using equation (S8)

	First lunar day		Second lunar day				
Data	N15	N16	N17-1	N17-2	N18-1	N18-2	Average
OLV	9.0±1.0	11.1±3.9	2.1±2.1	7.9±2.3	11.8±2.2	10.9±2.5	8.8±3.3
OPX	27.5±3.4	9.2±4.5	24.0±0.6	17.8±1.1	20.3±2.5	10.9±2.5	18.3±6.6
CPX	4.1±0.3	8.5±0.3	14.0±1.7	18.8±0.7	10.6±3.1	6.8±1.2	10.4±4.8
PLG	59.5±2.6	71.3±8.1	60.0±1.0	55.5±2.7	57.3±1.6	71.5±3.8	62.5±6.4
i/(°)	50.88	72.06	73.39	64.51	64.56	66.23	–
e/(°)	46.93	42.89	47.97	46.53	46.30	45.48	–
a/(°)	93.97	89.55	77.81	91.87	90.82	101.93	–

Note *i*, *e*, and α are solar zenith angle, sensor viewing zenith angle, and the solar phase angle, respectively. LUT=lookup table; OLV=olivine; OPX=orthopyroxene; CPX=clinopyroxene; PLG=plagioclase.

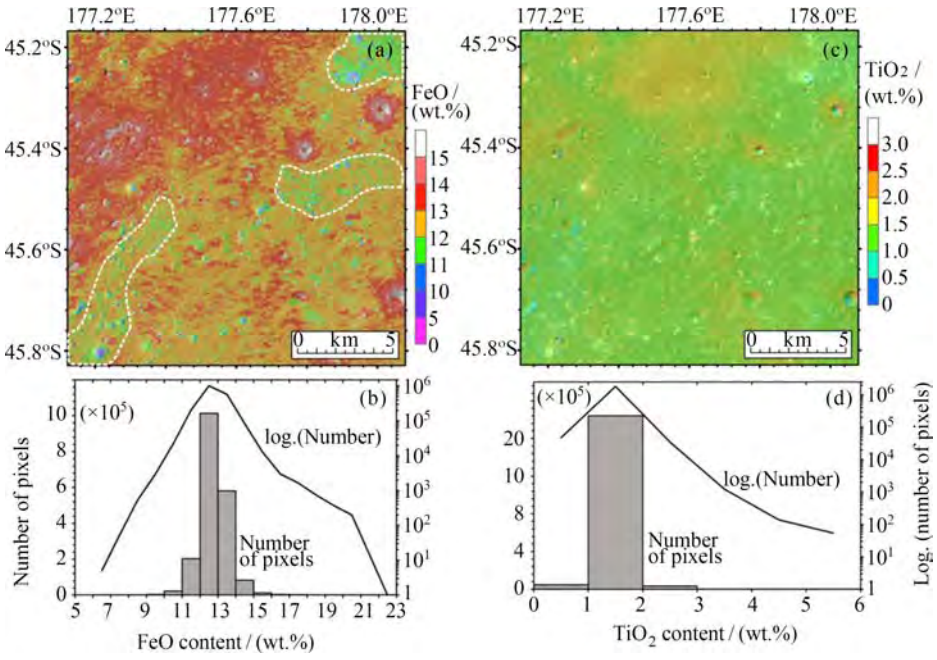

Fig. 15 FeO (a) and TiO_2 (c) abundance maps of the studied landing area and their histograms (b) (d). The dashed patches in (a) mark the strip-shaped areas with decreased iron contents

region with slightly lower FeO abundance (about 12%~13%wt., the mean value of 12.7%wt. with 1 δ =0.7).

Ling *et al.*[13] presented a comprehensive study of the composition, mineralogy, and chronology of the basaltic and non-mare units in this crater, with the intent to provide context for the compositional properties of the landing site. They produce the compositional maps such as FeO, TiO_2, $Mg^{\#}$ and Th, and analyze spatial distribution characteristics of monoclinic pyroxene and orthopyroxene. The mare surface in Von Kármán crater is relatively low in FeO (about 13%~18%wt.) and TiO_2 (about 1%~3%wt.) in comparison with basalt at the Chang'E-3 landing site (*i.e.*, about 22.8%wt. FeO and 5.0%wt. TiO_2). It is clear that the typical mare basalt belongs to a low-Fe (15.3%±0.6%wt.) and low-Ti (2.0_0.3%wt.) end-member, while the Mg composition suggests they are relatively high in $Mg^{\#}$ values (about 52±2). The related results are shown in Figure 16. Chang'E-4 mare basalt stands out as a special type of basalt with similar Fe, Ti contents, and $Mg^{\#}$ values with the very high K basalt and high aluminum basalt from Apollo 14 (*e.g.*, Apollo 14053, 14168, 14305, 14321 samples) and Luna 16 missions[10,13]. The characteristic chemical compositions of Chang'E-4 basalt may imply a unique view of farside volcanism[13].

3.4 Geological Evolution of the Von Kármán Carter

Ling *et al.*[9, 13] used the remote sensing data to identify two types of impact craters, which are indicated by 40 dark rings and 77 bright rings in the landing area. The dark ring impact crater can be regarded as the ejecta from Finsen crater, which can penetrate the surface layer of the landing area and excavate the lower basalt, whileas impact craters indicated by the bright ring are not able to penetrate the ejecta layer. The research teams produced the schematic of stratigraphy and subsurface structure of the Chang'E-4 landing site and analyze the coverage relationship of ejecta over multiple times in this area, as shown in Figure 17. The study reveals the stratigraphic structural characteristics and geological evolution history of the landing area. The related results are shown in Figure 17 and 18.

A brief geological history of the study area is proposed as follows.

(1) The South Pole-Aitken basin was formed more than four billion years ago[13,14] in the multiple cratering scenario created the SPA that eventually

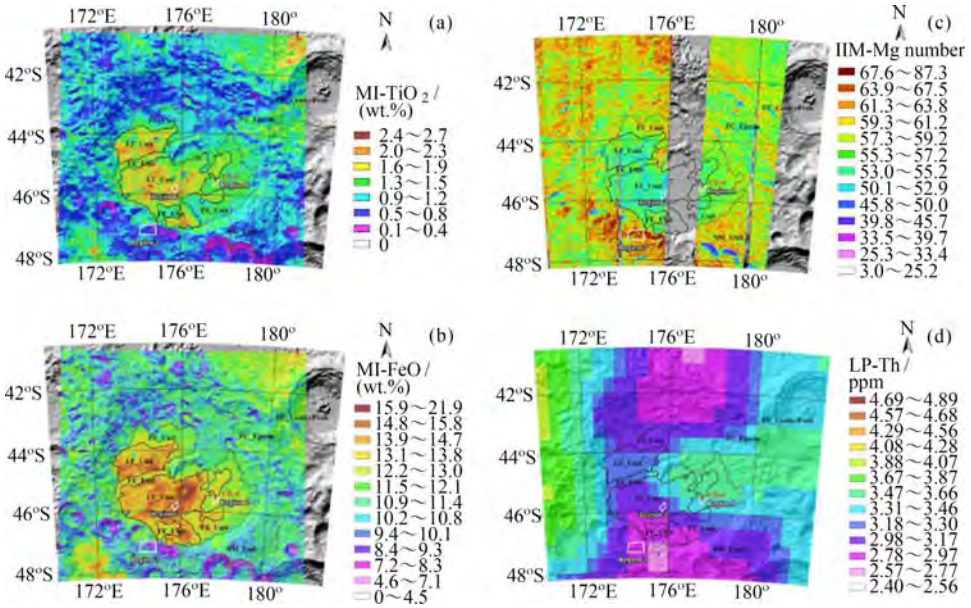

Fig. 16 Chemical compositions of Von Kármán crater. (a) TiO_2 map and (b) FeO map using Kaguya Multiband Imager (MI) data, (c) $Mg^{\#}$ (100×MgO/(MgO þ FeO)) map using Chang'E-1 IIM data, and (d) Th maps from Lunar Prospector data. The base map is LOLA shaded relief image. Black polygons are the unit division results: LT, low-titanium mare unit; FE, Finsen ejecta unit

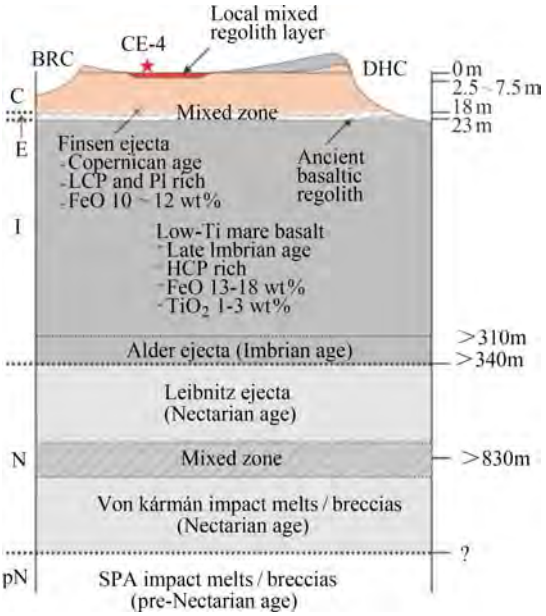

Fig. 17 Stratigraphy and subsurface structure. The red star indicates the Chang'E-4 landing site. Typical DHCs and BRCs are shown here. The shaded regions indicate the mixed zone between the impact ejecta and the underlying layer. The letters on the left represent lunar geological periods: pN for pre-Nectarian, N for Nectarian, I for Imbrian, E for Eratosthenian, and C for Copernican

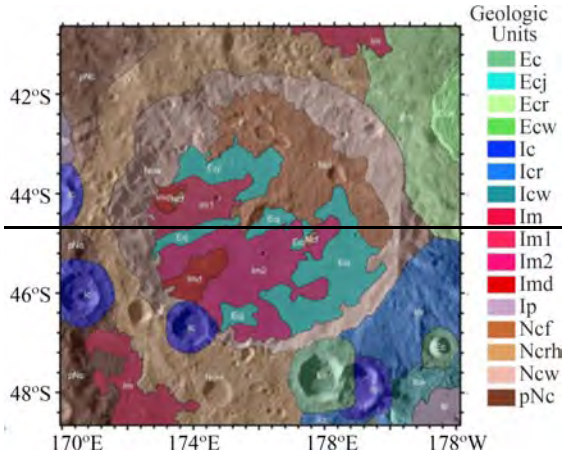

Fig. 18 Geologic map of Von Kármán crater. pNc is pre-Nectarian crater materials, Ncw, Ncrh, Ncf are Nectarian crater wall, hummocky rim, and floor materials, Ip is Imbrian plain materials, Im, Im1 and Im2 are Imbrian mare units, Imd is Imbriaum dome-like unit, Ic is Imbrian materials and can be sub-divided into rim (Icr) and wall (Icw) units, Ec is Eratoshenian crater materials and can be sub-divided into rim (Ecr), wall (Ecw) and ejecta (Ecj) units

excavated the lower crust and probably the upper mantle, resulting in a very thin crust region[14].

(2) A Nectarian impact event formed 186-km-

diameter Von Kármán; Then, the 240-km-diameter Leibnitz crater formed north of Von Kármán crater and destroyed part of the northern rim structure of Von Kármán crater and ejected material into the northern part of the Von Kármán crater floor[9,13]. The formation of Alder crater also transported a thin layer of exhumed materials[9].

(3) During the Imbrian period, regional lava-infilling events took place within the SPA basin interior, which generated small mare plains. The Von Kármán floor surface mare deposits are dated to be about 3.4~3.6 Ga, with buried mare flows to be about 3.7 Ga lava flow at a depth of >100 m[13]. Basaltic volcanism was active at 3.6 Ga, and low-Ti basalt flows filled most of the floor; A basaltic regolith layer formed on the surface of the mare basalt plain[9]. Mare basalts emplaced at the Von Kármán crater floor are characterized by a Ca- and Fe-rich pyroxene composition, with relatively low iron and titanium contents, but relatively higher magnesium[13].

(4) In the long Eratosthenian Period, no large crater formed in the adjacent area, and basaltic regolith formed on the surface of mare basalt; The Copernican Finsen impact ejecta overlay the basalt unit and covered the study area; The following small impact events struck the surface, and some of them excavated the underlying basaltic materials and formed the craters with dark halos. These Finsen ejecta materials are characterized by elevated FeO, TiO_2, and LCP content than typical lunar highlands[13].

3.5 Stratigraphy Structure of the Lunar Regolith

Lai *et al.*[16] interpreted the lunar penetrating radar detection data. Indicated at the Chang'E-4 site, the permittivity is about 4.3 at 130 ns, the instantaneous permittivity increases very rapidly at the near-surface section of the regolith (< 2 m) and then grows slowly to the maximum value of about 4.5 at the depth of 11 m. The study derives a bulk density for the regolith at Chang'E-4 of ρ =1.22~2.23 g·cm^{-3}, increasing with depth.

Radargrams of both LPR experiments show a complicated picture of the shallow stratigraphic profile (Figure 19): numerous short lateral reflectors caused by the accumulation of ejecta from small local craters appear in the near-surface region. Several rough and intermittent interfaces (hr1~3) with rocks and paleoregolith admixed are identified in the Chang'E-4 LPR results, which may correspond to more than one large-scale ejecta layers (hr1) or the transition zones between regolith and bedrock (hr2, hr3). The rough interface above the fractured bedrock at the depth of 25.8 m (hr4) and 33~35 m (hr5) are also revealed by the LPR. Hr3 might be caused by a rough interface of fractured bedrock and hr4 may indicate the rough interface of another fractured paleo basalt layer[16].

Li *et al.*[17] combined the information provided by the radargram, the tomographic image, and the quantitative analysis, concluded that the subsurface

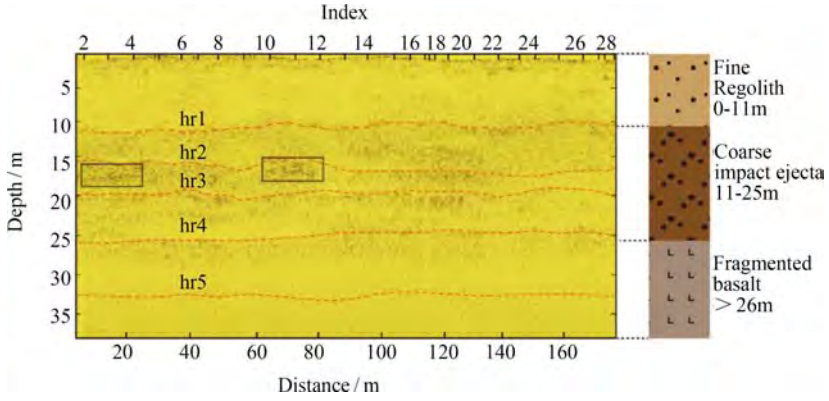

Fig. 19 LPR radargram of CE-4 site. The geologic interpretation of LPR results is given on the panel on the right. hr stands for the horizontal reflector, also indicated by the dotted line. The rectangles circled the hyperbolic signals caused by the discrete scatters within the ejecta layers

internal structure at the landing site is essentially made by low-loss, highly porous granular materials embedding boulders of different sizes. Given such a strong geological constraint, the most plausible interpretation is that the sequence is made of a layer of regolith overlaying a sequence of ejecta deposits from various craters (Figure 20), which progressively accumulated after the emplacement of the mare basalts on the floor of Von Karman crater. The layer of regolith (Unit 1) is quite thick (up to 12 m), is rather homogenous both laterally and vertically, and is mostly composed of fine materials. It developed from the uppermost portion of the ejecta deposits, which were thicker than 12 m and were delivered to this area by multiple impact craters, mostly Finsen, Von Karman L, and Von Karman L' craters. Unit 2 (depth, 12 to 24 m) is characterized by large rocks and boulders that are interbedded with thin layers of fine materials. It is likely formed due to a combination of (i) coarse ejecta that were not mobilized during the landing of impact ejecta, (ii) structural disturbances in local materials caused by the landing ejecta, and (iii) fine materials generated during or after the ejecta deposition. Unit 3 (24 to 40 m) contains alternating layers of coarse and fine materials. This unit can be interpreted as a combination of ejecta deposits, which were delivered by various craters older than Finsen and regolith developed during the impact intervals.

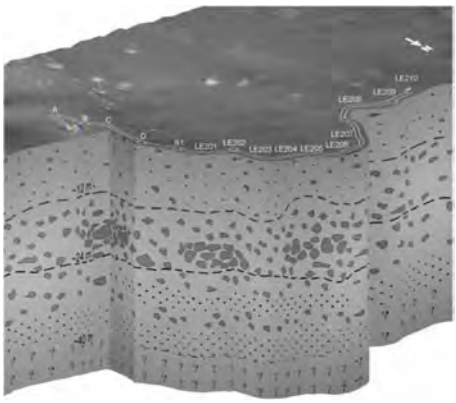

Fig. 20 Schematic representation of the subsurface geological structure at the Chang'E-4 landing site inferred from LPR observations. The subsurface can be divided into three units: Unit 1 (up to 12 m) consists of lunar regolith, Unit 2 (depth range, 12 to 24 m) consists of coarser materials with embedded rocks, and Unit 3 (depth range, 24 to 40 m) contains alternating layers of coarse and fine materials

4 Conclusions and Future Scientific Research

The research team of Chang'E-4 achieved preliminary results in some aspects of lunar science such as terrain, geomorphology, geological tectonic, mineral constitution and shallow subsurface structure by use of data acquired from Chang'E-4. The results of the radar data collected by the LPR provide the first electromagnetic image of the farside subsurface structure and the first "ground truth" of the stratigraphic architecture of an ejecta deposit. The results could provide strong evidence for the understanding of materials in the lunar interior as well as provide new constraints for revealing the important scientific issues, of which the geological evolution of the SPA basin of the Moon, the early evolutionary history of the lunar crust, the structure in the lunar interior and its formation mechanism.

The study on the lunar-based low-frequency radio astronomy, lunar neutron radiation and neutral atoms are still undergoing, with related papers under review. It is believed that more new scientific results are coming up next.

The rover of Chang'E-4 mission works very well on the Moon's far side. Based on the scientific results achieved in the past time, in situ exploration on the Moon's farside by Chang'E-4 is still concentrates on the Finsen crater ejecta and lunar mare basalt around the landing site. However, many scientific issues, such as in the following aspects, still await further investigation.

(1) To cumulate more scientific evidence of whether the deep-seated materials of the Moon's farside originate from the lunar mantle.

(2) To further analyze and interpret scientific data emphatically to study on the mixed-effects of the local basalt and exogenous feldspathic materials.

(3) To conduct further study on the layer structure and geological evolution of the landing area.

(4) To study the transformation of the lunar surface by impacts; volcanic activity scale and their history.

(5) To search clues to the early evolution of the universe, planetary radios of the solar system, and solar low-frequency radio bursts through Low-frequency radio detection.

(6) To study on the relationship between the neutral atom energy spectrum and the solar wind speed, and to measure the electron particle radiation dose, fast neutrons, thermal neutrons and γ-rays on the lunar surface. Discovery in the solar energetic particle acceleration and transport in the heliosphere are expected.

References

[1] XU Lin, ZOU Yongliao, QIN Lang. Latest Scientific Results of China's Lunar Exploration Program [J]. *Chin. J. Space Sci.*, 2018, **38**(5):598-603

[2] JIA Yingzhuo, ZOU Yongliao, PING Jinsong. The scientific objectives and payloads of Chang'E-4 mission [J]. Planet. Space Sci., 2018, **162**(SI):207-215

[3] LI Chunlai, LIU Dawei, LIU Bin, *et al.* Chang'E-4 initial spectroscopic identification of lunar far-side mantle-derived materials [J]. *Nature*, 2019, **569**:378-393

[4] SPUDIS P D; REISSE R A; GILLIS J J. Ancient multiring basins on the Moon revealed by Clementine laser altimetry [J]. *Science*, 1994, **266**(5192):1848-1851

[5] KAICHANG D I, ZHU Menghua, YUE Zongyu, LIN Yangting. Topographic evolution of Von Kármán crater revealed by the lunar rover Yutu-2 [J]. *Geophys. Res. Lett.*, 2019, **46** (22):12764-12770

[6] WU Weiren, LI Chunlai, WEI Zuo, *et al.* Lunar farside to be explored by Chang'E-4 [J]. *Nat. Geosci.*, 2019, **12**(4):222-223

[7] HUANG J, XIAO Z, FLAHAUT J, *et al.*, Geological characteristics of Von Kármán Crater, Northwestern South Pole-Aitken Basin: Chang'E-4 landing site region [J]. *J. Geophys. Res.: Planets*, 2018, 123:1684-1700

[8] LIU Jianjun, REN Xin, YAN Wei, *et al.*, Descent trajectory reconstruction and landing site positioning of Chang'E-4 on the lunar farside [J]. *Nat. Commun.*, 2019. DOI:10.1038/s41467-019-12278-3

[9] FU Xiaohui, QIAO Le, ZHANG Jiang, *et al.* The subsurface structure and stratigraphy of the Chang'E-4 landing site: orbital evidence from small craters on the Von Kármán crater floor [J]. *Res. Astron. Astrophys.*, 2020, **20**(1):1-14

[10] QIAO Le, LING Zongtheng, FU Xiaohui. Geological characterization of the Chang'E-4 landing area on the lunar farside [J]. *ICARUS*, 2019, **333**:37-51

[11] GOU Sheng, DI Kaichang, YUE Zongyu. Lunar deep materials observed by Chang'E-4 rover [J]. *Earth Planet. Sci. Lett.*, 2019, **528**:115829

[12] LIN Honglei, HE Zhiping, YANG Wei, Lin Yangting. Olivine-norite rock detected by the lunar rover Yutu-2 likely crystallized from the SPA impact melt pool [J]. *Natl. Sci. Rev.*, 2019, 183

[13] LING Z, QIAO L, LIU C, *et al.* Composition, mineralogy and chronology of mare basalts and non-mare materials in Von Kármán crater: landing site of the Chang'E-4 mission [J]. *Planet. Space Sci.*, 2019, 104741

[14] CHISENGA Chikondi, YAN Jianguo, ZHAO Jiannan, *et al.* Density structure of the Von Karman crater in the Northwestern South Pole-Aitken basin: initial subsurface interpretation of the Chang'E-4 landing site region [J]. *Sensors*, 2019, **19** (20):4445

[15] HU Xiaoyi, MA Pei, YANG Yazhou, *et al.* Mineral abundances inferred from in situ reflectance measurements of Chang'E-4 landing site in South Pole-Aitken Basin [J]. *Geophys. Res. Lett.*, 2019, **46** (16):9439-9447

[16] LAI Jialong, XU Yi, ZHANG Xiaoping, *et al*, Comparison of dielectric properties and structure of lunar regolith at Chang'E-3 and Chang'E-4 landing sites revealed by ground-penetrating radar [J]. *Geophys. Res. Lett.*, 2019, **46**:12783-12793

[17] LI Chunlai, SU Yan PETTINELLI Elena, *et al.*, The Moon's farside shallow subsurface structure unveiled by Chang'E-4 Lunar Penetrating Radar [J]. *Sci. Adv.*, 2020, **6**:6898

PAN Jianwei. Progress of the Quantum Experiment Science Satellite (QUESS) Micius Project. *Chin. J. Space Sci.*, 2020, **40**(5): 042-046. DOI:10.11728/cjss2020.05.042

Progress of the Quantum Experiment Science Satellite (QUESS) Micius Project

PAN Jianwei

(*Hefei National Laboratory for Physical Sciences at Microscale and Department of Modern Physics, University of Science and Technology of China, Hefei* 230026)

(*CAS Center for Excellence in Quantum Information and Quantum Physics, Hefei* 230026)

Abstract The Micius satellite was successfully launched on 16 August 2016, from Jiuquan, China, orbiting at an altitude of about 500 km. The main scientific goals, including satellite-to-ground quantum key distribution, satellite-based quantum entanglement distribution, ground-to-satellite quantum teleportation, and satellite relayed intercontinental quantum network, were achieved in 2017. As a starting point, the Micius satellite has become a platform for quantum science experiments at the space scale. Here, we introduce the latest experimental achievements (in 2018–2020) based on the Micius satellite.

Key words Quantum science satellite, Quantum key distribution, Quantum entanglement, Time-frequency transfer

Classified index V 524, P 35

1 Entanglement-based Quantum Key Distribution (QKD) from Satellite to Ground

The entanglement-based QKD is particularly attractive because of its inherent source-independent security where the security can be established without any assumption on the trusted relay.

Following the first satellite-based entanglement distribution[1,2], a later experiment[3] was performed between the ground stations of Delingha and Nanshan with a spatial separation of 1120 km, as shown in Figure 1.

The receiving efficiencies were considerably improved using higher efficiency telescope and follow-up optics. Both ground stations used newly built telescopes with diameters of 1.2 m. In each telescope, the main lens was re-coated, and the beam expander was re-designed. In the follow-up optics, the collection efficiency was enhanced by optical pattern matching, in particular, through shortening the optical path by reducing spectral splitting to avoid beam spread. These technical improvements allowed the authors to observe an average two-photon count rate of 2 Hz (corresponding to an increase of the two-photon link efficiency by a factor of 4), which is significant as it increased the obtained key rate and decreased the quantum bit error rate from 8.1% to 4.5%.

A special effort of this work was made to ensure its implementation is practically secure against all known side channels. Thanks to the source-independent nature of the entanglement-based QKD, the system is immune to any loophole in the source, and all left is to ensure the security on the detection sides in the two ground stations.

In general, the side channels, known and to be known, on the detection primarily violate the assumption of fair-sampling. Experimentally, it ensures the validity of the fair-sampling by filtering in different degrees of freedom including frequency, spatial

Received June 28, 2020
E-mail: pan@ustc.edu.cn

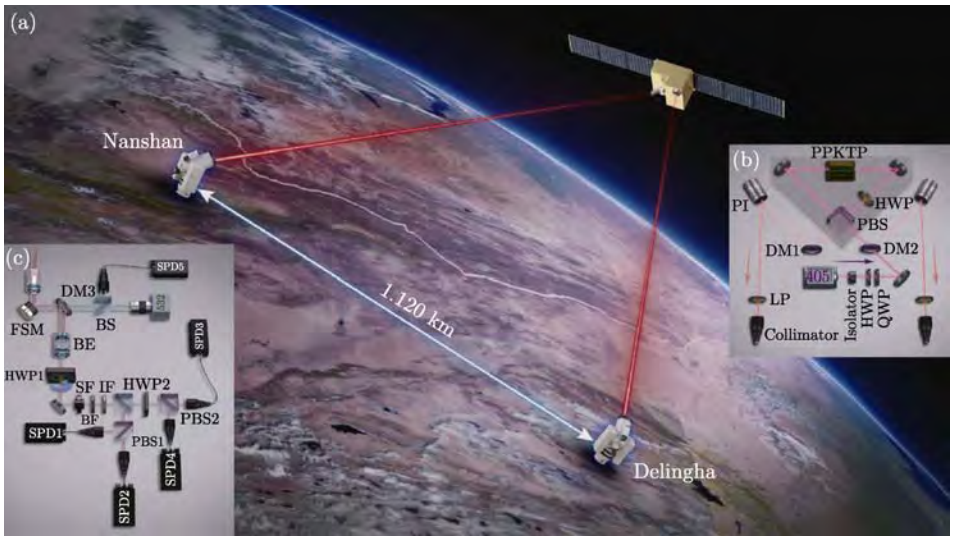

Fig. 1 Overview of the experimental set-up of entanglement-based quantum key distribution. (a) Illustration of the Micius satellite and two ground stations. (b) The spaceborne entangled-photon source. (c) The follow-up optics at the ground station

and temporal modes, and countermeasures were taken for the correct operation of the single-photon detectors. All known detection attacks were considered including the detector-related attacks, spatial-mode attack, and other possible side-channels. For example, for the side channels targeting at the operation of detectors such as blinding attacks, additional monitoring circuits were used to monitor the anode of the load resistance in the detection circuit to counter the blinding attack. For the time-shift attack and the dead-time attack, the countermeasure was to operate the detector in free-running mode, in which the detector records all the detection events and post-selects the detection windows such that the detection efficiency is guaranteed to be at a nominal level.

Consequently, the secret key, generated by our QKD system, is practically secure under realistic devices. By running 1021 trials of the Bell test during an effective collection time of 226 s, Yin *et al.* observed the parameter S to be 2.56±0.07 with a violation of local realism by 8 standard deviations. Having violated the Bell's inequality, we demonstrated the entanglement-based QKD using Bennett-Brassard-Mermin 1992 protocol (BBM92), where both Alice and Bob took measurements randomly along the H/V and basis.

Within 3100 s data collection time, Yin *et al.* obtained 6208 initial coincidence, which gave 3100 bits of sifted keys with 140 erroneous bits. The quantum bit error rate is 4.5%±0.4%. After error correction and privacy amplification, the secure key rate of 0.43 bit·s^{-1} was obtained in the asymptotic limit of the infinite long key. The secure key rate is 11 orders of magnitude higher than that would be obtained by direct transmission of entangled photons over 1120 km through the best commercial fibers. Note that with the newly developed entangled photon source with 1 GHz generation rate[4], the secure key rate can be increased by about 2 orders of magnitude directly. The results increase the secure distance of practical QKD for ground users by 10 times to the order of thousand kilometers, which represents a key step toward the Holy Grail of cryptography.

2 Satellite-based Quantum-secure Time-frequency Transfer

Today's time synchronization techniques are vulnerable to sophisticated, malicious adversaries, which require fundamentally new methods of securely distributing high-precision time information. Based on Micius satellite, the recent work is aimed at this direction, with the proposal and demonstration of a

satellite-based Quantum-Secure Time Transfer (QSTT) scheme from a two-way quantum key distribution in a free-space link, which is characterized by a quantum signal (*e.g.*, single photon) acting as the carrier for both time transfer and secret-key generation to realize information-theoretic security in the time information transfer[5].

Figure 2 presents a schematic diagram of QSTT. Satellite Alice, which has master Clock A, initiates two-way time transfer with the ground station, Bob, who has slave Clock B. The scheme is then implemented through four basic steps. In Step 1, Alice and Bob mutually transmit single photons over free space for both two-way QKD and two-way transmission of timing signals. In Step 2, Alice and Bob evaluate the Quantum Bit Error Rates (QBERs) in the polarization degree of freedom for the timing signals. In Step 3, Alice transmits the encrypted classical timing data to Bob through a public channel, using the keys generated from the QKD. In Step 4, Alice or Bob, having all the timing data, evaluates the clock offset and the ranging distance with the coincidence time events.

To verify the key technologies and show their feasibility, we performed an experimental study of satellite-based QSTT between the Micius satellite and the Nanshan ground observatory in China. In the downlink, we demonstrated satellite-based QKD by using single photons as carriers of time transfer. In the uplink, we performed standard optical time transfer using classical laser pulses. The experimental set-up is illustrated in Figure 3.

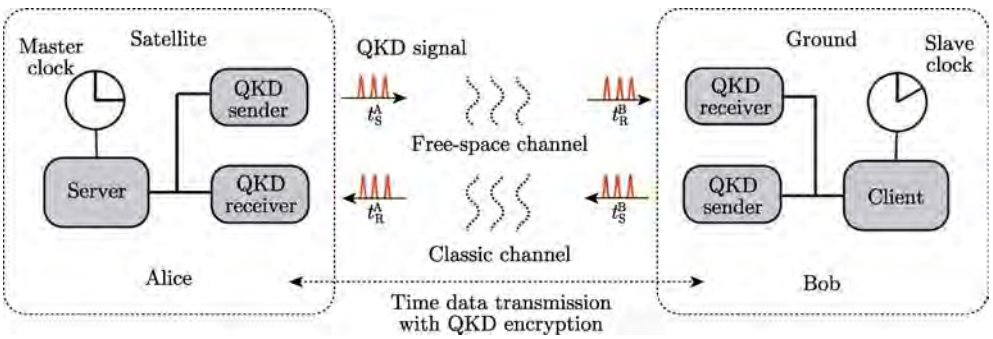

Fig. 2 Schematic of satellite-based QSTT

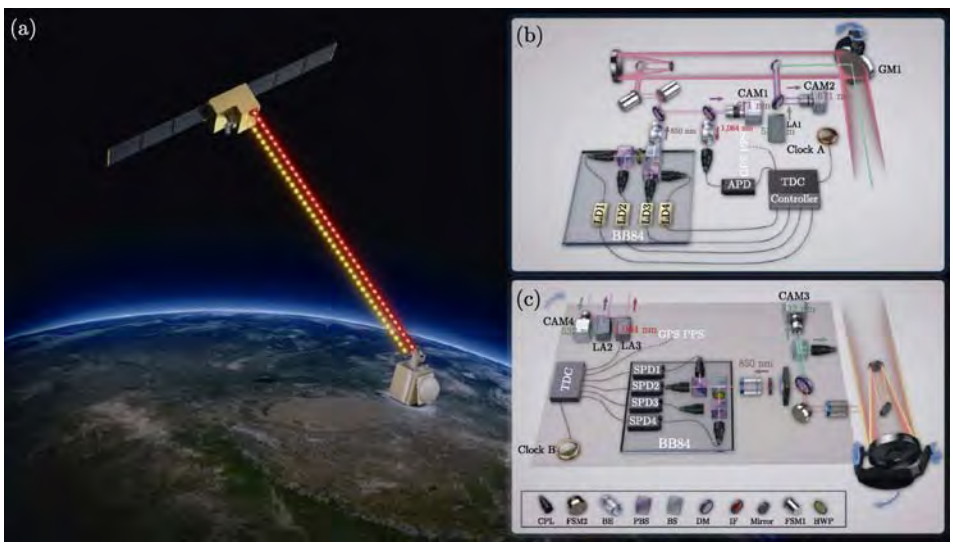

Fig. 3 Experimental set-up. (a) An overview of satellite-based QSTT. A two-way optical link is established between the Micius satellite and the Nanshan ground observatory. (b) Schematic of the transceiver on the satellite. (c) Schematic of the transceiver on the ground

Finally, the authors perform satellite-to-ground time synchronization using single-photon-level signals and achieve a quantum bit error rate of less than 1%, a time data rate of 9 kHz and a time-transfer precision of 30 ps. These results offer possibilities towards an enhanced infrastructure for a time-transfer network, whose security stems from quantum physics. We also anticipate that the findings of this study will generate new possibilities for a revolutionary quantum time-transfer network at a global scale.

3 Probing Gravity-induced Decoherence

The satellite Micius can also provide the feasibility for testing the entanglement decoherence induced by the gravitation of the Earth. Quantum mechanics and relativity form the bedrock of modern physics. General theory of relativity predicts a kind of exotic spacetime structure called Closed Time Curve (CTC). CTC is interesting because it violates causality and in principle can be formed from the quantum fluctuations of spacetime itself.

To theoretically describe the quantum fields in both exotic spacetime containing CTCs and ordinary spacetime, in recent years, scientists reported the event formalism of quantum fields. This theory predicts that the different evolutions of quantum fields may probabilistically induce time decorrelation of two entangled photons passed through different regions of curved spacetime, which are able to keep the entanglement in standard quantum theory. Considering about the curved spacetime brought by the Earth's gravitation, the decoherence effect can be tested via distributing entanglement between ground station and satellite.

Recently, Xu *et al.* implemented a quantum optical experimental test of event formalism of quantum fields using the Micius satellite[6]. We experimentally test a prediction of the theory that a pair of time-energy entangled particles probabilistically decorrelate passing through different regions of the gravitational potential of Earth.

In the implementation, polarization entangled photon pair is prepared in Ngari ground station, as shown in Figure 4. Photon in Path 2 is detected on the ground after passing through the ordinary spacetime, while its twin is received by the Micius satellite after propagating in the curved spacetime. Because the gravitation cannot induce the decoherence of

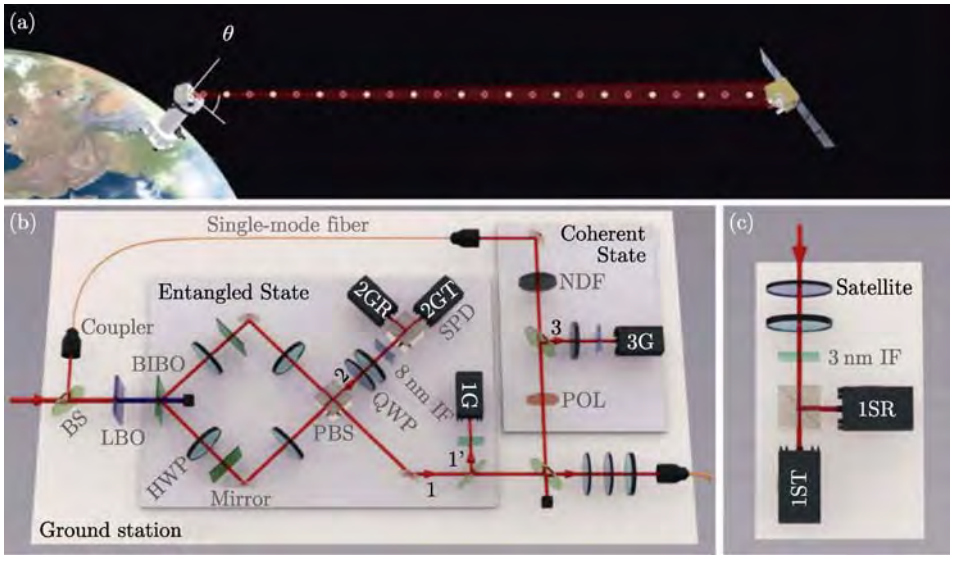

Fig. 4 Schematics of an experimental test of event formalism in Earth's gravitational field. (a) The ground station sends both entangled single photons and faint coherent laser pulses to the Micius satellite. (b) Preparation of entangled photon pairs and faint coherent laser pulses at the ground station. (c) Single photons received by the satellite are passed through polarization analysis and detected by single photon detectors

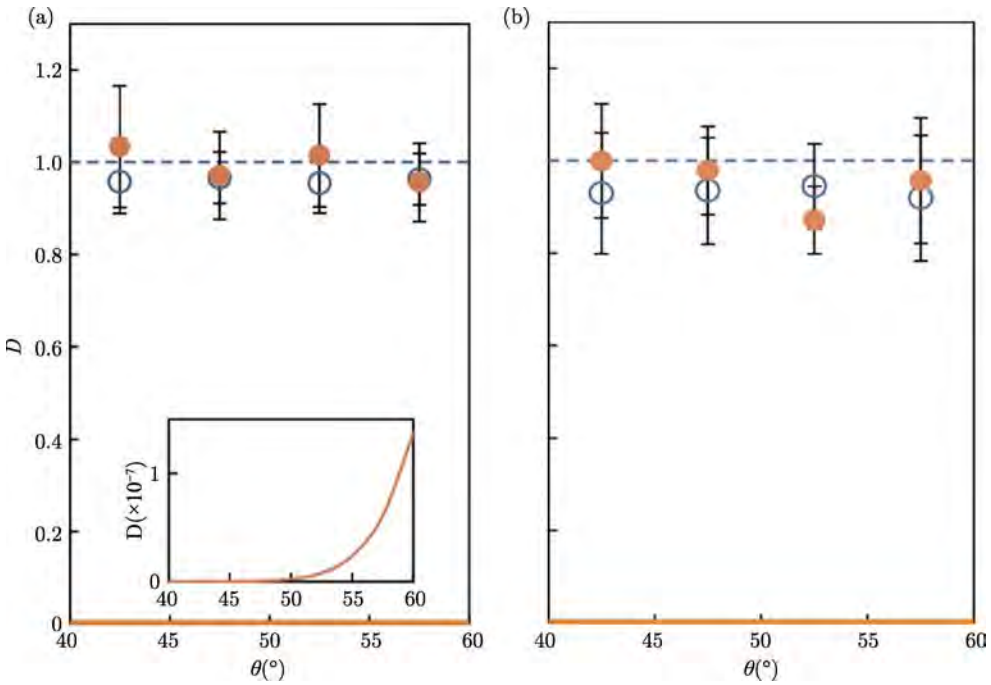

Fig. 5 Experimentally estimated decorrelation factors in different altitude angle of the satellite without (a) and with (b) fulfilling the non-signaling condition

classical correlation, the coherent laser is possible to be used as a reference. Before transmitting, the entangled photons are combined with the faint coherent laser pulses in Path 1. The transmitted coherent photons are classically correlated with the photons in Path 3 on the ground. Two trains of entangled and coherent photons are shifted by half a pulse interval about 6 ns, which make the satellite to distinguish the photons by their arrival times.

The experiment is implemented with and without fulfilling the no-signaling condition to account for the quantum collapse models. By using 1 km fiber to delay the photons in the ground station, the detection events of entangled photons on the ground and satellite are separated spacelike. By collecting data when the altitude angle of satellite varying from 40° to 60°, the estimated decoherence factors for both spacetime settings are shown in Figure 5. We then conclude that our experimental results are consistent with the descriptions of standard quantum theory and do not support the predictions of event formalism. The future testing of such model may be performed based on a satellite in a higher orbit.

References

[1] YIN J, CAO Y, LI Y H, *et al.* Satellite-based entanglement distribution over 1200 kilometers [J]. *Science*, 2017, **356**:1140-1144

[2] YIN J, CAO Y, LI Y H, *et al.* Satellite-to-ground entanglement-based quantum key distribution [J]. *Phys. Rev. Lett.*, 2017, **119**:200501

[3] YIN J, LI Y H, LIAO S K, *et al.* Entanglement-based secure quantum cryptography over 1120 kilometers [J]. *Nature*, 2020, **582**:501-505

[4] CAO Y, LI Y H, ZOU W J, *et al.* Bell test over extremely high-loss channel: towards distributing entangled photon pairs between Earth and the Moon [J]. *Phys. Rev. Lett.*, 2018, **120**:140405

[5] DAI H, SHEN Q, WANG C Z, *et al.* Towards satellite-based quantum-secure time transfer [J]. *Nat. Phys.*, 2020, **16**:848-852

[6] XU P, MA Y, REN J G, *et al.* Satellite testing of a gravitationally induced quantum decoherence model [J]. *Science*, 2019, **366**:132-135

HU Wenrui, KANG Qi, DUAN Enkui, LONG Mian. SJ-10 Recoverable Satellite for Space Microgravity Experiments. *Chin. J. Space Sci.*, 2020, **40**(5): 047-053. DOI:10.11728/cjss2020.05.047

SJ-10 Recoverable Satellite for Space Microgravity Experiments *

HU Wenrui[1,2] KANG Qi[1,2] DUAN Enkui[3] LONG Mian[1,2]

1 (*Institute of Mechanics, Chinese Academy of Sciences, Beijing* 100190)

2 (*School of Engineering Science, University of Chinese Academy of Sciences, Beijing* 100049)

3 (*Institute of Zoology, Chinese Academy of Sciences, Beijing* 100101)

Abstract SJ-10 is a recoverable scientific experiment satellite specially for the space experiments of microgravity physics science and space life science. This mission was officially started on 31 December 2012, and the satellite was launched on 6 April 2016. This paper introduces briefly the SJ-10 mission, the progress of SJ-10 engineering and the project constitution of sciences experiments onboard SJ-10. The purpose of this mission is to discover the law of matter movement and the rule of life activity that cannot be discovered on the ground due to the existence of gravity, and to know the acting mechanism on organisms by the complex radiation of space that cannot be simulated on the ground.

Key words Microgravity physics, Space life science, Space microgravity experiments, Recoverable satellite

Classified index V 524, V 4

1 Introduction

Shijian-10 (SJ-10) satellite is the second mission of the Strategic Priority Research Program (First-Stage) on Space Science, the Chinese Academy of Sciences (CAS). On 6 April 2016, at 01:38:04 BJT, Long March 2D was launched at Jiuquan Satellite Launch Center (Figure 1). And 559 seconds later, SJ-10 recoverable scientific experiment satellite was successfully sent into the near-circular orbit at the height of about 250 km. This is the 24th successful launch of China's recoverable satellite. In the past, we also carried out many microgravity science experiments with China's recoverable satellites.

Fig. 1 SJ-10 satellite was launched successfully at Jiuquan Satellite Launch Center

SJ-10 is the recoverable scientific experiment satellite specially for the space experiments of microgravity physics science and space life science. This mission was officially started on 31 December 2012. With the long period time in the microgravity environment and the radiation condition in space provided by SJ-10, a number of scientific and technological experimental studies on the law of matter movement and the rule of life activity were carried out through remote scientific and technological

* Supported by the Strategic Priority Research Program of the Chinese Academy of Sciences (XDA04020000) and United Funding from National Natural Science Foundation of China and Chinese Academy of Sciences

Received March 6, 2020

E-mail: wrhu@imech.ac.cn

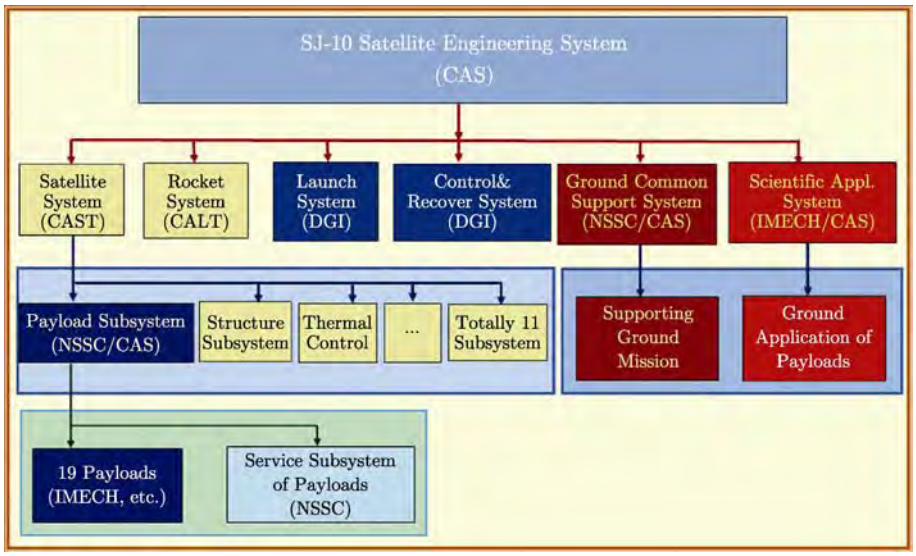

Fig. 2 Organization structure of SJ-10 engineering mission

methods and sample recovery analytic techniques of space experiments. These space experiments focused on some fundamental and hot issues in microgravity physics science and space life science, especially for the verification of the original physical model, the utilization of spacecraft technology and space environment, and the important applications and theoretical breakthrough in space science in the future. The purpose of this mission is to discover the law of matter movement and the rule of life activity that cannot be discovered on the ground due to the existence of gravity, and to know the acting mechanism on organisms by the complex radiation of space that cannot be simulated on the ground.

SJ-10 engineering includes six systems: Satellite, Rocket, Launching, Control and Recover, Ground Support, and Scientific Applications, as shown in Figure 2. The National Space Science Center of CAS is the general engineering management organization, the Institute of Mechanics of CAS is in charge of the scientific application system of the mission. Their tasks include overall organization, coordination, operation, and management of the scientific research work, as well as completing the planning and guiding the implementation of scientific experiments, *etc.*

2 Introduction on SJ-10 Engineering

There are 28 research topics on microgravity physics and space life science aboard the SJ-10 satellite, and they are integrated into 19 projects of payloads. Among them, there are 10 payloads about microgravity physics sciences, and the research fields include 3 subjects: microgravity fluid physics (A1), microgravity combustion science (A2), and space material science (A3). The satellite fully inherited China's recoverable satellite technology, and it is divided into the orbit capsule and the reentry capsule. All the 8 projects in the orbit capsule are about experiments of microgravity physics sciences, including 5 experimental payloads of fluid physics) and 3 experimental payloads of combustion, which all do not require sample recovery. In the reentry capsule, there are two experimental payloads about microgravity physics sciences: (i) synthetic furnace of multifunctional material in space; (ii) SCCO experimental payload of complex fluid, and nine other experimental payloads are all for life science research. All experimental samples in the reentry capsule need to be analyzed in the ground laboratory after the recovery.

The research and development of the payload

prototypes of SJ-10 were completed in September 2013. The development of engineering prototypes and flight prototypes was completed in December 2014 and January 2016 respectively. The total weight of the 10 experimental payloads of microgravity physics science is about 350 kg. Figure 3 shows the debugging and testing site of scientific experiment payloads and the satellite of SJ-10.

On 6 April 2016, four hours after the satellite was launched into the orbit, the orbit capsule firstly started the research experiment of colloidal crystals, and then the experimental payloads in the orbit capsule carried out cycled rounds of scientific experiments in a serial operating mode. In the reentry capsule, the experiment of SCCO payload lasted for 270 h, and the melting experiment on synthetic furnace of multifunctional materials accumulated totally 208 h with 6 working positions switched in turn. The scientific experimental data from the satellite were received by the three satellite ground stations of CAS at Miyun, Sanya and Kashi, and delivered to the integrated operating and control center of the ground support system at the National Space Science Center of CAS in Beijing in real time for primary processing; Then the first level data packages were distributed to the scientific experiment operating center of scientific application systems at the Institute of Mechanics of CAS. Scientists interpreted and processed the space experimental data on line and adjusted space experimental parameters, operating mode, and plans according to the space experimental status. After 12 days in orbit, the reentry capsule separated from the orbit capsule and returned to Siziwangqi recovery area in Inner Mongolia, China. The payloads and samples were disassembled on-site and taken back to laboratories for

(a)

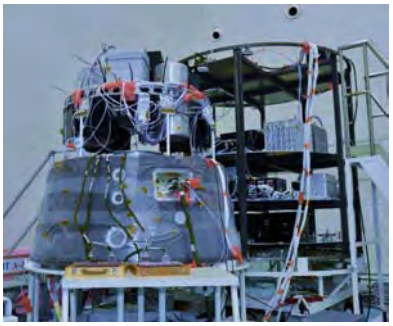

(b)

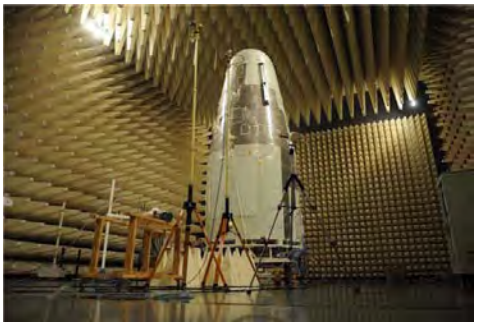

(c)

Fig. 3 Test of payloads and satellite (Photo courtesy of SJ-10 mission department) (a) Desktop test of payloads, (b) satellite test of payloads, (c) SJ-10 satellite test

post-processing. The orbit capsule continued to work 8 days in space to complete all the follow-up and expanded experiments.

3 Introduction to the Microgravity Physical Sciences Projects

The research on microgravity physical sciences depends heavily on advanced space technologies. It promotes the development of space science and applications. It fully demonstrates a country's ability in science and technology. It is an important driven force for the development of science and technology in the world. Therefore, microgravity physical sciences naturally become the hot subject of research in the world (especially in power countries in spaceflight). In recent years, the International Space Station (ISS) has become the main platform for research on microgravity physical sciences internationally. NASA, ESA, JAXA and Roskosmos/RKA established many special experimental racks for the research on microgravity physical sciences, and greatly improved the experimental platform in the space station to carry out studies on microgravity physical sciences. They are promoting the fast development of microgravity physical sciences at an unprecedented speed.

The study on microgravity physical sciences in China started in the late 1980s. Since then, more than ten batches of space experiments on microgravity physical sciences have been carried out mainly on Chine's recoverable satellites and Shenzhou spaceships. Chinese scientists have obtained some valuable first-hand experiences in space research, which has laid a good foundation for the development of this subject. In recent years, microgravity science, as an important content in space science, has been deeply demonstrated and planned for a medium and long term by the Strategic Priority Research Program on Space Science of CAS and China Space Station Program. Among the pre-research projects of the Strategic Priority Research Program on Space Science and the first batch of science projects of China Space Station Program, dozens of microgravity physical science projects have been supported.

Space experimental research on microgravity physical science in SJ-10 focuses on some frontier subjects in the field of microgravity science in the world, *i.e.,* microgravity fluid physics, microgravity combustion science, and space material science[4,5]. It is based on the fact that, some important physical processes could be understood clearly only in the long period time in the microgravity environment of space, and the research could increase people's knowledge of the laws of matter movement under the extreme condition of microgravity: the processes of convection, self-organizing and phase change, and the laws of heat and mass transfer; material ignition and combustion behavior, coal combustion mechanism under the microgravity condition; the growth and solidification processes of new material samples in the microgravity environment. It will improve and optimize engineering fluid and thermal power machinery as well as material processing technology on the ground and in space, obtain high-quality materials that are difficult to grow in the gravity field on the ground, and provide scientific basis and fundamental data for the safety of manned spacecraft in China and some major national requirements such as energy and carbon emission reduction, *etc.*

The project's objectives of microgravity physical sciences are as follows.

(1) Microgravity fluid physics. To study the internal mechanisms, dynamic processes and instabilities of heat and mass transfer in the convection and phase change (evaporation and boiling), and discover new laws and verify independently developed physical models; to verify the such molecule gas-liquid separation theory of granular gas; using a typical colloid system to study the establishment and evolution processes of the ordered phase driven by pure entropy, the establishment of liquid crystalline phase and the self-assembly mechanism of metal nano-particles; to accurately measure the Soret coefficient of the samples including Chinese petroleum, and study the cross diffusion rule of the multi-component medium.

(2) Microgravity combustion science. To dis-

cover the laws of ignition, combustion, flame spread, flue gas precipitation, soot emission and smoke distribution of typical non-metallic materials and wire insulations under microgravity condition; and to reveal the laws of pyrolysis, ignition, combustion and pollutant generation of typical coal of China under microgravity condition. To provide theoretical basis and technical support for ground combustion and space safety by microgravity research results.

(3) Space material science. To discover the selective occupation law of dopant atoms, the morphogenesis and evolution mechanisms of the alloy structure during the crystal growth process, and understand in depth the interface dynamics in the formation of materials from the melt and develop relative theories; to realize the mass transport process dominated by diffusion, and achieve a uniform and large scale semiconductor crystals, high-quality metal alloys and composite materials that are difficult to grow in the gravity field on the ground.

There are eleven space experiments on microgravity physical sciences.

4 Introduction to the Space Life Science Projects

The aforementioned projects attempt, from the viewpoint of space life science and biotechnology, to unravel the sensing and transduction mechanisms of various species under microgravity and space radiation and to develop the novel techniques in stem cell differentiation and embryonic development. Scientific issues are mainly focused on understanding the effect of space environment on the evolution of terrestrial life and the impact of space environment on the physiological homeostasis of organisms. Three specific aims are: (i) how do the terrestrial lives sense microgravity and/or space radiation signaling and what are the underlying transduction pathways; (ii) how do the organisms adapt themselves to the microgravity and/or space radiation environment; (iii) how are the microgravity and/or space radiation resources utilized to promote the perspective of space life science and the development of space biotechnology.

The outcomes of these projects would provide the fundamental understandings, propose new concepts, new ideas, and new methodology, and establish the integrated platforms in ground- or space-based studies for space life science and biotechnology. Expected results are to develop numerical simulation platforms and biologically-specific techniques and to further the understandings in sensation and transduction of microgravity and space radiation signaling for plant or animal cells or in tissue histogenesis.

4.1 Radiation Biology

The first project in this category, entitled "Molecular biology mechanism of space radiation mutagenesis", aims to (i) analyze the sequence information of genome methylation and transposon change caused by space radiation and explore the molecular mechanisms of space radiation induced genomic instability; to (ii) study the proteomics profiles of model organisms caused by different radiation qualities, mine the molecular mechanisms of functional proteins, and to establish the biological systems that evaluate radiation qualities. Plant and animal model organisms are located at three distinct radiation environments inside the satellite. By monitoring three tissue equivalent detector devices, the space radiation parameters such as absorbed dose, absorbed dose rate, linear energy transfer value, and dose equivalent are detected. The biological materials irradiated by different kinds of particles that belong to the same satellite orbit are then harvested and recovered. System biology analyses such as genome epigenetic scanning and proteomic approaches are conducted to obtain information of biological changes under different radiation qualities and to correlate biological effects with different radiation parameters.

The second project entitled "Roles of space radiation on genomic DNA and its genetic effects", attempts to elucidate the roles of space radiation on genomic DNA and its genetic effects in the real space environment in two aspects.

(1) Space radiation and genomic stability. Genomic stability of wild type and radiation-sensitive

mouse cells and fruit flies is investigated in pre- and post-flight or at different time points during the spaceflight. Quantitative parameters of space radiation of the genome and its genetic effects are then obtained in the real space environment.

(2) Gene expression profiles and sensitive response genes to space radiation. Gene expression profiles are obtained from the above mouse cells and of fruit flies. Novel and sensitive biological molecules are identified as space radiation markers. This work provides novel information for developing evaluation methods for the risk factors and protection tools against space radiation.

The third project, entitled "Effects of space environment on silkworm embryo development and mechanism of mutation", applies the selected silkworm embryos to pursue the following contents: (i) gene expression pattern of embryo under real space environment; (ii) proteome of silkworm embryo; (iii) mutation discovery and functional analysis; and (iv) embryo development and its characterization. Systematic approaches of the embryo development design and multiple sampling throughout the entire developmental stages are performed under space environment. Multiple platforms of gene expression, proteomics, and functional genomics, are employed to unravel the development characteristics of the silkworm in space and to find out the possible mutations through molecular approaches.

4.2 Gravitational Biology

The first project in this category, entitled "Biological effects and the signal transduction of microgravity stimulation in plants", focuses on elucidating the effects of microgravity (weightless) environment in space on plant growth and the molecular mechanisms underlined in two specific aims: (i) whether plant's sensation of the weight loss is also mediated by statoliths or other mechanisms; and (ii) whether there are any differences in transduction cascades between weight loss and gravitropic signaling. The hypothesis that the rigidity of the supporting tissue (*i.e.*, the cell wall in the plant) is regulated by microgravity is tested to understand how space microgravity affects the rigidity of plant cell wall and the metabolism of the plant cell wall, which in turn manipulates the growth of plants.

The second project, entitled "Biomechanics of mass transport of cell interactions under microgravity", attempts to (i) develop a novel space cell culture hardware consisting of the precisely controlled flow chamber and gas exchange system and to investigate the mass transport mechanisms in cell growth and cell-cell interactions under microgravity; and to (ii) distinguish the direct responses of cells from those indirect responses *via* the varied mass transport conditions induced by gravity changes. New data sets on the metabolism, proliferation, apoptosis, differentiation, and cytoskeleton of osteoblasts and mesenchymal stem cells are collected under well-defined mass transfer. This work provides an insight into quantifying the direct cellular responses in space, revealing the effects of gravity on cell-cell interactions, elucidating the mechanisms of cell growth and differentiation in space, and overcoming the methodological bottlenecks of space cell biology studies.

The third project, entitled "Photoperiod-controlling flowering of *Arabidopsis* and rice in microgravity", aims at deciphering how space microgravity regulates the transportation of flowering signals from leaf to shoot apex at a molecular level. Using transgenic *Arabidopsis thaliana* and rice plants (expressing FT or Hd 3a gene with the reporter genes GFP or GUS), living fluorescence imaging technique is developed to determine the induction of FT and Hd3a gene expression and floral initiation in shoot apex under long-day and short-day photoperiod condition under space microgravity or in normal gravity on the ground. This work sheds light on regulating mechanisms of photoperiod controlled flowering in both *Arabidopsis thaliana* and rice by microgravity.

4.3 Space Biotechnology

The first two projects, entitled "Three-dimensional cell culture of neural and hematopoietic stem cells in space", share the same hardware in SJ-10 satellite. They aim to understand whether microgravity environment is suitable for the self-renewal and differentiation of hematopoietic or neural stem cells. Three-dimensional cell culture of hematopoietic stem

cells and neural stem cells is conducted in space. With microscopic detection, image transmission, and gene/protein analysis through the recovered samples, the effects of microgravity on the self-renewal/differentiation of two types of stem cells are tested to reveal the characteristics of growth and differentiation of these 3D cultured stem cells under microgravity. The outcomes are crucial in regenerative medicine for the treatment of various blood diseases and neural injury, respectively.

5 Conclusion

The China National Space Administration (CNSA) promotes the microgravity experiments onboard the Chinese recoverable satellite in the period of late last century and early this century. The Program of SJ-8 recoverable satellite launched on 9 September 2006 was organized jointly by CNSA and the Chinese Academy of Sciences (CAS). The recoverable capsule was used for the breeding experiments, and the unrecoverable capsule was used for microgravity experiments which scientific results were summarized in Ref.[1]. The SJ-10 Mission was formally organized and then determines by CNSA in May 2006. Unfortunately, the engineering phase was stopped at the beginning due to the reform of CNSA, and then the missions of scientific satellite were moved from CNSA to CAS in 2011. The CAS restarted the demonstration phase at the end of 2012, and the engineering phase since the beginning of 2013. The introduction was published for the scientific program in Ref.[2], and for the experiments on the grand in Ref.[3].

A grant was supported jointly by the CAS and National Natural Science Foundation for research of space experiments, and the experimental results were summarized in two books published respectively by Science Press (Beijing) and Springer [4,5].

Acknowledgements The authors are grateful for all the individuals and institutions to implement the SJ-10 mission. They are (but not limited to) Prof. YIN Hejun and Prof. XIANGLI Bin as Chief of the mission, Prof. WU Ji as Acting Chief of the mission, Prof. TANG Bochang as the Chief Designer of the mission, Prof. MENG Xin as the Deputy Chief of mission; Prof. HUANG Chengguang as the Chief Commander of scientific application system; Prof. ZHANG Xiaohui, ZHAO Huiguang, QIU Jiawen, and XUE Changbin as the Director of SJ-10 engineer, satellite, and payload. The authors also acknowledge all the colleagues, experts, engineers, administrators, and participants from the six systems of Satellite, Rocket, Launching, Control and Recover, Ground Support, and Scientific Applications for the SJ-10 satellite mission. We are also particularly grateful to our scientist/payload teams.

References

[1] HU W R. Microgravity experiments on board the Chinese recoverable satellite [J]. *Microgravity. Sci. Tech.*, 2008, **20**(2):59-60

[2] HU W R, ZHAO J F, LONG M, *et al.* Space program SJ-10 of microgravity research [J]. *Microgravity Sci. Tech.*, 2014, **26**(1):59-69

[3] ZHAO J F, KANG Q. Ground-based researches related to microgravity science experiments aboard SJ-10 [J]. *Microgravity Sci. Tech.*, 2016, **28**(2):79-188

[4] HU W R, KANG Q. Physical Science under Microgravity: Experiments on Board the SJ-10 Recoverable Satellite [M]. Beijing: Science Press and Springer, 2019

[5] DUAN E K, LONG M. Life Science in Space: Experiments on Board the SJ-10 Recoverable Satellite [M]. Beijing: Science Press and Springer, 2019

ZHANG Shuangnan. Progress Report on Insight-HXMT: China's First X-ray Astronomy Satellite. *Chin. J. Space Sci.*, 2020, **40**(5): 054-060. DOI:10.11728/cjss2020.05.054

Progress Report on Insight-HXMT: China's First X-ray Astronomy Satellite

ZHANG Shuangnan

(*Institute of High Energy Physics, Chinese Academy of Sciences, Beijing* 100049)

Abstract Insight-HXMT is China's first X-ray astronomy satellite. It was launched on 15 June 2017 and is currently in service smoothly. Insight-HXMT has been used to scan the Galactic plane repeatedly, making pointing observations to neutron stars and black holes, and monitor the whole sky continuously in the MeV band. Insight-HXMT is also very flexible in making ToO observations, with the response time from about 3 hours to within a day. So far more than 50 refereed publications have been made with data from its observations; many more publications have used the data or results of Insight-HXMT one way or another. The scientific impacts of Insight-HXMT have been growing rapidly since launch. We expect Insight-HXMT to continue to operate for several more years.

Key words X-ray astronomy, Black holes, Neutron stars, Gamma-Ray Bursts (GRBs)

Classified index V 474, P 111

1 Mission Overview

Insight-HXMT, shown in Figure 1, is China's first X-ray astronomy satellite. It was launched on 15 June 2017 and is currently in service smoothly[1]; the nominal mission lifetime is 4 years. There are three main instruments onboard Insight-HXMT, the high energy X-ray telescope (20~250 keV for pointing observations and 0.2~3 MeV for all-sky monitoring, 5100 cm^2)[2], the medium energy X-ray telescope (8~35 keV, 952 cm^2)[3], and the low energy X-ray telescope (1~12 keV, 384 cm^2)[4]. The effective areas of the three X-ray telescopes for pointing observations are shown in Figure 2. For all-sky monitoring, the effective areas of the HE/CsI in two modes are shown in Figure 3, in comparison with most of the other all-sky monitors in similar energy bands.

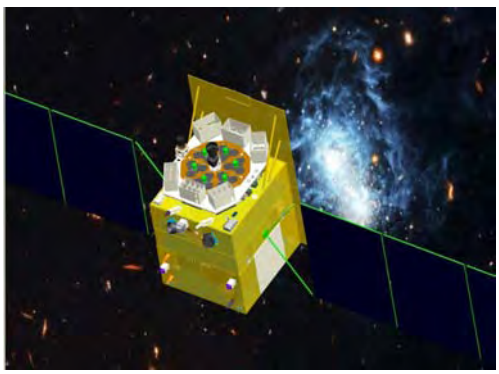

Fig. 1 A cartoon of Insight-HXMT

The main scientific objectives of Insight-HXMT are: (i) to scan the Galactic Plane to find new transient

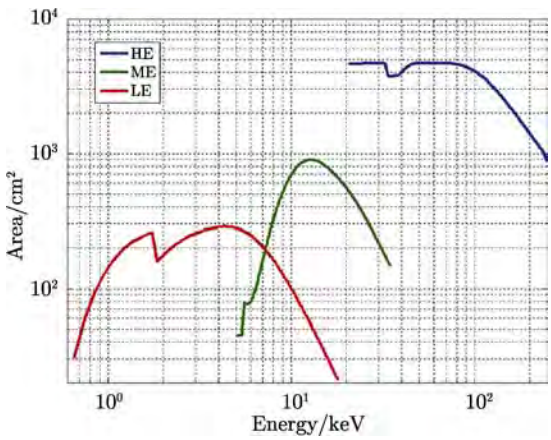

Fig. 2 Effective areas of the three telescopes (HE, ME and LE) of Insight-HXMT for pointing observations[1]

Received March 22, 2020

E-mail: zhangsn@ihep.ac.cn

sources and to monitor the known variable sources; (ii) to observe X-ray binaries to study the dynamics and emission mechanism in strong gravitational or magnetic fields; (iii) to monitor and study Gamma-Ray Bursts (GRBs) and Gravitational Wave Electromagnetic counterparts (GWEM).

2 Highlights of Insight-HXMT's Scientific Results

2.1 Galactic Plane Scanning Survey and Source Monitoring

Insight-HXMT has better capability in sky survey for weak and variable sources than other hard X-ray telescopes, thanks to its large effective area and narrow field of view in hard X-ray band. It will perform deep and high cadence survey of hard X-ray transient sources in the galaxy, produce the catalog of hard X-ray sources in the galaxy, and find some new hard X-ray variable sources or new phenomenon of hard X-ray emission. By 28 November 2019, Insight-HXMT has carried out 1322 small sky area scanning survey, which had fully covered the Galactic plane[6] (Figure 4); so far Insight-HXMT has been monitoring more than 2128 known sources. Figure 5 shows the result of an individual scanning observation.

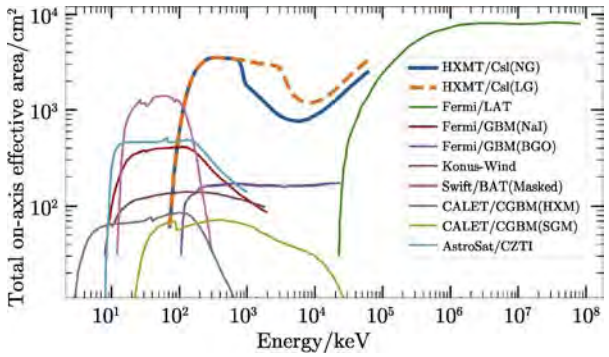

Fig. 3 Effective areas of Insight-HXMT/CsI and other gamma-ray monitors in operation. An averaged effective area over the unocculted sky is plotted for Fermi/GBM (NaI)[5]

2.2 New Window to Explore Black Holes and Neutron Stars with High Energy Timing and Spectral Observations

Insight-HXMT has a very wide energy band (1~250 keV) that covers both soft and hard bands of X-ray binaries. HE (20~250 keV) has the largest effective area among the space telescopes with narrow Field of View (FOV), which is an advantage in observing the X-ray binary outbursts and evolution in low/hard spectral state. Its soft X-ray band covers the energy as low as 1 keV and has adequate energy

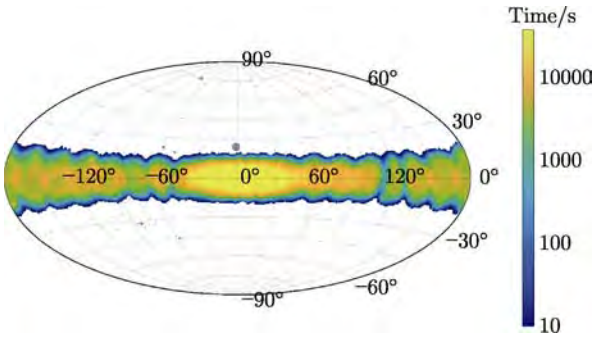

Fig. 4 Exposure map of the Galactic plane survey[6]

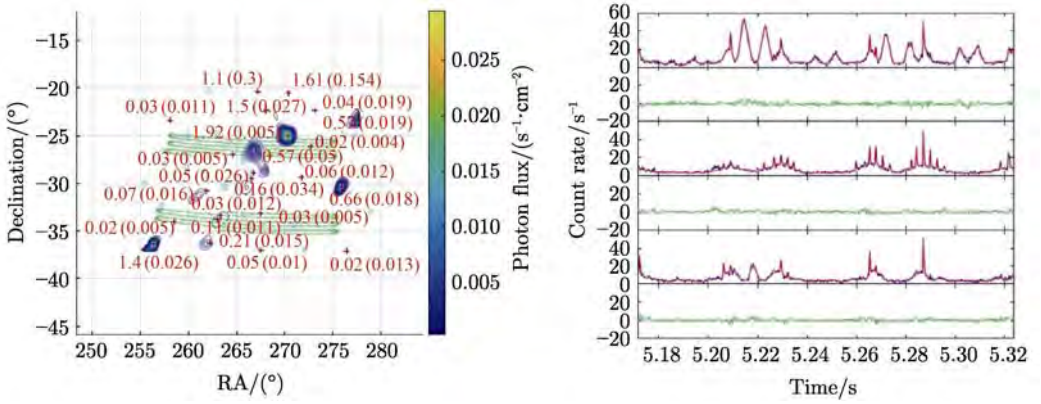

Fig. 5 Data processing result of an individual scanning observation with an improved direct demodulation method. (a) is the reconstructed sky map, while (b) is the comparison between the observed and predicted count rates (b) in three groups of LE detectors with three different orientations[7]

and time resolution. It can avoid the problem of detector saturation (photon pile-up) when observing bright sources, and has advantages in observing bright sources in soft X-ray energy band and outbursting sources in high/soft spectral state. Thus, Insight-HXMT will bring broad-band and high statistical observation samples for bright and outbursting sources in 1~250 keV. Such results can be used to study systematically on each spectrum of outburst and evolution of an X-ray binary, such as the low/hard state and high/soft state, to study the basic properties of a BH, the accretion disk behavior near its horizon, and to measure its spin. It will also help us to understand the basic characteristics of NSs, to study the magnetospheric characteristics and measure the magnetic field strength of NSs surface. For the overview on the mission and recent progress please refer to Ref.[1].

Figure 6 shows the RMS of the type-C Quasi-Periodic Oscillation (QPO) as a function of photon energy from the black hole X-ray binary candidate MAXI J1535-571 observed by Insight-HXMT[8]. It is the first time for Insight-HXMT to extend the RMS-energy study to the whole 1~100 keV energy band; previously the highest energy reached is around only 30 keV. The highest energy QPO (above 200 keV) was discovered with Insight-HXMT in the new black hole X-ray binary MAXI J1820+070[9] (Figure 7). The phase lag of the LFQPO is constant around zero below 30 keV, and becomes a soft lag above 30 keV. The soft lag gradually increases with energy and its maximum value is 1.3 s in the 150~200 keV band. The detection at high energies, the large soft lag, and the energy dependent behaviors of the LFQPO pose a great challenge for most currently existing models. These findings suggest that the LFQPOs probably originate from the precession of a small-scale jet[9]. Insight-HXMT observed the outburst of GRO J1008-57 and measured the CRSF line at around 85 keV at a significance more than 20

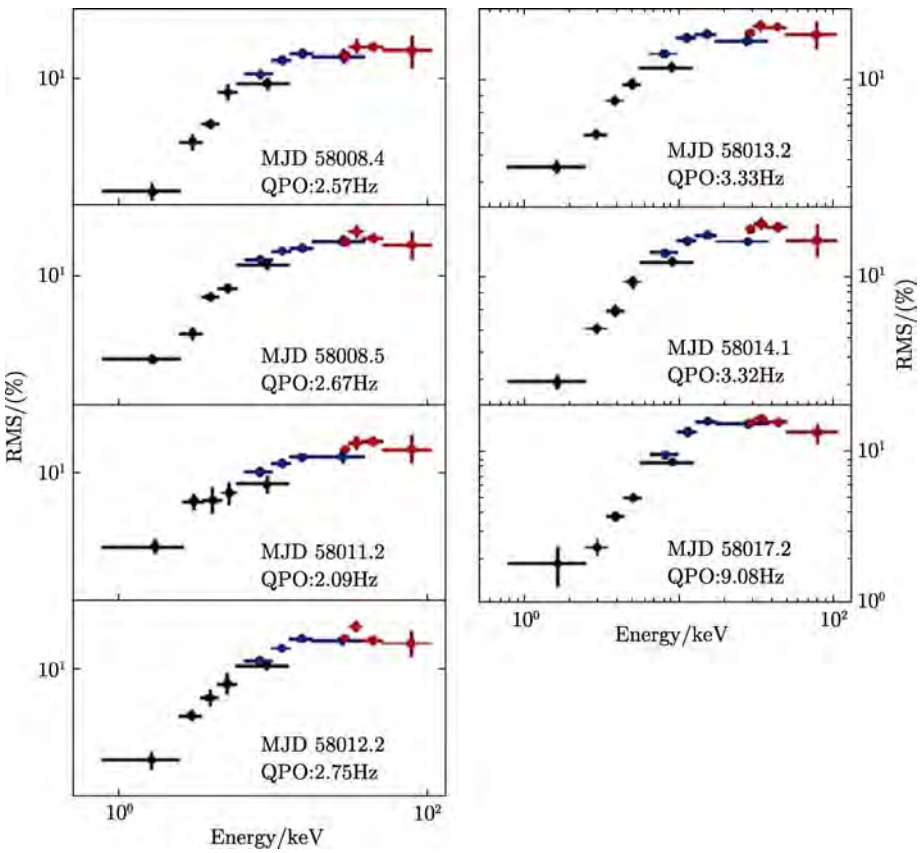

Fig. 6 RMS of Type-C QPO as a function of the photon energy of the BH candidate MAXI J1535-571 observed by Insight-HXMT. The results of LE, ME and HE are plot as black, blue and red dots, respectively[8]

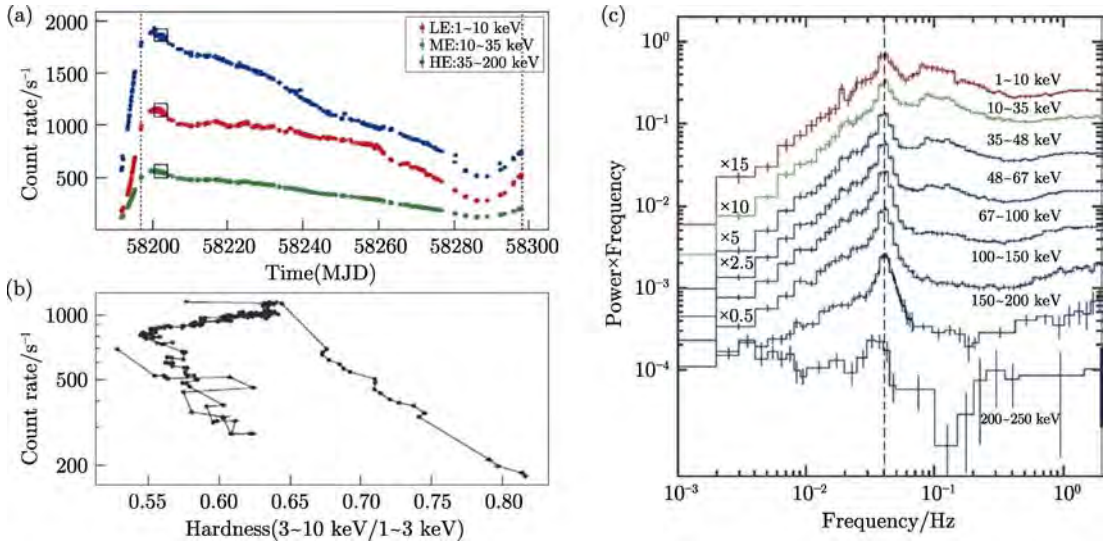

Fig. 7 Highest energy QPO discovered in MAXI J1820+070[9]

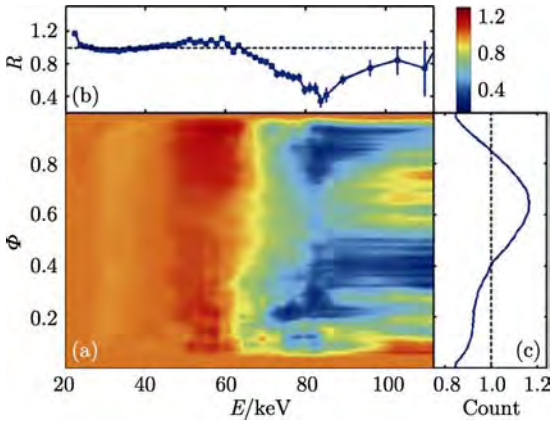

Fig. 8 CRSF around 80 keV detected in GRO J1008-57 with Insight-HXMT[10]

sigma[10] (Figure 8). Such a detection reveals so far the highest centroid energy that is measured directly from the NS system.

Type I X-ray bursts are thermonuclear explosions that occur on the surface of accreting NS in binary systems, which usually lasts for dozens to hundreds of seconds. Previous results from other satellites/telescopes had suggested a cooling corona during the thermonuclear bursts, based on the data combined by tens to hundreds of bursts. However, with Insight-HXMT observation, the cooling corona phenomenon had been found in a single burst of the NS X-ray binary 4U 1636-536. It is the first time that the decrease of hard X-ray emission has been found in the spectra of Type I burst on a time scale of seconds, as shown in Figure 9[11].

Concerning Z- and atoll-sources, although for Sco X-1 the kilo Hz QPO has been detected already, its origin remains a puzzle in the last 20 years, partially because of no detection of the kilo Hz QPO at high energy. Insight-HXMT detected for the first time the kilo Hz QPO from Sco X-1 at energy above 20 keV. Since X-rays at energy above 20 keV are not likely dominated by the disk emission, such a detection challenges the current popular kilo Hz QPO models[12] (Figure 10).

Insight-HXMT observed thoroughly the outburst of the first Galactic Ultra-Luminous X-ray source (ULX) Swift J0243.6+6124. The accumulated high cadence observations and high statistic data allow for systematical study of the source property, especially on the NS accretion and spin evolution. These studies revealed that near two critical luminosities the source was observed to have transitions in pulse profile, power spectrum, and energy spectrum[13] (Figure 11). The transition at higher critical luminosity denotes the transform of the disk accretion mode from gas pressure to radiation pressure dominated disk, which is consistent with the theoretical prediction made half a century ago. Similar behavior was detected as well in the HXMB 2S 1417-624[14].

2.3 MeV Gamma-ray All-sky Monitoring for Explosive Events

As shown in Figure 3, Insight-HXMT is the most sensitive all-sky monitor currently in operation, in the MeV energy region with modest energy resolution

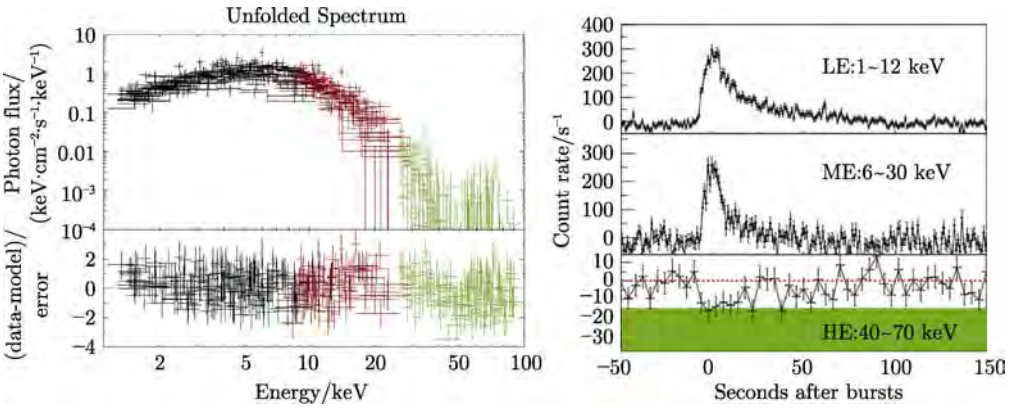

Fig. 9 Spectrum and light curves of Type-I X-ray burst of 4U 1636-536[11].

(a) Vertical axis is flux, (b) vertital axis is counts per second

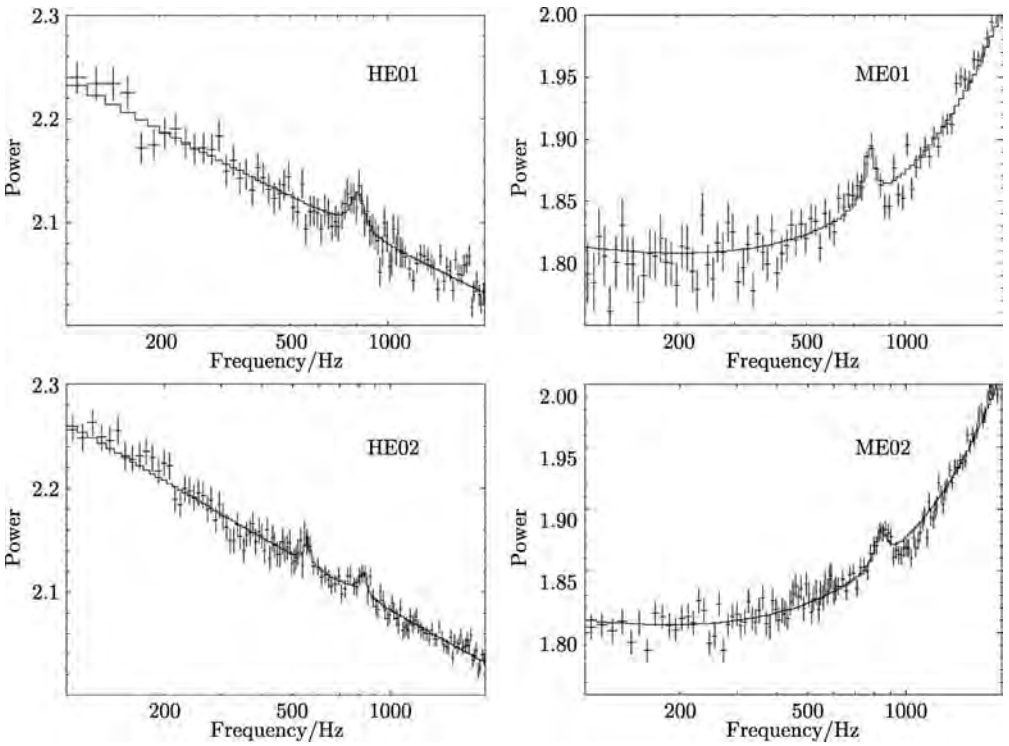

Fig. 10 High energy QPOs in Sco X-1 observed with Insight-HXMT[12]

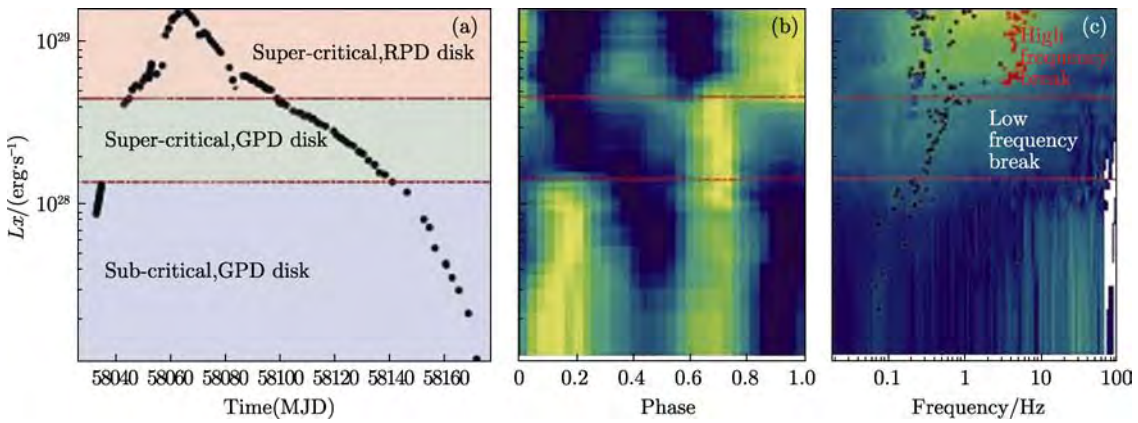

Fig. 11 Outburst evolution of the Galactic ULX Swift J0243.6+6124 monitored by Insight-HXMT[13], where MJD stands for Modified Julian Date

but excellent timing resolution. Insight-HXMT contributed to the observations of the electromagnetic counterpart of the first double neutron star merging event producing the GW20170817A gravitational event[15,16]. However, it does not have an in-flight trigger and real-time downlink, and thus all GRBs are found by the ground search of the CsI event data. Both blind search and targeted search have been implemented in the GRB processing pipeline. By using a much finer search parameter, the targeted search could find weaker GRBs than blind search. In general, the Insight-HXMT detection sensitivity to GRB prompt emission (in 0.2~3 MeV) could reach about 8×10^{-8} erg·cm^{-2} (10~1000 keV), as shown in Figure 12.

Since event data is recorded for CsI detector, the time accuracy of gamma-ray monitoring data is about several microseconds. In addition, CsI detector has an effective area of thousands square centimeters, which allows CsI to measure the fine temporal features of GRBs in MeV band. Figure 13 gives the Light curve of GRB170904A detected by Insight-HXMT/HE CsI detector.

Insight-HXMT can also monitor the MeV pulsars with this gamma-ray all-sky monitoring observation scenario. Especially, Gamma-ray emission from the Sun and the Earth could be monitored as well, including Solar Flares and Terrestrial Gamma-ray Flash (TGF).

TGF is a very short period (about 0.1 ms) of gamma-ray emission produced in the lightning process. Insight-HXMT can detect about 100 TGFs per year. The observation data of a typical TGF is shown in Figure 14. Figure 15 is the distribution of sub-satellite points of Insight-HXMT when TGFs were detected. Most TGFs were produced in the active region of lightning.

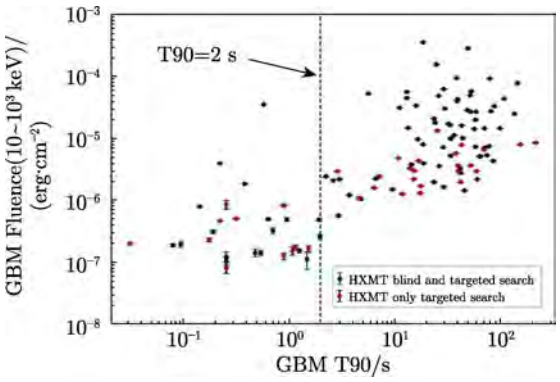

Fig. 12 GRBs jointly detected by Insight-HXMT and Fermi/GBM. Those GRBs in green could be found by both blind search and targeted search, while red ones are only revealed by targeted search

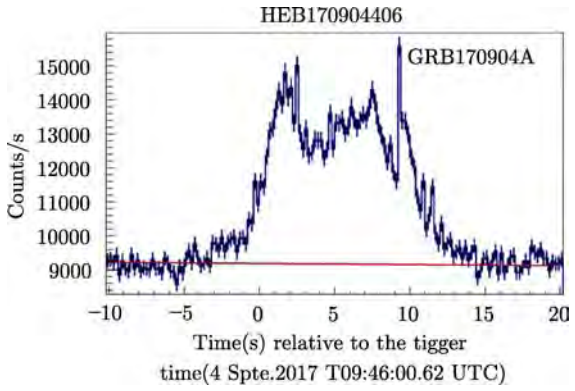

Fig. 13 Light curve of GRB170904A detected by Insight-HXMT/HE CsI detector. Fine temporal features (*e.g.* spikes) are seen with high statistics

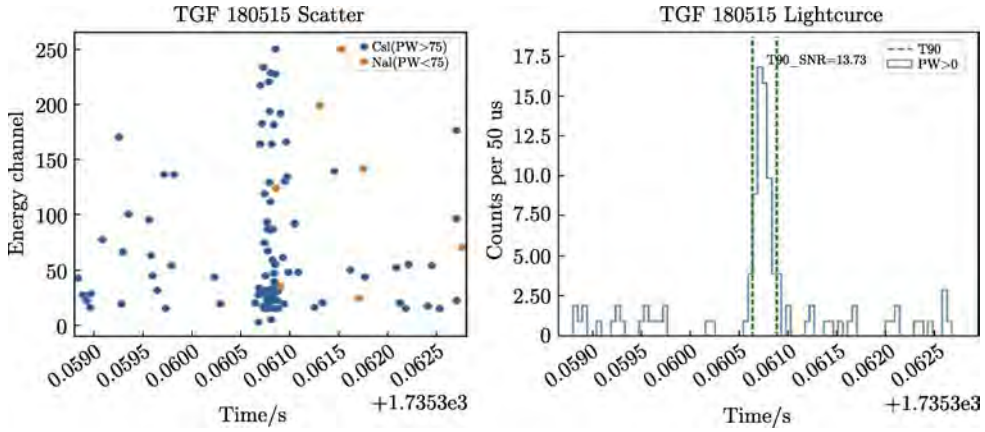

Fig. 14 Observation data of TGF180515. (a) Scatter plot of event data. (b) Light curve of the TGF. Dashed green lines indicate the time interval of T90

Finally, it should be pointed out that Insight-HXMT is very flexible in making ToO observations, either pre-approved or *ad hoc*, with the response time from about 3 h to within a day. So far more than 30 refereed publications have been made with data from its observations; many more publications have used the data or results of Insight-HXMT one way or another. Figure 16 shows all publications in which HXMT was mentioned. It is evident that the scientific impacts of Insight-HXMT have been growing rapidly since launch on 15 June 2017. Currently, all its instruments are performing normally and there are no consumables onboard and satellite's orbit can be maintained for about five more years. We therefore expect Insight-HXMT to continue to operate for several more years.

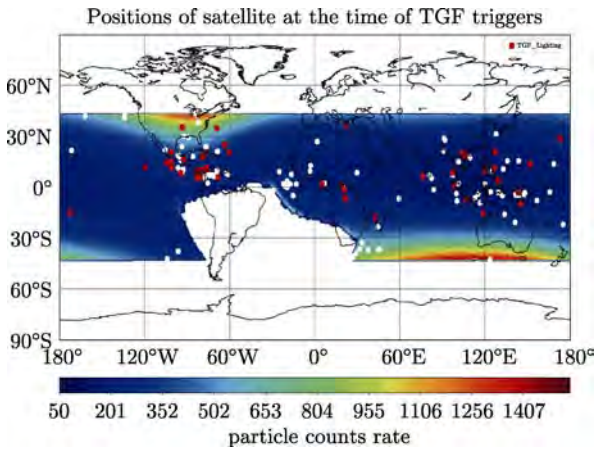

Fig. 15 Distribution of sub-satellite points of Insight-HXMT when TGFs were detected. Red blocks are TGFs with lightning association while white dots are without lightning association

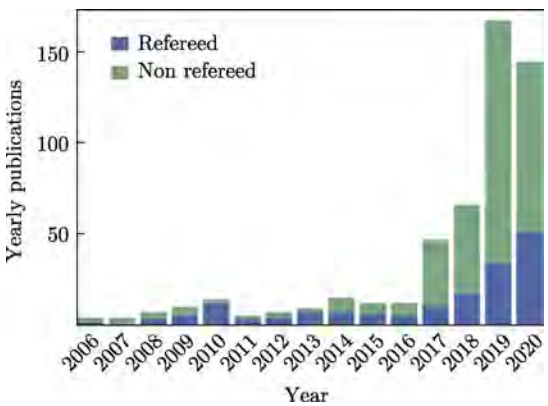

Fig. 16 Yearly publications in which HXMT was mentioned explicitly (From https://ui.adsabs.harvard.edu/, searched on 25 August 2020 with full text HXMT since 2006)

References

[1] ZHANG S N, LI T P, LU F J, *et al.* Overview to the hard X-ray modulation telescope (Insight-HXMT) satellite [J]. *Sci. China-Phys. Mech. Astron.*, 2020, **63**(4):249502

[2] CAO X L, JIANG W C, MENG B, *et al.* The Medium Energy (ME) X-ray telescope onboard the Insight-HXMT astronomy satellite [J]. *Sci. China-Phys. Mech. Astron.*, 2020, **63**(4):249504

[3] LIU C Z, ZHANG Y F, LI X F, *et al.* The High Energy X-ray telescope (HE) onboard the Insight-HXMT astronomy satellite [J]. *Sci. China-Phys. Mech. Astron.*, 2020, **63**(4):249503

[4] CHEN Y, CUI W W , LI W, *et al.* The Low Energy X-ray telescope (LE) onboard the Insight-HXMT astronomy satellite [J]. *Sci. China-Phys. Mech. Astron.*, 2020, **63**(4):249505

[5] LUO Q, LIAO J Y, XIONG S L, *et al.* Calibration of the instrumental response of Insight-HXMT/HE CsI detectors for gamma-ray monitoring [J]. *J. High Energy Astrophys.*, 2020, **27**:1-13

[6] SAI N, LIAO J Y, LI C K, *et al.* Methodology and performance of the two-year galactic plane scanning survey of Insight-HXMT [J]. *J. High Energy Astrophys.*, 2020, **26:**1-10

[7] GUAN J, LU F J, ZHANG S, *et al.* A modified direct demodulation method applied to Insight-HXMT Galactic plane scanning survey [J]. *J. High Energy Astrophys.*, 2020, **26**:11-20

[8] HUANG Y, QU J L, ZHANG S N, *et al.* INSIGHT-HXMT observations of the new black hole candidate MAXI J1535-571: timing analysis [J]. *Astrophys. J.*, 2018, **866**:122

[9] MA X, *et al.* Discovery of oscillations above 200 keV in a black-hole X-ray binary with Insight-HXMT [J]. *Nature Astron.*, 2020 (in press)

[10] GE M Y, JI L, ZHANG S N, *et al.* Insight-HXMT firm detection of the highest-energy fundamental cyclotron resonance scattering feature in the spectrum of GRO J1008-57 [J]. *Astrophys. J.*, 2020, **899**(1):L19

[11] CHEN Y P, ZHANG S, QU J L, *et al.* Insight-HXMT observations of 4U 1636-536: corona cooling revealed with single short Type-I X-Ray burst [J]. *Astrophys. J.*, 2018, **864**:L30-L35

[12] JIA S M, BU Q C, QU J L, *et al.* Insight-HXMT studies of the timing properties of ScoX-1 [J]. *Astrophys. J.. High Energy Astrophys.*, 2020, **25**:1-9

[13] DOROSHENKO V, ZHANG S N, SANTANGELO A, *et al.* (Insight-HXMT team) hot disk in swift J0243 revealed by HXMT-Insight [J]. *Month. Not. Roy. Astron. Soc.*, 2020, **491**:1857-1867

[14] JI L, DOROSHENKO V, SANTANGELO A, *et al.* Timing analysis of 2S 1417-624 observed with NICER and Insight-HXMT [J]. 2020, *Month. Not. Roy. Astron. Soc.*, **491**:1851-1856

[15] ABBOTT B P, ABBOTT R, ABBOTT T D, *et al.* Multi-messenger observations of a binary neutron star merger [J]. *Astrophys. J.*, 2017, **848**:L12-L71

[16] LI T P, XIONG S L, ZHANG S N, *et al.* Insight-HXMT observations of the first binary neutron star merger GW170817 [J]. *Sci. China: Phys. Mech. Astron.*, 2018, **61**(3):031011

ZHANG Peng, YANG Zhongdong, LIU Yi, YANG Dongxu, BI Yanmeng, LIN Manyun, WANG Qian, LIU Chengbao, XIAN Di, YAO Lu, LÜ Daren. Recent Progress of TanSat In-flight Performance, Data, and Applications. *Chin. J. Space Sci.*, 2020, 40(5): 061-069. DOI:10.11728/cjss2020.05.061

Recent Progress of TanSat In-flight Performance, Data, and Applications

ZHANG Peng[1] YANG Zhongdong[1] LIU Yi[2,3] YANG Dongxu[2,3] BI Yanmeng[1]
LIN Manyun[1] WANG Qian[1] LIU Chengbao[1] XIAN Di[1] YAO Lu[2,3] LÜ Daren[2,3]

1 (*National Satellite Meteorological Center, China Meteorological Administration, Beijing* 100081)
2 (*Key Laboratory of Middle Atmosphere and Global Environment Observation, Institute of Atmospheric Physics, Chinese Academy of Science, Beijing* 100029)
3 (*University of Chinese Academy of Sciences, Beijing* 100049)

1 General Introduction

TanSat is the first Chinese mission for global carbon dioxide (CO_2) monitoring. It is a research and development program jointly supported by the Ministry of Science and Technology of China (MOST), the Chinese Academy of Sciences (CAS), and the China Meteorological Administration (CMA). Since the successful launch on 22 December 2016, TanSat has being operated on the orbit for more than 3 years. TanSat has an about 702 km altitude Sun-synchronous orbit with about 98.16° inclination, 13:39 mean local time (ascending), and a 16-day (233 orbits) ground track repeat period[1].

TanSat carries the Atmospheric CO_2 Grating Spectrometer (ACGS) and the Cloud and Aerosol Polarization Imager (CAPI). ACGS sounding records will be used to retrieve XCO_2, while data from CAPI will be used to correct cloud and aerosol interferences. ACGS is a high-spectral resolution, 3-channel imaging grating spectrometer. It records spectra of reflected sunlight within the 0.76 μm O_2 A-band, and the CO_2 bands centered near 1.61 μm (WCO_2) and 2.06 μm (SCO_2)[2,3]. The spectral resolving power of ACGS is about 19000, 12800, and 12250 in the O_2 A-band, WCO_2, and SCO_2 band, respectively. More detailed specifications of ACGS are presented in Table 1, which gives all of the major spectral and

Table 1 Major spectral and radiometric specifications

	O_2 A	WCO_2	SCO_2
Dynamic range/(mW·m^{-2}·sr^{-1}·nm^{-1})	SNR=1@3.1e-02-362.17	SNR=1@7.06e-03-60.50	SNR=1@5.8e-03-15.50
SNR@(mW·m^{-2}·sr^{-1}·nm^{-1})	360@15.2	250@2.60	180@1.10
Abs/Rel Calibration error/(%)	<5%/<3%		
Calibration Nonlinearity error/(%)	<2%		
Dark Current (DNs) error	<5 DNs (After correction)		
Radiance response uniformity/(%)	>99.9% @ interior of band; >99% between bands		
Spectral ranges/nm	758~778	1594~1624	2042~2082
Spectral resolutions/nm	0.033~0.047	0.120~0.142	0.160~0.182
Spectral Sampling Number/FWHM	>2		
IFOV	2 km×2 km		
Frame rate/Hz	about 3		

Received August 24, 2020

radiometric parameters.

TanSat uses a pointing mirror in conjunction with satellite platform motions to point the ACGS boresight at the nadir, sun glint, or stationary surface targets. This measurement approach is expected to collect spectra with the sensitivity and accuracy needed to estimate XCO_2 with random errors of 1~4 ppm (0.25% to 1%) on regional scales (500 km× 500 km) at monthly intervals[4,5].

2 Calibration Procedure

2.1 Radiometric Calibration

The focal planes are read out in non-dimensional Digital Numbers (DN, Defined with math symbol of N_D). The first data processing step for ACGS is to apply dark correction. During thermal vacuum testing, a set of data was collected with the light source shuttered such that no light entered the instrument. This dark data is used to characterize the response of the focal planes with no illumination. This is important because a DN offset can introduce a linear error. On orbit, dark data will be collected and the dark subtraction will be updated early in the mission. The dark data will be monitored thereafter and updated if needed. The next step is to apply gain curves, which describe the relationship between DN and calibrated radiance.

Ambient temperature variations contribute to the dark background signal. The as-measured DN values can be corrected for these effects using the dark subtraction equation

$$N_{\mathrm{D,\,cor}} = N_{\mathrm{D}} - N_{\mathrm{D,\,dark.}}$$

Because atmospheric absorption is inferred from the ratio between continuum and line core radiances, the radiometric calibration must account for any nonlinearity in the instrument gain. Even though the instrument gain appears almost linear, it is described using a 5th order polynomial of radiance *vs.* signal to describe any nonlinear effects.

$$R = k\sum_{i=0}^{5} c_i (N_{\mathrm{D,\,cor}})^i$$

Here k is the attenuation coefficient, which will be set to 1.0 at launch. c_i is the radiometric calibration coefficient. $N_{\mathrm{D,cor}}$ is the N_{D} after corrected by dark current[6].

2.2 Spectral Calibration

The dispersion coefficients express the relationship between the spectral element index (an individual pixel) and its associated wavelength without any Doppler correction or dispersion adjustments. The coefficients are used as follows

$$\lambda_{\mathrm{column}} = \sum_{i=0}^{5} c_i \ \mathrm{column}^i ,$$

where column refers to the column number, c_i is the spectral calibration coefficient.

The main challenge of the TanSat ACGS spectral calibration comes from characterizing the Instrument Line Shape (ILS). There is not a single ILS, but rather the ILS for each and every spectral pixel index, footprint, and band. Theoretically speaking, 20178 individual ILS functions in total should be considered in the procedure.

ILS describes the response of each spectral element of the instrument versus wavelength, and can be used to convolve high spectral resolution spectra for comparison with ACGS spectra. An initial determination of the ILS was performed using tunable diode lasers that were stepped through a range of wavelengths covering the ACGS spectral range. On the whole, the consistency of the ILS values across the spatial and spectral dimensions is perfect in the three bands. Most of the ILS response variations are less than 0.63%. The maximum ILS variation was –1.62% in the last channel of O_2 A band. Most of the biases are presented at both wings of ILS profiles and can be negligible at the central wavelength of the ILS. Thus, the ILS variations resulting in changes in radiometric response and spectral dispersion are of little significance.

3 In-flight Performance

3.1 Radiometric Performance

The in-flight radiometric calibration accuracy and the stability are critical to realize high precision

measurements of global atmospheric CO_2 concentrations. The evaluations of dark current and Signal-to-Noise Ratio (SNR) are presented below.

Dark current is the response of an instrument detector when it is not actively being irradiated. The detectors of WCO_2 and SCO_2 bands of ACGS are sensitive to changes in temperature. Therefore, to minimize science impact, dark correction coefficients should be updated on-orbit where the ambient temperature is different from that of pre-launch. The way to correct dark current is to establish a functional relationship between shielded margin pixels and irradiated pixels by the measurements from the full-orbit dark current calibration observation. Thus the dark current can be subtracted for science observations. Considering that the temperature changes for different observation modes could lead to different dependencies, we calculated the coefficients individually for the solar, nadir, and glint observation modes.

The results for correction coefficients calculation show that there is a very good linear relationship between the response of shielded margin pixels and the irradiated pixels in the three observation modes of the WCO_2 and SCO_2 bands. These models have been used in the preprocessing algorithm of ACGS Level 1 products, and the performance has been validated in the XCO_2 retrieval processing. After the correction used in these models, the dark current error was below 5 DNs in the two CO_2 bands of ACGS. The O_2 A-band uses a Si detector with a dark current response of tens of DNs. And this result varies only between 2 and 3 DNs during the full-orbit dark current calibration, indicating very low temperature sensitivity. Because the ambient temperature is controlled to within 0.3 K in-flight, this sensitivity could be negligible in orbit[7].

SNR is a measurement that compares the level of the desired signal to the level of background noise. In flight, we use the measurement of the calibration lamp and solar diffuser to evaluate the SNR of ACGS according to the following formulas. The definition of SNR is the ratio of the mean to the standard deviation of a measured signal.

$$\mathrm{SNR}=\frac{\bar{S}}{\sqrt{\frac{1}{M-1}\sum_{k=1}^{M}(S_k-\bar{S})^2}},\bar{S}=\frac{1}{M}\sum_{k=1}^{M}S_k,$$

where S_k represents the sample of the measured radiance of lamp calibration or solar diffuser, M is the sample size of measured radiance, and it should be larger than 100, $\bar{S}$ indicates the mean of measured radiance.

We evaluate the SNR under the condition of typical radiance values which are based on the SNR model determined in the laboratory for the solar and lamp calibration observations. The in-flight SNRs for WCO_2 and O_2 A bands show a good consistency with the SNR model for all nine footprints. But for the SCO_2 band, the in-flight SNRs reduce by about 15% at the typical radiance. As for the temporal change for in-flight SNRs, they all show good stability.

The radiometric bias (Figure 1) compared with Kuruzs reference spectral radiance is less than 5%, and shows a very good consistency between footprints for the three bands of ACGS.

3.2 Spectroscopic Performance

The ILS is FWHM of a slit image on the FPA. The ILS of ACGS is determined by the slit width, pixel pitch, optical aberrations, diffraction, and detector crosstalk. The ILS profile and dispersion coefficient of ACGS are carefully characterized and calibrated prior to launch.

In order to validate the spectral accuracy of the centroid wavelength in-flight, the solar spectra collected during solar calibration observation of ACGS

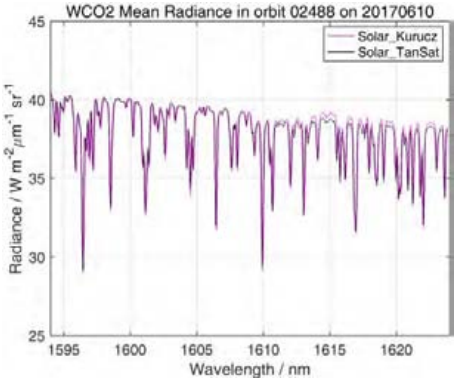

Fig. 1 Radiometric bias at WCO_2 band. This analysis is for footprint 4 on 10 June 2017 (Orbit No. 02488)

are used to compare with the high-resolution solar irradiance database after correcting for the Doppler effects. The results present remarkable consistencies in the footprints and agreements with the reference spectrum. The spectral calibration accuracy of the O_2 A band is 1.9×10^{-4} nm, that of the WCO_2 band is 2.7×10^{-4} nm, and that of the SCO_2 band is 4.75×10^{-3} nm, all of which satisfy the requirement of 0.05 FWHM[8]. Figure 2 shows the comparison of the normalized observed spectrum and reference solar spectrum for WCO_2 band. Figure 3 illustrates that there is no temporal variation for the central wavelength of the absorption line in observed WCO_2 spectrum in full-orbit nadir observation, which shows a very good spectral stability.

3.3 Geolocation Performance

The geolocation algorithm for TanSat is complex since TanSat often switched its operation mode from one working status to another to meet the CO_2 monitoring requirement[9]. There are two main kinds of operation modes, *i.e.*, scientific observation modes and calibration observation modes. The scientific observation modes include four detailed observation modes, *i.e.*, nadir principal plane observation mode, non-principal plane observation mode, glint observation mode, and target observation mode. The calibration observation mode includes three types of observation modes, *i.e.*, solar observation mode, moon observation mode, and lamp observation mode.

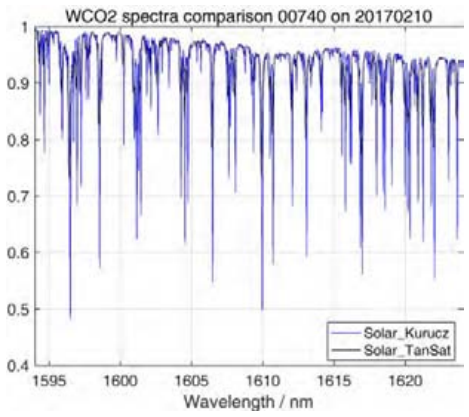

Fig. 2 Comparison of the normalized observed spectrum and reference solar spectrum for WCO_2 band

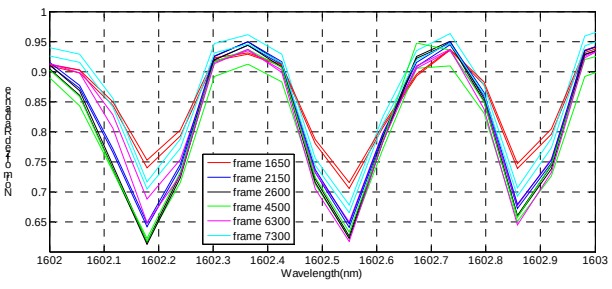

Fig. 3 Temporal variation of observed spectra in WCO_2 band for Orbit 01739 in nadir mode

In order to achieve high-precision geolocation results, the geolocation algorithm is designed correspondingly for remote sensing data under each observation mode. With the time-series correlation analysis of original attitude measurements, the attitude in every sample time is achieved by a high-precision matching and fitting method.

Meanwhile, the observation geometry of TanSat is closely related to the main plane which is defined by the Sun, the Earth, and the observation target. The rotation influence of the main plane observation mode is also a problem needed to be solved for improving the accuracy of the geolocation algorithm.

Besides the traditional geolocation requirements which only focus on the geolocation information in the WGS84 coordinate system, the special geolocation information related to the main plane spatial geometry also needs to be solved, which is the particularity and innovation for the geolocation algorithm of TanSat. Based on the on-orbit test of TanSat, all of the orbit and attitude parameters meet the design requirements.

As there is no landmark channel for ACGS, it is difficult to estimate its geolocation accuracy directly. Considering that the visible band of CAPI can identify landmarks and the optical boresight of CAPI is almost the same with that of ACGS, the landmarks of CAPI could be used to evaluate the geolocation accuracy of TanSat image. The landmarks shown in Figure 4 are the geolocation results when TanSat passing Port au Prince near Caribbean Sea, and Gulf of Venezuela on 2 June 2017. The red line is the ideal boundary between sea and land, and the background image is the remote sensing data of CAPI.

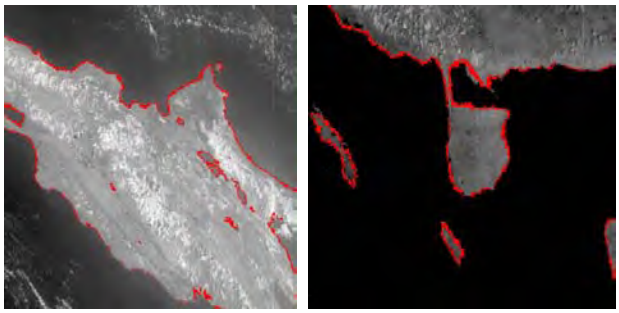

Port au Prince -Caribbean Sea Gulf of Venezuela

Fig. 4 Accuracy of geolocation is estimated by a visible band of CAPI on TANSat

Based on a high-precision attitude, stable trajectory, and the adaptive geolocation algorithm designed according to each observation mode, the geolocation accuracy achieves 1 pixel.

4 Data Services

4.1 Data Archive and Service Platform Design

TanSat data archive and service platform is constructed and operated by the National Satellite Meteorological Center (NSMC), CMA. The raw data acquired from Jiamusi, Wulumuqi, Kiruna Ground station are processed to produce Level 1 products with geolocation and calibration information in real time. After the Level 1 products are generated, the data will be archived in NSMC and distributed meanwhile to application segments, such as CAS and MOST for product retrievals and application services routinely.

TanSat data archive and service platform (Figure 5) is designed to fulfill the needs of scientists and the public user community. It is composed of two parts, *i.e.*, the front end and the back end. The back end was designed to focus on the quality and integrity of data. It also pays attention to the efficiency of data storage, IO, and retrieval. The back end obtains the output data from the processing system in real time. After quality inspection, data extraction, sorting, archiving, it arranges online caching for part of the data according to the established caching strategy which can quickly prepare and provide corresponding

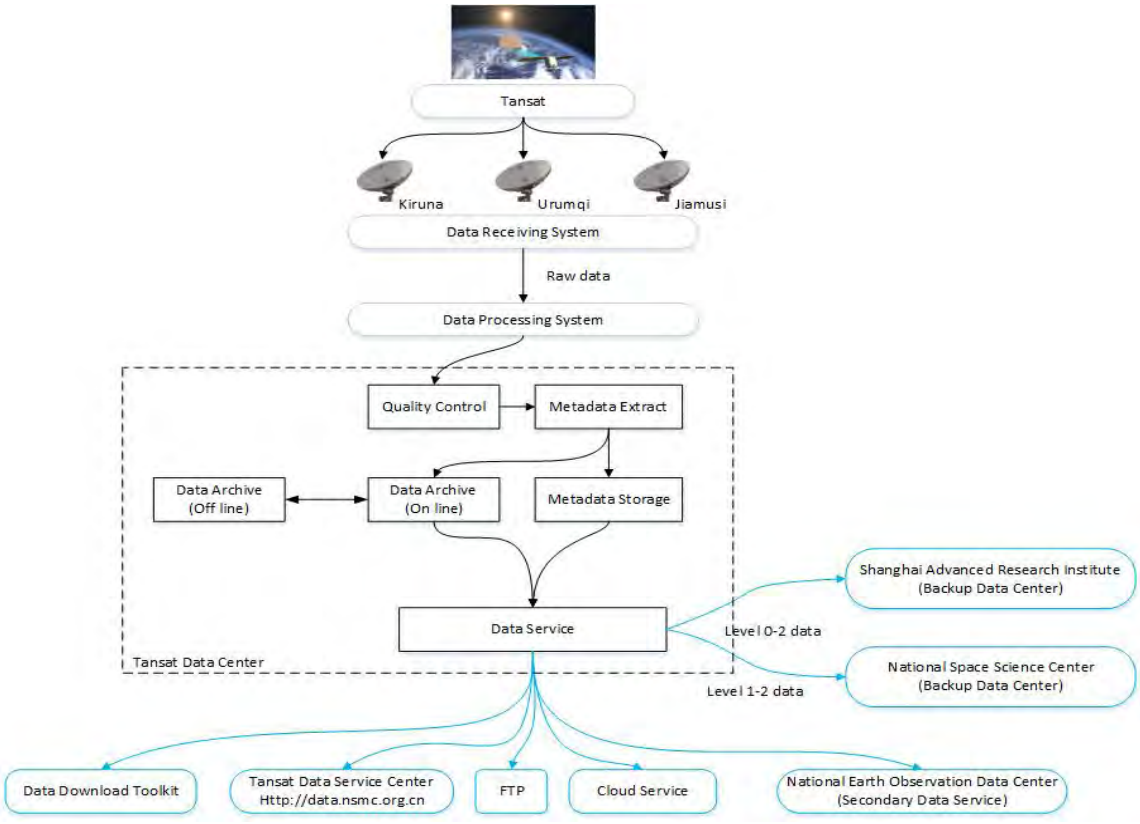

Fig. 5 Tansat data archive and service platform Architecture

data files to the front end requirements.

The front end is designed to focus on the users. It pays attention to the flexibility and convenience of users' access to data. On the one hand, through dedicated lines, all TanSat data are distributed to two TanSat data backup centers, the Shanghai Advanced Research Institute (SARI), CSA, and the National Space Science Center, CAS in real time. On the other hand, through the internet, Tansat data are open to the public in a variety of ways for convenient data track and access.

NSMC's satellite data service website (http://data.nsmc.org.cn) is the most important entry for the public to get the TanSat data. Registered users can track and download TanSat data from the web. The users can also order batch datasets, and go back to download them from NSMC FTP servers when the ordered data is prepared by the TanSat data archive and service platform. In another way, the users can install a data-download-toolkit provided by the website onto their computer which can download the batch datasets automatically. Data services based on cloud computing technology are also on the way at this stage and will improve the data services in the future.

Figure 5 shows the architecture of TanSat data flow. When TanSat data are acquired by the ground stations, level 1 data are processed in Data Processing System. Those data and products are delivered to the Tansat Data Archive and Services System. After data quality control, meta data extraction, and storage, Tansat data are ready to service via different ways and backup to two backup data centers.

4.2 TanSat Data Resource and Service

TanSat began science observations in January 2017 and delivered radiometrically-calibrated, geolocated (Level 1B) products on 24 October 2017 (http://satellite.nsmc.org.cn/PortalSite/Default.aspx).

Up to the end of 2019, NSMC had stored TanSat data volume up to more than 110 TB, including more than 80 product catalogs and 1.17 million files. According to CMA data policy, all L1 data (Seeing Table 2) is open to users all over the world.

Table 2 TanSat L1 datasets open to public

Payload	Level	Name of the data set	Number of files	Total size/TB
	L1	L1A Sample Z-Axis Solar Calibration Sample product v2.0		
	L1	L1A Sample Dark Calibration Sample product v2.0		
	L1	L1A Sample Lamp Calibration Sample product v2.0		
	L1	L1A Principal-Plane Nadir Sample product v2.0	51263	12.7
ACGS	L1	L1A Sample Glint Sample product v2.0		
	L1	L1B Sample Z-Axis Solar Calibration Science product v2.0		
	L1	L1B Sample Dark Calibration product v2.0		
	L1	L1B Sample Lamp Calibration product v2.0		
	L1	L1B Principal-Plane Nadir Science product v2.0		
	L1	L1B Sample Glint Science product v2.0		
	L1	L1A Principal-Plane Nadir Pixel product		
	L1	L1A Sample Glint Pixel product		
	L1	L1B Principal-Plane Nadir Geometry product (1000M)		
	L1	L1B Principal-Plane Nadir Geometry product (250M)	476237	45.1
CAPI	L1	L1B Principal-Plane Nadir Science product (1000M)		
	L1	L1B Principal-Plane Nadir Science product (250M)		
	L1	L1B Sample Glint Geometry product (1000M)		
	L1	L1B Sample Glint Geometry product (250M)		
	L1	L1B Sample Glint Science product (1000M)		
	L1	L1B Sample Glint Science product (250M)		
		Summary	527500	57.8

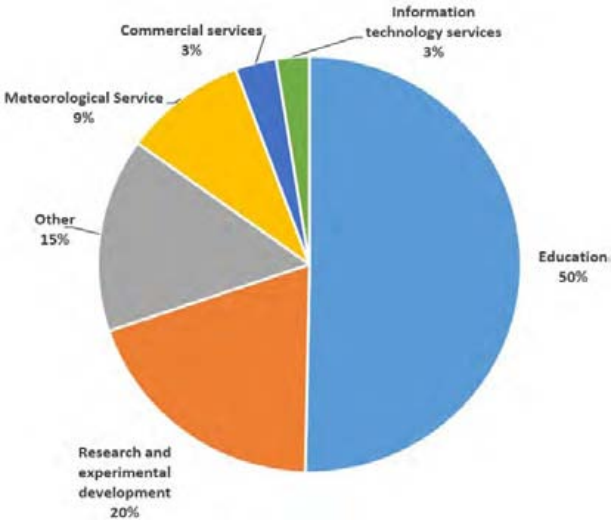

Fig. 6 TanSat data user distribution

Up to the end of 2019, almost 5 million files added up to more than 280TB TanSat data had been delivered to 158 domestic and international users, including users from 7 countries such as Germany, Australia, Iran, Colombia, the Netherlands, France, and the United States. Regarding the users' distribution (Figure 6), 50% users come from education, 20% users come from research, 9% users come from meteorological service, 3% users come from commercial services, 3% users come from information technology services and 15% users come from other fields.

TanSat data provides users with more information and the possibility to understand the distribution of CO_2 in the atmosphere. For example, users from CAS and other departments take advantage of TanSat data to conduct research on global carbon emissions and CO_2 distribution and many high quality papers have been published[10-13].

5 TanSat CO_2, Solar Induced Chlorophyll Fluorescence (SIF) Measurement and Data Application

5.1 Improvement of TANSAT CO_2 Retrieval Algorithms

The Institute of Atmospheric Physics Carbon Dioxide Retrieval algorithms for the Satellite Remote Sensing (IAPCAS, as the same acronym with Institute of Atmospheric Physics Chinese Academic of Sciences) were developed for spaceborne greenhouse gas measurement. This algorithm has been applied to GOSAT data retrieval studies and validation results show a reliable precision on XCO_2[17,20] and also XCH_4[15]. An Optimal Estimation Method (OEM) has been used in TanSat retrieval algorithm coupling with an accurate forward model that simulates satellite measured spectrum. The retrieval compares the simulated spectrum against measurement, and iteratively adjusting the atmospheric CO_2 content and relevant atmosphere and surface state, *e.g.* surface pressure, temperature, moisture, aerosols, surface reflectance *etc.*[14], until the consistency of the final simulated spectrum and the measured spectrum meets the residual threshold value that has been marked as 'good' fitting and hence convergence. The first global map of XCO_2 from TanSat measurement (April and July 2017) has been released to the public within three months after TanSat has ended in-flight test and calibration phase[11]. This result indicates the hot-pot of CO_2 in the northern hemisphere due to anthropogenic emissions in spring. It also shows the seasonal variation from the spring to summer in the northern hemisphere that was caused by the uptakes of the ecosystem. Total Carbon Column Observation Network (TCCON) is a global Carbon monitoring network whose measurements and data products have been well applied in greenhouse gas satellite validation studies[19]. This preliminary TanSat XCO_2 product was verified against with overlap measurement from OCO-2, and also has been validated against eight TCCON sites, and results show an average precision of 2.11 ppm, which meets the requirement of TanSat mission design[13]. Further studies on the measurement of TanSat O_2 A and CO_2 1.61 μm band provide a radiometric correction method on L1B data to improve retrieval qualities. After applying this method to TanSat retrieval, we approached a new TanSat XCO_2 data. A 15-months of XCO_2 retrieval validation study that against 20 TCCON sites over global indicate a 1.47 ppm mean

root-mean-square error (RMSE) and –0.08 ppm mean bias, which makes a step forward of TanSat data to a better application in carbon flux estimation study.

5.2 Retrieval of Solar-induced Chlorophyll Fluorescence (SIF) Measurement

Solar Induced chlorophyll Fluorescence (SIF), which is recognized as an ideal proxy of vegetation GPP and mostly linear correlated with Normalized Difference Vegetation Index (NDVI) and Enhanced Vegetation Index (EVI), has been found that can be approached from hyperspectral O_2 A band measurement from space by using the fill-in effect of solar lines[16]. The retrieval of top of atmosphere SIF emission from TanSat O_2 A band has been studied and two algorithms have been developed. A singular value decomposition (SVD), which is a retrieval method that using SVD data-driven and approach the first global terrain ecosystem SIF measurement[10]. Data training is performed before retrieval on the O_2 A band measurements in order to find the characteristic of SIF signal and back-reflected sunlight. The SIF signal can be extracted from non-SIF background signal in SVD data driven retrieval. Recently, a new Differential Optical Absorption Spectroscopy (DOAS) like a retrieval algorithm has been developed based on IAPCAS with sharing use modules of TanSat XCO_2 retrieval algorithm. The radiative transfer is simulated by using a non-scattering Beer-Lambert Law model in order to approach a physical solution. A bias correction by subtracting a temporal and spatial dependent background signal is required to remove the measurement induced bias. Those two data products have been inter-compared over the global and a regional bias has been found.

5.3 Joint Data Assimilation System for CO_2 Flux Estimation

A joint data assimilation system for CO_2 flux estimation, TanTracker, has been developed for TanSat mission[18]. The proper orthogonal decomposition (POD) based ensemble four-dimensional variational data assimilation method (PODEn4DVar) is implemented in the TanTracker. No assumption on perfect transport models is required in TanTracker and a complete dynamic model to consistently describe the time evolution of CO_2 Surface Fluxes (CFs) and the atmospheric CO_2 could be better using observation information in each assimilation step, which provides a fast and accurate solution on flux optimization. The new version of TanSat XCO_2 data produced will release in 2020 and the TanTracker will be applied in TanSat data assimilation to approach a better estimation on global CO_2 flux.

6 Broadly International Cooperation Promoted by TanSat Mission

The Chinese Government has made great efforts to support nationally-determined contributions (NDCs) defined in COP21 Paris Agreement and to global GHG to fulfill this target. In May 2019, 2019 Refinement to the 2006 IPCC Guidelines for National Greenhouse Gas Inventories was adapted at IPCC 49th General Assembly, it emphasizes the atmospheric CO_2 monitoring will play a crucial role to enhance the transparency and support. The TanSat is going to provide high quality global products which will fill the gaps among the other GHGs satellite observations, it will serve as the testing data to design the next generation of TanSat family, and it promotes the scientific collaboration within GHGs satellite communities. All these activities will support future actions related to the National Greenhouse Gas Inventories refinement.

TanSat achievements had been introduced in many important international meetings, such as COP21 2015 Paris Climate Conference, GEO Plenary meeting, IWGGMS, AGU, and EGU meetings. In 2017 GEO Plenary meeting, TanSat first provided Data Sharing service for L1 products, and later TanSat SIF products and XCO_2 products were shared gradually. Recently, The Protocol between National Remote Sensing Center of China Ministry of Science and Technology of China (MOST/NRSCC) and the European Space Agency (ESA) was signed, to include TanSat into the ESA Third Party Mission Program and TanSat data usage within the ESA

Climate Change Initiative (CCI) and Earthnet Data Assessment Pilot (EDAP) project. The NRSCC and ESA cooperating in the area of earth observation science and applications will greatly promote global GHGs emission monitoring. The project of the International Reanalysis Cooperation on Carbon Satellites Data (IRCSD) was implemented to facilitate data sharing, in which the TanSat data service has been provided by Cooperation on the Analysis of carbon Satellites data (CASA). In the future, the Chinese Government will certainly provide more strong support to a new generation of GHG satellites, such as TanSat-2. To cooperate with different space agencies more closely to (i) reduce the uncertainty of national emission inventory reporting, identify additional emission reduction opportunities and provide quantified guidance towards emission reduction strategies (NDCs); and (ii) track changes in the natural carbon cycle caused by human activities and climate variations.

References

[1] BI Yanmeng, WANG Qian, YANG Zhong-dong, *et al.* Advances on space-based hyper spectral remote sensing for atmospheric CO_2 in near infrared band [J]. *Chin. Opt.*, 2015, **8**(5):725-735

[2] BI Yanmeng, YANG Zhongdong, LU Naimeng, *et al.* Channel Selection for Hyper Spectral CO_2 Measurement at the Near-infrared Band [J]. *J. Appl. Meteor. Sci.*, 2014, **25**(2):143-149

[3] WANG Qian, BI Yanmeng, YANG Zhongdong. Simulation analysis of aerosol effect on shortwave infrared remote sensing detection of atmospheric CO_2[J]. *Acta Phys. Sin.*, 2018, **67**(3):039202-1:039202-13

[4] YANG Zhongdong, ZHENG Yuquan, YIN Zenshan, *et al.* Laboratory spectral calibration of the TanSat atmospheric carbon dioxide grating spectrometer [J]. *Geosci. Instrum. Method. Data Syst.*, 2018, **7**(3):245-252

[5] YANG Zhongdong, ZHENGYuquan, YINZenshan, *et al.* Prelaunch Radiometric Calibration of the TanSat Atmospheric Carbon Dioxide Grating Spectrometer [J]. *IEEE Trans. Geosci. Remote Sens.*, 2018, **56**(7):4225-4233

[6] YANG Zhongdong, BI Yanmeng, WANG Qian, *et al.* Inflight performance of the TanSat atmospheric carbon dioxide grating spectrometer [J]. *IEEE Trans. Geosci. Remote Sens.*, 2020(99):1-13

[7] AVIS C. OCO-2 Algorithm Specification Document-Level 1B Process [R]. Pasadena, California: Jet Propulsion Laboratory & California Institute of Technology, 2015

[8] DU Shanshan, LIU Liangyun, LIU Xinjie, *et al.* Retrieval of global terrestrial solar-induced chlorophyll fluorescence from TanSat satellite [J] *Sci. Bull.*, 2018, **63**(22):1502-1512

[9] YANG Dongxu, LIU Yi, CAI Zhaonan, *et al.* First global carbon dioxide maps produced from TanSat measurements [J]. *Adv. Atmos. Sci.*, 2018, **35**(6):621-623

[10] RAN Youhua, LI Xin. TanSat: a new star in global carbon monitoring from China [J]. *Sci. Bull.*, 2019, **64**(5):284-285

[11] LIU Yi, WANG Jing, LU Yao, *et al.* The TanSat mission: preliminary global observations [J]. *Sci. Bull.*, 2018, **63**(18):1200-1207

[12] CHEN X, LIU Y, YANG D, *et al.* A theoretical analysis for improving aerosol-induced CO_2 retrieval uncertainties over land based on TanSat nadir observations under clear sky conditions [J]. *Remote Sens.*, 2019, 11(9):1061

[13] DENG J, LIU Y, YANG D, *et al.* CH4 retrieval from hyperspectral satellite measurements in shortwave infrared: sensitivity study and preliminary test with GOSAT data [J]. *Chin. Sci. Bull.*, 2014, **59**(14):1499-1507

[14] GUANTER L, ALONSO L, GÓMEZ-CHOVA L, *et al.* Estimation of solar-induced vegetation fluorescence from space measurements [J]. *Geophys. Res. Lett.*, 2007, **34**(8):1-5

[15] LIU Y, YANG D, CAI Z. A retrieval algorithm for Tansat XCO2 observation: Retrieval experiments using GOSAT data [J]. *Chin. Sci. Bull.*, 2013, **58**:1520-1523

[16] TIAN X, XIE Z, LIU Y, *et al.* A joint data assimilation system (Tan-Tracker) to simultaneously estimate surface CO_2 fluxes and 3-D atmospheric CO_2 concentrations from observations [J]. *Atmos. Chem. Phys.*, 2014, **14**:13 281-13 293

[17] WUNCH D, TOON G C, BLAVIER J F L, *et al.* The total carbon column observing network [J]. *Phil. Trans. R. Soc. A*, 2011, **369**:2087-2112

[18] YANG D, LIU Y, CAI Z, *et al.* An advanced carbon dioxide retrieval algorithm for satellite measurements and its application to GOSAT observations[J]. *Sci. Bull.*, 2015, **60**:2063-2066

SHEN Xuhui, ZEREN Zhima, HUANG Jianping, YANG Yanyan, ZHAO Shufan, YAN Rui, ZHANG Zhenxia, LIU Dapeng, WANG Qiao, CHU Wei, LU Hengxin, XU Song, GUO Feng, TAN Qiao, LI Wenjing, ZHOU Na, SONG Fuxi. Current Status and Main Scientific Results of In-flight CSES Mission. *Chin. J. Space Sci.*, 2020, **40**(5): 070-086. DOI:10.11728/cjss2020.05.070

Current Status and Main Scientific Results of In-flight CSES Mission*

SHEN Xuhui ZEREN Zhima HUANG Jianping YANG Yanyan
ZHAO Shufan YAN Rui ZHANG Zhenxia LIU Dapeng
WANG Qiao CHU Wei LU Hengxin XU Song GUO Feng
TAN Qiao LI Wenjing ZHOU Na SONG Fuxi

(*Institute of Crustal Dynamics, China Earthquake Administration, Beijing* 100085)

Abstract The CSES (China Seismo-Electromagnetic Satellite) is the electromagnetism satellite of China's Zhangheng mission which is planned to launch a series of microsatellites within next 10 years in order to monitor the electromagnetic environment, gravitational field. The CSES 01 probe (also called ZH-1) was launched successfully on 2 February 2018, from the Jiuquan Satellite Launch Centre (China) and is expected to operate for 5 years in orbit. The second probe CSES 02 is going to be launched in 2022. The scientific objectives of CSES are to detect the electromagnetic field and waves, plasma and particles, for studying the seismic-associated disturbances. To meet the requirements of scientific objective, the satellite is designed to be in a sun-synchronous orbit with a high inclination of 97.4° at an altitude around 507 km. CSES carries nine scientific payloads including Search-coil magnetometer, Electric Field Detector, High precision Magnetometer, GNSS occultation Receiver, Plasma Analyzer, Langmuir Probe, two Energetic Particle Detectors (including an Italian one), and Tri-Band Transmitter. Up to now, CSES has been operating in orbit for 2 years with stable and reliable performance. By using all kinds of data acquired by CSES, we have undertaken a series of scientific researches in the field of global geomagnetic field re-building, the ionospheric variation environment, waves, and particle precipitations under disturbed space weather and earthquake activities, the Lithosphere-Atmosphere-Ionosphere coupling mechanism research and so on.

Key words CSES mission, Magnetic field model, Waves, Particles, LAIC, Geomagnetic storm

Classified index V 524, P 35

1 Introduction

On 2 February 2018, the China Seismo-Electromagnetic Satellite (CSES), also called ZHANGHENG-1 (ZH-1), was launched successfully in orbit by CZ-2D vehicle from Jiuquan Satellite Launching Site[1,2]. CSES is the first space-based platform in China for both earthquake observation and geophysical field measurement, which was first proposed early in 2003 and was approved in 2013 after ten years' scientific and engineering demonstration. During the past 15-year, the pre-studies and development of CSES have been continuously funded by CNSA, the Ministry of Sciences and Technologies (MOST), and China Earthquake Administration (CEA). Back to the cross point of the century, there occurred a hot scientific dispute in the community about whether an earthquake is predictable accompanied with a series

* Supported by National Key R&D Program of China (2018YFC1503501), Research Grant from Institute of Crustal Dynamics, China Earthquake Administration (ZDJ2019-22 and ZDJ2020-06) and the APSCO Earthquake Research Project Phase II
Received March 31, 2020
E-mail: zsf2008bj@126.com

of devastating earthquakes including the 2001 China Kunlunshan M8.1, 2004 Indonesia M9.2, 2008 China Wenchuan M8.0, and 2011 Japan M9.0 and so on. Regarding that earthquake prediction is a natural science based on observations, at the beginning of 2003, Chinese government decided to develop space-based observation system so as to help to develop new methods and theory on earthquake forecasting science, and to improve the understanding of physical processes in the preparation, occurrence, and development of earthquake. After ten yours' re-studies on science and engineering, the mission was finally initiated in 2013. In the middle of 2014, the development of Electrical Model was finished which was used to demonstrate the hardware and software design of the platform and payloads, to verify the compatibility between the platform and payloads, to test the payload performance, to validate the structure and mechanical designs as well as the satellite thermal control design and so on. In the middle of 2015, the Qualification Model was developed for the purpose of qualifying all newly built units and calibrating all payloads. The results show that the satellite platform and scientific payloads fulfill all the specifications. In the middle of 2017, the Flight Model was developed and performed as required for flight operation. The commission test had been carried out after the scientific payloads started to operate successively since 13 February 2018.

The CSES mission is the first satellite of Chinese space based geophysical field observation system and provides a lot of application prospects in Earthquake science, geophysics, space sciences, and so on. The scientific objectives of the mission are listed as follows.

(1) To obtain global data of the electromagnetic field, plasma and energetic particles in the ionosphere, especially those real-time data when the satellite passes over the Chinese territory.

(2) To monitor and study the ionospheric perturbations which could be possibly associated with seismic activity, especially with those destructive ones.

(3) To monitor and study the near-Earth space environment, and its disturbance caused by human activities.

(4) To analyze the features of seismic-ionospheric perturbations, therefore, to explore the possibility for short-term earthquake forecasting in terms of satellite observation and to search the new approaches for short-term and imminent prediction.

(5) To support the researches on geophysics, space science as well as radio science and so on.

(6) To provide the data sharing service for international cooperation and scientific community.

To meet the scientific goals, CSES is designed to carry nine scientific payloads including: the High Precision Magnetometer (HPM) for the total magnetic field observations[3-5]; the three-axis Search-Coil Magnetometer (SCM) and the Electric Field Detector (EFD) for the electromagnetic field detection at a broad frequency range from DC to HF[6,7]; a Langmuir Probe (LAP) and Plasma Analyzer Package (PAP) for in-situ plasma parameters measurements[8,9]; the High Energetic Particle Package (HEPP) and Italian Energetic Particle Detector (HEPD) for high energy particles[10,11]; the GNSS Occultation Receiver (GOR) and Tri-Band Beacon (TBB) to measure electron density profiles[12,13].

2 Satellite Platform and Ground Application System

The platform of CSES was remodeled upon the CAST2000 which offers a standard multi-mission platform at a very attractive cost. Technically, the platform architecture is generic, and adaptations are limited to relatively minor changes in several electrical interfaces and software modules. The platform includes eight units: Data Transmission subsystem (DTs), Structure and Mechanism Subsystem (SMs), Thermal Control subsystem (TCs), Attitude and Orbital Control subsystem (AOCs), Power Supply subsystem (PSs), Telemetry and Tele-Command subsystem (TTCs), on Board Data Handling subsystem (OBDHs) and scientific payloads. Satellite structure construction uses the dual-layer cabin design: payload layer cabin and platform layer cabin.

Satellite is flying in the direction of the satellite X axis, the satellite Z axis is pointing nadir, the satellite Y axis is then decided by right hand rule. Solar panel locates on the $+Y$ side of the satellite with 12° offset angle and rotates around the satellite Y axis. Housekeeping data are exchanged through CAN bus onboard, the OBDH Center Computer is used as a host for all other equipment. Onboard telemetry uses TM package to communicate. Satellite AOCs use earth oriented 3-axis stabilization. Three star-trackers, two groups of gyros, and one digital sun sensor are used to measure the attitude. Reaction wheel and magnetic torque are used to maintain the zero-momentum control. A propulsion system is used for attitude complementary control and orbit maintenance. An S-B and Telecommunication system assisted by GPS positioning is used for TMTC subsystem. The power supply subsystem is composed of 80 A·h Li-ion battery and GaInP2/GaAs/Ge solar cell panel.

The commissioning phase of the satellite was completed by November 2018 after 9 months of launch. Up to now, CSES has been operating in orbit for 2 years and has collected scientific data for more than 10000 orbits. Except some unknown contamination sources for Plasma Analyzer Package, the entire set of payloads and platform are all working in good condition. The configuration of CSES satellite platform is represented in Figure 1.

The main orbit parameters of CSES are listed in Table 1. The distance between neighboring orbit trajectories is around 2650 km in one day and is reduced to 530 km in a revisit period of 5 days (Table 1). The payloads and physical parameters of CSES satellite are listed in Table 2.

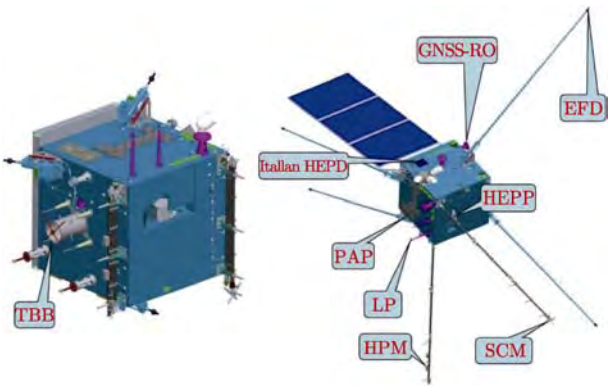

Fig. 1 Configuration of CSES satellite platform

The ground segment (as shown in Figure 2) of CSES consists of a science and application center, the satellite ground receiver networks, the field verification field, and comparison system for satellite-ground measurement. The science and application center is responsible for mission operation and control, data management, and data sharing service, as well as Earthquake Science. application, operated by China Earthquake Administration.

After the commission phase, every 3~4 months the satellite performs an orbit maneuver for ground track control so as to have a perfect recursive visit relative to all geophysical locations. The latest ground track keeping maneuver was performed on 20 January 2020. The remaining fuel of the satellite is about 35 kg (42 kg before launch), according to the current usage, the fuel is sufficient to support the entire life span.

The satellite establishes 6~8 times data transmission downlink and 4 times TMTC duplex links to the ground segment at each day, and both the data transmission link and TMTC link work steadily and efficiently.

Normally all payloads switch off over ±65° of latitude, however, the satellite can extend the working zone to cover the polar region for the specific experiments.

Table 1 Main parameters of CSES platform

Style of orbit	Sun-synchronous orbit
Altitude/km	507
Inclination/(°)	97.4
Period/min	94.6
Descending time (LT)	14:00
Revisiting period/d	5
Mass budget/kg	730
Volume budget/mm	About cube 1400
Length of booms/mm	4500
Data storage/GByte	160
Data transmission X-band, downlink rate/(Mbit·s^{-1})	120
Lifetime	>5 years

Table 2 Status of the scientific payloads

Payloads	Parameters	Status
High Precision Magnetometer (HPM)	DC to 15 Hz	Excellent performance
Search-Coil Magnetometer (SCM)	10~20 kHz	Excellent performance
Electric Field Detector (EFD)	DC~3.5 MHz	Good condition, but little high noises in HF band than expected
Plasma Analyzer Package (PAP)	Ion density, Ion temperature, Ion contents, and Ion drift velocity	Probe Contamination in orbit
Langmuir Probe (LAP)	Electron density, Electron temperature	Excellent performance
GNSS Occultation Receiver (GOR)	TEC, N_e Profile, Profile of air temperature and pressure	Excellent performance
Tri-Band Beacon (TBB): 50/400/1066 MHz	TEC, N_e Profile	Good performance but with 400 MHz band malfunction
Energetic Particle Detector (HEPP)	Proton flux: 1.5~200 MeV Electron flux: ⩾ 0.1 keV~10 MeV X ray: 0.9~35 keV	Excellent performance
Italian Energetic Particle Detector (HEPD)	Proton flux: 30~100 MeV Electron flux: 30~200 MeV	Excellent performance

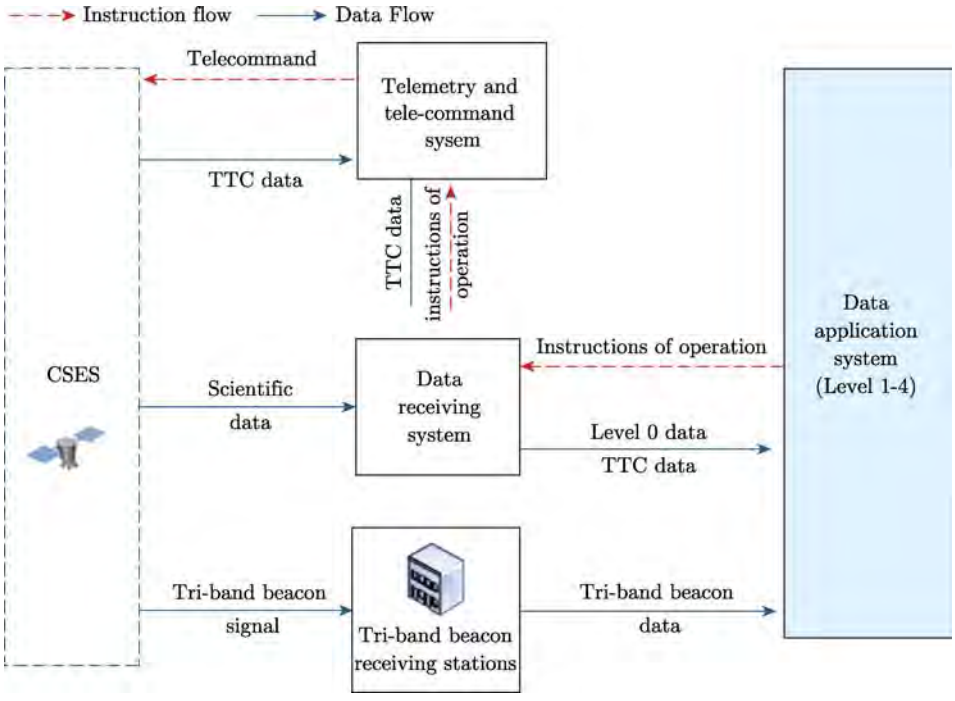

Fig. 2 Data flow between satellite and ground units

In order to provide reliable assistant information for all payloads, the performance of the satellite platform is evaluated every 6 months in terms of positioning accuracy, attitude information accuracy, and potential charging control, meanwhile the thermal control system and timing system are monitored all the time. So far, major specifications for CSES mission meet the expectations. The satellite is

working stably and continuously providing scientific data with great duty cycle percentage.

The ground receiving system consists of four stations, which are Miyun Station, Kashi Station, Sanya Station, and Southwest Station. Orbit prediction error keeps <30 s. All interfaces between satellite and ground stations such as coding, data rate, and modulation satisfy the requirement, and the transmission efficiency from all ground stations to data station meets the requirement.

Data Application system, which is in charge of the mission operation center, running control management subsystem, and data processing subsystem, is generally running stably, in which parallel processing architecture is embedded to realize automatic data process, and manual interactive process is optional. So far, the success rate for level-0 to level-2 data process could reach more than 90%. Data distribution website (www.leos.ac.cn) is established and ready for user to access.

3 Preliminary Results of CSES Satellite

3.1 Global Geomagnetic Field Reference Model

The International Geomagnetic Reference Field (IGRF) model is used to describe the main field and the secular variation of Earth's geomagnetic field. The building of IGRF model is an international behavior organized by International Association of Geomagnetism and Aeronomy (IAGA). IGRF is updated every five years, and 2019 is the final year for 12th generation IGRF. In March of 2019, IAGA announced the new call for 13th generation IGRF. Thanks to China Seismo-Electromagnetic Satellite (CSES) mission[1-2], this is the first time that China response to the open call from IAGA and started to build a candidate model. Until the final submission of IGRF-13 candidate model (1 October 2019), CSES has accumulated one and half a year dataset. Using this dataset, the main field for 2020 totally based on CSES's data was built, becoming the only one without using Swarm data in all the 12 candidate models of IGRF-13. The independent data source from CSES provides an opportunity for the cross-check with other models.

For the building of this proposed candidate model, the 1 Hz level 2 scientific HPM data were used. The data were calibrated using the procedure described in Zhou *et al.*[4] and provided by the Institute of Crustal Dynamics, China Earthquake Administration. It should be noted that, determined by the working mode of the satellite, HPM consists of two types data. The type 1 data is in geographic latitudes between 65°S and 65°N, which are down sampled to 1Hz from the original 60 Hz FGM and 30 Hz CDSM data. The data is carefully calibrated and opened for public. The type 2 data is available for North and South geographic latitudes higher than 65°. This dataset hasn't been opened yet because of continuous magnetic disturbance caused by the magnetic torque. To build the model entirely based on CSES data, however, some efforts still have to be made to make such data available.

For the model submitted to IAGA, we selected CSES data from 3 March 2018 (the date that CDSM successfully turned on to work) to 20 September 2019, which lasts about 19 months. In this work, however, we have updated the model using more data to 30 November 2019. Data selection criteria are similar to those typically used for dedicated internal field modeling[14](where some of the quantities used below are defined) with some special considerations related to the CSES mission.

(1) Common selection to all data: (i)dark region only (solar elevation angle at least 10° below horizon); (ii) magnetically quiet conditions, based on RC index <2 nT·h^{-1} and $Kp<2^{+}$; (iii) FLAG_MT=0 to remove data with disturbance from the magnetic torques. This flag is not used for type 2 data, as all data are affected by MT.

(2) Additional selection for scalar data: (i) for QD latitude above 55°, the merging electric field at magnetopause Em should be less than 0.8 mV·m^{-1}; (ii) decimation: 1 point every 30 points for Type 1 data, no decimation for Type 2 data.

(3) Additional selection for vector data: (i) only

vector data for QD latitudes less than 20° are selected; (ii) FLAG_TBB=0 to remove data with disturbance from Trip-Band Beacon; (iii) A final decimation (1 out of 15 data points) is being used to avoid over-representation along tracks.

Then, using the selected dataset, the model parameters were computed by minimizing the mismatch between data and model prediction[14], using iteratively reweighted least-squares with Huber weights, without any regularization, as shown in Figure 3. To validate our candidate model, we decided to rely on some comparison between the prediction of our parent model with that of the CHAOS6-x9 model[15]. The result illustrates that the difference in the Br values predicted by our CSES parent model and CHAOS6-x9 at Earth's surface, for the central epoch 11 December 2018 is about 20 nT in amplitude. The largest differences are in the zonal component. These differences most likely reflect some of the systematic boom deformations along the CSES orbits. We note, however, that such differences remain within a reasonable level acceptable by typical IGRF candidate models. More detailed information about modeling will be found in Yang *et al.* (in preparation).

3.2 ELF/VLF Electromagnetic Waves

The upper ionosphere is a highly dynamic region with a variety of intense electromagnetic emissions, especially the whistler-mode emissions at Extremely/Very Low Frequency (ELF/VLF) range[16]. The most common and typical ELF/VLF whistler-mode waves in the high-latitude ionosphere mainly include hiss[17,18], chorus[19,20], and Quasiperiodic (QP) waves[21,22], *etc.* Figure 4 shows two QP wave events represented by the sum of Power Spectral Density values (PSD) of three components of the magnetic field and electric field at frequency from 200 Hz to 2 kHz. These two events were captured on 25 August (Figure 4a), 18 December (Figure 4b), at dayside upper ionosphere, respectively. It can be seen that there exist fixed time-separations (*i.e.*, periods) between adjacent wave elements during each event at a broad frequency range from f_{cp} (the proton cyclotron frequency, see the black dashed lines) predominantly up to 1.5 kHz, occasionally up to about 2 kHz. The proton cyclotron frequency f_{cp} is computed by the scalar value of the total magnetic field measured by HPM.

CSES's observations are consistent with previous understanding that the QP wave is almost a dayside phenomenon[21], however, compared to the similar technically designed satellite DEMETER in the upper ionosphere, CSES seems that can record more well pronounced rising-tone structures. The DEMETER is a synchronous circular Low Earth Orbit (LEO) satellite with an altitude about 660 km[23], measuring generally the same space environment as CSES (507 km) in the upper ionosphere. To our knowledge, there are two reasons that might explain for less rising-tone QP events from DEMETER's observations. One reason might be due to the measurement capability of satellites: the frequency resolution of electromagnetic field measurement of DEMETER is 19.5 Hz in all time survey-mode, and 2.5 Hz only in short time burst-mode (so the observation chance is very limit), while the frequency

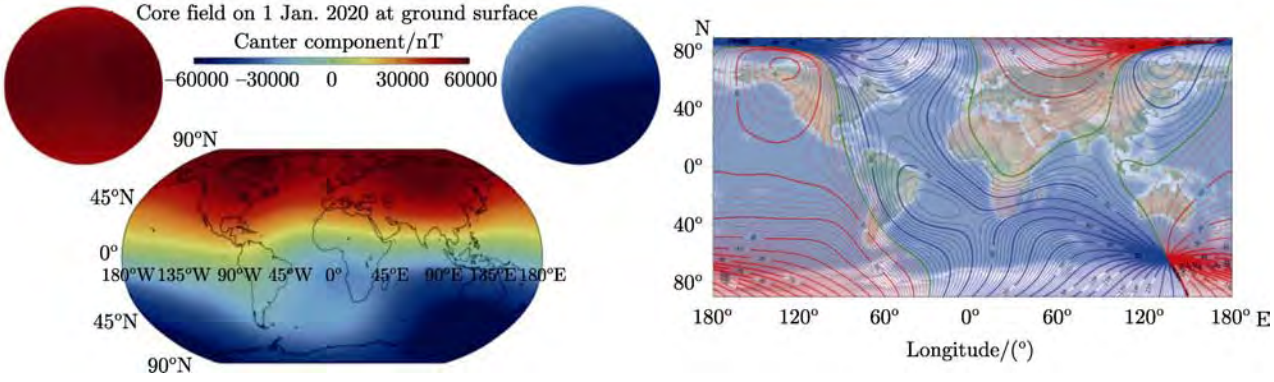

Fig. 3 Magnetic field center component (a) and inclination (b) calculated from CSES-IGRF 2020.0 candidate model

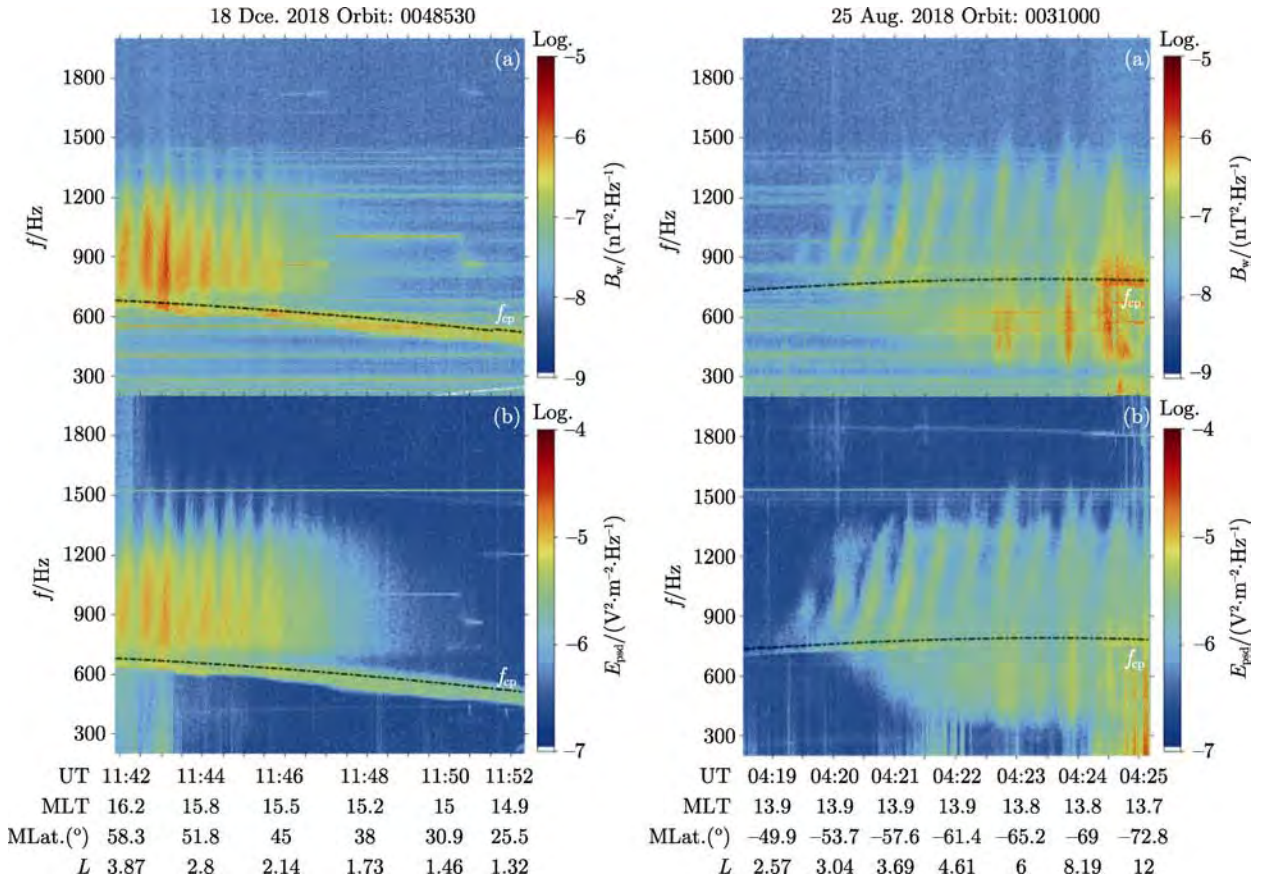

Fig. 4 Quasi-periodic electromagnetic waves recorded by CSES in the high-latitude upper ionosphere.(a) The event of 25 August 2018; (b) the event of 18 December 2018; the waves are represented by the sum of Power Spectral Density (PSD) values of three components of magnetic field (a) and the electric field at frequency band from 200 Hz to 2 kHz

resolution of CSES is 2.5 Hz in all time survey mode; another reason might be due to the observational time window: DEMETER operates at dayside around 10:30 LT while CSES around 14:00 LT. It is widely accepted that the QP emissions predominately occur around noon, but no further investigations on the occurrence of rising-tone QP waves have been reported. Considering CSES has recorded well pronounced rising-tone structures around 14:00 MLT, we speculate that 14:00 MLT might be a suitable time window for excitation of rising-tone QP structures, we will leave this topic for future study after CSES collects adequate evidence.

3.3 Particle Precipitations Induced by Wave-particle Interaction

The Earth's radiation belts, filled with energetic particles, consist of inner and outer radiation belts separated by a region known as the slot region with electron flux minimum, which lies around L=3. The electron enhancements in the radiation belts can be caused by wave heating or radial diffusion during storms by wave-particle interaction mechanism. Killer electrons, especially with energies greater than 1 MeV, are the main environmental hazard to Earth orbiting satellites and astronauts. And the energetic particle burst is closely related with the disturbance of the geomagnetic field. Therefore, it is very important and meaningful to study the high energy electron precipitation mechanism.

The onboard high energy particle detector (HEPP-L, H)[11] can measure the electron fluxes with energy ranging from 0.1 keV to 55 MeV with an energy resolution$\leqslant$8.9% at 1 MeV and wide pitch angles. The maximum field of view of HEPP-L is 100°×30°. So the launch of CSES satellite and the good performance of HEPP-L particle detector pro-

vide a good opportunity for studying the electron precipitation phenomenon. Here we introduce two kinds of electron precipitations associated with chorus acceleration during geomagnetic storms and ground VLF transmitters.

3.3.1 Electron Precipitation in Extremely Low *L*-Shell Induced by Chorus Waves during Storms

Whistler-mode waves are often observed during the geomagnetic storm and possibly excited by the energetic electron injection outside plasmasphere near the equator. Magnetospheric chorus wave can rapidly accelerate relativistic radiation-belt electrons. However, all the electron enhancements reported in the past located in the region of high *L*-shell (L>4) corresponding to outer radiation belts.

In the paper[24], based on ZH-1 satellite, for the first time, we provided compelling evidence that an intense and deep MeV electron penetration in extremely low *L*-shell is attributable to the chorus acceleration during the storm (Figure 6). Here we focus on the relativistic electron flux enhancement in

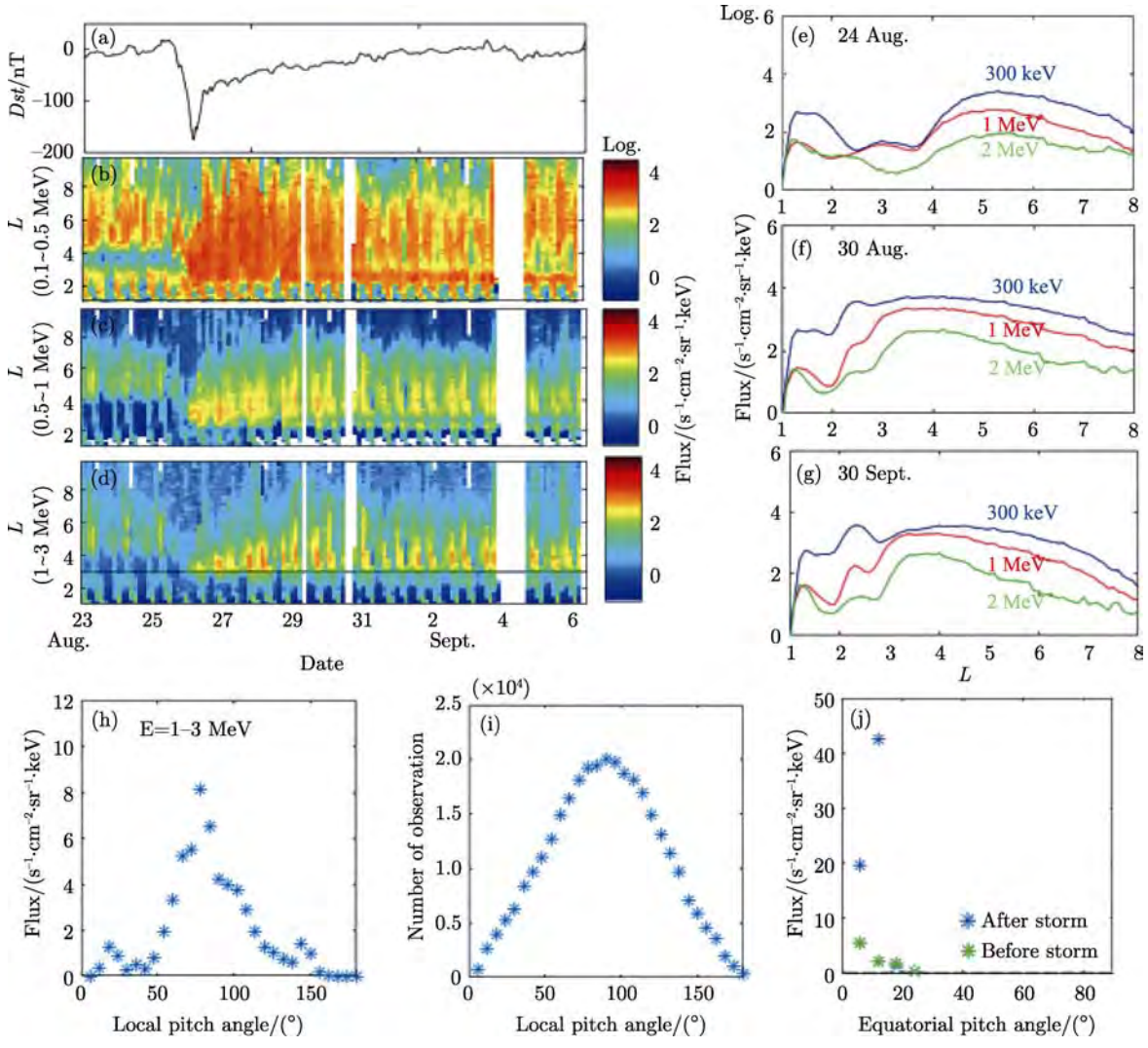

Fig. 5 Overview of the electron evolution during the storm of August 2018 measured by ZH-1. (a) The geomagnetic storm index *Dst*. (b)~(d) The electron evolution for the energy range of 0.1~0.5, 0.5~1, and 1~3 MeV, respectively. (e)~(g) Daily-averaged flux distributions in the *L*-shell. (h) and (j) The flux distributions of 1~3 MeV electrons in local pitch angle and equatorial pitch angle with L=2~5. (i) The number of observed electrons in each pitch angle channel. The solid black line in panel (d) denotes L=3[24]

low L shell (L=2.5~4) during August 2018 geomagnetic storm (minimum Dst= –190 nT). Strong whistler-mode (chorus and hiss) waves, with amplitudes 81~126 pT, were also observed in the extremely low L-shell simultaneously (reaching $L \approx 2.5$) where the plasmapause was suppressed. And then we explained this phenomenon by electron phase space density distribution and quasi-linear diffusion theory of wave-particle interaction.

Fig. 6(b)~(d) show the dynamical evolution of radiation belt relativistic (0.1~3 MeV) electrons observed by HEPP-L detectors onboard ZH-1 (including descending and ascending orbits). The electron measurements are color coded in logarithm and sorted in L-shell (L bin width: 0.1). The L-shell here used in HEPP-L data is McIlwain's L-shell, which is calculated based on the IGRF model with the external field OP77 model. Before the occurrence of a storm, the slot region, inner and outer radiation belts were clearly exhibited in those plots. The slot region lies around $L = 3$~3.8. The fact that there is a lack of measurable >1 MeV electrons in the inner belt agrees with previous longer-term measurements. The apparently periodic feature of fluxes is caused by the characteristic of Sun-synchronous orbits of the ZH-1 satellite.

3.3.2 Electron Precipitation Induced by Ground VLF Transmitter

Ground-based Very-Low-Frequency (VLF) EM signals can transmit across the atmosphere, expands into the ionosphere[25-27], and interacts with the energetic particles in the radiation belt[28]. This interaction accelerates the particles by changing their momentum or scattering their pitch angle, which causes them to enter the bounce or drift loss cones. As a result, a mass of energetic particles accumulates within a certain L-shell and yields particle-flux enhancement, which can be observed by the onboard particle detectors of satellites. The electron precipitation belts induced by VLF transmitter, which has attracted much attention in the past decades, is also observed by the particle detectors onboard ZH-1 satellite.

Figure 6 shows the North West Cape (NWC) electron precipitation between L-shells of L=1.4 and L=1.8 labeled by the blue dots-line on the top panel observed by ZH-1. The flux level, energy spectra, pitch angle distribution is displayed on the lower panels of Figure 7. We can find the clear electron precipitation wisp structures distributing in the energy range of 0.1~0.3 MeV in Figure 7. The electron precipitation induced by ground NWC VLF transmitter can be explained by pitch angle and momentum diffusion of the wave-particle interaction mechanism.

3.4 Seismo-lithosphere-atmosphere-ionosphere Coupling Mechanism

Earth, atmosphere, ionosphere, and magnetosphere are physically coupled together. Mantle convection drives plate movement, which leads to seismic activities, and will have a response in the near Earth space[29-32]. There are mainly three kinds of Seismo-Lithosphere-Atmosphere-Ionosphere coupling mechanisms at present. The electric field mechanism and the electromagnetic wave mechanism used as pre-earthquake mechanisms behave well, while the acoustic gravity wave mechanism could explain the co-seismic phenomena well[33,34].

The formation of LAIC electric field is mainly based on the p-hole mechanism of solid state physics. It is believed that the increase of rock stress before the earthquake will ionize the atmosphere near the surface and generate a large number of additional ions. Ions gather at the bottom of the atmosphere and generate an abnormal atmospheric electric field[35-38]. This atmospheric electric field penetrates into the ionosphere and produces extra $\boldsymbol{E}\times\boldsymbol{B}$ drift, which could cause the abnormal in the above and conjugate areas[38-41].

It is also believed that there are broadband electromagnetic waves from ultra-low-frequency to extra-low-frequency and very-low-frequency radiated from the seismogenic zone because of the piezoelectric and electro-kinetic effects[42,43]. The waves could penetrate the lithosphere and propagate in the ground-ionosphere waveguide for long distance. But there is still some energy linking into the ionosphere and magnetosphere which can be observed by the satellite[44,45].

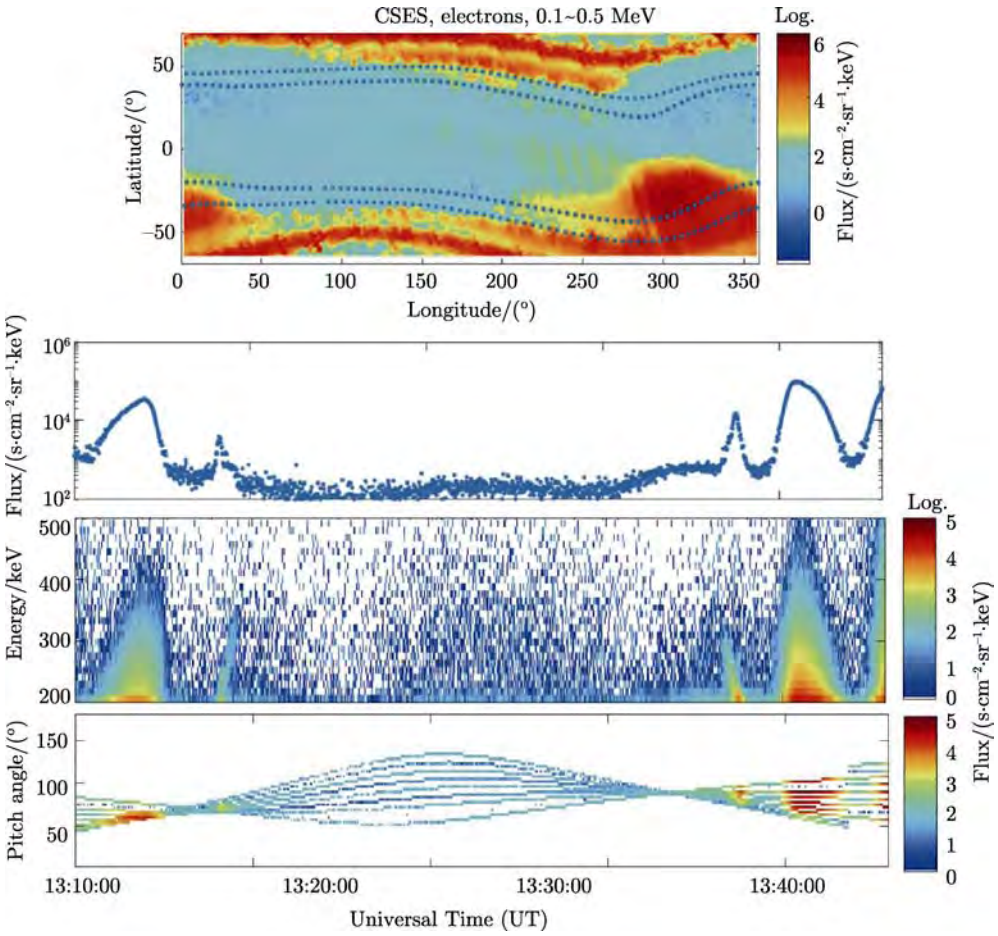

Fig. 6 NWC electron precipitation measured by HEPP-L particle detector onboard ZH-1

There are many ground based VLF transmitters around the world used for submarine communication with constant radiation frequencies and powers. With the help of the VLF signals, the electromagnetic wave LAIC model has been validated by comparing the model results with the satellite observation results. A full-wave method[46,47] seeks a solution of Maxwell equations for waves varying as $e^{j\omega t}$ in a horizontally-stratified medium. Considering the observation distance from the source to the satellite is just 507 km, which is much smaller than the radius of the Earth, the Earth's curvature is neglected. The simulation results show that the electromagnetic field attenuates gradually from the near center of VLF transmitters to the far away area, and the wave mode interference in the waveguide is also mapped into the ionosphere.

The VLF signals in the ionosphere propagating from ground-based transmitters are observed by the newly launched CSES satellite[27]. The features of VLF signals in the overhead ionosphere and their geomagnetic conjugate regions by CSES are presented. According to the revisit orbit analysis, it is found that the average values and standard deviations of electromagnetic field excited by the transmitters observed by CSES match well with the simulation results shown in Figure 7. It also shows that the electromagnetic field induced by NWC, NAA, and GBZ in the conjugate area is mainly distributed within $1.5<L<2.5$. However, NPM in the conjugate area is distributed at about $L<1.5$, implying a non-ducted propagation.

3.5 Ionospheric Disturbances Induced by the Geomagnetic Storms

Geomagnetic storms, last for several days, are the major space weather events. There are whole space disturbances involving thermosphere, ionosphere, and

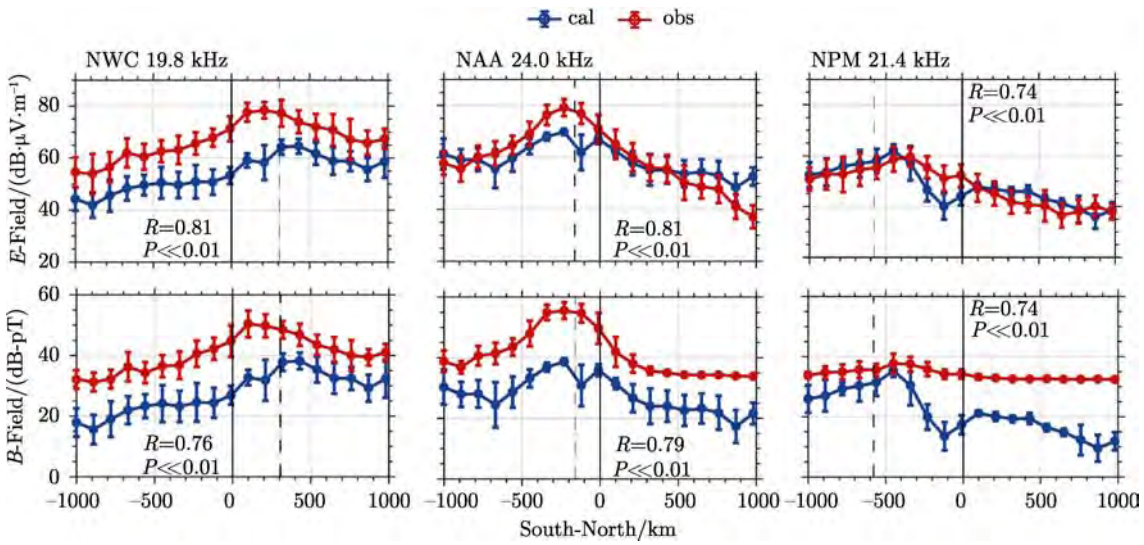

Fig. 7 Comparison of electric field (top panel) and magnetic field (bottom panel) excited by VLF transmitters (NWC, NAA, NPM) between CSES satellite observation and simulations. The R value represents the correlation coefficient. The P value represents whether the correlation coefficient has statistical significance. The vertical black solid lines show the geographical position of the transmitter; the black dashed lines show the geographical position of the crossing between the orbit of the satellite and the field line whose foot is at the height of 80 km above NWC transmitter

magnetosphere. Storms are thought to be related with activities in the Sun, *e.g.*, solar flares, CME. In the ionosphere, the solar Extreme Ultra Violet (EUV), Ultraviolet (UV) and X-rays related ionization can result in the enhancement of Electron density. Furthermore, the storm time ionosphere changing is also closely related with the physical process from the thermosphere and magnetosphere. During the storm, the increased energy input enhances the convection electric field in the magnetosphere, which can map down along magnetic field lines to high latitude of ionosphere, resulting in the strong plasma drift. The convection electric field can then penetrate into low latitude. At the same time, the energetic particles can inflow from the magnetosphere to ionosphere through Region 1 (R1) and Region 2 (R2) currents, expanding and intensifying the aurora activities, and considerably heating the ionized and neutral gases. The uneven expansion of thermosphere will then drive the neutral wind, altering the thermosphere circulation. This process, along with the penetration of electric fields to low latitude, will change the global dynamics in the ionosphere, resulting in the redistribution of neutral composition and plasma.

Low Earth orbit (LEO) can provide a good opportunity to conduct ionosphere observations during the storm. On 25–26 August 2018, CSES met the first intense storm event since its launch. In the work of Ref.[48], ionosphere multi-parameter disturbances observed during this storm are reported using conjunction observations from CSES data from HPM, SCM, LAP, PAP, EFD HEPD, and GOR payloads onboard CSES. The main purpose is to demonstrate the capabilities and performance of these payloads, as well as to reveal the mechanism of this storm event.

During this event, Swarm Alpha has close LT with CSES, so, we can make a comparison for the features detected by two missions. As presented in Figure 9, the residual field calculated from HPM/CDSM data by subtracting CHAOS main and crust field (reflecting currents from the ionosphere and magnetosphere) show very consistent results with Swarm observations. Both residual fields observed from CSES and Swarm shows very similar trends with storm activity, *i.e.*, during the storm initial phase, the residual fields enhanced and then reduced sharply for the storm's main phase; the value slowly

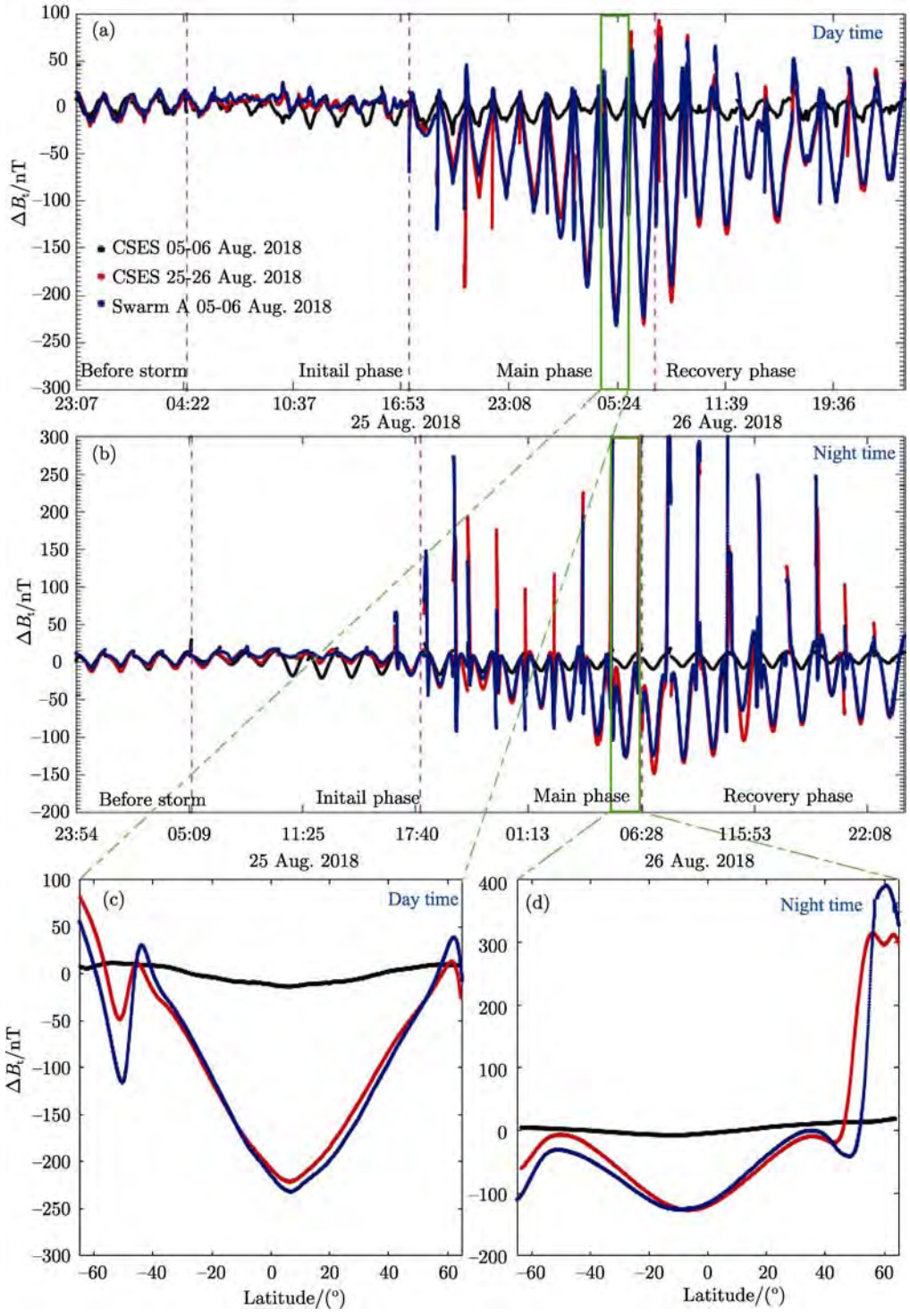

Fig. 8 Residual magnetic field evolution for CSES and Swarm during 25–26 August[48]

backs to a lower level during the recovery phase. The results indicate that the magnetic fields detected from CSES exhibit very good quality.

The joint observations from LAP, PAP, EFD, and GOR data can be used to investigate the possible mechanisms of this intense storm. Firstly, the plasma intensity (temperature) detected from LAP and PAP clearly increases (decreases) during the storm main phase and early recovery phase, and then backs to quiet time values. At the same time, the ULF PSD of

electric field behaves the similar way with plasma density. Besides, N_mF_2 and h_mF_2 observed from GOR (see Figure 9) are greatly enhanced and show a large deviation from quiet time. These phenomena imply that electric field penetration might be responsible for the generation of this positive ionosphere storm event.

Then, through SCM data, we observed very clear ELF/VLF waves during this storm event. For the daytime, very clear ELF/VLF waves are observed, which can last from storm main phase to several days of the recovery phase. While for the nighttime, the ELF/VLF waves are very weak during the whole storm event. The global distribution of energetic electron flux from HEPP is also checked in the study. We found a clear enhancement of <1 MeV energetic particles at the SAA, slot region, and outer radiation belt. At the same time, the pitch angle distribution shows that most particles are concentrate around 90°, indicating the locally mirroring (trapped/quasi-trapped) may be the dominant process for this storm time enhancement of energetic particles. These main features observed with SCM and HEPP are highly consistent with previous reported results. These observations also hint high potential applications of EFD/SCM and HEPP data on wave-particle studies.

3.6 Ionospheric Disturbances Associated with Strong Earthquakes

Electromagnetic precursors to seismic events have been reported since 1980s[49,50], serving as a new observing technique for studying seismic electromagnetic effects (*e.g.* Ref.[51] and references therein). The Lithosphere-Atmosphere-Ionosphere Coupling (LAIC) models explained these anomalous including the positive and the negative variation to a certain degree[52,53]). After CSES satellite was launched on 2 February 2018, the first earthquake with Ms>7.0 recorded by CSES was the Ms7.1 earthquake occurred in Mexico on February 17: the disturbances of low-frequency electromagnetic waves (Figure 10) and

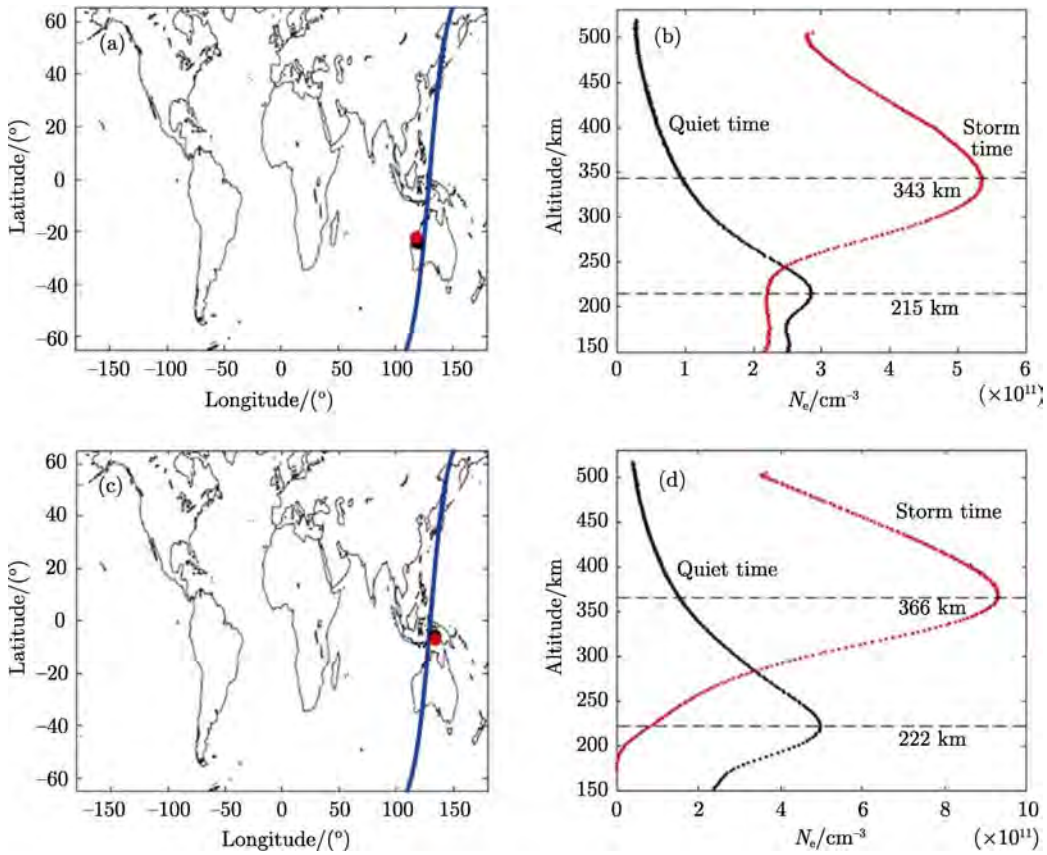

Fig. 9 Electron density profile obtained from GOR during the quiet time and storm time[49]

ionospheric plasma were found 2 or 3 days before the earthquake.

Then we examined the strong earthquake with Ms>6.0 in China and earthquake with Ms>7.0 all over the world since CSES launch with some data processing methods, and explored the disturbance characteristics and mechanism in the ionospheric before and after these earthquakes[51].

In this paper, we discussed another Ms 7.6 earthquake, which occurred about 46km southeast of Namatanai, Papua New Guinea on 14 May 2019 at 12:58:28 UT. It is also a shallow EQ with a depth of 30 km. The epicenter is located at geographic 4.15°S and 152.52°E. Ionospheric perturbations of N_e during 10 days before the EQ were studied using the moving median method. The nighttime data collected on one orbit within ±10° around the epicenter were resampled by 0.5° in the direction along the latitude. The background median value (A_b) and interquartile range (Q) were calculated using data from the previous 10 orbits (about 10 days), and then taking $A_b \pm Q$ as the upper and lower thresholds. We also introduce a similar method in detail in the reference[51]. The current resampled orbit data (A_o), background data (A_b), and upper and lower thresholds ($A_b \pm Q$) are shown at the same time in the upper panel Figure 11. The relative change, $[A_o-(A_b \pm Q)]/(A_b \pm Q)$, is calculated when the observation value is greater than the upper threshold or smaller than the lower threshold. If observation values are between the upper and lower thresholds, the relative change is then 0 (bottom panel Figure 11). From Figure 11, we can find that increases of N_e on 7 May and 11 May are obvious. Firstly, we check the Kp index during these two days and found that most Kp index is equal to 4 and 5 on 11 May. Hence, the N_e increases observed on 11 May is probably due to the magnetic storms. Then we found that the orbit on 7 May happened to be orbit passing by the epicenter (Figure 12) and in quiet magnetic days. So, we think the

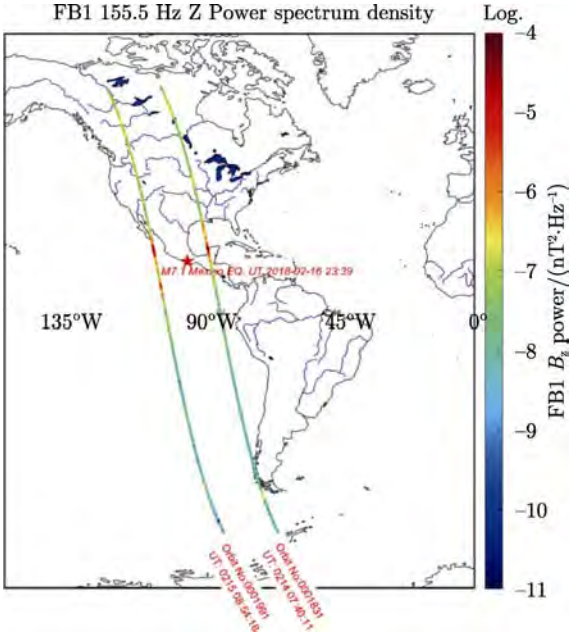

Fig. 10 Enhancement of ULF/ELF at 155.5 Hz magnetic field before Mexico earthquake

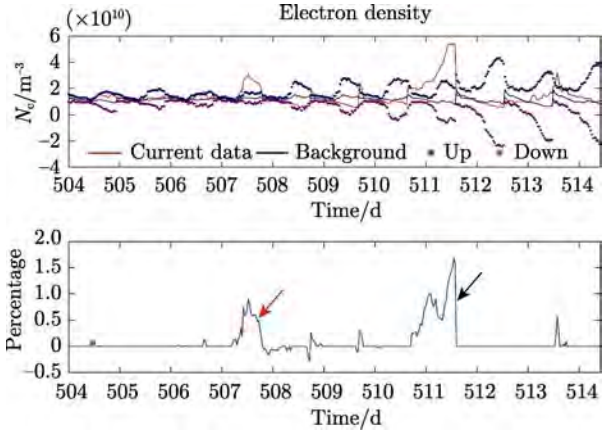

Fig. 11 Time series analysis of N_e moving average value

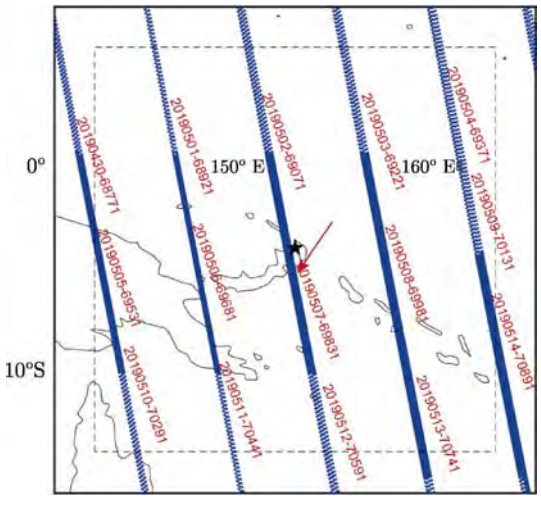

Fig. 12 Distribution of ascending revisited orbits close (less than 1000 km) to the epicenter

N_e enhancement is likely to be related to the earthquake (Figure 12) in magnetically quiet days.

It is found that CSES could record anomalies probably related to earthquakes after excluding the data disturbances caused by the satellite or payloads, magnetic storms, and disturbances at high latitudes. These findings are similar to those obtained on other satellites over the past decade. We summarized some abnormal phenomena probably related to the global earthquakes with $M \geqslant 7$ and depth $\leqslant 100$ km from February 2018 to February 2020 (not shown). Based on these results, we conclude that during strong earthquakes activities, CSES data are responsive to these earthquake events, the same parameters may not be reflected in each earthquake, perturbations in different parameters can occur at various locations and times. We also find that it is difficult to determine whether the abnormal is caused by an earthquake or not. The measured parameters display similar background variations in absence of seismic activity since the ionosphere is affected by a number of other factors. *Kp* and *Dst* can be used to examine whether perturbations are from earthquakes or magnetic storms, but they cannot be used to rule out other possibilities. This is one of the challenges in studying earthquake precursors[51]. Of course, the mechanism of ionospheric perturbation related to earthquakes still remains poorly understood and needs a long-term further study.

4 Conclusions

The current statuses of CSES platform, ground application system are briefly introduced in this report. Up to now, CSES has been operating in orbit for 2 years and has collected scientific data for more than 10000 orbits, except for some unknown contamination sources of Plasma Analyzer Package, the entire set of payloads and platform are all working in good condition. After the commission phase, every 3~4 months the satellite performs an orbit maneuver for ground track control so as to have a perfect recursive visit relative to all geophysical locations. The latest ground track keeping maneuver was performed on 20 January 2020. The remaining fuel of the satellite is about 35 kg (42 kg before launch), according to the current usage, the fuel is sufficient to support the entire life span. The ground segment of CSES consists of a science and application center, the satellite ground receiver networks, the verification field, and comparison system for satellite-ground measurement. CSES Satellite began its global observation since 13 February 2018, *i.e.* 10 d after its successful launching, and it has been collecting valuable scientific data. Using these first-hand data, we have achieved some good scientific results including some preliminary results on the global geomagnetic field modelling, the electromagnetic waves, the wave-particle interactions, the seismic-ionospheric mechanism as well as earthquake case study. The preliminary scientific applications indicate that CSES will benefit not only earthquake science but also geophysics, space science, radio wave science, and space weather monitoring.

Acknowledgments We acknowledge the CSES scientific mission which was funded by China National Space Administration (CNSA) and China Earthquake Administration (CEA), the data in this study can be download from the website http://www. leos.ac.cn/.

References

[1] SHEN X, ZONG Q, ZHANG X. Introduction to special section on the China Seismo-Electromagnetic Satellite and initial results [J]. *Earth Planet. Phys.*, 2018, **2**(6):439-443

[2] SHEN X, ZHANG X, YUAN S, *et al.* The state-of-the-art of the China Seismo-Electromagnetic Satellite mission [J]. *Sci. China Technol. Sci.*, 2018, **61**(5):634-642

[3] CHENG B, ZHOU B, MAGNES W, *et al.* High precision magnetometer for geomagnetic exploration onboard of the China Seismo-Electromagnetic Satellite [J]. *Sci. China Technol. Sci.*, 2018, **61**(5):659-668

[4] ZHOU B, YANG Y, ZHANG Y, *et al.* Magnetic field data processing methods of the China Seismo-Electromagnetic Satellite [J]. Earth Planet. Phys., 2018, **2**(6):455-461

[5] POLLINGER A, LAMMEGGER R, MAGNES W, *et al.* Coupled dark state magnetometer for the China Seismo-Electromagnetic Satellite [J]. *Meas. Sci. Technol.*, 2018, **29**(9):095103

[6] CAO J, ZENG L, ZHAN F, *et al.* The electromagnetic wave

experiment for CSES mission: Search coil magnetometer [J]. *Sci. China Technol. Sci.*, 2018, **61**(5):653-658

[7] HUANG J, SHEN X, ZHANG X, *et al.* Application system and data description of the China Seismo-Electromagnetic Satellite [J]. *Earth Planet. Phys.*, 2018, **2**(6):444-454

[8] YAN R, GUAN Y, SHEN X, *et al.* The Langmuir Probe onboard CSES: data inversion analysis method and first results [J]. *Earth Planet. Phys.*, 2018, **2**(6):479-488

[9] LIU C, GUAN Y, ZHENG X, *et al.* The technology of space plasma in-situ measurement on the China Seismo-Electromagnetic Satellite [J]. *Sci. China Technol. Sci.*, 2019, **62**(5):829-838

[10] CHU W, HUANG J, SHEN X, *et al.* Preliminary results of the High Energetic Particle Package onboard the China Seismo-Electromagnetic Satellite [J]. *Earth Planet. Phys.*, 2018, **2**(6):489-498

[11] LI X Q, XU Y B, AN Z H, *et al.* The high-energy particle package onboard CSES [J]. *Radiat. Detect. Technol. Methods*, 2019, 3(3). DOI: 10.1007/s41605-019-0101-7

[12] LIN J, SHEN X, HU L, *et al.* CSES GNSS ionospheric inversion technique, validation and error analysis [J]. *Sci. China Technol. Sci.*, 2018, **61**:669-677

[13] CHEN L, OU M, YUAN Y, *et al.* Preliminary observation results of the Coherent Beacon System onboard the China Seismo-Electromagnetic Satellite-1 [J]. *Earth Planet. Phys.*, 2018, **2**(6):505-514

[14] HULOT G, VIGNERON P, L GER J-M, *et al.* Swarm's absolute magnetometer experimental vector mode, an innovative capability for space magnetometry [J]. *Geophys. Res. Lett.*, 2015, **42**(5):1352-1359

[15] FINLAY C C, OLSEN N, KOTSIAROS S, *et al.* Recent geomagnetic secular variation from Swarm and ground observatories as estimated in the CHAOS-6 geomagnetic field model [J]. *Earth Planets Space*, 2016, **68**:112

[16] ZHIMA Z, CAO J, LIU W, *et al.* Storm time evolution of ELF/VLF waves observed by DEMETER satellite [J]. *J. Geophys. Res.: Space Phys.*, 2014. DOI: 10.1002/2013JA019237

[17] CHEN L, SANTOL K O, HAJOŠ M, *et al.* Source of the low-altitude hiss in the ionosphere [J]. *Geophys. Res. Lett.*, 2017. DOI: 10.1002/2016GL072181

[18] ZEREN Zhima, CHEN L, XIONG Y, *et al.* On the origin of ionospheric hiss: a conjugate observation [J]. *J. Geophys. Res.: Space Phys.*, 2017, **122**(11):11784-711793

[19] PARROT M, SANTOL K O, NĚMEC F. Chorus and chorus-like emissions seen by the ionospheric satellite DEMETER [J]. *J. Geophys. Res.: Space Phys.*, 2016, **121**(4):3781-3792

[20] ZEREN Zhima, CAO J, LIU W, *et al.* DEMETER observations of high-latitude chorus waves penetrating the plasmasphere during a geomagnetic storm [J]. *Geophys. Res. Lett.*, 2013, **40**(22):5827-5832

[21] HAYOSH M, NĚMEC F, SANTOL K O, *et al.* Propagation properties of quasiperiodic VLF emissions observed by the DEMETER spacecraft [J]. *Geophys. Res. Lett.*, 2016, **43**(3):1007-1014

[22] NĚMEC F, BEZDĚKOV B, MANNINEN J, *et al.* Conjugate observations of a remarkable quasiperiodic event by the low-altitude DEMETER spacecraft and ground-based instruments [J]. *J. Geophys. Res.: Space Phys.*, 2016, **121**(9):8790-8803

[23] PARROT M, BERTHELIER J, LEBRETON J, *et al.* Examples of unusual ionospheric observations made by the DEMETER satellite over seismic regions [J]. *Phys. Chem. Earth*, 2006, **31**(4-9):486-495

[24] ZHANG Z, CHEN L, LIU S, *et al.* Chorus acceleration of relativistic electrons in extremely low *L*-Shell during geomagnetic storm of August 2018 [J]. *Geophys. Res. Lett.*, 2020, **47**(4). DOI: 10.1029/2019GL086226

[25] ZHANG Z, CHEN L, LI X, *et al.* Observed Propagation Route of VLF Transmitter Signals in the Magnetosphere [J]. *J. Geophys. Res.: Space Phys.*, 2018, **123**(7):5528-5537

[26] ZHAO Shufan, LIAO Li, ZHANG Xuemin. Trans-ionspheric VLF wave power absorption of terrestrial VLF signal [J]. *Chin. J. Geophys.*, 2017, **60**(8):3004-3014 (in Chinese)

[27] ZHAO S, ZHOU C, SHEN X, *et al.* Investigation of VLF Transmitter Signals in the Ionosphere by ZH-1 Observations and Full-Wave Simulation [J]. *J. Geophys. Res.: Space Phys.*, 2019, **124**(6):4697-4709

[28] ZHANG Z-X, LI X-Q, WANG C-Y, *et al.* North west cape-induced electron precipitation and theoretical simulation [J]. *Chin. Phys. B*, 2016, **25**(11):119401

[29] ZHAO B Q, WANG M, YU T, *et al.* Is an unusual large enhancement of ionospheric electron density linked with the 2008 great Wenchuan earthquake [J]. *J. Geophys. Res.: Space Phys.*, 2008, **113**, A11. DOI: 10.1029/2008JA013613

[30] LIU J Y, CHEN Y I, PULINETS S A, *et al.* Seismo-ionospheric signatures prior to M⩾6.0 Taiwan earthquakes [J]. *Geophys. Res. Lett.*, 2000, **27**(19):3113-3116

[31] LIU J Y, CHEN Y I, CHEN C H, *et al.* Seismoionospheric GPS total electron content anomalies observed before the 12 May 2008 Mw7.9 Wenchuan earthquake [J]. *J. Geophys. Res.: Space Phys.*, 2009, **114**(A4). DOI: 10.1029/2008JA013698

[32] HAYAKAWA M, KASAHARA Y, NAKAMURA T, *et al.* A statistical study on the correlation between lower ionospheric perturbations as seen by subionospheric VLF/LF propagation and earthquakes [J]. *J. Geophys. Res.: Space Phys.*, 2010, **115**(A9). DOI: 10.1029/2009JA015143

[33] LIU J Y, TSAI Y B, CHEN S W, *et al.* Giant ionospheric disturbances excited by the M9.3 Sumatra earthquake of 26 December 2004 [J]. *Geophys. Res. Lett.*, 2006, 33(2). DOI: 10.1029/2005GL023963

[34] HAO Y Q, XIAO Z, ZHANG D H. Multi-instrument observation on co-seismic ionospheric effects after great Tohoku earthquake [J]. *J. Geophys. Res.: Space Phys.*, 2012, 117. DOI: 10.1029/2011JA017036

[35] FREUND F. Pre-earthquake signals: Underlying physical processes [J]. *J. Asian Earth Sci.*, 2011, **41**(4/5):383-400

[36] FREUND F, KULAHCI I G, CYR G, *et al.* Air ionization at rock surfaces and pre-earthquake signals [J]. *J. Atmos. Solar-Terr. Phys.*, 2009, **71**(17/18):1824-1834

[37] FREUND F, TAKEUCHI A, LAU B W, *et al.* Stress-

Induced Changes in the Electrical Conductivity of Igneous Rocks and the Generation of Ground Currents [J]. *Terr. Atmos. Ocean. Sci.*, 2004, **15**(3):437-467

[38] SOROKIN V M, CHMYREV V M, YASCHENKO A K. Electrodynamic model of the lower atmosphere and the ionosphere coupling [J]. *J. Atmos. Solar-Terr. Phys.*, 2001, **63**(16):1681-1691

[39] KUO C L, HUBA J D, JOYCE G, *et al.* Ionosphere plasma bubbles and density variations induced by pre-earthquake rock currents and associated surface charges [J]. *J. Geophys. Res.: Space Phys.*, 2011, **116**, A10

[40] KUO C L, LEE L C, HUBA J D. An improved coupling model for the lithosphere-atmosphere-ionosphere system [J]. *J. Geophys. Res.: Space Phys.*, 2014, **119**(4):3189-3205

[41] ZHOU C, LIU Y, ZHAO S F, *et al.* An electric field penetration model for seismo-ionospheric research [J]. *Adv. Space Res.*, 2017, **60**(10):2217-2232

[42] FREUND F, TAKEUCHI A, LAU B W S. Electric currents streaming out of stressed igneous rocks - A step towards understanding pre-earthquake low frequency EM emissions[J]. *Phys. Chem. Earth*, 2006, **31**(4-9):389-396

[43] GAO Y X, HARRIS J M, WEN J, *et al.* Modeling of the coseismic electromagnetic fields observed during the 2004 Mw 6.0 Parkfield earthquake [J]. *Geophys. Res. Lett.*, 2016, **43**(2):620-627

[44] HAYAKAWA M. Probing the lower ionospheric perturbations associated with earthquakes by means of subionospheric VLF/LF propagation [J]. *Earthquake Sci.*, 2011, **24**(6):609-637

[45] NĚMEC F, SANTOLíK O, PARROT M. Possible seismic influence on VLF wave intensity: observations by a low-altitude satellite [C]//WDS'08 Proceedings of Contributed Papers, 2008

[46] LEHTINEN N G, INAN U S. Radiation of ELF/VLF waves by harmonically varying currents into a stratified ionosphere with application to radiation by a modulated electrojet [J]. *J. Geophys. Res.*, 2008, **113**, A06301

[47] LIAO L, ZHAO S F, SHEN X H, *et al.* Characteristic analysis and full wave simulation of electrical field for China seismo-electromagnetic satellite observations radiated from VLF transmitter [J]. *Chin. J. Geophys.*, 2019, **62**(4):1210-1217

[48] YANG Y Y, ZHIMA Z R, SHEN X H, *et al.* The first intense storm event recorded by the China seismo-electromagnetic satellite [J]. *Space Weather*, 2019. DOI: 10.1029/2019SW002243

[49] LARKINA V I, MIGULIN V V, MOLCHANOV O A, *et al.* Some statistical results on very low frequency radiowave emissions in the upper ionosphere over earthquake zones [J]. *Phys. Earth Planet. Int.*, 1989, **57**(1):100-109

[50] PARROT M. VLF emissions associated with earthquakes and observed in the ionosphere and the magnetosphere [J]. *Phys. Earth Planet. Int.*, 1989, 57(1/2):86-99

[51] YAN R, SHEN X, HUANG J, *et al.* Examples of unusual ionospheric observations by the CSES prior to earthquakes [J]. *Earth Planet. Phys.*, 2018, **2**(6):515-526

[52] PULLINETS S, OUZOUNOV D. The Possibility of Earthquake Forecasting [M]. Bristol: IOP Publishing, 2018

[53] HAYAKAWA M. Electromagnetic phenomena associated with earthquakes: a frontier in terrestrial electromagnetic noise environment [J]. *Recent Res. Develop. Geophys.*, 2004, **6**:81-112

WANG Chi, CHEN Zhiqing, XU Jiyao. Recent Advances in Research of the Chinese Meridian Project. *Chin. J. Space Sci.*, 2020, **40**(5): 087-098. DOI:10.11728/cjss2020.05.087

Recent Advances in Research of the Chinese Meridian Project*

WANG Chi CHEN Zhiqing XU Jiyao

(*State Key Laboratory of Space Weather, National Space Science Center, Chinese Academy of Sciences, Beijing* 100190)

Abstract The Chinese Meridian Project is a ground-based space environment monitoring facility in China. The first phase of the project has been put into formal operation since 2012 after 4-year's construction. It consists of 15 observatories located roughly along 120°E longitude and 30°N latitude, with each observatory equipped with multiple instruments to monitor space environment. Based on the huge observational data accumulated, significant scientific achievements have been made with more than 300 peer-reviewed journal papers published. In this report, scientific results from the past two years have been reviewed with topics covering fields of geomagnetic, atmosphere, ionosphere, and their responses to solar activities. The excellent achievements from the Phase I of Chinese Meridian Project lay a good foundation for Phase II, which has already been approved with the official kick-off of construction in November 2019. It will conceive an unprecedented contribution to global space weather community from China.

Key words Chinese Meridian Project, Space weather, Ionosphere, Upper atmosphere

Classified index P 35

1 Brief Introduction of the Project

The Chinese Meridian Project, with a full name of Space Environment Ground Based Comprehensive Monitoring Network (SEGCMN), is a Major Science and Technology Infrastructure funded by the Chinese government. The project was scheduled to be constructed in two steps: the first step (Phase I) has led to tens of instruments deployed across China's territory and the Antarctic region, which has been put into operation since 2012. The second step (Phase II) of construction kicked off in November 2019, and is expected to complete in 2023. This report will briefly summarize the recent research progresses based on observations made by instruments that were constructed in Phase I of the Chinese Meridian Project.

Phase I of the project, also named East-sphere Space Environment Ground-based Comprehensive Monitoring Chain, consists of 15 ground-based observatories located roughly along 120°E longitude and 30°N latitude[1]. The longitudinal chain of observatories starts from Mohe, the northernmost city of China, and runs southward roughly through Beijing, Wuhan, Guangzhou, and the island of Hainan (with instruments at Haikou, Fuke, and Sanya) and extends to China's Zhongshan station in Antarctica[1]. Distances between neighbouring stations are roughly 4°~5° in latitude, or about 500 km near 120°E longitude, except the Zhongshan station in Antarctica. A chain of stations was also constructed roughly following 30°N, spanning from Lhasa to Shanghai. Each observatory is equipped with multiple instruments to comprehensively measure the key para-

* Supported by the Open Research Project of Large Research Infrastructures of Chinese Academy of Sciences, the Study on the Interaction between Low/Mid-latitude Atmosphere and Ionosphere Based on the Chinese Meridian Project, and the Chinese Meridian Project

Received March 16, 2020

E-mail: cw@spaceweather.ac.cn

meters such as the baseline and time-varying geomagnetic field, as well as the middle and upper atmosphere and ionosphere from about 20 to 1000 km. Parameters of the solar wind are also tentatively measured.

Instruments of the Meridian Project (Phase I) mainly include magnetometers, ionosondes, an incoherent scatter radar, a high-frequency backscatter radar, mesosphere-stratosphere-troposphere radars, meteor radars, lidars (light detection and ranging), Fabry-Perot Interferometers (FPI), and aurora spectrographs. Overall, the instruments can be grouped into four categories, named geomagnetic (geoelectric) field, radio wave, optical, and sounding rocket. Altogether, 87 instruments were built and installed at 15 stations.

The Phase I of the project was funded by China's National Development and Reform Commission as part of a series of major scientific infrastructures. Construction of the project started in January 2008 and completed in December 2012. It is a joint effort of 12 institutions or universities in China, led by National Space Science Center (NSSC), the Chinese Academy of Sciences.

2 Scientific Achievements in the Past Two Years

The Meridian Project was put into formal operation in December 2012. Up to the end of 2019, about 15570 thousand data files (6.54 TB) have been accumulated. Using these data, scientists have made significant progress in space physics and space weather study, publishing more than 300 peer-reviewed papers. More than 10 national or provincial level awards were obtained.

Among these achievements, there are more than 80 journal papers published in recent two years (2018–2019), which will be briefly summarized as follows.

2.1 Polar Region Ionosphere

The polar region ionosphere is distinctive from that of the mid-to-low latitudes, features with plasma patches, strong radio wave scintillations, particle precipitation and upflows, *etc.* A bundle of instruments deployed by Chinese Meridian Project at Antarctic region, such as the SuperDARN radar[2] and scintillation monitors, were available for relevant researches.

Recently, a newly identified high-density irregularity named polar cap hot patch was found at high latitudes. Compared with classical polar cap patches, hot patches are associated with higher electron temperature and particle precipitation. By using five years of in situ plasma observations from DMSP satellites, with SuperDARN data in comparison, Ma *et al.*[3] investigated the characteristics of hot patches versus classical patches. For the first time, they show that the difference/ratio of ion/electron temperature can be used to distinguish between classical and hot patches. The vertical ion flux is generally downward in the classical patches ($T_i/T_e > 0.8$ or $T_e < T_i + 600$ K), while the vertical ion flux is generally upward in the hot patches ($T_i/T_e < 0.8$ or $T_e > T_i + 600$ K). They also found that the T_i/T_e ratio (or $T_i - T_e$ difference) has a definite influence on behaviors of polar cap patches as, upon increasing T_i/T_e ratio, patches turn from hot to classical ones and vertical flux turns from upward to downward. The highest upflow occurrence was found in those hot patches which are near the polar cap boundary, and are associated with particle precipitation, strong convection speed, and localized field-aligned currents. This result shows that the polar cap hot patches may play a very important role in the solar wind-magnetosphere-ionosphere coupling processes.

For a long time, it was widely accepted that in the polar region the amplitude scintillation should be much weaker than the phase scintillation, even ignorable. Recently, this popular opinion has been challenged more and more based on simulations and some tests, which usually focused on the way adopted to obtaining these scintillation indices especially over the polar region. However, a direct experimental evidence is still required to deep the new understanding. On the plasma flow around the noon sector of polar ionosphere, Wang *et al.*[4] presented the first experimental proof of a clear and strong dependence

of the standard phase scintillation index by using the observation measurements from Global Positioning System and SuperDARN radars. They reported that the phase scintillation index presents a strong linear dependence on the plasma drift speed, but the amplitude scintillation index (S_4) does not. These different dependencies on the relative drift can be explained to be a consequence of changing Fresnel frequency, but also the fixed cutoff frequency (0.1 Hz) used to detrending the raw data to calculating the classical phase scintillation index. Moreover, other than the amplitude scintillation and the so-called phenomenon "phase without amplitude" scintillation in the high latitude region, a higher occurrence of phase scintillation can be probably explained by this dependence pattern. Furthermore, it can be concluded that the phase scintillation index in classical is much more sensitive to plasma drift. Therefore, if you are looking at the phase scintillation phenomenon especially over the polar region where the ionospheric plasma flow is much faster than those at equatorial and mid-latitude regions, one should be much careful to investigating the scintillation behaviors.

By analyzing five years' (2010–2014) DMSP plasma data, with SuperDARN data in comparison, Ma *et al.*[5] investigated the plasma parameters of ion upflow above the north polar cap under different Solar Zenith Angles (SZA), solar activity ($F_{10.7}$) levels, and convection speeds. In spatial distributions, high upflow occurrence rates are found in the dawn sector associated with regions of higher convection speed, while higher upflow fluxes are found in the dusk sector associated with higher density. By taking the solar illumination and activity into consideration, they find that the upflow occurrence shows a positive correlation with convection speed and solar activity, while it shows a negative correlation with SZA. Thus, when SZA>100° and the convection speed is low, the lowest upflow occurrence is observed. A clear seasonal dependence is found for upflow velocity and flux, which shown higher speed in the winter (high SZA) and higher flux in the summer (low SZA) during low convection conditions. It suggests that upflow density mainly contributes to upflow flux in summer, and upflow velocity mainly contributes to upflow flux in winter. For the first time, upflow velocity and density are found to be both higher in summer and high convection conditions, which implies the combined effect of evolution of flux tubes and joule/frictional heating variation done on the convection speeds. These results suggest that ion upflow in the polar cap is controlled by the combination of convection, solar activity, and solar illumination.

2.2 Study on Ionospheric Irregularities

Using Wuhan ionosonde of the Chinese Median Project, Wuhan Very High Frequency (VHF) coherent scatter radar and Mengcheng airglow imager, Zhou *et al.*[6] investigated the nighttime disturbances in E and F regions at the midlatitude China region. They presented two case studies of simultaneous observations of diffuse sporadic E (Es) layers, quasiperiodic echoes of E region irregularities, spread F, and medium-scale traveling ionospheric disturbances. Results indicate that diffuse Es layers and E region irregularities can be associated with the F region medium-scale traveling ionospheric disturbances or spread F through polarization electric field mapping along the field lines. Further analysis on the dataset of Wuhan ionosonde and Wuhan VHF radar during 2015–2016 finds that, the probability of coincidence of diffuse Es layers, quasiperiodic echoes of E region irregularities, and spread F is high at local nighttime. The results provide the first observational evidence in midlatitude China region to support the concept that polarization electric field generated in the E region irregularities could map along the magnetic field lines and excite electrodynamic disturbances in F region, such as Perkins instability.

Brazil is in the South American Magnetic Anomaly region. Research on the ionosphere, geomagnetic field, and other space weather physical processes in this region is a hot topic in international space weather communities. Moro *et al.*[7] did a comparative study using ionospheric sounding data of Chinese Meridian Project Wuhan station (30.5°N, 114.4°E, dip is 46°), together with data from Santa

Maria station (29.7°S, 53.7°W, dip is –38°) which is located in the South American Magnetic Anomaly area in Brazil. The differences of ionospheric parameters (f_0E, f_0F_2, h_mF_2, and thickness parameter B_0) between the northern and southern hemispheres, the geomagnetic anomaly area, and the non-anomaly area are revealed. It is found that the ionosphere in the South American Magnetic Anomaly area exhibits a greater variation than in the northern hemisphere under the same conditions. This study is of great significance as to deepening understanding of the influences of the South American Magnetic Anomaly on space weather.

Based on ground-based instruments, including an all-sky airglow imager, a spectrometer, and a Fabry-Perot Interferometer (FPI) from the Chinese Meridian Project and a Digisonde in midlatitude of China, Sun *et al.*[8] report a special mid-latitudinal Medium-Scale Traveling Ionospheric Disturbance (MSTID) event, accompanied by a poleward surge of airglow depletion/enhancement and a bifurcation of depletion during the magnetically quiet period. It is found that interaction of the passing MSTID and Nighttime Plasma Density Enhancement (NPDE) resulted in the poleward surge and bifurcation of airglow depletion. For the first time, the article provided observational evidence that midlatitudinal bubble-like bifurcation structure can be directly generated by the propagating MSTID, that most likely caused by the Secondary Gradient Drift Instability (SGDI). Meanwhile, for the first time, the article suggested the Midnight Brightness Wave (MBW) as one of the possible sources of the NPDE at midlatitude regions.

In the study of Chen *et al.*[9], the oblique-incidence ionosonde network in North China and the Beijing Digisonde were used to investigate the nighttime ionospheric disturbances, including the Premidnight Enhancements (PRMEs) and the Postmidnight Enhancements (POMEs) in January and February of 2011. Most of the two kinds of electron density enhancements present opposite latitudinal dependence, namely, the PRMEs appear earlier in the north and then travel southward and the POMEs occur in the south and then move to north. Thus, the two enhancements should be induced by different mechanisms. Further analysis reveals that the PRMEs are the peaks of the Large-Scale Travelling Ionospheric Disturbances (LSTIDs), which may be induced by the southward propagating gravity waves. Most of the POMEs are composed by an enhancement and a following depletion, which is considered to be induced by the downward $\boldsymbol{E}\times\boldsymbol{B}$ drift due to the westward electric field.

Equatorial Plasma Bubbles (EPBs) are frequently occurred phenomena in the ionosphere at low latitude of China, which have a great impact on navigation and communication. Wu *et al.*[10] used observational data from all-sky imager of the Chinese Meridian Project and the C/NOFS satellite to study the edge plasma enhancements of EPBs. By researching on four-year observations from 2012 to 2015, it was found that edge plasma enhancements are usually accompanied by EPBs. The observations of four years show that it is a high-incidence phenomenon, and the average incidence rate reaches about 82%. And the plasma enhancements only appeared at the east and west edges of EPBs, while none of them appeared at poleward edges. They show similar geographical longitude and local time distribution relative to pertaining EPBs. The results of observations show their occurrence rate made a peak between 20:00 LT to 22:00 LT. Zonal extents of those plasma enhancements present different scale characteristics at different altitudes. Occurrence characteristics of edge plasma enhancements of EPBs were also studied. Results indicate that the plasma related to EPBs is more likely to have been redistributed and, consequently formed depletions and enhancements. This study has provided a new perspective on the formation of EPBs.

In general, ionospheric plasma blobs as the density enhancement in the Equatorial Ionization Anomaly (EIA) regions are caused by the polarization electric field, which was generated within Equatorial Plasma Bubbles (EPBs) and mapped to the EIA regions along the magnetic field lines. A major characteristic of this view is that plasma blobs

occur at the poleward edges of EPBs. Wang *et al.*[11] reported three cases of concurrent plasma blobs and bubbles around 22:30 LT from low latitude stations Vanimo (geog. 2.7°S, 141.3°E; geom. 11.2°S, 146.2°W) and Hainan (geog. 19.5°N, 109.1°E; geom. 9.1°N, 179.1°W) in the same magnetic meridian in Asian-Oceanian sector during solar maximum, taking advantages of simultaneous observations by ROCSAT-1 satellite and ground ionosonde/GPS scintillations to examine the relative location of plasma bubbles and blobs. In these cases, the blobs were at the equatorward edges of equatorial plasma bubbles, contradicting to the traditional perception. All plasma blobs were observed at about 600 km height near to the equator. ESF and amplitude scintillations near the same magnetic meridian line indicated the existence of bubbles at higher latitude. Considering that both plasma bubbles and blobs are field-aligned elongated structures, in two of these cases, blobs were above bubbles, indicating an explanation that the eastward polarization electric field inside EPBs drives plasma upward and causes plasma blobs just above the upper boundary of the EPBs in the intermediate stage of the bubble development. In the third case, the blob might be slightly lower than EPBs, and the EPB and blob might be generated by eastward and westward electric fields in the parts of the perturbation produced by charging by gravitational electric current below the ionospheric peak.

2.3 Responses of Ionosphere/Thermosphere to Solar Activities and Geomagnetic Activities

Based on data collected by the meteor radars at the Davis Station (68.6°S, 77.9°E), Svalbard (78.3°N, 16°E), Tromsø (69.6°N, 19.2°E), Mohe (53.5°N, 122.3°E) and Beijing (40.3°N, 116.2°E), Yi *et al.*[12] presented a first inter-hemisphere observation of neutral mesospheric density response to geomagnetic storms. A superposed epoch analysis results show that strong geomagnetic storms can cause a greater than about 10% decrease at the polar region and about 5% decrease at higher mid-latitudes, which may indicate that geomagnetic storms could influence the polar mesospheric dynamics.

Using multiple data sets including Beidou geostationary orbit satellites Total Electron Contents (TECs), ionosonde, and meteor radar from Chinese Meridian Project combined with model simulations, Lei *et al.*[13] investigated the ionospheric responses during the September 2017 geomagnetic storm in the Asian-Australian sector. It was found that long-duration daytime TEC enhancements that lasted from 7 to 12 September 2017 were observed by the Beidou geostationary orbit satellite constellation. This is a unique event as the prominent TEC enhancements persisted during the storm recovery phase when geomagnetic activity became quiet. The model results predicted that the TEC enhancements on 7–9 September were associated with the geomagnetic activity, but it showed significant electron density depletions on 10 and 11 September in contrast to the observed TEC enhancements. The results suggested that the observed long-duration TEC enhancements from 7 to 12 September are mainly associated with the interplay of ionospheric dynamics and electrodynamics. Nevertheless, the root causes for the observed TEC enhancements seen in the storm recovery phase are unknown and require further observations and model studies.

Using the nighttime thermospheric temperature (about 250 km) measured by an FPI deployed at Xinglong (40.2°N, 117.4°E) station between 2010 and 2018, Liu *et al.*[14] studied the responses of the multiday oscillations in thermospheric temperature to oscillations in $F_{10.7}$ and Ap index. The results showed that the 27, 13.5, 9, and 7-day oscillations depended on solar phases. The 27-day oscillation was predominant during solar maximum and highly correlated with the $F_{10.7}$ and Ap index. The 13.5, 9, and 7-day oscillations were important and highly correlated with Ap index during solar ascending phase.

2.4 Responses of Ionosphere/thermosphere to Disturbances in Lower Atmosphere

Exploiting variation of the Equatorial Ionization Anomaly (EIA) crest derived from GPS observations in China and Brazilian sector, Mo *et al.*[15] investigated the longitudinal dependence of periodic meridional movement of EIA crest during Sudden Stratospheric Warming (SSW) events in 2003, 2006

and 2009. Results show that the locations of EIA crests in both China and Brazilian sectors exhibit obvious and constant 14~15 days periodic in-phase oscillation, which coincide with the half of the lunar revolution period (29.53 days) and the lunar phase. The temporal extent of wave power at 14~15 days is consistent with the temporal extent of stratospheric zonal wind, indicating that 14~15 days periodic meridional movement of EIA crest is due to enhanced lunar tide modulated by zonal wind. In addition, it is also found that the amplitude of 14~15 days periodic oscillation of EIA crest in China sector is larger than that in Brazilian sector, which may be caused by the longitudinal variation of tides and neutral wind pattern.

With ionospheric TEC, geomagnetic field data in East-Asia and American sectors, Liu *et al.*[16] studied the longitudinal differences of low-latitudinal ionospheric responses during the SSW winters from 2009–2018. The Time-shifted Semi-diurnal (TS) patterns and the amplitude, phase angle, and relative strength of the lunar semi-diurnal tide (M2) harmonic in TEC are compared between the two sectors. The study came out with main results as: (i) TS patterns, M2 amplitudes, and M2 relative strengths tend to be more discernible or larger in the American sector than in the East Asian sector; (ii) TS patterns and M2 phase angles correlated well to the lunar phase, and the occurrence of TS patterns coincides well with the enhancement of M2 amplitudes and M2 relative strengths; (iii) such patterns can sometimes occur before the polar peak warming and experience several cycles during one event, but the most significant one tends to follow the peak warming. These longitudinal differences suggest that the influences of M2 on the low-latitudinal ionosphere tend to be more prominent in the American sector than in the East Asian sector during SSWs. It has probably resulted from a combined effect of the longitudinal variety in atmospheric and electrodynamic processes.

To study the response characteristics of ionosphere during a strong lower atmospheric process, Liu *et al.*[17] analyzed the ionospheric TEC data measured by Chinese Meridian Project during a Sudden Stratospheric Warming event in 2018. Research result shows that the deviation of TEC presents remarkable perturbation after the reversal of the zonal wind, especially around the temperature peak. Wavelet power spectra analysis indicates that the variation of TEC exhibits a strong semidiurnal and diurnal oscillation pattern during the SSW period. The cross-correlation analysis reveals that the equatorial electrojet played a key role in the anomaly perturbation and periodic oscillation of TEC, while the correlation is weak at middle latitude. These results definitely confirm the energy transmission and coupling between the lower atmosphere and ionosphere, and the dynamic process interplaying between high latitude and low latitude.

Using TEC associated with Beidou geostationary satellites from GNSS receivers of Chinese Meridian Project and IGS network, Huang *et al.*[18] statistically analyzed the daytime periodic wave-like structures for the first time in the low-latitude ionosphere over the Asian-Australian sector during 2016–2017. These structures have periods of about 18~28 min, which frequently occur during 11:00 LT–17:00 LT in the winter at latitudes ranging between 17°N and 25°N (10°–18°N magnetic latitude MLAT) in the Northern Hemisphere, where they have a maximum occurrence rate of 80% at about 21°N (14°N MLAT). In the Southern Hemisphere, daytime periodic wave-like structures are also observed during 11:00 LT–15:00 LT in the winter within latitudes ranging between 6.0°S and 11.1°S (15.4°–21.6°S MLAT), although the peak occurrence rate is only approximately 40%. Compared with stratospheric Gravity Waves (GWs), the seasonal and latitudinal variations of daytime periodic wave- like structures are generally consistent with those of stratospheric GWs. This gives a possible argument that daytime periodic wave-like structures in the low-latitude ionosphere could be generated in the low-latitude ionosphere and triggered by GWs from the lower atmosphere. This study provides a typical example that the Chinese Meridian Project combined with other observation networks have been used to explore the coupling of the different Earth's at-

mosphere and provide a new understanding of the structure of the low-latitude daytime ionosphere.

By the help of ionosonde observations from Chinese Meridian Project and GNSS radio occultation measurements from COSMIC, Yu *et al.*[19] analyzed the long-term climatology of the intensity of ionospheric sporadic E (Es) layers during 2006–2014. A high-spatial-resolution map of Es intensity shows a peak of strong occurrence and intensity of Es layers in the mid-latitudes of the summer hemisphere. Some interesting distinctions between the occurrence and intensity of sporadic E layers were found. At high latitudes, the occurrence rates of Es are generally low, but the intensity of Es is relatively high. This pattern is more evident over the magnetic poles, likely resulting from the vertical motions of polar-gap gravity waves in concentrating ionizations within Es layers. Using wind fields from Whole Atmosphere Community Climate Model (WACCM), the summer maximum of Es layers can be explained by the vertical ion convergences of wind shear. However, the wind shear convergences at higher E-region altitudes cannot explain the observations. The results indicate that other dynamical and chemical processes of metallic ions, such as meteoric mass influx and geo-magnetic forces, should be considered in the temporal and spatial variation in the Es layers.

2.5 Study on Atmospheric Gravity Waves

Li *et al.*[20] reported a study of mesospheric Gravity Waves (GWs) for one year (August 2015 to July 2016) in the latitudinal band from 45°N to 75°N using an OH all sky airglow imager over Kazan (55.8°N, 49.2°E), Russia, for the first time. The observation, sponsored by Chinese Meridian Project, fills a huge airglow imaging gap in Europe and Russia region. Most of the waves propagate northeastward in all seasons, which was significantly different from airglow imager observations at other latitudes, such as Meridian Project Xinglong station that the propagation directions were seasonal dependent. The European Centre for Medium Range Weather Forecasts reanalysis data indicates that the convections near Caucasus Mountains region are the dominant source of the GWs in spring, summer, and autumn seasons. This study extends our knowledge that convection might also be an important source of GWs in the higher latitudes. Jet stream systems are considered to be the controlling generation mechanism of the GWs in winter. Another important finding is that the occurrence frequency of ripple is much lower than that of other stations. The present study provides some constraints in GW parameterization schemes in general circulation models in Europe and Russian region.

Using data from the meteor radar chain along 120°E, Jia *et al.*[21] revealed multiyear high-frequency Gravity Wave (GW) momentum fluxes and variances in the mesosphere and lower thermosphere region at Northern Hemisphere mid-latitudes for the first time. The meteor radars are located at Mohe (53.5°N, 122.3°E), Beijing (40.3°N, 116.2°E), Mengcheng (33.3°N, 116.5°E), and Wuhan (30.5°N, 114.2°E) respectively, with two of them from Chinese Meridian Project. The directions of the monthly mean zonal momentum fluxes are mostly against the background mean zonal winds, which agree well with the selective filtering mechanism. The seasonal variations of meridional momentum fluxes have similar trends over all four stations. The latitudinal differences in the seasonal variation of GW momentum fluxes are mainly due to the latitudinal differences of background winds and GW sources. Observations show unexpected eastward momentum flux in winter over Beijing, that is likely caused by the secondary GWs propagating eastward from the source region over the Tibetan Plateau (25°–40°N, 70°–100°E). The GW variances show a V-shaped structure indicating annual and semiannual variations over four stations in zonal component. A quasi-4-month oscillation was observed over Mohe, Mengcheng, and Wuhan in meridional component. The background winds play decisive roles in these GW variance structures.

Li *et al.*[22] presented a mesospheric bore event observed in the airglow layers of both OH and OI (557.7 nm) bands by two all-sky airglow imagers in Lhasa (29.66°N, 90.98°E) on the Tibetan Plateau and the Day Night Band (DNB) of the Visible Infrared Imaging Radiometer Suite (VIIRS) onboard

the Suomi National Polar-orbiting Partnership (NPP) satellite on the night of 16–17 December 2014. They also made a comparative study of the bore event observed at Chinese Meridian Project Xinglong Station. Temperature and OH intensity measurements from the Sounding of the Atmosphere using Broadband Emission Radiometry (SABER) instrument onboard the TIMED satellite and wind observation by a meteor radar were used to study the environment of the bore propagation. SABER temperature shows a large mesospheric inversion layer. Through hydraulic jump theory and observations, it is found that the duct initially shrank followed by an expansion. The horizontal wavelengths and observed phase speeds of the bore packet increased with the expansion of the duct and decreased with the contraction of the duct. The bore may leak out of the duct with the variation of the depth of the duct. This study provides new insight into mesospheric bore evolution and how the ducted environment influences the propagation of bores.

2.6 Study on Atmospheric Tide and Planetary Waves

Most previous studies about tidal climatology assume that tidal variations are quite stable over a couple of weeks, and it's safe to ignore its day-to-day variability. However, the day-to-day variability of tides is in itself an important scientific question that needs to investigate further. Zhou *et al.*[23] attempted to fix these questions and proposed a new approach to derive tidal climatology with its day-to-day variability taken into consideration. Combined with TIMED Doppler Interferometer (TIDI) wind measurements, 4-year continuous horizontal winds measured by a meteor radar chain over Mohe, Beijing, Wuhan, and Sanya are used in the study. Taking advantage of Empirical Tidal Mode (ETM), which is first derived from Global Scale Wave Model (GSWM) using Empirical Orthogonal Function (EOF) analysis, the daily variations of different mesosphere and lower thermosphere tides are then obtained. ETM displays latitudinal and vertical features of each tidal component in a realistic background atmosphere with dissipation effects. After fitting the observations by ETM day by day, the monthly mean of daily fitted results is used to describe tidal monthly features. Seasonal variations of three major tidal components were identified: DW1 in both zonal and meridional winds usually has two maxima around equinoxes, DE3 in zonal winds achieves its maximum in September, while that in meridional winds becomes strongest in February and November. SW2 in zonal winds reaches the largest amplitudes in May in the southern hemisphere, and meridional winds have minor peaks in February and November in the northern hemisphere.

Using data by a meteor radar chain of the Chinese Meridian Project in the period from December 2008 to November 2017, Gong *et al.*[24] presented an extensive analysis of quasi 5-Day Waves (5DWs) in the Mesosphere and Lower Thermosphere (MLT) and their responses to a major Sudden Stratospheric Warming (SSW) event. The ter-annual oscillation of the 5DWs is found to be as important as the commonly recognized annual oscillation and semiannual oscillation at the three stations in both neutral wind components. The 5DWs are strong mainly during the August/September in the meridional component, while they are primarily enhanced in the period of January, April/May, and late summer in the zonal component. An enhancement of 5DWs is observed during the 2013 SSW event in the MLT region at the three stations. The amplitudes during the SSW are more than 2 times larger than the January average. The strength of the amplification is most prominent at Mohe and reduces as latitude decreases. Results indicate that the amplification of the 5DWs is very likely associated with the 2013 SSW. This is the first time that an enhanced 5DW during a major SSW has been investigated.

By using observations from three meteor radars and a MST radar supported by the Chinese Meridian Project and reanalysis data, Yu *et al.*[25] studied the SFW in 2015 spring and PW activities from the troposphere to the MLT. The reanalysis data indicates that in the SFW, the polar mean temperature at 10 hPa level increases about 20 K, and the polar mean zonal wind decreases from about 30 $m \cdot s^{-1}$ to

-10 m·s^{-1}. In this way, the polar circulation completes a seasonal transition. The radar observations show that the Q10DW and Q16DW occur around the SFW. In the troposphere and stratosphere, the wave activities are intense before the SFW, while in the MLT, the waves are amplified following the SFW with an amplitude peak of about 10-day lag, and their latitudinal variation is roughly consistent with the Hough modes. This means that the Q10DW and Q16DW in the MLT are likely to be generated and strengthened in situ in the upper stratosphere and MLT.

The propagation and excitation of ISOs were extensively studied in the tropics. However, there are few reports on ISOs at higher latitudes. Using measurements of meteor radar and MST radar established by the Chinese Meridian Project and reanalysis data, Huang *et al.*[26] reported an ISO with about a 30-day period at mid and high latitudes. The oscillation propagates downward below 9 km and has an amplitude peak at about 9 km. At about 9~16 km, the oscillation gradually decays with height, and then strengthens again as it propagates into the stratosphere. In the mesosphere, the oscillation is robust at 78~86 km. Reanalysis data shows that in the troposphere, the oscillation propagates southward. In the lower stratosphere, the oscillation is gradually reflected back to propagate northward. Refractive index can explain these complex propagation characteristics very well. The phase progression indicates that the oscillation comes from the polar lower atmosphere. Hence, ISOs can not only originate from but also propagate in the atmosphere at mid and high latitudes.

Because the measurements of mesopause density remain scarce, the seasonal variations in the mesopause densities, especially with regard to its global structure, are still unclear. Yi *et al.*[27] reported a climatology of mesopause density estimated by using multiyear observations from a global distribution of meteor radars (including the meteor radars in the Chinese Meridian Project). They find that the seasonal variations of the southern polar mesopause densities are mainly dominated by an Annual Oscillation (AO). The mesopause densities of northern high latitudes show mainly an AO and a relatively weak SAO (semiannual oscillation). The mesopause densities over low latitudes show an Intra-Seasonal Oscillation (ISO) with a periodicity of 30~60 days. The latitudinal variation of mesopause densities exhibit a clear seasonal asymmetry, which may be related to latitudinal changes influenced by forcing of waves from the low atmosphere.

2.7 Characteristics of Metal Layers in Mesopause Region

Qiu *et al.*[28] used the combined observations from the sodium fluorescence lidar (Hefei, 31°N, 117°E) and ionosonde (Wuhan, 30°N, 114°E) of the Chinese Meridian Project to study the possibility of icy dust existing at the mesopause. The calculations for icy dust acting as a sodium reservoir are experimentally tested for the first time in details. The icy dust could form under extremely low temperature and appropriate humidity. Simultaneous temperature results from the nearby USTC T/W lidar show that the temperature minimum of 134.4 K was lower than the theoretical frost-point temperature, indicating the nucleation and growth for the water vapor. The formed icy-dust particles may have the capability to absorb enough sodium atoms in a given time period. Based on these results, an empirical model for the subtropical SSLs is proposed: first, icy dust is formed and then absorbed sodium species as a sodium store; after that, sodium atoms were released by the reservoir *via* special triggering (*e.g.*, by gravity wave braking). The overall finding of the study is such that three important conditions regarding zonal wind shear, temperature, and water vapor cycle must coincide for SSLs to form. Accordingly, if one or more of the three conditions vanish, then the sudden sodium layer disappears, which explains the occasional intermittency of the SSL phenomenon as observed. As it stated, this study discussed the mechanism of the formation of a sporadic sodium layer from a rather innovative viewpoint.

Xun *et al.*[29] reported the first concurrent observations of thermospheric Na layers from two nearby lidar stations, located at Yanqing (40.5°N, 116.0°E) and Pingquan (41.0°N, 118.7°E) respec-

tively. From one year data set, they identified four thermospheric Na layer events, including an unprecedented one reaching to the height of 200 km with a maximum density of 35 cm^{-3} and a very fast descending rate. Taking main Na layers into comparison, for three nights, thermospheric Na layers were observed only in one station (Yanqing). This suggests that thermospheric Na layers usually occur locally with a horizontal scale less than about 250 km.

Based on the sodium lidars, ionosondes, and meteor radars observations provided by Chinese meridian Project, the Solar-Terrestrial Environment Research Network and the China Research Institute of Radiowave Propagation, Ma *et al.*[30] analyzed the co-observed enhanced sodium layers and their association with the background wind, temperature as well as the ionospheric sporadic E layers from 8 years observational data. The co-observed enhanced sodium layers are the sporadic sodium layers or the thermospheric enhanced sodium layers, which expanded to a horizontal scale of approximate 350 km (*i.e.*, the distance between Hefei and Wuhan). In a statistical point of view, the co-observed enhanced sodium layers occurred more frequently during the summer time. Moreover, among the total 19 co-observed enhanced sodium layers, about 85% have been observed simultaneously over Hefei and Wuhan without a time delay. Most of them were associated with the enhancement of critical frequency of sporadic E layer. Further analysis showed that the enhanced sodium layers observed over Hefei and Wuhan, which last more than 2 hours, were highly correlated. It indicates the possible role of the large-scale tide/gravity wave-induced wind shear in formation of the large horizontal enhanced sodium layers. Meanwhile, the apparent time delay between Hefei and Wuhan was observed for a few enhanced sodium layers, which suggests the horizontal transport induced by wind might exist.

2.8 Comparisons between Observations and Modeling

Jiang *et al.*[31] investigated the characteristics of night time thermospheric wind during geomagnetically quiet times by using the observations of three mid-latitude FPIs at Xinglong (geog. 40.2°N, 117.4°E; geom. 35°N), Kelan (geog. 38.7°N, 111.6°E; geom. 34°N) and Millstone Hill (geog. 42.6°N, 71.5°W; geom. 52°N) and the model calculations of TIEGCM and HWM14. The results show that good agreement between TIEGCM winds and FPI winds occurs in the months around winter, especially for the NS winds; discrepancies between TIEGCM and the measurements occur mainly in the months around summer, especially for zonal winds. The output of TIEGCM overestimates the NS wind speeds at the two Asian stations from February to September, while generally produces the best replication to measurements at Millstone Hill. HWM14 generally agrees with quiet-time mid-latitude neutral wind measurements, especially the meridional component does very well throughout most of a year; discrepancies between HWM14 model and observations occur mainly in zonal winds during the winter season. HWM14 gives a preferable reproduction for the FPI wind dataset of Millstone Hill which already was used to construct the model, so inclusion of data from these new stations in the HWM empirical database will more likely improve the ability of HWM model products to be closer to the real thermospheric wind.

Ma *et al.*[32] presented a study of the mean wind variations in the MLT region from 2009 to 2017, using observations made by the Chinese Meridian Project meteor radar chain. The wind structures over Mohe, Beijing, Wuhan, and Sanya are analyzed based on the long-term observations and are further compared with the Horizontal Wind Model-07 (HWM-07). The annual oscillation dominates at mid-latitudes while both the annual oscillation and semiannual oscillations are important at low latitudes. A reversal of the mean zonal winds is observed in mid-latitudes around the spring equinox, which is likely due to the rapid change of the gravity wave forcing. In addition, a three-cell southward wind pattern is observed over Wuhan and Sanya. Composite-year comparisons between the observations and the HWM-07 show large discrepancies during winter time. HWM-07 predictions agree with the meteor radar observations better in the zonal component than in the meridional

component. The model predictions at low latitudes are not as accurate as that of the middle latitudes.

In the ionosphere and thermosphere community, it is Roble and Dickinson[33], who did the simulation for the first time to demonstrate the greenhouse gas effect on the ionosphere. After that, the community has done comprehensive studies on this topic involving both data analysis and modeling. However, there still exist differences between observations and simulations. Yue *et al.*[34] made use of Wuhan ionosonde data during 1947–2017 interval, which was digitized and unified recently, to evaluate the NCAR-TIEGCM simulation, which was driven by the realistic geomagnetic field and CO_2 level. They found that both data and model show the similar long term f_0F_2 (–0.0021 MHz·a^{-1}) and h_mF_2 (–0.106 km·a^{-1}) trend in terms of mean value and local time variation during the interval. Further control simulations indicate that CO_2 and geomagnetic field have a comparable effect on h_mF_2 trend, while geomagnetic field effect dominates f_0F_2 trend over Wuhan. In addition, the trend due to geomagnetic field is more complex than CO_2 increase versus years. Their results also testified the high quality of Wuhan ionosonde long-term data that produced by a series of different engineers during 70 years.

3 Conclusions and Outlook

In recent two years, using data from the Chinese Meridian Project, about 80 peer-reviewed journal papers were published embodying significant progresses in space weather and space physics research. The research topics covered a wide range, from ionosphere dynamics and regional characteristics to coupling between different spheres within the solar-terrestrial space. In this report, we categorized the scientific achievements into 8 subjects.

In addition to basic research, space science communities in China have made huge progresses to build a world leading ground-based space environment monitoring system, namely the Phase II of the Chinese Meridian Project. Meanwhile, the International Meridian Circle Program (IMCP) advocated by China is progressively stepping into realization stage. Altogether, these achievements will certainly contribute significantly to the global space science community.

Acknowledgements The article was written up based on materials provided by authors of the cited papers in the references. Much thanks for their generous help. We are also grateful to all members of the whole Chinese Meridian Project team, who have been making continuous efforts to perfect the operation of the project.

References

[1] WANG Chi. New chains of space weather monitoring stations in China [J]. *Space Weather*, 2010, **8**, S08001. DOI:10.1029/2010SW000603

[2] HU H Q, LIU E X, LIU R Y, *et al.* Statistical characteristics of ionospheric backscatter observed by SuperDARN Zhongshan radar in Antarctica [J]. *Adv. Polar Sci.*, 2013, **24**:19-31

[3] MA Y Z, ZHANG Q H, XING Z Y, *et al.* The ion/electron temperature characteristics of polar cap classical and hot patches and their influence on ion upflow [J]. *Geophys. Res. Lett.*, 2018, **45**. DOI.org/10.1029/2018GL079099

[4] WANG Y, ZHANG Q H, JAYACHANDRAN P T, *et al.* Experimental evidence on the dependence of the standard GPS phase scintillation index on the ionospheric plasma drift around noon sector of the polar ionosphere [J]. *J. Geophys. Res.: Space Phys.*, 2018, **123**:2370-2378

[5] MA Y Z, ZHANG Q H, XING Z Y, *et al.* Combined contribution of solar illumination, solar activity, and convection to ion upflow above the polar cap [J]. *J. Geophys. Res.: Space Phys.*, 2018, **123**:4317-4328

[6] ZHOU C, TANG Q, HUANG F, *et al.* The simultaneous observations of nighttime ionospheric E region irregularities and F region mediumscale traveling ionospheric disturbances in midlatitude China [J]. *J. Geophys. Res.: Space Phys.*, 2018, **123**:5195-5209

[7] MORO, XU J, DENARDINI J, *et al.* On the sources of the ionospheric variability in the South American Magnetic Anomaly during solar minimum [J]. *J. Geophys. Res.: Space Phys.*, 2019, **124**:7638-7653

[8] SUN L, XU J, XIONG C, *et al.* Midlatitudinal special airglow structures generated by the interaction between propagating medium-scale traveling ionospheric disturbance and nighttime plasma density enhancement at magnetically quiet time [J]. *Geophys. Res. Lett.*, 2019, **46**:1158-1167

[9] CHEN G, WANG J, ZHANG S, *et al.* Opposite latitudinal dependence of the premidnight and postmidnight oscillations in the electron density of midlatitude F layer [J]. *J. Geophys. Res.: Space*, 2018, **123**:796-807

[10] WU K, XU J, XIONG C, *et al.* Edge plasma enhancements of equatorial plasma depletions observed by all-sky imager and the C/NOFS satellite [J]. *J. Geophys. Res.: Space Phys.*, 2018, **123**:8835-8849

[11] WANG Z, LIU H, SHI J, *et al.* Plasma blobs concurrently observed with bubbles in the Asian-Oceanian sector during solar maximum [J]. *J. Geophys. Res.: Space Phys.*, 2019, **124**:7062-7071

[12] YI W, REID I M, XUE X, *et al.* High- and middle-latitude neutral mesospheric density response to geomagnetic storms [J]. *Geophys. Res. Lett.*, 2018, **45**:436-444

[13] LEI J, HUANG F, CHEN X, *et al.* Was magnetic storm the only driver of the long-duration enhancements of daytime total electron content in the Asian-Australian sector between 7 and 12 September 2017 [J]. *J. Geophys. Res.: Space Phys.*, 2018, **123**:3217-3232

[14] LIU Y, XU J, LIU X, *et al.* Responses of multiday oscillations in the nighttime thermospheric temperature to solar and geomagnetic activities measured by Fabry-Perot interferometer in China [J]. *J. Geophys. Res.: Space Phys.*, 2019, **124**. DOI.org/10. 1029/2019JA027237

[15] MO X H, ZHANG D H. Lunar tidal modulation of periodic meridional movement of equatorial ionization anomaly crest during sudden stratospheric warming [J]. *J. Geophys. Res.: Space Phys.*, 2018, **123**:1488-1499

[16] LIU J, ZHANG D H, HAO Y Q, *et al.* The comparison of lunar tidal characteristics in the low-latitudinal ionosphere between East Asian and American sectors during stratospheric sudden warming events: 2009–2018 [J]. *J. Geophys. Res.: Space Phys.*, 2019, **124**. DOI.org/10.1029/2019JA026722

[17] LIU G, HUANG W, SHEN H, *et al.* Ionospheric response to the 2018 sudden stratospheric warming event at middle- and low- latitude stations over China sector [J]. *Space Weather,* 2019, **17**:1230-1240

[18] HUANG F, OTSUKA Y, LEI J, *et al.* Daytime periodic wave-like structures in the ionosphere observed at low latitudes over the Asian-Australian sector using total electron content from Beidou geostationary satellites [J]. *J. Geophys. Res.: Space Phys.*, 2019, **124**:2312-2322

[19] YU Bingkun, XUE Xianghui, KUO Chengling, *et al.* The intensification of metallic layered phenomena above thunderstorms through the modulation of atmospheric tides [J]. *Atmos. Chem. Phys. Discuss*, 2018. DOI.org/10.5194/acp-2018-1025

[20] LI Q, YUSUPOV K, AKCHURIN A, *et al.* First OH airglow observation of mesospheric gravity waves over European Russia region [J]. *J. Geophys. Res.: Space Phys.*, 2018, **123**:2168-2180

[21] JIA M, XUE X, GU S, *et al.* Multiyear observations of gravity wave momentum fluxes in the midlatitude mesosphere and lower thermosphere region by meteor radar [J]. *J. Geophys. Res.: Space Phys.*, 2018, **123**:5684-5703

[22] LI Q, XU J, YUE J, *et al.* Evolution of a mesospheric bore in a duct observed by ground-based double-layer imagers and satellite observations over the Tibetan Plateau region [J]. *J. Geophys. Res.: Space Phys.*, 2019, **124**:1377-1388

[23] ZHOU X, WAN W, YU Y, *et al.* New approach to estimate tidal climatology from groundand space-based observations [J]. *J. Geophys. Res.: Space Phys.*, 2018, **123**:5087-5101

[24] GONG Y, LI C, MA Z, *et al.* Study of the quasi-5-day wave in the MLT region by a meteor radar chain [J]. *J. Geophys. Res.: Atmos.*, 2018, **123**:9474-9487

[25] YU F R, HUANG K M, ZHANG S D, *et al.* Quasi 10- and 16-day wave activities observed through meteor radar and MST radar during stratospheric final warming in 2015 spring [J]. *J. Geophys. Res.: Atmos.*, 2019, **124**. DOI.org/10.1029/2019JD030630

[26] HUANG K M, XI Y, WANG R, *et al.* Signature of a quasi 30-day oscillation at midlatitude based on wind observations from MST radar and meteor radar [J]. *J. Geophys. Res.: Atmos.*, 2019, **124**. DOI.org/10.1029/2019JD031170

[27] YI W, XUE X, REID I M, *et al.* Climatology of the mesopause relative density using a global distribution of meteor radars [J]. *Atmos. Chem. Phys.*, 2019, **19**(11):7567-7581

[28] QIU S, SOON W, XUE X, *et al.* Sudden sodium layers: Their appearance and disappearance [J]. *J. Geophys. Res.: Space Phys.*, 2018, **123**:5102-5118

[29] XUN Y, YANG G, SHE C Y, *et al.* The first concurrent observations of thermospheric Na layers from two nearby central midlatitude lidar stations [J]. *Geophys. Res. Lett.*, 2019, **46**:1892-1899

[30] MA Ju, XUE Xianghui, DOU Xiankang, *et al.* Large-Scale Horizontally Enhanced Sodium Layers Coobserved in the Midlatitude Region of China [J]. *J. Geophys. Res.: Space Phys.,* 2019**, 124**(9):7614-7628

[31] JIANG G, XU J, WANG W, *et al.* A comparison of quiet time thermospheric winds between FPI observations and model calculations [J]. *J. Geophys. Res.: Space Phys.*, 2018, **123**:7789-7805

[32] MA Z, GONG Y, ZHANG S D, *et al.* Study of mean wind variations and gravity wave forcing *via* a meteor radar chain and comparison with HWM-07 results [J]. *J. Geophys. Res.: Atmos.*, 2018, **123**(17):9488- 9501

[33] Roble R G, Dickinson R E. How will changes in carbon dioxide and methane modify the mean structure of the mesosphere and thermosphere [J] *Geophys. Res. Lett.*, 1989, **16**:1144-1441

[34] YUE X, HU L, WEI Y, *et al.* Ionospheric trend over Wuhan during 1947–2017: Comparison between simulation and observation [J]. *J. Geophys. Res.: Space Phys.*, 2018, **123**:1396-1409

LUO Ziren, ZHANG Min, WU Yueliang. Taiji-1 Satellite Mission. *Chin. J. Space Sci.*, 2020, **40**(5): 99–100. DOI:10.11728/cjss2020.05.99

Taiji-1 Satellite Mission*

LUO Ziren[1,2] ZHANG Min[1,3] WU Yueliang[1,3]

1 (*Taiji Laboratory for Gravitational Universe, University of Chinese Academy of Science, Beijing* 100049)

2 (*Institute of Mechanics, Chinese Academy of Science, Beijing* 100190)

3 (*International Centre for Theoretical Physics Asia-Pacific, University of Chinese Academy of Science, Beijing* 100190)

Abstract China's first satellite to conduct experiments on key technologies related to space-based gravitational wave detection, Taiji-1, has successfully completed its in-orbit tests, making a breakthrough in the country's gravitational wave detection. With the success of Taiji-1's in-orbit tests, the first goal of Chinese Academy of Science's three-step strategy to implement the Taiji program has been successfully achieved.

Key words Gravitational wave, Taiji program, Drag-free control system

Classified index V474

Taiji-1 was launched on 31 August 2019, and it was China's first satellite to conduct in-orbit experiments on the key technologies related to space-borne Gravitational Wave (GW) detection. It's also the first step of Taiji program, which is a Chinese space-borne GW detection mission leading by Chinese Academy of Sciences[1,2]. Unlike the ground-based GW observatory LIGO[3], Taiji is focused on GWs at lower frequencies to observe celestial bodies with greater mass or located farther away in the universe[4]. However, the gravitational wave signals from those sources are extremely weak, posing great challenges for detection. To ensure a successful mission performance for Taiji, it was set a 3-step plan to launch Taiji in early 2030s (see Figure 1).

The first step of Taiji program is to continue technology development in addition to the launch of a pilot study satellite called Taiji-1 (a glance at the Taiji-1 satellite please see Figure 2). The second step is to launch Taiji pathfinder (also called Taiji-2). Taiji-2, consisting of two satellites, is to demonstrate most of Taiji technology and to pave the way for Taiji.

Taiji-1 was approved on 30 August 2018, a year before its launching. The orbit of Taiji-1 was a circular

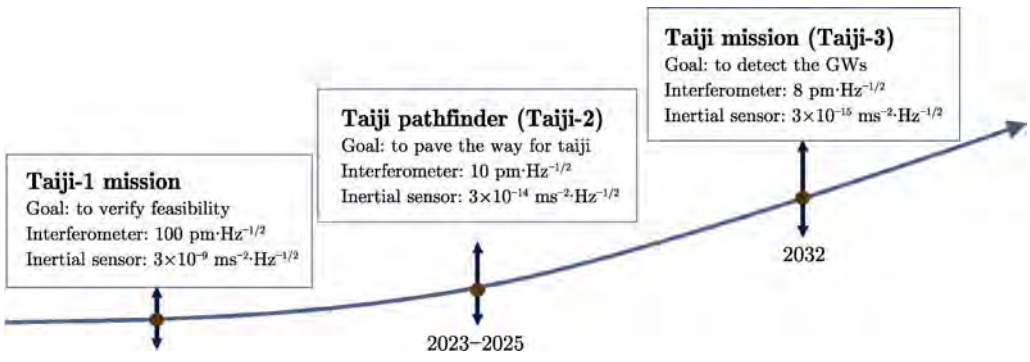

Fig. 1 3-step plan of Taiji program

* Supported by Strategic Priority Research Program of the Chinese Academy of Science (XDA15020709)
Received July 28, 2020
E-mail: zhang-min@ucas.ac.cn

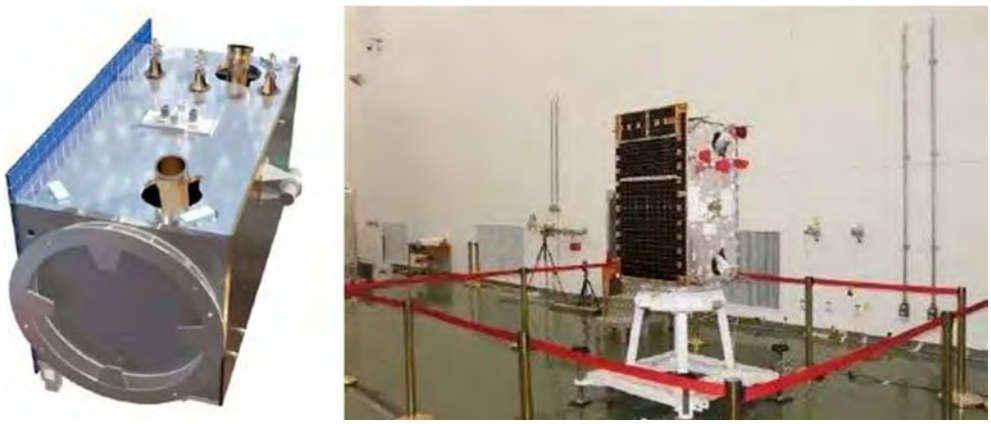

Fig. 2 Design picture (a) and photo (b) of Taiji-1

Sun-synchronous orbit inclined 97.79°. The altitude of Taiji-1 orbit is 600 km. The two major technology units, optical metrology system[5] and drag-free control system[6], were tested on Taiji-1. The optical metrology system consisted of an optical bench, phasemeter, and two laser sources. While the drag-free control system is composed of a gravitational reference sensor, a drag-free controller, and two types of μN-thrusters.

Taiji-1 now has completed its designed tasks, and all the payloads were successfully tested. The accuracy of displacement measurement of the laser interferometer on Taiji-1 reached 100 pm·Hz$^{-1/2}$, equivalent to the size of an atom. The accuracy of the gravitational reference sensor on the satellite reached 10^{-9} ms^{-2}·Hz$^{-1/2}$, ten billionths of the magnitude of the Earth's gravitational acceleration. The resolution of the micro-thruster on the satellite reached 0.1 μN·Hz$^{-1/2}$ order of magnitude. The residue acceleration of the satellite after drag-free control was below 10^{-7} ms^{-2}·Hz$^{-1/2}$.

The successful flight of Taiji-1 has verified the feasibility of Taiji's 3-step plan, and laid a solid foundation for future gravitational wave observation in space for China.

References

[1] LUO Z R, GUO Z K, JIN G, *et al.* A brief analysis to Taiji: science and technology [J]. *Results Phys.*, 2020, **16**:102918

[2] LUO Z R, JIN G, WU Y L, *et al.* The Taiji program: a concise overview [J]. *Prog. Theor. Exp. Phys.*, 2020. DOI: 10.1093/ptep/ptaa083

[3] LIGO Scientific Collaboration. Advanced LIGO [J]. *Class. Quant. Gravity*, 2015, **32**:074001

[4] GONG Xuefei, XU Shengnian, YUAN Yefei, *et al.* Laser interferometric gravitational wave detection in space and structure formation in the early universe [J]. *Chin. Astron. Astrophys.*, 2015, **39**(4):411-446

[5] HEATHER E A. LISA Path nder: optical metrology system monitoring during operations [J]. *IOP Conf. Ser.: J. Phys.*, 2017, **840**:012034

[6] FICHTER W, GATH P, VITALE S, *et al.* LISA pathfinder drag-free control and system implications [J]. *Class. Quant. Gravity*, 2005, **22**(10):S139-S148

JIA Yingzhuo, ZOU Yongliao, ZHU Yan, DU Qingguo, FAN Yu, CHEN Yuesong, WANG Chi. Development Progress of China's First Mars Exploration Mission: Its Scientific Objectives and Payloads. *Chin. J. Space Sci.*, 2020, **40**(5): 101-105. DOI:10.11728/cjss2020.05.101

Development Progress of China's First Mars Exploration Mission: Its Scientific Objectives and Payloads*

JIA Yingzhuo ZOU Yongliao ZHU Yan DU Qingguo

FAN Yu CHEN Yuesong WANG Chi

(*National Space Science Center, Chinese Academy of Sciences, Beijing* 100190)

Abstract China's first Mars exploration mission is scheduled to be launched in 2020. It aims not only to conduct global and comprehensive exploration of Mars by use of an orbiter but also to carry out in situ observation of key sites on Mars with a rover. This mission focuses on the following studies: topography, geomorphology, geological structure, soil characteristics, water-ice distribution, material composition, atmosphere and ionosphere, surface climate, environmental characteristics, Mars internal structure, and Martian magnetic field. It is comprised of an orbiter, a lander, and a rover equipped with 13 scientific payloads. This article will give an introduction to the mission including mission plan, scientific objectives, scientific payloads, and its recent development progress.

Key words China's first Mars exploration mission, Scientific objectives, Scientific payloads

Classified index V 524, P 35

1 Overview of China's First Mars Exploration Mission

China's first Mars exploration mission got approval in 2016. It is comprised of five systems, which are the probe system, the launch vehicle system, the launching site system, the TT&C (Tracking, Telemetry and Command) system, and ground research and application system.

The probe system consists of an orbiter, a lander platform, and a rover. The mission is scheduled to make a soft landing after the lander carrying the rover separates from the orbiter. The orbiter provides the service of communication relay links for the rover on the relay communication orbit as well as to conduct its own exploration mission[1]. The launch vehicle system will use Long March 5 launch vehicle, which will send the probe to the Earth-Mars transfer orbit directly in July 2020. The launch site system is expected to work at Wenchang satellite launch center, located in Hainan province.

Based on the existing spaceflight TT&C network and deep-space TT&C network, the TT&C system has additionally constructed three 35 m aperture antenna in Kashgar deep-space station to implement the TT&C task with assistance of the VLBI network. Ground research and application system will receive the scientific data while completing the observation tasks, and subsequently, carry out the work of data analysis.

The mission is designed to implement a sequence of spacecraft orbiting, landing, and roving on Mars with only a single launch. This mission is scheduled to be launched in July 2020 and expected to reach Mars in 2021. The project objectives of the mission include the following key technology tasks: Mars orbit braking and capture, entering/descending/landing, long-term independent management, long-distance

* Supported by the Major Program of the National Science Foundation of China (41590851) and the Beijing Municipal Science and Technology Commission (Z181100002918003)
Received March 10, 2020
E-mail: fanyu@nssc.ac.cn

Tracking, Telemetry, and Command (TT&C) and communication, roving on the Martian surface.

2 Scientific Objectives and Payloads

The orbiter of the mission is scheduled to conduct Mars global survey. The rover is to carry out a detailed comprehensive investigation in some critical areas. The scientific objectives of China's first Mars mission are as follows[2].

(1) To study the characteristics of Martian topography and geomorphology, acquire the data with high-precision to characterize global terrain of Mars and conduct the study on the processes that formed and modified the geologic record within a field exploration area on Mars.

(2) To study the characteristic of soil on the Martian surface and the distribution of water ice, characterize a variety of soils, rocks, and global distribution, search for the clue to past water activity to conduct the study on the surface layer of the Martian soil.

(3) To investigate the composition of the Martian surface, identify the types of rocks and search for the secondary mineral to analyze the mineral composition on the Martian surface.

(4) To study atmosphere and ionosphere, surface climate, and environmental characteristics of Mars; monitor space environmental conditions, temperature, air pressure, and wind field to study the Martian ionosphere structure and the seasonal variation of surface weather.

(5) To study the Martian internal structure and magnetic field, investigate the Mars magnetic field to carry out the study on the history of early geological evolution, internal mass distribution, and gravity field.

There are 13 scientific payloads equipped for the mission, 7 scientific payloads installed on the orbiter including Moderate Resolution Imaging Camera, High Resolution Imaging Camera, Mars Orbiter Scientific Investigation Radar, Mars Mineralogical Spectrometer, Mars Orbiter Magnetometer, Mars Ions and Neutral Particle Analyzer, Mars Energetic Particles Analyzer; 6 scientific payloads installed on the rover including Multispectral Camera, Navigation and Terrain Camera, Mars Rover Penetrating Radar, Mars Surface Composition Detector, Mars Rover Magnetometer, and Mars Mineralogical Spectrometer. There are two payload controllers separately installed on the orbiter and the rover, combined to command the payloads power supply, instruction control, data acquisition, and data processing[3]. The main technical parameters of scientific payloads and their scientific tasks are shown in Table 1.

Table 1 Main technical parameters of scientific payloads

Scientific payloads	Scientific observation tasks	Main technical parameters
Moderate resolution imaging camera	Imaging Mars surface and acquire the remote sensing images from a global view Characterize Mars topographic mapping and geomorphological structure	Spectral range: visible spectrum Resolution: better than 100 m at 400 km Effective pixel number: 4096×3072
High resolution imaging camera	Imaging the critical region of Mars surface Imaging topography and geomorphology of Mars surface in a detailed way	Mars surface Pixel resolution (below 265 km orbit altitude). Panchromatic: better than 2.5 m, local key area better than 0.5 m. Color: better than 10 m, local key area better than 2.0 m
Mars orbiter scientific investigation radar	Investigate Mars subsurface structure and underground water-ice distribution. Acquire the radar echo data with dual-frequency and dual-polarization to study Mars surface topography On Earth-Mars transfer orbit, it is used to observe spectrograms of very low frequency interplanetary radio emissions	Frequency: 10~20 MHz; 30~50 MHz Detecting depth: Mars subsurface structure, 100 m; Mars polar ice layer, 1000 m Thickness resolution: meter level

(Continued)

Scientific payloads	Scientific observation tasks	Main technical parameters
Mars mineralogical spectrometer	Analyze mineral composition and distribution. Investigate integral chemical composition and evolution history of Mars Analyze resources and distribution on Mars	Spectrum: Visible near-infrared, 0.45~1.05 μm; intermediate infrared and near-infrared, 1.00~3.40 μm Spectral resolution: Visible near-infrared, better than 10 nm; intermediate infrared and near-infrared, better than 12 nm at 1.0~ 2.0 μm, better than 25 nm at 2.0~3.4 μm
Mars orbiter magnetometer	Observe the space magnetic field of Mars, and study the interaction mechanism between Mars ionosphere, magnetic field, and solar wind Revert generator current of Mars ionosphere and research conductivity character of Martian ionosphere cooperating with Mars Magnetic Field Observation Station	Measurement range: ± 2000 nT Resolution: better than 0.01 nT
Mars ions and neutral particle analyzer	Study the particle characteristics of Mars plasma and understand the escape of the Mars atmosphere Study the interaction mechanism between the solar wind and the Martian atmosphere, and the acceleration mechanism of neutral particles near the Mas shock wave	Low energy ions Energy range: 0.005~25 keV Energy resolution $(\Delta E / E)$: 15% Mass: 1~70 amu Low energy neutral particles Energy range: 0.05~3 keV Energy resolution $(\Delta E / E)$: 100% Mass: 1~32 amu
Mars energetic particles analyzer	Observe the changes of the energy spectrum of energy particles, elementary composition and flux in the near-Mars space environment and Earth-Mars transfer orbit Survey the spatial distribution of different types of energetic particle radiation on Mars and Earth-Mars transfer orbit	Energy range: Electronic 0.1~12 MeV; Proton 2~100 MeV; α-particle, heavy ion 25~300 MeV Energy resolution $(\Delta E / E)$: 15% Elementary composition: H~Fe ($1 \leqslant Z \leqslant 26$) Heavy ion mass resolution $(\Delta E / E)$: $\leqslant$25% ($Z \leqslant 9$, energy range 25~300 MeV); $\leqslant$25% ($10 \leqslant Z \leqslant 26$, energy range 100~300 MeV); $\leqslant$60% ($10 \leqslant Z \leqslant 26$, energy range 25~100 MeV)
Multispectral camera	Acquire the multispectral images of landing and roving site, and study material type distribution on the Mars surface	Spectral range (nm): there are 9 spectra, which are 480 (20), 525 (20), 650 (12), 700 (15), 800 (25), 900 (30), 950 (50), 1000 (50) Viewing Sun Panchromatic spectrum, note: contents in brackets are full width at half height Normal imaging distance: 1.5 m to ∞
Navigation and terrain camera	Imaging terrain and geological structure of the roving area	Spectral range: Visible spectrum Color: Multicolor (RBG) Normal imaging distance: 0.5 m to ∞ Effective pixel number: 2048×2048
Mars rover penetrating radar	Investigate soil thickness and ice layer structure of the roving area and acquire ultra-wideband full polarized echo data on both of the Mars surface and subsurface Survey subsurface structure of the roving site, acquire geologic structure data on the Mars subsurface	First channel Center frequency: 55 MHz Bandwidth: 40 MHz Resolution of ice thickness: meter level Detection depth: $\geqslant$100 m (ice, ε_γ=3.0), $\geqslant$10 m (soil, ε_γ=3.0~4.0) Second channel

(Continued)

Scientific payloads	Scientific observation tasks	Main technical parameters
		Center frequency: 1300 MHz Bandwidth: 1000 MHz Resolution of thickness: cm level Detection depth: ⩾ 10m (ice, ε_γ =3.0), ⩾ 3 m (soil, ε_γ=3.0~4.0)
Mars surface composition detector	Analyze chemical component of material on Mars surface Analyze mineral and identify rocks on Mars surface	LIBS detection. Types of element: no less than 10 element (Si, Al, Fe, Mg, Ca, Na, O, C, H, Mn, Ti, S, *etc.*) Detection distance: 2~5 m (best detection distance), as far as to 10 m Short-wave infrared spectroscopy. Spectral range: 850~2400 nm. Spectral resolution: ⩽12 nm. Spectrum band: no less than 130 band
Mars rover magnetometer	Investigate the magnetic field of the landing area, and detect Mars' interior Investigate Mars space magnetic field and character of Mars ionosphere, invert Mars ionosphere generator current cooperating with orbiting investigation	Measure range: ± 2000 nT Resolution: better than 0.01 nT
Mars mineralogical spectrometer	Conduct in-situ investigation on wind field parameters of Mars surface Monitor the sound on Mars surface Measure environment temperature and air pressure on Mars	Temperature Measure range: –120~ +50°C Resolution: 0.1°C Pressure Measure range: 1~1500 Pa. Resolution: 0.1 Pa Wind speed Measure range: 0~70 $m \cdot s^{-1}$ Resolution: 0.1 $m \cdot s^{-1}$ Sound Frequency range: 0.02~2.5 kHz, 2.5~20 kHz Sensitivity: better than 50 $mV \cdot Pa^{-1}$

3 Key Technologies of Scientific Payloads

After over four years' development, breakthroughs in the following key technologies have been achieved in scientific payloads.

(1) High resolution imaging camera: aiming at high elliptic orbit, it breaks through the real-time image motion compensation calculation of push-broom imaging and attitude control technology, so as to realize sub-meter level fine imaging observation.

(2) Mars orbiter scientific investigation radar: the technology of dual-frequency and dual-polarization Linear Frequency Modulation (LFM) pulse is used to realize the layered structure detection of different geological targets.

(3) Mars mineralogical spectrometer: it uses Off-axis three reflective mirrors telescope, free-formed surface plane reflection grating technology to realize a wide band, compact and efficient spectrometer, and makes breakthroughs in the key technologies in infrared wide band light detector components.

(4) Mars rover penetrating radar: it uses ultra-wideband frequency Modulated Interrupting Continuous Wave (FMICW) to realize time-shared receiving/transmitting and solve receiving and transmitting channel segregation.

(5) Mars surface composition detector: it breaks

Laser-Induced Breakdown Spectros (LIBS) quantitative inversion technology.

4 Summary

At present, the scientific payloads have been completely manufactured and will be transported to the launching site for installation and test as planned in April 2020. The five systems of the Mars mission schedule to be completed all the research and manufacture works before July 2020. The scientific data processing methods and application research will continue to proceed. The scientific payloads aim at a global investigation of Mars such as terrain, geomorphology, atmosphere, and magnetic fields. Chinese scientists are making efforts to deepen the study on methods and applications of scientific data, and eager to obtain a new understanding of Mars, such as Mars atmosphere, ionosphere, and Mars surface composition.

With the development of the Mars mission, China makes efforts to promote more missions in deep-space exploration such as the asteroid exploration, sample-return from Mars, Jupiter system and beyond exploration. CNSA (China National Space Administration) attaches great importance to international cooperation and has openly announced "Announcement of Opportunities for Scientific Payloads and Projects onboard Asteroid Exploration Mission" in April 2019. Currently, CNSA has received the relevant proposals from some countries, for instance, Russia, Italy, Sweden, Germany, Belgium, and so forth. In the near future, the selection process organized by CNSA will be underway.

References

[1] GENG Y, ZHOU J S, LI S, *et al.* Review of first Mars exploration mission in China [J]. *J. Deep Space Explor.*, 2018, **5**(5):399-405

[2] LI C L, LIU J J, GENG Y, *et al.* Scientific objectives and payload configuration of China's first Mars exploration mission [J]. *J. Deep Space Explor.*, 2018, **5**(5):406-413

[3] ZHU Y, BAI Y F, WANG L G, *et al.* Integral technical scheme of payloads system for Chinese Mars-1 exploration [J]. *J. Deep Space Explor.*, 2017, **4**(6):510-514

WEI Jianyan. Progress on SVOM Satellite Development. *Chin. J. Space Sci.*, 2020, **40**(5): 106-107. DOI:10.11728/cjss2020.05.106

Progress on SVOM Satellite Development

WEI Jianyan

(*National Astronomical Observatories, Chinese Academy of Sciences, Beijing* 100101)

Abstract SVOM (Space-based multiband astronomical Variable Objects Monitor) is a Chinese-French space mission dedicated to studying Gamma-Ray Bursts. The satellite has four instruments to detect and localize the prompt GRB emission and measure the evolution of the afterglow in the visible band and in X-rays, and a VHF communication system enabling the fast transmission of SVOM alerts to the ground. The ground segment includes an array of wide-angle cameras and two follow-up telescopes. It was planned to be in orbit in 2021, and now has to be delayed about six months because of COVID-19 epidemic.

Key words Space astronomy, Gamma-ray burst

Classified index V 474

SVOM (Space-based multiband astronomical Variable Objects Monitor) is a mission dedicated to studying Gamma-Ray Bursts (GRBs)[1]. The mission has been approved jointly by both Chinese and French space agencies. The satellite will have an orbit with an altitude of 600~650 km and an inclination of 29°. The system Critical Definition Review (CDR) was carried out by CNSA and CNES in July 2020. It was planned to be in orbit in 2021, and now has to be delayed about six months because of COVID-19 epidemic.

GRBs are extremely luminous transient sources appearing when a newborn stellar mass black hole or magnetar emits an ultra-relativistic jet towards the Earth. Consequently, the study of GRBs not only has the potential to expand or revolutionize our understanding of key astrophysical issues on the mechanisms driving stellar explosions and the radiation processes of relativistic jets. In the next years GRBs will also undoubtedly shed new light on the evolution of the young universe, particularly on the history of star formation, the metal enrichment of galaxies, and the reionization of the intergalactic medium[2]. GRB 170817A, a normal short GRB detected by Fermi-GBM, was the first confirmed counterpart of gravitational-wave transients, which made GRBs even hotter topic[3].

The scientific objectives of SVOM put a special emphasis on two categories of GRBs: very distant GRBs at $z>5$ which constitute exceptional cosmological probes, and faint/soft nearby GRBs which allow probing the nature of the progenitors and the physics at work in the explosion. These goals have a major impact on the design of the mission: the on-board hard X-ray imager is sensitive down to 4 keV and computes online image and rate triggers, and the follow-up telescopes on the ground are sensitive in the NIR.

In order to take advantage of the astrophysical potential of GRBs, SVOM is designed to (i) permit the detection of all known types of GRBs; (ii) provide fast, reliable GRB positions; (iii) measure the spectral shape of the GRB prompt emission from visible to MeV; (iv) measure the temporal properties of the GRB prompt emission from visible to MeV; (v) identify quickly the afterglows of detected GRBs at both X-ray and visible bands, including the ones that are highly redshifted ($z>5$); (vi) measure the spectral shape of the early and late GRB afterglow from visible to X-rays; (vii) measure the temporal evolution of the early and late GRB afterglow from visible to X-rays.

Received July 28, 2020

E-mail: wjy@nao.cas.cn

SVOM mission is designed to consist of a set of scientific instruments to implement the synergy between space and ground observations. The space-based instruments include: (i) ECLAIRs, a wide field-of-view hard X-ray imager and spectrometer; (ii) GRM, a wide field-of-view soft gamma-ray spectrometer; (iii) MXT, a narrow field-of-view low-energy X-ray telescope; (iv) VT, a narrow field-of-view visible/near infrared (NIR) telescope. An artist view of the SVOM satellite is showed in Figure 1. And the ground-based instruments include: (i) GFTs, two follow-up telescopes (one of which featuring efficient NIR capabilities); (ii) GWAC, an array of wide field-of-view cameras in visible band.

At the beginning of the next decade, SVOM will be the main provider of GRB positions and spectral parameters. The SVOM instrumentation, primarily designed for GRB studies, composes a unique multi-wavelength observatory with rapid slew capability and quick command up-link capability. Therefore, SVOM will also be a powerful target-of-opportunity observatory for the whole astronomy community beyond the specific objectives linked to GRBs. For example, the SVOM mission has been conceived to promptly point to the celestial fields where sources have been detected by wide field of view astronomical devices such as the upgraded generation of gravitational wave detectors (advanced Virgo/LIGO) and high-energy neutrino detectors (IceCube, KM3NeT).

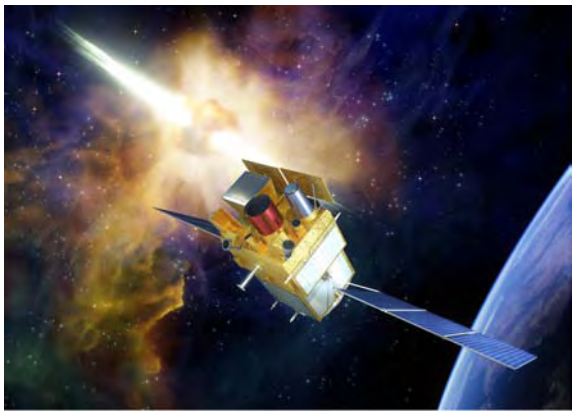

Fig. 1 Artist view of the SVOM satellite

References

[1] WEI J, CORDIER B, ANTIER S, *et al.* The deep and transient universe in the SVOM era: new challenges and opportunities–scientific prospects of the SVOM mission [J]. arXiv161006892W, 2016

[2] GEHRELS N, RAMIREZ-RUIZ E, FOX D B. Gamma-ray bursts in the swift era [J]. *Ann. Re. Astron. Astrophys.*, 2009, **47**(1):567-617

[3] GOLDSTEIN A, VERES P, BURNS E, *et al.* An ordinary short gamma-ray burst with extraordinary implications: fermi-GBM detection of GRB 170817A [J]. *Astrophys. J. Lett.*, 2017, **848**(2):14

WANG Chi, BRANDUARDI-RAYMONT Graziella. Update on the ESA-CAS Joint Solar Wind Magnetosphere Ionosphere Link Explorer (SMILE) Mission. *Chin. J. Space Sci.*, 2020, **40**(5): 108-111. DOI:10.11728/cjss2020.05.108

Update on the ESA-CAS Joint Solar Wind Magnetosphere Ionosphere Link Explorer (SMILE) Mission*

WANG Chi[1] BRANDUARDI-RAYMONT Graziella[2]

1 (*State Key Laboratory of Space Weather, National Space Science Center, Chinese Academy of Sciences, Beijing* 100190)

2 (*Mullard Space Science Laboratory, University College London, London RH5 6NT*)

Abstract The SMILE (Solar wind Magnetosphere Ionosphere Link Explorer) mission aims at deepening our understanding of the interaction of the solar wind with the Earth magnetosphere. It is the first time that ESA and CAS jointly select, design, implement, launch, and operate a space mission. The mission was adopted by CAS in November 2016 and by ESA in March 2019 with a target launch date by the end of 2023.

Key words SMILE, Soft X-ray Imager (SXI), Ultra-Violet Imager (UVI), Light Ion Analyzer (LIA), MAGnetometer (MAG)

Classified index P 35

1 Introduction

The SMILE (Solar wind Magnetosphere Ionosphere Link Explorer) mission was proposed as a candidate in response to the ESA and CAS (Chinese Academy of Sciences) joint call for a small class mission released in January 2015. SMILE aims at deepening our understanding of the interaction of the solar wind with the Earth magnetosphere by making global images of the dayside magnetosheath and cusps of the magnetosphere, and the aurorae at the North Pole simultaneously, while monitoring the in-situ plasma environment. Following the recommendation of the joint Scientific Evaluation Panel, SPC reached the consensus to select SMILE in November 2015, with a target launch date by the end of 2023. The mission was adopted by CAS in November, 2016 (the 13th Five-Year Plan Period) and by ESA in March 2019.

It is the first time that ESA and China jointly select, design, implement, launch, and operate a space mission. CAS is responsible for the study and development of satellite Platform (PF), TC/TM (CLTC), Science Application System (SAS) as well as Ground Support System (GSS), and provides in-situ measurement instruments MAGnetometer (MAG) and Light Ion Analyzer (LIA). While ESA is responsible for the study and development of Payload Module (PLM), Launch Vehicle, Launch Site, and science operation and ground receiving station supports when necessary, and also the development of the Soft X-ray Imager (SXI) and Ultra-Violet Imager (UVI).

2 Scientific Objectives

As pointed out by the ESA/CSA Joint Scientific Evaluation Panel, the SMILE Mission will use novel soft X-ray imaging technology to obtain, for the first time, the global image of the solar wind-magnetosphere ionosphere interaction. This is critical to quantitatively analyzing and understanding of the global feature of the solar-terrestrial system.

Understanding and thus predicting the non-

* Supported by Strategic Priority Program on Space Science, CAS(XDA15350000), National Natural Science Foundation of China (41731070), Key Research Program of Frontier Sciences, CAS(QYZDJ-SSW-JSC028), and Strategic Pionner Program on Space Science, CAS(XDA15052500)

Received February 2, 2020

E-mail: cw@spaceweather.ac.cn

linear global systematic behaviours of the magnetosphere have remained both the key objectives and grand challenges of the solar-terrestrial physics in particular for more than 50 years. In-situ data has dramatically improved our understanding of the localized physical processes involved. However, piecing the individual parts together to make a coherent overall picture, capable of explaining and predicting the dynamics of the magnetosphere at the system level has proved to be extremely difficult. Remote sensing of the cusps and magnetosheath with X-ray imaging is now possible thanks to the relatively recent discovery of the solar wind charge exchange (SWCX) X-ray emission. Based on this mechanism, SMILE's Soft X-ray Imager (SXI) can be used to determine the nature of the dayside solar wind-magnetosphere interaction from conditions prevailing at the Earth's bow shock, magnetopause, and cusps. The system-level magnetospheric dynamics can be further sensed via time sequences of auroral images, which can be provided by SMILE's high-heritage Ultraviolet Imager (UVI). Therefore, SMILE is a novel space mission that will revolutionize the magnetospheric physics by providing simultaneous images and movies of the magnetopause, cusps, and auroral oval using state-of-the-art detection techniques.

The interaction of the solar wind with the Earth's atmosphere leads to the formation of the large-structures of the magnetosphere, including the bow shock, magnetopause, and cusp regions. The position and shape of the magnetopause and cusps change constantly as the Earth's magnetosphere responds to varying solar wind dynamic pressures and interplanetary magnetic field orientations. Both the fast and slow solar wind can be interrupted by large, fast-moving bursts of plasma called interplanetary Coronal Mass Ejections (CMEs). When a CME impacts the Earth's magnetosphere, it temporarily deforms the Earth's magnetic field, changing its direction and strength, and induces large electrical currents; this is called a geomagnetic storm and it is a global phenomenon. The southward interplanetary magnetic fields, as presented in a CME event, could induce magnetic reconnection in the Earth's magnetotail; this launches protons and electrons downward toward the Earth's atmosphere, where they form the aurora, resulting in substorms.

The Science objectives of SMILE mission are summarized as: (i) explore the fundamental modes of the dayside solar wind/magnetosphere interaction; (ii) understand the substorm cycle; (iii) determine how CME-driven storms arise and their relationship to substorms.

3 Modeling Update

The solar wind-magnetosphere interaction can be modeled by global MHD codes. Figure 1 is the SXI intensity simulation result during a magnetic storm event on 17 Mar 2015, based on the 3D PPMLR (the extended Lagrangian version of the piecewise parabolic method) MHD code. The left panel shows the time variation of solar wind parameters and the *Dst* index. From top to bottom, the parameters are: interplanetary magnetic field, plasma velocity, number density, temperature, and *Dst*. The orbit of SMILE is plotted in the middle panel. The right panel presents the simulated X-ray image, with the white box showing the field of view of SXI. The crescent-shaped region with relatively high X-ray emission provides information about the magnetopause boundary position, important to the study of system-level magnetospheric dynamics.

To extract location and motion of the dayside boundaries such as bow shock, magnetopause, low- and high-latitude cusp boundaries from X-ray images, the SMILE Modelling Working Group (MWG) performs studies on the reconstruction techniques. So far, four approaches have been developed to derive the 3D magnetopause position from X-ray images, namely the Boundary Fitting Approach (BFA), Tangent Fitting Approach (TFA), Tangential Direction Approach (TDA), and Computed Tomography Approach (CTA). These approaches are developed based on different assumptions about the shapes of boundaries or features of the X-ray emissions, and preliminary model studies show that they work well with desired X-ray information provided. Figure 2 is a brief summary of the reconstruction approaches.

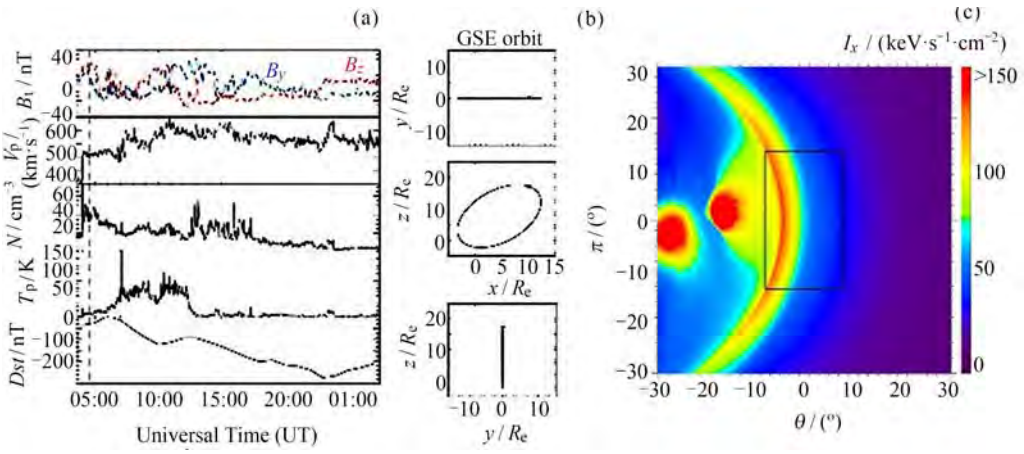

Fig. 1 MHD simulation of the X-ray intensity

Fig. 2 Current approaches to derive the magnetopause position from X-ray images

4 Mission Overview

4.1 Satellite System

Satellite orbit has a big inclination and the highly elliptical orbit has an apogee altitude of about 19 R_e and perigee of about 5000 km. The inclination is 70° if launched with Vega-C as baseline, or 98.0° if launched with Ariane 62.

The SMILE satellite system is constituted by Platform (PF) and Payload Module (PLM), and is a three-axis stabilized satellite. The mass of the satellite is less than 2250 kg. X-band transmission will meet CCSDS standard, with data rate 65 Mbit·s^{-1} and data volume 35.5 Gbit per orbit. Telemetry and telecommand will be Unified S-band TT&C system. The lifetime will be more than 3 years after delivered to user.

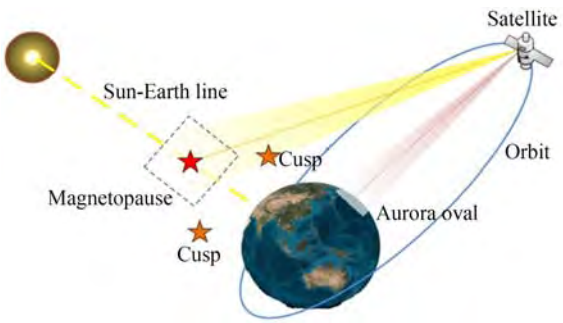

Fig. 3 SMILE satellite HEO orbit

Fig. 4 Diagram of satellite structure

4.2 Launch Vehicle

Launch Vehicle is ESA's responsibility. The options include single launching with Vega-C as baseline, or dual launching with Ariane 62 at Kourou.

4.3 Launch Site

ESA is responsible for the Launch Site and Launch service, and will provide the ground segment support and logistics.

4.4 TC/TM

China Satellite Launch and Tracking Control General (CLTC) will be responsible for the TC/TM of SMILE satellite. European Space Operation Center (ESOC) will be responsible for the TC/TM before the satellite separation with Launch Vehicle. In addition, ESA will also provide the support of ground station in case of emergency.

4.5 Ground Support System (GSS)

GSS has been constructed during the 12th Five-Year Plan Period and it will undergo some modifications according to the new requirements of the space science missions during the 13th Five-Year Plan Period. It is mainly responsible for the operation and management of the payloads, scientific data receiving, L_0 data processing, data archiving of different levels, and distribution service of scientific data to the science community.

4.6 Science Application System (SAS)

CAS will set up SAS located at NSSC, and ESA will set up Science Operation Center (SOC) located in European Space Astronomy Center (ESAC). Both parties will cooperate coordinately to make a science strategic plan and observation plan, monitor the execution of the plan, analyze the performance of the payloads in orbit, implement the calibration of the payloads, produce quick look scientific data, and produce L1 and above scientific data products.

5 Development Plan and Current Status

The CAS part of the SMILE mission has already been adopted by Bureau of Major Research and Development (BMRD) in November 2016. After SMILE was selected by SPC in November 2015, the ESA part of the SMILE mission proceeded into Phase A study. SMILE mission has already completed Instrument Consolidation Review, PF, and PLM Consolidation Review in 2017. Joint Mission Consolidation Review (MCR) was completed in October 2018, which was the first joint review of the SMILE mission. SMILE mission passed through ESA mission adoption in March 2019 and went into Phase B study. With the effort of CAS and ESA study and engineering team, Joint Ground Segment Preliminary Design Review (PDR) was completed in October 2019. Based on Payload Instrument PLM and PF PDRs, the joint Mission PDR was completed successfully in January 2020 in Europe, which is the third joint review of the SMILE mission, marking the kick-off of Phase C. The next milestone will be the Mission Critical Design Review (CDR) scheduled in August 2021.

Acknowledgments SMILE Mission is a joint project with the support from CAS and ESA. Thanks for the great support of CAS Strategic Priority Research Program and the ESA science program. Also thanks to the study and engineering teams for their cooperation and hard work: National Space Science Center, Innovation Academy for microsatellites of CAS, CLTC, Shanghai Institute of Space Propulsion, National Center for Space Weather, Polar Research Institute of China, *etc.* from Chinese side; University College London, University of Leicester, Imperial College, University of Calgary, Rutherford Appleton Laboratory, Finnish Meteorological Institute, *etc.* from ESA side, as well as Canadian Space Agency and NASA Goddard Space Flight Center.

Reference

[1] SUN T, WANG C, CONNOR H K, *et al.* Deriving the magnetopause position from the soft X-ray image by using the tangent fitting approach [J]. *J. Geophys. Res.: Space Phys.*, 2020, 125. DOI.org/10.1029/2020JA028169

YUAN Weimin. Report on the Einstein Probe Mission. *Chin. J. Space Sci.*, 2020, 40(5): 112-116. DOI:10.11728/cjss2020.05.112

Report on the Einstein Probe Mission*

YUAN Weimin

(*National Astronomical Observatories, Chinese Academy of Sciences, Beijing* 100012)

Abstract The Einstein Probe (EP) is a mission dedicated to time-domain astronomy to monitor the sky in the soft X-ray band, led by the Chinese Academy of Sciences with the participation from ESA and MPE. Its wide-field imaging capability is achieved by using established technology of the micro-pore lobster-eye X-ray focusing optics. Complementary to this is deep X-ray follow-up capability enabled by a Wolter-I type X-ray telescope. EP is also capable of fast transient alerts triggering and downlink, aiming at multi-wavelength follow-up observations by the world-wide community. EP will enable systematic survey and characterization of high-energy transients at unprecedented sensitivity, spatial resolution, grasp, and monitoring cadence. Its scientific goals are mainly concerned with discovering new or rare types of transients, including tidal disruption events, supernova shock breakouts, high-redshift GRBs, and electromagnetic sources of gravitational wave events. EP is currently in Phase C and is aimed for launch by the end of 2022.

Key words X-ray all-sky monitor, Time-domain astronomy, High-energy astrophysics, X-ray transients, Lobster-eye MPO

Classified index P4

1 Introduction

The Einstein Probe (EP) [1,4] is a space mission dedicated to time-domain astrophysics to monitor the universe in the soft X-ray band and to perform detailed X-ray follow-up observations. The project was formally adopted at the end of 2017 and is fully funded by the Chinese Academy of Sciences (CAS) in its Strategic Priority Programme on Space Science (2nd phase). It is also an international collaboration endeavour with the participation of the European Space Agency (ESA) and the Max-Planck-Institute for Extraterrestrial Physics (MPE), Germany.

The X-ray sky is rich in transients and variables of various types. With diverse timescales from subseconds to years, a large variety of such dramatic objects have been discovered and extensively studied ever since the early days of X-ray astronomy, thanks to successive all-sky monitors in the X-ray waveband. In recent years the successful operations of Swift[2], Integral, and MAXI[3] have greatly expanded our horizon in monitoring the X-ray sky and advanced our knowledge about the dynamic high-energy universe. New transients, particularly of previously unknown and scientifically important types, continue to be discovered. To characterize and understand these new phenomena, large samples of events, and detailed observations are needed[1]. With the advent of major wide-field sky-monitoring facilities across the entire electromagnetic spectrum and even in the non-electromagnetic regimes, the next decade will see a golden age of time-domain astronomy with flourishing discoveries.

In the X-ray band, the next generation of monitoring instruments are highly invoked with higher sensitivity and improved angular resolution (a few arcminutes or better) than those currently available. One promising technology is the novel X-ray focusing optics–the lobster-eye micro-pore optic. Such X-ray focusing optics results in an enhanced gain in signal

* Supported by the Strategic Pioneer Program on Space Science, Chinese Academy of Sciences(XDA15310300, XDA15052100, XDA15310100)

Received June 28, 2020

E-mail: wmy@nao.cas.cn

to noise, and thus high sensitivity, while a wide Field-of-View (FoV) can be maintained. The wide-field X-ray monitoring capability of EP is enabled by this technology.

2 Scientific Objectives

The Einstein Probe will carry out systematic sky monitoring surveys with a large instantaneous field-of-view in the soft X-ray band with the sensitivity one order of magnitude better than those currently in orbit. The mission will address some of the challenging questions in astrophysics and cosmology, by discovering and studying more distant and fainter cosmic transient events[5]. These questions include the demography of black holes in the Universe by finding tidal disruption events (Figure 1) and how they formed and evolved, and how black holes accrete mass and launch jets; the astrophysical origins and underlying processes of gravitational wave events; details of the physics which operate in extreme conditions of strong gravity; stars in the early Universe and how they re-ionize the Universe; the progenitors of supernovae.

The primary science objectives are listed as follows.

(1) Discover and characterize cosmic X-ray transients, to reveal their properties and gain insight into their nature and underlying physics.

(2) Discover and characterize X-ray outbursts from normally quiescent black holes, for better understanding of the demography of black holes and their origin and evolution, as well as accretion physics.

(3) Search for X-ray sources associated with gravitational-wave events and precisely locate them.

Fig. 1 Artist's impression of a stellar tidal disruption event by a massive black hole (credit: NASA)

3 Instruments

EP carries two scientific instruments: an X-ray monitoring instrument Wide-field X-ray Telescope (WXT) with a large instantaneous FoV, and a narrow-field Follow-up X-ray Telescope (FXT). Some of the specifications of WXT and FXT are listed in Table 1. To achieve both wide FoV and X-ray focusing, the novel micro-pore optics in the lobster-eye configuration is adopted for WXT. WXT consists of 12 identical modules with a 375 mm focal length, each of which is composed of 36 mosaicking MPO plates, subtending a solid angle of approximately 300 $(^{\circ})^2$. An optical baffle is attached at the front end of the module to shield optical stray light. The focal plane detector of each module comprises 4 scientific CMOS imaging sensors. One WXT module includes the MPO mirror assembly, detector, and electronics units, optical baffle, structure, and thermal control (Figure 2). The nominal detection bandpass of WXT is 0.5~4.0 keV. The peak effective area is about 3 cm^2 at around 1 keV for most of the directions within the FoV except at the edge of the MPO plates. Thought the effective area is small, it has nearly the same value across the entire FoV. The 12 modules make a total FoV of WXT of no less than 3600$(^{\circ})^2$ (about 1.1 steradians; Figure 3). Thereby EP WXT has a large grasp (effective area times FoV) of the order of 10^4 $cm^2 \cdot (^{\circ})^2$, which is the largest among all focusing telescopes in X-rays ever built. WXT has a nominal theoretical sensitivity of 10^{-11} erg $s^{-1} \cdot cm^{-2}$ for 1000 s exposure in

Table 1 Specifications of WXT and FXT

Parameters	WXT	FXT
Number of modules	12	2
Telescope optic	lobster-eye MPO	Wolter-I
Detector	sCMOS	CCD
Field of view	⩾3600 sq.deg.	⩾38′ (diameter)
Focal length/mm	375	1600
Effective area/cm^2 @1.25 keV	2.7	300(×2)
Spatial resolution (1 keV)	5′ (FWHM)	30″ (HPD)
Bandpass/keV	0.5–4	0.3–10
E-resolution/eV @1.25 keV	170	120
Sensitivity/(erg·s^{-1}·cm^{-2})	~1×10^{-11}@1 ks	~1×10^{-14}@10 ks

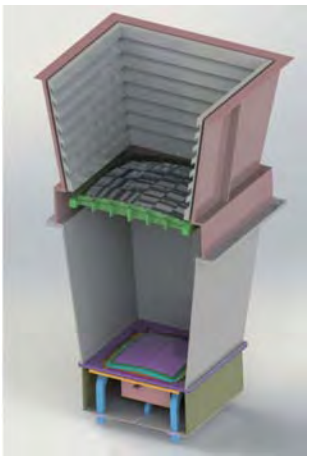

Fig. 2 Design of one module of the Wide-field X-ray Telescope (WXT), consisting mainly of an optical baffle, MPO plates, and focal plane detectors (credit: NAOC)

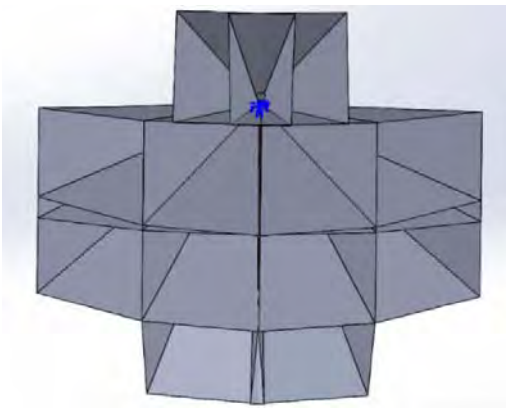

Fig. 3 Combined fields of view of the 12 WXT modules.

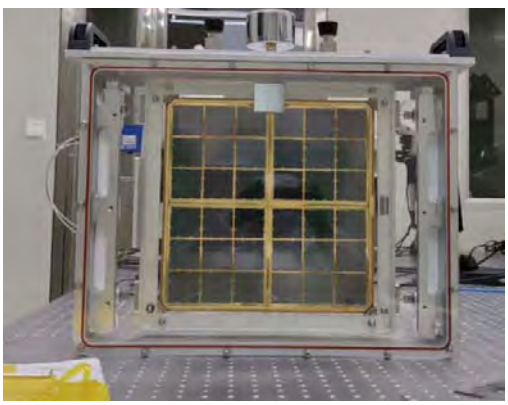

Fig. 4 Prototype of an MPO mirror assembly for one WXT module (credit: NAOC).

the 0.5~4 keV band. Figure 4 shows a prototype of an MPO mirror assembly for one WXT module developed at NAOC, CAS.

The EP FXT is composed of a pair of Wolter-I focusing mirror assemblies, each with a focal length of 1.6m and a field of view no less than 38 arcmin in diameter. For each of the telescope, a CCD detector is mounted on the focal plane. FXT covers an energy passband of 0.5~8 keV and has an effective area of about 300 cm^2 each at around 1keV.

4 Mission Profile

The design of the EP satellite is shown in Figure 5. The total weight is approximately 1.4 tons. The spacecraft will be in a circular orbit at an altitude of 600 km and a period of about 97 min, and an inclination angle of about 29°. The basic survey strategy is to monitor the night sky with a series of WXT pointings in the directions avoiding the Sun, with Sun avoidance angles to the edge of the WXT FoV greater than 90°. In this way most of the night sky will be mosaiced and monitored at a cadence of several times in one day on average. With the movement of the Sun about 1° daily in the sky, the entire sky will be covered within half-a-year. The typical daily detection sensitivity of WXT is expected to be about 6×10^{-12} erg·s^{-1}·cm^{-2}.

There are three basic observation modes for EP: the monitoring survey mode with WXT, the follow-up observation mode using mainly FXT (while WXT continues taking data), as well as ToO observations of both WXT and FXT upon command uplink from the ground segment. During monitoring observations with WXT, the fields are generally such chosen that FXT is pointed to pre-planned targets of known sources, making the most of its large light collecting power.

During monitoring observations of WXT, the onboard computer will search for transients from X-ray photon events collected in real time over a range of timescales. Once a transient source is detected and triggered by the onboard data processing system, the satellite will slew to a new position to target the new source within the FoV of FXT and to enable pointed follow-up observations. Meanwhile,

the alerts information about the transient source will be transmitted quickly to the ground segment, in most cases within several minutes, by making use of the Beidou satellite navigation system. During follow-up observations, WXT continues to take data to monitor the new sky region. ToO observations can be carried out by sending observing command uplink from the ground segment via the telecommand system and via the Beidou systems for urgent requests. Follow-up observations of faint transient sources detected from elaborated data reduction and analysis by the ground segment will be enabled by ToO observations.

The ground segment of the Einstein Probe project is composed of the Mission Operation Centre, hosted at the National Space Science Centre of the CAS, and the Science and Operation Centre, hosted at the National Astronomical Observatories and Institute of High-Energy Physics of the CAS. The alert information of the detected transients will be made public immediately after their detections to invoke multi-wavelength follow-up observations. The telemetry data will be transmitted to the ground segment *via* the X-band using the ground tracking stations of the CAS and ESA. The data reduction and calibration will be carried out at the Science & Operation Centre of the CAS. The observational data of both WXT and FXT will be made public to the entire community after a proprietary period of one year or less.

5 Collaboration Consortium

The Einstein Probe project is led by the CAS with the participation of the European Space Agency and the Max-Planck-Institute for Extraterrestrial Physics in Germany *via* the provision of hardware and ground segment contributions.

6 Status report

The project was formally adopted at the end of 2017 and is fully funded by the Chinese Academy of Sciences (CAS) in its Strategic Priority Programme on Space Science (2nd phase). The satellite mechanical model was completed and passed qualified-level mechanical and acoustic tests in December 2019 (Figure 6 and 7). The project passed the mission-level phase B conclusion review at the end of 2019, and is currently in phase C. Reviews for the qualification

Fig. 5 Layout of the Einstein Probe spacecraft and scientific payloads, which include 12 modules of WXT aligned to different directions and 2 coaligned modules of FXT (credit: MicroSat)

Fig. 6 Preparation for thermal balance test for a WXT module

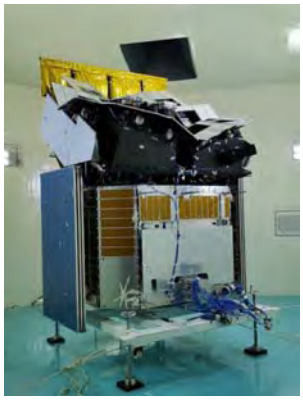

Fig. 7 Structural and thermal model of the EP payload and spacecraft (credit: MicroSat)

model at the subsystem level have been completed in April, and the qualification model manufacturing procedure has been started and is expected to complete in April 2021. The mission is planned for launch by the end of 2022, with an operational lifetime of three years and five years as a goal. The project development has been inevitably affected to some extent by the COVID-19 pandemic since early 2020, and the EP team is making every effort to minimize its impact aiming at keeping the project on schedule.

References

[1] YUAN W, AMATI L, CANNIZZO J K, *et al.* Perspectives on gamma-ray burst physics and cosmology with next generation facilities [J]. *Space Sci. Rev.*, 2016, **202**:235-277

[2] GEHRELS N, CHINCARINI G, GIOMMI P, *et al.* The Swift gamma-ray burst mission [J]. *Astrophys. J.*, 2004, **611**: 1005-1020

[3] MATSUOKA M, KAWASAKI K, UENO S, *et al.* The MAXI mission on the ISS: Science and instruments for monitoring all-sky X-ray images [J]. *Publ. Astron. Soc. Jpn.*, 2009, **61**:999-1010

[4] YUAN W, ZHANG C, FENG H, *et al.* Einstein Probe - a small mission to monitor and explore the dynamic X-ray universe [C]//Proceedings of Swift: 10 Years of Discovery. Rome: La Sapienza University, 2015. DOI: 10.22323/1.233.0006

[5] YUAN Weimin, ZHANG Chen, CHEN Yong, *et al.* Einstein Probe: Exploring the ever-changing X-ray Universe [J]. *Sci. Sin.: Phys. Mech. Astron.*, 2018, **48**:039502 (in Chinese)

GAN Weiqun. Status of the Advanced Space-based Solar Observatory. *Chin. J. Space Sci.*, 2020, **40**(5): 117-119. DOI:10.11728/cjss2020.05.117

Status of the Advanced Space-based Solar Observatory*

GAN Weiqun

(*Key Laboratory of Dark Matter and Space Astronomy, Purple Mountain Observatory, Chinese Academy of Sciences, Nanjing* 210033)

Abstract The Advanced Space-based Solar Observatory (ASO-S) was formally approved at the end of 2017. In the past two years, ASO-S underwent its official Phase-B and Phase-C studies. The Phase-B study was successfully accomplished by the end of April 2019, and the Phase-C study is being now undertaken until August 2020. Then the flight model is planned to finish within 16 months. Around the end of 2021, ASO-S will be ready in the launch state. We briefly summarize the history of ASO-S, the phase-B studies, and the phase-C studies.

Key words Space astronomy, Solar physics, Spacecraft

Classified index P 35

1 Brief History of ASO-S

The idea of Advanced Space-based Solar Observatory (ASO-S) was proposed in 2010, referring partially to SMESE, a joint Chinese-French mission[1]. Then in 2011 ASO-S was selected to do concept study (Phase-0/A) by a new program named as Strategic Priority Research Program of Space Science sponsored by the Chinese Academy of Sciences (CAS). Two years later, ASO-S satisfactorily finished the concept study and was successfully selected to undertake further intensive study (Phase-A/B) supported by the same channel. During that period, NNSFC (National Natural Science Foundation of China) provided even stronger financial support to ASO-S. In April 2016, ASO-S got a good mark in an assessment report issued by a top level committee organized by NSSC (National Space Science Center, CAS). Supported continuously by NNSFC, at the end of 2017 ASO-S was formally accepted by CAS after a serious competition with other candidates. Since then ASO-S has been going into the engineering study of official Phase-B and subsequent Phase-C.

There are three payloads on ASO-S, which are the Full-disc vector MagnetoGraph (FMG), the Lyman-alpha Solar Telescope (LST), and the Hard X-ray Imager (HXI), respectively. For the first time in a single platform they will simultaneously observe the solar magnetic field, non-thermal image of solar flares, and the initiation of Coronal Mass Ejection (CME) and its early propagation, so as to study the relationships among solar magnetic field, solar flares, and CMEs. Explicitly, four major scientific objectives can be described as: (i) to observe simultaneously non-thermal images of solar flares in hard X-rays, and the initiations of CME in Lyman-alpha waveband, in order to understand the relationships between flares and CMEs; (ii) to observe simultaneously full-disc vector magnetic field, energy build up and release of solar flares, and the formation of CMEs, in order to understand the causality among them; (iii) to observe the response of solar atmosphere to the eruptions, in order to understand the mechanisms of energy release and transport; (iv) to observe solar eruptions and the evolution of magnetic field, in order to provide clues for forecasting space

* Supported by Chinese Academy of Sciences (XDA15052200) and by National Natural Science Foundation of China (U1731241, 11921003, U1931138)
Received February 13, 2020
E-mail: wqgan@pmo.ac.cn

weather.

In November 2019, a special issue about ASO-S, including a total of 14 papers[2-15], was published in Research in Astronomy and Astrophysics (RAA). These papers summarized comprehensively the general framework, the scientific objectives, systematic designs, the payload schemes, prototype models, engineering models, scientific systems, the synthetic studies, and so on, up to the end of Phase-B and the beginning of Phase-C. The readers are encouraged to refer to that special issue for more details. We here mention briefly only the rough milestones in chronological order for the past two years.

2 Phase-B Studies

Officially, the Phase-B studies continued 16 months, from January 2018 to the end of April 2019. During this period, the work focused mainly on the satellite system, including the payloads.

2.1 Satellite System in Phase-B

Besides coordinating all the issues related to payloads, the satellite system has its own tasks like mission requirement analysis, preliminary scheme design, key technology solutions, validating experiments, and so on. Quite a number of documents were generated during this period, which summarized the tasks done and provided the scheme for the following works. Although the platform does not seem to be special, all the sub-systems should be considered and designed. How to ensure all the payloads pointing to the Sun with rather high accuracies is one of the key issues, which was finally solved through both smart design and process control. The whole architecture of the mission was mechanically experimented at the beginning of 2019. The evaluation on the entire work of the Phase-B was passed at the end of April 2019.

2.2 Payloads in Phase-B

The requirement analysis was first finished in the initial stage of this period. Besides the interface parameters like weight, power, and dimensions, the detailed specification parameters of all three instruments were definitely defined. The solutions of key technologies for each payload are the main work during Phase-B. For the FMG, the key issues include the entrance window, imaging stabilization system, the bubble suppression in the filter, and so on. For the LST, the key issues include the suppression of stray-light, the measurement of stray-light, imaging stability, and so on. For the HXI, the key issue is concerned about the assembly of the grids, like grid stack technique, the alignment of front and rear grids, the stability of collimator, and so on. All of these key technologies were properly identified during the Phase-B. The engineering proto-type models of the FMG, LST, and HXI were produced and tested. The integration of the payloads with the platform was also performed and some experiments like assembly, mechanics, vibration, thermal control were carried out.

3 Phase-C Studies

Officially, the Phase-C studies started from May 2019 and will finish at the end of July 2020. During this period, besides the satellite system, the scientific application system (including science preparations) has also been put on the agenda.

3.1 Satellite System in Phase-C

Based on the work done in Phase-B, at the beginning of Phase-C, the satellite system finished and improved the design of the whole platform, including seven subsystems of Mechanics, Thermal Control, AOCS, Electrical Power, OBDH, TT&C, and Data Transmission. The interfaces with other systems and detailed schedule were drawn up. Then the individual parts have been under fabrication. In July 2019, the electric performances of the platform together with all three payloads were jointly debugged. The integration and test work is scheduled to start no later than March 2020. All the work related to the qualification model is planned to finish by the end of July 2020.

3.2 Payloads in Phase-C

Like the satellite system, the schematic designs for FMG, LST, and HXI were first improved and finished. Then the individual parts for these three instruments were in parallel manufactured and the assembly for each instrument has almost been com-

pleted by the end of December 2019. As of the time of writing (the end of January 2020), the experiment, calibration, and environment tests are being done for these instruments separately. In March 2020, the qualification models of FMG, LST, and HXI will be delivered to the satellite system for integration and the overall test.

3.3 Scientific Issues

Besides the hardware work, scientific preparations have also been progressing for quite a time. Two major research grants were provided by NNSFC and CAS respectively. The science team, led by the chief scientist of ASO-S, was organized, which focuses mainly on the data deductions and usages for the outputs of the payloads in the future. Certainly, this kind of work is closely related to the Science Operation and Data Center (SODC)[11], which consists in fact four divisions: scientific operation, data management, data analysis center, and user service. So far SODC has finished its schematic design and the software work has started accordingly. Besides, the first ASO-S international workshop was held in 15–18 January, 2019 at Nanjing. More than 100 participants from over ten countries attended the meeting.

4 Conclusions

By now ASO-S is undertaking its Phase-C study. All the works look smooth and are on the track of the schedule, although the timetable shows a little tense sometimes. It is expected that the flight model can be started from August 2020 and then at the end of 2021 or in the early of 2022, ASO-S could be launched. In this period, the special issue of ASO-S[2-15] is highly recommended to the readers who would like to know more details about the mission.

References

[1] VIAL J C, AUCHERE F, CHANG J, *et al.* SMESE: a small explorer for solar eruptions [J]. *Adv. Space Res.*, 2007, **40**:1787

[2] GAN W Q, DING M D, HUANG Y, *et al.* Preface: Advanced Space-based Solar Observatory (ASO-S) [J]. *Res. Astron. Astrophys.*, 2019, **19**:155

[3] GAN W Q, ZHU C, DENG Y Y, *et al.* Advanced Space-based Solar Observatory (ASO-S): an overview [J]. *Res. Astron. Astrophys.*, 2019, **19**:156

[4] DENG Y Y, ZHANG H Y, YANG J F, *et al.* Design of the Full-disk Magneto Graph (FMG) onboard the ASO-S [J]. *Res. Astron. Astrophys.*, 2019, **19**:157

[5] LI H, CHEN B, FENG L, *et al.* The Lyman-alpha Solar Telescope (LST) for the ASO-S mission - I. Scientific objectives and overview [J]. *Res. Astron. Astrophys.*, 2019, **19**:158

[6] CHEN B, LI H, SONG K F, *et al.* The Lyman-alpha Solar Telescope (LST) for the ASO-S mission - II. Design of LST [J]. *RAA*, 2019, **19**:159

[7] ZHANG Z, CHEN D Y, WU J, *et al.* Hard X-ray Imager (HXI) onboard the ASO-S mission [J]. *Res. Astron. Astrophys.*, 2019, **19**:160

[8] SU J T, BAI X Y, CHEN J, *et al.* Data reduction and calibration of the FMG onboard ASO-S [J]. *Res. Astron. Astrophys.*, 2019, **19**:161

[9] FENG L, LI H, CHEN B, *et al.* The Lyman-alpha Solar Telescope (LST) for the ASO-S mission - III. Data and potential diagnostics [J]. *Res. Astron. Astrophys.*, 2019, **19**:162

[10] SU Y, LIU W, LI Y P, *et al.* Simulations and software development for the Hard X-ray Imager onboard ASO-S [J]. *Res. Astron. Astrophys.*, 2019, **19**:163

[11] HUANG Y, LI H, GAN W Q, *et al.* The Science Operations and Data Center (SODC) of the ASO-S Mission [J]. *Res. Astron. Astrophys.*, 2019, **19**:164

[12] LI C, FANG C, LI Z, *et al.* Chinese Hα Solar Explorer (CHASE) – A complementary space mission to the ASO-S [J]. *Res. Astron. Astrophys.*, 2019, **19**:165

[13] VIAL J C. The synergy between the payloads on the ASO-S mission [J]. *Res. Astron. Astrophys.*, 2019, **19**:166

[14] KRUCKERS S, HURFORD G, SU Y, *et al.* Joint hard X-ray observations with ASO-S/HXI and SO/STIX [J]. *Res. Astron. Astrophys.*, 2019, **19**:167

[15] VOURLIDAS A. Lyα science from the LST aboard the ASO-S mission [J]. *Res. Astron. Astrophys.*, 2019, **19**:168

Guo Huadong, Chen Hongyu, Chen Liangfu, Fu Bihong. Progress on CASEarth Satellite Development. *Chin. J. Space Sci.*, 2020, **40**(5): 120-130. DOI:10.11728/cjss2020.05.120

Progress on CASEarth Satellite Development*

GUO Huadong[1] CHEN Hongyu[2] CHEN Liangfu[1,3] FU Bihong[2]

1 (*Aerospace Information Research Institute, Chinese Academy of Sciences, Beijing* 100101)

2 (*Innovation Academy for Microsatellites, Chinese Academy of Sciences, Shanghai* 201204)

3 (*University of Chinese Academy of Sciences, Chinese Academy of Sciences, Beijing* 100049)

Abstract CASEarth satellite is the first space Earth science satellite produced by the Chinese Academy of Sciences. The satellite has three payloads: high-definition Thermal Infrared Spectrometer (TIS), high-definition Glimmer Imager for Urbanization (GIU), and high-definition Multispectral Imager for Inshore (MII). These payloads are used to explore the urbanization level and residential layout, the coastal ecosystem, and new methods and approaches of environmental detection during night-time and even under conditions of polar aurora and provide scientific evidence for the refined depiction of human traces. The CASEarth satellite can provide space observation data for A Project on Big Earth Data Science Engineering as well as scientific and application studies inside and outside China.

Key words CASEarth satellite, Human traces, Thermal infrared spectrometer, High-definition glimmer imager for urbanization, Multispectral imager for inshore

Classified index P 4

1 Introduction

As an organic component of Project on Big Earth Data Science Engineering dominated by the Chinese Academy of Sciences, the CASEarth satellite, also known as the Guangmu Earth science satellite, was established in July 2018. The satellite is the first space Earth science satellite in China developed by Chinese Academy of Sciences. It is intended for a refined depiction of human traces based on the requirements of residential layout, energy consumption, and coastal environment. Apart from three optical payloads in this satellite, a ground support system and a scientific application system are constructed. This satellite aims to provide spatial observations and support relevant scientific explorations domestically and internationally.

2 Scientific Objectives

The philosophy of the CASEarth satellite design is owning what others do not have and owning what better than others. The satellite is used to explore the urbanization level and residential layout, coastal ecosystem and new methods and approaches of environmental detection during night-time and even under conditions of polar aurora and provide scientific evidence for the refined depiction of human traces. The scientific objectives to be achieved through the CASEarth satellite are as followed.

(1) Comprehensively evaluate the development levels and social and economic development status of the cities involved in the Belt and Road Initiative. Use the thermal infrared and glimmer sensors to provide continuous and stable wide-range thermal infrared and glimmer remote sensing observations, then to quantify the magnitude of thermal radiation and light intensity. After that, the modelling relationship between urban spatial distribution, urban energy consumption, urban light data and thermal radiation data will be obtained. Finally, analyze and

* Supported by Chinese Academy of Sciences Strategic Leading Science and Technology Project (XDA19010000)
Received March 16, 2020
E-mail: liangdong@radi.ac.cn

disclose social and economic patterns, such as social and economic status, human activity status and energy consumption, and therefore realize dynamic monitoring and analysis of urban development levels and social and economic development status for the economic and energy corridors of the Belt and Road Initiative by combining urban spatial layouts and other social and economic statistics.

(2) Evaluate the regional differences and spatial layouts of the economic development in China. Based on infrared, glimmer, and multispectral comprehensive remote sensing data, detect urban and rural space human activity status and study the development differences, urbanization levels, and city and town distribution on both sides of the Hu Line. Explore the characteristics of urban functional areas, differences between old and new urban areas in a city, and characteristics of urban thermal environment and residential layout space distribution.

(3) Study the ecological environment quality of the coastal environment and the coastal zone. Use the three loads configured for the satellite to detect colored dissolved organic matter, chlorophyll and other water pollutants, locate the sources of coastal heat emission and pollutant discharge, detect port function areas, scales, and activity levels, and comprehensively evaluate the impact degrees of human activities along the coastal zone.

Based on the above-mentioned items, the CASEarth satellite will blaze the trail in the detection of nighttime urban particulate pollution and study the mechanism, using quantitative moonlight observation in snow-covered polar regions during polar nights to fill a gap in moonlight remote sensing in such regions.

3 Scientific Payloads

For a refined depiction of human trace information, such as residential layouts, energy consumption, and coastal ecology, the CASEarth satellite equipped with three payloads: high-definition Thermal Infrared Spectrometer (TIS), high-definition Glimmer Imager for Urbanization (GIU), and high-definition Multispectral Imager for Inshore (MII). The high-definition GIU and the high-definition MII share a common optical path and are integrated into one device called Glimmer and Multispectral Imager (GMI). The TIS is used for global thermal radiation detection, the GIU for observing lamplight on the Earth surface during night, and the MII mainly for coastal zone and specially for water environment observation.

3.1 TIS

Based on traditional surface temperature infrared split-window method (within the bands of 10.3~11.3 μm and 11.5~12.5 μm), a new band of 8~10.5 μm is added to TIS. The new configuration ensures higher surface temperature retrieval accuracy. The specific indexes are as follows.

(1) Imaging range width: ⩾300 km at 505 km.

(2) Pixel resolution: 30 m at 505 km (sub-satellite point).

(3) Detection spectra.

Waveband B1: 8~10.5 μm.

Waveband B2: 10.3~11.3 μm.

Waveband B3: 11.5~12.5 μm.

(4) NETD. Waveband B1: ⩽0.2 K at 300 K. Waveband B2: ⩽0.2 K at 300 K. Waveband B3: ⩽ 0.2 K at 300 K.

(5) Dynamic range: 220~340 K.

(6) Digitalizing bit: ⩾12 bit.

(7) Static/Dynamic MTF: ⩾0.17/0.10.

(8) Radiometric calibration uncertainty: absolute calibration better than 1 K at 300 K, relative calibration better than 5%.

3.2 GIU

The GIU is mainly used to obtain wide-range and high-resolution panchromatic and RGB glimmer data at night in the orbit, perform high-precision radiation calibration, provide nighttime glimmer images for big data scientific engineering of the Earth and evaluate residential layouts and urbanization development levels through lamplight distribution and lamplight quality. To comprehensively collect and detect lamplight data of different types (incandescent lamp, neon light, high voltage mercury lamp, xenon lamp, LED lamp, and others), the wide waveband of 430~900 nm is adopted for design, and panchromatic band data

are collected to improve the SNR. Considering the requirements of lamplight type differentiation and nighttime particle detection in cities, the wavebands are sub-divided into three bands of RGB.

(1) Spectrum range. Panchromatic: 430~900 nm. B: 430~520 nm. G: 520~615 nm. R: 615~900 nm.

(2) Panchromatic spatial resolution: 10 m at 505 km.

(3) RGB spectral spatial resolution: 40 m at 505 km.

(4) Imaging range width: ⩾300 km at 505 km.

(5) SNR. Panchromatic: City's main road lamplight (1.0×10^{-2} W·m^{-2}·sr^{-1})⩾50; city and town residential area (1.6×10^{-3} W·m^{-2}·sr^{-1}) ⩾10; polar moonlight ⩾10. RGB: City's main road lamplight (1.0×10^{-2} W·m^{-2}·sr^{-1}) ⩾50; city and town residential area (1.6×10^{-3} W·m^{-2}·sr^{-1}) ⩾10.

(6) Digitalizing bit: ⩾12 bit.

(7) Static/Dynamic MTF: ⩾0.23/0.10.

(8) Camera radiometric calibration uncertainty (RMS, the full field of view). Relative calibration: better than 2%. Absolute calibration: better than 5%.

3.3 MII

Retrieval study results of existing water quality parameters and simulation and analysis of water quality measurement spectra for the Yangtze River mouth, the Tai Lake and other locations show that, for suspended sediment detection, the traditional red light wave band (660±30 nm) is sensitive to a low sediment content, while the red edge wave band (785±20 nm) is more sensitive to a high sediment content; the deep blue wave band (440±20 nm) and the blue waveband (490±30 nm) are relatively sensitive for chlorophyll A detection in water, and deep blue wave band (400±20 nm) shows better performance in CDOM detection. To differentiating mangroves and extracting on-land vegetation coverage, the green light wave band (560±40 nm) and the near-infrared waveband (852.5±47.5 nm) must both be involved. Therefore, the indices of the CASEarth MII are designed as follows.

(1) Spectrum settings:

B1 (deep blue 1) 380~420 nm,

B2 (deep blue 2) 420~460 nm,

B3 (blue) 460~520 nm,

B4 (green) 520~600 nm,

B5 (red) 630~690 nm,

B6 (red edge) 765~805 nm,

B7 (near-infrared) 805~900 nm.

(2) Each spectrum's pixel resolution: 10 m at 505 km.

(3) Imaging range width: ⩾300 km at 505 km.

(4) SNR: B1>130, B2~B7>150.

(5) Code rate: not more than 2.4 Gbit·s^{-1} (uncompressed, total).

(6) Static/Dynamic MTF: ⩾0.23/0.10.

(7) Camera radiation calibration uncertainty (RMS, the full field of view). Relative calibration: better than 2%. Absolute calibration: better than 5%.

4 Guangmu Earth Science Satellite Mission

4.1 Satellite System

4.1.1 Satellite Orbit

It is desirable to use the CASEarth GIU to observe the cities and towns during the period (19:00 LT–22:00 LT) at night when there are relatively intense activities. It is required that the observation area's solar elevation angle be ⩾30° to ensure enough SNR when the MII is used for observation. Based on these two requirements and considering the need to use ground reception stations through staggering to avoid competing with other in-orbit remote sensing satellites for arc resources, the Sun-synchronous orbit with the descending node of 09:30 LT is selected. During orbit ascending, the sub-satellite point is at night (18:00 LT–22:00 LT) and glimmer observation is performed; during orbit descending, the sub-satellite point is at daytime and MII observation is performed (09:00 LT–10:00 LT). The TIS can work at any point in the orbit. The specific orbit parameters are as follows.

(1) Orbit type: Sun-synchronous orbit.

(2) Standard orbit height: 505 km.

(3) Inclination angle: 97.5° (+0.1° compared with SSO small bias to ensure orbit injection descending node).

(4) Descending node: 09:30 LT.

(5) Height variation range: 500~510 km.

On the orbit of 500 km to 510 km, the time required for the satellite payload with a 300 km range width to cover the entire Earth is about 11 to 15 days.

4.1.2 Observation Mode and Pointing Direction

The satellite task includes three observation modes: general survey observation, expansion observation, and emergency observation. There are six calibration modes for three types of payload.

4.1.2.1 General Survey Observation Mode

It is the most common in-orbit observation mode. The observation is implemented through on-satellite autonomous task planning by default. The satellite attitude is Earth center pointing and the drift angle is corrected. The ground observation areas (city, country, region, and others) are divided into not more than 100 polygonal areas. Based on the orbit extrapolation sub-satellite position and solar elevation angle and the autonomously determined power-on type on the satellite, autonomous preparation of payload and DDT, power-on, imaging, data storage, and power-off is performed.

For key observation areas (top priority areas: Beijing-Tianjin-Hebei, Yangtze River Delta, Zhujiang River Delta, the biggest three lakes in China and the Silk Road on Sea), observation performs at each orbit if possible. Based on coverage simulation, the observation longest time for each orbit is summarized in Table 1.

After the observation of the key areas is completed, observation performs for areas with level-2 (inland cities of The Belt and Road, cities with a population of over one million and the capital; Silk Road on Land) and level-3 (the entire world with the focus on global metropolises) priority to cover key areas of The Belt and Road and the areas across the globe.

Table 1 Maximum observation time summary per orbit (Unit min)

No.	Payload	Key areas	Belt and Road areas and China
1	TIS	6.3	16.9
2	GIU	6.3	16.8
3	MII	5.4	16.8

4.1.2.2 Expansion Observation Mode

Arctic and Antarctic observation is an expansion task for the CASEarth satellite. When the satellite flies over the Arctic and the Antarctic, it is planned that it will use as little time as possible with a resolution as high as possible and with as fewer times of attitude maneuvers to cover the entire regions through infrared, glimmer and multispectral observation using satellite side swing and payload imaging parameter settings.

With a satellite orbit inclination of 97.5°, the sub-satellite point cannot cover the entire Arctic and Antarctic regions (66.5°N/S to 90°N/S) and therefore the observation of these regions is made through satellite side swings. The satellite needs to make a side swing of 40° and therefore to observe the poles to reduce big-angle side swing time and increase as much resolution as possible. Two angles are adopted for observation of the Arctic and Antarctic regions. With the side swing of 40°, it takes 0.5 days to cover the areas from 84.5°N/S to the North Pole or the South Pole. For details, see Figure 1. With the side swing of 25°, it takes 2.5 days to cover the areas from 66.5°N/S to 84.5°N/S. Considering coverage time, ground resolution, data volume and TIS thermal constrains, it takes 5 days for polar night coverage and 12 days for polar day coverage without side way.

Five minutes before polar region range entry for each orbit, the satellite performs side swing maneuver to enter polar region observation mode and resume its original position and enter standby mode after leaving the corresponding polar region.

The observation sub-modes include Arctic polar night observation, Arctic polar day observation, Antarctic polar night observation, and Antarctic polar day observation. Polar day observation will be carried out in the polar summer. The Sun elevation angle is the main factor that affects irradiance in the

polar region. The changes of the Sun elevation angle in the polar regions of different latitude with time are shown in Figure 2.

Polar night observation is based on ice and snow detection experiments under the moonlight during winter nights in the polar regions. The Moon elevation angle is the main factor that affects irradiance in the polar region. The changes of the Moon elevation angle in the polar regions of the different latitude with time are shown in Figure 3.

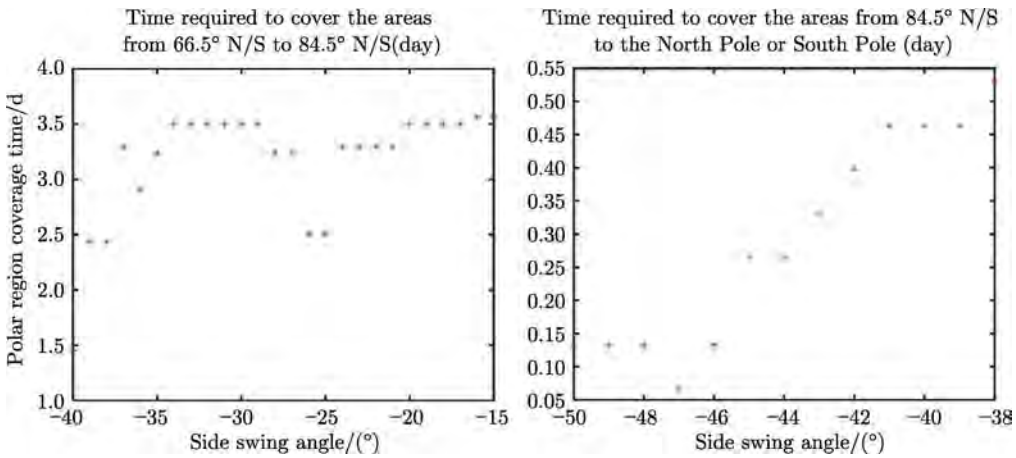

Fig. 1 Relationship between side swing angles and polar region coverage time

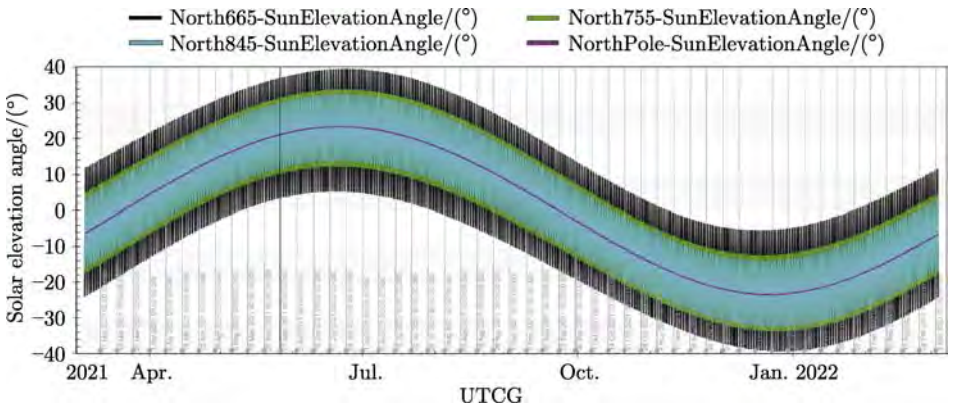

Fig. 2 Relationship between Solar elevation angle and the different latitude

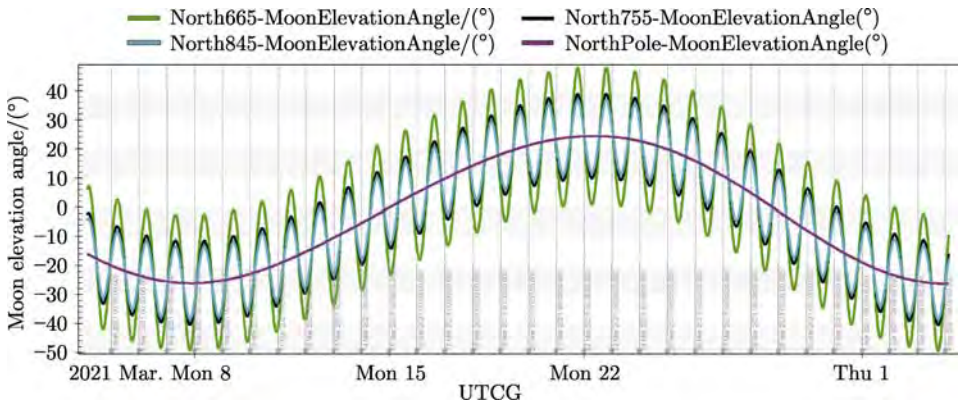

Fig. 3 Relationship between Moon elevation angle and the different latitude

The ideal condition for polar region observation is when the Moon elevation angle is over 24°. The GIU adopts image motion compensation to increase exposure time and improve the glimmer observation capability.

4.1.2.3 Emergency Observation Mode

The CASEarth satellite is flexible and mobile and can track and shoot photos of specific targets in emergencies in a directional manner. It can adjust its attitude through simultaneous rolling and yawing to perform tracking and observation for targets more than 300 km away from the sub-satellite point.

4.1.2.4 Payload Calibration Mode

(Ⅰ) TIS black body + cold sky calibration

The TIS combines the full-aperture black body and cold sky background to perform radiation calibration. There are two calibration modes: black body calibration and cold sky calibration. The mode switch is realized through the inner scanning mirror of the payload. The optical path of the optical system is shown in the following Figure 4.

Satellite pointing and calibration time sequences are shown in Figure 5.

(Ⅱ) GMI Internal Calibration through LED

The LED light source is the standard calibration light source for in-orbit internal calibration. On its basis, the quantitative relationship between the camera's spectral radiation input and image gray value output. Radiation transmission model parameters of different spectrum channels are calculated regularly in an in-orbit manner to monitor sensor variation and stability and verify and correct the sensor radiation response coefficient.

There are seven sets of LEDs inside each camera, with each set providing main and standby calibration data for adjacent two sensors, as shown in Figure 6. The main data are used for relative radiation correction and the alternate data are used for analyzing light source changes.

In-orbit internal calibration through LEDs is

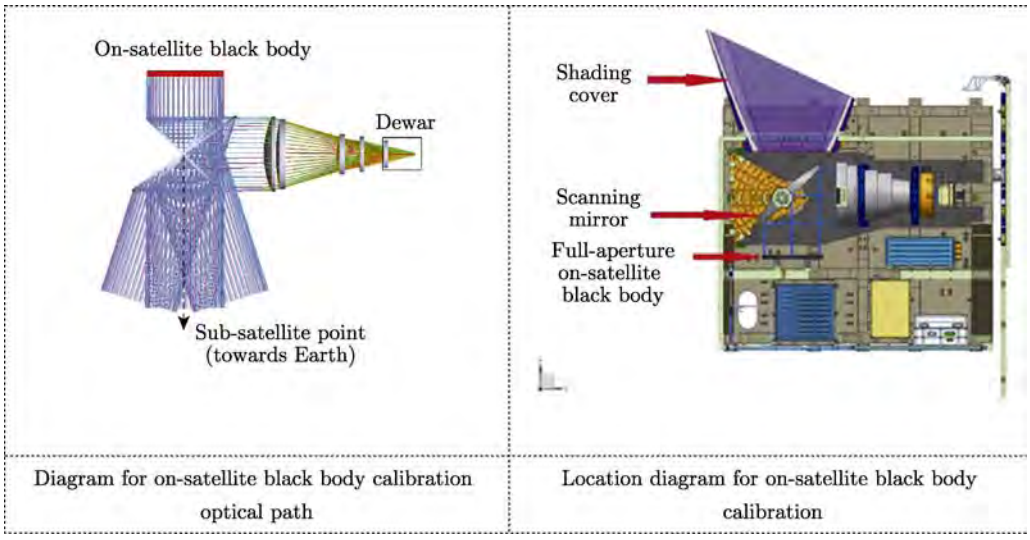

Fig. 4 Optical path of TIS optical system

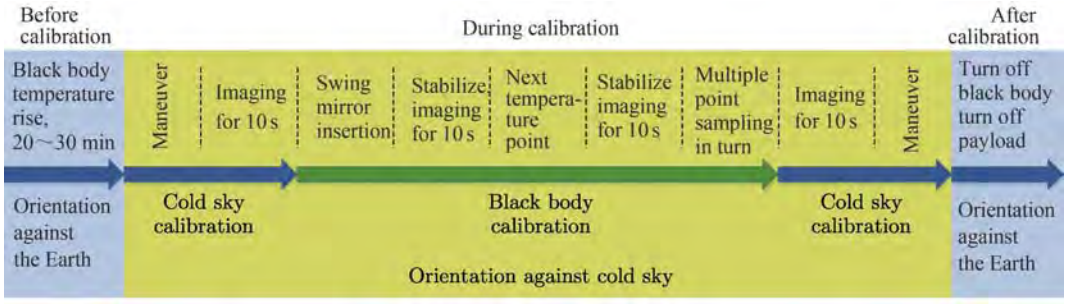

Fig. 5 Calibration process diagram of the TIS

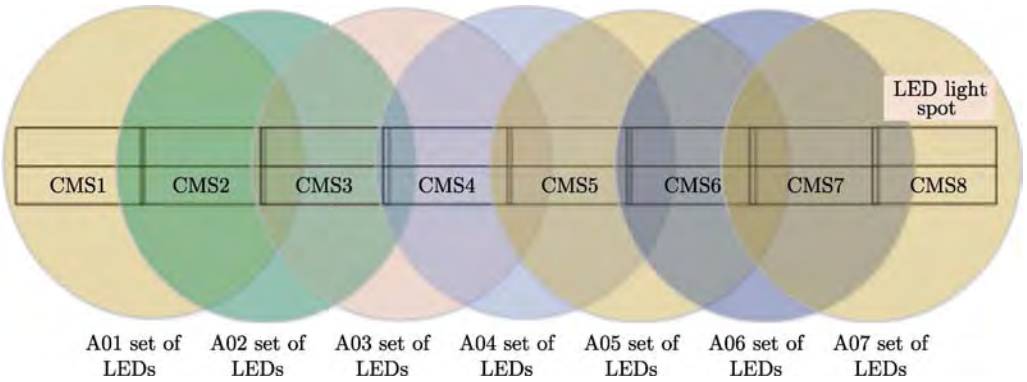

Fig. 6 Diagram of light spots on the LED focal plane

performed for the cameras with the satellite pointing towards the Earth from the 29th day of a month to the 1st day of the next month every month on the lunar calendar during cloudless nights when the satellite pass through a deep-sea area.

(III) GMI Calibration against the Moon

Since the attenuation of calibration light sources cannot be measured for the internal calibration method, outside-satellite calibration against the Moon is performed in addition to in-satellite LED calibration. The detector performs push-broom scanning for the entire Moon disk for each spectrum during Moon imaging. The detector push-broom direction is similar to that of the push-broom for the Earth, as shown in Figure 7.

The calibration needs to be performed in two orbits. In each orbit, rectangular scanning is performed for eight detectors of a camera in turn, as shown in Figure 8.

4.1.3 Payload Solution

4.1.3.1 TIS

The TIS adopts a one-dimension whisk-broom system for wide-range thermal infrared observation and channels the collected optical information into the transmission-type low-temperature optical system in the payload and concentrates it on the long-wave focusing plane assembly. The detector then receives the optical information and transforms it into electrical signals through photoelectric conversion. The scanning mode is shown in Figure 9. During the scanning process, forward scanning with a range of 300 km is performed and images are generated. Images are not generated in reverse scanning. Both scanning processes are performed at an even speed.

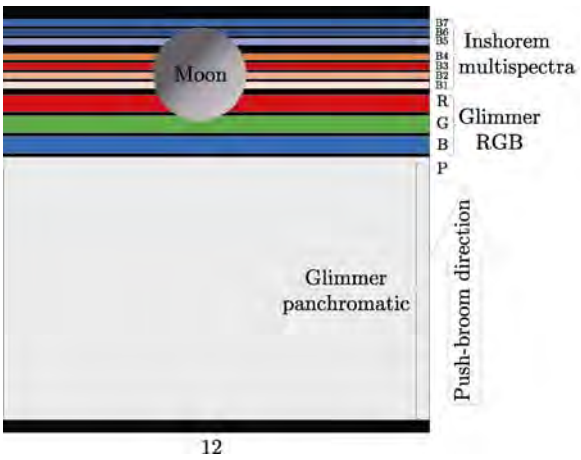

Fig. 7 Diagram of the Moon, detector and push-broom direction

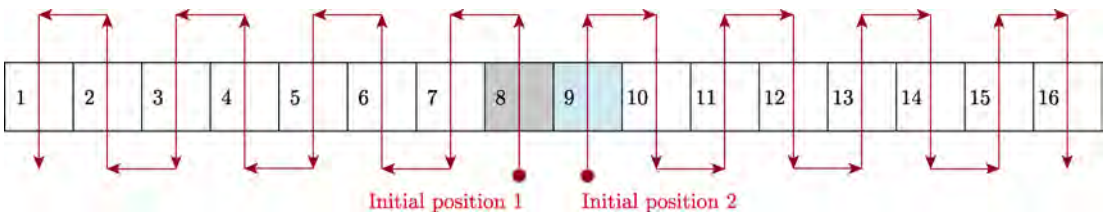

Fig. 8 Planning for whisk-broom path for the Moon

The TIS mainly consists of an optical machine main body, a comprehensive electrical box, and a cooler control circuit box. The composition and external ports the TIS system is shown in Figure 10.

4.1.3.2 GMI

To meet the imaging requirements under the city and town glimmer at night and of inshore multiple spectra during the daytime, a low-illumination CMOS detector and the off-axis TMA optical system with a small F-number are used and the technology system combining digital TDI push-broom with a large field of view and plane-array staring imaging is adopted. The digital TDI imaging mode is adopted by default to realize high-efficiency imaging with a large field of view, while for weak target signals, the staring imaging mode based on image motion compensation is adopted to increase exposure time and improve the detection capability. The imaging range of one camera is more than 150 km, with a ground pixel resolution of 10 m. A range of 300 km can be achieved by joining two cameras.

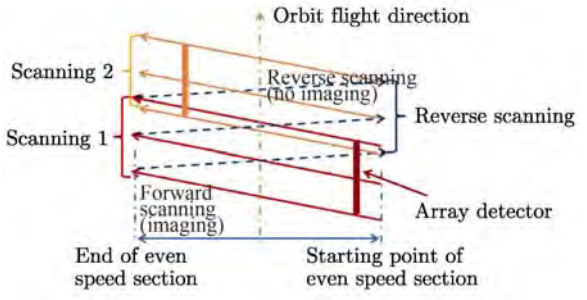

Fig. 9 Diagram of TIS whisk-broom

The GMI consists of the camera lens, the focusing plane assembly and the electrical control assembly. The overall structure of its components and external ports is shown in Figure 11.

Images of surface feature targets are formed on the focusing plane through the camera lens and then processed through on-satellite registration following photoelectric conversion. Image information is output through the imaging circuit. Image data are transmitted to the satellite DDT component for data compression and storage, sent to the ground station at a proper time after real-time or in-orbit storage, and processed by the ground application system.

4.1.4 Platform Solution

The satellite's containing structure is a rectangle. The center of the interconnection circle between the satellite and the rocket is defined as the coordinate origin, the direction that the payload lens is pointing in the interconnection plane is defined as the $+z$ direction (that is, the Earth-pointing direction of the general survey mode during in-orbit flight) and the direction perpendicular to the interconnection plane and pointing from the platform to the payload is the $+x$ direction (the flight direction in general survey mode during in-orbit flight). The satellite adopts three-axis stable attitude control, with the three axes stably pointing to fixed direction against the Earth in general survey mode. The sunlight mainly shines on the satellite from the $-x$ and $-y$ directions. When the satellite is placed on the ground, from top to bottom

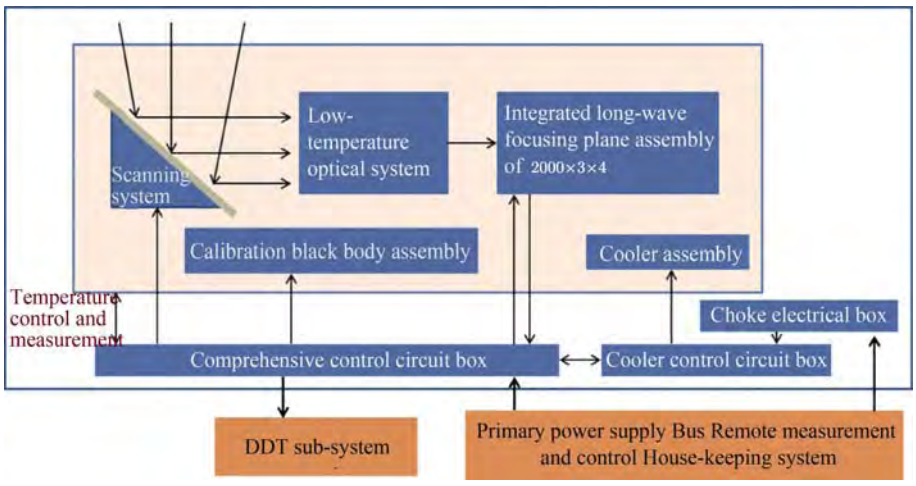

Fig. 10 Diagram of TIS system composition and external ports

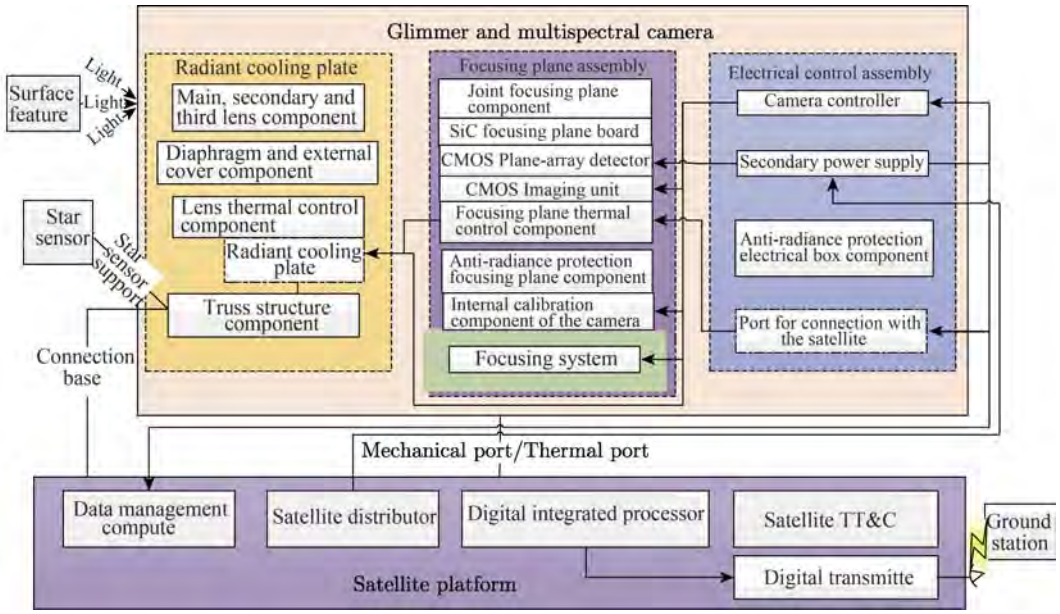

Fig. 11 Diagram of GMI system composition and external ports

are the GMI, the TIS, and the satellite platform cabin, as shown in Figure 12.

A single-wing fold-up solar panel is adopted for the satellite power supply. When the satellite is launched, the solar panel is folded up on the $-y$ side board. The solar panel is unfolded and locked in the $-y$ axis direction after the satellite enters its orbit, with an angle of 30° between the solar panel and the $-y$ axis. The night side and $+y$ side are the heat dissipation sides of the payload, the $-z$ side is the main heat dissipation side of the satellite platform, and $+z$ and $-x$ sides are the auxiliary heat dissipation sides of the satellite platform, as shown in Figure 13.

The house-keeping computer is the satellite information management and control center which performs centralized management for on-satellite remote sensing data collection, flying program, attitude and orbit control, and thermal control. A power controller provides power supply and distribution for each computer in a uniform manner. The on-satellite payload DDT information flow centers on a multiplex modulator to perform data multiplexing, assembling frames, encoding, modulation, amplification, and downlink to ground stations through the antenna, and complete payload data and satellite

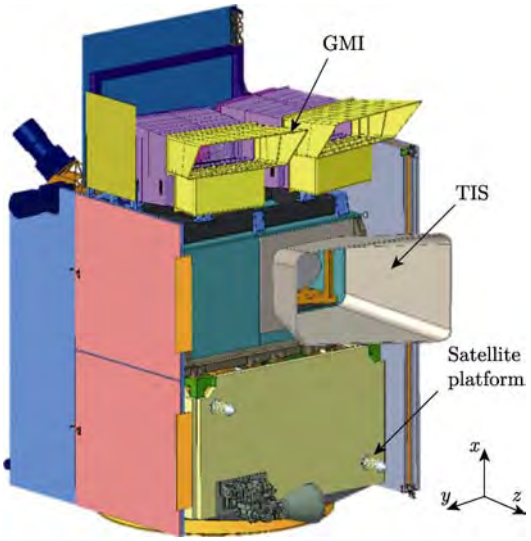

Fig. 12 Diagram of the static satellite placed on ground

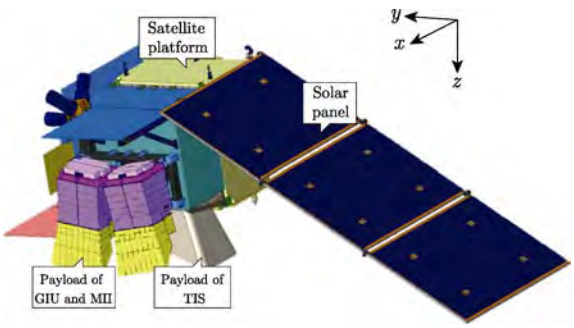

Fig. 13 In-orbit flying status diagram

platform data transmission. For DDT, the X band is adopted to realize scientific data downlink from the satellite to the ground at 2×810 Mbit·s^{-1}.

The satellite time system is managed by a housekeeping computer uniformly. The computer supports functions such as time service, centralized time calibration, uniform time calibration, and GPS/Beidou time calibration. The computer keeps the time by itself after synchronization of GPS/Beidou time calibration and centralized time calibration on the ground.

The satellite adopts three-axis zero-momentum stability control and double star sensors and gyro EKF for attitude measurement accuracy of 10", and uses angular momentum feed-forward to compensate for the impact of the movement of the thermal infrared oscillating mirror to meet the requirements of ground pointing accuracy of 0.08° and stability of 0.0012(°)·s^{-1}.

The satellite dry weight is 715 kg, among which 355 kg is the payload weight and 15 kg is the fuel. The average power dissipation of the entire satellite is 576 W and the peak power dissipation is 1086 W.

4.2 Launch Vehicle and Launch Site

LM-6 is the New Generation innocuous and no-pollution launch vehicle, mainly used to launch satellites for various purposes to Sun-Synchronous Orbit (SSO) and Low-Earth Orbit (LEO).

The LM-6 uses three horizons (horizontal integral test, horizontal integral Satellite and Launch Vehicle docking, horizontal integral transportation and erection) test-launch mode, realizing quick test and launching (see Figure 14 and 15).

Launch Site is in Taiyuan Satellite Launch Center.

4.3 Measurement and Control System

Satellite ground TT&C system adopt the USB measurement and control mechanism for satellite tracking, range finding, orbit measurement, remote measurement, and remote control.

4.4 Ground Support System

The Ground Support System (GSS) is responsible for in-orbit operation management and services for the satellite, including satellite status monitoring and fault warnings, payload status monitoring, data reception plan preparation, scientific data reception, and forwarding and others.

The ground data reception station includes three X band reception stations in Miyun, Sanya, and Kashi. When necessary, use the Antarctic reception station to make up for the insufficient reception time. The technical indices are listed as follows.

(1) Operating band: X band.

(2) Polarization method: simultaneous left-handed + right-handed circular polarization (data), left-handed/right-handed circular polarization self-adaption (tracking).

(3) Antenna aperture: 12 m.

(4) Antenna G/T value: 33.5 dB·K^{-1}.

(5) Ground station reception rate: main 2×810 Mbit·s^{-1} (8 PSK) and emergency 2×540 Mbit·s^{-1} (QPSK).

4.5 Scientific Application System

The Scientific Application System (SAS) is responsible for verifying scientific objectives, payload configuration solutions, satellite technology indices and usage requirements, constructing scientific application

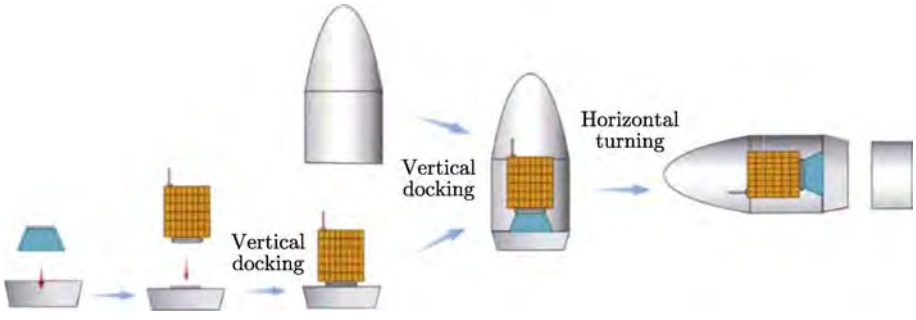

Fig. 14 Single satellite docking flow

Fig. 15 LM-6 launch vehicle

system software and hardware, producing and providing level 0~4 standard products, advanced products, and dedicated scientific application products as well as providing data support for scientific application research, realizing in-orbit on-satellite calibration through observation of the cold sky, on-satellite black bodies, LED lights, the Moon and other light sources or objects to obtain and provide calibration parameters and organizing in-orbit tests with the CASEarth satellite in the fields of panoramic beautiful China, the digital Belt and Road, 3D information ocean, biodiversity and ecological security, three poles and others.

5 Ground Reception and Data Processing

The ground part of the CASEarth satellite mainly consists of a measurement and control system, the ground support system, and the scientific application system.

The measurement and control system is responsible for receiving the payload control instructions from the ground support system and encode them and perform instruction transmission to the satellite through the S-band satellite ground measurement and control station, receiving remote measurement data of the satellite S-band and sending the data to the ground support system.

The ground support system is responsible for generating payload control instruction through payload imaging planning based on the scientific observation plan, receiving the satellite remote measurement data from the measurement and control system, analyzing and handling remote measurement data to monitor satellite status and payload status and give fault warnings, as well as receiving downlink DDT data of the X band from the satellite through the ground data reception station and sending them to the scientific application system.

The scientific application system is responsible for generating an observation plan based on the scientific observation requirements, receiving the satellite DDT data from the ground support system to handle data products, producing and providing level 0~4 standard products, advanced products and dedicated scientific application products, providing ground calibration parameters through ground calibration, collaborating with each dedicated applications of the dedicated Earth big data project, and providing high-quality data support for dedicated scientific application research.

6 Development Plan and Current Status

The satellite is now at the prototype phase and is scheduled to be launched at a proper time after May 2021. Data services will be available within half a year after the launch.

WANG Chi, Chen Zhiqing, XU Jiyao. Introduction to Chinese Meridian Project – Phase II. *Chin. J. Space Sci.*, 2020, **40**(5): 131–135. DOI:10.11728/cjss2020.05.131

Introduction to Chinese Meridian Project – Phase II *

WANG Chi Chen Zhiqing XU Jiyao

(*State Key Laboratory of Space Weather, National Space Science Center, Chinese Academy of Sciences, Beijing* 100190)

Abstract The Chinese Meridian Project is a ground-based space environment monitoring network, which is constructed in two steps. The first step (Phase I) of the project consists of 15 observation stations located roughly along 120°E longitude and 30°N latitude. The second step (Phase II) of the project will additionally deploy 16 stations to better cover China's territory, and build a stereo monitoring capability to monitor the cause and effect of the space weather chain in the solar terrestrial system. Based on the existing two monitoring chains in Phase I, two more chains will be established along 100°E longitude and 40°N latitude, respectively, forming a double-cross network configuration. After the two-step construction, the whole project will run nearly 300 instruments deployed at 31 stations. Aside from standard instruments, quite a few innovative and powerful instruments will be developed, such as radioheliographs with a very wide frequency band, a 3-station incoherent scattering radar to make a 3D measurement of the ionosphere, and a helium lidar to measure atmosphere density up to an altitude of 1000 km.

Key words Meridian Project, Ground-based observation, Space weather

Classified index P 4

1 Overview of the Chinese Meridian Project

The Chinese Meridian Project is a ground-based space environment monitoring facility funded by China's National Development and Reform Commission as one of a series of major scientific infrastructures. It is a joint effort of more than 10 research institutions and universities in China, led by the National Space Science Center (NSSC), the Chinese Academy of Sciences.

The space environment here refers to the vast area between the Sun and Earth that includes solar atmosphere, interplanetary space, Earth's magnetosphere, ionosphere, middle and upper atmosphere. This huge area constitutes the space weather cause and effect chain, whereby solar activities influence near Earth environment. Variations of the solar-terrestrial space environment contain a great deal of physical processes such as magnetic reconnection, coronal heating, energetic particles acceleration and transportation, and charge exchange between ionized particles and neutrals, *etc.* The solar eruptions will disturb space environment significantly, resulting in space weather events. Space weather could subsequently influence the performance and reliability of space-borne and ground-based technological systems, even endanger human life or health. Adverse conditions in the space environment can cause disruptions of satellite operations, communications, navigations, and electric power grids, leading to a variety of socioeconomic losses.

The space weather monitoring systems include both space-borne satellites and ground-based observatories. Chinese Meridian Project is a ground-based space weather monitoring network.

Due to the bounding of charged particles by the Earth's magnetic field and latitudinal difference of

* Supported by the Chinese Meridian Project
Received March 16, 2020
E-mail: cw@spaceweather.ac.cn

solar radiation, space environment disturbances usually occur along the meridian lines. As a result, observing along a specific meridian line owns a great deal of advantages. The Chinese Meridian Project has fully exploited these advantages, by taking into configuration the meridian line at east longitude 120°E that has the longest cut through China's territory.

The scientific objectives of the Chinese Meridian Project are: (i) to study the propagation processes of disturbances caused by solar activities, from the sun to interplanetary, magnetosphere, ionosphere, until mid-to-upper atmosphere; (ii) to study mechanisms behind coupling between different space spheres/layers, namely solar atmosphere, interplanetary, magnetosphere, ionosphere, and mid-to-upper atmosphere; (iii) to study the regional characteristics of the space environment above China's territory, and its relationship with the global variations.

The conception of the Chinese Meridian Project was initially proposed as early as in 1990s, and rolled into realization stage in 2008 upon being approved by the government as one of the major scientific infrastructures. The construction of Phase I of this project was completed in 2012 and has been put into operation from then on. The construction of the Phase II kicked off in 2019, and is scheduled to complete by 2023.

2 Phase I of the Project

The first phase of the project, with the full name of East-hemisphere Space Environment Ground-based Comprehensive Monitoring Chain, consists of 15 ground-based observatories located roughly along 120°E longitude and 30°N latitude[1]. The chain along the 120°E longitude starts from Mohe, the northernmost city of China, and runs south through Beijing, Wuhan, Guangzhou, and the island of Hainan (with instruments at Haikou, Fuke, and Sanya) and extends to China's Zhongshan station in Antarctica. Distances between neighboring stations are roughly 4°–5° in latitude or about 500 km apart, except the Zhongshan station in Antarctica. Another chain of stations was constructed roughly following 30°N, spanning from Lhasa to Shanghai. Each observatory is equipped with multiple instruments to comprehensively measure the key parameters of the baseline and time-varying geomagnetic field as well as of the middle and upper atmosphere and ionosphere. Parameters of the solar wind are also tentatively measured. There are totally 87 instruments which have been built and installed.

In addition to the space environment monitoring system provided by these instruments, Data & Communication System and Research & Forecasting System have also been built, and the headquarter is located in Beijing. The Data and Communications System is in charge of collecting, transferring, processing, storing, and distributing data in quasi real time. All data is made public *via* the website data.meridianproject.ac.cn. The Research and Forecasting System coordinates observations, develops relevant data analysis and space weather forecasting tools, and promotes international collaborations.

Exploring the huge volume of data that instruments have accumulated, scientists have made huge progresses into key scientific problems such as space weather characteristics in middle and low latitude regions, laws of zonal or meridional propagation of disturbances. According to incomplete statistics, more than 300 journal papers have been published.

3 A Grand Upgrade by Phase II

In 2018, the Chinese government approved an even more ambitious program to make a grand upgrade to the Chinese Meridian Project: Phase II of this project, which will deploy 16 more comprehensive stations with two main goals: (i) to better cover China's territory; (ii) to build a 3D monitoring capability covering the cause and effect of the space weather chain in the solar terrestrial system, including the solar atmosphere, interplanetary space, magnetosphere, ionosphere, and middle-upper atmosphere[2].

The configuration of the second phase of the Chinese Meridian Project can be set forth by explaining its core elements as follows[3].

3.1 One Cause and Effect Chain

The first phase of the project lacks the capability to monitor the solar atmosphere and the interplanetary space, even though it indeed has tentatively built an Interplanetary Scintillation (IPS) monitoring instrument. The domain of the Phase I of the project was basically confined to the near-Earth region, or geospace. That prevents it from reaching the ultimate source of the space weather.

In the second phase of the project, a series of instruments will be constructed to monitor activities on the solar atmosphere, such as sunspots on photosphere, solar flares on chromosphere, coronal mass ejections, and so on. Further into the interplanetary space, radio signals and cosmic rays will be utilized to monitor the complete route that solar activities follow to reach Earth, nearly without any significant space gap. These instruments comprise the cause and effect chain of the project.

3.2 Three Networks

In complement to the existing two monitoring chains deployed in the first phase, two more chains will be established along 100°E longitude and 40°N latitude respectively, forming a double-cross network configuration. Including the 15 stations from Phase I of the project, there will be 31 comprehensive stations in total. Thus, the whole territory of China plus the polar region will be covered by this project.

Multiple types of space weather monitoring instruments will be installed for each station, endowing with a versatile capability to monitor various parameters pertaining to space regions at different heights. These are three instrument networks for monitoring geomagnetic field, mid-to-upper atmosphere, and ionosphere respectively.

3.3 Four Focuses

In addition to the three networks, four key regions are focused including the high, middle, low latitudes, and the third pole of Earth. The polar region in high latitude is where the high energy particles from the solar wind or magnetotail precipitate directly into ionosphere and atmosphere along the polar magnetic field. The north part of China in the middle latitude is the pathway for disturbances from high latitude regions propagating towards the mid and low latitude regions of China. The Hainan island in the low latitude is closest to the equatorial ionospheric anomaly, where ionosphere disturbances and anomalies occur very frequently. The Tibetan plateau region is also regarded as the third pole of Earth besides the north/south poles where unique geographic conditions give rise to particularly complex atmospheric convections.

Aside from such a much wider geographical extension and the ability to reach the solar atmosphere, comparing with Phase I, the most important upgrade for Phase II lies in that quite a few innovative and powerful instruments will be employed especially for the four focus regions. Instrumentation will be elaborated in the following section.

4 Instrumentation

For the Cause and Effect Chain, the project has a multi-layer magnetograph which is able to map the magnetic field vector across the whole solar disk by a single snap, a coronagraph with an outer field of view radius of 2 solar radii, several radioheliographs that make up a super-broad observation frequency band, a triangle configured Interplanetary Scintillation (IPS) telescope array, and several cosmic ray detectors for muons and neutrons respectively.

For the Three Networks, standard instruments are adopted in a great number. The main instruments include more than 100 magnetometers, tens of traditional or digital ionosondes, tens of airglow imagers, tens of meteor radars, tens of GNSS ionospheric TEC, and scintillation monitors, Mesosphere-Stratosphere-Troposphere (MST) radars, lidars, and aurora spectrographs. Generally, these kinds of instruments are able to run in a fully automatic mode and produce continuous data.

For the Four Focuses, innovative and powerful space environment instruments will be constructed

as a part of the second phase, except for the polar region which will be mainly equipped with a set of standard instruments.

The most powerful instruments are radio heliographs with a very wide combined frequency band, 3-station Interplanetary Scintillation telescope (IPS) for interplanetary monitoring, 3-station incoherent scattering radar to make a 3D measurement of the low-latitude ionosphere, a high frequency radar array for mid-to-high latitude ionosphere observation, and a synthetic aperture helium lidar to measure atmosphere density up to an altitude of 1000 km. Please see Figure 1 for the design illustrations.

On completion of the construction, altogether, the Chinese Meridian Project will run nearly 300 instruments deployed at 31 different stations.

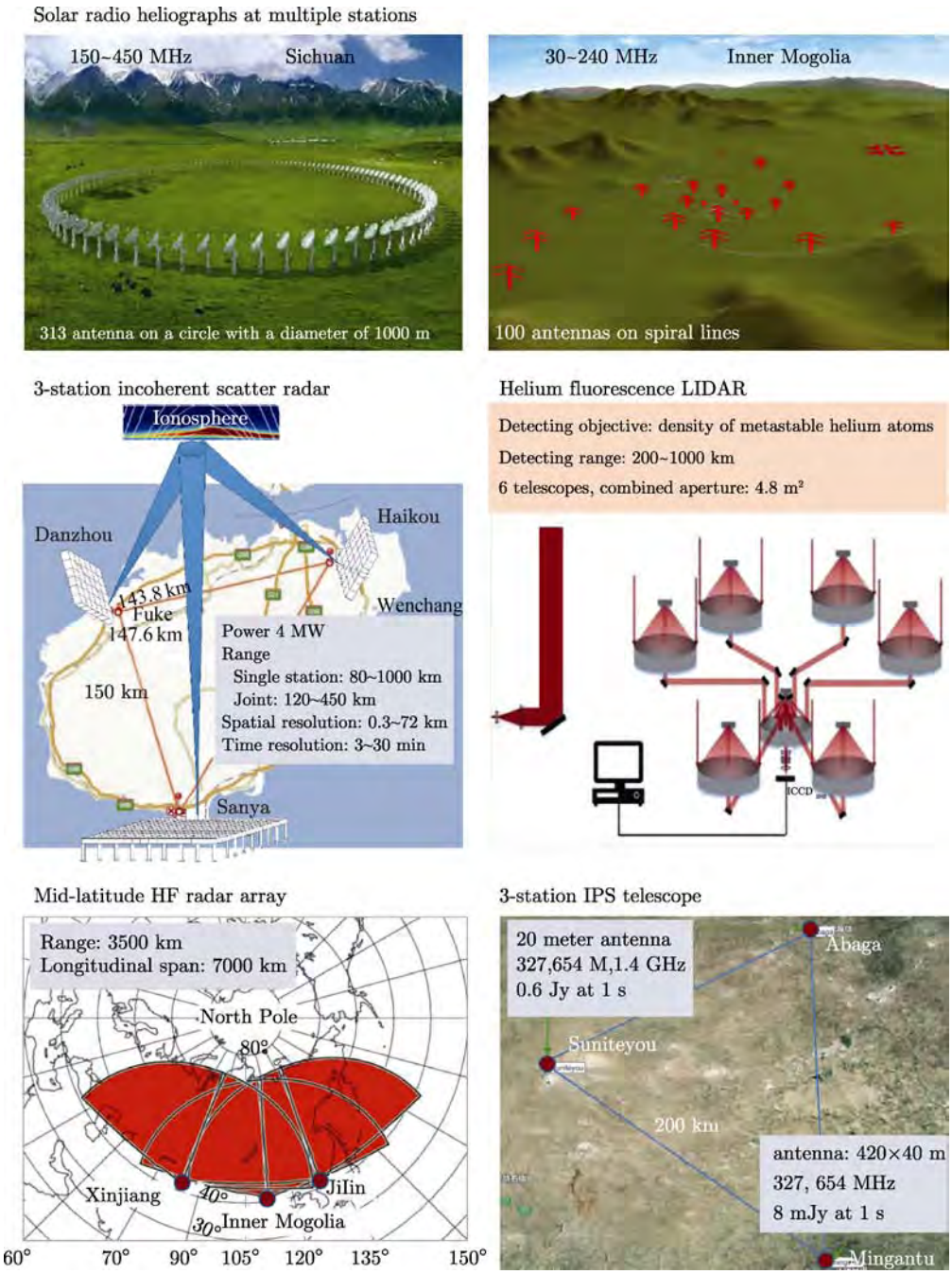

Fig. 1 Some innovative instruments of the Phase II of the Chinese Meridian Project

5 Data Storage and Processing

Aside from the Space Environment Monitoring System comprised of the nearly 300 instruments, the project also has a Data & Communication System and a Science Application System. These two additional systems will be constructed anew rather than a minor upgrade to the existing systems in Phase I, since the estimated data volume is astonishingly huge compared to that of Phase I, and much more research and data applications will be developed.

It is estimated that the Data and Communication System has to cope with an annual data volume of about 2 PBs (petabytes). The data center will have 10 PBs storage capacity upon acceptance, with an expansion capacity of up to 30 PBs. To facilitate data transfer, based on the internet, VPN links connecting the data center and instruments will be established. Thus, most kinds of data will be collected in real-time and made public *via* a website within 15 minutes.

The Science Application System will construct facilities and software for observation coordination, data analysis, modeling and simulation, space weather forecasting methods development, and international collaboration.

At the same time, mainly for accommodating these two systems, a 6-floor-building will be erected on the Huairou campus of NSSC in Beijing. It will serve as the headquarter of the Chinese Meridian Project.

6 Construction Plan and Current Status

Starting from 2015, the study team with members from more than 10 research institutes and universities has been working hard on the framework and detailed design of the Phase II of the project forward. In 2018, China's National Development and Reform Commission approved the proposal of the project, to be followed by an approval for the Feasibility Study report in February 2019.

Construction of the project officially kicked off in November 2019. It is expected to finish by 2023. Now, the whole project is going through a detailed design stage. Due to the diversity of complexity, instruments are scheduled to finish construction on different dates. Standard instruments are hopeful to be ready by the end of 2021. From then on, these instruments will be put into operation.

7 Outlook and Concluding Remarks

Based on the Chinese Meridian Project, China is pushing forward an international collaboration initiative to carry out observation along the unique meridian circle of 120°E/60°W, which is called International Meridian Circle Program (IMCP). The proposal has been raising huge interests around the world. The proposal to initiate this international collaboration has been submitted to the Ministry of Science and Technology of China at the end of 2019.

The Chinese Meridian Project, including the already running Phase I and the Phase II under construction, will endow China and the world with solid ground-based capabilities to monitor space environment. After combined with the IMCP, an unprecedentedly comprehensive data set will be available for the whole science community, which is very much worthy looking forward to, and please stay tuned.

References

[1] WANG Chi. New chains of space weather monitoring stations in China [J]. *Space Weather*, 2010, **8**, S08001. DOI: 10.1029/2010SW000603

[2] WANG Chi, XU Jiyao. Preliminary design report for Space Environment Ground-based Comprehensive Monitoring Network [R]. Beijing: Chinese Academy of Sciences, 2018

[3] WANG Chi. Recent advances in observation and research of the Chinese Meridian Project [J]. *Chin. J. Space Sci.*, 2018, **38**(5):640-649

LIU William, WANG Chi, SHEN Xuhui, WU Jian, BLANC Michel, YAN Yihua, FU Suiyan, YUE Xinan, LEI Jiuhou, GONG Wei, ZHANG Shaodong, ZHANG Qinghe, WANG Xin, YANG Jing, ZHANG Xiaoxin, GAO Jing, XU Jiyao, YANG Guotao, LI Hui, REN Liwen, YANG Fang. International Meridian Circle Program. *Chin. J. Space Sci.*, 2020, **40**(5): 136-138. DOI:10.11728/cjss2020.05.136

International Meridian Circle Program*

LIU William[1] WANG Chi[1] SHEN Xuhui[2] WU Jian[3] BLANC Michel[1] YAN Yihua[4]
FU Suiyan[5] YUE Xinan[6] LEI Jiuhou[7] GONG Wei[8] ZHANG Shaodong[8]
ZHANG Qinghe[9] WANG Xin[10] YANG Jing[10] ZHANG Xiaoxin[11] GAO Jing[12]
XU Jiyao[1] YANG Guotao[1] LI Hui[1] REN Liwen[1] YANG Fang[1]

1 (*National Space Science Center, Chinese Academy of Sciences, Beijing* 100190)
2 (*National Institute of Natural Hazards, Ministry of Emergency Management of China, Beijing* 100085)
3 (*China Electronics Technology Group Corporation No.22 Research Institute, Xinxiang* 259008)
4 (*National Astronomical Observatories, Chinese Academy of Sciences, Beijing* 100101)
5 (*School of Earth and Space Sciences, Peking University, Beijing* 100871)
6 (*Institute of Geology and Geophysics, Chinese Academy of Sciences, Beijing* 100083)
7 (*School of Earth and Space Sciences, University of Science and Technology of China, Hefei* 230026)
8 (*School of Electronic Information, Wuhan University, Wuhan* 430079)
9 (*School of Space Science and Physics, Shandong University, Weihai* 264209)
10 (*Institute of Atmospheric Physics, Chinese Academy of Sciences, Beijing* 100029)
11 (*China Meteorological Administration, Beijing* 100089)
12 (*Institute of Tibetan Plateau Research, Chinese Academy of Sciences, Beijing* 100101)

Abstract The Earth is buffered from the ferocious onslaught of the solar wind by a thin layer of matter known as the atmosphere and geospace. This layer absorbs energy from irradiance and outburst from the Sun, as well as from disasters, transient phenomena and anthropogenic emissions originated from Earth. Through complicated physics, the absorbed energy changes the atmospheric and geospace state and sometimes gets re-released to power extreme events such as space weather. Taking place globally, these complicated processes cannot be understood unless they are studied globally. The Chinese scientists have proposed the International Meridian Circle Program (IMCP) to meet this demand. By operating nearly 1000 instruments encompassing all latitudes along with the 120°E–60°W longitudes, IMCP aims, for the first time, to construct comprehensive 3D data representation of the atmosphere and geospace on a global scale and empower interdisciplinary research to tackle key questions related to Earth's environment and climate change.

Key words International Meridian Circle Program, Chinese Meridian Project, Ground-based observation, Space weather, Solar-terrestrial physics

Classified index P 4

The changing environment is one of the greatest challenges humanity faces in the 21st century. In spite of enormous progress, our science is still not in a position to offer clear solutions to many environmental problems confronting us today. Since the environment is a global whole, its understanding demands a global effort from all countries. The International Meridian Circle Program is a call for global action to tackle one of the most critical scientific questions of the century, namely, how does

* Supported by Beijing Municipal Science and Technology Commission (Z181100002918001)
Received March 30, 2020
E-mail: cw@spaceweather.ac.cn

energy from the Sun and Earth change the atmosphere, how can the resulting change pose a threat to the human society, and how can we mitigate and manage the negative consequences of this change.

The atmosphere and its extension into space (known together as Geospace) are fundamental to the survival of humanity; a 1% deviation of some Geospace parameters from their present values could have catastrophic consequences. The Geospace system is driven by an ever-present flow of energy from the Sun and Earth. The light energy from the Sun maintains the delicate balance in the ecosphere and regulates the tropospheric weather. The magnetic energy from the Sun stirs the often-stormy solar wind through which the Earth sails uneasily. The heat energy within Earth drives tectonic movement and oceanic circulation. The land features of Earth perturb the air circulation and feedback on local and global weather. All these inputs and interactions account for the high variability of Earth's climate and weather and are often associated with natural disasters or undesirable long-term trends.

The Ionosphere and Mid-Upper Atmosphere (IMUA), located in the altitude range 20~1000 km, is crucial to Geospace Change. Energy extracted from the solar-terrestrial interaction and energy propagating upward from the troposphere give rise to a complex pattern of motion and turbulence, which can change significantly the distribution of species participating in the chemistry of Global Change. IMUA is also the seat of extreme Space Weather, an electromagnetic meltdown in space posing a major threat to economy and potentially human life. According to a 2008 report by the US National Research Council[1], if the largest recorded space weather incident, the Carrington event in 1859 (when the use of electric power was still a novelty), were to recur today, the potential economic loss could exceed $2 trillion in the US alone, with a potential loss in life measured in millions. Moreover, the pattern of IMUA motion and turbulence is a mirror image of their respective solar and terrestrial energy sources, raising the possibility of using IMUA perturbation patterns to predict space weather and Earth-originated disruptions.

Till now we have not understood fully Space Weather or how Global Change responds to energy flows from the Sun and Earth, much less making robust predictions based on the understanding. However, there is a strong foundation to achieve this understanding. Over the years, the scientists have built powerful regional and continent-scale arrays of sophisticated ground-based instruments capable of taking the snapshots of IMUA over a large area. Combined these snapshots gives a fuzzy collage of Geospace, but not a smooth movie. The goal of the International Meridian Circle Program is to obtain, on a continuous basis, global movie of Geospace in motion, by (i) synchronizing the observations from the existing networks around the globe, (ii) harmonizing data formats and analytics standards, (iii) building strategically important new research capacities, and (iv) establishing an International Meridian Organization to oversee the research and operational activities of the combined global network.

The majority of the existing Geospace-observing networks are distributed along the Great Meridian Circle along with the 120°E and 60°W longitudes, cutting across China, Russia, Canada, the United States, Latin America, Antarctica, Australia, and Southeast Asia, with about 1000 instruments in operation or under construction. In particular, in China, the Chinese Meridian Project (Phase 1 and 2) will deliver, by 2023, the world's most extensive ground-based Geospace-observing network with more than 300 instruments measuring 38 different parameters.

Once integrated, the 1000 instruments deployed along the 120°E–60°W meridian circle can give a complete cross-sectional scan of Geospace from ground level to up to 3000 km altitude, including density, temperature, electric and magnetic fields, wind fields, planetary waves, and distribution of minor species involved in Global Change. By virtue of Earth's rotation, this network can give a complete three-dimensional representation of these key Geospace parameters every 12 h. Accumulated over years and decades, this dataset will provide valuable insight on how Climate and long-term atmospheric change are influenced by the solar and terrestrial energy input. By detecting and tracking short-term anomalies in Geospace parameters, the network can

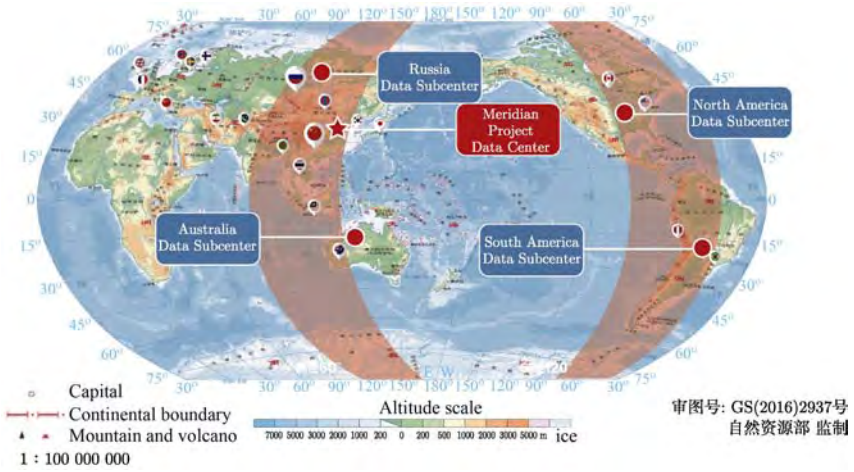

Fig. 1 Illustrative map of IMCP

provide advanced warnings on space weather and terrestrial disasters such as earthquakes.

The idea of a circumpolar chain of ground-based instruments for space weather study was first conceived by Prof. Wei Fengsi in 1994, just about the time when space weather became an international concern. In 2004, this idea was crystallized in the proposal of the Chinese Meridian Project (CMP) and received formal support from the National Development and Reform Commission in 2008.

The International Meridian Circle Program emphasizes the development of new research capacities to tackle scientific questions arising from the expanded view of Geospace, first as a system driven by energy flows from both solar and terrestrial sources, and second by taking into account longer time-scale variability associated with Global Change. These new capacities could include innovative use of nanosatellite technology to complement and complete the ground-based observations.

For program direction and management, we envision a new type of international research organization, with a permanent and fully staffed headquarters in Beijing, and four program platforms, namely, research, coordinated network operations, data sharing, and HQP training distributed around the globe. An International Meridian Organization will be created through an international charter approved by participating countries and given independent power and authority to manage the International Meridian Circle Program in the best interest of science.

Now, IMCP is selected as a candidate mission for the International Big Science Initiative supported by Chinese Academy of Sciences, and has been funded as a concept study by Beijing Municipal Science and Technology Commission. Besides, Government of Beijing already allocated funds for an 8000 m^2 IMCP HQ building.

IMCP is building international support at an impressive rate. To date, close to 20 countries have expressed an interest to cooperate. These include major advanced economies such as Great Britain and France, BRICS countries such as Russia and Brazil, countries with major existing capabilities and crucial territories such as Canada and Australia, leading developing countries such as Indonesia and possibly India. Despite temporary strains in relationship, scientists from the United States have been very active in supporting the IMCP. Many international organizations have endorsed IMCP as a valuable contribution to global science, including IUGG, COSPAR, SCOSTEP, URSI, SCAR, and ISWI.

IMCP will be a major step forward from the outstanding foundation of CMP Phases 1 and 2. Set in an international context demanding greater global cooperation to tackle grand challenges humanity faces as a whole, IMCP will be a compelling entry point for Chinese research to reach an elevated altitude in international science.

References

[1] COUNCIL N R. Severe Space Weather Events: Understanding Societal and Economic Impacts: A Workshop Report [R]. Washington D C: National Academies Press, 2008:144

GAN Weiqun. Space Solar Physics in China. *Chin. J. Space Sci.*, 2020, **40**(5): 139–141. DOI:10.11728/cjss2020.05.139

Space Solar Physics in China*

GAN Weiqun

(*Key Laboratory of Dark Matter and Space Astronomy, Purple Mountain Observatory, Chinese Academy of Sciences, Nanjing* 210033)

Abstract The activities of Chinese space solar physics in 2018–2020 are going on smoothly. Besides the missions of ASO-S and CHASE which are in the engineering phases, there are quite a number of projects which are in the pre-study stage (conception study) or have finished the pre-study stage, constituting a rich pond for the selection of next solar mission(s). This paper describes in brief the status of all these related projects.

Key words Space astronomy, Solar physics

Classified index P 353

1 Missions Undertaken

Mission-level solar projects in China have gone a long way[1-8]. Unprecedentedly, there are two solar missions in engineering phases currently: the Advanced Space-based Solar Observatory (ASO-S), and Chinese H-alpha Solar Explorer (CHASE).

ASO-S is a mission proposed for the 25th solar maximum by the Chinese solar community[9,10]. The scientific objectives are to study the relationships among solar magnetic field, solar flares, and coronal mass ejections (CMEs). Three payloads are Full-disk Magnetograph (FMG)[11,12], Lyman-alpha Solar Telescope (LST)[13-15], and Hard X-ray Imager (HXI)[16,17], respectively. ASO-S has a solar synchronous orbit at an altitude of 720 km with an inclination angle of around 98.2°. Since the formal approval at the end of 2017, ASO-S underwent the official Phase-B study from January 2018 to April 2019. Then from May 2019, ASO-S has been undertaking the Phase-C study. The Phase-D study (flight model) is expected to start at August 2020. ASO-S is planned to launch either at the end of 2021 or in early 2022.

CHASE[18] is a unique science payload onboard a new experimental platform. It is designed to spectrally image the whole Sun at lines of H-alpha (6562.8 Å) and FeI (6569.2 Å). A scheme of grating spectrometer plus scanning mirrors is used in its optical system. Total weight of the telescope is about 35 kg. Now the mission is under engineering study and the expected launch date is in early 2021.

2 Pre-study Projects: Finished

In the report for 2016–2018[8], we listed some proposals which were selected into the first batch of pre-study projects supported by the CAS's Strategic Priority Program on Space Science during the 13th five-year plan. Two years later, a few of them have finished their pre-studies, which are as follows.

(1) Multi-scale Solar Spectral Observatory (MSSO) (January 2018 to December 2019): As expected, this project finished all the works on time at the end of 2019. Being a mission conception it proposed in fact a comprehensive framework: a full waveband radiation monitor plus a multi-wave band spectral imaging of coronagraph. The former, taking the Sun as a star, aims at observing the whole ra-

* Supported by Chinese Academy of Sciences (XDA15052200) and by National Natural Science Foundation of China (U1731241, 11921003 and U1931138)
Received February 13, 2020
E-mail: wqgan@pmo.ac.cn

diation from the infrared to gamma-rays by using several individual detectors, so as to study the long time variation of the Sun and the short time influence like the influence by the solar flares. The latter would like to observe with unprecedently high resolution the corona from 1.5 to 90 solar radii by using a group of spectrometers and imagers, so as to study how the solar wind, CMEs, shock-waves, and energetic particles evolve from the Sun to the Earth.

(2) Dual observations at solar polar orbit (January 2018 to December 2019): This mission conception was also finished its study on time at the end of 2019. The idea is to use two identical satellites at conjugate positions of solar polar orbit (the perihelion and aphelion is comparable to the Sun-Earth distance), so as to observe the whole Sun always, especially for the solar polar regions. The proposed payloads include temporally the full disk magnetograph, ultraviolet polarized telescope, wide field coronagraph, and in-situ detectors for the solar wind. The proposers believe that this mission could make a breakthrough in understanding the origin of solar magnetic field besides monitoring the Sun globally.

(3) Solar Transition region Observation and Research Mission (STORM) (January 2018 to December 2019): The completed mission concept includes both a EUV telescope (diameter 20 cm; Ne VII 465 Å, FOV $250'' \times 250''$) and a spectrometer (400~475 Å, 745~795 Å, 995~1045 Å), in order to observe for the first time the connections from the lower atmosphere continuously to the upper transition region and corona, so as to provide a better understanding for the mechanism of coronal heating and the origin of solar wind.

(4) Close observation on solar eruptions (January 2018 to December 2019): Close to the Sun to make both in-situ and remote observations is certainly an exciting task. Differing from Solar Orbiter and Park Solar Probe, this mission proposes to measure the magnetic reconnection region directly, like the current sheet which leads to solar flares and CMEs. The proposed payloads consist of detectors for measuring energetic particles, electric field, magnetic field, EUV coronal spectrometers (for measuring high temperature plasma), and so on.

Obviously, these finished pre-study projects are being improved at present and looking for opportunities to do further studies.

3 Pre-study Projects: Undertaking

In 2019 the second batch of pre-study projects supported by the CAS's Strategic Priority Program on Space Science during the 13th five years plan is started. Furthermore, there are also several projects supported by other sources. They are summarized as follows.

(1) The Formation Flying of Focused Solar Hard X-ray Telescope: it is a conception study, which plans to propose a feasible mission with two spacecraft separated about 150 m. The front one is the focused grazing telescope, while the rear one is the detector, so as to get unprecedently high spacial resolution in solar hard X-ray imaging. This proposal has gotten financial supports from both CAS and NNSFC. The key of the study is around the feasibility.

(2) Solar Observatory at L5: in fact there are two independent proposals for the solar and terrestrial observations at L5. One is proposed by NSSC, paying more attention to the space weather domain; and the other by Nanjing University, emphasizing more on solar physics. Both proposals are more or less similar in the payload deployments, including obviously a couple of in-situ and remote instruments.

(3) Solar Observation at L2: this proposal is proposed also by NSSC and has gotten pre-study support from CAS. The idea is to launch a mission working at L2, to observe the solar corona through a natural coronagraph, *i.e.*, using the Earth as a natural shelter for the Sun. Both scientific and technical issues are the topic to be studied.

(4) Space Weather Mission at L1: for quite a time it was heard that National Satellite Meteorological Center would build a space weather mission working at L1. But no more information has been publicly released so far. Therefore no progress can be reported. However, their Fengyun-3E mission will be launched in 2020, on which an X (0.6~8.0 nm, 0.6~6.0 nm, 0.6~5.0 nm, 0.6~2.0 nm, 0.6~6 nm, 0.6~1.2 nm)

and EUV (19.5 nm) telescope will make a routine observation of the Sun.

(5) Three-dimensional Imaging for Inner Heliosphere: this proposal proposes to launch a group of 6 identical spacecraft into the Earth orbit, two of which work together as a sub-group and separate from other sub-groups by 120°. This kind of distributions is believed to be able to make some key observations on the solar structures and the eruptions.

(6) Close Imaging the Sun: it is another proposal proposed by the different affiliations from what in Section 2. A series of technical and scientific issues are being studied with the supports by CAS and NNSFC.

(7) A New Kind Telescope for Solar Hard X-rays and Gamma-rays: the traditional high energy solar telescopes use either spatial or temporal modulation. This proposal proposes a new kind of telescope based on a new principle, so-called double modulations.

(8) Solar Observatory on the Moon: it seems to be long term envision and no real progress has been made so far, although it is proposed in response to the call by the Chinese Lunar Program.

(9) Some proposal candidates for the Space Station: in response to the call issued by the Chinese space station, several solar proposals are submitted, like Multi-waveband and Wide-Field EUV Spectral Imaging, the EUV Polarization Observation, Wide-field X-ray Telescope/Coronagraph, Super-wide Dynamic Frequency Spectrometer in Millimeter Waveband, and so on. At the moment, it is still unknown which one could be selected.

4 Conclusions

We have seen from the above that the zero-breakthrough of the first Chinese Solar spacecraft will soon be realized either in 2021 or 2022. The scientific researches on the data from ASO-S and CHASE are intensively being prepared. On the other hand, quite a number of pre-study mission concepts have been proposed. It is really a good situation for the Chinese solar physics community. However, at the moment it is still unclear where and what is the real chance for the next solar mission. Furthermore, how to select the mission from so many proposals is another challenge. Anyway, with the launch of ASO-S and CHASE, the second Chinese solar spacecraft will soon be put on the agenda.

References

[1] GAN W Q, XUE S J. Space astronomy in China: 2002–2004 [J]. *Chin. J. Space Sci.*, 2004, **24**: (Sppl.):99-101

[2] GAN W Q. Space astronomy in China during 2004–2006 [J]. *Chin. J. Space Sci.*, 2006, **26**: (Sppl.):76-78

[3] GAN W Q. Space astronomy in China: 2006–2008 [J]. *Chin. J. Space Sci.*, 2008, **28**(5):424-425

[4] GAN W Q, ZHANG S N, YAN Y H, CHANG J. Space astronomy in China: 2008–2010 [J]. *Chin. J. Space Sci.*, 2010, **30**(5):424-426

[5] ZHANG S N, YAN Y H, GAN W Q. China's space astronomy and solar physics in 2011–2012 [J]. *Chin. J. Space Sci.*, 2012, **32**(5):605-617

[6] GAN W Q. Space solar physics in 2012–2014 [J]. *Chin. J. Space Sci.*, 2014, **34**(5):563-564

[7] GAN W Q. Space solar physics in 2014–2016 [J]. Chin. J. Space Sci., 2016, **36**(5):636-638

[8] GAN W Q, FAN Q L. Space solar physics: 2016–2018 [J]. *Chin. J. Space Sci.*, 2018, **38**(5):662-664

[9] GAN W Q, DING M D, HUANG Y, *et al.* Preface: Advanced Space-based Solar Observatory (ASO-S) [J]. *RAA*, 2019, **19**:155

[10] GAN W Q, ZHU C, DENG Y Y, *et al.* Advanced Space-based Solar Observatory (ASO-S): an overview [J]. *RAA*, 2019, **19**:156

[11] DENG Y Y, ZHANG H Y, YANG J F, *et al.* Design of the Full-disk Magnetograph (FMG) onboard the ASO-S [J]. *RAA*, 2019, **19**:157

[12] SU J T, BAI X Y, CHEN J, *et al.* Data reduction and calibration of the FMG onboard ASO-S [J]. *RAA*, 2019, **19**:161

[13] LI H, CHEN B, FENG L, *et al.* The Lyman-alpha Solar Telescope (LST) for the ASO-S mission – I. Scientific objectives and overview [J]. *RAA*, 2019, **19**:158

[14] CHEN B, LI H, SONG K F, *et al.* The Lyman-alpha Solar Telescope (LST) for the ASO-S mission – II. Design of LST [J]. *RAA*, 2019, **19**:159

[15] FENG L, LI H, CHEN B, *et al.* The Lyman-alpha Solar Telescope (LST) for the ASO-S mission – III. Data and potential diagnostics [J]. *RAA*, 2019, **19**:162

[16] ZHANG Z, CHEN D Y, WU J, *et al.* Hard X-ray Imager (HXI) onboard the ASO-S mission [J]. *RAA*, 2019, **19**:160

[17] SU Y, LIU W, LI Y P, *et al.* Simulations and software development for the Hard X-ray Imager onboard ASO-S [J]. *RAA*, 2019, **19**:163

[18] LI C, FANG C, LI Z, *et al.* Chinese $H\alpha$ Solar Explorer (CHASE)–A complementary space mission to the ASO-S [J]. *RAA*, 2019, **19**:165

JI Jianghui, WANG Su. China's Future Missions for Deep Space Exploration and Exoplanet Space Survey by 2030. *Chin. J. Space Sci.*, 2020, **40**(5): 142-144. DOI:10.11728/cjss2020.05.142

China's Future Missions for Deep Space Exploration and Exoplanet Space Survey by 2030*

JI Jianghui[1,2] WANG Su[1]

1 (*CAS Key Laboratory of Planetary Sciences, Purple Mountain Observatory, Chinese Academy of Sciences, Nanjing* 210008)

2 (*CAS Center for Excellence in Comparative Planetology, Hefei* 230026)

Abstract Four future missions for deep space exploration and future space-based exoplanet surveys on habitable planets by 2030 are scheduled to be launched. Two Mars exploration missions are designed to investigate geological structure, the material on Martian surface, and retrieve returned samples. The asteroids and main belt comet exploration is expected to explore two objects within 10 years. The small-body mission will aim to land on the asteroid and get samples return to Earth. The basic physical characteristics of the two objects will be obtained through the mission. The exploration of Jupiter system will characterize the environment of Jupiter and the four largest Moons and understand the atmosphere of Jupiter. In addition, we further introduce two space-based exoplanet survey by 2030, Miyin Program and Closeby Habitable Exoplanet Survey (CHES Mission). Miyin program aims to detect habitable exoplanets using interferometry, while CHES mission expects to discover habitable exoplanets orbiting FGK stars within 10 pc through astrometry. The above-mentioned missions are positively to achieve breakthroughs in the field of planetary science.

Key words Deep space exploration, Exoplanet surveys, Mars, Jupiter, Habitable planets

Classified index P 4

1 Deep Space Exploration Program of China by 2030

Four missions for deep space exploration in China are scheduled to be launched by 2030, which includes two Mars exploration missions, Near-Earth asteroid sample return and main belt comet rendezvous mission, and the exploration on the Jupiter and its moons. Here we summarize the major subjects on these missions as follows in a chronological order.

1.1 First Mars Exploration Mission in 2020

The first China's Mars exploration mission was approved in 2016, and it has been launched on 23 July 2020 by CZ-5 carrier rocket. The Mars mission includes an orbiter, a lander, and a rover. Through the Martian orbiting phase, the global mapping of the surface of Mars will be carried out. The partial extensive investigations will survey surface material composition, landform, and geological structure, while Martian atmosphere and climate environment will be investigated in detail in the patrol phases. Now, the spacecraft is launched from Wenchang, Hainan Province to the Earth-Mars transfer orbit. After seven-month travel in the space, the spacecraft will be captured by the gravity of Mars about February 2021.

Main Scientific Goals[1, 2]

(1) To characterize the global landform and

* Supported by the B-type Strategic Priority Program of the Chinese Academy of Sciences (XDB41000000), the National Natural Science Foundation of China (11773081, 11573073), CAS Interdisciplinary Innovation Team, Foundation of Minor Planets of the Purple Mountain Observatory and Youth Innovation Promotion Association

Received June 25, 2020

E-mail: jijh@pmo.ac.cn

geological structure, surface material composition, and internal structure, *etc.*

(2) To characterize the soil and water-ice distribution on Mars.

(3) To assess the characteristics of atmosphere and climate environment surrounding Mars.

1.2 Asteroid and Main Belt Comet Exploration Mission

The Near-Earth asteroid and main belt comet exploration mission is expected to be carried out in 2024. The primary targets are the near Earth object 469219 Kamo'oalewa (also known as 2016 HO_3) which is the fifth quasi-satellite of Earth[3] and the main belt comet 133P/Elst-Pizarro. The mission will fly around the asteroid, then land on it, carry out in-situ measurement, obtain some samples, and return Earth. For the comet phase, the spacecraft will orbit 133P to explore its physical property. The entire mission for two objects will almost last for 10 years.

Main Scientific Goals

For the stage of the asteroid exploration: (i) measure the parameters of its orbit, rotation, shape, and thermo-physical characteristics, *etc.*; (ii) characterize the global landform and geological structures, surface composition, internal structure; (iii) analyze the returned sample and retrieval its physical and chemical parameters, chemical composition, age, and establish the relationship between the samples and in situ measurement.

For the stage of main belt comet exploration: (i) measure the parameters of comet's orbit, rotation, shape, and thermal feature, *etc.*; (ii) characterize the global landform and geological structures, surface material composition, internal structure, the space environment, the existence of water, and the activity of the comet.

1.3 Second Mars Exploration Mission around 2028

The second exploration on Mars is scheduled in 2028 and will take some Martian samples back to Earth.

Main Scientific Goals[2]

(1) To characterize the terrain and chemical composition through in situ measurement.

(2) To analyze the returned samples and get its physical and chemical properties, which can help us to reveal the origin and evolution of Mars.

1.4 Exploration of Jupiter System

The exploration of Jupiter system is scheduled to be launched about 2030. The main targets are Jupiter and its four largest Moons, and perform large-scale remote-sensing observations[2].

Main Scientific Goals

(1) To investigate the environment around Jupiter system, including the magnetic fields and plasmas interaction.

(2) To characterize the structure and composition of Jupiter's atmosphere.

(3) To establish the atmosphere model, the ice surface terrain and internal structures of the Galilian satellites.

(4) To study the structures of solar wind from the Earth to Venus and Jupiter.

2 Exoplanet Space Surveys on Habitable Planets by 2030

China is actively involved in its own space exploration programs of exoplanets, to characterize habitable planets around the neighborhood of the solar system using astrometry measurements and direct imaging observations in the next decades. There are mainly several future exoplanet space surveys on habitable planets by 2030, Miyin, and CHES mission. Miyin program aims to detect habitable exoplanets using interferometry, while CHES expects to discover habitable exoplanets through astrometry.

2.1 Miyin Program

Miyin program expects to find habitable planets around the stars in our neighborhood. The mission will launch spacecraft with groups of telescopes to search for exoplanets with interferometry in the intermediate infrared band. The spatial resolution of the mission will reach 0.01 arcseconds.

Main Scientific Goals

(1) To detect and locate exoplanets in our neighborhood by retrieving their direct images and assess their habitability.

(2) To investigate the objects in our Solar sys-

tem and study the water distribution on the objects.

2.2 Closeby Habitable Exoplanet Survey (CHES Mission)

CHES mission will discover the nearby Earth-like planets around FGK stars within 10 pc from our solar system *via* astrometry. Astrometry can minimize the detection bias of other techniques, like RV or transit, thereby being one of the most important methods of detecting exoplanets. The FOV of CHES is 0.44°× 0.44°, based on 1.2 m primary. CHES will utilize the Space Astrometry technique in the optical band. In order to keep the high stability of the pointing accuracy, minimizing the temperature effect *etc.*, the mission will occupy the L2 orbit. The micro arcsecond astrometry in space will deserve to be the highest precision mission, which may produce fruitful achievements in planetary science, cosmology science, and many other astrophysical research fields. CHES is expected to discover at least 50 Earth-like planets or super Earths during its five-year mission.

Main Scientific Goals

(1) To search for the nearby terrestrial exoplanets in habitable zones, especially Earth-like planet around FGK stars within 10 pc.

(2) To comprehensively survey and detect the nearby planetary systems within 10 pc, to discover the planets with orbital periods ranging from 30 days to 10 years, and further to determine its orbital parameters and the masses.

On the other hand, the high-contrast exoplanet imager mounted on the Chinese Space Station Optical Survey Telescope (CSST), scheduled for launching in 2022, will observe the mature Jupiter-like planets, cold Neptunes and super Earths in the neighborhood of solar-type stars, which expects to detect tens of exoplanetary candidates and brown dwarfs[8]. In addition, there are also other missions proposed to detect Earth twins, such as Super-Kepler Mission, *etc.*

In summary, the above-mentioned missions are positively expected to achieve breakthroughs in the field of planetary sciences.

References

[1] JIA Yingzhuo, FAN Yu, ZOU Yongliao. Scientific objectives and payloads of Chinese first Mars exploration [J]. *Chin. J. Space Sci.*, 2018, **38**(5):650-655

[2] XU Lin, ZOU Yongliao, JIA Yingzhuo. China's planning for deep space exploration and lunar exploration before 2030 [J]. *Chin. J. Space Sci.*, 2018, **38**(5):591-592

[3] DE LA FUENTE MARCOS C, DE LA FUENTE MARCOS R. Asteroid (469219) 2016 HO_3, the smallest and closest earth quashi-satellite [J]. *Mon. Not. Roy. Astron. Soc.*, 2016, **462**:3441-3456

[4] China National Space Administration. Announcement of opportunities for the asteroid exploration mission payload and payload project [EB/OL]. [2019-04-19]. http://www.cnsa.gov.cn/n6758823/n6758839/c6805886/content.html

[5] Science and Technology Daily. Chinese scientists have put forward a plan to explore Jupiter [N/OL]. [2016-07-06]. http://finance.china.com.cn/roll/20160706/3798458.shtml

[6] WU Ji. Calling Taikong: A Study Report on the Future Space Science Program in China [M]. Beijing: Science Press, 2016

[7] China News. China will launch its "Sound-finding Mission" to explore habitable planets near its solar system [N/OL]. [2019-12-13]. http://www.hn.chinanews.com/news/gnxw/2019/1213/374838.html

[8] LIU B B, JI J H. A tale of planet formation: from dust to planets [J]. *Res. Astron. Astrophys.*, 2020 (in press)

ZHAO Xinhua, SHEN Chenglong, HE Jiansen, NING Hao. Research Progress of Interplanetary Physics in Mainland China. *Chin. J. Space Sci.*, 2020, **40**(5): 145-190. DOI:10.11728/cjss2020.05.145

Research Progress of Interplanetary Physics in Mainland China*

ZHAO Xinhua[1] SHEN Chenglong[2] HE Jiansen[3] NING Hao[4]

1 (*State Key Laboratory of Space Weather, National Space Science Center, Chinese Academy of Sciences, Beijing* 100190)

2 (*CAS Key Laboratory of Geospace Environment, Department of Geophysics and Planetary Sciences, University of Science and Technology of China, Hefei* 230026)

3 (*School of Earth and Space Sciences, Peking University, Beijing* 100871)

4 (*Institute of Space Sciences, Institute of Frontier and Interdisciplinary Science, Shandong University, Weihai* 264209)

Abstract Significant progress has been made by Chinese scientists in research of interplanetary physics during the recent two years (2018–2020). These achievements are reflected at least in the following aspects: Activities in solar corona and lower solar atmosphere; solar wind and turbulence; filament/prominence, jets, flares, and radio bursts; active regions and solar eruptions; coronal mass ejections and their interplanetary counterparts; other interplanetary structures; space weather prediction methods; magnetic reconnection; Magnetohydrodynamic (MHD) numerical modeling; solar energetic particles, cosmic rays, and Forbush decreases; machine learning methods in space weather and other aspects. More than one hundred and forty papers in the academic journals have been published in these research directions. These fruitful achievements are obtained by Chinese scholars in solar physics and space physics either independently or through international collaborations. They greatly improve people's understanding of solar activities, solar eruptions, the corresponding space weather effects, and the Sun-Earth relations. Here we will give a very brief review on the research progress. However, it must be pointed out that this paper may not completely cover all achievements in this field due to our limited knowledge.

Key words Solar wind, Solar eruptions, Energetic particles, Interplanetary transients, Space weather

Classified index P 353

1 Activities in Solar Corona and Lower Solar Atmosphere

Solar UV bursts are a new type of small-scale activity discovered with NASA's IRIS mission. Tian *et al.*[1] studied the temporal evolution of UV bursts in the earliest stage of solar flux emergence, and found that the appearance of UV bursts is a good indicator of local heating during flux emergence. They also found that the occurrence frequency of UV bursts is closely related to the rate of flux emergence. By investigating the 3D magnetic field topology through a magneto-hydrostatic model, they found that almost all UV bursts are located in regions of a large squashing factor at a height of about 1 Mm. The relationship between Elleman bombs and UV bursts is highly debated. Chen *et al.*[2] investigated the spatial and temporal relationship between Elleman bombs

* Supported by the B-type Strategic Priority Research Program of Chinese Academy of Sciences (XDB41000000), the National Natural Science Foundation of China (41531073, 41731067, 41861164026, 41874202, 41474153), the Youth Innovation Promotion Association of Chinese Academy of Sciences (2016133) and Chinese Academy of Sciences Research Fund for Key Development Directions

Received March 27, 2020

E-mail: xhzhao@spaceweather.ac.cn

and UV bursts using joint near-limb observations of GST and IRIS. They find that many UV bursts tend to appear at the upper parts of their associated flame-like EBs. The intensity variations of most EB-related UV bursts and their corresponding EBs match well. These results suggest that UV bursts and EBs likely form at different heights during a common reconnection process.

Solar spicules are the most abundant small-scale dynamic features in the solar chromosphere. The origin of these small-scale jets is poorly understood. Using GST's high-resolution and high-sensitivity magnetic field measurements of the photosphere, Samanta *et al.*[3] found clear signatures of opposite-polarity magnetic fluxes at the footpoints of the jets. Interaction between these fluxes leads to the generation of the jets. These observations provide a strong evidence for the reconnection driven spicule mechanism. Their observations have also revealed obvious heating of these spicules to coronal temperatures, thus revealing the previously missing link between magnetic activities in the lower solar atmosphere and coronal heating. Through a detailed analysis of the coordinated GST and IRIS observations, Tian *et al.*[4] identified signatures of shock waves and unambiguous evidence of reconnection at light brights. They found frequently occurring inverted Y-shaped jets in the *Hα* wings and UV burst-type profiles of the transition region lines. This work demonstrated that the surge-like activity above light bridges has two components: the ever-present short and slow surges likely to be related to the upward leakage of magneto-acoustic waves from the photosphere, and the occasionally occurring long and fast surges that are obviously caused by the intermittent reconnection jets. Their study has solved the debate regarding the nature of these surge-like activities.

From the highest-resolution sunspot images obtained with GST, Zhang *et al.*[5] discovered a new type of fine structures in light bridges: striking knot-like dark structures within the central dark lane. These dark knots divide the central dark lane into multiple sections, and they appear to be very common in narrow light bridges. The evolution of these highly dynamic dark structures could provide detailed information about the magneto-convection in light bridges. IRIS Observations often reveal significantly broadened and non-reversed Mg II k and h line profiles at flare ribbons. Zhu *et al.*[6] performed plane-parallel radiative hydrodynamics modeling for the formation of the Mg II k and h lines in flares, and reproduced their significantly broadened and single-peak profiles observed with IRIS for the first time

Coronal loops interconnecting two Active Regions (Ars), called Interconnecting Loops (Ils), are prominent large-scale structures in the solar atmosphere. They carry a significant amount of magnetic flux and therefore are considered to be an important element of the solar dynamo process. Earlier observations showed that eruptions of Ils are an important source of Coronal Mass Ejections (CMEs). It is generally believed that Ils are formed through magnetic reconnection in the high corona (>150″~200″), and several scenarios have been proposed to explain their brightening in Soft X-rays (SXRs). However, the detailed IL formation process has not been fully explored, and the associated energy release in the corona still remains unresolved. Du *et al.*[7] reported the complete formation process of a set of Ils connecting two nearby Ars, with successive observations by STEREO-A on the far side of the Sun and by Solar Dynamics Observatory (SDO) and Hinode on the Earth side. They concluded that Ils are formed by gradual reconnection high in the corona, in line with earlier postulations. In addition, they showed evidence that Ils brighten in SXRs and EUVs through heating at or close to the reconnection site in the corona (*i.e.*, through the direct heating process of reconnection), a process that has been largely overlooked in earlier studies of Ils.

Extreme-Ultraviolet (EUV) waves are spectacular horizontally propagating disturbances in the low solar corona. They always trigger horizontal Secondary Waves (SWs) when they encounter the ambient coronal structure. Zheng *et al.*[8] presented the first example of upward SWs in a streamer-like structure after the passing of a EUV wave. This event occurred on 1 June 2017. The EUV wave happened

during a typical solar eruption including a filament eruption, a CME, and a C6.6 flare. The EUV wave was associated with Quasi-periodic Fast Propagating (QFP) wave trains and a type II radio burst that represented the existence of a coronal shock. The EUV wave had a fast initial velocity of similar to 1000 km·s^{-1}, comparable to high speeds of the shock and the QFP wave trains. Intriguingly, upward SWs rose slowly (similar to 80 km·s^{-1}) in the streamer-like structure after the sweeping of the EUV wave. The upward SWs seemed to originate from limb brightenings that were caused by the EUV wave. All of the results show that the EUV wave is a fast-mode Magnetohydrodynamic (MHD) shock wave, likely triggered by the flare impulses. They suggested that part of the EUV wave was probably trapped in the closed magnetic fields of the streamer-like structure, and upward SWs possibly resulted from the release of slow-mode trapped waves. It was believed that the interplay of the strong compression of the coronal shock and the configuration of the streamer-like structure is crucial for the formation of upward SWs.

The morphologies of the wavefronts of EUV waves can shed light on their physical nature and driving mechanism, which are still strongly debated. In reality, the wavefronts always deform after interacting with ambient coronal structures during their propagation. Zheng *et al.*[9] studied the initial wavefront morphologies of four selected EUV waves that were closely associated with jets or flux-rope eruptions, using the high spatio-temporal resolution observations and different perspectives from SDO and STEREO. For the jet-driven waves, the jets originated from one end of the overlying closed loops, and the arc-shaped wavefront formed around the other, far end of the expanding loops. The extrapolated field lines of the Potential Field Source Surface model show the close relationships between the jets, the wavefronts, and the overlying closed loops. For the flux-rope-driven waves, the flux ropes (sigmoids) lifted off beneath the overlying loops, and the circular wavefronts had an intimate spatio-temporal relation with the expanding loops. All of the results suggest that the configuration of the overlying loops and their locations relative to the erupting cores are very important for the formation and morphology of the wavefronts, and two jet-driven waves and two flux-rope-driven waves were likely triggered by the sudden expansion of the overlying closed loops. They also proposed that the wavefront of EUV wave was possibly integrated by a chain of wave components triggered by a series of separated expanding loops.

Fast sausage modes in solar magnetic coronal loops are only fully contained in unrealistically short dense loops. Otherwise, they are leaky, losing energy to their surroundings as outgoing waves. This causes any oscillation to decay exponentially in time. Simultaneous observations of both period and decay rate therefore reveal the eigenfrequency of the observed mode, and potentially insight into the tubes' nonuniform internal structure. Cally and Xiong[10] presented a global spectral description of the oscillations in an implicit matrix eigenvalue equation where the eigenvalues were associated predominantly with the diagonal terms of the matrix. The off-diagonal terms vanish identically if the tube is uniform. A linearized perturbation approach, applied with respect to a uniform reference model, was developed that makes the eigenvalues explicit. The implicit eigenvalue problem was easily solved numerically though, and it was shown that knowledge of the real and imaginary parts of the eigenfrequency is sufficient to determine the width and density contrast of a boundary layer over which the tubes' enhanced internal densities drop to ambient values. Linearized density kernels were developed that show sensitivity only to the extreme outside of the loops for radial fundamental modes, especially for small density enhancements, with no sensitivity to the core. Higher radial harmonics did show some internal sensitivity, but these would be more difficult to observe. Only kink modes are sensitive to the tube centers. Variation in internal and external Alfvén speed along the loop was shown to have little effect on the fundamental dimensionless eigenfrequency, though the associated eigenfunction became more compact at the loop apex as stratification increases, or might even displace from the apex.

A new method to quantitatively and comprehensively diagnose shock waves responsible for heating and ionizing solar atmosphere is proposed. Shock wave is supposed to be one of the main energy sources of heating and ionizing the lower atmosphere of the sun. The longitudinal oscillation of the solar shock on the surface of the photosphere is the source of the shock wave. In order to understand the physical process of the lower atmosphere of the sun, it is necessary to conduct the comprehensive and quantitative diagnosis of shock wave. However, the remote sensing diagnosis of the shock wave in the partially ionized solar atmosphere is more difficult than the in-situ diagnosis of the shock wave in the interplanetary solar wind. Thanks to the IRIS space-based telescope, the spectroscopy + imaging observation of the low transition region of the sun provides necessary conditions for the comprehensive and quantitative diagnosis of shock waves. Ruan *et al.* [11] established a new method of shock analysis based on imaging spectroscopy (abbreviated as the shock-ABIS method). The steps of this method are as follows: (i) based on the imaging spectroscopic observation, five parameters of the upstream and downstream of the shock wave (the velocity in the line of sight direction, the radiation intensity of the upstream and downstream, and the propagation velocity in the sky plane projection) are given; (ii) these five parameters are used as known quantities to be substituted into the nonlinear equation with the propagation velocity in the line of sight direction as unknown quantities for the iterative solution; (iii) further use the propagation velocity in the direction of line of sight to calculate the density, temperature, velocity, Mach number and other residual parameters of the upstream and downstream. The remarkable features of this method are: (i) combining the imaging spectroscopic observation data with the RH jump to the greatest extent; (ii) considering the temperature response function of the spectroscopic observation; (iii) considering the heating ionization effect downstream of the shock wave; (iv) being able to provide a full set of parameters of quasi-parallel shock wave to realize the comprehensive and quantitative diagnosis. The validity of the diagnosis method is verified by forward simulation. The diagnosis results applied to the observation cases show that the temperature in the downstream of the shock wave in the low transition region is significantly higher than that in the upstream (more than 30000° higher), the compression ratio of the shock wave is generally less than 2, and the propagation speed of the shock wave is slightly higher than the local sound speed in the upstream.

2 Solar Wind and Turbulence

Magnetic holes are common features with a prominent dip of magnetic field strength in space plasma turbulence. As to their nature, there exists a dispute of explanations among discontinuities, magnetic reconnection, solitons, kinetic-scale electron vortexes, slow waves, and mirror-mode instability. As magnetic holes are often accompanied by thermal anisotropy, at MHD scales double-polytropic equations can serve as an appropriate description. The reason for the long-lasting dispute lies in the fact that both mirror-mode structures and oblique slow-mode waves are characterized by anti-correlation between plasma density (or temperature) and magnetic field strength, which, as often used in preceding works, is also the characteristic feature of magnetic holes. Therefore, to finally and unambiguously diagnose the nature of magnetic holes above ion scales, Zhang *et al.*[12] proposed to resort to other features, among which $v_{\parallel}$ and its phase relation with $|B|$ and n behave differently between mirror mode structures and slow-mode waves. Herewith they established a model with a superposition of both slow and mirror modes to reproduce the observed types of behaviors (n, $v_{\parallel}$, $|B|$, $T_{\parallel}$, $T_{\perp}$). This model inspires a new understanding of the nature of magnetic holes: the magnetic hole in reality is not solely contributed by only one mode, but a mixture of the two modes with an adjustable amplitude ratio.

The compressible component of solar wind turbulence displays a slow-mode feature. However, the

nature of the slow-mode fluctuations remains open. Based on numerical simulations of the driven compressible MHD turbulence with a uniform mean magnetic field, Yang *et al.*[13] used polarization of the MHD modes to decompose turbulent velocity and magnetic fields into Alfvén modes, slow modes, and fast modes. The numerical results with different cross-helicity, plasma beta (β), and Alfvén Mach number noted that fast modes are a marginal component among the three decomposed modes, and the compressible component of the MHD turbulence behaves mainly as the slow modes. Both of the decomposed slow modes and Alfvén modes exhibit a Kolmogorov-like power-law spectrum and evident anisotropy, with wave vectors mainly distributing around the directions perpendicular to the uniform mean field. For the first time, it was found that the propagating slow magnetosonic waves as well as the non-propagating slow-mode structures are combined to contribute to the compressible fluctuations, and the propagating Alfvén waves, as well as the non-propagating Alfvén-mode structures, coexist for the non-compressible fluctuations. However, there is unlikely a one-to-one match between the identified slow waves and Alfvén waves, or between the identified slow-mode structures and Alfvén-mode structures. These findings provide a new perspective on the understanding of the compressible and non-compressible fluctuations.

Time History of Events and Macroscale Interactions during Substorms (THEMIS) data are used to investigate the magnetic field structures in the vicinity of the magnetopause. Generally, the tendency that the farther away is from the Earth, the weaker the detected magnetic field is expected inside the dayside magnetopause. Song *et al.*[14] showed two cases which conflict with the expectation that the magnetic field gradient direction reverses from inward to outward in a short time interval. After further analysis, it was found that the THEMIS probes encountered a magnetopause indentation moving along the magnetopause towards the dawn in one case, and for the other case, they crossed an evolutive indented magnetopause that was produced locally and then recovered to its normal state. These two magnetopause indentations may be related with the fast magnetosheath flow. Accordingly, they supposed that the fast magnetic gradient direction reverse was caused by the abnormal magnetic field distribution adjacent to the deformed magnetopause.

Structures and propagating waves are often observed in solar wind turbulence. Their origins and features remain to be uncovered. Yang *et al.*[15] used 3D driven, compressible MHD turbulence simulations to investigate the global signatures of the driven fluctuations in the whole spatial and temporal domain. With four-dimensional spatial-temporal (x, y, z, t) Fourier transformations implemented, they identified two distinct main populations: waves, which satisfy the ω-k dispersion relations and were propagating; and structures, which satisfied the polarization relations but non-propagating ($\omega=0$). Whereas the overall turbulent energy spectrum was still consistent with $k^{-5/3}$, the contributions from waves and structures showed very different behavior in k space, with structures dominating at small k but waves became comparable to structures at large k. Overall, the fluctuations in the directions perpendicular to the large-scale mean field $\boldsymbol{B}_0$ were a manifestation of structures, while along the parallel direction, the fluctuations were dominated by waves. Also, a significant portion of the incompressible structures was the Alfvénic nature, and with imbalanced increased, the waves predominantly propagated in one direction and nearly perpendicular to $\boldsymbol{B}_0$. Differentiating the relative contributions from waves and structures could have important implications for understanding the non-linear cascade processes in the inertial range as well as particle-fluctuation interactions at small scales.

The power spectrum of magnetic fluctuations has a break at the high-frequency end of the inertial range. Beyond this break, the spectrum becomes steeper than the Kolmogorov law $f^{-5/3}$. The break frequency was found to be associated with plasma beta (β). However, the full-range β dependence of the ion-scale spectral break has not been presented before in observational studies. Wang *et al.*[16] showed

the continuous variation of the break frequency on full-range β in the solar wind turbulence. By using measurements from the WIND and Ulysses spacecraft, they showed the break frequency (f_b) normalized, respectively, by the frequencies corresponding to ion inertial length (f_{di}), ion gyroradius ($f_{\rho i}$), and cyclotron resonance scale (f_{ri}) as a function of β for 1306 intervals. Their β values spread from 0.005 to 20, which nearly cover the full β range of the observed solar wind turbulence. It was found that f_b/f_{di} ($f_b/f_{\rho i}$) generally decreases (increases) with β_γ while f_b/f_{ri} is nearly a constant. They performed a linear fit on the statistical result, and obtained the empirical formulas $f_b/f_{di} \approx \beta^{-1/4}$, $f_b/f_{\rho i} \approx \beta^{1/4}$, and $f_b/f_{ri} \approx 0.90$ to describe the relation between f_b and β. They also compared the observations with a numerical simulation and the prediction by ion cyclotron resonance theory. The result favors the idea that the cyclotron resonance is an important mechanism for energy dissipation at the spectral break. When $\beta \ll 1$ and $\beta \gg 1$, the break at f_{di} and $f_{\rho i}$ may also be associated with other processes.

The slow wind anisotropy has been observed as elongation along the magnetic field direction in the magnetic self-correlation contours calculated from data sets of two-day-long data and averaged for five years in 1998–2002, which is consistent with prediction by the critical balance cascade theory. More pronounced elongation at smaller scales than at larger scales has also been predicted by this theory. However, this prediction has not yet been checked by observations. Wang *et al.*[17] presented a check of the variation trend of the anisotropy with scales by presenting level contours of magnetic field and velocity self-correlations using intervals with durations varying from two days to one hour as observed by ACE during 1998–2002 in the slow wind. They found that the level contours elongate along the magnetic field direction at durations of two days and one day. But they become isotropic for shorter intervals from about 10 hours to 1 hour. They also found that in the fast wind, the variation of the anisotropy with the scale has the same trend as in the slow wind. The 2D isotropic feature of the solar wind fluctuations shown by these statistical results is not consistent with the existing theory and will open a new avenue for studying solar wind turbulence.

The Quiet Sun (QS) and helmet Streamer (STR) are generally considered to account for sources of slow solar wind with low Alfvénicity and low proton temperature. The solar wind with high Alfvénicity is often associated with Coronal Holes (CHs). Recently, the solar wind measured by ACE spacecraft at 1 AU was mapped back to its magnetic footpoints. Depending on the proximity of the solar wind footpoints to a given coronal or heliospheric structure, Wang *et al.*[18] classified solar winds into different types based on their sources: QS, STR, Active Region (AR), and CH. They compared the properties of the solar winds originated from QS, STR, AR, and CH using 2 h data. It was found that at solar maximum 34% of the quiet-Sun-associated slow wind (V_{sw}< 450 km·s^{-1}) has high Alfvénicity ($|\sigma_c| > 0.7$). This significantly higher proportion of Alfvénic fluctuations indicated that the quiet-Sun-associated wind at 1 AU has similar properties as fast wind, which originates from the CH. Accordingly, they speculate that this type of solar wind at 1 AU could come from open fields within the quiet-Sun region. This observational study will help us understand more about the coronal source regions of the solar wind in interplanetary space.

On the mechanism of the isotropy of the turbulent power spectral break position: the isotropy of the turbulent diffusion effect. The break point of the solar wind turbulence power spectra has an important physical meaning: it is the transition from the energy cascade region at the MHD scales to the kinetic scales. There is a great controversy about the physical process related with the scale of break point: is it the dissipation of the ion cyclotron wave or the dispersion of the kinetic Alfven wave. If one of them is dominant, then the break point frequency should have anisotropic characteristics. Duan *et al.*[19] developed a set of methods to fit the double power-law spectra and identify the location of spectral break points. It was found that the frequency of break points did not change with the angle, suggesting the

isotropic characteristics. Why is the break point frequency isotropic? Therefore, they studied the relationship between three effects with their initials being "d" (diffusion, dissipation, and dispersion), and found that diffusion effect (a combination of both dissipation effect and dispersion effect) can better characterize the physics. It was found that the indicator for diffusion effect is quasi-isotropic in the wave vector space, which provides a physical explanation for the isotropic observation results of spectral break points.

The formula of energy conversion rate spectrum in wave number space was put forward, and it was applied to the dissipation diagnosis of plasma turbulence in space by He *et al.*[20]. The profile of the dissipation rate spectrum of ion cyclotron wave is observed for the first time, and the parallel and vertical dissipation rate spectra are compared. It is found that the vertical dissipation rate spectrum dominates, indicating that the turbulent energy dissipation is mainly used to heat plasma vertically. They theoretically gave two equivalent forms of the distribution of dissipation rate spectrum in the wavenumber space, and expounds that one of them is relatively intuitive but cannot be applied to the actual observation, while the other seems to be relatively indirect but can be applied to the actual observation. With regard to in which reference system turbulent electric field should be used to calculate the dissipation rate spectrum. They pointed out through demonstration that the electric field under the average flow reference frame rather than the local flow reference frame should be used, otherwise the dissipation rate spectrum will be obviously underestimated. The dissipation of ion cyclotron wave is supposed to be one of the main mechanisms of turbulence dissipation of solar wind, but there is no direct evidence. Through the proposed method, people can directly determine whether the turbulence including the ion cyclotron wave is dissipating rather than growing, and gives the dissipation rate spectrum of the turbulence. The results show that the dissipation rate spectrum of turbulence has the following characteristics: (i) at the MHD scales in the cascade inertial range, the dissipation rate spectrum is maintained near 0; (ii) at the ion and sub-ion scales in the kinetic range, the dissipation rate spectrum begins to rise to positive and has obvious protrusion; (iii) after the frequency integration, the dissipation rate spectrum is 0.5×10^{6} J·kg^{-1}·s^{-1}.

A model has been established by He *et al.*[21] to describe the intermittent characteristics of the inertial and dissipative ranges of solar wind turbulence quantitatively. The reason and explanation are found for the multifractals of the inertial range and the mono-fractals of the dissipative range. They extended the function of the application of casting probability distribution function. Based on two parameters of Casting probability distribution (μ and λ^2: the most probable values and variances of logarithmic form of turbulent local standard deviation, respectively), the mathematical formulas describing multi-order structure functions, flatness and scaling law index were derived for the first time. They found that using the mathematical formula of casting function and multi-order structure function to perform joint fitting, compared with simply using the probability distribution as the object to fit, can better determine the change of μ and λ^2 with the scale (τ). It was found that only λ^2 controls the scale change trend of Flatness: λ^2 is saturated or even slightly decreased with the decrease of the scale, which leads to the flatness approaching saturation or even not rising or falling in the sub ion scale. More importantly, they revealed the formation reasons of multifractal in inertia range and mono-fractal in dissipation range: $\mathrm{d}\mu/\mathrm{d}(\ln\tau)$ and $\mathrm{d}\lambda^2/\mathrm{d}(\ln\tau)$ are the coefficients of linear term and second-order term of scaling law index with scale change, the existence of multifractal is due to $|\mathrm{d}\mu/\mathrm{d}(\ln\tau)|\sim|\mathrm{d}\lambda^2/\mathrm{d}(\ln\tau)|$, while the appearance of a single fractal is due to $|\mathrm{d}\mu/\mathrm{d}(\ln\tau)|)|\mathrm{d}\lambda^2/\mathrm{d}(\ln\tau)|$. In addition, they also found that the kinks of μ and λ^2 appear at different scales: the kink of μ and the kink of power spectrum appear at a smaller scale, while the kink of λ^2 and the kink of flatness appear at a larger scale.

For the turbulence at the kinetic scales (from the ion scale to the sub-electron scale), a wide-band

wave mode decomposition method has been proposed by Zhu *et al.*[22]. It was found that the wave modes from the ion scale to the sub-electron scale are multiple: the kinetic Alfvén wave, the quasi-parallel propagating whistler wave, and the ion acoustic wave. They used the data of MMS satellite with high precision and high time resolution to study the wave mode properties of these turbulences from the ion scale (about 1 Hz) to the sub electron scale (about 1000 Hz), and showed the new observation results. Based on the theory of two fluids, the energy ratio of different types of wave modes and their changes with scales are analyzed quantitatively for the first time. They found that the Kinetic Alfvén Wave (KAW) is dominant at 1~30 Hz. Whistler Wave (WW) causes the magnetic field power spectrum to rise above 30 Hz, while Ion Acoustic Wave (IAW) causes the electric field power spectrum to rise above 30 Hz. Furthermore, the quantitative analysis of the three-wave mode energy ratios shows that: (i) the vertical magnetic field disturbance is mainly contributed by KAW at <30 Hz and WW at >30 Hz; (ii) the parallel magnetic field disturbance and the vertical electric field disturbance are mainly contributed by KAW in the whole frequency range; (iii) the parallel electric field disturbance is mainly contributed by IAW in the whole frequency range.

3 Filament/Prominence, Jets, Flares and Radio Bursts

Awasthi *et al.*[23] studied the source region of a complex ejecta, focusing on a flare precursor with definitive signatures of magnetic reconnection, *i.e.*, non-thermal electrons, flaring plasma, and bidirectional outflowing blobs. Aided by nonlinear force-free field modeling, they concluded that the reconnection occurs within a system of multiple braided flux ropes with different degrees of coherency. This study signifies the importance of internal structure and dynamics in understanding CMEs and in predicting their impacts on Earth. Su *et al.*[24] studied flares occurring in an Arch Filament System (AFS) consisting of multiple bundles of dark filament threads enclosed by semicircular flare ribbons. They constructed coronal magnetic field models using two independent methods, *i.e.*, the nonlinear force-free field extrapolation and the flux rope insertion method, and concluded that these circular shaped flares were caused by 3D magnetic reconnection at the Quasi-Separatrix Layers (QSLs) associated with the AFS possessing mixed signs of helicity.

It is often envisaged that dense filament material lies in the dips of magnetic field lines belonging to either a sheared arcade or a magnetic flux rope. But it is also debated which configuration correctly depicts filaments' magnetic structure, due to the incapacity to measure the coronal magnetic field. Awasthi *et al.*[25] addressed this issue by employing mass motions in an active-region filament to diagnose its magnetic structure, using $H\alpha$ line-center and line wing (±0.4 Å) images obtained by the 1 m New Vacuum Solar Telescope (NVST). Filament material predominately exhibits two kinds of motions, namely, rotation about the spine and longitudinal oscillation along the spine, which indicates a double-decker host structure with mixed signs of helicity, comprising a flux rope atop a sheared-arcade system. Prominence bubbles are cavities rising into quiescent prominences from below. Not only the origin of prominence bubbles is poorly understood, but most of their physical characteristics are still largely unknown. Awasthi and Liu[26] investigated the dynamical properties of a prominence bubble, which was observed since its early emergence beneath the spine of a quiescent prominence in the $H\alpha$ line-center and line-wing (±0.4 Å) by NVST. Combining Doppler maps with flow maps in the plane of sky derived from a Nonlinear Affine Velocity Estimator, they obtained a comprehensive picture of mass motions revealing a counter-clockwise rotation inside the bubble; with blue shifted material flowing upward and red-shifted material flowing downward. This sequence of mass motions was interpreted to be either outlining a kinked flux rope configuration of the prominence bubble or providing observational evidence of the internal kink instability in the prominence plasma.

Wang *et al.*[27] analyzed high-resolution observations from the 1.6 m telescope at Big Bear Solar Observatory that cover an active region filament. Counter-streaming motions in the filament extend to a light bridge, forming a spectacular circulation pattern around a sunspot. They analyzed the power of oscillations with the image sequences of constructed Dopplergrams, and found that the counter-streaming motion in the filament was due to physical mass motion along fibrils, while in the light bridge due to oscillation along the line-of-sight. The disintegration of solar filaments via mass drainage is a frequently observed phenomenon during a variety of filament activities. It is generally considered that the draining of dense filament material is directed by both gravity and magnetic field, yet the detailed process remains elusive. Liu *et al.*[28] reported on a partial filament eruption during which filament material drained downward to the surface not only along the filament's legs, but to a remote flare ribbon through a fan-out curtain-like structure. It is the interaction of the filament with the overlying QSLs that led to the splitting and disintegration of the filament.

Plasma motions within flaring regions provide key information to understanding flare processes. Cheng *et al.*[29] constructed EVE plasma dynamic spectrum charts, a 2D map of Doppler shift against temperature and time and identified three kinds of plasma motions: chromospheric evaporation (100~200 km·s^{-1}) above 1 MK, cooling inside post-flare loops (approximately 150 km·s^{-1}) between 0.3 and 1 MK, and condensation at footpoints ($<$30 km·s^{-1}) below 0.3 MK. The chromospheric evaporation and condensation at footpoints started in the impulsive phase almost simultaneously, while the cooling occurred later in the gradual phase, with a time delay of more than 10 min. The reversal temperature between blue/redshifts is close to 1 MK, implying that the boundary of upflowing/downflowing plasma is located at the lower corona or the upper transition region.

The second peak in extreme ultraviolet sometimes appears during the gradual phase of solar flares, which is known as EUV Late Phase (ELP). Stereo-typically ELP is associated with two separated sets of flaring loops with distinct sizes, and it has been debated whether ELP is caused by additional heating or extended plasma cooling in the longer loop system. Chen *et al.*[30] carried out a survey of 55 M-and-above GOES-class flares with ELP during 2010–2014, which are categorized as circular-ribbon (19 events), two-ribbon (23 events), and complex-ribbon (13 events) flares, and found that additional heating is more likely present during ELP in two-ribbon than in circular-ribbon flares, but that cooling may be the dominant factor causing the delay of the ELP peak relative to the main-phase peak, because the loop system responsible for the ELP emission is generally larger than, and well separated from, that responsible for the main-phase emission. They suggested a composite "dome-plate" QSL as a general and robust structure characterizing circular-ribbon flares rather than a magnetic null point.

Small-scale solar wind transients looking like "blobs" or "ripples" are very common in the solar wind. They mostly appear to emerge from coronal streamers as clear density enhancements but eventually diffuse to become part of the slow solar wind. Li *et al.*[31] developed a new method to identify and locate the transients automatically from simultaneous images from the two inner telescopes, known as HI-1, based on a correlation analysis. Correlation Coefficient (CC) maps along the Sun-Earth line were constructed for the period from 1 January 2010 to 28 February 2011. From the maps, transients propagating along the Sun-Earth line were identified, and a 27-day periodic pattern was revealed, especially for small-scale transients. Besides, it was suggested by the cc map that small-scale transients along the Sun-Earth line are more frequent than large-scale transients by a factor of at least 2, and that they quickly diffused into background solar wind within about 40 R_s in terms of the signal-to-noise ratio of white-light emissions. The method provides a new tool to reconstruct inhomogeneous structures in the heliosphere from multiple perspectives.

Quiescent solar prominences are generally considered to have a stable large-scale structure. How-

ever, they consist of multiple small-scale structures that are often significantly dynamic. To understand the nature of prominence plasma dynamics, Ruan *et al.*[32] used the high spatial, temporal, and spectral resolution observations obtained by Interface Region Imaging Spectrograph (IRIS) during a coordinated campaign with the Multichannel Subtractive Double Pass spectrograph at the Meudon Solar Tower. Detailed analysis of the IRIS observations of Mg II lines, including the analysis of Doppler shift and line width obtained with two different methods (quantile method and Gaussian-fit method) were discussed in the frame of the dynamic nature of the structures. Large-scale coherent blue shift and redshift features were observed in Mg II lines and $H\alpha$ exhibiting a slow evolution during 100 min of observations. They explained the presence of several significantly asymmetric peaks in the observed Mg II line profiles by the presence of several prominence fine structures moving with different velocities located along the Line of Sight (LOS). In such a case, the decrease of the intensity of individual components of the observed spectra with the distance from the central wavelength can be explained by the Doppler dimming effect. They showed that C II line profiles may be used to confirm the existence of multi-components along the LOS.

Ruan *et al.*[33] also derived the physical conditions of the prominence observed on 30 March 2017. They used a unique set of data in Mg II lines obtained with the space-borne IRIS and in $H\alpha$ line with the ground-based Multi-Channel Subtractive Double Pass spectrograph operating at the Meudon solar tower. They analyzed the prominence spectra of Mg II h and k lines, and the $H\alpha$ line in the part of the prominence which is visible in both sets of lines. They computed a grid of 1D NLTE (*i.e.*, departures from the local thermo-dynamical equilibrium) models providing synthetic spectra of Mg II k and h, and $H\alpha$ lines in a large space of model input parameters (temperature, density, pressure, and micro-turbulent velocity). They compared Mg II and $H\alpha$ line profiles observed in 75 positions of the prominence with the synthetic profiles from the grid of models. With these models, they could compute the relationships between the integrated intensities and between the optical thickness in $H\alpha$ and Mg II k lines. The optical thickness $t_{H\alpha}$ is between 0.05 and 2, and $t_{\mathrm{MgII}k}$ is between 3 and 200. They showed that the relationship of the observed integrated intensities agrees well with the synthetic integrated intensities for models with a higher micro-turbulence (16 $\mathrm{km\cdot s^{-1}}$) and T around 8000 K, n_e=1.5×10^{10} $\mathrm{cm^{-3}}$, p=0.05 dyne. In this case, large micro-turbulence values could be a way to take into account the large mixed velocities existing in the observed prominence.

The magnetic orientation of CMEs near the Earth's magnetosphere is one major parameter that influences the geoeffectiveness of CMEs. The orientation often varies during the eruption and propagation from the Sun to the Earth due to the deflection and/or rotation of CMEs. It is common to observe the Counterclockwise (CCW) or Clockwise (CW) rotation (viewed from above) of solar prominences in the corona, which can be used to predict the space weather effect of associated CMEs. Song *et al.*[34] reported an intriguing failed prominence eruption that occurred on 10 December 2010, exhibiting the CCW and CW rotations sequentially in the corona. The eruption was recorded by both SDO/AIA and the Extreme Ultraviolet Imager on board STEREO. This stereoscopic combination makes it possible to reconstruct the three-dimensional structure and identify the rotation reversal without ambiguity. The prominence first rotates CCW about its ascending direction by 135° in 26 min and then reverses to the CW rotation by 45° in 15 min; *i.e.*, the average CCW and CW rotation speeds are 5.2 and 3.0(°)·$\mathrm{min^{-1}}$, respectively. The possible mechanisms leading to the rotation and reversal were discussed. The kinematics of the prominence was also analyzed, which indicates that an upward force acts on the prominence during the entire process.

Filament eruptions, one of the most energetic explosions on the Sun, release large quantities of magnetized plasma into the interplanetary space. Hence, the understanding of the initiation and evolution of filament eruptions can provide broader im-

plications for space weather and geospace climate. Zheng *et al.*[35] presented a confined partial eruption of a double-decker structure that consisted of two vertically separated filaments on 16 April 2016. Only the upper filament erupted, and the eruption was closely associated with an episode of flux cancellation, surrounding transient brightenings, and unambiguous tether-cutting reconnections of the overlying sheared loops. However, the lower filament was nearly intact through the eruption. Interestingly, the erupting material moved along large-scale external loops and eventually arrived at remote sites, indicating a confined partial eruption. All the results show that the partial eruption involved two magnetic reconnections at least, and the bottom magnetic cancellation and internal tether-cutting reconnections between filaments both play critical roles in triggering the eruption. They conjectured that the newly formed low-lying loops due to tether-cutting reconnections and the flare loops resulting from the partial eruption likely contributed to maintaining the equilibrium of the lower filament. It was also suggested that the restriction of some large-scale external magnetic structures was crucial to turn the successful partial eruption into a confined event.

Coronal jets are always produced by magnetic reconnection between emerging flux and pre-existing overlying magnetic fields. When the overlying field is vertical/oblique or horizontal, the coronal jet will appear as anemone type or two-sided-loop type. Most observational jets are of the anemone type, and only a few two-sided-loop jets have been reported. Using the high-quality data from New Vacuum Solar Telescope, Interface Region Imaging Spectrograph, and Solar Dynamics Observatory, Zheng *et al.*[36] presented an example of two-sided-loop jets simultaneously observed in the chromosphere, transition region, and corona. The continuous emergence of magnetic flux brought in successively, the emergence of coronal loops and the slow rise of overlying horizontal filament threads. The following occurred sequentially: the deformation of the loops, the plasmoid ejection from the loop top, and pairs of loop brightenings and jets moving along the untwisting filament threads. All of the observational results indicate that magnetic reconnection exists between the emerging loops and the overlying horizontal filament threads, and it was the first example of two-sided-loop jets associated with ejected plasmoids and twisted overlying fields.

Ruan *et al.*[37] reported on bidirectional coronal reconnection outflows reaching ±200 km·s^{-1} as observed in an active region with the Si IV and C II spectra of IRIS. The evolution of the active region with an emerging flux, a failed filament eruption, and a jet is followed in SDO/AIA filters from 304 to 94 Å, IRIS slit jaw images, and SDO/HMI movies. The bidirectional outflow reconnection is located at a bright point visible in multi-wavelength AIA filters above an arch filament system. This suggests that the reconnection occurs between rising loops above the emergence of magnetic bipoles and the longer, twisted magnetic field lines remnant of the failed filament eruption one hour before. The reconnection occurs continuously in the corona between quasi-parallel magnetic field lines, which is possible in a 3D configuration. The reconnection also triggers a jet with transverse velocities around 60 km·s^{-1}. Blueshifts and redshifts along its axis confirm the existence of a twist along the jet, which could have been transferred from the filament flux rope. The jet finally blows up the material of the filament before coming back during the second phase. In the $H\alpha$ Dopplergrams provided by the MSDP spectrograph, they saw more redshift than blueshift, indicating the return of the jet and filament plasma.

A complete understanding of the onset and subsequent evolution of confined flares has not been achieved. Earlier studies mainly analyzed disk events so as to reveal their magnetic topology and cause of confinement. Ning *et al.*[38] presented dynamic details of a confined flare observed on the northwestern limb of the solar disk on 24 July 2016, taking advantage of a tandem of instruments working at different wavelengths of X-rays, EUVs, and microwaves. The entire dynamic evolutionary process starting from its onset is consistent with a loop-loop interaction scenario. The X-ray profiles manifest an intriguing double-

peak feature. From spectral fitting, it was found that the first peak is non-thermally dominated while the second peak is mostly multi-thermal with a hot (about 10 MK) and a super-hot (about 30 MK) component. This double-peak feature is unique in that the two peaks are clearly separated by 4 minutes, and the second peak reaches up to 25~50 keV; in addition, at energy bands above 3 keV the X-ray fluxes decline significantly between the two peaks. This, together with other available imaging and spectral data, manifest a two-stage energy release process. They carried out a comprehensive analysis to investigate the nature of this two-stage process, and conclude that the second stage with the hot and super-hot sources mainly involves direct heating through loop-loop reconnection at a relatively high altitude in the corona. The uniqueness of the event characteristics and complete data set make the study a nice addition to present literature on solar flares.

In solar flares, Hard X-Rays (HXRs) appear in the form of either footpoint sources or coronal sources. Each individual source provides its own critical information on the acceleration of non-thermal electrons and plasma heating. Earlier studies found that the HXR emission in some events manifests a broken-up power-law spectrum, with the break energy around a few hundred keV based on spatially-integrated spectral analysis, and it does not distinguish the contributions from individual sources. Ning *et al.*[39] reported the observation of the broken-up spectra of a coronal source studied using HXR data recorded by Reuven Ramaty High Energy Solar Spectroscopic Imager (RHESSI) during the GOES X8.2-class flare on 10 September 2017. The flare occurred behind the western limb and its footpoint sources were mostly occulted by the disk. They could clearly identify such broken-up spectra pertaining solely to the coronal source during the flare peak time and after. Since a significant pileup effect on the RHESSI spectra is expected for this intense solar flare, they have selected the pileup correction factor, p=2. In this case, they found the resulting RHESSI temperature (about 30 MK) to be similar to the GOES soft X-ray temperature and break energies of 45~60 keV. Above the break energy, the spectrum hardens with time from the spectral index of 3.4 to 2.7, and the difference in spectral indices below and above the break energy increases from 1.5 to 5 with time. However, they note that when p=2 is assumed, a single power-law fitting is also possible with the RHESSI temperature higher than the GOES temperature by about 10 MK. Possible scenarios for the broken-up spectra of the loop-top HXR source are briefly discussed.

Non-thermal loop-top sources in solar flares are the most prominent observational signature that suggests energy release and particle acceleration in the solar corona. Although several scenarios for particle acceleration have been proposed, the origin of the loop-top sources remains unclear. Kong *et al.*[40] presented a model that combines a large-scale MHD simulation of a two-ribbon flare with a particle acceleration and transport model for investigating electron acceleration by a fast-mode termination shock at the loop top. Their model provides spatially resolved electron distribution that evolves in response to the dynamic flare geometry. They found a concave-downward magnetic structure located below the flare termination shock, induced by the fast reconnection downflows. It acts as a magnetic trap to confine the electrons at the loop top for an extended period of time. The electrons are energized significantly as they cross the shock front, and eventually build up a power-law energy spectrum extending to hundreds of keV. They suggested that this particle acceleration and transport scenario driven by a flare termination shock is a viable interpretation for the observed non-thermal loop-top sources.

Solar radio spikes are narrowband, short duration radio bursts. Feng *et al.*[41] presented the latest observations from the newly built solar radio spectrograph at the Chashan Solar Observatory. On 18 July 2016, the spectrograph records a solar spike burst event, which has several episodes showing harmonic structures, with the second, third, and fourth harmonics. The lower harmonic radio spike emissions are observed later than the higher harmonic bands, and the temporal delay of the second

(third) harmonic relative to the fourth harmonic is about 30~40 (10) ms. Based on the electron cyclotron maser emission mechanism, they analyzed possible causes of the temporal delay and further infer relevant coronal parameters, such as the magnetic field strength and the electron density at the radio source.

Solar radio spikes are excited by the energetic electrons accelerated during small scale magnetic reconnections. Spikes play an important role in diagnosing magnetic reconnections and studying electron accelerations. Feng[42] reported the solar radio spikes observed by the Chashan Solar Observatory (CSO) spectrograph combined with observations from SDO, to study the properties of spikes with harmonics. The CSO data show that the central frequency ratio of the third to the second harmonic is 1.35±0.01 and the third harmonic has a larger absolute and relative bandwidth, but a shorter duration than the second one. By studying the correlation between light curves of the solar radio spike and those of bright points at different EUV passbands, the best associated EUV bright point and passbands were determined. The spike source properties were discussed based on the extrapolated magnetic field around the associated EUV bright point.

Source imaging of solar radio bursts can be used to track energetic electrons and associated magnetic structures. Vasanth *et al.*[43] presented a combined analysis of data at different wavelengths for an eruption associated with a moving Type IV (T-IVm) radio burst. In the inner corona, the sources are correlated with a hot and twisted eruptive EUV structure, while in the outer corona, the sources are associated with the top front of the bright core of a white-light CME. This reveals the potential of using T-IVm imaging data to continuously track the CME by lighting up the specific component containing radio-emitting electrons. It was found that the T-IVm burst presents a clear spatial dispersion with observing frequencies. The burst manifests broken power law-like spectra in brightness temperature, which is as high as 10^7~10^9 K, while the polarization level is generally weak. In addition, the T-IVm burst starts during the declining phase of the flare with a duration as long as 2.5 h. From the differential emission measure analysis of AIA data, the density of the T-IVm source is found to be at the level of 10^8 cm^{-3} at the start of the burst, and the temperature may reach up to several MK. These observations do not favor gyro-synchrotron to be the radiation mechanism but are in line with a coherent plasma emission excited by energetic electrons trapped within the source. Further studies are demanded to elucidate the emission mechanism and explore the full diagnostic potential of T-IVm bursts.

Liu *et al.*[44] reported a stationary Type IV (IVs) radio burst observed on 24 September 2011. Observations from the Nançay Radio Heliograph (NRH) show that the Brightness Temperature (TB) of this burst is extremely high, over 10^{11} K at 150 MHz and over 10^8 K in general. The degree of circular polarization (q) is between –60%~–100%, which means that it is highly left-handed circularly polarized. The flux-frequency spectrum follows a power-law distribution, and the spectral index is considered to be roughly –3 ~ –4 throughout the IVs. Radio sources of this event are located in the wake of the CMEs and are spatially dispersed. They line up to present a formation in which lower-frequency sources are higher. Based on these observations, it was suggested that the IVs were generated through electron cyclotron maser emission.

For the first time, Koval *et al.*[45] presented simulation results of the focusing effect of the ionospheric plasma density irregularities, namely, Medium-Scale Traveling Ionospheric Disturbances (MSTIDs), on solar radio emission by applying a ray tracing method to the Earth's ionosphere with MSTIDs. With this technique, they investigated the focusing effect that manifests itself in the form of peculiar spectral disturbances in intensity with specific morphology, so-called Spectral Caustics (SCs), occasionally appearing in dynamic spectra of different solar radio instruments operating in the meter-decameter wavelength range. They showed that the simulated spectral shapes of SCs are in good agreement with the ones detected in real solar radio spectrograms. In particular, SCs that are classified as inverted V-like,

V-like, X-like, and fiber-like types have been reproduced. It was also found that the seasonal dependence in the occurrence of SCs, which has been discovered recently, can be understood through a strong relationship between the focusing frequency, the most important characteristic point in most SC patterns, and the elevation angle of the Sun. They found that under typical parameters of MSTIDs with spatial and temporal periods set to be 300 km and 40 min, respectively, the focusing frequency decreases with the growth of the elevation angle. Physical interpretations of the results and implications on the analysis of solar radio data with SCs are discussed.

Koval *et al.*[46] also presented the first direct observations of SCs induced by MSTIDs, using solar dynamic spectra with SCs obtained by different European radio telescopes on 8 January 2014 and simultaneous two-dimensional detrended Total Electron Content (dTEC) maps over Europe. Spatial examination of dTEC maps as well as precise timing analysis of the maps and the dynamic spectra have been performed. Firstly, they found several pairs of one-to-one (TID-SC) correspondences. The study provides strong observational evidence supporting the suggestion that MSTIDs are the cause of SCs.

It has been suggested that the Z-mode instability driven by energetic electrons with a loss-cone type velocity distribution is one candidate process behind the continuum and zebra pattern of solar type-IV radio bursts. Both the temperature of background plasma (T_0) and the energy of energetic electrons (v_e) is considered to be important to the variation of the maximum growth rate (γ_{max}). Li *et al.*[47] presented a detailed parameter study on the effect of T_0 and v_e, within a regime of the frequency ratio ($10 \leqslant \omega_{pe}/\Omega_{ce} \leqslant 30$). In addition to γ_{max}, they also analyzed the effect on the corresponding wave frequency (ω^r_{max}) and propagation angle (θ_{max}). They found that: (i) γ_{max} generally decreases with increasing v_e, while its variation with T_0 is more complex depending on the exact value of v_e; (ii) with increasing T_0 and v_e, ω^r_{max} presents stepwise profiles with jumps separated by gradual or very weak variations, and due to the warm plasma effect on the wave dispersion relation ω^r_{max} can vary within the hybrid band (the harmonic band containing the upper hybrid frequency) and the higher band; (iii) the propagation is either perpendicular or quasi-perpendicular, and θ_{max} presents variations in line with those of ω^r_{max}, as constrained by the resonance condition. They also examined the profiles of γ_{max} with ω_{pe}/Ω_{ce} for different combinations of T_0 and v_e to clarify some earlier calculations which show inconsistent results.

The latest observational reports of solar flares reveal some uncommon features of microwave spectra, such as unusually hard (or even positive) spectra and/or a super-high peak frequency. For a better understanding of these features, Wu *et al.*[48] conducted a parameter study to investigate the effect of broken-power-law spectra of energetic electrons on microwave emission on the basis of the gyro-synchrotron mechanism. The electron broken-power-law energy distribution is characterized by three parameters–the break energy (E_B) and the power-law indices below (d_1) and above (d_2) the break energy. They found that with the addition of the d_2 component of the electron spectra, the total flux density can increase by several times in the optically thick regime, and by orders of magnitude in the optically thin regime; the peak frequency (v_p) also increases and can reach up to tens of gigahertz; and the degree of polarization (r_c) decreases in general. They also found that (i) the variation of the flux density is much larger in the optically thin regime, and the microwave spectra around the peak frequency manifest various profiles with a softening or soft-hard pattern; (ii) the parameters d_1 and E_B affect the microwave spectral index (α) and the degree of polarization (r_c) mainly in the optically thick regime, while d_2 mainly affects the optically thin regime. The results are helpful in understanding the recently reported microwave bursts with unusual spectral features and indicate the demands for a more complete spectral coverage of microwave bursts, especially in the high-frequency regime, say >10~20 GHz.

Quasi-periodic oscillations are usually detected as spatial displacements of coronal loops in imaging

observations or aperiodic shifts of line properties (*i.e.*, Doppler velocity, line width, and intensity) in spectroscopic observations. They are often applied for remote diagnostics of magnetic fields and plasma properties on the Sun. Li *et al.*[49] combined the imaging and spectroscopic measurements of available space missions, and investigated the properties of non-damping oscillations at flaring loops. They used the Interface Region Imaging Spectrograph (IRIS) to measure the spectrum over a narrow slit. The double-component Gaussian fitting method was used to extract the line profile of Fe XXI1354.08Å at the O I spectral window. The quasi-periodicity of loop oscillations was identified in the Fourier and wavelet spectra. A periodicity at about 40 s is detected in the line properties of Fe XXI 1354.08 Å, hard X-ray emissions in GOES 1~8 Å derivative, and Fermi 26~50 keV. The Doppler velocity and line width oscillate in phase, while a phase shift of about $\pi/2$ is detected between the Doppler velocity and peak intensity. The amplitudes of Doppler velocity and line width oscillation are about 2.2 km·s^{-1} and 1.9 km·s^{-1}, respectively, while peak intensity oscillates with amplitude at about 3.6% of the background emission. Meanwhile, a quasi-period of about 155 s is identified in the Doppler velocity and peak intensity of the Fe XXI 1354.08 Å line emission, and AIA 131 Å intensity. The oscillations at about 40 s are not damped significantly during the observation; this might be linked to the global kink modes of flaring loops. The periodicity at about 155 s is most likely a signature of recurring downflows after chromospheric evaporation along with flaring loops. The magnetic field strengths of the flaring loops are estimated to be about 120~170 Gs using the MHD seismology diagnostics, which are consistent with the magnetic field modeling results using the flux rope insertion method.

Quasi-Periodic Pulsations (QPPs) are usually found in the light curves of solar and stellar flares; they carry the features of time characteristics and plasma emission of the flaring core, and could be used to diagnose the coronas of the Sun and remote stars. Yuan *et al.*[50] combined SDO/AIA and the Nobeyama Radio-heliograph (NoRH) to observe an M7.7 class flare that occurred at active region 11520 on 19 July 2012. A QPP was detected both in the AIA 131 Å bandpass and the NoRH 17 GHz channel; it had a period of about four minutes. In the spatial distribution of Fourier power, they found that this QPP originated from a compact source and that it overlapped with the X-ray source above the loop top. The plasma emission intensities in the AIA 131 Å bandpass were highly correlated within this region. The source region is further segmented into stripes that oscillated with distinctive phases. Evidence in this event suggests that this QPP was likely to be generated by intermittent energy injection into the reconnection region.

CMEs play a decisive role in driving space weather, especially the fast ones (*e.g.*, with speeds above 800 km·s^{-1}). Understanding the trigger mechanisms of fast CMEs can help us gain important information in forecasting them. The filament eruptions accompanied with CMEs provide a good tracer in studying the early evolution of CMEs. Zou *et al.*[51] surveyed 66 filament-accompanied fast CMEs to analyze the correlation between the trigger mechanisms, namely either magnetic reconnection or ideal MHD process, associated flares, and CME speeds. Based on the data gathered from SDO, GONG, and STEREO, they found that: (i) Active Region (AR) filament and intermediate filament (IF) eruptions show a higher probability for producing fast CMEs than quiet Sun (QS) filaments, while the probability of Polar Crown (PC) filament eruptions is zero in their statistic; (ii) AR filament eruptions that produce fast CMEs are more likely to be triggered by magnetic reconnection, while QS filaments and IFs are more likely to be triggered by an ideal MHD process; (iii) for AR filaments and IFs, it seems that the specific trigger mechanism does not have a significant influence on the resulting CME speeds, while for the QS filaments, the ideal MHD mechanism can more likely generate a faster CME; (iv) comparing with previous statistical studies, the onset heights of filament eruptions and the decay indexes of the overlying field show some differences: for AR filaments

and IFs, the decay indexes are larger and much closer to the theoretical threshold, while for QS filaments, the onset heights are higher than those obtained in previous results.

Two X-class solar flares occurred on 6 September 2017 from active region NOAA 12673: the first one is a confined X2.2 flare, and it is followed only 3 h later by the second one, which is the strongest flare in solar cycle 24, reaching X9.3 class and accompanied by a CME. Why did these two X-class flares occur in the same position with similar magnetic configurations, but one is eruptive while the other is not. Zou *et al.*[52] tracked the coronal magnetic field evolution via nonlinear force-free field extrapolations from a time sequence of vector magnetograms with a high cadence. A detailed analysis of the magnetic field shows that a Magnetic Flux Rope (MFR) forms and grows gradually before the first flare, and shortly afterward, the MFR's growth is significantly enhanced with a much faster rise in height, from far below the threshold of torus instability to above it, while the magnetic twist only increases mildly. Combining EUV observations and the magnetic field extrapolation, they found that overlying the MFR is a null-point magnetic topology, where recurrent brightening is seen after the first flare. They thus suggested a scenario to interpret the occurrence of the two flares. The first flare occurred since the MFR reached a high enough height to activate the null point, and its continuous expansion forces the null-point reconnection recurrently. Such reconnection weakens the overlying field, allowing the MFR to rise faster, which eventually crosses the threshold of torus instability and triggers the second, eruptive flare.

Using SDO/AIA, Samanta *et al.*[53] reported a wavelike or oscillating plasma flow propagating upward against the Sun's gravitational force. After carefully analyzing this event, they concluded that this phenomenon is likely a manifestation of vortex shedding in the supra-arcade region of a solar flare. The computed Strouhal number is also consistent with the prediction from previous simulations of vortex shedding in MHD environments. Song and Tian[54] performed the first statistical study of circular-ribbon flares. They used SDO/HMI observations from 2010 to 2017 and identified 90 circular-ribbon flares. Interestingly, they found that about 1/3 of these flares are white-light flares, which is much higher than previous thought. Compared to normal flares, these white-light flares tend to have a shorter duration, smaller size, stronger electric current, and more complicated magnetic field, suggesting that the timescale, spatial scale, and magnetic field complexity may play important roles in the generation of white-light emission.

4 Active Regions and Solar Eruptions

Ye *et al.*[55] presented a combined analysis of the applications of the weighted horizontal magnetic gradient (denoted as G_M) method and the magnetic helicity tool employed for three Active Regions (ARs), namely NOAA AR 11261, AR 11283 and AR 11429. They analyzed the time series of photospheric data from SDO taken between August 2011 and March 2012. During this period the three ARs produced a series of flares (eight M- and six X-class) and CMEs. AR 11261 had four M-class flares and one of them was accompanied by a fast CME. AR11283 had similar activities with two M- and two X-class flares, but only with a slow CME. Finally, AR 11429 was the most powerful of the three ARs as it hosted five compact and large solar flare and CME eruptions. For applying the G_M method they employed the Debrecen sunspot data catalogue, and, for estimating the magnetic helicity at a photospheric level they used the Space-weather HMI Active Region Patches (SHARP's) vector magnetograms from SDO/HMI (Helioseismic and Magnetic Imager). They followed the evolution of the components of the G_M and the magnetic helicity before the flare and CME occurrences. They found a unique and mutually shared behaviour, called the U-shaped pattern, of the weighted distance component of G_M and of the shearing component of the helicity flux before the

flare and CME eruptions. This common pattern is associated with the decreasing-receding phases yet reported only known to be a necessary feature prior to solar flare eruption(s) but found now at the same time in the evolution of the shearing helicity flux. This result leads to the conclusions that (i) the shearing motion of photospheric magnetic field may be a key driver for a solar eruption in addition to the flux emerging process, and that (ii) the found decreasing-approaching pattern in the evolution of shearing helicity flux may be another precursor indicator for improving the forecasting of solar eruptions.

Wang *et al.*[56] reported the observations of a moderate but relatively intense geoeffective solar eruption on 4 November 2015 from the peripheral diffusive polarities of active region 12443. They used space-borne SDO and ACE observations. EUV images identified a helical pattern along a filament channel, and they regard this channel as flux-rope structure. Flow velocity derived from tracked magnetograms inferred converging motion along the polarity inversion line beneath the filament channel. An associated magnetic cancellation process was detected in the converging region. Further, the pre-eruptive EUV brightening was observed in the converging region, the most intense part of which appeared in the magnetic cancellation region. These observations implied that the converging and canceling flux probably contributed to the formation of the helical magnetic fields associated with the flux rope. A filament-height estimation method suggested that the middle part of the filament probably lies at a low altitude and was consistent with the initial place of the eruption. A thick current channel associated with the flux rope was also determined. For an expanding thick current channel, the critical height of the decay index for torus instability lied in the range of 37~47 Mm. Southward magnetic fields in the sheath and the ejecta induced a geomagnetic storm with a *Dst* global minimum of about −90 nT.

After that, Wang *et al.*[57] studied the magnetic field evolution in the AR 12673 that produced the largest solar flare in the past decade on 6 September 2017. Fast flux emergence was one of the most prominent features of this AR. They calculated the magnetic helicity from photospheric tangential flows that shear and braid field lines (shear helicity) and from normal flows that advected twisted magnetic flux into the corona (emergence helicity), respectively. Their results showed that the emergence helicity accumulated in the corona is -1.6×10^{43} Mx^2 before the major eruption, while the shear helicity accumulated in the corona was -6×10^{43} Mx^2, which contributed about 79% of the total helicity. The shear-helicity flux was dominant throughout the overall investigated emergence phase. Their results implied that the emerged fields initially contained relatively low helicity. Much more helicity was built up by shearing and converging flows acting on preexisting and emerging flux. Shearing motions were getting stronger with the flux emergence, and especially on both sides of the polarity inversion line of the core field region. The evolution of the vertical currents showed that most of the intense currents did not appear initially with the emergence of the flux, which implied that most of the emerging flux was probably not strongly current carrying. The helical magnetic fields (flux rope) in the core field region were probably formed by long-term photospheric motions. The shearing and converging motions were continuously generated, driven by the flux emergence. AR 12673 was representative, as photospheric motions contributed most of the non-potentiality in the AR with vigorous flux emergence.

Hu *et al.*[58] investigated a global Extreme-Ultraviolet (EUV) wave associated with a CME-driven shock on 10 September 2017. The EUV wave was transmitted by north- and south-polar Coronal Holes (CHs), which was observed by SDO and STEREO-A from opposite sides of the Sun. They obtained key findings on how the EUV wave interacted with multiple coronal structures, and its connection with the CME-driven shock: (i) the transmitted EUV wave was still connected with the shock that was incurvated to the Sun, after the shock had reached the opposite side of the eruption; (ii) the south CH transmitted EUV wave was accelerated inside an

on-disk, low-density region with closed magnetic fields, which implies that an EUV wave can be accelerated in both open and closed magnetic field regions; (iii) part of the primary EUV wavefront turned around a Bright Point (BP) with a bipolar magnetic structure when it approached a dim, low-density filament channel near the BP; (iv) the primary EUV wave was diffused and apparently halted near the boundaries of remote active regions (ARs) that were far from the eruption, and no obvious AR related secondary waves were detected; (v) the EUV wave extended to an unprecedented scale of 360° in latitudes, which was attributed to the polar CH transmission. These results provide insights into the effects of coronal density and magnetic field distributions on the evolution of a EUV wave, and into the connection between the EUV wave and the associated CME-driven shock.

Solar eruptions occurring at different places within a relatively short time interval are considered to be sympathetic. However, it is difficult to determine whether there exist a cause and effect between them. Wang *et al.*[59] found slipping-like magnetic reconnection of the large-scale field in the quiet-Sun corona could continually transform magnetic fluxes overlying one filament to the other, which strengthened the strapping field of the filament that underwent a failed eruption but weakened the strapping field of the filament that erupted successfully. The effects of the slipping-like magnetic reconnection were manifested as serpentine flare ribbons extending along the chromospheric network, coronal dimmings, apparently growing hot loops, contracting cold loops, *etc.*

Large-scale propagating fronts are frequently observed during solar eruptions, yet whether or not they are waves is still an open question. Studying EUV fronts associated with three homologous CMEs from pseudo-multi-viewing angles, Liu *et al.*[60] found that each primary front directly associated with the CME consistently transmits through various coronal structures while producing slow and stationary fronts. The primary front also propagates along an arcade of coronal loops and slows down due to foreshortening at the far side, yielding local plasma heating. Based on these characteristics, the strength of the coronal magnetic field is estimated to be 2 Gs in the polar coronal hole and 4 Gs in the coronal arcade neighboring the AR. These observations substantiate the wave nature of the primary front and shed new light on slow fronts.

Solar eruptions, mainly eruptive flares with CMEs, represent the most powerful drivers of space weather. Due to the low plasma-β nature of the solar corona, solar eruption has its roots in the evolution of the coronal magnetic field. Although various theoretical models of the eruptive magnetic evolution have been proposed, they still oversimplify the realistic process in observation, which shows a much more complex process due to the invisible complex magnetic environment. Jiang *et al.*[61] studied a complex sigmoid eruption in solar active region11283, which is characterized by a multipolar configuration embedding a null-point topology and a sigmoidal magnetic flux rope. Based on extreme ultraviolet observations, it has been suggested that a three-stage magnetic reconnection scenario might explain the complex flare process. They reproduced the complex magnetic evolution during the eruption using a data-constrained high-resolution MHD simulation. The simulation clearly demonstrates three reconnection episodes, which occurred in sequence in different locations in the corona. Through these reconnections, the initial sigmoidal flux rope breaks one of its legs, and quickly gives birth to a new tornado-like magnetic structure that is highly twisted and has multiple connections to the Sun due to the complex magnetic topology. The simulated magnetic field configuration and evolution are found to be consistent with observations of the corona loops, filaments, and flare ribbons. Their study demonstrates that significant insight into a realistic, complex eruption event can be gained by a numerical MHD simulation that is constrained or driven by observed data.

Three-dimensional magnetic topology is crucial to understanding the explosive release of magnetic energy in the corona during solar flares. Much at-

tention has been given to the pre-flare magnetic topology to identify candidate sites of magnetic reconnection, yet it is unclear how the magnetic reconnection and its attendant topological changes shape the eruptive structure and how the topology evolves during the eruption. Jiang *et al.*[62] employed a realistic, data-constrained MHD simulation to study the evolving magnetic topology for an X9.3 eruptive flare that occurred on 6 September 2017. The simulation successfully reproduces the eruptive features and processes in unprecedented detail. The numerical results reveal that the pre-flare corona contains multiple twisted flux systems with different connections, and during the eruption, these twisted fluxes form a coherent flux rope through tether-cutting-like magnetic reconnection below the rope. Topological analysis shows that the rising flux rope is wrapped by a quasi-separatrix layer, which intersects itself below the rope, forming a topological structure known as a hyperbolic flux tube, where a current sheet develops, triggering the reconnection. By mapping footpoints of the newly reconnected field lines, they were able to reproduce both the spatial location and, for the first time, the temporal separation of the observed flare ribbons, as well as the dynamic boundary of the flux rope's feet. Furthermore, the temporal profile of the total reconnection flux is comparable to the soft X-ray light curve. Such a sophisticated characterization of the evolving magnetic topology provides important insight into the eventual understanding and forecasting of solar eruptions.

Solar eruptions are manifestations of explosive release of magnetic energy in the Sun's corona. Large solar eruptions originate mostly within active regions, where strong magnetic fields concentrate on the solar surface. Jiang *et al.*[63] studied the magnetic field structure for an exception, which is a peculiar GOES X1.2 flare accompanied with a very fast coronal mass ejection taking place between two active regions, where the magnetic field is relatively weak. The pre-flare magnetic field is reconstructed from the SDO/HMI vector magnetogram, using a non-linear force-free field extrapolation method. It was found that prior to the flare, there is a highly twisted magnetic flux rope with magnetic field lines winding over 6 turns, which connects the border of a leading sunspot of one active region and the following polarity of the neighboring active region. The basic configuration of the flux rope is consistent with the observed sigmoidal coronal loops and filament channels by SDO/AIA. It resides rather low-lying between the active regions such that the torus instability is not able to be triggered. Thus, it is likely that, due to the strong magnetic twist, the kink instability of the flux rope triggers the eruption.

Magnetic Flux Ropes (MFRs) are thought to be the central structures of solar eruptions, and their ideal MHD instabilities can trigger the eruption. Duan *et al.*[64] performed a study of all the MFR configurations that led to major solar flares, either eruptive or confined, from 2011 to 2017 near the solar disk center. The coronal magnetic field was reconstructed from observed magnetograms, and based on magnetic twist distribution, they identified the MFR, which is defined as a coherent group of magnetic field lines winding an axis with more than one turn. It was found that 90% of the events possess pre-flare MFRs, and their 3D structures are much more complex in detail than theoretical MFR models. They further constructed a diagram based on two parameters, the magnetic twist number which controls the Kink Instability (KI), and the decay index which controls the Torus Instability (TI). It clearly shows lower limits for TI and KI thresholds, which are $n_{\rm crit}$=1.3 and $|T_w|_{\rm crit}$=2, respectively, as all the events above $n_{\rm crit}$ and nearly 90% of the events above $|T_w|_{\rm crit}$ erupted. Furthermore, by such criterion, over 70% of the events can be discriminated between eruptive and confined flares, and KI seems to play a nearly equally important role as TI in discriminating between the two types of flares. More than half of the events with both parameters are below the lower limits, and 29% are eruptive. These events might be triggered by magnetic reconnection rather than MHD instabilities.

Solar eruptions are the most powerful drivers of space weather. To understand their cause and nature, it is crucial to know how the coronal magnetic field

evolves before the eruption. He *et al.*[65] studied the formation process of a relatively large-scale Magnetic Flux Rope (MFR) in active region NOAA 12371 that erupted with a major flare and CME on 21 June 2015. A data-driven numerical MHD model was employed to simulate 3D coronal magnetic field evolution of 1 day duration before the eruption. Comparison between the observed features and their modeled magnetic field discloses how the pre-eruption MFR forms. Initially, the magnetic field lines were weakly twisted as being simply sheared arcades. Then a long MFR was formed along the polarity inversion line due to the complex photospheric motion, which is mainly shearing rather than twisting. The presence of the MFR is evidenced by a coherent set of magnetic field lines with twist number above unity. Below the MFR a current sheet is shown in the model, suggesting that tether-cutting reconnection plays a key role in the MFR formation. The MFR's flux grows as more and more field lines are twisted due to continuous injection of magnetic helicity by the photospheric motions. Meanwhile, the height of the MFR's axis increases monotonely from its formation. By an analysis of the decay index of its overlying field, they suggested that this is because the MFR runs into the torus instability regime and becomes unstable, which finally triggers the eruption.

Miao *et al.*[66] reported a detailed observational study of two Quasi-periodic Fast-Propagating (QFP) magnetosonic wave events that occurred on 2011 March 9 and 10, respectively. Interestingly, both the events have two Wave Trains (WTs): a strong main one (WT-1) and a small and weak secondary one (WT-2). Peculiar and common characteristics of the two events are observed, namely, (i) the two QFP waves are accompanied with brightenings during the whole stage of the eruptions; (ii) both the two main WTs are nearly propagating along the same direction; (iii) extreme ultraviolet (EUV) waves were found to be associated with the two events. Investigating various aspects of the target events, they argued that: (i) the second event is accompanied with a flux rope eruption during the whole stage; (ii) the second event eruption produces a new filament-like dark feature; (iii) the ripples of the two WT-2 QFP waves seem to result from different triggering mechanisms. Based on the obtained observational results, they proposed that the funnel-like coronal loop system is indeed playing an important role in the two WT-1 QFP waves. The development of the second WT-2 QFP wave can be explained as due to the dispersion of the main EUV front. The coexistence of the two events offers thereby a significant opportunity to reveal what driving mechanisms and structures are tightly related to the waves.

Artifacts could mislead interpretations in astrophysical observations. A thorough understanding of an instrument will help in distinguishing physical processes from artifacts. Yuan *et al.*[67] investigated an artifact of AIA onboard SDO. Time-series data and wavelet spectra revealed periodic intensity perturbations in small regions over the entire image in certain AIA Extreme Ultraviolet (EUV) passbands at a period of about 45 seconds. These artificial intensity variations are prominently detected in regions with sharp intensity contrast, such as sunspot light bridges. This artifact was caused by a periodic pointing wobble of the two AIA telescopes ATA 2 (193 and 211 Å channels) and ATA 3 (171 Å and UV channels), to a lesser extent, while the other two telescopes were not found to be affected. The peak-to-peak amplitude of the wobble was about 0.2 pixels in ATA 2 and 0.1 pixels in ATA 3. This artifact was intermittent and affected the data of seven months from 18 January to 28 August 2012, as a result of a thermal adjustment to the telescopes. They recommended that standard pointing-correction techniques, such as local correlation tracking, should be applied before any detailed scientific analysis that requires sub-pixel pointing accuracy. Specifically, this artificial 45-second periodicity was falsely interpreted as abnormal sub-minute oscillations in a light bridge of a sunspot.

The Kelvin-Helmholtz (KH) instability is commonly found in many astrophysical, laboratory, and space plasmas. It could mix plasma components of different properties and convert dynamic fluid energy from large-scale structures to smaller ones. Yuan

et al.[68] combined the ground-based New Vacuum Solar Telescope (NVST) and SDO/AIA to observe the plasma dynamics associated with active region 12673 on 9 September 2017. In this multi-temperature view, they identified three adjacent layers of plasma flowing at different speeds, and detected KH instabilities at their interfaces. They could unambiguously track a typical KH vortex and measure its motion. They found that the speed of this vortex suddenly tripled at a certain stage. This acceleration was synchronized with the enhancements in emission measure and the average intensity of the 193 Å data. They interpreted this as evidence that KH instability triggers plasma heating. The intriguing feature in this event is that the KH instability observed in the NVST channel was nearly complementary to that in the AIA 193 Å. Such a multi-thermal energy exchange process is easily overlooked in previous studies, as the cold plasma component is usually not visible in the extreme-ultraviolet channels that are only sensitive to high-temperature plasma emissions. Their finding indicates that embedded cold layers could interact with hot plasma as invisible matters. They speculated that this process could occur at a variety of length scales and could contribute to plasma heating.

Solar flares are often associated with coronal eruptions, but there are confined ones without eruptions, even for some X-class flares. How such large flares occurred and why they are confined are still not well understood. Zou *et al.*[69] studied a confined X2.2 flare in NOAA Active Region 12673 on 6 September 2017. It exhibits two episodes of flare brightening with rather complex, atypical ribbons. Based on topology analysis of the extrapolated coronal magnetic field, they revealed that there is a two-step magnetic reconnection process during the flare. Prior to the flare, there is a Magnetic Flux Rope (MFR) with one leg rooted in a rotating sunspot. Neighboring the leg is a magnetic null-point structure. The sunspot drives the MFR to expand, pushing magnetic flux to the null point, and reconnection is first triggered there. The disturbance from the null-point reconnection triggers the second reconnection, *i.e.*, a tether-cutting reconnection below the rope. However, these two reconnections failed to produce an eruption, because the rope is firmly held by its strapping flux. Furthermore, they compared this flare with an eruptive X9.3 flare in the same region 2 h later, which has a similar MFR configuration. The key difference between them is that, for the confined flare, the MFR is fully below the threshold of torus instability, whereas for the eruptive one, the MFR reaches entirely above the threshold. This study provides good evidence supporting that reconnection alone may not be able to trigger eruption; rather, MHD instability plays a more important role.

5 Coronal Mass Ejections and Their Interplanetary Counterparts

Recent years have seen growing evidence of the existence of Alfvén waves within interplanetary magnetic flux ropes, which are believed to be an important aspect of dynamics connecting the Sun and the heliosphere. Previous studies, due to localized observation by single spacecraft, focused on sunward or antisunward Alfvén waves propagating along with magnetic field lines. Wang *et al.*[70] used multi-spacecraft observations to verify and analyze two large-scale Magnetic Clouds (MCs), when the spacecraft had quite different spatial separations. What surprises them was that not only unidirectional but bidirectional Alfvén waves existed in the large-scale MC, which was rooted to the Sun. They speculated that unidirectional Alfvén waves within an MC were generated by distortions produced within a pre-existing flux rope, and bidirectional Alfvén waves were emitted from the center of reconnection and then traveled outward along with two loop legs of an MC.

He *et al.*[71] investigated how a weak CME launched on 8 October 2016 without obvious signatures in the low corona produced a relatively intense geomagnetic storm. Remote sensing observations from SDO, STEREO, and SOHO and in situ measurements from WIND are employed to track the

CME from the Sun to the Earth. Using a graduated cylindrical shell model, they estimated the propagation direction and the morphology of the CME near the Sun. CME kinematics were determined from the wide-angle imaging observations of STEREO A and are used to predict the CME arrival time and speed at the Earth. They compared ENLIL MHD simulation results with in situ measurements to illustrate the background solar wind where the CME was propagating. They also applied a Grad-Shafranov technique to reconstruct the flux-rope structure from in situ measurements in order to understand the geoeffectiveness associated with the CME magnetic field structure. Key results were obtained concerning how a weak CME could generate a relatively intense geomagnetic storm: (i) there were coronal holes at low latitudes, which could produce High Speed Streams (HSSs) to interact with the CME in interplanetary space; (ii) the CME was bracketed between a slow wind ahead and an HSS behind, which enhanced the southward magnetic field inside the CME and gave rise to the unexpected geomagnetic storm.

Liu *et al.*[72] investigated the kinetic properties of a typical fast-mode shock inside an Interplanetary Coronal Mass Ejection(ICME) observed on 6 August 1998 at 1 AU, including particle distributions and wave analysis with the in situ measurements from WIND. Key results were obtained concerning the shock and the shock-ICME interaction at kinetic scales: (i) gyrating ions, which may provide energy dissipation at the shock in addition to wave-particle interactions, are observed around the shock ramp; (ii) despite the enhanced proton temperature anisotropy of the shocked plasma, the low plasma β inside the ICME constrains the shocked plasma under the thresholds of the ion cyclotron and mirror-mode instabilities; (iii) whistler heat flux instabilities, which can pitch-angle scatter halo electrons through a cyclotron resonance, were observed around the shock, and can explain the disappearance of Bi-Directional Electrons (BDEs) inside the ICME together with normal betatron acceleration; (iv) whistler waves near the shock are likely associated with the whistler heat flux instabilities excited at the shock ramp, which is consistent with the result that the waves may originate from the shock ramp; (vi) the whistlers share a similar characteristic with the shocklet whistlers, providing possible evidence that the shock is decaying because of the strong magnetic field inside the ICME.

An unexpected strong geomagnetic storm occurred on 26 August 2018, which was caused by a slow CME from a gradual eruption of a large quiet-region filament. Chen *et al.*[73] investigated the eruption and propagation characteristics of this CME in relation to the strong geomagnetic storm with remote sensing and in situ observations. Coronal magnetic fields around the filament were extrapolated and compared with extreme ultraviolet observations. They determined the propagation direction and tilt angle of the CME flux rope near the Sun using a Graduated Cylindrical Shell (GCS) model and the Sun-to-Earth kinematics of the CME with wide-angle imaging observations from STEREO A. They reconstructed the flux-rope structure using a Grad-Shafranov technique based on the in situ measurements at the Earth and compared it with those from solar observations and the GCS results. Their conclusions are as follows: (i) the eruption of the filament was unusually slow and occurred in the regions with relatively low critical heights of the coronal field decay index; (ii) the axis of the CME flux rope rotated in the corona as well as in interplanetary space, which tended to be aligned with the local heliospheric current sheet; (iii) the CME was bracketed between slow and fast solar winds, which enhanced the magnetic field inside the CME at1 AU; (iv) the geomagnetic storm was caused by the enhanced magnetic field and a southward orientation of the flux rope at 1 AU from the rotation of the flux rope.

A powerful CME occurred on 10 September 2017 near the end of the declining phase of the historically weak solar cycle 24. Liu *et al.*[74] obtained new insights concerning the geometry and kinematics of CME driven shocks in relation to their heliospheric impacts from the optimal, multi-spacecraft observations of the eruption. The shock, which together with the CME driver can be tracked from the early stage

to the outer corona, shows a large oblate structure produced by the vast expansion of the ejecta. The expansion speeds of the shock along the radial and lateral directions are much larger than the translational speed of the shock center, all of which increase during the flare rise phase, peak slightly after the flare maximum and then decrease. The near simultaneous arrival of the CME-driven shock at the Earth and Mars, which are separated by 156.6° in longitude, is consistent with the dominance of expansion over translation observed near the Sun. The shock decayed and failed to reach STEREO A around the backward direction. Comparison between ENLIL MHD simulations and the multi-point in situ measurements indicates that the shock expansion near the Sun is crucial for determining the arrival or non-arrival and space weather impact at certain heliospheric locations. The large shock geometry and kinematics have to be taken into account and properly treated for accurate predictions of the arrival time and space weather impact of CMEs.

In order to have a comprehensive view of the propagation and evolution of CMEs from the Sun to deep interplanetary space beyond 1 AU, Zhao *et al.*[75] carried out a kinematic analysis of seven CMEs in solar cycle 23. The events are required to have coordinated coronagraph observations, interplanetary type II radio bursts, and multi-point in situ measurements at the Earth and Ulysses. A graduated cylindrical shell model, an analytical model without free parameters, and an MHD model were used to derive CME kinematics near the Sun, to quantify the CME/shock propagation in the Sun-Earth space, and to connect in situ signatures at the Earth and Ulysses, respectively. They found that each of the seven CME-driven shocks experienced a major deceleration before reaching 1 AU and thereafter propagated with a gradual deceleration from the Earth to larger distances. The resulting CME/shock propagation profile for each case was roughly consistent with all the data, which verifies the usefulness of the simple analytical model for CME/shock propagation in the heliosphere. The statistical analysis of CME kinematics indicates a tendency that the faster the CME, the larger the deceleration, and the shorter the deceleration time period within 1 AU. For several of these events, the associated geomagnetic storms were mainly caused by the southward magnetic fields in the sheath region. In particular, the interaction between a CME-driven shock and a preceding ejecta significantly enhanced the pre-existing southward magnetic fields and gave rise to a severe complex geomagnetic storm.

It is paramount from both scientific and societal perspectives to understand the generation of extreme space weather. Liu *et al.*[76] discussed the formation of solar superstorms based on a comparative study of the 23 July 2012 and 23 July 2017 eruptions. The first one is Carrington-class, and the second could rival the 1989 March event that caused the most intense geomagnetic storm of the space age. Observations of these events in the historically weak solar cycle 24 indicate that a solar superstorm can occur in any solar cycle and at any phase of the cycle. Recurrent patterns are identified in both cases, including the long-lived eruptive nature of the active region, a complex event composed of successive eruptions from the same active region, and in-transit interaction between the successive eruptions resulting in exceptionally strong ejecta magnetic fields at 1 AU. Each case also shows unique characteristics. Preconditioning of the upstream solar wind leading to unusually high solar wind speeds at 1 AU is observed in the first case, but not in the latter. This may suggest that the concept of "preconditioning" appears to be necessary for making a Carrington-class storm. They found a considerable deflection by nearby coronal holes in the second case, but not in the first. On the basis of these results, they proposed a hypothesis for further investigation that superstorms are "perfect storms" in nature, *i.e.*, a combination of circumstances that results in an event of unusual magnitude. Historical records of some extreme events seem to support their hypothesis.

The Sun's atmosphere is frequently disrupted by CMEs, coupled with flares and energetic particles. The coupling is usually attributed to magnetic reconnection at a vertical current sheet connecting the

flare and CME, with the latter embedding a helical magnetic structure known as flux rope. However, both the origin of flux ropes and their nascent paths toward eruption remain elusive. Gou *et al.*[77] presented an observation of how a stellar-sized CME bubble evolving continuously from plasmoids, mini flux ropes that are barely resolved, within half an hour. The eruption initiated when plasmoids springing from a vertical current sheet merged into a leading plasmoid, which rose at increasing speeds and expanded impulsively into the CME bubble, producing hard X-ray bursts simultaneously. This observation illuminates a complete CME evolutionary path capable of accommodating a wide variety of plasma phenomena by bridging the gap between microscale and macroscale dynamics.

Liu *et al.*[79] studied the twists released by 30 off-limb rotational solar coronal jets, and compare the observational findings with theoretical kink instability thresholds. The results suggest that the kink instability threshold in the solar atmosphere should not be a constant. They found the lower limit of a twist number of 1.3 turns should be merely a necessary but not a sufficient condition for a finite solar Magnetic Flux Rope (MFR) to become kink unstable. Wang *et al.*[79] investigated the continuous evolution of a pre-existing MFR in the corona, whose gradual expansion is associated with the development of a pair of coronal dimming regions on the surface, suggesting that the dimmings map the MFR's feet. Quantitative measurements indicate that the magnetic twist of the MFR increases from 1.0±0.5 to 2.0±0.5 turns during the five-hour expansion, and further increases to about 4.0 turns per AU when it is detected as a magnetic cloud at 1 AU. Besides, Magnetic Clouds (MCs) were also used to study the twist distribution inside the magnetic flux rope. Wang *et al.*[80] reported a rare event, in which a MC was observed sequentially by four spacecraft near Mercury, Venus, Earth, and Mars, respectively. With the aids of a uniform-twist flux rope model and a newly developed method that can recover a shock-compressed structure, they found that the axial magnetic flux and helicity of the magnetic cloud decreased when it propagated outward but the twist increased. Their analysis suggests that the "pancaking" effect and "erosion" effect may jointly cause such variations. The MC was eroded significantly leaving its inner core exposed to the solar wind at a far distance. The increase of the twist together with the presence of the erosion effect suggests that the post-eruption magnetic flux rope may have a high-twist core enveloped by a less-twisted outer shell. Besides, by peeling off equal azimuthal magnetic flux from both the front and rear boundary of an MC, just like peeling an onion, the average twist and the twist in each layer of the cross section of the MC were analyzed by Zhao *et al.*[81]. And they also found that the absolute value of twists exhibits a roughly monotonous decrease from the axis to the edge. Furthermore, Zhao *et al.*[82] showed that there's a clear positive correlation between the twist and the plasma poloidal angular velocity in peeled flux ropes or flux rope layers of the MC.

Similar to the Sun, other stars shed mass and magnetic flux via ubiquitous quasi-steady wind and episodic stellar CMEs. Mishra *et al.*[83] investigated the mass loss rate via solar wind and CMEs as a function of solar magnetic variability represented in terms of sunspot number and solar X-ray background luminosity during solar cycles 23 and 24. The study confirms a true physical increase in CME activity relative to the sunspot number in cycle 24, and shows that the CME occurrence rate and associated mass loss rate can be better predicted by X-ray background luminosity than the sunspot number. In contrast, the solar wind mass loss rate which is an order of magnitude more than the CME mass loss rate shows no obvious dependency on cyclic variation.

From 4–6 September 2017, heliospheric activity suddenly and drastically increased starting from a simple sunspot which transformed into a complex region with four X-class flares accompanied by several Earth-directed CMEs and largely disturbed the Earth's geomagnetic field. The two CMEs launched on 4 September 2017, 20:24 UT and 6 September 2017, 12:24 UT interacted with each other in the interplanetary space and formed a Shock-ICME

complex structure. When the Shock-ICME arrived at Earth, it caused a strong multi-step magnetic storm. By recovering the shocked part of the Shock-ICME to an uncompressed state, and substituting both the observational data and recovered state into various *Dst* prediction models, Shen *et al.*[84] found that the compression of the shock enhanced the intensity of this geomagnetic storm by roughly a factor of two. For the first time, this work quantitatively analyzed the effects of shock compression on enhancing the geoeffectiveness of an ICME. In addition, in this case, the interaction between the shock and the host ICME increased the intensity of solar energetic particles by a factor of five.

For a deeper comprehension of the space weather effects of S-ICMEs, Xu *et al.*[85] analyzed 18 geomagnetic storms caused by shock-ICMEs since 1995. The results showed that due to the compression of the shock, the peak values of the southward magnetic field and the dawn-dusk electric field in ICMEs were increased by 2.0 and 2.2 times, respectively, and the intensity of the geomagnetic storm was increased by 1.4 times. Besides, Xu *et al.*[86] studied 12 ICMEs with extraordinary energetic particle enhancements, 9 of which were shock-interplanetary coronal mass ejection complex structures (shock-ICMEs), and 3 were Isolated Interplanetary Coronal Mass Ejections (I-ICMEs). Energetic-particle intensities increase more in the shock-ICMEs than in the I-ICMEs in all energy channels, especially in the high-energy channels. In addition, shocks inside energetic-particle-enhanced shock-ICMEs are relatively fast and strong. These results indicate that shock-ICME interaction may be an effective local acceleration mechanism.

CMEs are frequently associated with filament eruptions. Theoretical studies propose that both magnetic reconnection and ideal MHD instability of magnetic flux ropes can convert coronal magnetic energy into the filament/CME kinetic energy. Numerical simulations and analytical considerations demonstrate that both mechanisms can have significant contributions to the filament/CME acceleration. Many observational studies support that reconnection plays an important role during the acceleration, while the question on how to resolve observationally the contribution of the ideal instability to the acceleration remains open. On the other hand, it is difficult to separate and compare their contributions through observations as both mechanisms often work in a close time sequence. The above issues are addressed by Song *et al.*[87], through analyzing the eruption process of a quiescent filament. The filament started to rise from 00:00 UT on 25 December 2011, 20 min earlier than the starting time of the flare impulsive phase (00:20 UT), and reached the maximum velocity at the flare peak time (00:50 UT). They divided the acceleration process into two stages, corresponding to the pre-flare and flare impulsive phases, respectively. The analysis indicates that an ideal flux-rope instability is dominant in the first stage, while reconnection below the flux rope becomes important during the second stage, and both mechanisms may have comparable contributions to the net acceleration of the filament.

CMEs often exhibit the classic three-part structure in a coronagraph, *i.e.*, the bright front, dark cavity, and bright core, which are traditionally considered as the manifestations of coronal plasma pileup, Magnetic Flux Rope (MFR), and filament, respectively. However, a recent survey based on 42 CMEs all possessing the three-part structure found that a large majority (69%) do not contain an eruptive filament at the Sun. Therefore, a challenging opinion is proposed and claims that the bright core can also correspond to the MFR, which is supported by the CME simulation. Then what is the nature of the CME core. Song *et al.*[88] studied a CME associated with the eruption of a filament-hosting MFR on 29 September 2013. This CME exhibits the three-part morphology in multiple white-light coronagraphs from different perspectives. The new finding is that the bright core contains both a sharp and a fuzzy component. Through tracking the filament motion continuously from its source region to the outer corona, they conclude that the sharp component corresponds to the filament. The fuzzy component was suggested to result from the MFR that supports the filament against the gravity in the corona. The study

can shed more light on the nature of CME cores, and explain the core whether or not the filament is involved with a uniform scenario. The nature of the CME cavity was also discussed.

So far, most studies on the structure of CMEs are conducted through white-light coronagraphs, demonstrating that about one-third of CMEs exhibit the typical three-part structure in the high corona (*e.g.*, beyond 2 R_S). Song *et al.*[89] reported the observation of the CME structure in the low corona (*e.g.*, below 1.3 R_S) through EUV passbands and found that the three-part CMEs in the white-light images can possess a similar three-part appearance in the EUV images, *i.e.*, a leading edge, a low-density zone, and a filament or hot channel. The analyses identified that the leading edge and the filament or hot channel in the EUV passbands evolve into the front and the core later within several solar radii in the white-light passbands, respectively. What is more, they found that the CMEs without an obvious cavity in the white-light images can also exhibit the clear three-part appearance in the EUV images, which means that the low-density zone in the EUV images (observed as the cavity in white-light images) can be compressed and/or transformed gradually by the expansion of the bright core and/or the reconnection of the magnetic field surrounding the core during the CME propagation outward. Their study suggests that more CMEs can possess the clear three-part structure in their early eruption stage. The nature of the low-density zone between the leading edge and the filament or hot channel was discussed.

Zhou *et al.*[90] performed a statistical study on the intermittency and the associated local heating in the front Boundary Layers (BLs) of 74 Magnetic Clouds (MCs). The intermittent structures are identified by the Partial Variance of Increments (PVI) method. The probability distribution function of PVI-values reveals that the BLs are more intermittent than adjacent sheath regions, and they contain a greater concentration of strong intermittencies. These strong intermittencies are accompanied by local enhancement of the proton temperature, while the enhancement is not prominent at weaker intermittencies inside the BLs. Since the strong intermittencies are associated with Magnetic Reconnection (MR) processes according to previous studies, these results indicate that MR processes may account for the local heating in the MCBLs to a large extent.

Coherent structures such as current sheets have been usually regarded to be sites of proton heating in the solar wind. Zhou *et al.*[91] statistically investigated the proton heating effects around the coherent structures within the turbulent sheath regions of Magnetic Clouds (MCs) based on WIND observations. It was found that the proton temperature enhancement near coherent structures in the MC sheath is not as remarkable as in the solar wind. Significant temperature increase only exists near coherent structures with great directional changes ($>45°$) in magnetic field or intensity changes ($\geqslant 10\%$ of the mean magnetic field magnitude), which merely account for 13% of the total of 12426 identified intermittent events in the 71 studied MC sheaths. The temperature increment is more evident near strong current sheets with great directional changes ($>45°$) at smaller scales than those at larger scales. It suggests that the heating effects in the MC sheath regions are likely to be highly localized. The local proton heating effects in the turbulent sheath are probably caused by the magnetic reconnection processes that are frequently associated with the strong current sheets.

6 Other Interplanetary Structures

Small Flux Ropes (SFRs) have been studied for decades, but their source regions and formation mechanisms are still under debate. Huang *et al.*[92] focused on the formation mechanism of the twisted structures of SFRs. Current research on magnetic clouds suggests five-type distributions of the time structure of iron average charge states ($Q_{<Fe>}$), which imply different formation mechanisms of twisted structures. They used a similar method to identify the $Q_{<Fe>}$ types of 25 SFRs. However, only four of

these five types of distributions were found among these SFRs. Because different origins of SFRs are characteristically affecting the formation of $Q_{<Fe>}$ types, the possible source regions of these SFRs are distinguished. With additional compositional parameters, SFRs are reconfirmed to originate from two types of source regions: the solar corona and the interplanetary medium. Based on these results, their analysis indicates that the twisted structures of SFRs originating from the solar corona may be formed predominately during eruptions. SFRs originating from interplanetary space are related to complex magnetic reconnection processes, which may result in intricate $Q_{<Fe>}$ distributions due to the reconstruction of magnetic field topology.

The global shape of the intersection of the Heliospheric Current Sheet (HCS) with the heliospheric equatorial plane is usually considered to be an Archimedean spiral, however, so far this has not been measured directly. Peng *et al.*[93] used multi-spacecraft measurements to determine its global shape. The time-shifted measured locations are fitted with Archimedean spirals. In most cases, the locations are fitted very well with Archimedean spirals, in addition to the direction of HCS determined by the Minimum Variation Analysis. However, there is one case in which the direction of the HCS does not fit well with the Archimedean spiral and therefore they fit it with a sinusoidal function in addition to an Archimedean spiral. The result showed that in some cases, the HCS is better described with an Archimedean spiral, superposed by small-scale ripples.

Liu *et al.*[94] reported on two small solar wind transients embedded in the corotating interaction region, characterized by surprisingly lower proton density compared with their surrounding regions. In addition to lower density, these two small solar wind transients showed other interesting features like higher proton temperature, higher alpha-proton ratios, and lower charge states (C^{+6}/C^{+5} and O^{+7}/O^{+6}). A synthesized picture for event one combining the observations by STEREO B, ACE, and WIND showed that this small solar transient has an independent magnetic field. Back-mapping links the origin of the small solar transient to a small coronal hole on the surface of the Sun. Considering these special features and the back-mapping, they concluded that such small solar wind transients may have originated from a small coronal hole at low latitudes.

Zhang *et al.*[95] presented a statistical study of the ion upflow associated with Sub-auroral Polarization Streams (SAPS) in the ionospheric sub-auroral region at different substorm times using three DMSP satellites (F16, F17, F18) data for five years (2010–2014) in the northern hemisphere. The results show similarities between SAPS and the ion upflow at a different intensity of substorms both in occurrence rate distribution and velocity distribution. In comparison to SAPS, the distribution of the ion upflow shows the smaller occurrence region and lower velocity. They also found that frictional heating plays an important role in ion upflow from the SAPS region. The intense substorms can trigger strong SAPS channels, enhanced frictional heating and large ion upflow. In addition, there is a moderate linear correlation between SAPS velocity and field-aligned velocity which is consistent with some previous findings. Their results also show that frictional heating can gradually dominate the ion upflow process in intense substorms, while it may not be the only factor to affect the whole upflow process.

7 Space Weather Prediction Methods

A solar magnetic flux transport model has the ability to demonstrate the magnetic evolution of the Sun, thus providing a foundation for space weather forecasting. Solar activities have close relationships with the Sun's magnetic fields. To predict the Sun's magnetic environment more precisely, many versions of magnetic flux rope models have been developed. Liu *et al.*[96] utilized two models that were created by Yeates *et al.* (hereinafter referred to as the Y model) and Worden and Harvey (hereinafter referred to as the WH model) to predict the short-term changes of 10.7 cm radio flux ($F_{10.7}$) during 2003–2014. Both

models performed very well in estimating $F_{10.7}$ values. The statistical results of analyzing the correlation coefficient, mean absolute error, mean square error, relative error, frequency distribution, and so on, show that the Y model is superior to the WH model. The meridional flow and diffusion process used in the WH model do not agree with the observations. Such discrepancies may influence estimates of the global flux.

Qin and Wu[97] studied solar cycles with the Version 2 monthly smoothed international Sunspot Number (SSN), and found that the variations of SSN were well represented by a modified logistic differential equation with four parameters: maximum cumulative sunspot number or total sunspot number x_m, initial cumulative sunspot number x_0, maximum emergence rate r_0, and asymmetry α. A two-parameter function was obtained by taking α and r_0 as fixed values. In addition, it was found that x_m and x_0 can be well determined at the start of a cycle. Therefore, a predictive model of sunspot number is established based on the two-parameter function. The prediction for Cycles 4~23 shows that the solar maximum can be predicted with an average relative error of 8.8% and a maximum relative error of 22% in Cycle 15 at the start of solar cycles if solar minima are already known. The quasi-online method for determining the moment of solar minimum shows that the solar minimum of 14 months can be obtained after the start of a cycle. Besides, their model can predict the cycle length with an average relative error of 9.5% and a maximum relative error of 22% in Cycle 4. Furthermore, they predicted the variations in sunspot number of Cycle 24 with the relative errors of the solar maximum and ascent time being 1.4% and 12%, respectively, and the predicted cycle length is 11.0 a (95% confidence interval is 8.3~12.9 a). A comparison to the observations of Cycle 24 shows that their predictive model has good effectiveness.

8 Magnetic Reconnection

Magnetic reconnection is prevalent in the solar wind and is usually associated with interplanetary coronal mass ejections. Zhou *et al.*[98] examined a Petschek-like Reconnection Exhaust (RE) in the front boundary of a magnetic cloud observed by the WIND spacecraft on 2 June 1998 and presented the first observation of a slow shock pair bounding the Petschek-like outflow jet in the interplanetary space. The whole structure contained an Alfvénic accelerated outflow and a pair of reverse slow shocks. The Alfvénic accelerated outflow was identified by Walén analysis. Rankine-Hugoniot relations were applied to confirm the slow shocks bounding the RE. Both shocks strictly satisfied the characteristics of slow shocks: (i) the intermediate Alfvén Mach numbers were both below unit in the up/downstream region; (ii) the slow Mach number was above unit in the upstream side but below unit in the downstream side. Plasma was compressed and heated across the trailing slow shock, especially in the shock jump layer that has a temperature 2.4 times that of the upstream.

As the Sun rotates, a fast stream can overtake a preceding slow stream, leading to the formation of a Stream Interaction Region (SIR). Two neighboring SIRs may eventually coalesce to produce a Merged Interaction Region (MIR) en route to the outer heliosphere. However, instances of significant interaction and merging of two neighboring SIRs within 1 AU are thought to be extremely rare. Wang *et al.*[99] presented a case report of two interacting and merging SIRs observed near 1 AU, which was associated with two adjacent low-latitude coronal holes. The two SIRs were filled with outward propagating Alfvénic fluctuations associated with MHD turbulence. A reconnection exhaust associated with a current sheet was identified. They suggested that magnetic reconnection represented a potentially important mechanism for the merging of two neighboring SIRs. This observation may shed light on the understanding of the structure and formation of a MIR within 1 AU.

Liu *et al.*[100] investigated the evolution of reconnection inflow using a fully kinetic approach. Three types of inflow were detailed, namely the collapse inflow, the vortex inflow, and the reverse inflow.

They were formed dynamically at different stages of reconnection *via* self-organizing processes, but were closely interrelated with each other. The reconnection starts from a small perturbation, which could trigger off a chain of pressure-induced collapses propagating into the inflow region. The pressure gradient resulted in the collapse inflow toward the reconnection site. Then due to the continuous injection of hot plasma carried by the reconnection outflows, the expanding exhaust caused its adjacent region to be compressed. The combined effects of the compression and the reflection of conducting walls led to the formation of the vortex inflow. Subsequently, the reverse inflow developed gradually within the exhaust. Under the modulation of these inflows, the reconnection rate showed a transient oscillation. They also discussed the possible occurrence of the self-organization inflow available in different contexts.

On the two-step energy conversion mechanism of the solar wind magnetic reconnection outflow region: Magnetic reconnection outflow/exhaust region is an important region of energy conversion, and its role in energy conversion is not less significant than that of magnetic reconnection diffusion region. Most of the energy conversion related to magnetic reconnection occurs in the outflow/exhaust region. The magnetic reconnection outflow region in the solar wind has the advantages for investigation, since it has a large extension scale and in-situ measurement compared with other reconnection outflow regions. By analyzing an event of WIND satellite passing through the magnetic reconnection outflow/exhaust region, He *et al.*[101] analyzed the changes of proton and electron velocity distribution in the upstream and downstream of reconnection in detail, and found that the proton and electron were heated obviously in the parallel direction. The reason for parallel heating may come from the fact that the back-to-back rotational discontinuities bend the particles upstream of both sides to flow counter stream in pairs, thus causing parallel heating. Further analysis shows that the solar wind particles heated in parallel are not stable, which makes the magnetic field line subject to the firehose instability. Moreover, they observed the excitation and emission of Alfven waves, which enhances the Alfven turbulence in the reconnection outflow region.

9 MHD Numerical Modeling

All kinds of upwind schemes can be combined very flexibly for different problems to achieve the perfect combination of Conservation Element and Solution Element (CESE) and Finite Volume Method (FVM). However, Yang *et al.*[102] pointed out that in many physical applications it needs to consider geometries that are more sophisticated. Hence, the main objective of their work was to extend the upwind CESE scheme to multi-dimensional MHD in general curvilinear coordinates by transforming the MHD equations from the physical domain (general curvilinear coordinates) to the computational domain (rectangular coordinates) and the new equations in the computational domain can be still written in the conservation form. For the three-dimensional (3D) case, the derivations of some formulas are much more abstract and complex in a 4D Euclidean hyperspace, and some technical problems need to be solved in the debugging process. Unlike in HD, keeping the magnetic field divergence-free for MHD problems is also a challenge especially in general curvilinear coordinates. These are the main obstacles they have overcome in their study. The test results of benchmarks demonstrate that they have successfully extended the upwind CESE scheme to general curvilinear coordinates for both 2D and 3D MHD problems.

Three-dimensional MHD numerical simulation is an important tool in the prediction of solar wind parameters. Shen *et al.*[103] improved their corona interplanetary total variation diminishing MHD model by using a new boundary applicable to all phases of solar cycles. This model used synoptic magnetogram maps from the Global Oscillation Network Group as the input data. The empirical Wang-Sheeley-Arge relation was used to assign solar wind speed at the lower boundary, while the temperature was specified accordingly based on its em-

pirical relation with the solar wind speed. Magnetic field intensity and solar wind density at the boundary were obtained from observational data in the immediate past Carrington rotations, permitting the persistence of these two parameters in a short time period. The boundary conditions depended on only five tunable parameters when simulating the solar wind for different phases of the solar cycle. They applied this model to simulate the background solar wind from 2007 to 2017 and compare the modeled results with the observational data in the OMNI database. Visual inspection showed that their model could capture the time patterns of solar wind parameters well at most times. Statistical analysis showed that the simulated solar wind parameters were all in good agreement with the observations. This study demonstrated that the improved interplanetary total variation diminishing model could be used for predicting all solar wind parameters near the Earth.

Li *et al.*[104] employed a path-conservative HLLEM FVM to solve the solar wind MHD systems of Extended Generalized Lagrange Multiplier (EGLM) formulation with Galilean invariance (G-EGLM MHD equations). The governing equations of single-fluid solar wind plasma MHD were advanced by using a one-step MUSCL-type time integration with the logarithmic space time reconstruction. The code was programmed in FORTRAN language with Message Passing Interface parallelization in spherical coordinates with a six-component grid system. Then, the large-scale solar coronal structures during Carrington Rotations (CRs) 2048, 2069, 2097, and 2121 were simulated by inputting the line-of-sight magnetic field provided by the Global Oscillation Network Group (GONG). These four CRs belong to the declining, minimum, rising, and maximum phases of solar activity. Numerical results basically generated the observed characteristics of structured solar wind and thus show the code's capability of simulating solar corona with complex magnetic topology.

The MHD modeling of the steady solar wind is an essential and important ingredient in numerical space weather study. Numerically solving the MHD equation system is not an easy work due to its complexity by combining the Euler equations of gas dynamics with Maxwell's equations of electromagnetics and the solenoidal constraint. Moreover, the vast physical temporal and spatial scales of the solar wind simulation propose harsh requirements for computational efficiency and memory storage. Considering these factors, Wang *et al.*[105] developed an easily implemented Finite Volume (FV) scheme using the GMRES algorithm with an LU-SGS preconditioner for the 3D MHD-based simulation. The steady-state solar wind from 1 Rs to 20 Rs during Carrington Rotation (CR) 2051 was simulated for the validation of the proposed matrix-free implicit solver. Compared with the explicit solver, the implicit one could effectively enlarge the CFL number to 100 and achieved speedup ratios of 31.27 and 28.05, which reduced the computational time for the steady-state study from several days to only a few hours. The simulation captured the main features of the solar corona and the mapped in-situ solar wind measurements. The scheme proposed here provided a promising choice to conduct the 3D MHD simulation of the solar wind background from the Sun to the Earth beyond.

Deep-space exploration of the inner heliosphere is in an unprecedented golden age, with the recent and forthcoming launches of the Parker Solar Probe (PSP) and Solar Orbiter (SolO) missions, respectively. In order to both predict and understand the prospective observations by PSP and SolO, Xiong *et al.*[106] performed forward MHD modeling of the 3D inner heliosphere at solar minimum, and synthesized the White-Light (WL) emission that would result from Thomson scattering of sunlight from the coronal and heliospheric plasmas. Both solar rotation and spacecraft trajectory should be considered when reconstructing quiescent large-scale solar-wind streams from PSP and SolO WL observations. When transformed from a static coordinate system into a corotating one, the elliptical orbit of PSP becomes a multi-winding spiral. The innermost spiral winding of this corotating PSP orbit takes the form of a closed "heart shape" within around 80 R_s of the Sun.

PSP, when traveling along this "heart-shaped" trajectory, can cross a single Corotating Interaction Region (CIR) twice. This enables in situ measurements of the same CIR to be made in both the corona and heliosphere. As PSP approaches perihelion, the WL radiance from the corona increases. Polarization can be used to localize the main WL scattering region in the corona. Large-scale structures around PSP can be further resolved in the longitudinal dimension, using additional WL imagery from the out-of-ecliptic perspective of SolO. Coordinated observations between PSP and SolO are very promising in the quest to differentiate background CIRs from transient ejecta.

Zhang *et al.*[107] have used a 3D numerical MHD model to study the reconnection process between magnetic cloud and heliospheric current sheet. Within a steady-state heliospheric model that gives a reasonable large-scale structure of the solar wind near solar minimum, they injected a spherical plasmoid to mimic a magnetic cloud. When the magnetic cloud moves to the heliospheric current sheet, the dynamic process causes the current sheet to become gradually thinner and the magnetic reconnection begins. The numerical simulation can reproduce the basic characteristics of the magnetic reconnection, such as the correlated/anti-correlated signatures in $\boldsymbol{V}$ and $\boldsymbol{B}$ passing a reconnection exhaust. Depending on the initial magnetic helicity of the cloud, magnetic reconnection occurs at points along the boundary of the two systems where anti-parallel field lines are forced together. They found the magnetic field and velocity in the MC have an effect on the reconnection rate, and the magnitude of velocity can also effect the beginning time of reconnection. These results are helpful in understanding and identifying the dynamic process occurring between the magnetic cloud and the heliospheric current sheet.

Li and Feng[108] modified the CESE-HLL 3D MHD solar wind model to be able to work in a corona-heliosphere integrated approach and then simulated the evolution of solar wind from the solar surface to the Earth's orbit during the year 2008. Here high-cadence photospheric magnetic field data were used to drive the model at the solar surface via the projected normal characteristic boundary equations. The simulated results were analyzed and quantitatively evaluated by comparing the simulated results with solar and interplanetary observations. The analyses demonstrated that their model reproduces the main pattern and the evolutionary feature of large-scale coronal structures. The simulated results showed that the height of the pseudostreamer X point was positively correlated with the distance of the coronal holes connected by the pseudostreamer. During the year 2008, the helmet streamer belt was found to have a net southward displacement from the equator while the pseudostreamer belts were biased to the Northern Hemisphere. Both helmet streamer belt and pseudostreamer belts exhibited a general trend of becoming more concentrated along the equator throughout 2008. The evaluation of the simulated results at the L1 point showed that the general structures could be generated by the model, and that speed was the best among the solar wind parameters reproduced. However, the temperature of the fast solar wind and the magnitude of the interplanetary magnetic field were underestimated. The success rate of prediction and arrival time error was also calculated for magnetic field polarity reversals and stream interaction regions.

Yang *et al.*[109] successfully used their newly developed numerical method to study the process of the emergence of magnetic flux rope from the solar convection zone into the atmosphere with a stratified hydro-static equilibrium as the initial ambient state. Their simulation obtained some key characteristics revealed by observation or other researchers' simulations. To achieve the process from emergence until eruption required a numerical scheme with low numerical diffusion. Otherwise, the emergence process would be suppressed by the diffusion of magnetic flux during the long emergence period caused by the great gradient for density and pressure in the ambient state. The results demonstrated that their code can simulate the emergence process very well, which allows to explore flux emergence mechanisms.

Liu *et al.*[110] proposed a Hyperbolic Cell-centered Finite Volume Solver (HCCFVS) to obtain the potential magnetic field solutions prescribed by the solar observed magnetograms. By introducing solution gradients as additional unknowns and adding a pseudo-time derivative, HCCFVS transformed the second-order Poisson equation into an equivalent first-order pseudo-time-dependent hyperbolic system. Thus, instead of directly solving the Poisson equation, HCCFVS obtained the solution to the Poisson equation by achieving the steady-state solution to this first-order hyperbolic system. The code was established in FORTRAN 90 with Message Passing Interface parallelization. To preliminarily demonstrate the effectiveness and accuracy of the code, two test cases with exact solutions were first performed. The numerical results showed its second-order convergence. Then, the code was applied to numerically solve the solar potential magnetic field problem. The solutions demonstrated the capability of HCCFVS to adequately handle the solar potential field problem, and thus it could provide a promising method of solving the same problem, except for the spherical harmonic expansion and the iterative finite difference method. Finally, by using the potential magnetic fields from HCCFVS and the spherical harmonic expansion as initial inputs, they made a comparative study on the steady-state solar corona in Carrington rotation 2098 to reaffirm the HCCFVS's performance. Both simulations showed that their modeled results were similar and capture the large-scale solar coronal structures. The average relative divergence errors, controlled by solving the Poisson equation in the projection method with HCCFVS for both simulations, were kept at an acceptable level.

Temporal evolution of magnetic structures of the solar Active Region (AR) NOAA AR 11158, was simulated by Hayashi, Feng *et al.*[111] with their MHD simulation models using time-dependent solar-surface electric field or plasma flow data. Using the SDO/HMI vector magnetogram data, the solar surface boundary electric field maps are derived with their recently developed algorithm to reproduce the temporal evolution of solar-surface vector magnetic field as observed. The plasma motion velocity maps were calculated through the Differential Affine Velocity Estimator for Vector Magnetograms. In both data-driven models, the simulated evolutionary magnetic field structures at strong-field low-beta regions appeared near force-free state, as the current helicity density ($\boldsymbol{J}\cdot\boldsymbol{B}/B^2$) was roughly constant along each field line. Although the magnetic energy simulated with the newly developed plasma-velocity-driven model was about 10% of that by the electric-field driven model, the plasma-velocity-driven model could maintain the frozen-in condition, and evolution of current and free energy generated by the solar-surface plasma motions could be spatially and temporally traced. The present MHD simulation models for AR system could be a step toward better, more realistic data-driven evolutionary modeling, in particular, establishing boundary treatments for introducing the time-dependent observation data in a physically and mathematically consistent manner.

MHD simulations in the domain of spherical shell are a crucial and challenging subject in many fields such as geophysics and solar-terrestrial physics, due to the complication of the MHD equations and the specificity of the domain. Besides, due to the real-time requirement, accelerating the heavy computation is proposed in many practical problems, of which the space weather simulation and forecast from the Sun to Earth is a typical case. Considering these factors, Wang *et al.*[112] first developed a new, spatially second-order accurate Finite Volume (FV) solver for 3D MHD simulations with the multiple time steps strategy, which was based on the six-component grid for spherical shell domain. Then to speed up the simulation, they implemented the solver on multiple GPUs with optimizations of CUDA and established an effective multi-GPU FV solver on the spherical shell domain. An MHD manufactured solution was used to validate the solvers' spatial accuracy, and to measure their performances. Results showed that both solvers had nice scalability, and speedup ratios of 27.7× to 30.06× are obtained on GPUs. Then they utilized them to study the ambient solar wind for Carrington Rotation (CR)

2060. The multi-GPU FV solver could not only obtain speedup ratios of about 29.0, but captured main features of the solar corona and the mapped in-situ solar wind measurements.

Feng *et al.*[113] applied the rotated-hybrid scheme for the first time to 3D MHD equations in the finite-volume frame. This scheme was devised by decomposing a cell-face normal vector into two orthogonal directions and combining the Roe solver, a full-wave or complete Riemann solver, and the Rusanov solver, an incomplete Riemann solver, into one rotated-hybrid Riemann solver. To keep the magnetic field divergence-free, they proposed two kinds of divergence-cleaning approaches by combining the least-squares reconstruction of magnetic field with divergence-free constraints. One was the locally solenoidality-preserving method designed to locally maintain the magnetic solenoidality exactly, not just in a least-squares sense, and another was the globally Solenoidality-Preserving (SP) approach that was implemented by adding a global constraint but abandoned the exactness of the locally divergence-free condition. Both SP methods were employed for 3D MHD with a rotated-hybrid scheme in the finite-volume frame. To validate and demonstrate the capabilities of the rotated-hybrid scheme for MHD, they performed an Orszag-Tang MHD vortex problem and a numerical study for the steady-state coronal structures of Carrington rotation 2068 during the solar activity minimum. The numerical tests showed the robustness of the proposed scheme and demonstrated the capability of these two SP approaches to keep the magnetic divergence errors to the expected accuracy.

Liu *et al.*[114] presented a 3D numerical MHD data-driven model for the simulation of the CME that occurred on 22June 2015 in the active region NOAA12371. The numerical results showed two elbow-shaped loops formed above the Polarity Inversion Line (PIL), which was similar to the tether-cutting picture previously proposed. The temporal evolutions of magnetic flux showed that the sunspots underwent cancellation and flux emergence. The signature of velocity field derived from the tracked magnetograms indicated the persistent shear and converging motions along with the PIL. The simulation showed that two elbow-shaped loops were reconnected and formed an inverse S-shaped sigmoid, suggesting the occurrence of the tether-cutting reconnection, which was supported by observations of the AIA telescope. Analysis of the decline rate of the magnetic field indicated that the flux rope reached a region where the torus instability was triggered. They concluded that the eruption of this CME was caused by multiple factors, such as photosphere motions, reconnection, and torus instability. Moreover, their simulation successfully reproduced the three-component structures of typical CMEs.

Zhang *et al.*[115] performed a 3D time-dependent, numerical MHD simulation to investigate the propagation of a CME occurring on 12 December 2008. The background solar wind was obtained by using a splitting finite-volume scheme based on a six-component grid system in spherical coordinate, with Parker's one-dimensional solar wind solution and measured photospheric magnetic fields as the initial values. A spherical plasmoid was superposed on the realistic ambient solar wind to study the 12 December 2008 coronal mass ejection event. The plasmoid was assumed to have a Spheromak magnetic structure with a high-density, high-velocity, and high-pressure near the Sun. The dynamical interaction between the CME and the background solar wind flow was then investigated. They compared the model results with observations, and the model provided a relatively satisfactory comparison with the WIND spacecraft observations at 1 AU. They also investigated the numerical results assuming different parameters of the CME, and found that initial magnetic fields in the CME had a larger influence on the solar wind parameters at the Earth.

Previous research has shown that the deflection of CMEs in interplanetary space, especially fast CMEs, is a common phenomenon. The deflection caused by the interaction with background solar wind is an important factor to determine whether CMEs could hit Earth or not. As the Sun rotates, there will be interactions between solar wind flows

with different speeds. When faster solar wind runs into slower solar wind ahead, it will form a compressive area corotating with the Sun, which is called a Corotating Interaction Region (CIR). These compression regions always have a higher density than the common background solar wind. When interacting with CME, will this make a difference in the deflection process of CME? Liu *et al.*[116] established a 3D flux-rope CME initialization model based on the Graduated Cylindrical Shell (GCS)model. Then this CME model was introduced into the background solar wind, which was obtained using a 3D IN (Interplanetary)-TVD-MHD model. The Carrington Rotation (CR) 2154 was selected as an example to simulate the propagation and deflection of fast CME when it interacted with background solar wind, especially with the CIR structure. The simulation results showed that: (i) the fast CME will deflect eastward when it propagates into the background solar wind without the CIR; (ii) when the fast CME hits the CIR on its west side, it will also deflect eastward, and the deflection angle will increase compared with the situation without CIR.

Wang *et al.*[117] presented a method of forced-field (*i.e.*, non-force-free field: NFFF) extrapolation of the global magnetic field in the corona, on the basis of single-layer vector magnetogram, by extending an extrapolation technique of local magnetic field. The forced coronal magnetic field is described by a system with the Minimum Dissipation Rate (MDR) which is appropriate for the corona as a forced and open system. The obtained solution of the magnetic field can be decomposed into three components including one potential field and two Linear Force-Free Fields (LFFF). Starting from the given single-layer vector magnetogram, the bottom boundary condition for each component is determined with an iterative method to achieve a minimum difference of the transverse component between the extrapolated field and the original magnetogram. The final extrapolated forced field is given by the sum of the three-component fields with the obtained bottom boundaries. The method was tested with an analytic Magnetohydrostatic (MHS) solution. It was shown that the extrapolated forced field is highly consistent with the MHS solution at least from the solar disk to the heliocentric distance of 1.5 solar radii. For instance, the complements of normalized and mean vector errors ($\boldsymbol{E}'_{\rm n}$, $\boldsymbol{E}'_{\rm m}$) are as high as about 97% and 95%, respectively. Further comparisons between magnetic strength, force, and field line distributions indicate that the MHS solution has been successfully reconstructed.

10 Solar Energetic Particles, Cosmic Rays, and Forbush Decreases

Lembège and Yang[118] analyzed self-consistently the impact of the non-stationarity of the heliospheric termination shock in the Presence of Pickup Ions (PUIs) on the energy partition between different plasma components by using a 1D particle-in-cell simulation code. Solar Wind Ions (SWIs) and PUIs were introduced as Maxwellian and shell distributions, respectively. For a fixed time, (i) with a percentage of 25% PUIs, a large part of the downstream thermal pressure was carried by reflected PUIs, in agreement with previous hybrid simulations; (ii) the total downstream distribution includes three main components: a low-energy component dominated by Directly Transmitted (DT) SWIs, a high-energy component dominated by reflected PUIs, and an intermediate-energy component dominated by reflected SWIs and DT PUIs. Moreover, results showed that the front non-stationarity (self-reformation) persisted even in presence of 25% PUIs, and had some impacts on both SWIs and PUIs: (i) the rate of reflected ions suffered some time fluctuations for both SWIs and PUIs; (ii) the relative percentage of downstream thermal pressure transferred to PUIs and SWIs also suffered some time fluctuations, but depended on the relative distance from the front; (ii) the three components within the total downstream heliosheath distribution persisted in time, but the contribution of the ion subpopulations to the low- and intermediate-energy components were redis-

tributed by the front non-stationarity. Their results allowed clarifying the respective roles of SWIs and PUIs as a viable production source of energetic neutral atoms and were compared with previous results.

The solar eruption on 27 January 2012 resulted in a wide-spread solar energetic particle event observed by STEREO A and the near-Earth spacecraft (separated by 108°). The event was accompanied by an X-class flare, Extreme-Ultraviolet (EUV) wave, and fast coronal mass ejection. Zhu *et al.*[119] investigated the particle release by comparing the release times of particles at the spacecraft and the times when magnetic connectivity between the source and the spacecraft was established. The EUV wave propagating to the magnetic footpoint of the spacecraft in the lower corona and the shock expanding to the open field line connecting the spacecraft in the upper corona are thought to be responsible for the particle release. They tracked the evolution of the EUV wave and modeled the propagation of the shock using EUV and white-light observations. No obvious evidence indicates that the EUV wave reached the magnetic footpoint of either STEREO A or L1-observers. Their shock modeling showed that the release time of the particles observed at L1 was consistent with the time when the shock first established contacted with the magnetic field line connecting L1-observers. The release of the particles observed by STEREO A was delayed relative to the time when the shock was initially connected to STEREO A via the magnetic field line. They suggested that the particle acceleration efficiency of the portion of the shock connected to the spacecraft determined the release of energetic particles at the spacecraft.

Yang *et al.*[120] investigated electron dynamics at low-Mach-number collisionless shocks by using two-dimensional electromagnetic particle-in-cell simulations with various shock normal angles, and found the following results.

(1) The reflected ions and incident electrons at the shock front provide an effective mechanism for the quasi-electrostatic wave generation due to the charge-separation. A fraction of incident electrons can be effectively trapped and accelerated at the leading edge of the shock foot.

(2) At quasi-perpendicular shocks, the electron trapping and reflection is non-uniform due to the shock rippling along the shock surface and is more likely to take place at some locations accompanied by intense reflected ion-beams. The electron trapping process has a periodical evolution over time due to the shock front self-reformation, which is controlled by ion dynamics. Thus, this is a cross-scale coupling phenomenon.

(3) At quasi-parallel shocks, reflected ions can travel far back upstream. Consequently, quasi-electrostatic waves can be excited in the shock transition and the foreshock region. The electron trajectory analysis shows these waves can trap electrons at the foot region and reflect a fraction of them far back upstream. Simulation runs in this paper indicated that the micro-turbulence at the shock foot can provide a possible scenario for producing the reflected electron beam, which is a basic condition for the type II radio burst emission at low-Mach-number interplanetary shocks driven by CMEs.

Only a few days later, on 10 September 2017 starting at about 15:53 UT, the same region launched another extremely fast magnetic cloud accompanied by an intense shock which spread rapidly across the entire solar surface. The study by Guo *et al.*[121] reported that particles accelerated at the Sun arrived at Earth only 10~20 min later after the solar-surface eruption and caused a ground-level enhancement of radiation seen by multiple neutron monitors. A few hours later and shortly before 20:00 UT, the Radiation Assessment Detector (RAD) started detecting the biggest event since the landing of the Curiosity rover in August 2012 on the surface of Mars which is about 160° east from Earth in the heliosphere. This was the first SEP event seen on the surface of two planets. SEPs were also transported across magnetic field lines throughout the heliosphere and were detected at the back side of the Sun where the eruption was centered. Meantime, the intense and wide shock also propagated into the interplanetary space,

reached Earth on its west edge after about 50.5 h and hit Mars on its east flank after about 59 h, causing the biggest depression of the galactic cosmic ray flux measured by RAD on Mars.

In particular, they combined both remote-sensing and in-situ observations of the 10 September 2017 eruptions at Earth, STEREO-A and also at Mars to study this event in a thorough manner. They addressed both the CME and shock propagation as well as the arrival of energetic protons at these locations using a data-constrained modeling approach to improve the understanding of the complexity of such extreme events in order to better forecast them and to mitigate their potential damages. First, they analyzed the event starting from the eruptions at the surface of the Sun and noticed the launch of 3 CMEs within hours from the same active region heading towards similar directions based on multi-viewpoint solar images. With the help of such stereoscopic images and 3D CME reconstruction techniques, they obtained the early kinematics of the 3 CMEs and modeled their propagation as they headed out from the Sun towards a direction more oriented towards Mars than to Earth (which are about 160° apart in heliospheric longitude). The CME-related shock was very wide and they derived it to be at least 220 degrees in its longitudinal extent in the solar equatorial plane. It impacted Earth in about 2 days after the launch. In the direction of Mars, it propagated faster and arrived at Mars (1.5 AU from the Sun) only about 10 hours later than its arrival at Earth. Using both an analytic drag-based model and the MHD ENLIL model, they simulated the propagation of 3 CMEs and the shock arrivals at two planets. In order to best match the modeled results with observations, they concluded that the shock experienced rather different interplanetary journeys in two directions. Towards Earth, the shock was not driven by a magnetic structure and experienced more deceleration on its way. Towards Mars, the very fast CME and its driven shock caught up with the previous 2 CMEs which likely swept the way for the successive one to experience less drag; all three CMEs had similar directions and speeds one faster than another and they likely merged as an entity and propagated further together. The arrival of the shock and the merged CME caused the biggest Forbush decrease in the Galactic Cosmic Ray flux RAD measures (about 23%).

The SEPs were widely spread and observed at 3 different locations in the heliosphere: Earth, Mars, and also STEREO-A spacecraft which was about 230° east from Earth. Upon the event onset at the Sun, Earth was already nicely connected to the central of the shock and flare region favoring high-energy particles triggering the Ground Level Enhancement (GLE) at multiple neutron monitors on the ground within tens of minutes. The high energy particle fluxes observed at Earth also had a rather gradual declining time profile especially after the shock passed Earth. This is likely caused by particles trapped by a Stream Interaction Region (SIR) before it reached Earth. Alternatively, STEREO-A was connected to the back side of the Sun where the eruption was centered and energetic proton fluxes only started gradually increasing 16 hours later. This delay was most probably attributed to cross-field diffusion of particles transported across the interplanetary magnetic field lines. More interestingly, the SEP onset at Mars was nearly 4 hours later than the eruption at the Sun. Their investigation suggested three scenarios for explaining the trigger of the GLE at Mars. (i) Particles were continuously accelerated and/or re-accelerated by the interplanetary shock as it was propagating outwards and started connecting to east-side interplanetary magnetic field lines. This magnetic connection was established upon/shortly after the SEP onset at Mars; (ii) particles were transported across the field lines and arrived at Mars similar to the situation at STEREO-A; (iii) an SIR structure (a different one from the previous one passing Earth) located closer to the central of the eruption was injected with SEPs at an earlier phase of the event and served as a reservoir of particles and favored the GLE onset at Mars when it passed by Mars. They believed that the 3 scenarios are not contradictory and could be complementary.

Their detailed study on the 10 September 2017

event suggested that in order to better predict the ICME and SEP arrival and their potential space weather impact at different heliospheric locations, it is important to consider (i) the eruption of the flare and CME at the Sun, (ii) the evolution of the ICME kinematics, especially during interactions of different CMEs and (iii) the dynamic heliospheric conditions at different locations in the heliosphere such as the varying solar wind speeds and the stream interaction regions. Besides, it is also necessary to include, as much as possible, both the remote-sensing and in-situ observations of the events in all possible aspects. If STEREO-B were still in service, it could have had the most head-on observation of the shock of the magnetic structure of the CMEs and people would learn in better detail how the 3 CMEs were merged/interacted and how fast the central part of the shock was propagating.

To better understand and forecast the potential radiation impacts induced by extreme SEP events, Guo *et al.*[122,123] developed a GEANT4-based particle transport model implemented with Martian atmospheric and regolith properties to transport Galactic Cosmic Ray (GCR) particles from deep space down to the surface of Mars. Guo *et al.*[124] also benchmarked this model using in-situ RAD measurements of charged particle spectra on the surface of Mars. Recently, Guo *et al.*[125] used this validated model to calculate the surface radiation for different input spectra at the top of the atmosphere. It is well known that the deep-space SEP differential energy spectrum at high energies is often given by a power law. They calculated the induced Martian surface radiation by a variety of SEP events with different properties such as their energy range, intensity, power-law index, and studied the correlation between the induced radiation and their properties statistically. For the first time, they found a pivot energy (about 300 MeV) at which the SEP flux alone can be used to determine the Martian surface dose rate for large SEP events with proton energy extending above about 500 MeV. In other words, with a fixed flux at this pivot energy, the variation of the power-law spectral index does not affect the surface radiation. This finding advances understanding of the radiation risks during possibly adverse space weather conditions. Together with SEP injection and interplanetary transport models, people can provide instantaneous and quantitative alerts for future human missions at Mars upon the onset of large SEP events at the Sun.

Because of the precise measurements of the cosmic ray electron flux by the PAMELA and AMS02, electron Forbush decreases (F_d) have recently been observed for the first time. This serves as motivation of Luo *et al.*[126] to perform a numerical study of electron Forbush decreases with an advanced time-dependent, three-dimensional (3D) stochastic differential equation model, developed earlier to study proton F_d. The model includes a realistic interstellar electron spectrum reconstructed from Voyager observations, and diffusion and drift coefficients to reproduce the modulated spectrum observed by PAMELA in 2009. On the basis of this numerical model, electron F_d profiles for a range of rigidities are simulated. In addition, a systematic comparison between electron and proton F_d during different solar polarity epochs is performed. This approach gives insight into the rigidity dependence of the heliospheric diffusion coefficients and of drift effects over two magnetic field polarity cycles. They found that during an $A>0$ epoch, the recovery time of a 1 GV proton F_d is remarkably shorter than the 1 GV electrons, whereas the electron F_d displays a faster recovery during an $A<0$ epoch. This model clear predicts a charge-sign dependent effect in the recovery time of F_d but less so for their magnitude.

In modeling the transport process of Solar Energetic Particles (SEPs) in the heliosphere, the previous simulation works often simplify the solar wind velocity as radial and constant, and treat the magnetic field as Parker spiral. In order to fully understand the effect of solar wind velocity and interplanetary magnetic field on the particles' transport process, a realistic background solar wind and magnetic field are required. Wei *et al.*[127] used the focused transport model to investigate the transport of SEPs in the solar wind velocity and the magnetic field generated by the 3D high-resolution MHD

model with a six-component grid. They found that in the uncompressed solar wind, the time intensity profiles of energetic particles showed a similar trend in both the MHD background and the Parker magnetic field assumption. However, the simulated SEP flux displayed an enhancement in the decay phase when a compression region swept past the local observer. Through investigating various effects, they found that the magnetic focusing effect was primarily responsible for the intensity enhancement, suggesting that the magnetic focusing effect had an important influence on the transport of SEPs. Further, they showed that the magnetic focusing could also be effective in large heliocentric distances.

Since May 2011, the Alpha Magnetic Spectrometer (AMS-02) on board the International Space Station has provided monthly cosmic proton fluxes for various low-rigidity levels ($P<50$ GV). These precise measurements, in terms of high time and rigidity resolution, have provided a good opportunity to study cosmic ray modulation over a wide range of rigidities, together with transient events. Luo *et al.*[128] constructed a comprehensive numerical transport model, which was based on Parker's transport equation that included all known physical mechanisms: diffusion, convection, drift, and adiabatic cooling. Propagating diffusion barriers to simulate Forbush decreases ($F_{\rm d}$) and Global Merged Interaction Regions (GMIRs) had also been incorporated: (i) utilizing a time-varying tilt angle of the heliospheric current sheet and interplanetary magnetic field, the general trend of the time variation of cosmic proton fluxes has been reproduced; (ii) the $F_{\rm d}$ events in October 2011 and March 2012 have been simulated, and the first GMIR event in solar cycle 24 has also been simulated and studied; and (iii) the rigidity dependence of the proton fluxes, as revealed by the AMS-02 data, had been reproduced with the appropriate chosen rigidity dependent diffusion coefficients. In order to reproduce the proton observations, they found that apart from the transient events, the derived mean free paths in interplanetary space also needed to be changed with time.

A 3D MHD solar wind model is an important tool for research and forecast of ambient solar wind. Employing boundary condition driven by solar photospheric magnetic field observation, Li *et al.*[129] developed a time-dependent 3D MHD interplanetary solar wind model. Using this model, they simulated the solar wind of Year 2008, and analyzed the evolution of global solar wind structures and the connection between interplanetary in-situ measurements and corona structures during that year. They realized a set of procedures, which evaluate the quality of predictions for both continuous solar wind parameters and characteristic structures of the solar wind. The evaluation results indicated that their model satisfactorily reproduced the large sale structure of the ambient solar wind during Year 2008. The correlation coefficient between observed and simulated speeds is higher than 0.6. The strength of simulated interplanetary magnetic field matched observation well. All interplanetary magnetic field reverses and 82.76% of the stream interaction regions were captured by their model. The false alarm rate of the interplanetary magnetic field reverse prediction is only 6.67% while that of the stream interaction region is only 11.11%. The errors in predicting the arrival time of these two structures were about one day.

Kong *et al.*[130] presented numerical modeling of particle acceleration at coronal shocks propagating through a streamer-like magnetic field by solving the Parker transport equation with spatial diffusion both along and across the magnetic field. They showed that the location on the shock where the high-energy particle intensity is the largest, depends on the energy of the particles and on time. The acceleration of particles to more than 100 MeV mainly occurs in the shock-streamer interaction region, due to perpendicular shock geometry and the trapping effect of closed magnetic fields. A comparison of the particle spectra to that in a radial magnetic field shows that the intensity at 100 MeV (200 MeV) is enhanced by more than one order (two orders) of magnitude. This indicates that the streamer-like magnetic field can be an important factor in producing large solar energetic particle events. They also showed that the energy spectrum integrated over the simulation domain

consists of two different power laws. Further analysis suggested that it may be a mixture of two distinct populations accelerated in the streamer and open field regions, where the acceleration rate differs substantially. Their calculations also showed that the particle spectra are affected considerably by a number of parameters, such as the streamer tilt angle, particle spatial diffusion coefficient, and shock compression ratio. While the low-energy spectra agree well with standard diffusive shock acceleration theory, the break energy ranges from 1 MeV to 90 MeV and the high-energy spectra can extend to 1 GeV with a slope of 2~3.

Shock acceleration is considered one of the most important mechanisms for the acceleration of astrophysical energetic particles. Kong *et al.*[131] investigated the time evolution of the accelerated particle energy spectrum in the downstream of the shock, in order to understand the acceleration mechanism of energetic particles. From simulation results they obtained power-law energy spectra with bend-over energy, E_0, increasing with time. With the particle mean acceleration time and mean momentum change during each cycle of the shock crossing from the diffusive shock acceleration model (following Drury), a time-dependent differential equation for the maximum energy, $E_{\rm acc}$, of particles accelerated at the shock can be approximately obtained. They assumed the theoretical bend-over energy as $E_{\rm acc}$. It was found that the bend-over energy from simulations agrees well with the theoretical bend-over energy using the nonlinear diffusion theory, NLGCE-F, in contrast to that using the classic quasi-linear theory.

Using test particle simulations, Qin *et al.*[132] studied electron acceleration at collisionless shocks with a two-component model turbulent magnetic field with slab component including dissipation range. They investigated the importance of the shock-normal angle $\theta_{\rm Bn}$, magnetic turbulence level $(b/B_0)^2$, and shock thickness on the acceleration efficiency of electrons. It is shown that at perpendicular shocks the electron acceleration efficiency is enhanced with the decrease of $(b/B_0)^2$, and at $(b/B_0)^2$=0.01 the acceleration becomes significant due to a strong drift electric field with longtime particles staying near the shock front for Shock Drift Acceleration (SDA). In addition, at parallel shocks, the electron acceleration efficiency is increasing with the increase of $(b/B_0)^2$, and at $(b/B_0)^2$=10.0 the acceleration is very strong due to sufficient pitch-angle scattering for first-order Fermi acceleration, as well as due to the large local component of the magnetic field perpendicular to the shock-normal angle for SDA. On the other hand, the high perpendicular shock acceleration with $(b/B_0)^2$= 0.01 is stronger than the high parallel shock acceleration with b $(b/B_0)^2$=10.0, the reason might be the assumption that SDA is more efficient than first-order Fermi acceleration. Furthermore, for oblique shocks, the acceleration efficiency is small no matter whether the turbulence level is low or high. Moreover, for the effect of shock thickness on electron acceleration at perpendicular shocks, they showed that there exists the bend over thickness, $L_{\rm diff,b}$. The acceleration efficiency does not noticeably change if the shock thickness is much smaller than $L_{\rm diff,b}$. However, if the shock thickness is much larger than $L_{\rm diff,b}$, the acceleration efficiency starts to drop abruptly.

Shen and Qin[133] studied the 11- and 22-year modulation of Galactic Cosmic Rays (GCRs) in the inner heliosphere using a numerical model. Based on the numerical solutions of Parker's transport equations, the model incorporates a modified Parker heliospheric magnetic field, a locally static time-delayed heliosphere, and a time-dependent diffusion coefficients model in which an analytical expression of the variation of magnetic turbulence magnitude throughout the inner heliosphere is applied. Furthermore, during solar maximum, the solar magnetic polarity is determined randomly with the possibility of $A>0$ decided by the percentage of the solar north polar magnetic field being outward and the solar south polar magnetic field being inward. The computed results are compared at various energies with several GCR observations, *e.g.*, IMP 8, EPHIN on board SOHO, Ulysses, and Voyager 1 and 2, and they show good agreement. They showed that their model had successfully reproduced the 11- and 22-year modulation cycles.

Galactic Cosmic-Ray (GCR) helium and heavier ions are important sources of space radiation, and their elemental spectra and composition can help us better understand the transport in both the galaxy and the heliosphere. Shen *et al.*[134] used a model based on the numerical solution of Parker's transport equation to study the modulation of GCR helium and heavier ions in the inner heliosphere. The model incorporates a modified Parker heliospheric magnetic field, time-dependent diffusion and drift model, time-delayed heliosphere, and randomly determined solar magnetic polarity during solar maximum. They set the outer boundary of modulation at 85 AU, and the reference unmodulated GCR energy spectra for GCR helium and heavier ions, which are assumed to have a general form, are determined by fitting the numerical results to the selected GCR measurements, *e.g.*, BESS, ACE/CRIS, HEAO-3-C2, *etc.* In addition, they used the Sun's polar magnetic field data from NSO/NISP to determine the possibility of $A>0$ during the recent solar maximum, and it gives an improved numerical result during the period 2013–2015. Finally, the fitted unmodulated GCR energy spectra were used to study the long-term modulation of GCRs of helium and heavier ions, and the computed results show good agreement with various GCR measurements.

The equation $k_{zz}=\mathrm{d}\sigma^2/(2\mathrm{d}t)$ describing the relation of the parallel diffusion coefficient k_{zz} with the displacementvariance σ^2 (hereafter DCDV) is a well-known formula. Wang and Qin[135] found that DCDV is only applicable to two kinds of transport equations of the isotropic distribution function, one without cross-terms and the other without a convection term. Here, by employing the more general transport equation, *i.e.*, the variable coefficient differential equation derived from the Fokker-Planck equation, a new equation of k_{zz} as a function of σ^2 is obtained. They found that DCDV is the special case of the new equation. In addition, another equation of k_{zz} as a function of σ^2 corresponding to the telegraph equation is also investigated preliminarily.

It is very important to understand the stochastic diffusion of energetic charged particles in the non-uniform background magnetic field in plasmas of astrophysics and fusion devices. Using different methods considering an along-field adiabatic focusing effect, various authors derived a parallel diffusion coefficient $k_\parallel$ and its correction T to $k_{\parallel 0}$, where $k_{\parallel 0}$ is the parallel diffusion coefficient without an adiabatic focusing effect. Using the improved perturbation method developed by He and Schlickeiser and iteration process, Wang and Qin[136] obtained a new correction T' to $k_{\parallel 0}$. Furthermore, by employing the isotropic pitch-angle scattering model $D_{\mu\mu}=D(1-\mu^2)$, they found that T' has a different sign from that of T. In this paper, the spatial perpendicular diffusion coefficient $k_\perp$ with the adiabatic focusing effect is also obtained.

Interplanetary collisionless shocks are known to be a strong source of energetic charged particles up to tens of MeV (or even to a few hundred MeV). However, the acceleration of electrons at collisionless shocks is still not well understood, but it is suspected that the suprathermal electrons of the solar wind including the strahl, halo, and super halo populations could provide seed particles for the shock acceleration in the interplanetary medium. On the issue of ICME-driven Shock Acceleration of Solar Wind Suprathermal Electrons, Yang *et al.*[137-139] made a comprehensive study of in situ electron acceleration during 74 shocks driven by ICMEs with good suprathermal electron observations by the Wind 3DP instrument at 1 AU from 1995 through 2014. Among the selected 59 quasi-perpendicular (15 quasi-parallel) shock cases, about 86% (60%), 62% (36%), and 17% (7%) show significant electron flux enhancements of $J_D/J_A>1.5$ across the shock, respectively at 0.43, 1.95, and 40 keV, where J_D and J_A are the electron flux in the shock's downstream and the preceding ambient solar wind. For significantly shocked suprathermal electrons, the differential flux J_D positively correlates most with the magnetosonic Mach number, while the flux enhancement J_D/J_A positively correlates most with the magnetic compression ratio, among the shock parameters. Both J_D and J_A generally fit well to a double-power-law spectrum at 0.4~100 keV, $J\propto E^{-\beta}$, with an index of $\beta_1\approx 2\sim 6$ below break energy

of e_b (which is typically about 2 keV) and an index of $\beta_2 \approx 2.0$~3.2 at energies above. Furthermore, J_D/J_A mostly peaks in the directions perpendicular to the interplanetary magnetic field at 0.4~50 keV. These results suggest that both quasi-parallel and quasi-perpendicular shocks accelerate electrons in situ at 1 AU mainly via shock drift acceleration, with an acceleration efficiency probably affected by the induced electric field at the shock surface.

Liu *et al.*[140] made a case study of the in situ acceleration of solar wind suprathermal electrons at the two quasi-perpendicular bow-shock crossings on 4 November 2015, combining the Wind 3D Plasma and Energetic Particle measurements of ambient solar wind suprathermal electrons and Magnetospheric Multiscale mission measurements of shocked suprathermal electrons. In both cases, the omni-directional differential fluxes of shocked suprathermal electrons in the downstream exhibit a double-power-law energy spectrum with a spectral index of about 3 at energies below a downward break e_b near 40 keV and index of 6 at energies above, different from the unshocked suprathermal electrons observed in the ambient solar wind. At energies below (above) e_b, the observed electron flux ratio between the downstream and ambient solar wind, J_D/J_A, peaks near 90° PA (becomes roughly isotropic). Electrons at e_b have an average electron gyrodiameter (across bow shock) comparable to the shock thickness. These suggested that the bow-shock acceleration of suprathermal electrons is likely dominated by the shock drift acceleration mechanism. For electrons at energies below (above) e_b, their estimated drift time appears to be roughly energy independent (decrease with energy), leading to the formation of a double-power-law spectrum substantially steepening at a break that's determined by the shock thickness.

11 Machine Learning Methods in Space Weather and Other Aspects

A hybrid intelligent source surface model applying the artificial neural network tactic for solar wind speed prediction was given by Yang *et al.*[141]. The model was a hybrid system merging various observational and theoretical information as input. Different inputs were tested including individual parameters and their combinations in order to select an optimum. Then, the optimal model was implemented for prediction. The prediction was validated by both error analysis and event-based analysis from 2007 to 2016. The overall correlation coefficient is 0.74, and the root-mean-square error is 68 km·s^{-1}. The probability for detecting a high-speed-event is 0.68, the positive predicted value is 0.73, and the threat score is 0.55.

As arriving at the Earth, ICME will interact with the Earth's magnetosphere and cause geomagnetic storms. Ye and Feng[142] obtained the ICME event set from Richardson and Cane's near Earth ICME list, and the input features were extracted based on interplanetary solar wind and magnetic data during ICME disturbance. A total of 483 ICME events from 1996 to 2006 were chosen. 13 magnetic and kinetic features were finally selected for the training of the machine learning model. Rank of each feature's Fisher score indicated that the duration of the south-directed interplanetary magnetic field that was larger than 10 nT and the increase of solar wind speed at the upstream shock or wave disturbance was closely related to the geoeffectiveness of ICME events, which was consistent with those former statistical results. The trained Radial Basis Function Support Vector Machine (RBF-SVM) could determine whether an ICME event would trigger moderate or stronger geomagnetic storms ($Dst \leqslant -50$ nT) effectively with an accuracy of 0.78±0.08. The results showed that RBF-SVM could be used as a powerful tool in further analysis, and the better prediction of the geoeffectiveness of ICME would be obtained.

The global distribution of magnetic field and other plasma parameters on the source surface, which Yang and Shen[143] set at 2.5 solar radii, is important for coronal and heliospheric modeling. They introduced a new data-driven self-consistent method to obtain the global distribution of different parameters.

The magnetic and polarized Brightness (pB) observations were used to derive the magnetic field and electron density on the source surface, respectively. Then, an Artificial Neural Network (ANN) machine learning technique was applied to establish an empirical relation among the solar wind velocity, the magnetic field properties, and the electron density. The ANN was trained with global observational data, and is validated to be more reliable than the Wang-Sheeley-Arge (WSA) model for reconstructing the solar wind velocity, especially at high latitudes. The plasma temperature distribution was derived by solving a simplified 1D MHD equation system on the source surface. Using the method introduced above they obtained the global distribution for all the parameters self-consistently based on magnetic and polarized brightness observations. The modeling results of four Carrington rotations from different solar cycle phases were presented to validate the method.

Lu *et al.*[144] presented a kind of large area subwavelength cavity antenna with artificial permeability-negative metamaterials at GHz range. The antenna has the advantages of flatness, ultra-thin thickness, high gain, and good directivity. The optimal receiving area of the antenna is mainly determined by the size of the radiation source. Its directivity and side lobe cancellation mainly depend on the patterns of the patch array as the radiation source. It was found that the antenna with non-uniform distributed patch array as the radiation source has better performance than that with uniform distributed patch array patterns. Otherwise, this type of metamaterial antenna has nearly the same performance compared to that of parabolic antenna with equal radiation aperture, so it has potential applications to replace the traditional large aperture parabolic antenna.

References

[1] TIAN H, ZHU X S, PETER H, *et al.* Magnetic reconnection at the earliest stage of solar flux emergence [J]. *Astrophys. J.*, 2018, **854**(2):174

[2] CHEN Y J, TIAN H, PETER H, *et al.* Flame-like Ellerman bombs and their connection to solar UV bursts [J]. *Astrophys. J. Lett.*, 2019, **875**:L30

[3] SAMANTA T, TIAN H, YURCHYSHYN V, *et al.* Generation of solar spicules and subsequent atmospheric heating [J]. *Science*, 2019, **366**:890-894

[4] TIAN H, YURCHYSHYN V, PETER H, *et al.* Frequently occurring reconnection jets from sunspot light bridges [J]. *Astrophys. J.*, 2018, **854**:92

[5] ZHANG J W, TIAN H, SOLANKI S K, *et al.* Dark structures in sunspot light bridges [J]. *Astrophys. J.*, 2018, **865**:29

[6] ZHU Y J, KOWALSKI A F, TIAN H, *et al.* Modeling Mg II *h*, *k* and triplet lines at solar flare ribbons [J]. *Astrophys. J.*, 2019, **879**:19

[7] DU G H, CHEN Y, ZHU C M, *et al.* Formation of large-scale coronal loops interconnecting two active regions through gradual magnetic reconnection and an associated heating process [J]. *Astrophys. J.*, 2018, **860**:40

[8] ZHENG R S, CHEN Y, FENG S W, *et al.* An extreme-ultraviolet wave generating upward secondary waves in a streamer-like solar structure [J]. *Astrophys. J.*, 2018, **858**(1). DOI:10.3847/2041-8213/aabe87

[9] ZHENG R S, XUE Z K, CHEN Y, *et al.* The initial morphologies of the wavefronts of extreme ultraviolet waves [J]. *Astrophys. J.*, 2019, **871**(2):9

[10] CALLY P S, XIONG M. Sensitivity of coronal loop sausage mode frequencies and decay rates to radial and longitudinal density inhomogeneities: a spectral approach [J]. *J. Phys. A: Math. Theor.*, 2018, **51**:025501

[11] RUAN W Z, YAN L M, HE J S, *et al.* A new method to comprehensively diagnose shock waves in the solar atmosphere based on simultaneous spectroscopic and imaging observations [J]. *Astrophys. J.*, 2018, **860**:99

[12] ZHANG L, HE J S, ZHAO J S, *et al.* Nature of magnetic holes above ion scales: a mixture of stable slow magnetosonic and unstable mirror modes in a double-polytropicscenario [J]. *Astrophys. J.*, 2018, **864**:355

[13] YANG L P, ZHANG L, HE J S, *et al.* Coexistence of slow-mode and Alfvén-mode waves and structures in 3D compressive MHD turbulence [J]. *Astrophys. J.*, 2018, **866**: 41

[14] SONG X J, ZUO P B, FENG X S, *et al.* Abnormal magnetospheric magnetic gradient direction reverse around the indented magnetopause [J]. *Astrophys. Space Sci.*, 2019, **364**:146

[15] YANG L P, LI H, LI S T, *et al.* Energy occupation of waves and structures in 3D compressive MHD turbulence [J]. *Mon. Not. Roy. Astron. Soc.*, 2019, **488**: 859-867

[16] WANG X, TU C Y, HE J S, *et al.* On the full-range β dependence of ion-scale spectral break in the solar wind turbulence [J]. *Astrophys. J.*, 2018, **857**:136

[17] WANG X, TU C Y, HE J S. 2-D isotropic feature of solar wind turbulence as shown by self-correlation level contours at hours time scales [J]. *Astrophys. J.*, 2019, **871**:93

[18] WANG X, ZHAO L, TU C Y, *et al.* 2 Alfvenicity of quiet-Sun-associated wind during solar maximum [J]. *Astrophys. J.*, 2019, **871**:204

[19] DUAN D, HE J S, PEI Z T, *et al.* Angular independence of break position for magnetic power spectral density in solar wind turbulence [J]. *Astrophys. J.*, 2018, **865**:89

[20] HE J S, DUAN D, WANG T Y, *et al.* Direct measurement of the dissipation rate spectrum around ion kinetic scales in space plasma turbulence [J]. *Astrophys. J.*, 2019, **880**:121

[21] HE J S, WANG Y, SORRISO VALVO L. Unified quantitative description of solar wind turbulence intermittency in both inertial and kinetic ranges [J]. *Astrophys. J.*, 2019, **873**:80

[22] ZHU X Y, HE J S, VERSCHAREN D, *et al.* Composition of wave modes in magnetosheath turbulence from sub-ion to sub-electron scales [J]. *Astrophys. J.*, 2019, **878**:48

[23] AWASTHI A K, LIU R, WANG H M, *et al.* Pre-eruptive magnetic reconnection within a multi-flux-rope system in the solar corona [J]. *Astrophys. J.*, 2018, **857**: 124

[24] SU Y N, LIU R, LI S W, *et al.* High-resolution observations of flares in an arch filament system [J]. *Astrophys. J.*, 2018, **855**:77

[25] AWASTHI A K, LIU R, WANG Y M. Double-decker filament configuration revealed by mass motions [J]. *Astrophys. J.*, 2019, **872**:109

[26] AWASTHI A K, LIU R. Mass motion in a prominence bubble revealing a kinked flux rope configuration [J]. *Front. Phys.*, 2019, **7**:218

[27] WANG H M, LIU R, LI Q, *et al.* Extending counter-streaming motion from an active region filament to a sunspot light bridge [J]. *Astrophys. J. Lett.*, 2018, **852**:L18

[28] LIU R, .CHEN J, WANG Y M. Disintegration of an eruptive filament via interactions with quasi-separatrix layers [J]. *Sci. China: Phys., Mech. Astron.*, 2018, **61**:069611

[29] CHENG Z X, WANG Y M, LIU R, *et al.* Plasma motion inside flaring regions revealed by Doppler shift information from SDO/EVE observations [J]. *Astrophys. J.*, 2019, **857**:93

[30] CHEN J, LIU R, LIU K, *et al.* Extreme ultraviolet late phase of solar flares [J]. *Astrophys. J.*, 2020, 890(2): 158

[31] LI X L, WANG Y M, LIU R, *et al.* Reconstructing solar wind inhomogeneous structures from stereoscopic observations in white-light: small transients along the Sun-Earth line [J]. *J. Geophys. Res.*, 2018, **123**:7257-7270

[32] RUAN G, SCHMIEDER B, MEIN P, *et al.* On the dynamic nature of a quiescent prominence observed by IRIS and MSDP spectrographs [J]. *Astrophys. J.*, 2018, **865**:123

[33] RUAN G, JEJ I S, SCHMIEDER B, *et al.* Diagnostics of the prominence plasma from *Hα* and Mg II spectral observations [J]. *Astrophys. J.*, 2019, **886**:134

[34] SONG H Q, ZHOU Z J, LI L P, *et al.* The reversal of a solar prominence rotation about its ascending direction during a failed eruption [J]. *Astrophys. J.*, 2018, **864**:L37

[35] ZHENG R S, YANG S H, RAO C H, *et al.* A confined partial eruption of double-decker filaments [J]. *Astrophys. J.*, 2019, **875**:71

[36] ZHENG R S, CHEN Y, HUANG Z H, *et al.* Two-sided-loop jets associated with magnetic reconnection between emerging loops and twisted filament threads [J]. *Astrophys. J.*, 2018, **861**:108

[37] RUAN G, SCHMIEDER B, MASSON S, *et al.* Bidirectional reconnection outflows in an active region [J]. *Astrophys. J.*, 2019, **883**:52

[38] NING H, CHEN Y, WU Z, *et al.* Two-stage energy release process of a confined flare with double HXR peaks [J]. *Astrophys. J.*, 2018, **854**:178

[39] NING H, CHEN Y, LEE J, *et al.* Broken-up spectra of the loop-top hard X-ray source during a solar limb flare [J]. *Res Astron. Astrophys.*, 2019, **19**:173

[40] KONG X, GUO F, SHEN CC, *et al.* The acceleration and confinement of energetic electrons by a termination shock in a magnetic trap: an explanation for nonthermal loop-top sources during solar flares [J]. *Astrophys. J.*, 2019, **887**:L37

[41] FENG S W, CHEN Y, LI C Y, *et al.* Harmonics of solar radio spikes at metric wavelengths [J]. *Sol. Phys.*, 2018, **293**:39

[42] FENG S W. The properties of solar radio spikes with harmonics and the associated EUV brightenings [J]. *Astrophys. Space Sci.*, 2019, **364**:4

[43] VASANTH V, CHEN Y, LV M S, *et al.* Source imaging of a moving type IV solar radio burst and is role in tracking coronal mass ejection from the inner to the outer corona [J]. *Astrophys. J.*, 2019, **870**:30

[44] LIU H, CHEN Y, CHO K, *et al.* A solar stationary type IV radio burst and its radiation mechanism [J]. *Sol. Phys.*, 2018, **293**:58

[45] KOVAL A, CHEN Y, STANISLAVSKY A, *et al.* Simulation of focusing effect of traveling ionospheric disturbances on meter-decameter solar dynamic spectra [J]. *J. Geophys. Res.: Space Phys.*, 2018, **123**(11):8940

[46] KOVAL A, CHEN Y, TSUGAWA T, *et al.* Direct observations of traveling ionospheric disturbances as focusers of solar radiation: spectral caustics [J]. *Astrophys. J.*, 2019, **877**(2):98

[47] LI C, CHEN Y, KONG X, *et al.* Effect of the temperature of background plasma and the energy of energetic electrons on Z-mode excitation [J]. *Astrophys. J.*, 2019, **880**:31

[48] WU Z, CHEN Y, NING H, *et al.* Gyrosynchrotron emission generated by nonthermal electrons with the energy spectra of Na broken power law [J]. *Astrophys. J.*, 2019, **871**:22

[49] LI D, YUAN D, SU Y N, *et al.* Non-damping oscillations at flaring loops [J]. *Astron. Astrophys.*, 2018, 617:A86

[50] YUAN D, FENG S, LI D, *et al.* A compact source for quasi-periodic pulsation in an M-class solar flare [J]. *Astrophys. J. Lett*, 2019, **886**:L25

[51] ZOU P, JIANG C W, WEI F S, *et al.* A statistical study of solar filament eruptions that form high-speed coronal mass ejections [J]. *Astrophys. J. Lett*, 2019, **884**:157

[52] ZOU P, JIANG C W, WEI F S, *et al.* Continuous null-point magnetic reconnection builds up a Torus unstable magnetic flux rope triggering the X9.3 flare in solar AR12673 [J]. *Astrophys. J.*, 2020, **890**:10

[53] SAMANTA T, TIAN H, NAKARIAKOV V M. Evidence for vortex shedding in the Sun's hot corona [J]. *Phys. Rev. Lett.*,

2019, **123**:035102

[54] SONG Y L, TIAN H. Investigation of white-light emission in circular-ribbon flares [J]. *Astrophys. J.*, 2018, **867**:159

[55] YE Y D, KORSÓS M B, ERDÉLYI R. Detailed analysis of dynamic evolution of three Active Regions at the photospheric level before flare and CME occurrence[J]. *Adv. Space Res.*, 2018, **61**:673-682

[56] WANG R, LIU Y D, HU H D, *et al.* A solar eruption with relatively strong geoeffectiveness originating from active region peripheral diffusive polarities [J]. *Astrophys. J.*, 2018, **863**:81

[57] WANG R, LIU Y D, HOEKSEMA J T, *et al.* Roles of photospheric motions and flux emergence in the major solar eruption on 2017 September 6 [J]. *Astrophys. J.*, 2018, **869**:90

[58] HU H D, LIU Y D, ZHU B, *et al.* Effects of coronal density and magnetic field distributions on a global solar EUV wave [J]. *Astrophys. J.*, 2019, **878**:106

[59] WANG D, LIU R, WANG Y M, *et al.* Unraveling the links among sympathetic eruptions [J]. *Astrophys. J.*, 2018, **869**:177

[60] LIU R, WANG Y M, LEE J, *et al.* Impacts of EUV wavefronts on coronal structures in homologous coronal mass ejections [J]. *Astrophys. J.*, 2019, **870**:15

[61] JIANG C W, FENG X S, HU Q. Formation and eruption of an active region sigmoid. II. Magnetohydrodynamic simulation of a multistage eruption [J]. *Astrophys. J.*, 2018, **866**:96

[62] JIANG C W, ZOU P, FENG X S, *et al.* Magnetohydrodynamic simulation of the X9.3 flare on 2017 September 6:evolving magnetic topology [J]. *Astrophys. J.*, 2018, **869**:13

[63] JIANG C W, DUAN A Y, FENG X S, *et al.* Reconstruction of a highly twisted magnetic flux rope for an interactive-region X-class solar flare [J]. *Front. Astron. Space Sci.,* 2019, **6**:63

[64] DUAN A Y, JIANG C W, HE W, *et al.* A study of pre-flare solar coronal magnetic fields: magnetic flux ropes [J]. *Astrophys. J.,* 2019, **884**:73

[65] HE W, JIANG C W, ZOU P, *et al.* Data-driven MHD simulation of the formation and initiation of a large-scale preflare magnetic flux rope in AR 12371 [J]. *Astrophys. J.,* 2019, **892**:9

[66] MIAO Y H, LIU Y, ELMHAMDI A, *et al.* Two quasi- periodic fast-propagating magnetosonic wave events observed in active region NOAA 11167 [J]. *Astrophys. J.,* 2020, **889**:139

[67] YUAN D, LIU W, WALSH R. Investigating sub-pixel 45-second periodic wobble in SDO/AIA data from January to August 2012 [J]. *Sol. Phys.,* 2018, **293**:147

[68] YUAN D, SHEN Y D, LI H B, *et al.* Multilayered Kelvin-Helmholtz instability in the solar corona [J]. *Astrophys. J. Lett*, 2019, **884**:L51

[69] ZOU P, JIANG C W, FENG X S, *et al.* A two-step magnetic reconnection in a confined X-class flare in solar active region12673 [J]. *Astrophys. J.*, 2019, **870**:97

[70] WANG Z H, FENG X S, ZHANG J C. Multispacecraft observation of unidirectional and bidirectional Alfvén waves within large-scale magnetic clouds [J]. *Astrophys. J. Lett.*, 2019, **887**:L18

[71] HE W, LIU Y D, HU Y D, *et al.* A stealth CME bracketed between slow and fast wind producing unexpected geoeffectiveness [J]. *Astrophys. J.*, 2018, **860**:78

[72] LIU M Z, LIU Y D, YANG Z W, *et al.* Kinetic properties of an interplanetary shock propagating inside a coronal mass ejection [J]. *Astrophys. J.*, 2018, **859**:L4

[73] CHEN C, LIU Y D, WANG R, *et al.* Characteristics of a gradual filament eruption and subsequent CME propagation in relation to a strong geomagnetic storm [J]. *Astrophys. J.*, 2019, **884**:90

[74] LIU Y D, ZHU B, ZHAO X W. Geometry, kinematics, and heliospheric impact of a large CME-driven shock in 2017 September [J]. *Astrophys. J.*, 2019, **871**:8

[75] ZHAO X W, LIU Y D, HU H D, *et al.* Quantifying the propagation of fast coronal mass ejections from the Sun to interplanetary space by combining remote sensing and multi-point in situ observations [J]. *Astrophys. J.*, 2019, **882**:122

[76] LIU Y D, ZHAO X W, HU H D, *et al.* A comparative study of 2017 July and 2012 July complex eruptions: are solar superstorms "perfect storms" in nature [J]. *Astrophys. J.*, 2019, **241**:15

[77] GOU T Y, LIU R, KLIEM B, *et al.* The birth of a coronal mass ejection [J]. *Sci. Adv.*, 2019, **5**:7004

[78] LIU J J, WANG Y M, ERDELYI R. How many twists do solar coronal jets release [J]. *Front. Astron. Space Sci.*, 2019, **6**:44

[79] WANG W S, ZHU C M, QIU J, *et al.* Evolution of a magnetic flux rope toward eruption [J]. *Astrophys. J.*, 2019, **871**:25

[80] WANG Y M, SHEN C L, LIU R, *et al.* Understanding the twist distribution inside magnetic flux ropes by anatomizing an interplanetary magnetic cloud [J]. *J. Geophys. Res.*, 2018, **123**:3238-3261

[81] ZHAO A, WANG Y M, FENG H Q, *et al.* The twist profile in the cross-section of interplanetary magnetic clouds [J]. *Astrophys. J. Lett.*, 2018, **869**:L13

[82] ZHAO A, WANG Y M, FENG H Q, *et al.* The relationship of magnetic twist and plasma motion in a magnetic cloud [J]. *Astrophys. J.*, 2019, **885**:122

[83] MISHRA W, SRIVASTAVA N, WANG Y M, *et al.* Mass loss via solar wind and coronal mass ejections during solar cycles 23 and 24 [J]. *Mon. Notic. Roy. Astron. Soc.*, 2019, **486**(4): 4671-4685

[84] SHEN C L, XU M J, WANG Y M, *et al.* Why the shock-ICME complex structure is important: Learning from the early 2017 September CMEs [J]. *Astrophys. J.*, 2018, **861**:28

[85] XU M J, SHEN C L, WANG Y M, *et al.* Importance of shock compression in enhancing ICME's geoeffectiveness [J]. *Astrophys. J. Lett.*, 2019, **884**:L30

[86] XU M J, SHEN C L, CHI Y T, *et al.* The enhancement of

the energetic particle intensities in ICMEs [J]. *Astrophys. J.*, 2019, **885**:54

[87] SONG H Q, CHEN Y, QIU J, *et al.* The acceleration process of a solar quiescent filament in the inner corona [J]. *Astrophys. J.*, 2018, **857**:L21

[88] SONG H Q, ZHANG J, CHENG X, *et al.* On the nature of the bright core of solar coronal mass ejections [J]. *Astrophys. J.*, 2019, **883**:43

[89] SONG H Q, ZHANG J, LI L P, *et al.* The structure of solar coronal mass ejections in the extreme-ultraviolet passbands [J]. *Astrophys. J.*, 2019, **887**:124

[90] ZHOU Z L, ZUO P B, FENG X S, *et al.* Intermittencies and local heating in magnetic cloud boundary layers [J]. *Sol. Phys.*, 2019, **294**:149

[91] ZHOU Z L, ZUO P B, WEI F S, *et al.* Intermittent heating in the magnetic cloud sheath regions [J]. *Astrophys. J. Lett*, 2019, **885**:L13

[92] HUANG J, LIU Y C M, PENG J, *et al.* The distributions of iron average charge states in small flux ropes in Interplanetary space: clues to their twisted structures [J]. *J. Geophys. Res.: Space Phys.*, 2018, **123**(9):7167-7180

[93] PENG J, LIU Y C M, HUANG J, *et al.* The warped heliospheric current sheet [J]. *J. Geophys. Res.: Space Phys.*, 2019, **124**(12):9814-9823

[94] LIU Y C M, QI Z H, HUANG J, *et al.* Unusually low density regions in the compressed slow wind: solar wind transients of small coronal hole origin [J]. *Astron. Astrophys.*, 2020, **635**:A49

[95] ZHANG Q, LIU Y C M, ZHANG Q H, *et al.* Statistical study of ion upflow associated with Subauroral Polarization Streams (SAPS) at substorm time [J]. *Geophys. Res.: Space Phys.*, 2020, **125**(3). DOI:org/10.1029/2019JA027163

[96] LIU C A, ZHAO X H, CHEN T, *et al.* Predicting short-term F10.7 with transport models [J]. *Astrophys. Space Sci.*, 2018, **363**:266

[97] QIN G, WU S S.A model of sunspot number with a modified logistic function [J]. *Astrophys. J.*, 2018, **869**:48

[98] ZHOU Z L, WEI F S, FENG X S, *et al.* Observation of interplanetary slow shock pair associated with reconnection exhaust in magnetic cloud boundary layer [J]. *Astrophys. J.*, 2018, **863**:84

[99] WANG Z H, GUO J P, FENG X S, *et al.* The merging of two stream interaction regions within 1 AU: the possible role of magnetic reconnection [J]. *Astrophys. J. Lett.*, 2018, **869**:L6

[100] LIU C X, FENG X S, WANG M P, GUO J P. Dynamic patterns of self-organization inflow in collisionless magnetic reconnection [J]. *Astrophys. Space Sci.*, 2019, **364**:127

[101] HE J S, ZHU X Y, CHEN Y J, *et al.* Plasma heating and Alfvénic turbulence enhancement during two steps of energy conversion in magnetic reconnection exhaust region of solar wind [J]. *Astrophys. J.*, 2018, **856**:148

[102] YANG Y, FENG X S, JIANG C W. An upwind CESE scheme for 2D and 3D MHD numerical simulation in general curvilinear coordinates [J]. *J. Comput. Phys.*, 2018, **371**:850-869

[103] SHEN F, YANG Z C, ZHANG J, *et al.* Three-Dimensional MHD simulation of solar wind using a new boundary treatment: comparison within situ data at Earth [J]. *Astrophys. J.*, 2018, **866**:18

[104] LI C X, FENG X S, XIANG C Q, *et al.* Solar coronal modeling by path-conservative HLLEM Riemann solver [J]. *Astrophys. J.*, 2018, **867**:42

[105] WANG Y, FENG X S, XIANG C Q. An effective matrix-free implicit scheme for the magnetohydrodynamic solar wind simulations [J]. *Comput. Fluids*, 2018, **179**:67-77

[106] XIONG M, DAVIES J A, FENG X S, *et al.* Prospective white-light imaging and in situ measurements of quiescent large-scale solar-wind streams from the Parker Solar Probe and Solar Orbiter [J]. *Astrophys. J.*, 2018, **868**:137

[107] ZHANG M, ZHOU Y F, FENG X S, *et al.* Numerical study of the reconnection process between magnetic cloud and heliospheric current sheet [J]. *Astron. Astrophys.*, 2018, **619**:A82

[108] LI H C, FENG X S. CESE-HLL magnetic field-driven modeling of the background solar wind during year 2008 [J]. *J. Geophys. Res.: Space Phys.*, 2018, **123**:4488-4509

[109] YANG Y, FENG X S, JIANG C W, *et al.* A study of the emergence of flux rope from the solar convection zone into the atmosphere by using a novel numerical method [J]. *Phys. Plasmas*, 2018, **25**:090702

[110] LIU C X, FENG X S, XIANG C Q, *et al.* Hyperbolic cell-centered finite volume method for obtaining potential magnetic field solutions [J]. *Astrophys. J.*, 2019, **887**:33

[111] HAYASHI K, FENG X S, XIONG M, *et al.* Magnetohydrodynamic simulations for solar active regions using time-series data of surface plasma flow and electric field inferred from Helioseismic Magnetic Imager vector magnetic field measurements [J]. *Astrophys. J. Lett.*, 2019, **871**:L28

[112] WANG Y, FENG X S, ZHOU Y F, *et al.* A multi-GPU finite volume solver for magnetohydrodynamics-based solar wind simulations [J]. *Comput. Phys. Commun.*, 2019, **238**:181-193

[113] FENG X S, LIU X J, XIANG C Q, *et al.* A new MHD model with a rotated-hybrid scheme and solenoidality-preserving approach [J]. *Astrophys. J.*, 2019, **871**:226

[114] LIU C A, CHEN T, ZHAO X H. New data-driven method of simulating coronal mass ejections [J]. *Astron. Astrophys.*, 2019, **626**:A91

[115] ZHANG M, FENG X S, YANG L P. Three-Dimensional MHD simulation of the 2008 December 12 coronal mass ejection: from the Sun to interplanetary space [J]. *J. Space Weather Space Clim.*, 2019, **9**:A33

[116] LIU Y S, SHEN F, YANG Y. Numerical simulation on the propagation and deflection of fast coronal mass ejections (CMEs) interacting with a corotating interaction region in interplanetary space [J]. *Astrophys. J.*, 2019, **887**:150

[117] WANG B, CHEN Y, HU Q, *et al.* A method of forced extrapolation of the global magnetic field in the solar corona [J]. *Sci. China Technol. Sci.*, 2019, **63**(2):234

[118] LEMBÈGE B, YANG Z W. Physical roles of interstellar-origin pickup ions at heliospheric termination shock. II.

Impact of the front nonstationary on the energy partition and particle velocity distribution [J]. *Astrophys. J.*, 2018, **860**:84

[119] ZHU B, LIU Y D, KWON R Y, *et al.* Investigation of energetic particle release using multi-point imaging and in situ observations [J]. *Astrophys. J.*, 2018, **865**:138

[120] YANG Z W, LU Q M, LIU Y D, *et al.* Impact of shock front rippling and self-reformation on the electron dynamics at low-Mach-number shocks [J]. *Astrophys. J.*, 2018, **857**:36

[121] GUO J N, DUMBOVIC M, WIMMER SCHWEINGRUBER R F, *et al.* Modeling the evolution and propagation of September 2017 CMEs and SEPs arriving at Mars constrained by remote sensing and in situ measurement [J]. *Space Weather*, 2018, **16**:1156-1169

[122] GUO J N, ZEITLIN C, WIMMER SCHWEINGRUBER R F, *et al.* A generalized approach to model the spectra and radiation dose rate of solar particle events on the surface of Mars [J]. *Astrophys. J.*, 2018,**155**:49

[123] GUO J N, WIMMER SCHWEINGRUBER R F, GRANDE M, *et al.* Ready functions for calculating the Martian radiation environment [J]. *J. Space Weather Space Clim.*, 2019, **9**:A7

[124] GUO J N, BANJAC S, RÖSTEL L, *et al.* Implementation and validation ofthe GEANT4/AtRIS code to model the radiation environment at Mars [J]. *J. Space Weather Space Clim.*, 2019, **9**:A2

[125] GUO J N, WIMMER SCHWEINGRUBER R F, WANG Y M, *et al.* The pivot energy of solar energetic particles affecting the Martian surface radiation environment [J]. *Astrophys. J. Lett.*, 2019,**883**:L12

[126] LUO X, POTGIETER M S, ZHANG, *et al.* A study of electron Forbush decreases with a 3D SDE numerical model [J]. *Astrophys. J.*, 2018, **860**:160

[127] WEI W W, SHEN F, YANG Z C, *et al.* Modeling solar energetic particle transport in 3D background solar wind: influences of the compression regions [J]. *J. Atmos. Sol.: Terr. Phys.*, 2019, **182**:155-164

[128] LUO X, POTGIETER M S, BINDI V, *et al.* A numerical study of cosmic proton modulation using AMS-02 observations [J]. *Astrophys. J.*, 2019, **878**:6

[129] LI H C, FENG X S, XIANG C Q. Time-dependent simulation and result validation of interplanetary solar wind [J]. *Chinese J. Geophys.*, 2019 , **62**(1): 1-18, 2019

[130] KONG F G, QIN G, WU S S, *et al.* Study of time evolution of the bend-over energy in the energetic particle spectrum at a parallel shock [J]. *Astrophys. J.*, 2019, **877**:97

[131] QIN G, KONG F J, ZHANG L H. Effects of shock and turbulence properties on electron acceleration [J]. *Astrophys. J.*, 2018, **860**:3

[132] SHEN Z N, QIN G. Modulation of galactic cosmic rays in the inner heliosphere over solar cycles[J]. *Astrophys. J.*, 2018, **854**:137

[133] SHEN Z N, QIN G, ZUP P B, *et al.* Modulation of galactic cosmic rays from helium to nickel in the inner heliosphere [J]. *Astrophys. J.*, 2019, **887**:132

[134] WANG J F, QIN G. The diffusion coefficient with displacement variance of energetic particles caused by adiabatic focusing [J]. *Astrophys. J.*, 2019, **886**:89

[135] WANG J F, QIN G. Parallel and perpendicular diffusion coefficients of energetic charged particles with adiabatic focusing [J]. *Astrophys. J.*, 2018, **868**:139

[136] YANG L, BERGER L, ROBERT F, *et al.* The pitch-angle distributions of suprathermalions near an interplanetary shock [J]. *Astrophys. J. Lett.*, 2020, **888**:L22

[137] YANG L, WANG L H, LI G, *et al.* Electron acceleration by ICME-driven shocks at 1 AU [J]. *Astrophys. J.*, 2019, **875**:140

[138] YANG L, WANG L H, LI G, *et al.* The strongest acceleration of >40 keV electrons by ICME-driven shocks at 1 AU [J]. *Astrophys. J.*, 2018, **853**:89

[139] LIU Z X, WANG L H, SHI Q Q, *et al.* Case study of solar wind suprathermal electron acceleration at the Earth's bow shock [J]. *Astrophys. J. Lett.*, 2020, **889**: L2

[140] YANG Y, SHEN F, YANG Z C, *et al.* Prediction of solar wind speed at 1 AU using an artificialneural network [J]. *Space Weather*, 2018, **16**:1-18

[141] YE Y D, FENG X S. Study on geoeffectiveness of interplanetary coronal mass ejections by support vector machine [J]. *Chin. J. Space Sci.*, 2019, **39**(3):295-302

[142] YANG Y, SHEN F. Modeling the global distribution of solar wind parameters on the source surface using multiple observations and the artificial neural network technique [J]. *Sol. Phys.*, 2019, **294**:111

[143] LU G, WANG W, YAN F, *et al.* Large area subwavelength cavity antenna with planar metamaterials [J]. *AIP Adv.*, 2019, **9**(2):025032

CAO Jinbin, YANG Junying. Magnetospheric Physics in China. *Chin. J. Space Sci.*, 2020, **40**(5): 191-268. DOI:10.11728/cjss2020.05.191

Magnetospheric Physics in China*

CAO Jinbin YANG Junying

(*Space Science Institute, School of Space and Environment, Beihang University, Beijing* 100191)

(*Key Laboratory of Space Environment Monitoring and Information Processing of MIIT, Beijing* 100191)

Abstract In the past two years, many progresses were made in Magnetospheric Physics by using the data of SuperMAG, Double Star Program, Cluster, THEMIS, RBSP, DMSP, DEMETER, NOAA, Van Allen probe, Swarm, MMS, ARTEMIS, MESSENGER, Fengyun, BeiDa *etc.*, or by computer simulations. This paper briefly reviews these works based on papers selected from the 248 publications from January 2018 to December 2019. The subjects covered various sub-branches of Magnetospheric Physics, including geomagnetic storm, magnetospheric substorm, magnetic reconnection, solar wind-magnetosphere-ionosphere interaction, radiation belt, ring current, whistler waves, plasmasphere, outer magnetosphere, magnetotail, planetary magnetosphere, and technique.

Key words Magnetospheric physics, Data, Computer simulations

Classified index P 352

1 Geomagnetic Storms

In Ref.[1], the occurrence probability of extreme geomagnetic storms is estimated by applying Extreme Value Theory (EVT) to the geomagnetic activity *Aa* index. The *Aa* index has 172 years' observation time span, which is much longer than other geomagnetic indices, and thus is more suitable for analysis for rarely occurred extreme geomagnetic storms. They use two newly developed EVT methods, Block Maxima Method (BMM) and Peak Over Threshold (POT), and find that the extreme geomagnetic storm happened in March 1989 may happen once per century. This result implies that they should pay more attention to such extreme geomagnetic storms that can cause Space Weather hazards.

Based on the data from the SuperMAG collaboration in 2000–2014, the Magnetic Latitude (MLAT) location of the Ring Current (RC) denoted by the MLAT of the maximum horizontal magnetic disturbance during the main phase of 67 intense geomagnetic storms ($Dst \leqslant -100$ nT) are derived. The results of Liu *et al.*[2] show that the maximum horizontal magnetic disturbance does not always occur in the magnetic equator, indicating that the RC might be tilted in the latitudinal direction during these storms. Specifically, the tilt of the RC near the day-night line is affected by the direction of solar wind. When the solar wind flows southward against the magnetic equatorial plane, the RC is more likely to show a dayside-lifted tilt. When the solar wind flows northward, the pattern is opposite. Tilts of the RC near the dawn-dusk line are also found in most of these storms. The location of the RC is mainly lifted in the dusk side and declined in the dawn side for positive IMF B_y, while the tilt is reversed for negative IMF B_y. A possible interpretation might be the IMF B_y-related twisting of the geomagnetic field. Besides, the monthly averaged MLAT of the fitted RC also varies with seasons. It is shifted to the southern hemisphere in the northern summer and to the northern hemisphere in the northern winter, which might indicate that the RC is not centered on a single

* Supported by National Natural Science Foundation of China Grants (41821003, 41941001)
Received March 16, 2020
E-mail: jbcao@buaa.edu.cn

plane. Such a seasonal variation might be related to the angle between the solar wind and the magnetic equatorial plane.

The temporal and spatial evolution of Electromagnetic Ion Cyclotron (EMIC) waves during the magnetic storm of 21–29 June 2015 is investigated by Wang *et al.*[3] using high-resolution magnetic field observations from Swarm constellation in the ionosphere and Van Allen Probes in the magnetosphere. Magnetospheric EMIC waves had a maximum occurrence frequency in the afternoon sector and shifted equatorward during the expansion phase and poleward during the recovery phase. However, ionospheric waves in subauroral regions occurred more frequently in the nighttime than during the day and exhibited less obvious latitudinal movements. During the main phase, dayside EMIC waves occurred in both the ionosphere and magnetosphere in response to the dramatic increase in the solar wind dynamic pressure. Waves were absent in the magnetosphere and ionosphere around the minimum Sym-*H*. During the early recovery phase, He^+ band EMIC waves were observed in the ionosphere and magnetosphere. During the late recovery phase, H^+ band EMIC waves emerged in response to enhanced earthward convection during substorms in the pre-midnight sector. The occurrence of EMIC waves in the noon sector was affected by the intensity of substorm activity. Both ionospheric wave frequency and power were higher in the summer hemisphere than in the winter hemisphere. Waves were confined to an MLT interval of less than 5 h with a duration of less than 186 min from coordinated observations. The results could provide additional insights into the spatial characteristics and propagation features of EMIC waves during storm periods.

During periods of storm activity and enhanced convection, the plasma density in the afternoon sector of the magnetosphere is highly dynamic due to the development of Plasmaspheric Drainage Plume (PDP) structure. This significantly affects the local Alfvén speed and alters the propagation of ULF waves launched from the magnetopause. Therefore, it can be expected that the accessibility of ULF wave power for radiation belt energization is sensitively dependent on the recent history of magnetospheric convection and the stage of development of the PDP. This is investigated using a 3D model for ULF waves within the magnetosphere in which the plasma density distribution is evolved using an advection model for cold plasma, driven by a (VollandStern) convection electrostatic field (resulting in PDP structure). The wave model includes magnetic field day/night asymmetry and extends to a paraboloid dayside magnetopause, from which ULF waves are launched at various stages during the PDP development. Degeling *et al.*[4] find that the plume structure significantly alters the field line resonance location, and the turning point for MHD fast waves, introducing strong asymmetry in the ULF wave distribution across the noon meridian. Moreover, the density enhancement within the PDP creates a waveguide or local cavity for MHD fast waves, such that eigenmodes formed allow the penetration of ULF wave power to much lower L within the plume than outside, providing an avenue for electron energization.

Based on a calculated open $\boldsymbol{E}\times\boldsymbol{B}$ convection passage of a flux tube with Subauroral Polarization Streams (SAPS) electric field involved, Qiao *et al.*[5] use the Dynamic Fluid-Kinetic model to simulate the transport of major ion species (H^+, He^+, and O^+) along magnetic field line (field-aligned) within the flux tube during the 2015 St. Patrick's Day storm. The drift trajectory is confirmed to be quite realistic based on observations and empirical models, meanwhile, the foot print of flux tube is initiated from subauroral latitudes toward polar latitudes along this drift pass. The Dynamic Fluid-Kinetic simulation displays interesting temporal evolution of the field-aligned plasma distribution at subauroral latitudes: The storm enhanced density region continuously provides upward ion flux filling into plasmasphere, but the equatorial mass loading in plasmaspheric plume increases at first and then decreases. Further analyses found that the SAPS particularly impact the field-aligned transport of O^+ particles from ionosphere to plasmasphere but have much less effect on H^+ and He^+ particles at subauroral latitudes, which

causes significant enhancements of equatorial O^+ density. The results show that the SAPS have significant effects on both drifting trajectory of the flux tube and associated field-aligned ion dynamics. This work reveals intimate storm time interaction between the inner magnetosphere and ionosphere which may affect the dynamics in outer magnetosphere or even at magnetopause with flux tube convection.

Three different episodes of Prompt Penetration Electric Field (PPEF) disturbances are observed during the main phase of the St. Patrick's Day storm on 17 March 2015 under steady southward Interplanetary Magnetic Field (IMF) B_z conditions unlike the conventional PPEF associated with southward or northward turnings of IMF B_z. As reported by Tulasi *et al.*[6], these PPEF events took place during the period when strong disturbance dynamo fields are prevailing in the background. The first event is triggered by a solar wind dynamic pressure pulse that caused a sharp eastward PPEF and strong enhancement of equatorial electrojet current in Brazilian dayside. The second event caused another short but strong westward PPEF on dayside due to the reversal of IMF B_y from duskward to dawnward under steady IMF B_z. The third event caused a longer eastward PPEF in association with a solar wind dynamic pressure pulse followed by the onset of a substorm, which has led to strong enhancement of equatorial electrojet, quick rejuvenation and symmetric redistribution of equatorial ionization anomaly in the Brazilian sector. The signatures of the PPEF with opposite polarity and smaller magnitudes are also observed in the Asian sector on the nightside. The possible mechanisms for the observed PPEF events under steady IMF B_z are discussed in terms of changes in the high-latitude field-aligned currents and reconfiguration of high-latitude convection fields using Active Magnetosphere and Planetary Electrodynamics Response Experiment and Super Dual Auroral Radar Network high-frequency radar observations.

Balan *et al.*[7] investigate the capability of geomagnetic storm parameters in the disturbance storm-time (Dst), Kp, and AE indices to distinguish between Severe Space Weather (SvSW) that causes the reported electric power outages and/or telecommunication failures and Normal Space Weather (NSW) that does not cause these severe effects in a 50-year period (1958–2007). The parameters include the storm intensities $Dst_{\min}$ (minimum Dst during the main phase, MP, of the storm), $(\mathrm{d}Dst/\mathrm{d}t)MP_{\max}$, $Kp_{\max}$, and $AE_{\max}$. In addition, the impulsive parameter is derived for the storms that are automatically identified in the Kyoto Dst and USGS Dst. $\int_{TMP}|Dst_{\mathrm{MP}}|\mathrm{d}t$ is the integral of the modulus of the Dst from onset of the MP (MPO) to the $Dst_{\min}$. T_{MP} is the MP duration from MPO to $Dst_{\min}$. The corresponding mean values Kp_{MP} and AE_{MP} are also calculated. Regardless of the significant differences in the storm parameters between the two Dst indices, the $I_{\mathrm{ps}}Dst$ in both indices seems to identify four of the five SvSW events (and the Carrington event) in more than 750 NSW events that have been reported to have occurred in 1958–2007, while all other parameters separate one or two SvSWs from the NSWs. Using the Kyoto $I_{\mathrm{ps}}Dst$ threshold of –250 nT, they demonstrate a 100% true SvSW identification rate with only one false NSW. Using the false NSW event (on 4 August 1972), they investigate whether using a higher resolution Dst might result in more accurate identification of SvSWs. The mechanism of the impulsive action leading to large $I_{\mathrm{ps}}Dst$ and SvSW involves the coincidence that the fast interplanetary coronal mass ejection velocity V contains its shock (or front) velocity ΔV and large interplanetary magnetic field B_z southward covering ΔV.

Conventionally, the minimum value of Dst ($Dst_{\min}$) and maximum values of Kp and AE ($Kp_{\max}$ and $AE_{\max}$) representing the geomagnetic storm intensities have been used for investigating Space Weather in Earth's environment. Balan *et al.*[8] use the derived parameters ($I_{\mathrm{ps}}Dst$, $I_{\mathrm{ps}}Kp$ and $I_{\mathrm{ps}}AE$) giving the mean values of Dst, Kp, and AE during the Main Phase (MP) of Dst storms for investigating ionosphere-thermosphere storms and low-latitude (630 nm) aurora. The derived parameters ($I_{\mathrm{ps}}Dst$, $I_{\mathrm{ps}}Kp$, and $I_{\mathrm{ps}}AE$) representing the impulsive strength of geomagnetic storms seem to have more systematic

dependence among themselves than among the intensities (Dst_{min}, Kp_{max}, and AE_{max}). The ionosphere-thermosphere storms observed by the CHAMP (Challenging Minisatellite Payload) satellite and low-latitude auroras observed by optical imagers are much more intense during high impulsive storms than high intensity storms. In a statistical sense, over 175 positive ionospheric storms ($\Delta N_m F_2$) observed in 1985–2005 and the intensity of 20 red auroras observed in 1989–2004 at mid-latitudes correlate better with the impulsive parameters than the intensity parameters, with the best correlation being with $I_{ps}Dst$. The mechanism of the impulsive action (high-energy input over a short duration) leading to large $I_{ps}Dst$ arises from the impact of fast solar storms (interplanetary coronal mass ejections) with large IMF B_z southward at their front (or shock). The impulsive action results in bright low-latitude auroras and strong ionosphere-thermosphere storms.

He *et al.*[9] report multi-satellite observations of the oscillations in the Subauroral Polarization Stream (SAPS) during a severe magnetic storm on 20 November 2003. The SAPS oscillations (SAPSOs) occurred during the main phase of the magnetic storm when the y component of the southward interplanetary magnetic field (IMF B_y) turned from positive to negative. The SAPSOs were first observed in the pre-midnight sector and propagated toward the dusk sector. The formation and evolution of SAPSO corresponded well with the plasma sheet ions injection and precipitation, indicating that the SAPSOs are possibly generated by the interaction between the hot plasma sheet and the cold plasmasphere under particular conditions (*e.g.*, change of the polarity of IMF B_y accompanied with a sudden enhancement of plasma sheet ion density). The hemispheric asymmetry of the SAPS channels is suggested to be related to the hemispheric differences in the ionospheric plasma condition and the ionospheric convection.

The Magnetic Local Time (MLT) distributions of the horizontal geomagnetic disturbance (ΔH) are investigated with the SuperMAG data set during 330 magnetic storms from 2000 to 2015. Then the MLT distributions of ΔH are verified and interpreted with the SuperMAG-based partial ring current indices (SMR indices) and the Burton equation. It is shown by Liu *et al.*[10] that the ΔH is positive at most MLTs and slightly stronger on the dayside during the initial phase. Such distribution might be mainly attributed to the global positive impact of the magnetopause currents, while the Ring Current (RC) only produces weak negative disturbances, which are slightly stronger on the dusk side. In the main phase, the ΔH decreases prominently with the peak on the dusk side. The RC particles injection plays a major role, especially for large Electric field of Solar Wind (E-SW). The region with ΔH larger than –20 nT is concentrated on the dawnside for small ESW, which might be attributed to earthward bursty bulk flows. Besides, larger solar wind dynamic pressure might cause stronger disturbances under the same magnitude of E-SW. In the recovery phase, the ΔH is weaker and more uniform distributed than in the main phase for negative ESW. For positive E-SW, similar dawn-dusk asymmetry occurs as that in the main phase, but the peak of strongest disturbance tends to weaken and move toward the dayside. Based on the dawn-dusk asymmetric decay rate derived from the Burton equation, it is speculated that the contribution of partial RC might be no less than the FACs.

He *et al.*[12] present multisatellite observations of the large-scale structures of Subauroral Polarization Streams (SAPS) during the main phase of a severe geomagnetic storm that occurred on 31 March 2001. Observations by the Defense Meteorological Satellite Program F12 to F15 satellites indicate that the SAPS were first generated around the dusk sector at the beginning of the main phase. The SAPS channel then expanded toward the midnight sector and moved to lower latitudes as the main phase progressed. The peak velocity, latitudinal width, latitudinal alignment, and longitudinal span of the SAPS channel were highly dynamic during the storm main phase. The large westward velocities of the SAPS were located in the region of low electron densities, associated with low ionospheric conductivity. The large-scale structures of the SAPS also corresponded closely to those of the Region-2 field-

aligned currents, which were mainly determined by the azimuthal pressure gradient of the ring current.

Spacecraft surface charging during geomagnetically disturbed times is one of the most important causes of satellite anomalies. Predicting the surface charging environment is one prevalent task of the geospace environment models. Therefore, the Geospace Environment Modeling (GEM) Focus Group "Inner Magnetosphere Cross-energy/Population Interactions" initiated a community-wide challenge study to assess the capability of several inner magnetosphere ring current models in determining surface charging environment for the Van Allen Probes orbits during the 17 March 2013 storm event. The integrated electron flux between 10 and 50 keV is used as the metrics. Various skill scores are applied to quantitatively measure the modeling performance against observations. Results indicate that no model consistently performs the best in all of the skill scores or for both satellites. Yu *et al.*[13] find that from these simulations the ring current model with observational flux boundary condition and Weimer electric potential driver generally reproduces the most realistic flux level around the spacecraft. A simple and weaker Volland-Stern electric field is not capable of effectively transporting the same plasma at the boundary toward the Earth. On the other hand, if the ring current model solves the electric field self-consistently and obtains similar strength and pattern in the equatorial plane as the Weimer model, the boundary condition plays another crucial role in determining the electron flux level in the inner region. When the boundary flux spectra based on Magnetohydrodynamics (MHD) model/empirical model deviate from the shape or magnitude of the observed distribution function, the simulation produces poor skill scores along Van Allen Probes orbits.

2 Magnetospheric Substorms

Substorm injections are one of the most dynamic processes in Earth's magnetosphere and have global consequences and broad implications for Space Weather modeling. They can be monitored using energetical electron detectors on geosynchronous satellites. The Imaging Electron Spectrometer (IES) onboard a Chinese navigation satellite, launched on 16 October 2015 into an Inclined Geosynchronous Satellite Orbit (IGSO), provides the first energetic electron measurement in IGSO orbit to the best of our knowledge. The IES was developed by Peking University and is named hereafter as BD-IES. Using a pinhole technique, the BD-IES instrument measures 50~600 keV incident electrons in eight energy channels from nine directions covering a range of 180° in polar angle. Data collection by the BD-IES instrument have passed the 1-year mark by the time of issue of Zong *et al.*[14], which reflects a successful milestone for the mission. The innermost and outermost signatures of substorm injection at $L \approx 6$ and 12 have been observed by the BD-IES with a high L shell spatial coverage, complementary to the existing missions such as the Van Allen Probes that covers the range below $L \approx 6$. There are other two BD-IES instruments to be installed in the coming Chinese Sun-synchronous and geosynchronous satellites, respectively. Such a configuration will provide a unique opportunity to investigate inward and outward radial propagation of the substorm injection region simultaneously at high and low L shells. It will further elucidate potential mechanisms for the particle energization and transport, two of the most important topics in magnetospheric dynamics.

The interaction between Interplanetary (IP) shocks and the Earth's magnetosphere would generate/excite various types of geomagnetic phenomena. In order to analyze what kind of IP shock is more likely to trigger intense substorms ($SME/AE > 1000$ nT) and how the energetic electrons respond to intense substorms at geosynchronous orbit, Ma *et al.*[15] perform a systematic survey of 246 IP shock events using SuperMag and LANL observations between 2001 and 2013. The statistical analysis shows that intense substorms ($SME > 1000$ nT) triggered by IP shocks are most likely to occur under the southward Interplanetary Magnetic Field (IMF) and fast solar wind preconditions. Besides, intense substorms after the IP shock arrival are much more likely to occur

when IMF points toward (away from) the Sun around spring (autumn) equinox, which can be ascribed to the Russell-McPherron effect. Thus, the IMF B_s precondition of an IP shock and the Russell-McPherron effect can be considered as precursors of an intense substorm. Furthermore, after the shock arrival associated with intense substorms, low-energy (<200 keV) electron fluxes increase significantly at geosynchronous orbit, and high-energy (>200 keV) electron fluxes decrease. The spectral index becomes softer with intense substorms and remains almost unchanged with moderate substorms no matter whether the IMF precondition is southward or northward.

Exohiss is a low-frequency structureless whistler-mode emission potentially contributing to the precipitation loss of radiation belt electrons outside the plasmasphere. Exohiss is usually considered as the plasmaspheric hiss leaked out of the dayside plasmapause. However, the evolution of exohiss after the leakage has not been fully understood. Gao *et al.*[16] report the prompt enhancements of exohiss waves following substorm injections observed by Van Allen Probes. Within several minutes, the energetic electron fluxes around 100 keV were enhanced by up to 5 times, accompanied by an up to 10-time increase of the exohiss wave power. These substorm-injected electrons are shown to produce a new peak of linear growth rate in the exohiss band ($<0.1\ f_{ce}$). The corresponding path-integrated growth rate of wave power within 10° latitude of the magnetic equatorial plane can reach 13.4, approximately explaining the observed enhancement of exohiss waves. These observations and simulations suggest that the substorm-injected energetic electrons could amplify the preexisting exohiss waves.

Tang and Wang[17] investigate the large-scale substorm current systems developed from its onset in an idealized substorm event simulated by global Magnetohydrodynamic (MHD) models. Mainly three current systems (loops) are revealed: (i) the classical substorm current wedge, which is composed by the disputed cross-tail current in the magnetotail, the nightside westward electrojet in the high-latitude ionosphere and a pair of Region 1 Field-Aligned Currents (FAC); (ii) the partial-ring current system, which is braced by two Region 2 FACs; and (iii) the meridional current system, which is formed by an equatorial radial current (outward/inward in the morning/evening sector), and Region 1 and Region 2 FACs at its two ends. The Region 2 FAC connects with Region 1 FAC by a latitudinal horizontal current at each morning/evening ionosphere to complete Loops 2 and 3. A quantitative study shows the significant enhancement of these current systems during the substorm expansion phase, while Loop 1 dominates, which can reach a magnitude of about 1 *Ma*. Empirical relations among the ionospheric currents and the related magnetotail currents are established based on the simulation results, implying that the substorm current systems are not evolved locally or separately, but must be viewed from a global perspective. This knowledge of large-scale substorm current system would deepen our understanding of the substorm development and could be validated by observations in the future.

The Polar Cap Boundary (PCB) is a fundamental indicator of magnetospheric activities especially during a substorm cycle. Taking a period on 8 March 2008 as an example, Wang *et al.*[18] investigate the location of PCB and its dynamics during a substorm event. The PCB location is determined from the Piecewise Parabolic Method with a Lagrangian Remap (PPMLR) Magnetohydrodynamic (MHD) simulation data and Defense Meteorological Satellite Program (DMSP) observations, respectively. Model-observation comparison indicates that the PPMLR-MHD model gives a reliable estimate of PCB location during a complex substorm sequence. They further analyze the evolution of PCB in that period. The polar cap expands under southward Interplanetary Magnetic Field (IMF), since the low-latitude dayside reconnection produces new open magnetic flux. Meanwhile, more solar wind energy enters and stores in the magnetosphere with the decreasing SML (SuperMAG Auroral Lower) index. After the substorm expansion onset, the polar cap contracts for a while due to the explosive increase of nightside re-

connection. When the IMF direction turns northward, the polar cap contracts continuously, since the dayside reconnection ceases and no more open magnetic flux are supplied, and the stored energy in the magnetosphere releases with the increasing SML index. The model results are in good accord with the features from observations.

Electromagnetic field and plasma data from the Time History of Events and Macroscale Interactions during Substorms (THEMIS) near-Earth probes are used by Sun *et al.*[19] to investigate magnetic dipolarizations inside geosynchronous orbit on 27 August 2014 during an intense substorm with AE_{max}≈1000 nT. THEMIS-D (TH-D) was located inside geosynchronous orbit around midnight in the interval from 09:25 UT to 09:55 UT. During this period, two distinct magnetic dipolarizations with tailward ion flows are observed by TH-D. The first one is indicated by the magnetic elevation angle increase from 15 to 250 around 09:30:40 UT. The tailward perpendicular velocity is $V_{\perp x}$ ≈–50 km·s^{-1}. The second one is presented by the elevation angle increase from 25 to 450 around 09:36 UT, and the tailward perpendicular velocity is $V_{\perp x}$ ≈–70 km·s^{-1}. These two significant dipolarizations are accompanied with the sharp increase in the energy flux of energetic electron inside geosynchronous orbit. After a 5 min expansion of the Near-Earth Plasma Sheet (NEPS), THEMISE (TH-E) located outside geosynchronous orbit also detected this tailward expanding plasma sheet with ion flows of –150 km·s^{-1}. The dipolarization propagates tailward with a speed of –47 km·s^{-1} along a 2.2 R_e distance in the x direction between TH-D and TH-E within 5 min. These dipolarizations with tailward ion flows observed inside geosynchronous orbit indicate a new energy transfer path in the inner magnetosphere during substorms.

Electron flux measurements outside Geosynchronous Orbit (GSO) obtained by the BeiDa Imaging Electron Spectrometer instrument onboard a 55° inclined GSO satellite and inside GSO obtained by the Van Allen Probes are analyzed to investigate the temporal and spatial evolutions of the substorm injection region. In 1 year data started from October 2015, 63 injection events are identified. First, Liu *et al.*[20] show that the injection signatures can be detected in a large radial extent in one single event, for example, from L≈4.1 to L≈9.3. Second, injection onset times are derived from the energy dispersion of particle injection signatures of each satellite. The difference of the onset times among satellites reveals that the injection boundary, termed as "injection front" in this paper, can propagate both earthward and tailward with a speed varying from a few km·s^{-1} to 100 km·s^{-1}. Third, evolutions of the upper-cutoff magnetic moments (μ_{uc}) of injected electrons are analyzed, upon which the injection events are classified into two categories. In one category, the μ_{uc} observed by two radially separated satellites are equal taking into account the error caused by the finite width of energy channels, whereas in the other category, μ_{uc} at lower L shells are smaller than those at higher L shells.

As reported by Li and Wang[21], after the passage of an Interplanetary (IP) shock at 06:13 UT on 24 August 2005, the enhancement ($>$ 6 nPa) of solar wind dynamic pressure and the southward turning of IMF cause the earthward movement of dayside magnetopause and the drift loss of energetic particles near geosynchronous orbit. The persistent electron drift loss makes the geosynchronous satellites cannot observe the substorm electron injection phenomenon during the two substorm expansion phases (06:57 UT–07:39 UT) on that day. Behind the IP shock, the fluctuations (0.5~3 nPa) of solar wind dynamic pressure not only alter the dayside auroral brightness but also cause the entire auroral oval to swing in the day-night direction. However, there is no Pi2 pulsation in the nightside auroral oval during the substorm growth phase from 06:13 UT to 06:57 UT. During the subsequent two substorm expansion phases, the substorm expansion activities cause the nightside aurora oval brightening from substorm onset site to higher latitudes, and meanwhile, the enhancement (decline) of solar wind dynamic pressure makes the nightside auroral oval move toward the magnetic equator (the magnetic pole). These observations demonstrate that solar wind dynamic pressure changes and substorm expansion activities can jointly control the luminosity and location of the

nightside auroral oval when the internal and external disturbances occur simultaneously. During the impact of a strong IP shock, the earthward movement of dayside magnetopause probably causes the disappearance of the substorm electron injections near geosynchronous orbit.

Yu *et al.*[22] report a new modeling capability that self-consistently couples physics-based magnetospheric electron precipitation with its impact on the ionosphere. Specifically, the ring current model RAM-SCBE is two-way coupled to an ionospheric electron transport model GLOW (GLobal airglOW), representing a significant improvement over previous models, in which the ionosphere is either treated as a 2D spherical boundary of the magnetosphere or is driven by empirical precipitation models that are incapable of capturing small-scale, transient variations. The new model enables us to study the impact of substorm-associated, spectrum-resolved electron precipitation on the 3D ionosphere. They found that after each substorm injection, a high-energy tail of precipitation is produced in the dawn sector outside the plasmapause, by energetic electrons ($10 < E < 100$ keV) scattered by whistler-mode chorus waves. Consequently, an ionospheric sublayer characterized by enhanced Pedersen conductivity arises at unusually low altitude (about 85 km), with its latitudinal width of about 5°~10° in the auroral zone. The sublayer structure appears intermittently, in correlation with recurrent substorm injections. It propagates eastward from the nightside to the dayside in the same drift direction of source electrons injected from the plasma sheet, resulting in a global impact within the ionosphere. This study demonstrates the model's capability of revealing complex cross-scale interactions in the geospace environment.

3 Magnetic Reconnection

The magnetic structure and topology of the three-dimensional (3D) magnetic reconnection region are significantly dynamic and complex. Small-scale flux ropes and magnetic null points are frequently detected in the reconnection outflow region and diffusion region due to the increased in-situ measurements at high temporal cadences. Previous studies have demonstrated that X-line and small-scale flux ropes are both related to null points. By applying a fitting-reconstruction method with the input of the Cluster dataset, Guo *et al.*[23] reveal three types of spiral null pairs that serve as the skeleton of the flux ropes. Two spiral nulls can be connected by a spine, or by a separator, or by both spine and separator. A theoretical model is proposed to explain these spiral null pairs. The observational results and the model indicate that the number of magnetic loops of the flux rope is restricted by the linkage pattern of two nulls, while the flux rope is confined by the two nulls and their fan surfaces. The model predicts that the magnetic perturbations in the reconnection region can transform the linkage types of the nulls and eventually lead to the evolution of flux ropes.

Plasma waves are believed to play an important role during magnetic reconnection. However, the specific role of Upper Hybrid (UH) waves in the electron diffusion region (EDR) remains elusive, owing to the absence of high-resolution measurements. Jiang *et al.*[24] analyzed one EDR event in the magnetotail on 11 July 2017 observed by the Magnetospheric Multiscale (MMS) mission. To the best of our knowledge, this is the first time that intense UH waves have been observed in the EDR by MMS. The agyrotropic crescent-shaped electron distributions could result in the observed UH waves. Concomitant with the observations of UH waves, the agyrotropy parameter $\sqrt{Q}$ of the electrons decreases, implying that the UH waves could effectively scatter the electrons in the EDR. The good accordance of positive energy conversion ($\boldsymbol{J}\cdot\boldsymbol{E}' > 0$, likely dissipation) and the observed UH waves indicates that UH waves may contribute to the energy conversion from the magnetic fields to the plasma particles during magnetic reconnection.

Huang *et al.*[25] report in-situ observations of an electron jet generated by secondary reconnection within the outflow region of primary reconnection in the terrestrial magnetotail by the Magnetospheric Multiscale (MMS) mission. The MMS spacecraft first

passed through the primary X-line and then crossed the electron jet in the outflow of primary reconnection. There are a series of small-scale flux ropes in the secondary reconnection region. Decoupling from the magnetic field for both ions and electrons, an intense out-of-plane current, unambiguous Hall currents, and a Hall electromagnetic field appear in the electron jet. Strong electron dissipation ($\boldsymbol{J}\cdot\boldsymbol{E}'>0$), a nonzero electric field in the electron frame, and electron crescent-like shaped distributions are detected in the center of the electron jet, implying that MMS spacecraft were likely passing through the electron diffusion region. The significant electron dissipation indicates that the electrons can be accelerated in the electron jet and the electron jet may be another important electron acceleration channel along with the electron diffusion region.

The separatrix region is the region between the separatrix and the reconnection jet. Due to the $\boldsymbol{E}\times\boldsymbol{B}$ drift and velocity filter effect in which high-energy particles with high parallel speed can be seen prior to low-energy particles along the field line, electrons are separated from ions. The electron dynamics in this region is of interest; however it has not been studied in detail, because of the insufficient resolution of plasma data. Bai *et al.*[26] present a slow separatrix crossing event observed by Magnetospheric Multiscale (MMS) satellite constellation on 1 January 2016, from the magnetosheath side with high-resolution burst mode data. The electron edge and ion edge are clearly distinguished in the separatrix region. Two types of electron dispersion, one with a short duration (about 0.3 s) and the other with a longer duration (about 13 s) were detected between the electron and ion edges. The rapid dispersion (with a small time scale) is mainly in the parallel direction, which might originate from a thin layer with non-frozen-in electrons close to the separatrix. The gradual (long time scale) dispersion is seen from parallel to perpendicular directions, which comes from the $\boldsymbol{E}\times\boldsymbol{B}$ drift of a curved D-shape distribution of electrons. The width of the electron diffusion region on the magnetosheath side is estimated based on MMS observation. The observation also reveals an unexpected parallel electron beam outside of the electron edge. Wave-particle interaction or parallel potential in the inflow region may be responsible for the generation of this electron population.

Unlike a quadrupolar Hall magnetic field in symmetric magnetic reconnection, a bipolar or quadrupolar Hall magnetic field occurs in asymmetric reconnection as indicated by recent observations from the Magnetospheric Multiscale (MMS) mission. Dai[27] presents analytic calculations of the structures of Hall magnetic fields in asymmetric reconnection. The Hall magnetic fields are analyzed in terms of kinetic Alfvén wave eigenmodes of the reconnection layer. The bipolar and quadrupolar patterns of Hall magnetic fields correspond to a dominance of the n=0 and n=1 kinetic Alfvén wave eigenmode, respectively. The asymmetry of Hall fields is linked to the asymmetry of the Alfvén speed profile. The Hall magnetic fields are shifted toward and enhanced on the low Alfvén speed side of the reconnection layer. The asymmetry in the magnetic field strength of the reconnection layer has a major effect on the structures of Hall magnetic fields.

Secondary flux ropes are suggested to play important roles in energy dissipation and particle acceleration during magnetic reconnection. However, their generation mechanism is not fully understood. Zhong *et al.*[28] present the first direct evidence that a secondary flux rope was generated due to the evolution of an electron vortex, which was driven by the electron Kelvin-Helmholtz instability in an ion diffusion region as observed by the Magnetospheric Multiscale mission. The sub-ion scale (less than the ion inertial length) flux rope was embedded within the electron vortex, which contained a secondary electron diffusion region at the trailing edge of the flux rope. They propose that intense electron shear flow produced by reconnection generated the electron Kelvin-Helmholtz vortex, which induced a secondary reconnection in the exhaust of the primary X line and then led to the formation of the flux rope. This result strongly suggests that secondary electron Kelvin-Helmholtz instability is important for reconnection dynamics.

It has been proposed that, in the near-Earth magnetotail, earthward propagating flux ropes can merge with the Earth's dipole magnetic field and dissipate its magnetic energy. However, the reconnection diffusion region related to this process has not been identified. Man *et al.*[29] report the first in situ observation of magnetic reconnection between an earthward propagating flux rope and the closed magnetic field lines connecting to Earth. Magnetospheric Multiscale (MMS) spacecraft crossed a vertical current sheet between the leading edge of the flux rope (negative B_z) and the geomagnetic field (positive B_z). The sub-ion-scale current sheet, super-Alfvénic electron outflow, Hall magnetic and electric field, conversion of magnetic energy to plasma energy ($\boldsymbol{J}\cdot\boldsymbol{E} > 0$), and magnetic null were observed during the crossing. All the above signatures indicate that MMS detected the reconnection diffusion region. This result is also relevant to other planets with intrinsic magnetosphere.

Magnetic reconnection efficiently converts magnetic energy into kinetic and thermal energy of plasmas. The electric field at the X-line, which represents the reconnection rate, is commonly used to measure how fast the reconnection proceeds. However, the Energy Conversion Rate (ECR) has rarely been investigated. Using a 2.5D particle-in-cell simulation, Yi *et al.*[30] examined the temporal evolution of the ECR in collisionless reconnection. It is found that the ECR reaches peak significantly later than the reconnection rate does. This is because the energy conversion primarily occurs at the reconnection fronts rather than at the X-line. With the increase of the inflow density, both the reconnection rate and the conversion rate decrease. The presence of a guide field leads to the reduction of both the reconnection rate and the conversion rate, though reconnection remains fast. They further find that ECR does not depend on the mass ratio but is sensitive to the length of the simulation domain.

Reconnection Front (RF) has frequently been observed in the magnetotail and is well known as the depolarization front in the near-Earth tail. Whether the RF exists in reconnection with distinct plasma/field properties across the reconnecting current sheet (*i.e.* asymmetric reconnection) is unknown yet. Song *et al.*[31] use 2.5D particle-in-cell simulations to investigate the properties of RF in asymmetric reconnection and compare it to RFs in symmetric reconnection. They find that RF is a robust structure in asymmetric reconnection. Its moving speed and thickness are smaller than those in symmetric reconnection. Its properties, such as the current density, electromagnetic field structure, are examined. Some features of RF in asymmetric reconnection are drastically different than those in symmetric reconnection. These results are of great help for studying RF in plasma environments with asymmetric reconnection, such as Earth's magnetopause.

Magnetic holes have been widely observed in various space plasma systems. The origin of magnetic holes and their influence on background plasma are under debate. Zhong *et al.*[32] show a kinetic-scale electron vortex magnetic hole in a non-ideal region of an active X line, which was observed by the Magnetospheric Multiscale mission at the dayside magnetopause. Intense current and non-ideal electric field in the electron frame were observed within the magnetic hole, which led to strong energy dissipation. Thus, the electron vortex magnetic hole probably provided an additional energy dissipation channel besides the electron diffusion region adjacent to the hole. They suggest that magnetic reconnection provided favorable conditions for the formation of this kinetic-scale magnetic hole and is an important source of magnetic holes in space plasma.

It has been shown that the guide field substantially modifies the structure of the reconnection layer. For instance, the Hall magnetic and electric fields are distorted in guide field reconnection compared to reconnection without guide fields (*i.e.* anti-parallel reconnection). Fu *et al.*[33] performed 2.5D electromagnetic full particle simulation to study the electric field structures in magnetic reconnection under different initial guide fields (B_g). Once the amplitude of a guide field exceeds 0.3 times the asymptotic magnetic field B_0, the traditional bipolar Hall electric field is clearly replaced by a tripolar electric field,

which consists of a newly emerged electric field and the bipolar Hall electric field. The newly emerged electric field is a convective electric field about one ion inertial length away from the neutral sheet. It arises from the disappearance of the Hall electric field due to the substantial modification of the magnetic field and electric current by the imposed guide field. The peak magnitude of this new electric field increases linearly with the increment of guide field strength. Possible applications of these results to space observations are also discussed.

Cold ions of plasmaspheric origin have been observed to abundantly appear in the magnetospheric side of the Earth's magnetopause. These cold ions could affect the magnetic reconnection processes at the magnetopause by changing the Alfven velocity and the reconnection rate, while they could also be heated in the reconnection layer during the ongoing reconnections. Zhang *et al.*[34] report in-situ observations from a partially crossing of a reconnection layer near the subsolar magnetopause. During this crossing, step-like accelerating processes of the cold ions were clearly observed, suggesting that the inflow cold ions may be separately accelerated by the rotation discontinuity and slow shock inside the reconnection layer.

Magnetic reconnection is the most fundamental energy transfer mechanism in the universe that converts magnetic energy into heat and kinetic energy of charged particles. For reconnection to occur, the frozen-in condition must break down in a localized region, commonly called the "diffusion region". In Earth's magnetosphere, ion diffusion regions have already been observed, while electron diffusion regions have not been detected due to their small scales (of the order of a few km). Zong and Zhang[35] report, for the first time, in-situ observations of an active electron diffusion region by the four Cluster spacecraft at the Earth's high-latitude magnetopause. The electron diffusion region is characterized by nongyrotropic electron distribution, strong field-aligned currents carried by electrons and bi-directional super-Alfvénic electron jets. Also observed were multiple micro-scale flux ropes, with a scale size of about $5c/\omega_{pe}$ (12 km, with c/ω_{pe} the electron inertial length), that are crucial for electron acceleration in the guide-field reconnection process. The data demonstrate the existence of the electron diffusion region in collisionless guide-field reconnection at the magnetopause.

Terrestrial dayside dynamics associated with a southward turning, oblique IMF carried by an interplanetary Tangential Discontinuity (TD) is investigated by performing a three-dimensional global-scale hybrid simulation systematically for cases in which the incoming solar wind TD possesses various magnetic field rotation angles $\Delta\Phi$ =90° to 180° and half widths $w = 2d_{i0}$ to $w = 30d_{i0}$, where d_{i0} is the ion inertial length in the solar wind. Overall, the TD is compressed while being transmitted into the magnetosheath, with different compression processes downstream of the quasi-parallel ($Q_{-\parallel}$) and quasi-perpendicular ($Q_{-\perp}$) shocks. It is found that magnetosheath reconnection may take place downstream of both the $Q_{-\parallel}$ and $Q_{-\perp}$ shocks due to interaction of the directional TD with the bow shock and magnetopause, but the existence of magnetosheath reconnection depends on w and $\Delta\Phi$. Magnetosheath flux ropes are formed through three-dimensional patchy reconnection in the thinned current sheet, with a longer rope length under a larger $\Delta\Phi$. There exists a dawn-dusk asymmetry in the spatial extent of the flux ropes, which becomes more significant as $\Delta\Phi$ decreases. When $\Delta\Phi$ decreases to 90°, no reconnection flux ropes are found. Magnetopause reconnection is initiated when the magnetic fluxes with a southward turning IMF (on the sunward side) reach the magnetopause, and the magnetopause flux ropes can be mixed with the magnetosheath ones. Simulation of Guo *et al.*[36] demonstrates that the effects of a southward turning of the IMF may not be a simple field direction change that leads to reconnection only at the magnetopause.

Magnetic reconnection is essentially a multi-scale phenomenon, driven by kinetic processes in microscopic region and enabling explosive energy conversion from magnetic field energy to plasma kinetic energy in large areas. It has been poorly

understood how the kinetic process around the X-line connects to the Magnetohydrodynamics (MHD) scale process in the reconnection downstream region. Fujimoto[37] investigated the energy conversion process in the region far downstream of the X-line, by means of the Particle-in-Cell (PIC) simulation with the Adaptive Mesh Refinement (AMR). The AMR-PIC model enables efficient kinetic simulation of multi-scale phenomena using dynamically adaptive meshes. It is found that the ion energy gain dominates in the reconnection region and is carried out mainly in the exhaust center rather than the exhaust boundaries. The simulation results suggest that the energy conversion process in collisionless magnetic reconnection is significantly different from that in the MHD reconnection model in which most energy conversion occurs at slow mode shocks formed at the exhaust boundaries.

Suprathermal electrons with energy from tens to hundreds of keV are frequently observed in the Earth's magnetotail. The generation of such electrons is typically attributed to magnetic reconnection, Dipolarization Fronts (DFs), or flux transport. However, which of these contributes more to this generation remains unclear. Xu *et al.*[38] quantitatively compared the electron acceleration by these processes, using the Cluster data. They analyze an event detected in the mid-tail and find that the suprathermal electrons there are first accelerated by magnetic reconnection and transported earthward, and then further accelerated locally at the DF. The acceleration process by reconnection and transport, resulting in an isotropic pitch angle distribution, contributes about 70% to the total flux enhancement, while the acceleration process by the DF, resulting in a pancake distribution, contributes about 30% to the flux enhancement. The electron acceleration at the DF is primarily attributed to a local betatron process that is successfully reproduced using an analytic model. In order to better understand this phenomenon, they examine an additional 16 similar events and find that the DFs and magnetic reconnection statistically contribute 11%~38% and 62%~89% to the total flux enhancement, respectively. This study greatly improves our understanding of the electron energization process in the magnetotail.

Magnetic nulls, where magnetic field strength becomes zero, play a crucial role in energy conversion and particle acceleration during magnetic reconnection. Recent simulations have suggested that Reconnection Fronts (RFs) inside the reconnection jet can be host to magnetic nulls. However, observational evidence for the RF-associated magnetic nulls remains absent so far. In this study, Liu *et al.*[39] presents such evidence by using the First-Order Taylor Expansion (FOTE) method and Cluster measurements. They confirm for the first time the existence of magnetic nulls around RFs, and find that the dip region ahead of RFs and the nearby magnetic flux ropes around RFs can be host to magnetic nulls. The observed magnetic nulls are all spiral types, and the reconstructed topologies are consistent with theoretical models. Their results verify the existence of magnetic nulls around RFs and may shed new lights on the study of magnetic reconnection and RF dynamics.

Using MMS high-resolution measurements, Liu *et al.*[40] present the first observation of fast electron jet ($V_e \approx 2000$ km·s^{-1}) at a Dipolarization Front (DF) in the magnetotail plasma sheet. This jet, with a scale comparable to the DF thickness (about $0.9d_i$), is primarily in the tangential plane to the DF current sheet and mainly undergoes the $\boldsymbol{E}\times\boldsymbol{B}$ drift motion; it contributes significantly to the current system at the DF, including a localized ring-current that can modify the DF topology. Associated with this fast jet, they observed a persistent normal electric field, strong lower hybrid drift waves, and strong energy conversion at the DF. Such strong energy conversion is primarily attributed to the electron-jet-driven current ($\boldsymbol{E}\cdot j_e \approx 2\,\boldsymbol{E}\cdot j_i$), rather than the ion current suggested in previous studies.

Kinetic Alfvén Waves (KAWs) are believed to be capable of efficiently transporting energy and play an important role in facilitating magnetic reconnection. KAW eigenmode theory suggests that Hall fields can be considered as the components of KAW, providing a mechanism for the generation and dissipation of KAW in magnetic reconnection. Using

particle-in-cell simulations, Huang *et al.*[41] examined Hall fields in the magnetic reconnection region and found that (i) hall electric filed is balanced by the ion pressure gradient and (ii) the ratio of Hall electric field to Hall magnetic field is on the order of Alfvén speed. These results are consistent with KAW physics. Simulation results also indicate that KAWs are excited in the reconnection site and then transmitted along the separatrices. The wave Poynting flux propagates parallel to the magnetic field lines, carrying substantial energy. It is further found that a thinner current sheet provides a favorable condition for the excitation of KAW and results in a higher ratio of the Hall fields.

Theoretically, magnetic reconnection, the process responsible for solar flares and magnetospheric substorms, occurs at the X-line or radial null in the Electron Diffusion Region (EDR). However, whether this theory is correct is unknown, because the radial null (X-line) has never been observed inside the EDR due to the lack of efficient techniques and the scarcity of EDR measurements. Fu *et al.*[42] report such evidence, using data from the recent MMS mission and the newly developed First-Order Taylor Expansion (FOTE) Expansion technique. They investigate 12 EDR candidates at the Earth's magnetopause and find radial nulls (X-lines) in all of them. In some events, spacecraft are only 3 km (one electron inertial length) away from the null. They reconstruct the magnetic topology of these nulls and find it agrees well with theoretical models. These nulls, as reconstructed for the first time inside the EDR by the FOTE technique, indicate that the EDR is active and the reconnection process is ongoing.

Magnetic reconnection, the process typically lasting for a few seconds in space, is able to accelerate electrons. However, the efficiency of the acceleration during such a short period is still a puzzle. Previous analyses, based on spacecraft measurements in the Earth's magnetotail, indicate that magnetic reconnection can enhance electron fluxes up to 100 times. This efficiency is very low, creating an impression that magnetic reconnection is not good at particle acceleration. By analyzing Cluster data, Fu *et al.*[43] report here a remarkable magnetic reconnection event during which electron fluxes are enhanced by 10000 times. Such acceleration, 100 times more efficient than those in previous studies, is caused by the betatron mechanism. Both reconnection fronts and magnetic islands contribute to the acceleration, with the former being more prominent.

Using data from the MMS mission and the First-Order Taylor Expansion (FOTE) method, Wang *et al.*[44] revealed electron distribution functions around a reconnection X-line at the Earths magnetopause. They find cigar distribution of electrons in both the magnetosphere-side and magnetosheath-side inflow regions, isotropic distribution of electrons at the separatrix, and loss of high-energy electrons in the antiparallel direction in the magnetosheath-side inflow region. They interpret the formation of cigar distribution in the inflow regions using the Fermi mechanism, as suggested in previous simulations, the loss of high-energy electrons in the magnetosheath side using the parallel electric fields, which evacuate electrons to escape the diffusion region along the antiparallel direction, and the isotropic distribution at the separatrix using the pitch angle scattering by whistler waves, which exist frequently at the separatrix. They also find that the electron distribution functions can change rapidly (within 60 ms) from isotropic to cigar as the spacecraft moves slightly away from the separatrix.

Complex magnetic structures are ubiquitous in turbulent astrophysical plasmas. Such structures can be host to many dynamic processes, such as magnetic reconnection and energy dissipation. Thus, revealing the 3D topologies of these structures is necessary. Liu *et al.*[45] propose a new method to reconstruct complex magnetic topologies in quasi-steady space plasmas, by utilizing eight-point measurements of magnetic fields and particles. Such a method, based on the Second-Order Taylor Expansion (SOTE) of a magnetic field, is nonlinear; it is constrained by $\nabla\cdot\boldsymbol{B}=0$ and $\nabla\times\boldsymbol{B}=\mu_0\boldsymbol{J}$, where $\boldsymbol{J}=n_e(V_i-V_e)$ is from particle moments. A benchmark test of this method, using the simulation data, shows that the method can give accurate reconstruction results within an area about

three times the size of a spacecraft tetrahedron. By comparing to the previous First-Order Taylor Expansion (FOTE) method, this method (SOTE) gives similar results for reconstructing quasilinear structures but exhibits better accuracy in reconstructing nonlinear structures. Such a method will be useful to the multi-scale missions, such as the future European Space Agency's "cross-scale" mission and China's "self-adaptive" mission. Also, it can be applied to four-point missions, such as Cluster and the Magnetospheric Multiscale Mission. They demonstrated how to apply this method to the four-point missions. In principle, this method will be useful to study shocks, magnetic holes, dipolarization fronts, and other nonlinear structures in space plasmas.

With high-resolution data of the Magnetospheric Multiscale (MMS) mission, Chen *et al.*[46] observed a Magnetic Flux Rope (MFR) in the Earth's magnetosheath. This MFR, showing a clear bipolar variation of the magnetic field in the normal component to local current sheet, contains a strong core field. They use the FOTE method to reconstruct the topology of this MFR and find it is consistent with previous expectation. For the first time, the spiral field and core field of the MFR are both revealed from the FOTE method. Comparing topologies reconstructed at different times, they suggest that the axis of the MFR rotates about 88° at different spatial location. Shape and size of the normal projection to axis vary with the spatial location as well. Inside the MFR, a significant increase of plasma density from 40 to 80 cm^{-3}, a sharp decrease of ion temperature from 200 to 50 eV, an enhancement of cold ions and a series of filamentary currents are found.

Electrostatic Solitary Waves (ESWs) have been reported inside reconnection jets, but their source and role remain unclear hitherto. Liu *et al.*[47] present the first observational evidence of ESWs generation by cold ion beams inside the jet, by using high- cadence measurements from the Magnetospheric Multiscale spacecraft in the Earth's magnetotail. Inside the jet, intense ESWs with amplitude up to 30 $mV{\cdot}m^{-1}$ and potential up to about 7% of the electron temperature are observed in association with accelerated cold ion beams. Instability analysis shows that the ion beams are unstable, providing free energy for the ESWs. The waves are observed to thermalize the beams, thus providing a new channel for ion heating inside the jet. Their study suggests that electrostatic turbulence can play an important role in the jet dynamics.

Radial nulls, where magnetic field strength becomes zero and the magnetic field lines point radially in the fan plane, are believed to be crucial for particle acceleration and energy dissipation during magnetic reconnection. Recent simulations have suggested that Reconnection Fronts (RFs) embedded in the reconnection jet can be host to radial nulls. However, observational evidence for radial nulls near the RFs remains elusive hitherto, owing to the absence of an efficient null-detection method and high-resolution measurements. Liu *et al.*[48] present such evidence by using the newly developed First-Order Taylor Expansion method and the high-resolution measurements from the recent MMS mission. For the first time, they confirm the existence of radial nulls near the RFs and find that the upstream region ahead of the RFs can preferentially host the radial nulls. The reconstructed topologies of the observed radial nulls are consistent with theoretical models. Associated with these radial nulls, no clear particle and wave activities were found, meaning that they were inactive during the observations.

4 Solar Wind-magnetosphere-ionosphere Interaction

By using 10-year of Challenging Mini-satellite Payload satellite observations, Wang *et al.*[49] investigated the average conditions of the Interplanetary Magnetic Field (IMF) prevailing during the westward Counter Equatorial Electrojet (CEJ). Equally, they compared the average IMF conditions accompanying high-latitude field-aligned currents of the Region 1 (R1) and Region 2 (R2). It shows that both CEJ and high-latitude field-aligned currents events when R2 is greater than R1 tend to happen preferably during the

northward turning of the IMF B_z and the substorm recovery phase. Sunlight has an important influence on the longitudinal distribution of the Equatorial Electrojet (EEJ), and the effect is opposite to the tidal electric field at E region. The anti-correlation between $\cos^{0.5}(\theta_{SZA})$ (Solar Zenith Angle effect) average values during CEJ events and EEJ intensity is most prominent around June solstice. By using combined measurements from Challenging Minisatellite Payload and DMSP satellites, it is found that before the occurrence and in the initial phase of a subauroral polarization stream the EEJ gets enhanced, and after about 30 min it reduces in intensity. The CEJ occurrence rate more than doubles during subauroral polarization stream periods compared to normal conditions.

The polar outflows, as an important plasma source of the Earth's magnetosphere, usually exhibit significant north-south asymmetries, which can strongly affect the plasma distributions in the magnetotail lobe and perhaps contribute to the substorm triggering. But the mechanism of the asymmetric transport of these outflows is still unclear. In this Letter, 3D global Magnetohydrodynamic (MHD) simulations are performed to investigate the development of the polar outflows after their escapes from the inner boundary under influences of the IMF B_x. It is found that the velocity of northern polar outflows is much stronger than the south. Wang *et al.*[50] suggest that the IMF B_x causes the north-south asymmetries in the magnetospheric configuration, and subsequently, great differences of the force and mass distributions appear between the two hemispheres, which lead to the significant north-south asymmetries in the transport of the polar outflows. They also discuss the differences in the acceleration mechanisms of the polar outflows between the northward and southward IMF cases.

In Ref.[51], the Space Weather Modeling Framework (SWMF) is used to simulate the real-time response of the magnetosphere to a solar wind event on 5 June 1998, in which the interplanetary magnetic field shifted its direction from north to south. Since most current models do not take into account convective effects of the inner magnetosphere, they first study the importance of Rice Convection Model (RCM) in the global model. They then focus on the following four aspects of the magnetosphere's response: the magnetosphere's density distribution, the structure of its magnetic field lines, the area of the polar cap boundary, and the corresponding ionospheric current change. They find that (i) when the IMF changes from north to south in this event, high magnetosheath density is observed to flow downstream along the magnetopause with the solar wind, low-latitude reconnection at dayside occurs under the southward IMF, while the magnetic field lines in the tail lobe caudal, caused by the nightside high latitude reconnection, extend into the interplanetary space, open magnetic field lines exist simultaneously at both high and low latitudes at the magnetopause; (ii) the area of the polar cap is obviously increased if the IMF turns from the north to the south, this observation is highly consistent with empirical observations; (iii) the ionospheric field align current in the northern hemisphere is stronger than in the southern hemisphere and also increases as the IMF changes from north to south. SWMF with the Rice Convection effect provides reliable modeling of the magnetospheric and ionospheric response to this solar wind variation.

Utilizing ACE satellite observations from 1998 to 2009, Zhang *et al.*[52] performed the elaborate study on the properties of the clock angle θ_{CA} ($\arctan(B_y/B_z)$, –90° to 90°) of the IMF in the solar wind at 1 AU. The solar wind with northward IMF (NW-IMF) and southward IMF (SW-IMF) are analyzed, independently. Statistical analysis shows that the solar wind with SW-IMF and NW-IMF has similar properties in general, including their durations, the IMF B_z and B_y components, and the IMF θ_{CA}. Then, the solar wind with NW-IMF (SW-IMF) is classified into five different temporal scales according to the duration of the NW-IMF (SW-IMF), *i.e.*, very-short wind of 10~30 min, short-scale wind of 0.5~1 h, moderate-scale wind of 1~3 h, long-scale wind of 3~5 h, and super-long wind >5 h. They reveal that the IMF θ_{CA} has a distinct decrease with the increase of the

temporal scale of the solar wind. Next, the solar wind is classified into two groups, *i.e.*, the high-speed solar wind (>450 km·s^{-1}) and the low-speed solar wind (<450 km·s^{-1}). Their analysis indicates that the IMF θ_{CA} depends highly on the solar wind speed. Statistically, high-speed solar wind tends to have larger IMF θ_{CA} than low-speed solar wind. The evolutions of the solar wind and IMF with the solar activity are further studied, revealing no clear solar variation of the IMF θ_{CA}. Finally, they analyze the monthly variation of the IMF θ_{CA}. Superposed epoch result strongly suggests the seasonal variation of the IMF θ_{CA}.

A Transpolar Arc (TPA), which extended from postmidnight to prenoon, was seen on 16 September 2001 in the Northern Hemisphere under northward IMF-B_z and weakly dawnward IMF-B_y conditions. Super Dual Auroral Radar Network detected significant westward plasma flows just equatorward of the poleward edge of the midnight sector auroral oval. These plasma flows were confined to closed field lines and are identified as the ionospheric plasma flow signature of Tail Reconnection during IMF Northward Nonsubstorm Intervals (TRINNIs). These TRINNI flows persisted for 53 min from prior to the TPA appearance to the cessation of TPA growth. They are usually observed before (and during) intervals when TPAs are present, but in this case, subsided after the TPA was completely connected to the dayside. Additional slower flows across the open/closed polar cap boundary were seen at the TPA onset time in the same magnetic local time sector as the nightside end of the TPA. These ionospheric flows suggest that magnetotail reconnection significantly contributed to the TPA formation, as proposed by Milan *et al* (https://doi.org/10.1029/2004JA010835). Nowada *et al.*[53] proposed a possible scenario for an absence of the TRINNI flows during the TPA brightening by considering the relation between the extent of the magnetotail reconnection line mapped onto nightside auroral oval and the TPA width; TRINNI flows would subside when the extent of X-line is comparable to the TPA width. Therefore, our results suggest that the fate (absence or presence) of TRINNI flows on closed field lines during the TPA formation would be closely related with magnetotail reconnection extent.

Pitkänen *et al.*[54] investigated THEMIS satellite measurements made in a tail-aligned constellation during a time interval on 1–2 January 2009, which has previously been attributed to an interval of an interplanetary magnetic field B_y-driven magnetotail twisting. They find evidence for that the orientation of the convection electric field in the tail is twist-mode dependent. For earthward flow and a negative twist (induced tail $B_y < 0$), the electric field is found to have northward E_z and tailward E_x components. During a positive twist (induced tail $B_y > 0$), the directions of E_z and E_x are reversed. The E_y component shows the expected dawn-to-dusk direction for earthward flow. The electric field components preserve their orientation across the neutral sheet, and a quasi-collinear field is observed irrespective of the tail distance. The electric field associated with the tailward flow has an opposite direction compared to the earthward flow for the negative twist. For the positive twist, the results are less clear. The corresponding plasma convection and thus the magnetic flux transport have an opposite dawn-dusk direction above and below the neutral sheet. The directions depend on the tail twist mode. The hemispherically asymmetric earthward plasma flows are suggested to be a manifestation of an asymmetric Dungey cycle in a twisted magnetotail. The role of tailward flows deserves further investigation.

Using results from a new drift kinetic model in the topside ionosphere, Shi *et al.*[55] captured the mode conversion from kinetic Alfven waves to electron acoustic waves. When the kinetic Alfven waves propagate into the transition region, where the electron density of ionospheric origin becomes comparable to that of magnetospheric origin, the steep temperature gradient leads to the mode conversion. The electron acoustic waves are short-lived by dissipating their energy into the electron energization, thus revealing a new type of electron acceleration in the topside ionosphere.

Polar cap patches are common irregularities in

the polar ionosphere, where their formation and evolution can directly affect satellite navigations and communications as well as over-the-horizon radar observations, *etc.* However, affected by the various dynamic processes during the solar wind-magnetosphere-ionosphere coupling, there is no fully accepted formation mechanism of polar cap patches. A statistical analysis of 345 patches at the dayside sectors during 09:00 MLT–15:00 MLT (Magnetic Local Time), observed by EISCAT Svalbard Radar (ESR) 42 m antenna from 2010 to 2013, has been performed by Jin *et al.*[56]. The dependence of their occurrence on solar wind and IMF conditions as well as their MLT distribution has been statistically investigated. The results show that the polar cap patches are preferentially formed during southward IMF conditions. In particular, the MLT dependence of the patches presents a clear IMF B_y-related prenoon-postnoon asymmetry, suggesting the patch formation is clearly modulated by the IMF B_y polarity. Moreover, their statistical results indicate that the patches should not be caused by the variations of the solar wind dynamic pressure or the solar wind velocity. All the results indicate that the pulsed dayside magnetic reconnection is possibly a significant formation mechanism of polar cap patches.

Geomagnetic crochet is believed to be directly related to solar flares. Relevant studies are important to understand the influence of solar eruptions on near-earth space environment, and to develop Space Weather forecasting techniques. Using the data from the geomagnetic station of Shandong University (Weihai), the Intermagnet Geomagnetic chain and the Meridian Space Weather Monitoring Project, the GOES satellite and the digital ionosonde system, Lei *et al.*[57] investigated a geomagnetic crochet associated with an M5.6 solar flare. Their conclusions are listed as follows. The characteristics of geomagnetic crochet are different between the northern and southern hemispheres and prenoon/postnoon, and the geomagnetic response has about 3 minutes' delay in comparison to the peak time of the solar flare. Geomagnetic disturbance is not obvious at night. They use the data of more than 50 magnetic stations located in the dayside hemisphere and found that the amplitude of geomagnetic crochet had a normal distribution, with the maximum being near noon. At last, they use geomagnetic data to get the crochet current system S_s during the event and the quiet current system S_q during quiet days. Their statistical study on the geomagnetic crochets and solar flares from 1996 to 2015 shows that the x-class flare is most likely the cause of magnetic crochets, and the possibility is about 42%; most magnetic crochets are caused by M-class flares; smaller flares, like A-, B-, C-class flares are hardly associated with magnetic crochets.

Dynamical nightside auroral structures are often observed by the All Sky Imagers (ASI) at the Chinese Yellow River Station (CYRS) at Ny-Ålesund, Svalbard, located in the polar cap near the poleward edge of the nightside auroral oval. The boundaries of the nightside auroral oval are stable during quiet geomagnetic conditions, while they often expand poleward and pass through the overhead area of CYRS during the substorm expansion phase. The motions of these boundaries often give rise to strong disturbances of satellite navigations and communications. Two cases of these auroral boundary motions have been introduced to investigate their associated ionospheric scintillations: one is Fixed Boundary Auroral Emissions (FBAE) with stable and fixed auroral boundaries, and another is Bouncing Boundary Auroral Emissions (BBAE) with dynamical and largely expanding auroral boundaries. Observations of Shishir *et al.*[58] show that the auroral boundaries, identified from the sharp gradient of the auroral emission intensity from the ASI images, were clearly associated with ionospheric scintillations observed by Global Navigation Satellite System (GNSS) scintillation receiver at the CYRS. However, amplitude scintillation (S_4) and phase scintillation (σ_ϕ) respond in an entirely different way in these two cases due to the different generation mechanisms as well as different IMF (Interplanetary Magnetic Field) condition. S_4 and σ_ϕ have similar levels around the FBAE, while σ_ϕ was much stronger than S_4 around BBAE. The BBAE were associated with stronger particle pre-

cipitation during the substorm expansion phase. IU/IL, appeared to be a good indicator of the poleward moving auroral structures during the BBAE as well as FBAE.

Xing *et al.*[59] report results from the analysis of a case of conjugate Polar Cap Arcs (PCAs) observed on 5 February 2006 in the Northern Hemisphere by the ground-based Yellow River Station all-sky imager (Svalbard) and in both hemispheres by the space-based DMSP/SSUSI and TIMED/GUVI instruments. The PCA's motion in dawn-dusk direction shows a clear dependence on the IMF B_y component and presents a clear asymmetry between Southern and Northern Hemispheres, that is, formed on the dusk side and moving from dusk to dawn in the Northern Hemisphere and vice versa in the other hemisphere. The already existing PCAs' motion is influenced by the changes in the IMF By with a time delay of similar to 70 min. They also observed strong flow shears/reversals around the PCAs in both hemispheres. The precipitating particles observed in the ionosphere associated with PCAs showed properties of boundary layer plasma. Based on these observations, they might reasonably expect that the topological changes in the magnetotail can produce a strip of closed field lines and local processes would set up conditions for the formation and evolution of PCAs.

The term "polar cap hot patch" is a newly identified high-density plasma irregularity at high latitudes, which is associated with high electron temperature and particle precipitation, while a classical polar cap patch has lower electron temperature. To investigate characteristics of hot patches versus classical patches, five years of in situ database of plasma observations from the DMSP satellites was analyzed. For the first time, Ma *et al.*[60] show how the ion/electron temperature ratio (or temperature difference) can be used to distinguish between classical and hot patches. For classical patches ($T_i/T_e > 0.8$ or $T_e < T_i + 600$ K), the vertical ion flux is generally downward. For hot patches ($T_i/T_e < 0.8$ or $T_e > T_i + 600$ K), the vertical ion flux is generally upward. The highest upflow occurrence was found near the polar cap boundary, associated with hot patches, particle precipitation, strong convection speed, and localized field-aligned currents. This result shows that the polar cap hot patches may play a very important role in solar wind-magnetosphere-ionosphere coupling processes.

By analyzing a five-year period (2010–2014) of Defense Meteorological Satellite Program (DMSP) plasma data, Ma *et al.*[61] investigated ion upflow occurrence, speed, density, and flux above the polar cap in the northern hemisphere under different Solar Zenith Angle (SZA), solar activity ($F_{10.7}$), and convection speed. Higher upflow occurrence rates in the dawn sector are associated with regions of higher convection speed, while higher upflow flux in the dusk sector is associated with higher density. The upflow occurrence increases with convection speed and solar activity but decreases with SZA. Upflow occurrence is the lowest when the SZA $>$ 100° and the convection speeds are low. While, the upflow velocity and flux show a clear seasonal dependence with higher speed in the winter and higher flux in the summer during low convection conditions. However, they are detected for the first time to be both higher in summer during high convection conditions. These results suggest that ion upflow in the polar cap is controlled by the combination of convection, solar activity, and solar illumination.

First experimental proof of a clear and strong dependence of the standard phase scintillation index (σ_ϕ) derived using Global Positioning System measurements on the ionospheric plasma flow around the noon sector of polar ionosphere is presented by Wang *et al.*[62]. σ_ϕ shows a strong linear dependence on the plasma drift speed measured by the Super Dual Auroral Radar Network radars, whereas the amplitude scintillation index (S_4) does not. This observed dependence can be explained as a consequence of Fresnel frequency dependence of the relative drift and the used constant cutoff frequency (0.1 Hz) to detrend the data for obtaining standard σ_ϕ. The lack of dependence of S_4 on the drift speed possibly eliminates the plasma instability mechanism(s) involved as a cause of the dependence. These observations further confirm that the standard phase

scintillation index is much more sensitive to plasma flow; therefore, utmost care must be taken when identifying phase scintillation (diffractive phase variations) from refractive (deterministic) phase variations, especially in the polar region where the ionospheric plasma drift is much larger than in equatorial and midlatitude regions.

The 616 mid and high altitude cusp crossings, collected from Cluster observation for the time interval from 1 February 2001 to 31 December 2010, are used to study IMF effect on cusp locations. Although the statistical errors in their study are quite significant, Xu *et al.*[63] show that with the increasing of the negative B_x, the invariant latitude of the cusp moves to poleward for northward IMF, while it slightly shifts to equatorward for southward IMF. For the increasing positive B_x, the invariant latitude of the cusp doesn't change too much. This phenomenon is observed obviously for the southern hemisphere, but no apparent phenomenon merges on the northern hemisphere. Moreover, when the negative B_y is enhanced, the magnetic local time of cusp turns to dawnward (duskward) for northern (southern) hemisphere under southward IMF. Consistent with previous study, they also find that with the increasing of southward B_z, the invariant latitude of the cusp moves equatorward for both northern and southern hemisphere, while it keeps almost unchanged for northward B_z.

The Cold-Dense Plasma Sheet (CDPS) plays an important role in the entry process of the solar wind plasma into the magnetosphere. Investigating the seasonal variation of CDPS occurrences will help us better understand the long-term variation of plasma exchange between the solar wind and magnetosphere, but any seasonal variation of CDPS occurrences has not yet been reported in the literature. Bai *et al.*[64] investigated the seasonal variation of the occurrence rate of CDPS using Geotail data from 1996 to 2015 and find a semiannual variation of the CDPS occurrences. Given the higher probability of solar wind entry under stronger northward IMF conditions, 20 years of IMF data (1996–2015) are used to investigate the seasonal variation of IMF B_z under northward IMF conditions. They find a semiannual variation of IMF B_z, which is consistent with the Russell-McPherron (R-M) effect. They therefore suggest that the semiannual variation of CDPS may be related to the R-M effect.

Studies on Sun-climate connection have been carried out for several decades, and almost all of them focused on the effects of solar total irradiation energy. As the second major terrestrial energy source from outer space, the solar wind energy flux exhibits more significant long-term variations. However, its link to global climate change is rarely concerned and remains a mystery. As a fundamental and important aspect of the Earth's weather and climate system, tropical cyclone activity has been causing more and more attentions. Li *et al.*[65] investigated the possible modulation of the total energy flux input from the solar wind into the Earth's magnetosphere on the global tropical cyclone activity during 1963–2012. From a global perspective, the accumulated cyclone energy increases gradually since 1963 and starts to decrease after 1994. Compare to the previously frequently used parameters, *e.g.*, the sunspot number, the total solar irradiation, the solar $F_{10.7}$ irradiation, the tropical sea surface temperature, and the south oscillation index, the total solar wind energy flux input exhibits a better correlation with the global tropical cyclone activity. Furthermore, the tropical cyclones seem to be stronger with more intense geomagnetic activities. A plausible modulation mechanism is thus proposed to link the terrestrial weather phenomenon to the seemingly-unrelated solar wind energy input.

Galactic Cosmic Rays (GCRs), modulated by the Heliospheric Magnetic Field (HMF), are speculated to provide a possible link between solar activities and the Earth's lightning variation. To test this hypothesis, Wu *et al.*[66] investigated the correlation between the sudden decrease of GCR in a few hours to one day, known as Forbush Decrease (FD), and the lightning incidence in the tropics and subtropics. During the operating period of the TRMM Satellite, 28 FD events are identified with their Decrease Amplitudes (DAs) greater than 4%. For a

typical FD event occurred on 10 January 2002, the daily Cosmic Ray (CR) intensity presents an intense counts decline from 5830.33 min^{-1} to 5675.96 min^{-1} in one day. Correspondingly, the daily lightning count decreases right after the FD's onset without any obvious time delay, specifically from 3474 d^{-1} to 672 d^{-1} in one day, and reaches its minimum of 355 d^{-1} another day later. Based on the Superposed Epoch Analysis (SEA), a similar statistical correlation is further confirmed. On average, the adjusted daily lightning anomaly decreases from 0.33 to − 0.31 in three days after the FD's onset. The result of the Monte Carlo test indicates that such positive relevance between the CR intensity and the lightning incidence during an FD event is statistically significant.

Ionospheric outflow from the polar cap through the polar wind plays an important role in the evolution of the atmosphere and magnetospheric dynamics. Both solar illumination and solar wind energy input are known to be energy sources of the polar wind. However, observational studies of the energy transfer from these two energy sources to the polar wind are difficult. Because of their low energy, polar wind ions are invisible to regular ion detectors onboard a positively charged spacecraft. Using a new technique that indirectly measures these low-energy ions, Li *et al.*[67] are able to estimate the energy budget of the polar wind. Their results show that solar illumination provides about 10^7 W of the kinetic energy of the polar wind, in addition to the energy transferred from the solar wind with a maximum rate of about 10^8 W. The energy transfer efficiency of solar illumination to the kinetic energy of the polar wind is about 6 to 7 orders of magnitude lower than that of the solar wind. Moreover, daily and seasonal changes in the orientation of the geomagnetic dipole axis control solar illumination over the polar cap, modulating both energies of the polar wind and energy transfer efficiencies from the two energy sources.

Previous studies mostly focused on ionosphere and thermosphere responses to strong southward IMF B_z conditions. However, it is not clear how the Ionosphere and Thermosphere (IT) system responds to Alfvénic quasi-periodic oscillating IMF B_z conditions. In Ref.[68], simulations by the Coupled Magnetosphere Ionosphere Thermosphere model have been used to investigate the effects of IMF B_z temporal variations with 10, 30, and 60 min oscillation periods on the coupled IT system. The simulation results show that the cross polar cap potential and auroral peak electron energy flux are stronger when the IMF B_z oscillation frequency is lower. The relatively small periodic wind responses in the 10 min IMF oscillation case indicate a low-pass filter nature of the magnetosphere-ionosphere-thermosphere system. Two different thermospheric wind (V_n) responses are revealed. One is the almost simultaneous responses at all latitudes, and the other shows a typical traveling atmospheric disturbances signature with a time delay with respect to the latitude for all UTs. The simultaneous V_n responses at all latitudes appear in the daytime Northern Hemisphere, which are mainly caused by the ion drag force in association with penetration electric fields induced plasma density and ion drifts changes. The short-period traveling atmospheric disturbances occurring in the nighttime of both hemispheres and the daytime of the Southern Hemisphere propagate from high to low latitudes showing latitudinal dependence. Both responses oscillate with the same frequencies as those of IMF B_z oscillations.

The temporal and spatial variations in thermospheric neutral winds at an altitude of 400 km in response to Subauroral Polarization Streams (SAPS) are investigated by Wang *et al.*[69] using global ionosphere and thermosphere model simulations under the southward IMF condition. During SAPS periods the westward neutral winds in the subauroral latitudes are greatly strengthened at dusk. This is due to the ion drag effect, through which SAPS can accelerate neutral winds in the westward direction. The new findings are that for SAPS commencing at different universal time, the strongest westward neutral winds exhibit large variations in amplitudes. The ion drag and Joule heating effects are dependent on the solar illumination, which exhibit UT varia-

tions due to the displacement of the geomagnetic and geographic poles. With more sunlight, stronger westward neutral winds can be generated, and the center of these neutral winds shifts to a later magnetic local time than neutral winds with less solar illumination. In the Northern Hemisphere and Southern Hemisphere, the disturbance neutral wind reaches a maximum at 18:00 UT and 04:00 UT, and a minimum at 04:00 UT and 16:00 UT, respectively. There is a good correlation between the neutral wind velocity and $\cos^{0.5}(\theta)$ (Solar Zenith Angle). The reduction in the electron density and the enhancement in the air mass density at an altitude of 400 km are strongest when the maximum solar illumination collocates with the SAPS. The correlation between the neutral wind velocity and $\cos^{0.5}(\theta)$ is also good during the northward IMF period. The effect of a sine-wave oscillation of SAPS on the neutral wind also exhibits UT variations in association with the solar illumination.

Using the in situ measurements of ROCSAT-1 satellite during 181 geomagnetic storms happened from July 1999 to June 2004, a superposed epoch analysis of the Equatorial Plasma Depletions (EPDs) occurrence is conducted by Wan *et al.*[70]. At postsunset hours (18:00UT – 22:00LT), the EPDs occurrence is enhanced shortly at the storm onset, but afterward, a long-last suppression dominates. The EPDs occurrence at Midnight (22:00 LT–02:00 LT) generally shares a similar pattern to that at postsunset hours. The occurrence at predawn (02:00 LT–04:00 LT) gradual increases near storm onset and reach its maximum at 6~9 h and decays until 18 h. For a given longitude at postsunset/midnight, the EPDs occurrence tends to be suppressed or promoted when the EPDs do or do not prevail. The disturbed vertical plasma drift generally determines the inhibition/promotion of the EPDs occurrence at postsunset/predawn. However, for predawn EPDs occurrence, the plasma vertical drift cannot well explain the longitudinal variation. The continuous observations from consecutive orbits of ROCSAT-1 are carefully compared and the result suggests that the geomagnetic storm-induced additional predawn EPDs are preferred to be the longer-lived developed EPDs rather than fresh EPDs. In addition, a possible mechanism concerning the background plasma density enhancement which might be related with the energetic electrons induced nighttime ionization is proposed.

Wang and Luehr[71] investigated the longitudinal variations in the mean densities of Field-Aligned Currents (FACs) at high latitudes in different seasons, by using magnetic field data from SWARM A and C satellites. There appears a wave-1 longitudinal structure in FACs in both hemispheres. Longitudinal variations are about a factor of 1.2~3.2 larger in the Southern Hemisphere than in the Northern. Variations in solar illumination can explain certain longitudinal variations in FACs, with more solar illumination and stronger FACs at near pole longitudes than at far-from-pole longitudes. On the nightside in the local winter a higher value of FACs is generally associated with more intense auroral precipitation in the same area. The theoretical study from the global ionosphere and thermosphere model revealed that the role of neutral wind is comparable to that of electric field in the longitudinal modulation of FACs. A tidal analysis was applied to both FACs and $\cos^{0.5}(\theta)$ (Solar Zenith Angle). FACs contain a large DW2 component, in particular during summer and equinox, which is absent for $\cos^{0.5}(\theta)$. Factors like the geomagnetic field strength, conductivity gradient, and dipole tilt angle might contribute to the observed DW2 features in FACs.

With the advantage of fast plasma measurements of the Magnetospheric Multiscale (MMS) mission in the magnetotail, Chen *et al.*[72] first investigated the particle carriers of Field-Aligned Currents (FACs) in the plasma sheet boundary layer for three cases. In all cases, electrons are the main carriers of FACs, while the contribution of ions can be neglected. The analysis of these cases indicates that thermal electrons (energy range from $0.5T_e$ to $5T_e$, where T_e is the electron parallel temperature) are the main carrier of the FACs. However, cold electrons (energy less than $0.5T_e$) can also significantly contribute to the FACs. In one of three cases,

suprathermal electrons (energy greater than $5T_e$) contribute but a small portion to the total current. The difference between the cases may depend on the local dynamics in the magnetotail. Then a statistical analysis was performed, which also shows that the thermal electrons are dominant in most of the FACs, while the cold electrons can be dominant in some cases. However, the suprathermal electrons cannot support the FACs solely, and they and the cold electrons are more often supporting the FACs together with the thermal electrons.

Field-aligned currents play a significant role in the magnetosphere-ionosphere coupling. With the multipoint measurements and the advanced instruments of the four Magnetosphere Multiscale spacecraft, Chen *et al.*[73] estimated the fine structure of field-aligned currents in the Plasma Sheet Boundary Layer (PSBL) by using the plasma moment data from the Fast Plasma Investigation. Those fine field-aligned currents under higher temporal resolutions could be quite different from that under the lower temporal resolution: Bipolar current signals can be observed under higher resolutions, while no current signal appears under the lower resolution; higher current density magnitude and shorter time scale of the current layer under higher resolutions are observed than that under the lower resolution. The essential reason could be that the spatial scale of some field-aligned current layers in the PSBL is too small to be found by low temporal measurements; thus, their results demonstrate the necessity of high data resolutions in resolving the subproton-scale structure of the field-aligned current and dynamics in the PSBL.

Observations of vertical ion drift velocities (V_z) at the topside of the ionosphere by Defense Meteorological Satellite Program (DMSP) satellites have been accumulated over decades and provide us a unique opportunity to study the vertical ion drifts through the ionosphere on different temporal and spatial scales. In Ref.[74], V_z data of F13, which are of high quality, are taken as the reference to rescale the measurements of DMSP F11, F12, F14, F15, and F16 at high latitudes from 50°N/S to 90°N/S, which show significant differences from each other in magnitudes. Through rescaling, all V_z data of F11~F16 are in a similar order of magnitudes. Moreover, their spatial and temporal distributions resemble each other on average and are consistent with the excepted averaged behaviors reported in previous studies. Thus, the rescaling is basically effective, which provides an opportunity to construct a data set of V_z from 1995 to 2014 that covers nearly two solar cycles for further statistical analysis. Meanwhile, it should be noted that the rescaling results are qualitative/semiqualitative with some uncertainty, which needs more detailed discussion and analysis in future studies.

Ouyang *et al.*[75] studied Ultralow-Frequency (ULF) waves at frequencies 17~100 mHz observed in the topside ionosphere by the DEMETER satellite in a 5-year period from January 2006 to November 2010. Their results show that two types of ULF oscillations occur on the nightside in the $L<2$ region. These two kinds of ULF oscillations are separated based on cross-covariance analysis between electric field in the DC/ULF range and electron density. Type I ULF oscillations, accompanied by electron density perturbations (average $|\delta N_e / N_{e0}| > 5\%$), are found to lag behind density variations, and the longitudinal distribution of type I ULF oscillations is quite similar to the longitudinal distribution of plasma irregularities at about 600 km. These signatures suggest that Type I ULF oscillations are related to plasma irregularities that are common phenomena in the nightside F region ionosphere. The characteristics of Type II ULF oscillations (without significant electron density perturbations) agree well with those features of midlatitude ionospheric electric field fluctuations, which are not thought to be related to magnetospheric origins.

Ionospheric outflow has been shown to be a dominant ion source of Earth's magnetosphere. However, most studies in the literature are about ionospheric outflow injected into the nightside magnetosphere. We still know little about ionospheric outflow injected into the dayside magnetosphere and its further energization after it enters the

magnetosphere. With data from Magnetospheric Multiscale mission, Liu *et al.*[76] reports direct observations of the modulation of dayside ionospheric outflow ions by Ultralow Frequency (ULF) waves. The observations indicate that the modulation is mass dependent, which demonstrates the possibility of using ULF waves as a mass spectrometer to identify ion species. Moreover, the measurement suggests that polarization drift may play a role in O^+ modulation, which may lead to a true acceleration and even nonadiabatic behavior of O^+. This interaction scenario can work throughout the whole magnetosphere and impact upon the plasma environment and dynamics.

In Earth's high-latitude ionosphere, the poleward motion of east–west elongated auroral arcs has been attributed to standing hydromagnetic waves, especially when the auroral arcs appear quasi- periodically with a recurrence time of a few minutes. The validation of this scenario requires spacecraft observations of ultra-low-frequency hydromagnetic waves in the magnetosphere and simultaneous observations of poleward-moving auroral arcs near the spacecraft footprints. Zhao *et al.*[77] presented the first observational evidence from the multi-spacecraft THEMIS (Time History of Events and Macroscale Interactions during Substorms) mission and the conjugated all-sky imager to support the scenario that standing hydromagnetic waves can generate the quasi-periodic appearance of poleward-moving auroral arcs. In this specific event, the observed waves were toroidal branches of the standing hydromagnetic waves, which were excited by a pulse in the solar wind dynamic pressure. Multi-spacecraft measurements from THEMIS also suggest higher wave frequencies at lower L shells (consistent with the distribution of magnetic field line eigenfrequencies), which indicates that the phase difference across latitudes would increase with time. As time proceeds, the enlarged phase difference corresponds to a lower propagation speed of the auroral arcs, which agrees very well with the ground-based optical data.

The flux variations of energetic electrons are one of the most important topics to understand dynamic processes in the space environment and the forecast for high-energy electron burst. BeiDa Image Electron Spectrometer (BD-IES), an imaging energetic electron spectrometer onboard a Chinese navigation satellite at an inclined geosynchronous orbit, can provide 50~600 keV electron flux data, which is used to investigate electron flux variations at GEO orbit during Co-rotating Interaction Region events (CIRs). The superposed epoch analysis is applied to study the electron flux variations in different energy channels of BD-IES during CIRs and the results support previous works. Yin *et al.*[78] revealed that electron fluxes in different channels all have a dropout before or at CIR interface and then the recovery of electrons with low energy reaches maximum earlier than that of electrons with high energy, with longer time differences for larger energy gap, which is consistent with two major mechanisms for energizing particles: inward radial diffusion and local acceleration. In addition, they investigate the relationship between electron flux enhancement in each energy channel and magnetic local time and the extent of enhancement for electron flux peak value compared with average value before the interface. These results can contribute to our understanding of electron flux variations at GEO during CIRs, and thus lay foundations for forecast research on high-energy electron enhancement during CIRs.

Previous observations indicate that there are mainly unstructured plasmaspheric hiss in the high-density plasmasphere, whereas structured whistler mode chorus waves with the lowest frequency of $0.1f_{ce}$ (f_{ce} is the electron gyrofrequency) are observed mostly outside the plasmapause. Yu *et al.*[79] observed ultrawide band rising-tone chorus waves with frequencies extending to lower hybrid resonance frequency ($f_{LHR} \approx$ 101 Hz) in a dawnside high-density region (07:00 MLT and $N_e \approx 75$ cm^{-3}) inside the oscillating plasmapause. The ultrawideband chorus waves have also typical two-band structures separated by a power gap at $0.5f_{ce}$, but their lowest frequency ($f_{LHR} \approx 0.023\ f_{ce}$) in the high-density region is much smaller than that of the normal chorus waves ($> 0.1f_{ce}$) in the low-density trough ($N_e < 40$ cm^{-3}).

The Poynting fluxes of the waves indicate that the ultrawideband chorus waves are excited near the magnetic equator. By comparing the linear wave growth rate to the nonlinear growth rate, they found that the ultrawideband chorus waves are probably amplified through the nonlinear excitation mechanism.

Samanes *et al.*[80] studied the dynamics of the nighttime lower ionosphere height through continuous monitoring of the VLF modal interference distance (so-called distance D). Since the distance D is related to the nighttime propagation modes within the Earth-Ionosphere waveguide, it provides information of the nighttime reflection height (h_N). They have used a long-term VLF narrowband database of almost 8 years (2006–2014) from a long transequatorial VLF propagation path between the transmitter NPM (Hawaii, 21.4 kHz) and the receiver ATI (Atibaia, Brazil). Their results show that h_N assumes lower values during northern hemisphere wintertime as compared with summertime. By using the Lomb-Scargle periodogram, periodicities around 180 (SAO), 365 (AO) and 800 (QBO) days have been found, being the periodicity around 180 days stronger than all other oscillations. Since these large-scale oscillations are commonly observed in several measurable parameters of the Mesosphere-Lower Thermosphere (MLT) region, their results suggest that the nighttime lower ionosphere can be strongly influenced by the dynamics of the MLT region. The effect of the long-term solar activity on h_N is also studied, resulting in a high negative correlation ($R = -0.91$). This effect makes h_N decrease around 1.2 km from low to high solar activity. This result suggests a control of the solar radiation on the nighttime lower ionosphere, and hence, on the electron density at night.

While Subauroral Polarization Streams (SAPS) are well recognized as representatively one of the most important features of magnetosphere-ionosphere (M-I) coupling processes in the subauroral region, the Double-Peak Subauroral Ion Drifts (DSAIDs) is a newly recognized ionospheric phenomenon, categorized as a subset of Subauroral Ion Drifts (SAIDs). Wei *et al.*[81] investigated both SAPS and DSAIDs that appear during the storm main phase of the 17 March 2015 event through a combination of multipoint observations and numerical simulations. They find that when SAPS/DSAIDs are observed by the DMSP spacecraft near the dusk subauroral region, strong electric fields are detected minutes later by the Van Allen Probes almost in the same conjugate region near the equatorial plane. Numerical simulations are carried out not only to reveal the global context and dynamic evolution of the SAPS in both the magnetospheric and ionospheric systems, but also to aid the understanding of the effect of conductance on the DSAIDs. Their results confirm that SAPS are indeed associated with Region 2 Field-Aligned Currents (FACs) flowing into the low conductance region. On the other hand, the DSAIDs may be related to the double-conductance-trough in the subauroral region.

Double-peak Subauroral Ion Drifts (DSAIDs), characterized by two high-speed flow channels, is a newly identified flow structure in the subauroral ionosphere. Two Region 2 field-aligned currents (R2 FACs) might cause the DSAIDs. However, the underlying physical process that drives the double R2 FACs is unknown. Wei *et al.* [82] report a DSAIDs event and reveal its magnetospheric drivers. Defense Meteorological Satellite Program F18 satellite observed DSAIDs in the dusk side subauroral region, which corresponded well to two low-density troughs and two R2 FACs. The Van Allen Probe B demonstrated that intense substorm ion injections recurrently occurred prior to the formation of DSAIDs, suggesting a potential magnetospheric driver of DSAIDs. Simulation confirms that recurrent ion injections intensify the partial ring current and create double pressure peaks in the near-Earth dusk-to-midnight region, leading two R2 FACs to flow into the ionosphere. The two R2 FACs are thus responsible for the DSAIDs formation. This study unveils the generation mechanism of DSAIDs and deepens the knowledge of the complex magnetosphere-ionosphere system.

Yang *et al.*[83] investigated the statistical, dual-spacecraft correlations of Field-Aligned Current (FAC)

signatures between two Swarm spacecraft. For the first time, they infer the orientations of the current sheets of FACs by directly using the maximum correlations obtained from sliding data segments. The current sheet orientations are shown to broadly follow the mean shape of the auroral boundary for the lower latitudes and that these are best ordered on the dusk side. Orientations at higher latitudes are less well ordered. In addition, the maximum correlation coefficients are explored as a function of magnetic local time and in terms of either the time shift (δ_t) or the shift in longitude (δ_{lon}) between Swarms A and C for various filtering levels and choice of auroral region. They find that the low-latitude FACs show the strongest correlations for a broad range of magnetic local time centered on dawn and dusk, with a higher correlation coefficient on the dusk side and lower correlations near noon and midnight. The positions of maximum correlation are sensitive to the level of low-pass filter applied to the data, implying temporal influence in the data. This study clearly reflects the two different domains of FACs: small-scale (some tens of kilometers), which are time variable, and large-scale (>50 km), which are rather stationary. The methodology is deliberately chosen to highlight the locations of small-scale influences that are generally variable in both time and space. They may fortuitously find a potential new way to recognize bursts of the 1st type of irregular pulsations of $\boldsymbol{B}$ (Pi1B) using low-Earth orbit satellites.

5 Radiation Belt, Ring Current and Whistler Waves

Wave number vectors $\boldsymbol{k}$ and minimum cyclotron resonant electron energies E_{min} of Electromagnetic Ion Cyclotron (EMIC) waves are analyzed via the phase differencing technique by using Magnetospheric Multiscale Mission data. It is demonstrated that the phase differencing method provides an estimate of the dominant wave number when finite $\boldsymbol{k}$ spectrum broadenings occur. A case study is conducted for the EMIC event on 20 November 2015, showing remarkable agreements with spectral analysis in wave propagation directions. Liu *et al.*[84] find that obtained wave vectors, roughly agreeing with the validity of cold plasma theory, might significantly vary from wave packet to wave packet. Numerical calculations indicate that E_{min} can range from 0.5 to tens of MeV, suggesting that EMIC waves can effectively interact with those relativistic electrons. This study enriches our understanding of the applicability of phase differencing. It further supports that EMIC waves can be responsible for the loss of electrons with an extremely broad energy range in the magnetosphere.

Sudden changes of the solar wind dynamic pressure have significant impacts on the dynamics of the magnetosphere-ionosphere system. As reported by Zhao *et al.*[85], on 18 February 2011, a sudden decrease in solar wind dynamic pressure was observed by the Wind satellite, which drove the entire magnetosphere-ionosphere system as recorded in many ground-based and space-based measurements. In the magnetosphere, Time History of Events and Macroscale Interactions during Substorms (THEMIS) spacecraft observed a counterclockwise plasma flow vortex propagating tailward. Near the magnetic footprints of the THEMIS spacecraft, the ground magnetometers observed magnetic field variations that corresponded to a counterclockwise vortex in the equivalent ionospheric currents, which in turn indicated the presence of upward field-aligned currents. The all-sky imager at RANK station near the THEMIS footprints also observed a simultaneous enhancement of the auroral brightness. Therefore, this comprehensive case study demonstrates a causal chain that links the solar wind dynamic pressure variations to magnetospheric, ionospheric, and auroral activities.

Recently, interplanetary shocks have been reported to cause "electron dropout echoes" in the outer radiation belt, which is manifested as repeated dropout and recovery signals in electron fluxes. Both previous case and statistical studies have shown that electron dropout echoes are mostly found for high-energy (>300 keV) electrons, and the initial

dropout region is mainly located at the dusk magnetosphere, regardless of shock parameters such as shock normal. To understand these properties, Liu *et al.*[86] modeled the electron dropout echoes at geosynchronous orbit by tracing electrons in the analytic field model of the shock-induced propagating pulse. It is shown that the characteristics of shock-induced electron dropout echo events including energy dependence and localization are well reproduced by their model. By analyzing the trajectories of typical electrons, they find that electrons are inward transported and accelerated through "drift-resonance-like" interactions with the magnetosonic pulse. Two causes of the dawn-dusk asymmetric response are presented: (i) the difference between the interaction time of electrons with the magnetosonic pulse and (ii) the opposite radial $\nabla \boldsymbol{B}$ drift of the electrons at dawnside and dusk side. Further, they calculate the contributions to electron dynamics and phase space density variations from three terms: $\boldsymbol{E} \times \boldsymbol{B}$ drift, radial $\nabla \boldsymbol{B}$ drift, and gyrobetatron acceleration. The details of electron flux variations could vary with the form of the shock-induced pulse and the initial electron distribution, thus be different from their results; however, the basic ingredients of the electron interaction with the pulse could provide a general frame for understanding and evaluating electron flux responses.

High-energy trapped particles in the radiation belts constitute potential threats to the functionality of satellites as they enter into those regions. In the inner radiation belt, the characteristics of high- energy (>20 MeV) protons variations during geomagnetic activity times have been studied by implementing 4-year (2013–2016) observations of the Van Allen probes. An empirical formula has been used by Xu *et al.*[87] to remove the satellite orbit effect, by which proton fluxes have been normalized to the geomagnetic equator. Case studies show that the region of $L<1.7$ is relatively stable, while $L>1.7$ is more dynamic and the most significant variation of proton fluxes occurs at L=2.0. The 4-year survey at L=2.0 indicates that for every geomagnetic storm, sharp descent in proton fluxes is accompanied by the corresponding depression of Sym-H index, with a one-to-one correspondence, regardless of the storm intensity. Proton flux dropouts are synchronous with Sym-H reduction with similar short timescales. Their observational results reveal that high-energy protons in the inner radiation belt are very dynamic, especially for the outer zone of the inner belt, which is beyond our previous knowledge.

Whistler mode chorus waves play a key role in controlling electron dynamics in Earth's inner magnetosphere. A criterion has been previously suggested whereby if the maximum value of the linear growth rate of whistler mode waves exceeds a certain critical bound, then fully nonlinear wave growth occurs and chorus waves are generated. This criterion corresponds to a boundary curve in (N_h/N_0, A_T) space where N_h is the hot electron number density, N_0 is the cold electron number density, and A_T is the thermal anisotropy. Chorus waves are generated in the region above the boundary curve, while no chorus waves are generated below the boundary curve. Tang and Summers[88] make use of a recently published set of 36 particle simulations of chorus, and they thereby are able to confirm the validity of the criterion. It is expected that this simple concept of the theoretical boundary curve based on linear theory will be useful in guiding the choice of parameters in future simulations of the chorus and also of practical use in interpreting experimental chorus wave data.

Strong electrostatic Electron Cyclotron Harmonic (ECH) waves on the dayside magnetosphere have been reported based on observations of the Magnetospheric Multiscale (MMS) spacecraft. Lou *et al.*[89] analyzes high-quality wave data from the four MMS satellites between 1 September 2015 and 30 August 2018 to investigate the statistical properties of dayside ECH emissions. The results show that dayside ECH waves are preferentially observed on the prenoon side in the outer magnetosphere (L = 8~12), with average wave amplitude $E_w > 0.1\ \mathrm{mV \cdot m^{-1}}$. In addition, besides the typical near-equatorial ($|\mathrm{MLAT}| \leqslant 15°$) region, dayside ECH waves exhibit moderate occurrence rate and wave amplitude in higher latitudinal regions (*i.e.*, $15 < |\mathrm{MLAT}| \leqslant 40°$),

possibly due to the off-equatorial geomagnetic field minimum. Their reported double peaks of dayside ECH wave occurrence zone and considerable occurrence rates of pre-noonside ECH waves suggest that dayside ECH waves can be a potentially important contributor to the formation of dayside diffuse aurora.

VLF (Very Low Frequency) electromagnetic waves at 3~30 kHz have the characteristics of long wavelength and long propagation distance. They can propagate along the Earth-lower ionosphere waveguide, and are widely used in many fields including communication and navigation. The Long Wavelength Propagation Capability (LWPC) model based on the waveguide mode theory provides a useful tool to evaluate the propagation path and amplitude of VLF waves, which can be analyzed to investigate ionospheric disturbances caused by solar flares, magnetic storms, earthquakes and other extreme events. In Ref.[90], the very simple electron density and collision frequency modules originally embedded in LWPC are updated by the International Reference Ionosphere (IRI) model for simulation improvements. The obtained numerical results are then compared to the observed amplitude of NWC VLF transmitter signals by Wuhan University VLF receiver at the Wuhan station. It is found that the amplitude variations of NWC VLF transmitter signals modeled using the LWPC and IRI models are much closer to the observations, which mainly results from the improved nighttime electron density profile from the IRI model and justifies the importance of electron density of the lower ionosphere to the VLF signal propagation properties. In addition, the dawn-dusk electron density variation on the wave propagation path largely modulates the NWC VLF signal amplitude, and forms an obvious transition region during the sunrise and sunset periods. Therefore, incorporation of the IRI model into LWPC improves quantitative analyses and prediction performance of the propagation processes of VLF transmitter signals, and provides an evaluation method of long wave navigation and communication quality.

As an important loss mechanism of radiation belt electrons, Electromagnetic Ion Cyclotron (EMIC) waves show up as three distinct frequency bands below the hydrogen (H^+), helium (He^+), and oxygen (O^+) ion gyro frequencies. Compared to O^+-band EMIC waves, H^+- and He^+-band emissions generally occur more frequently and result in more efficient scattering removal of < 5 MeV relativistic electrons. Therefore, knowledge about the occurrence of these two bands is important for understanding the evolution of the relativistic electron population. To evaluate the occurrence pattern and wave properties of H^+- and He^+-band EMIC waves when they occur concurrently, Fu *et al.*[91] investigated 64 events of multi-band EMIC emissions identified from high quality Van Allen Probes wave data. Their quantitative results demonstrate a strong occurrence dependence of the multi-band EMIC emissions on Magnetic Local Time (MLT) and L-shell to mainly concentrate on the dayside region of L=4~6. They also find that the average magnetic field amplitude of H^+-band waves is larger than that of He^+-band waves only when $L<4.5$ and $AE'<300$ nT and He^+-band emissions are more intense under all other conditions. In contrast to 5 events that have average H^+-band amplitude over 2 nT, 19 events exhibit >2 nT He^+-band amplitude, indicating that the He^+-band waves can be more easily amplified than the H^+-band waves under the same circumstances. For simultaneous occurrences of the two EMIC wave bands, their frequencies vary with L-shell and geomagnetic activity: the peak wave frequency of H^+-band emissions varies between $0.25f_{cp}$ and $0.8f_{cp}$ with the average between $0.25f_{cp}$ and $0.6f_{cp}$, while that of He^+-band emissions varies between 0.03 and $0.23f_{cp}$ with the average between $0.05f_{cp}$ and $0.15f_{cp}$. These newly observed occurrence features of simultaneous H^+- and He^+-band EMIC emissions provide improved information to quantify the overall contribution of multi-band EMIC waves to the loss processes of radiation belt electrons.

Wang *et al.*[92] present a detailed investigation of bounce-resonant pitch angle scattering of ring current electrons caused by Electromagnetic Ion Cyclotron (EMIC) waves. It is found that H^+ band EMIC waves can resonate with near-equatorially

mirroring electrons over a wide range of L-shells (*i.e.*, $3 \leqslant L \leqslant 6$) and energies and lead to the efficient transport of ring current electrons (*i.e.*, 10 keV to 100 keV) from near 90° pitch angles to lower pitch angles. Computations of the bounce-resonant pitch angle scattering rates show a strong dependence on the L-shell, electron energy, and resonance harmonics. When the L-shell increases, the orders of bounce resonance contributing to the whole scattering coefficient decrease, and meanwhile, it becomes difficult for the bounce resonance of higher orders to occur. Furthermore, when the electron energy increases, the bounce resonance orders decrease. Their results demonstrate that bounce-resonant scattering by H^+ band EMIC waves can be an important loss mechanism for 10~100 keV electrons because of the absence of cyclotron resonance for ring current electrons interacting with EMIC waves. They conclude that bounce resonant scattering by H^+ band EMIC waves should be incorporated into future modeling efforts of the ring current electron dynamics.

A statistical analysis on the radiation belt dropouts is performed based on 4 years of electron phase space density data from the Van Allen Probes. The μ, K, and L' dependence of dropouts and their driving mechanisms and geomagnetic and solar wind conditions are investigated using electron phase space density data sets for the first time. Results of Xiang *et al.*[93] suggest that Electromagnetic Ion Cyclotron (EMIC) wave scattering is the dominant dropout mechanism at low L' region, which requires the most active geomagnetic and solar wind conditions. In contrast, dropouts at high L' have a higher occurrence and are due to a combination of EMIC wave scattering and outward radial diffusion associated with magnetopause shadowing. In addition, outward radial diffusion at high L' is found to cause larger dropouts than EMIC wave scattering and is accompanied with active geomagnetic and solar wind drivers.

Hua *et al.*[94] analyzed an energetic electron flux enhancement event in the inner radiation belt observed by Van Allen Probes during an intense geomagnetic storm. The energetic electron flux at $L \approx 1.5$ increased by a factor of 3 with pronounced butterfly Pitch Angle Distributions (PADs). Using a three-dimensional radiation belt model, they simulate the electron evolution under the impact of radial diffusion, local wave-particle interactions including hiss, very low frequency transmitters, and magnetosonic waves, as well as Coulomb scattering. Consistency between observation and simulation suggests that inward radial diffusion plays a dominant role in accelerating electrons up to 900 keV and transporting the butterfly PADs from higher L-shells to form the butterfly PADs at $L \approx 1.5$. However, local wave-particle interactions also contribute to driving butterfly PADs at $L \geqslant 1.9$. Their study provides a feasible mechanism to explain the electron flux enhancement in the inner belt and the persistent presence of the butterfly PADs at $L \approx 1.5$.

Recently, Cosmic Ray Albedo Neutron Decay (CRAND) has been identified as the main source of relativistic electrons measured at the inner edge of inner radiation belt. Xiang *et al.*[95] introduced a drift-source model that includes azimuthal drift and a CRAND electron source to simulate the quasi-trapped electron distribution measured by the DEMETER satellite during 20–30 April 2010. The simulated longitude distribution of quasi-trapped electron fluxes at the inner edge of inner radiation belt successfully reproduces the DEMETER observations, confirming CRAND as the main source for these electrons. Furthermore, a comparison of the energy spectrum and the L distribution of the quasi-trapped relativistic electrons between simulations and observations further suggests that CRAND is likely the dominant source for 300~700 keV quasi-trapped electrons at $L < 2$ and $L \approx 3$.

Wei *et al.*[96] report multi-spacecraft observations of ULF waves from Van Allen Probes (RBSP), Magnetospheric Multiscale (MMS), Time History of Events and Macroscale Interactions during Substorm (THEMIS), and Geostationary Operational Environmental Satellites (GOES). On 31 August 2015, global-scale poloidal waves were observed in data from RBSP-B, GOES, and THEMIS from L = 4 to L = 8 over a wide range of Magnetic Local Time

(MLT). The polarization states varied towards purely poloidal polarity. In two consecutive orbits over 18 h, RBSP-A and RBSP-B recorded gradual variation of the polarization states of the poloidal waves; the ratio ($|B_a|/|B_r|$) decreased from 0.82 to 0.13. After the variation of polarization states, the poloidal ULF waves became very purely poloidal waves, localized in both L and MLT. They identify the poloidal wave as second harmonic mode with a large azimuthal wave number (m) of −232. From RBSP particle measurements they find evidence that the high-m poloidal waves during the polarization variations were powered by inward radial gradients and bump-on-tail ion distributions through the N=1 drift-bounce resonance. Most of the time, the dominant free energy source was inward radial gradients, compared with the positive gradient in the energy distribution of the bump-on-tail ion distributions.

By investigating the resonant energy and latitudinal resonance region of Landau resonance between H^+ band Electromagnetic Ion Cyclotron (EMIC) waves and radiation belt electrons and performing calculations of quasi-linear diffusion coefficients, Fu *et al.*[97] find that Landau resonance with EMIC waves, characterized by a very broad range of resonant energies from below 1 eV to above 10 MeV and the strikingly small extent of the latitudinal resonance region well below 0.1°, can be a feasible candidate accounting for the pitch angle scattering of near-equatorially mirroring electrons. Compared to the dominant pitch angle scattering caused by the cyclotron resonance for greater than about 2 MeV electrons at equatorial pitch angles less than about 80° with the rates well above 10^{-4} s^{-1}, Landau resonance with H^+ band EMIC waves has the potential to drive more efficient pitch angle scattering of radiation belt electrons from about 10 MeV down to tens of kiloelectron volts at equatorial pitch angles greater than about 85°.

Both Magnetosonic (MS) waves and plasmaspheric hiss can resonantly scatter outer radiation belt electrons, leading to various electron pitch angle distribution. Based on electron diffusion coefficients calculations and 2D Fokker-Planck diffusion simulations, Hua *et al.*[98] performed a parametric study to quantitatively investigate the net electron scattering effect and the relative contributions of simultaneously occurring hiss and MS waves with groups of different wave amplitude combinations. It is found that the combined scattering effects are dominated by pitch angle scattering due to hiss emissions at L=4, when their amplitude is comparable to or stronger than that of MS waves, thereby producing the butterfly, top-hat, flat-top, and pancake pitch angle distributions, while the butterfly distributions can evolve over a broader energy range when MS waves join the combined scattering effects. Their results demonstrate that the relative intensities of various plasma waves play an essential role in controlling the radiation belt electron dynamics.

Electromagnetic ion cyclotron waves have long been recognized to play a crucial role in the dynamic loss of ring current protons. While the field-aligned propagation approximation of electromagnetic ion cyclotron waves was widely used to quantify the scattering loss of ring current protons, in this study, Cao *et al.*[99] find that the wave normal distribution strongly affects the pitch angle scattering efficiency of protons. Increase of peak normal angle or angular width can considerably reduce the scattering rates of ⩽10 keV protons. For >10 keV protons, the field-aligned propagation approximation results in a pronounced underestimate of the scattering of intermediate equatorial pitch angle protons and overestimates the scattering of high equatorial pitch angle protons by orders of magnitude. Their results suggest that the wave normal distribution of electromagnetic ion cyclotron waves plays an important role in the pitch angle evolution and scattering loss of ring current protons and should be incorporated in future global modeling of ring current dynamics.

Fu *et al.*[100] developed a general 3D relativistic Test Particle (TP) simulation code to examine the trajectories and pitch angle variations of test electrons. They investigate the conditions when the electrons transit broadband, parallel propagating H^+ band Electromagnetic Ion Cyclotron (EMIC) waves to find whether the classical Quasilinear Theory

(QLT) can be applied to interactions between H^+ band EMIC waves and radiation belt relativistic (and ultra-relativistic) electrons. They find that to reach good consistency between TP scattering coefficients and QLT calculations, the wave-particle resonant interaction time (which indicates the time of particles traveling in the wave fields and being resonant with the wave fields) must be carefully calculated to ensure the validity of the linear diffusion process. This wave-particle resonant interaction time depends largely on the wave amplitude, the bandwidth, and the initial parameters of electrons for TP simulations; once the time of electrons traveling in the wave fields becomes large enough when the pitch angles of electrons scattered by wave fields reach the maximal value limited by the resonance condition and cannot be diffused any longer, the linear diffusion process of particles defined by QLT will not be valid any longer. When the resonant electrons start to travel through the wave field, they undergo the linear diffusion process resulting from the pitch angle scattering by the H^+ band EMIC wave field. As the time of traveling in the wave fields increases, the test electrons will suffer effective pitch angle scattering and the pitch angles of these electrons will reach the maximum value limited by the resonance condition, which is determined by the wave and electron parameters. These electrons are then reflected by the wave fields and the linear wave-particle interactions defined by QLT will not be valid anymore. This kind of wave-particle interaction subsequently introduces considerable deviation of TP diffusion coefficients from those predicted by QLT calculations. Their results demonstrate that the general validity of QLT in describing how broadband EMIC waves affect radiation belt relativistic electrons is highly related to the time of electron traveling in the wave fields, which tends to increase for smaller wave power and broader wave frequency spectra.

Spatial distributions of plasma waves play an essential role in the dynamics of Jovian magnetospheric electrons. Despite that most previous observations of whistler waves in the Jovian magnetosphere are limited to $|\lambda| \leqslant 15°$ of the magnetic equator, the data availability from JUNO WAVES instrument provides a good opportunity to capture plasma waves over a broader range of latitude and distance. By using the datasets obtained from JUNO WAVES instrument, the spatial distribution features of whistler waves in the Jovian magnetosphere are studied in detail. The observations indicate that whistler waves occur widely in the region between 35~75 R_J (the Jupiter's radius) within 30° of the magnetic equator. The average amplitude of whistler waves in the Jovian magnetosphere is generally at the level of several pT, weaker than that in the terrestrial magnetosphere. Whistler wave intensities at Jupiter are also found to exhibit a tendency of slow increase with increasing L_J and gradual stability with decreasing magnetic latitude. Based on these observational results, Huang *et al.*[101] implement fits of exponential power-law function to develop an empirical model of the variation of Jovian whistler wave amplitude with L_J and magnetic latitude, which can be used readily to contribute to improved understanding of the importance of whistler waves to the dynamical variations of high energy electrons in the Jovian magnetosphere.

Hua *et al.*[102] report a typical event that fast Magnetosonic (MS) waves, exohiss, and two-band chorus waves occurred simultaneously on the dayside observed by Van Allen Probes on 25 December 2013. By combining calculations of electron diffusion coefficients and 2D Fokker-Planck diffusion simulations, they quantitatively analyze the combined scattering effect of multiple waves to demonstrate that the net impact of combined scattering does not simply depend on the wave intensity dominance of various plasma waves. Although the observed MS waves are most intense, the electron butterfly distribution is inhibited by exohiss and chorus, and electrons are considerably accelerated by combined scattering of MS and chorus waves. The simulated electron pitch angle distributions exhibit the variation trend consistent with the observations. Their results strongly suggest that competition and cooperation between resonant interactions with concurrently occurring magnetospheric waves need to be carefully treated in

modeling and comprehending the radiation belt electron dynamics.

Fu *et al.*[103] develop a full relativistic test particle code to model the combined electron scattering effect of Landau and bounce resonances with magnetosonic waves. Test particle simulations of magnetosonic wave-electron interactions indicate that the two resonances coexist to affect radiation belt electrons at different energies and pitch angles, and the resultant combined pitch angle scattering and energy diffusion can reach the rates of about 10^{-4} and 10^{-5} s, respectively, for electrons 40~500 keV at pitch angles 70°~80° for the given wave model (about 200 pT) inside the plasmapause at L=4.5. Comparisons with the quasi-linear theory results show that the test particle combined scattering rates are generally an order of magnitude weaker, possibly because the electrons are moved out of the Landau resonance by the advective effect of the bounce resonance. Their investigation demonstrates that the Landau and bounce resonances with magnetosonic waves cannot be treated independently or additively in terms of quasi-linear theory to simulate the associated radiation belt electron dynamics.

Fast Magnetosonic (MS) waves are commonly regarded as electromagnetic waves that are characteristically confined within ±3° of the geomagnetic equator. Ni *et al.*[104] report two typical off-equatorial MS events observed by Van Allen Probes, that is, the 8 May 2014 event that occurred at the geomagnetic latitudes of 7.5°–9.2° both inside and outside the plasmasphere with the wave amplitude up to 590 pT and the 9 January 2014 event that occurred at the latitudes of – (15.7°–17.5°) outside the plasmasphere with a smaller amplitude about 81 pT. Detailed test particle simulations quantify the electron resonant scattering rates by the off-equatorial MS waves to find that they can cause the pitch angle scattering and momentum diffusion of radiation belt electrons with equatorial pitch angles $<75°$ or $<58°$ (depending on the wave latitudinal coverage) on timescales of a day. Subsequent two-dimensional Fokker-Planck diffusion simulations indicate that the strong off-equatorial MS waves are capable of efficiently transporting high pitch angle electrons to lower pitch angles to facilitate the formation of radiation belt electron butterfly distributions for a broad energy range from 100 keV to >1 MeV within an hour. Their study clearly demonstrates that the presence of off-equatorial MS waves, in addition to equatorial MS waves, can contribute importantly to the dynamical variations of radiation belt electron fluxes and their pitch angle distribution.

To investigate the hot plasma effects on the cyclotron-resonant interactions between Electromagnetic Ion Cyclotron (EMIC) waves and radiation belt electrons in a realistic magnetospheric environment, calculations of the wave-induced bounce-averaged pitch angle diffusion coefficients are performed by Ni *et al.*[105] using both the cold and hot plasma dispersion relations. The results demonstrate that the hot plasma effects have a pronounced influence on the electron pitch angle scattering rates due to all three EMIC emission bands (H^+, He^+, and O^+) when the hot plasma dispersion relation deviates significantly from the cold plasma approximation. For a given wave spectrum, the modification of the dispersion relation by hot anisotropic protons can strongly increase the minimum resonant energy for electrons interacting with O^+ band EMIC waves, while the minimum resonant energies for H^+ and He^+ bands are not greatly affected. For H^+ band EMIC waves, inclusion of hot protons tends to weaken the pitch angle scattering efficiency of >5 MeV electrons. The most crucial differences introduced by the hot plasma effects occur for >3 MeV electron scattering rates by He^+ band EMIC waves. Mainly due to the changes of resonant frequency and wave group velocity when the hot protons are included, the difference in scattering rates can be up to an order of magnitude, showing a strong dependence on both electron energy and equatorial pitch angle. Their study confirms the importance of including hot plasma effects in modeling the scattering of ultra-relativistic radiation belt electrons by EMIC waves.

Currently, the generation mechanism for the lower L-shell dayside chorus has still remained an open question. He *et al.*[106] report two storm events:

6–7 March 2016 and 20–21 January 2016, when Van Allen Probes observed enhanced dayside chorus with lower and higher wave normal angles (the angles between the wave vector and the geomagnetic field) in the region of L=3.5~6.3 and MLT=5.6~13.5. Hot and energetic (1~100 keV) electrons displayed enhancements in fluxes and anisotropy when they were injected from the plasma sheet and drifted from midnight through dawn toward the dayside. Calculations of chorus local growth rates under different wave normal angles show that the upper cutoff and peak wave frequencies display similar patterns to the observations. Chorus growth rates maximize for the parallel propagation and drop with increasing wave normal angles. The current results confirm that the observed lower L-shell dayside chorus can be excited by anisotropic electrons originating from the plasma sheet in drifting from the nightside to the dayside.

Previous theoretical studies have shown that dayside chorus can produce butterfly distribution of energetic electrons in the Earth's radiation belts by preferentially accelerating medium pitch angle electrons, but this requires the further confirmation from high resolution satellite observation. Jin *et al.*[107] report correlated Van Allen Probes data on wave and particle during the 11–13 April 2014 geomagnetic storm. They find that a butterfly pitch angle distribution of relativistic electrons is formed around the location L=4.52, corresponding to the presence of enhanced dayside chorus. Using a Gaussian distribution fit to the observed chorus spectra, they calculate the bounce-averaged diffusion rates and solve two-dimensional Fokker-Planck equation. Numerical results demonstrate that acceleration by dayside chorus can yield the electron flux evolution both in the energy and butterfly pitch angle distribution comparable to the observation, providing a further evidence for the formation of butterfly distribution of relativistic electrons driven by Very Low Frequency (VLF) plasma waves.

Degeling *et al.*[108] examined the effect on drift-resonant particle dynamics of a strongly peaked internally driven poloidal mode FLR (with specified frequency ω in the Pc5 range and azimuthal mode number $m \gg 1$). Using an analytic MHD model in a dipole field to describe the ULF wave mode, they use the bounce-averaged formalism of Northrop (1963) to obtain equations of motion for charged particles in the wave frame, and find an analytic solution for the case of a temporally constant ULF wave amplitude prole. Focusing on equatorially mirroring electrons in this study, they demonstrate that, for sufficiently peaked radial proles, multiple drift resonances appear that are associated with the FLR peak. These are in addition to the well-known zeroth order drift resonance location, occurring when the unperturbed drift speed Φ_0 satisfies the resonance condition ($m\Phi - \omega = 0$). The additional resonances arise because the strongly peaked FLR wave field components provide sufficiently strong perturbations to the azimuthal drift speed to cause multiple zero-crossings in the resonance condition. These additional resonances have trapping periods much lower than that of the zeroth order resonance, and considerably complicate the electron dynamics. Further properties of these resonances and their measurable effect on electron dynamics are discussed. For example, their effect on observations of energetic electron flux onboard satellites in the vicinity of an FLR is calculated, and shown to significantly distort the typical signature associated with drift resonance (modulations in electron flux at the wave frequency with a 180° phase change across the resonant energy).

To better understand rapid enhancements of the seed populations (hundreds of keV electrons) in the heart of the Earth's outer radiation belt ($L' \approx 3.5$~5.0) during different geomagnetic activities, Tang *et al.*[109] investigated three enhancement events measured by Van Allen Probes in detail. Observations of the fluxes and the pitch angle distributions of energetic electrons are analyzed to determine rapid enhancements of the seed populations. They show that three specified processes associated with substorm electron injections can lead to rapid enhancements of the seed populations, and the electron energy increases up to 342 keV. In the first process, substorm electron injections accompanied by the transient and intense substorm electric fields can directly lead to rapid

enhancements of the seed populations in the heart of the outer radiation belt. In the second process, the substorm injected electrons are first trapped in the outer radiation belt and subsequently transported into $L'<4.5$ by the convection electric field. In the third process, the lower energy electrons are first injected at $L'\approx5.3$ and then undergo drift resonance with ultralow-frequency waves. These accelerated electrons by ultralow-frequency waves are further transported into $L'<4.5$ due to the convection electric field. This process is consistent with the radial diffusion. Their results suggest that these specified processes are important for understanding the dynamics of the seed populations in the heart of the outer radiation belt.

Recent studies have indicated that highly oblique lower band chorus could be excited by temperature anisotropy with a low-energy electron plateau. Zhou *et al.*[110] present another excitation mechanism of highly oblique lower and upper band chorus by using the simultaneous observations and numerical modeling. During 23:00 UT–24:00 UT on 3 July 2016, Van Allen probe A observed chorus with the wave normal angle close to the resonance cone both in the lower and upper bands around L=5.0 and MLT=3. Enhanced flux and pitch angle anisotropy of energetic electrons were observed in the same spatial region. Calculations of chorus growth rates show that highly oblique chorus waves can be excited by the energetic electrons with a loss cone feature and distinct temperature anisotropy, particularly more efficient in the presence of a low-energy plateau. The temperature anisotropy for the oblique upper band is higher than that for the lower band.

Electrostatic electron Cyclotron Harmonic (ECH) waves can yield diffuse aurora primarily at higher L-shells by driving efficient precipitation loss of plasma sheet electrons. Using the Van Allen Probes high resolution data, Chen *et al.*[111] examine in detail the global occurrences of ECH waves during the period from 1 October 2012 to 30 June 2017 and find that there are totally 419 events of enhanced ECH waves. The statistical results demonstrate that ECH waves can be present over a broad region of L=4~6 and MLT=0~24, with a higher occurrence in the region of L=5~6 and MLT=6~19. The electron phase space density exhibits a distinct ring distribution ($\frac{\partial f}{\partial v_\perp}>0$) with the peak energy around a few kiloelectron volts. Both ECH wave events and the electron ring distributions are closely related and tend to be more distinct with increasing geomagnetic activity. Auroral Kilometric Radiation (AKR) can potentially produce serious damage to space-borne systems by accelerating trapped radiation belt electrons to relativistic energies. Zhao *et al.*[112] examined the global occurrences of AKR emissions in radiation belts based on Van Allen Probes observations from 1 October 2012 to 31 December 2016. The statistical results (1848 events in total) show that AKR covers a broad region of L=3~6.5 and 00:00 MLT–24:00 MLT, with a higher occurrence on the night side (20:00 MLT–24:00MLT and 00:00 MLT–04:00 MLT) within L=5~6.5. All the AKR events are observed to be accompanied with suprathermal (about 1 keV) electron flux enhancements. During active geomagnetic periods, both AKR occurrences and electron injections tend to be more distinct, and AKR emission extends to the dayside. The current study shows that AKR emissions from the remote sources are closely associated with electron injections.

Liu *et al.*[113] present a Magnetospheric Multiscale mission observation of quasiperiodic Electromagnetic Ion Cyclotron (EMIC) variations on 24 December 2015 corresponding to magnetic field depressions as well as proton pitch angle anisotropy enhancements. Proton dynamic pressure obtained by WIND indicates that the solar wind was periodically compressing the magnetosphere with a period of about 7.5 min, which is consistent with the EMIC modulation period observed by the Magnetospheric Multiscale. Numerical calculations demonstrate that the EMIC modulation period is comparable with the magnetic field line resonance period, suggesting that quasiperiodic solar wind enhancement compressing the magnetosphere and propagating as the fast mode can lead to the magnetic field line oscillation and hence the presence of quasiperiodic magnetic compressions and discrete proton anisotropy elements,

which provides optimal conditions for modulating the EMIC instability. Current results provide a complete chain of self-consistent observational evidences to illustrate the process connecting solar wind variations to EMIC wave amplitude modulation in the magnetosphere.

Whistler-mode waves play an important role in the inner magnetospheric particle dynamics. The direction and efficiency of energy transfer between waves and particles strongly depend on the wave frequency distribution characteristics. Recent observations have drawn attention to the low-frequency whistler-mode chorus waves below 0.1 times the equatorial gyrofrequency f_{ce} of electrons outside the plasmasphere. On the basis of the analysis of the Van Allen Probes wave data, Gao *et al.*[114] described a new type of low-frequency hiss-like whistler-mode wave around or below $0.1f_{ce}$. They show that two normal chorus wave bands split by the $0.5f_{ce}$ gap can produce the low-frequency hiss-like whistler-mode waves through the nonlinear three-wave interaction.

During the 13–14 November 2012 storm, Van Allen Probe A simultaneously observed a 10 h period of enhanced chorus (including quasi-parallel and oblique propagation components) and relativistic electron fluxes over a broad range of L=3~6 and 02:00 MLT–10:00 MLT within a complete orbit cycle. By adopting a Gaussian fit to the observed wave spectra, Yang *et al.*[115] obtain the wave parameters and calculate the bounce-averaged diffusion coefficients. They solve the Fokker-Planck diffusion equation to simulate flux evolutions of relativistic (1.8~4.2 MeV) electrons during two intervals when Probe A passed the location L=4.3 along its orbit. The simulating results show that chorus with combined quasi-parallel and oblique components can produce a more pronounced flux enhancement in the pitch angle range 45°~80°, consistent well with the observation. The current results provide the first evidence on how relativistic electron fluxes vary under the drive of almost continuously distributed chorus with both quasi-parallel and oblique components within a complete orbit of Van Allen Probe.

Previous studies have revealed a typical picture that seed electrons are transported inward under the drive of radial diffusion and then accelerated via chorus to relativistic energies. Liu *et al.*[116] show a potentially different process during the 2–3 October 2013 storm when Van Allen Probes observed extremely rapid (by about 50 times in 2 h) flux enhancements of relativistic (1.8~3.4 MeV) electrons but without distinct chorus at lower L-shells. Meanwhile, Time History of Events and Macroscale Interactions during Sub- storms satellites simultaneously measured enhanced chorus and fluxes of energetic (100~300 keV) seed electrons at higher L-shells. Numerical calculations show that chorus can efficiently accelerate seed electrons at $L\approx8.3$. Then radial diffusion further increased the phase space density of relativistic electrons throughout the outer radiation belts, with a remarkable agreement with the observation in magnitude and timescale. The current results provide a different physical scenario on the interplay between radial diffusion and local acceleration in outer radiation belt.

Electromagnetic whistler-mode chorus and electrostatic Electron Cyclotron Harmonic (ECH) waves can contribute significantly to auroral electron precipitation and radiation belt electron acceleration. In the past, linear and nonlinear wave-particle interactions have been proposed to explain the occurrences of these magnetospheric waves. By analyzing Van Allen Probes data, Gao *et al.*[117] present here the first evidence for nonlinear coupling between chorus and ECH waves. The sum-frequency and difference-frequency interactions produced the ECH sidebands with discrete frequency sweeping structures exactly corresponding to the chorus rising tones. The newly generated weak sidebands did not satisfy the original electrostatic wave dispersion relation. After the generation of chorus and normal ECH waves by hot electron instabilities, the nonlinear wave-wave interactions could additionally redistribute energy among the resonant waves, potentially affecting to some extent the magnetospheric electron dynamics.

In Ref. [118], a detailed evolution process of parallel electromagnetic ion cyclotron waves in the inner magnetosphere is investigated through qua-

silinear theory. A new saturation has been found to occur after the usual first saturation. During the interval between these two saturations, the energy transfers from H^+ band to He^+ band electromagnetic ion cyclotron waves. Moreover, through the best fitting, they obtain new model parameters for the anisotropy-beta inverse relation of hot H^+, which identifies the threshold of ion cyclotron instabilities in the inner magnetosphere. In situ observations of the Van Allen Probe mission also verify these new model parameters. Therefore, their results reveal the evolution process and saturation characteristics of parallel electromagnetic ion cyclotron waves in the inner magnetosphere.

Electromagnetic ion cyclotron waves and fast magnetosonic waves are found to be simultaneously modulated by background plasma density: both kinds of waves were observed in high plasma density regions but vanished in low-density regions. Theoretical analysis based on Snell's law and linear growth theory has been utilized to investigate the physical mechanisms driving such modulation. It is suggested that the modulation of fast magnetosonic waves might be due to trapping by plasma density structures, which results from the conservation of the parameter Q during their propagation. Here $Q=nr\sin\psi$, with n as the refractive index, r as the radial distance, and ψ as the wave azimuthal angle. As for electromagnetic ion cyclotron waves, the modulation might be owed to the ion composition difference between different plasma density regions. Yuan *et al.*[119] indicate the alternative mechanism for the simultaneous appearance of electromagnetic ion cyclotron waves and fast magnetosonic waves (rather than wave excitations of both two wave emissions), which might take combined effects on the evolution of radiation belt electrons.

Low-frequency chorus emissions have recently attracted much attention due to the suggestion that they may play important roles in the dynamics of the Van Allen Belts. However, the mechanism(s) generating these low-frequency chorus emissions have not been well understood. Yu *et al.*[120] reported an interesting case in which background plasma density lowered the lower cutoff frequency of chorus emissions from above $0.1f_{ce}$ (typical ordinary chorus) to $0.02\ f_{ce}$ (extremely low-frequency chorus). Those extremely low-frequency chorus waves were observed in a rather dense plasma, where the number density N_e was found to be several times larger than has been associated with observations of ordinary chorus waves. For suprathermal electrons whose free energy is supplied by anisotropic temperatures, linear growth rates (calculated using in-situ plasma parameters measured by the Van Allen Probes) show that whistler mode instability can occur at frequencies below $0.1\ f_{ce}$ when the background plasma density N_e increases. Especially when N_e reaches 90 cm^{-3} or more, the lowest unstable frequency can extend to $0.02f_{ce}$ or even less, which is consistent with satellite observations. Therefore, their results demonstrate that a dense background plasma could play an essential role in the excitation of extremely low- frequency chorus waves by controlling the wave growth rates.

Yuan *et al.*[121] present unique conjugated satellite observations of MeV relativistic electron precipitation caused by Electromagnetic Ion Cyclotron (EMIC) waves. On the outer boundary of the plasmasphere, the Van Allen probe observed EMIC waves. At ionospheric altitudes, the National Oceanic and Atmospheric Administration (NOAA) 16 satellite at the footprint of Van Allen probe simultaneously detected obvious flux enhancements for precipitating $>$ MeV radiation belt electrons but not for precipitating $<$ MeV electrons. Theoretical calculations of pitch angle diffusion coefficients for radiation belt electrons indicate that observed EMIC waves can solely lead to flux enhancements of precipitating $>$MeV radiation belt electrons. Their result provides a direct magnetic conjugated observational link between in situ inner magnetospheric EMIC waves and precipitation of MeV relativistic electrons at ionospheric altitudes so as to reveal that EMIC waves can solely scatter MeV radiation belt electrons into the loss cone so as to precipitate into the atmosphere.

With observations of Van Allen Probe A, Yu *et al.*[122] display a typical event where banded whistler waves shifted up their frequencies with frequency

bands broadening as a response to the enhancement of solar wind dynamic pressure. Meanwhile, the anisotropy of electrons with energies about several tens of keV was observed to increase. Through the comparison of the calculated wave growth rates and observed wave spectral intensity, they suggest that those banded whistler waves observed with frequencies shifted up and frequency bands broadening could be locally excited by these hot electrons with increased anisotropy. The current study provides a great in situ evidence for the influence on frequencies of banded whistler waves by the enhancement of solar wind dynamic pressures, which reveals the important role of solar wind dynamic pressures playing in the frequency properties of banded whistler waves.

A typical case of Electromagnetic Ion Cyclotron (EMIC) emissions with both He^+ band and O^+ band waves was observed by Van Allen Probe A on 14 July 2014. These emissions occurred in the morning sector on the equator inside the plasmasphere, in which region O^+ band EMIC waves prefer to appear. Through property analysis of these emissions, it is found that the He^+ band EMIC waves are linearly polarized and propagating quasi-parallelly along the background magnetic field, while the O^+ band ones are of linear and left-hand polarization and propagating obliquely with respect to the background magnetic field. Using the in situ observations of plasma environment and particle data, the excitation of these O^+ band EMIC waves has been investigated with the linear growth theory. The calculated linear growth rate shows that these O^+ band EMIC waves can be locally excited by ring current protons with ring velocity distributions. The comparison of the observed wave spectral intensity and the calculated growth rate suggests that the density of H^+ rings providing the free energy for the instability has decreased after the wave grows. Therefore, Yu *et al.*[123] provided a direct observational evidence to the excitation mechanism of O^+ band EMIC waves: ring current protons with ring distributions provide the free energy supporting the instability in the presence of rich O^+ in the plasmasphere.

Fifty-two CMEs from 2012 to 2017 are categorized into four types according to different IMF preconditions, and behaviors of 1.8, 3.4, 5.2, and 7.7 MeV electrons are quantitatively investigated using a Radiation Belt Content (RBC) index improved for nondipolar geomagnetic field configuration due to interaction with CMEs. Statistical analyses show that CMEs with continuous southward IMF from upstream of shock front to CME leading edge are the most efficient in the production of megaelectronvolt electron content, with RBC five times larger after shock arrival for 1.8 MeV channel, seven times larger for 3.4 MeV channel, and three times larger for 5.2 MeV channel; the 7.7 MeV channel also experiences less pronounced enhancements. For CMEs with continuous northward IMF from upstream of shock front to CME leading edge, clear dropouts of RBC are revealed. The depletion is the most significant for 1.8 MeV, and the magnitude of depletion gradually decreases when the electron energy goes higher. It is suggested by Yuan and Zong[124] that the location of magnetopause and plasmapause, and thus magnetopause shadowing and magnetospheric waves like whistler mode chorus, contributes to the dynamics of mega-electron volt electrons in the outer radiation belt, with energy dependence, in response to CMEs with different preconditions.

Electromagnetic Ion Cyclotron (EMIC) waves are important for the loss of high-energy electrons in the radiation belt. Based on the measurements of Van Allen Probes, two events during the same storm period are presented by Wang *et al.*[125] to study the propagation of EMIC waves. In the first event, left-handed polarized EMIC waves were observed near the plasmapause, while right-handed waves were observed in the inner plasmasphere. The Poynting flux of the right-hand waves was mainly directed inward and equatorward, and no positive growth rates were obtained in the region of these right-hand waves, indicating the inward propagation of the waves from a higher L-shell. In the second event, the wave vectors were quasi-perpendicular to the background magnetic field inside the plasmaspheric plume but became quasi-parallel outside. This phenomenon can be explained by the refraction of the

large density gradient, which qualitatively satisfies Snell's law. These observations provide indirect evidence of the inward propagation of the EMIC waves and give a new insight into how density gradients may modify wave properties.

Hao *et al.*[126] studied electron behavior in the outer radiation belts during the 16 July 2017 Storm Sudden Commencement (SSC), in which prompt intensification of ultra-relativistic electron fluxes was observed at around L=4.8 by Van Allen Probe B immediately after an interplanetary shock. The electron fluxes in multiple energy channels show clear oscillations in the Pc5 frequency range, although the oscillation characteristics are quite different in different energy channels. At energies above 1 MeV, the oscillation periods were very close to the electron drift period, which resembles an energy spectrogram evolution expected for an energetic particle injection event and its drift echoes. At lower energies, however, the oscillation periods hardly depended on the energy: they were very close to the Ultralow Frequency (ULF) wave period derived from electric field measurements (about 250 s according to wavelet analysis). These complex signatures are consistent with the picture of drift resonance between electrons and short-lived ULF waves with low azimuthal wave numbers. Good agreement between the observations and numerical simulations confirms that shock-induced global-scale ULF waves can efficiently accelerate outer belt ultra-relativistic electrons up to 3.4 MeV over a time scale shorter than 1 h.

Six years of Van Allen Probes data are used to investigate cold plasmaspheric electrons affected by ULF waves in the inner magnetosphere ($L<7$) including spatial distributions, occurrence conditions, and resonant energy range. Events exhibit a global distribution within L=4~7 but preferentially occur at $L\approx$5.5~7 in the dayside, while there is a higher occurrence rate in the dusk side than dawnside. They can occur under different geomagnetic activities and solar wind velocities (V_s), but the occurrence rates are increasing with larger AE, |Sym-H|, and V_s. These features are closely associated with the generation and propagation of ULF waves in Pc4 (45~150 s) and Pc5 (150~600 s) bands. Combined with electron observations from HOPE instrument, the resonant energies inferred from wave power indicate that cold electrons at ones to hundreds of electron volts can be affected by ULF waves. Ren *et al.*[127] may shed new light on further investigations on the acceleration and transportation of cold plasmaspheric particles that would affect plasmaspheric material release to the Earth's magnetosphere and instabilities for exciting various waves.

Chen *et al.*[128] present multi-period modulation of energetic electron flux observed by the BeiDa Imaging Electron Spectrometer (BD-IES) onboard a Chinese navigation satellite on 13 October 2015. Electron flux oscillations were observed at a dominant period of about 190 s in consecutive energy channels from 50 keV to 200 keV. Interestingly, flux modulations at a secondary period of about 400 s were also unambiguously observed. The oscillating signals at different energy channels were observed in sequence, with a time delay of up to about 900 s. This time delay far exceeds the oscillating periods, by which they speculate that the modulations were caused by localized ULF waves. To verify the wave-particle interaction scenario, they revisit the classic drift-resonance theory. They adopt the calculation scheme therein to derive the electron energy change in a multi-period ULF wave field. Then, based on the modeled energy change, they construct the flux variations to be observed by a virtual spacecraft. The predicted particle signatures well agree with the BD-IES observations. They demonstrate that the particle energy change might be underestimated in the conventional theories, as the Betatron acceleration induced by the curl of the wave electron field was often omitted. In addition, they show that azimuthally localized waves would notably extend the energy width of the resonance peak, whereas the drift-resonance interaction is only efficient for particles at the resonant energy in the original theory.

Oxygen (O^+) enhancements in the inner magnetosphere are often observed during geomagnetically active times, such as geomagnetic storms. Yue *et al.*[129] quantitatively examined the difference in

ring current dynamics with and without a substantial O^+ ion population based on almost 6-year of Van Allen Probes observations. Their results have not only confirmed the previous finding of the role of O^+ ions to the ring current but also found that abundant O^+ ions are always present during large storms when Sym-$H < -60$ nT without exception, while having the pressure ratio (R) between O^+ and proton (H^+) larger than 0.8 and occasionally even larger than 1 when $L < 3$. Simultaneously, the pressure anisotropy decreases with decreasing Sym-H and increasing L shell. The pressure anisotropy decrease during the storm main phase is likely related to the pitch angle isotropization processes. In addition, they find that R increases during the storm main phase and then decreases during the storm recovery phase, suggesting faster buildup and decay of O^+ pressure compared to H^+ ions, which are probably associated with some species dependent source and/or energization as well as loss processes in the inner magnetosphere.

In Earth's inner magnetosphere, electromagnetic waves in the ULF range play an important role in accelerating and diffusing charged particles via drift resonance. In conventional drift resonance theory, linearization is applied under the assumption of weak wave-particle energy exchange so particle trajectories are unperturbed. For ULF waves with larger amplitudes and/or durations, however, the conventional theory becomes inaccurate since particle trajectories are strongly perturbed. Li *et al.*[130] extend the drift resonance theory into a nonlinear regime, to formulate nonlinear trapping of particles in a wave-carried potential well, and predict the corresponding observable signatures such as rolled-up structures in particle energy spectrum. After considering how this manifests in particle data with finite energy resolution, they compare the predicted signatures with Van Allen Probes observations. Their good agreement provides the first observational evidence for the occurrence of nonlinear drift resonance, highlighting the importance of nonlinear effects in magnetospheric particle dynamics under ULF waves.

In Earth's magnetosphere, the behavior of charged particles in response to ULF waves has long been understood in the framework of their resonant interactions with standing hydromagnetic waves. It has been argued that for impulse-excited waves, it may take a few wave cycles for the standing structure to be fully established; during these initial cycles, the waves should propagate along magnetic field lines before they are reflected from the ionosphere and are superimposed to form standing waves. However, it has been unclear how particles behave during the initial, traveling stage of the ULF wave evolution. Yang *et al.*[131] use a simplistic model of ULF wave evolution from traveling to standing waves, to investigate the response of low-energy electrons (presumably of plasmaspheric and/or ionospheric origin) immediately after the wave excitation. They find that an off-equatorial spacecraft would observe dispersive signatures in both energy and pitch angle spectra of electron fluxes, and the flux modulation may appear (at specific pitch angle and energy ranges) prior to the electromagnetic oscillations. These predicted signatures, consistent with the scenario of field-aligned streaming electrons surfing on traveling ULF waves, are indeed observed by the Cluster spacecraft during a ULF wave event on 25 September 2001. Their identification of such signatures, therefore, provides a new understanding of ULF wave evolution and wave-particle interactions in the inner magnetosphere.

Yu *et al.*[132] find that hot He^+ ions significantly alter the kinetic dispersion relation of Electromagnetic Ion Cyclotron (EMIC) waves and thus strongly affect the wave-driven electron pitch angle scattering rates. Increasing hot He^+ ion parallel temperature, temperature anisotropy, or abundance raises the pitch angle scattering rates of MeV electrons driven by the H^+ band EMIC waves. During the electron resonance with the He^+ and O^+ band EMIC waves, the electron pitch angle scattering rates are more sensitive to the variation of temperature anisotropy and abundance of hot He^+ ions than their parallel temperature. The increase of hot He^+ ion abundance (temperature anisotropy or abundance) generates a reduction of the energy range of electrons interacting

with the He^+ (O^+) band EMIC waves. Therefore, the effect of hot He^+ ions on the EMIC wave-driven electron pitch angle scattering should be involved in the radiation belt modeling.

Magnetosonic (MS) waves are believed to have the ability to affect the dynamics of ring current protons both inside and outside the plasmasphere. However, previous studies have focused primarily on the effect of high-frequency MS waves ($f>20$ Hz) on ring current protons. Yu *et al.*[133] investigated interactions between ring current protons and low-frequency MS waves (<20 Hz) inside the plasmasphere. They find that low-frequency MS waves can effectively accelerate <20 keV ring current protons on time scales from several hours to a day, and their scattering efficiency is comparable to that due to high-frequency MS waves (>20 Hz), from which they infer that omitting the effect of low-frequency MS waves will considerably underestimate proton depletion at middle pitch angles and proton enhancement at large pitch angles. Therefore, ring current proton modeling should take into account the effects of both low- and high-frequency MS waves.

Tao *et al.*[134] analyzed plasma perturbations occurring in the coexisting environment of powerful VLF transmitter emission, intense lightning strokes, and strong seismic activity during the pregnant period. The results suggest that anomalous electron bursts with energy dispersion in the range of 100~350 keV, forming the "wisp" signature, are due to cyclotron resonance of electrons with monochromatic waves from the powerful NWC VLF transmitters during nighttime. The intense broad band VLF emissions (up-going O^+ whistlers) are observed while the DEMETER satellite goes through the region of intense thunderstorm activities at mid-latitudes. However, the effects of intense lightning activity and pregnant earthquake have little impact on this kind of stable energy-dispersed electron structures, despite the fact that they are presumably two primary reasons for the particle precipitation in the ionosphere. The case studied here provides us a valuable opportunity to address the various sources triggering the anomalous plasma perturbations in the ionosphere.

Zhang *et al.*[135] investigated the characteristics of impulsive electric fields in the Earth's magnetosphere, as measured by the Van Allen Probes, in association with interplanetary shocks, as measured by Advanced Composition Explorer and Wind spacecraft in the solar wind from January 2013 to July 2016. It is shown that electric field impulses are mainly induced by global compressions by the shocks, mostly in the azimuthal direction, and the amplitudes of the initial electric field impulses are positively correlated with the rate of increase of the dynamic pressure across the shock in the dayside. It is also shown that the temporal profile of the impulse is related to the temporal profile of the solar wind dynamic pressure, P_d. It is suggested that during the first period of the impulse, the evolution of the electric field is directly controlled by external solar wind forcing, and thus, finite rates of change of P_d should be considered in the study of the interactions between solar wind and magnetosphere. The implications of shock-induced impulsive electric fields on the acceleration and transport of radiation belt electrons are also discussed.

Lü and Liu[136] studied the characteristic of large-scale convection electric field in the inner magnetosphere, using Magnetospheric Multiscale (MMS) observations between $L=5$ and $L=8$ over the period from 1 September 2015 to 31 October 2016, covering almost all Magnetic Local Time (MLT). Observations show that the DC convection electric field generally has small variations in this region. They investigate whether the convection electric field is correlated with geomagnetic indices and solar wind parameters. It is found that, among the studied parameters, solar wind electric field, z component of interplanetary magnetic field, AE and Kp indices show good correlations with the averaged convection electric field. The results in this paper provide valuable information for understanding the role of electric field on the dynamics of the inner magnetosphere.

Whistler wave-particle interactions play an important role in the Earth inner magnetospheric

dynamics and have been the subject of numerous investigations. By running a global kinetic ring current model (RAM-SCB) in a storm event occurred on 23–24 October 2002, Yu *et al.*[137] obtained the ring current electron distribution at a selected location at MLT of 9 and L of 6 where the electron distribution is composed of a warm population in the form of a partial ring in the velocity space (with energy around 15 keV) in addition to a cool population with a Maxwellian-like distribution. The warm population is likely from the injected plasma sheet electrons during substorm injections that supply fresh source to the inner magnetosphere. These electron distributions are then used as input in an implicit Particle-in-Cell Code (iPIC3D) to study whistler-wave generation and the subsequent wave-particle interactions. They find that whistler waves are excited and propagate in the quasi-parallel direction along the background magnetic field. Several different wave modes are instantaneously generated with different growth rates and frequencies. The wave mode at the maximum growth rate has a frequency of around $0.62\,\omega_{ce}$, which corresponds to a parallel resonant energy of 2.5 keV. Linear theory analysis of wave growth is in excellent agreement with the simulation results. These waves grow initially due to the injected warm electrons and are later damped due to cyclotron absorption by electrons whose energy are close to the resonant energy and can effectively attenuate waves. The warm electron population overall experiences net energy loss and anisotropy drop while moving along the diffusion surfaces towards regions of lower phase space density, while the cool electron population undergoes heating when the waves grow, suggesting the cross-population interactions.

Based on the statistical data measured by Van Allen Probes from 2012 to 2016, Li *et al.*[138] analyzed the effects of solar wind plasma flow and IMF on the spatial distribution of Earth's radiation belt electrons (>100 keV). The statistical results indicate that the increases in solar wind plasma density and flow speed can exert different effects on the spatial structure of the radiation belts. The high solar wind plasma density ($\geqslant 6$ cm^{-3})/flow pressure ($\geqslant 2.5$ nPa) and a large southward IMF ($B_z < -6$ nT) usually appear in the front of high-speed solar wind streams ($\geqslant 450$ km·s^{-1}), and they tend to narrow the outer radiation belt but broaden the slot region. In contrast, the increase in solar wind flow speed can broaden the outer radiation belt but narrows the slot region. When the solar wind speed exceeds 500 km·s^{-1}, the outer radiation belt electrons can penetrate into the slot region ($L < 3$) and even enter the inner radiation belt ($L < 2$). The lower-energy electrons penetrate into the deeper (smaller-L) region than the higher-energy electrons.

6 Plasmasphere

Yu *et al.*[139] presented two observational cases and simulations to indicate the relationship between the formation of butterfly-like electron pitch angle distributions and the emission of Low-Harmonic (LH) Fast Magnetosonic (MS) waves inside the high-density plasmasphere. In the wave emission region, the pitch angle of relativistic (>1 MeV) electrons becomes obvious butterfly-like distributions for both events (near-equatorially mirroring electrons are transported to lower pitch angles). Unlike relativistic (>1 MeV) electrons, energetic electrons (<1 MeV) change slightly, except that relatively low-energy electrons (<150 keV) show butterfly-like distributions in the 21 August 2013 event. In theory, the LH MS waves can affect different-energy electrons through the bounce resonance, Landau resonance, and transit time scattering. By performing the Fokker-Planck diffusion simulations, they demonstrate that the bounce resonance with the LH MS waves mainly leads to the butterfly pitch angle distribution of MeV electrons, whereas the Landau resonance and transit time scattering mainly affect energetic electrons in the high-density region.

A localized Pc 4~5 Ultralow-Frequency (ULF) wave event associated with a plasmaspheric plume was observed by THEMIS-E on the dawnside near L=6, which is identified by Zhang *et al.*[140] as a second harmonic poloidal wave. The plume was identified as a sudden density enhancement during an outbound

pass. The charged particle populations in the plume have a variety of periodic modulation characteristics at different energies. First, there is an antiphase relationship between magnetic field Br and particle flux across a wide energy range both for ions and electrons (50 keV to 1 MeV). Second, there is a 180° phase shift in the modulated ion flux within an energy range of 2~6 keV, with negative slope dispersions of ion pitch angle distributions at 2~6 keV and 50~75 keV, which are characteristics of drift-bounce resonances. Third, the lower-energy ($<$ 32 eV) ion flux is modulated at double the wave frequency, which is the result of $\boldsymbol{E}\times\boldsymbol{B}$ effect. Considering the generation mechanism of this poloidal mode wave within the plume, they find that it is likely generated by drift-bounce resonance from an unstable population of ions, due to an inward radial phase space density gradient. They suggest that the localization of waves to the plume is because the high plasma density reduces the local poloidal mode eigenfrequency, enabling a match to the drift-bounce frequencies of these ions, and resonant energy transfer from these particles to the eigenfunction at this location. This generates the Pc4~5 second harmonic poloidal waves at a much lower L region than would otherwise be expected.

Fast Magnetosonic (MS) waves play an important role in the dynamics of the inner magnetosphere. Theoretical prediction and simulation have demonstrated that MS waves can heat cold ions. However, direct observational evidence of cold ion heating by MS waves has so far remained elusive. Yuan *et al.*[141] show a typical event of cold ion heating by magnetosonic waves in a density cavity of the plasmasphere with observations of the Van Allen Probe mission on 22 August 2013. During enhancements of the MS wave intensity in the density cavity, the fluxes of trapped H^+ and He^+ ions with energies of 10~100 eV were observed to increase, implying that cold plasmaspheric ions were heated through high-order resonances with the MS waves. Based on simultaneous observations of ring current protons, they have calculated local linear growth rates, which demonstrate that magnetosonic waves can be locally generated in the density cavity. Their results provide a direct observational proof of the energy coupling process between the ring current and plasmasphere; that is, through exciting MS waves, the free energy stored in the ring current protons with ring distributions is released. In the density cavity of the plasmasphere, both cold H^+ and He^+ ions are heated by MS waves. As a result, the energy of the ring current can be transferred into the plasmasphere.

Plasmaspheric hiss is known to play an important role in radiation belt electron dynamics in high plasma density regions. Zhang *et al.*[142] present observations of two crossings of a plasmaspheric plume by the Van Allen Probes on 26 December 2012, which occurred unusually at the post-midnight- to-dawn sector between $L \approx 4$~6 during a geomagnetically quiet period. This plume exhibited pronounced electron densities higher than those of the average plume level. Moderate hiss emissions accompanied the two plume crossings with the peak power at about 100 Hz. Quantification of quasi-linear bounce-averaged electron scattering rates by hiss in the plume demonstrates that the waves are efficient to pitch angle scatter 10~100 keV electrons at rates up to 10^{-4} s^{-1} near the loss cone but become gradually insignificant to scatter the higher energy electron population. The resultant timescales of electron loss due to hiss in the nightside plume vary largely with electron kinetic energy over 3 orders of magnitude, that is, from several hours for tens of keV electrons to a few days for hundreds of keV electrons to well above 100-day for $>$1 MeV electrons. Changing slightly with L-shell and the multiquartile profile of hiss spectral intensity, these electron loss timescales suggest that hiss emissions in the nightside plume act as a viable candidate for the fast loss of the $\leqslant$100 keV electrons and the slow decay of higher energy electrons.

Whistler mode hiss acts as an important loss mechanism contributing to the radiation belt electron dynamics inside the plasmasphere and plasmaspheric plumes. Based on Van Allen Probes observations from September 2012 to December 2015, Zhang *et al.*[143] conduct a detailed analysis of hiss

properties in plasmaspheric plumes and illustrate that corresponding to the highest occurrence probability of plumes at L=5.0~6.0 and 18:00 MLT–21:00 MLT, hiss emissions occur concurrently with a rate of >80%. Plume hiss can efficiently scatter 10 to 100 keV electrons at rates up to 10^{-4} s^{-1} near the loss cone, and the resultant electron loss timescales vary largely with energy, that is, from less than an hour for tens of kiloelectron volt electrons to several days for hundreds of kiloelectron volt electrons and to >100 d for >5 MeV electrons. These newly obtained statistical properties of plume hiss and associated electron scattering effects are useful to future modeling efforts of radiation belt electron dynamics.

The generation of a High-Frequency Plasmaspheric Hiss (HFPH) wave observed by Van Allen Probes is studied in Ref.[144] for the first time. The wave has a moderate power spectral density (about 10^{-6} $nT^2 \cdot Hz^{-1}$), with a frequency range extending from 2 to 10 kHz. The correlated observations of waves and particles indicate that HFPH is associated with the enhancement of electron flux during the substorm on 6 January 2014. Calculations of the wave linear growth rate driven by the fitted electron phase space density show that the electron distribution after the substorm onset is efficient for the HFPH generation. The energy of the contributing electrons is about 1~2 keV, which is consistent with the observation. These results support that the observed HFPH is likely to be generated locally inside the plasmasphere due to the instability of injected kiloelectron volt electrons.

Plasmaspheric hiss waves have been frequently invoked to explain the slow loss of the radiation belt electrons. However, the effect of hiss waves outside the plasmasphere on the radiation belt electrons remains unclear. On the basis of Van Allen Probes observations and quasilinear simulations, He *et al.*[145] show that the hiss waves outside the plasmasphere are able to cause the significant precipitation loss of energetic electrons on a timescale of 1 day. In the event of interest, the hiss wave power spectra density reached up to 10^{-6} $nT^2 \cdot Hz^{-1}$, and the obtained pitch-angle diffusion coefficients are found to be 10^2~10^4 times larger than the momentum and cross diffusion coefficients. During a period of 1 day, the modeled hiss waves caused the depletion of 300~500 keV electrons by up to 10 times. These results suggest that the hiss waves outside the plasmasphere should be taken into account in the future radiation belt modeling.

Scattering by plasmaspheric hiss is responsible for the newly reported reversed energy spectra with abundant high-energy but fewer low-energy electrons between hundreds of kilo-electron volt and about 2 MeV in the inner magnetosphere. To deepen their understanding of the contributions of plasmaspheric hiss to the formation of reversed electron energy spectrum, Ni *et al.*[146] conduct a detailed theoretical parametric analysis through numerical simulations to explore the sensitivity of hiss-induced reversed electron energy spectrum to the ambient magnetic field, plasma density, and hiss wave distribution properties. Given L-shell, variations of ambient plasma density and wave frequency spectrum contribute importantly to the formation of reversed electron energy spectrum, while variations of background magnetic field (which usually shows small changes in the plasmasphere) and wave normal angle distribution play a less effective role. Their study suggests that the reversed electron energy spectrum has important implications for unveiling the sophisticated energy-dependent nature of wave-particle interactions and energetic particle dynamics in geospace.

Using the Van Allen Probe-A observations, Yuan *et al.*[147] obtained the global distribution of proton rings and calculated the linear wave growth rate of fast Magnetosonic (MS) waves in the region $L \approx 3$~6. Statistical and calculated results demonstrate that MS waves can be locally excited on the dayside outside the plasmapause, as well as in the dusk sector inside the plasmapause. The frequency range of unstable MS waves is strongly modulated by the ratio of the proton ring velocity (V_r) to the local Alfvén speed (V_A). High harmonic MS waves ($\omega > 20$ Ω_{H^+}) can be excited outside the plasmapause where $V_r / V_A < 1$, while low harmonic MS waves ($\omega < 10$ Ω_{H^+}) with frequencies less than 30 Hz are found to be

excited both outside and inside the plasmapause where $1< V_r/V_A< 2$.

By analyzing observations from Van Allen Probes in its inbound and outbound orbits, Ren *et al.*[148] presents evidence of coherent enhancement of cold plasmaspheric electrons and ions due to drift-bounce resonance with Ultralow Frequency (ULF) waves. From 18:00 UT on 28 May 2017 to 10:00 UT on 29 May 2017, newly formed poloidal mode standing ULF waves with significant electric field oscillations were observed in two consecutive orbits when Probe B was traveling inbound. In contrast to observations during outbound orbits, the cold (<150 eV) electrons measured by the HOPE instrument were characterized by flux enhancements several times larger and bidirectional pitch angle distributions during inbound orbits. The electron number density inferred from upper hybrid waves is twice as larger as during inbound orbits, which were also confirmed by an increase of spacecraft potential. The observed ULF waves are identified as second harmonic modes that satisfy the drift-bounce resonant condition of N=1 with cold electrons. An enhancement of the plasmaspheric ion number density to restore charge neutrality of plasmas in inbound orbits is observed, which is associated with an increase of ULF wave periods. The observations suggest that the dynamics of plasmaspheric electrons are modified by ULF waves through drift-bounce resonance and that plasmaspheric ions are indirectly impacted.

The spatio-temporal distribution of the field of Alfvén waves excited by the plasma tubes/shock wave front interaction is studied by Zong *et al.*[149]. This process results in localized pulses of Fast Magnetosonic (FMS) oscillations at the plasma tube boundary, which are stretched along the tube boundary/shock wave front intersection lines. These pulses move along the cylinder boundary together with the shock wave front. FMS oscillations generate Alfvén waves on the resonance magnetic shells. The polarization of the resonant Alfvén waves depends on the observation point and changes with time. The field dynamics of the resonant Alfvén waves are calculated for the Earth's plasmasphere/interplanetary shock interaction. A cylindrical plasma tube is used to simulate the magnetospheric near-equatorial region. Based on the calculations, the poloidal Alfvén waves excited inside the magnetosphere due to the plasmasphere/interplanetary shock wave front interaction are explained. These waves are particular in that they result from Alfvén resonance and are not associated with any high-energy particle fluxes.

Based on the wave and proton observations by Van Allen Probes A and B, Liu *et al.*[150] examined the effects of hot protons (0.01~50 keV) on fast Magnetosonic (MS) waves inside and outside the Earth's plasmasphere. In the low-density plasma trough outside the plasmapause, the gyroresonance interactions between hot protons and MS waves not only cause the MS wave growth at some frequencies but also lead to the damping of MS waves at other frequencies, which depends on the proton phase space density gradient and the ambient plasma density. The gyroresonance of the observed hot protons cannot excite MS waves near the lower hybrid resonance frequency and even causes the MS wave damping. Thus, the frequencies of the observed MS waves outside the plasmapause are usually lower than the lower hybrid resonance frequency. In the high-density plasmasphere, the observed hot protons merely lead to the weak gyrodamping of MS waves. The persistent existence of lower band MS waves indicates that the weak gyrodamping effect of hot protons on MS waves is ignorable in the high-density plasmasphere.

7 Outer Magnetosphere

Magnetosheath properties, particularly those related to magnetopause Magnetic Reconnection (MR), are investigated by Zhang *et al.*[151]. (i) Asymmetries are found to exist in the distributions of plasma and magnetic field parameters in the magnetosheath. These asymmetries are related to the IMF orientation, and they are produced either on the bow shock

or inside the magnetosheath. Thus, one must be very cautious in directly using the upstream solar wind and IMF properties as the magnetopause MR initiation conditions, since the magnetosheath parameters are not the same everywhere. (ii) A unique method is introduced to estimate how much IMF magnetic flux passes through the magnetosphere *via* MR on either the low-latitude or the high-latitude magnetopause. This flux mainly varies with three independent parameters: the IMF clock angle θ_{CL}, the magnetosheath plasma β, and the solar wind sound Mach number MS. Surprisingly, the magnetic fluxes passing through the magnetosphere are comparable under the southward and northward IMF conditions. (iii) The dipole tilt angle, the property from the inside of the magnetosphere, also controls the magnetosheath parameters. As the Earth's dipole tilt angle varies, the plasma pressure ridge shifts its location but remains near the magnetic equator. The stagnation point of the magnetosheath flow on the magnetopause, however, remains at the subsolar point no matter how large the dipole tilt angle is. These behaviors may be determinative of the locations of MR and the generation of flux transfer events on the magnetopause.

The spatiotemporal structure of Alfvén waves excited by a moving pressure pulse on the magnetopause is analytically explored by Klimushkin *et al.*[152]. These waves are supposed to be responsible for field aligned currents generating traveling convection vortices in the ionosphere. It is found that a moving source generates two wave modes, a primary and a secondary mode, having different azimuthal wave vectors and frequencies. Both modes represent surface waves with amplitudes exponentially decreasing from the magnetopause. At a given azimuthal location, they also decrease with time as the source passes away. For the primary mode, the wave frequency equals the Alfvén resonant frequency on the surface of the source, while for the secondary mode the frequency equals the local resonant frequency. The dependence of the frequency of the secondary mode on the radial coordinate results in phase mixing, which leads to a change of the wave polarization from mixed into toroidal polarization. For both primary and secondary modes, the azimuthal component of the wave vector equals the corresponding wave frequency divided by the speed of the source. Superposition of the primary and secondary modes produces plasma vortices behind the source.

Magnetic cavities (sometimes referred to as magnetic holes) at electron kinetic scale are thought to be one of the extremely small intermittent structures formed in magnetized turbulent plasmas, where the turbulence energy cascaded down to electron scale may finally be dissipated and consequently energize the electrons. However, the geometry and formation of these structures remain not definitively resolved. Liu *et al.*[153] discussed an electron scale magnetic cavity embedded in a proton scale magnetic cavity observed by the MMS spacecraft in the magnetosheath. By applying an innovative particle sounding technique, they directly depict the boundary of the electron scale magnetic cavity and uncover the geometry. They find that this structure is nearly circular with a radius of 10.0 km and its formation is due to the diamagnetic current. Investigation of the electron scale structure is only recently made possible by the high spatial and temporal resolution provided by MMS observations.

As one type of driver of magnetospheric Alfvén waves, foreshock transients have received less attention than, for example, the Kelvin-Helmholtz instability, discrete, and broadband frequency solar wind dynamic pressure oscillations, and interplanetary shocks. Previous works show that foreshock transients can induce both Alfvén mode and compressional mode Pc 3~5 ULF waves inside the magnetosphere. However, to our knowledge, none of these reported Pc 3~5 waves, induced by foreshock transients, are proved to be localized in the magnetosphere. In this paper, using in situ and ground-based observations, Shen *et al.*[154] reports the generation of localized magnetospheric compressional waves and Field Line Resonances (FLRs) by a foreshock transient. Both the foreshock transient and Pc5 ULF waves were found on the dusk side; while on the morning side of the magnetosphere, no clear wave

signatures were captured. Their results demonstrate that in addition to the global effects of foreshock transients on the magnetosphere reported earlier, foreshock transients can also generate localized magnetospheric responses in the Pc5 range with clear dawn-dusk asymmetry. A suite of eight dayside spacecraft plus ground magnetometer measurements make possible the determination of the foreshock transient driver and dawn-dusk asymmetry of the magnetospheric response not previously reported with such a complete data set.

A new type of electron-scale coherent structure, referred to as electron vortex magnetic holes, was identified recently in the Earth's magnetosheath turbulent plasma. These electron-scale magnetic holes are characterized by magnetic field strength depression, electron density enhancement, temperature and temperature anisotropy increase (a significant increase in perpendicular temperature and a decrease in parallel temperature), and an electron vortex formed by the trapped electrons. The strong increase of electron temperature indicates that these magnetic holes have a strong connection with the energization of electrons. Using high time resolution in situ measurements from the MMS mission, it is further shown that electron-scale whistler waves coexist with electron-scale magnetic holes. These whistler waves were found not propagating from remote regions, but generated locally due to electron temperature anisotropy ($T_{e\perp}/T_{e\parallel} > 1$) inside the magnetic holes. Huang *et al.*[155] provided new insights into the electron-scale plasma dynamics in turbulent plasmas.

Flux ropes are frequently observed in the space plasmas, such as solar wind, planetary magnetosphere and magnetosheath *etc.*, and play an important role in the reconnection process and mass and flux transportation. One usually uses bipolar signature and strong core field to identify the flux ropes. Huang *et al.*[156] proposed one new method to identify flux ropes based on the correlations between the variables of the data from in situ spacecraft observations and the "Target Function to be Correlated" (TFC) from the ideal flux rope model. Through comparing the correlation coefficients of different variables at different times and scales, and performing weighted-average techniques, this method can derive the scales and locations of the flux ropes. They compare it with other methods and also discuss the limitation of their method.

Conjunction observations of the magnetic field and plasma by Cluster and TC-1 at the dayside magnetosphere are presented to investigate the sequential flux ropes transferred from the Low Latitude Boundary Layer (LLBL) to the high altitude cusp on 10 March 2004. Three sequential flux ropes originating from the dayside low latitude magnetopause are first detected by TC-1. After 5.3 min, three sequential flux ropes accumulated with energetic oxygen ions are also detected by Cluster in the high altitude cusp. The recurrence period of these flux ropes is 3 min. The number density of energetic oxygen ions in the cusp flux rope is 0.25 cm^{-3} detected from CIS/CODF instrument on Cluster. It is found that oxygen ions with energy lager than 10 keV have a narrow pitch angle (less than 90°) distribution in the southern high altitude cusp. While oxygen ions with energy less than 10 keV are distributed in a wide pitch angle from 0 to 180°. Counter-streaming energetic oxygen ions are found in these flux ropes in the high altitude cusp. Duan *et al.*[157] suggest that the oxygen ions with energy less than 10 keV in the high altitude cusp have two source regions. One is from the dayside magnetopause and the other is from the low altitude cusp. Their investigations first provide evidence that flux ropes at dayside low latitude magnetopause can carry energetic oxygen ions into the high altitude cusp region.

Wang *et al.*[158] use the bow shock crossings contained in the Space Physics Data Facility database, collected by four spacecraft (IMP 8, Geotail, Magion-4, and Cluster1) to analyze the effect of the Interplanetary Magnetic Field (IMF) B_y component on the bow shock position and shape. Although the IMF B_z component is usually considered much more geoeffective than B_y, they find that the dayside bow shock is more responsive to the eastward component of the IMF than the north-south one. They believe

that the explanation lies in the changes that the B_z component induces on the magnetopause location and shape, which largely compensate for the corresponding changes in the dayside bow shock location. In the tail, they find that the bow shock cross section is elongated roughly in the direction perpendicular to the IMF direction, which agrees with earlier modeling studies.

The small-scale mirror mode excited by electron dynamics is a fundamental physical process, attracting research interest in space, laboratory, and astrophysical plasma physics over the past half century. However, the investigations of this process were mostly limited to theories and numerical simulations, with no direct observational evidence for their existence. Yao *et al.*[159] present clear observations of electron mirror-mode using Magnetospheric Multiscale data at unprecedented high temporal cadence. These structures are train-like, compressible, non-propagating, and satisfy the theoretical excitation and electron trapping conditions. They were observed near the Earth's foreshock and its downstream turbulence during the corotating interaction region events, which could be involved with the interaction between solar wind and Earth.

Using the bow shock crossing events from four spacecraft: IMP 8, Geotail, Magion-4, and Cluster 1, a new three-dimensional asymmetric bow shock model is constructed by Lu *et al.*[160]. The model is parameterized by the solar wind dynamic pressure, the interplanetary magnetic field, magnetosonic Mach number, solar wind β, and the Earth's dipole tilt angle. It is shown that the shape and size of bow shock are both affected by the dipole tilt angle. The dipole tilt angle causes asymmetries in the meridional plane: (i) the bow shock subsolar standoff distance and the north-south asymmetry increase with the dipole tilt angle; (ii) as the dipole tilt angle increases, the shock flaring angle in the equatorial plane is slightly reduced, while in the meridional plane the flaring angle obviously decreases in Southern Hemisphere and keeps almost unchanged in the Northern Hemisphere, the flaring angle in the Northern Hemisphere is larger than in the Southern Hemisphere; (iii) the effects of negative dipole tilt angle on shock flaring are just the opposite of those for positive tilt, and the effects of dipole tilt angle on the shape of the bow shock are north-south symmetric. The model results are also validated by comparing with one previous empirical model and with observational crossings, and it is demonstrated that the new model is able to predict the observed crossings more accurately and can better describe the rotational asymmetry and north-south asymmetry of the Earth's bow shock.

Tang *et al.*[161] report an ion-scale magnetic flux rope (the size of the flux rope is about 8.5 ion inertial lengths) at the trailing edge of Kelvin-Helmholtz (KH) waves observed by the Magnetospheric Multiscale (MMS) mission on 27 September 2016, which is likely generated by multiple X-line reconnection. The currents of this flux rope are highly filamentary: in the central flux rope, the current flows are mainly parallel to the magnetic field, supporting a local magnetic field increase at about 7 nT, while at the edges the current filaments are predominantly along the antiparallel direction, which induce an opposing field that causes a significant magnetic depression along the axis direction (>20 nT), meaning the overall magnetic field of this flux rope is depressed compared to the ambient magnetic field. Thus, this flux rope, accompanied by the plasma thermal pressure enhancement in the center, is referred to as a crater type. Intense Lower Hybrid Drift Waves (LHDWs) are found at the magnetospheric edge of the flux rope, and the wave potential is estimated to be about 17% of the electron temperature. Though LHDWs may be stabilized by the mechanism of electron resonance broadening, these waves could still effectively enable diffusive electron transports in the cross-field direction, corresponding to a local density dip. This indicates LHDWs could play important roles in the evolution of crater flux ropes.

At the Earth's magnetopause, the electron transport due to Kinetic Alfvén Waves (KAWs) is investigated in an ion-scale flux rope by the Magnetospheric Multiscale mission. Clear electron dropout around 90° pitch angle is observed throughout the

flux rope, where intense KAWs are identified. The KAWs can effectively trap electrons by the wave parallel electric field and the magnetic mirror force, allowing electrons to undergo Landau resonance and be transported into more field-aligned directions. The pitch angle range for the trapped electrons is estimated from the wave analysis, which is in good agreement with direct pitch angle measurements of the electron distributions. The newly formed beam-like electron distribution is unstable and excites whistler waves, as revealed in the observations. Tang *et al.*[162] suggest that KAWs could be responsible for the plasma depletion inside a flux rope by this transport process, and thus be responsible for the formation of a typical flux rope.

Kinetic-Scale Magnetic Dips (KSMDs), with a significant depression in magnetic field strength, and scale length close to and less than one proton gyroradius, were reported in the turbulent plasmas both in recent observation and numerical simulation studies. These KSMDs likely play important roles in energy conversion and dissipation. Yao *et al.*[163] present observations of the KSMDs that are labeled whistler mode waves, electrostatic solitary waves, and electron cyclotron waves in the magnetosheath. The observations suggest that electron temperature anisotropy or beams within KSMD structures provide free energy to generate these waves. In addition, the occurrence rates of the waves are higher in the center of the magnetic dips than at their edges, implying that the KSMDs might be the origin of various kinds of waves. They suggest that the KSMDs could provide favorable conditions for the generation of waves and transfer energy to the waves in turbulent magnetosheath plasmas.

Mirror-mode structures are widely observed in space plasma environments. Although plasma features within the structures have been extensively investigated in theoretical models and numerical simulations, relatively few observational studies have been made, due to a lack of high-cadence measurements of particle distributions in previous space missions. Electron dynamics associated with mirror-mode structures are studied by Yao *et al.*[164] based on Magnetospheric Multiscale observations of electron pitch angle distributions. They define mirror-mode peaks/troughs as the region where the magnetic field strength is greater/smaller than the mean field. The observations show that most electrons are trapped inside the mirror-mode troughs and display a donut-like pitch angle distribution configuration. Besides the trapped electrons in mirror-mode troughs, they find that electrons are also trapped between ambient mirror-mode peaks and coexisting untrapped electrons within the mirror-mode structure. Analysis shows that the observed donut-like electron distributions are the result of betatron cooling and the spatial dependence of electron pitch angles within the structure.

Kelvin-Helmholtz Waves (KHWs), which have been widely observed at the magnetopause in the region near the Earth, play an essential role in the transport of solar wind plasma and energy into the magnetosphere under dominantly northward IMF conditions. In this study, Ling *et al.*[165] present simultaneous observations of KHWs under the northward IMF observed by both the Acceleration, Reconnection, Turbulence, and Electrodynamics of Moon's Interaction with the Sun (ARTEMIS) spacecraft in the Earth's magnetotail around the lunar orbit (at $x \approx -50\,R_e$, $y \approx 30\,R_e$, dusk side) and the Geotail in the near-Earth space (at $x \approx -5\,R_e$, $y \approx -10\,R_e$, dawn side). The KHWs are quantitatively characterized by their dominant period, phase velocity, and wavelength, utilizing wavelet analysis and an approximation of their center-of-mass velocity. Their results suggest that the phase velocity and spatial scale of KHWs may increase as they propagate along with the boundary layer toward the tail. Alternatively, the differences between the ARTEMIS and Geotail observations may indicate the possibility of dawn-dusk asymmetry in the excited KHWs in this study. Their results strongly evidence the existence of the development of KHWs in terms of their wave frequency and scale size in the magnetotail and provide insight into the time evolution of KHWs along the magnetopause.

The sudden enhancements of magnetic strength,

named Magnetic Peaks (MPs), are often observed in the magnetosheath of magnetized planets. They are usually identified as Flux Ropes (FRs) or magnetic mirror mode structures. Previous studies of MPs are mostly on the Magnetohydrodynamics (MHD) scale. In Ref.[166], an electron scale MP is reported in the Earth magnetosheath. They present a typical case with a scale of about 7 electron gyroradii and a duration of about 0.18 s. A strong magnetic disturbance and associated electrical current are detected. Electron vortex is found perpendicular to the magnetic field line and is self-consistent with the peak. They use multipoint spacecraft techniques to determine the propagation velocity of the MP structure and find that the magnetic peak does propagate relative to the plasma (ion) flow. This is very different from the magnetic mirror mode that does not propagate relative to the plasma flow. Furthermore, they develop an efficient method that can effectively distinguish "magnetic bottle like" and "FRs like" structures. The MP presented in this study is identified as magnetic bottle like type. The mechanism to generate the electron scale magnetic bottle like structure is still unclear, suggesting that new theory needs to be developed to understand such small-scale phenomena.

Crescent-shaped electron distributions perpendicular to the magnetic field are an important indicator of the electron diffusion region in magnetic reconnection. They can be formed by the electron finite gyroradius effect at plasma boundaries or by demagnetized electron motion. Tang *et al.*[167] present Magnetospheric Multiscale mission observations of electron crescents at the flank magnetopause on 20 September 2017, where reconnection signatures are not observed. These agyrotropic electron distributions are generated by electron gyromotion at the thin electron-scale magnetic boundaries of a magnetic minimum after magnetic curvature scattering. The variation of their angular range in the perpendicular plane is in good agreement with predictions. Upper hybrid waves are observed to accompany the electron crescents at all four Magnetospheric Multiscale spacecraft as a result of the beam-plasma instability associated with these agyrotropic electron distributions. This study suggests electron crescents can be more frequently formed at the magnetopause.

Using Global MHD model the spatial distribution of Flux Transfer Events (FTE) at the dayside magnetopause under high solar wind speed is investigated by Chen[168]. The solar wind conditions of this case are: v_{sw}=1200 km·s^{-1}, n_{sw}=3 cm^{-3}, B_z =– 8.3 nT, B_y= 8.3 nT and B_x= 0 nT. The simulation results virtually agree with those expected FTE signatures from observations, and bipolar signatures and related variations of number density pressure and velocity are found. A total number of 39 FTE are observed by ten virtual probes which are spread over the magnetopause from y=–5 R_e to y=5 R_e. 14 FTE are found when the probe is near to the noon. However, when the probe is located near y =–5 R_e and y = 5 R_e, the same number, 3, of FTE in both locations is found. Furthermore, 8 FTE are found when the probe is adjacent to y=–2.5 R_e and 11 FTE are found near y= 2.5 R_e. In a nutshell, the number of FTE decreases as the observed probes approach the flank of the magnetopause which could be caused by the distribution of solar wind velocity in the magnetosheath.

The Kelvin-Helmholtz (K-H) waves predominantly excited at the Earth's low-latitude magnetopause were suggested to be dawn-dusk asymmetric. Lu *et al.*[169] report a prolonged simultaneous observation of the K-H waves on the dawn and dusk magnetopause by Magnetospheric Multiscale (MMS) and THEMIS-A (THA) spacecraft, respectively. The quasi-periodic K-H waves on both flanks have unambiguous low-density and high-speed patterns. The wave periods vary gradually on both flanks, with similar average periods (303±107 s for MMS and 266±102 s for THA). The lag time between the variations of the wave periods is close to the wave propagation time from THA to MMS, which suggests that the K-H waves generate and propagate quasi-symmetrically on both flanks. Larger local magnetic shear angles are observed on the trailing edges by MMS than by THA, which is probably due to the strong magnetic field distortion during the tailward

propagation. The increased magnetic shear may excite magnetic reconnection, thus contributing to the formation of the low-latitude boundary layer.

Although many works have investigated the occurrence rate of Flux Transfer Events (FTEs) under different upstream conditions, the relation between the upstream Mach number and the occurrence rate of FTEs remains unclear. By using global magnetohydrodynamics simulations, Chen *et al.*[170] studied the occurrence rate of FTEs under different upstream Alvénic Mach numbers (*Ma*). A recently developed method is used to identify the FTEs throughout the dayside magnetopause. It shows that the occurrence rate of FTEs decreases with increasing value of *Ma*. They suggest that the magnetosheath β, which increases with increasing *Ma*, plays an important role in the process of reconnection and thus affects the occurrence rate of FTEs. As the solar wind Ma increases with increasing distance from the Sun, they speculate that the planet with a larger heliocentric distance may have fewer FTEs because of the increasing value of upstream *Ma*.

By using global MHD simulation, Sun *et al.*[171] presented the large-scale characteristics of Flux Transfer Events (FTEs) on the dayside magnetopause during periods of generic southward interplanetary magnetic field. It is revealed that FTEs can be generated both at lower and higher latitudes, and also at almost all local times. The occurrence rate of FTEs has an apparent longitudinal/latitudinal dependence, with a higher occurrence rate near noon/at lower latitudes. It is further shown that even under constant solar wind conditions, the azimuthal lengths of FTEs can have large variability, changing from as short as $<1\,R_e$ to as long as $>10\,R_e$ for different FTEs. Moreover, FTEs generated closer to the subsolar point tend to have longer extensions along their axes. This new knowledge of large-scale properties of FTEs will improve our understanding of the solar wind-magnetosphere interaction.

The soft X-ray emissions from the Earth's magnetosheath and cusp regions are simulated under different solar wind conditions, based on the PPMLR-MHD code. The X-ray images observed by a hypothetical telescope are presented, and the basic responses of the magnetopause and cusp regions are discernable in these images. From certain viewing geometries, the magnetopause position in the equatorial plane, as well as the latitudinal scales and azimuthal extent of cusp can be directly extracted from the X-ray images. With these reconstructed positions, the issues that Sun *et al.*[172] are able to analyze include but are not limited to the compression of magnetopause and widening of the cusp after enhancement of solar wind flux, as well as the erosion of the magnetopause and equatorward motion of cusp after the southward turning of the interplanetary magnetic field. Hence, the X-ray imaging is an appropriate technique to study the large-scale motion of magnetopause and cusps in response to solar wind variations.

Two ion-scale Flux Ropes (FRs) embedded in southward flow at the dayside magnetopause were encountered by Magnetosphere Multiscale (MMS) spacecraft sequentially in 9 s, as reported by Jiang *et al* [173]. Super-Alfvénic electron jet, non-zero electric field in electron frame, and strong current are observed in these two FRs. Specifically, whistler waves are observed inside and outside the FRs. The properties of whistler waves inside the FRs are quite different from whistler waves outside the FRs. Whistler waves outside the FRs have a frequency range between $0.1f_{ce}$ and f_{ce} (f_{ce} is the electron gyro-frequency) and they propagate parallel to the magnetic field. Whistler waves inside the FRs have a frequency range between $0.5f_{ce}$ to f_{ce} and they propagate antiparallel to the magnetic field. The intensity of whistler waves outside FRs is stronger than the whistler waves inside FRs. Electron beam instability may be the reason for the generation of whistler waves observed here. The difference between whistlers inside and outside FRs may have a close relationship with different magnetic topology and electron distribution inside and outside FRs.

Wang *et al.*[174] use the AMR-CESE-MHD model to investigate the influences of the IMF B_z and the upstream solar wind dynamic pressure (D_p) on

Earth's magnetopause and bow shock. Their results present that the earthward displacement of the magnetopause increases with the intensity of the IMF B_z. The increase of the northward IMF B_z also brings the magnetopause closer to the Earth even though with a small distance. Their simulation results show that the subsolar bow shock during the southward IMF is much closer to the Earth than during the northward IMF. As the intensity of IMF B_z increases (also the total field strength), the subsolar bow shock moves sunward as the solar wind magnetosonic Mach number decreases. The sunward movement of the subsolar bow shock during southward IMF is much smaller than that during northward IMF, which indicates that the decrease of solar wind magnetosonic Mach number hardly changes the subsolar bow shock location during southward IMF. Their simulations also show that the effects of upstream solar wind dynamic pressure (D_{P}) changing on both the subsolar magnetopause and bow shock locations are much more significant than those due to the IMF changes, which is consistent with previous studies. However, in their simulations, the earthward displacement of the subsolar magnetopause during high solar wind D_{P} is greater than that predicted by the empirical models.

Using the Cluster data from 2001 to 2010, Pang *et al.*[175] studied the spatial distribution of effective ion polytropic index in the southern high latitude magnetosheath, and joint-modulation of ion polytropic index by temperature anisotropy and MHD disturbances. The magnetosheath ions generally experience various polytropic processes with different polytropic index. The median polytropic indexes of magnetosheath ions in the GSE xy plane decrease toward the bow shock. Near the magnetopause, the median polytropic indexes are basically between isothermal and adiabatic except in the dusk side flank close to the terminator. The analysis of correlation coefficient of perturbed ion number density with parallel magnetic field CC_ $\delta n \delta B_{||}$ and ion temperature anisotropy parameter A_{T}, indicates that the dominant MHD disturbance near magnetopause is a slow mode with larger ion temperature anisotropy, and there are various modes of MHD disturbances with insignificant ion temperature anisotropy near the bow shock. The polytropic index modulated by slow mode disturbances is generally larger than that modulated by fast mode disturbances, and the larger ion temperature anisotropy, the larger polytropic index. The median polytropic indexes modulated jointly by slow mode disturbances and the strong ion temperature anisotropy can be larger than 1.0, while those modulated by fast mode disturbances and weak temperature anisotropy can be even possibly close to zero. Moreover, because of pronounced dusk-favored asymmetry of ion temperature anisotropy, the median polytropic index in the dawnside flank of the magnetosheath near the terminator is smaller than that in the dusk side flank of the magnetosheath. The good correspondence between the distributions of median polytropic indexes and ion temperature anisotropy and MHD disturbances indicates that the ion temperature anisotropy and MHD disturbances determine the distribution of the polytropic index in the magnetosheath.

On 6 December 2015, the Magnetospheric Multiscale satellites traversed the southward outflow of a magnetic reconnection on the magnetopause from the outside in. The magnetic structures or the geometries of the field lines inside this outflow are distinguished in detail by using the plasma and magnetic field observations. A flux rope and the magnetic flux piling-up against this flux rope are found embeded in this outflow. The strong magnetosheath magnetic field allows the formation of a magnetic mirror in the flux pileup region. As the Magnetospheric Multiscale satellites approached the flux rope inside this mirror, the pitch angles of electrons converge toward 90°, indicating that the electrons are trapped inside the mirror. The local loss cones of these electrons along the satellite trajectory are estimated. It is found by Zhu *et al.*[176] that the triangle-like pitch angle distribution is well embraced by the curves of the estimated local loss cones. The energy spectra inside the mirror show that the electrons are accelerated in the direction perpendicular to the magnetic field. A test particle method is used

to reproduce the acceleration process in a fitted 3D magnetic field model. The results show that the quasi-perpendicular electrons experience the betatron acceleration when drifting into the stronger field region and that the electrons may also experience the Fermi acceleration when their pitch angles enlarge. The mirror structure on the magnetopause provides a unique opportunity to explore the behaviors of the magnetic reconnection associated with electrons.

An interplanetary shock impinged on the Earth's magnetosphere on 17 March 2015, and caused an instant change of Total Electron Content (TEC) measured by Ground-based global Positioning System (GPS) receivers. Hao *et al.*[177] attribute the sudden TEC variation to magnetospheric compression by the shock, and in this paper they follow to examine the process by incorporating high time resolution (1 s) TEC data from some GPS receivers as well as TEC measurements from Beidou Navigation Satellite System. These observations add new understandings to the reaction of magnetosphere to a strong shock. The compression drives plasma in dayside magnetosphere to move earthward, and the contraction of the Earth's magnetic field will make plasma concentrate near the equatorial plane. The scenario involves dynamics of the plasmasphere where the plasma is dense enough to contribute to the variations of both GPS and Beidou TEC. In addition, they also inspect TEC measured on board sever allow Earth orbit satellites, but no significant change is identified possibly due to inappropriate satellite position. The above TEC measurements, known collectively as Global Navigation Satellite System (GNSS) TEC techniques, exhibit an unprecedented capability of remote sensing and will hopefully provide new insight into the dynamics of magnetosphere.

Dong *et al.*[178] investigated the current carriers and current sources of an ion scale tangential magnetopause current layer using the Magnetospheric Multiscale four spacecraft data. Within this magnetopause current layer, ions and electrons equally contribute to the perpendicular current, while electrons carry nearly all the parallel current. The energy The energy range of all these current carriers is predominantly from middle to high (>100 eV), where particles with higher energies are more efficient in producing the current. By comparing each term, two-fluid Magnetohydrodynamic (MHD) theory is able to describe the current sources to a large degree because the sum of all the perpendicular currents from MHD theory could account for the currents observed. In addition, they find that the ion diamagnetic current is the main source of the total perpendicular current, while the curvature current can be neglected. Nevertheless, ions and electrons both carry comparable current due to the redistribution of the electric field and show features beyond the classic Chapman-Ferraro model, particularly on the front side of the boundary layer where the electric field reversal is most intense. They also show a second, comparative event in which ions do not satisfy MHD theory, while the electrons do. The small-scale, adiabatic parameter (square of curvature radius/gyroradius) supports their interpretation that this second event contains ion scale substructure. They suggest that comparing the predicted MHD current with plasma current can be a good method to judge whether the MHD theory is satisfied in each specific circumstance, especially for high-precision Magnetospheric Multiscale data.

Xiao *et al.*[179] use the multiple-point magnetic measurements from the Cluster mission to investigate the curvature and gradient of the magnetic field as well as their relations with the current density inside the cusp region under different IMF conditions. From two event studies, it is shown that the curvature radius of magnetic field line is on average 5.13 R_e under southward IMF and 19.75 R_e under northward IMF condition. The directional angle of curvature is more distributed in a wider range under southward condition. The gradient of the magnetic field strength B is larger with a larger standard deviation under southward IMF condition. These results imply that the cusp region has more complicated magnetic structures under southward IMF condition. Through the correlation analysis between the magnetic field parameters and the current density, it is found that

the magnetic gradient has a strong relation with total current density j_t and perpendicular current density $j_\perp$ when the ratio of parallel component $j_\parallel$ to j_t decreases, possibly due to gradient B drift. Furthermore, they present a statistical study on the 19 cusp crossing events from July 2003 to September 2003. The results from the statistical study are consistent with the event studies.

The Low-Latitude Boundary Layer (LLBL) plays an important role as a transition layer in coupling the magnetosheath and magnetosphere. Using high-resolution Magnetospheric Multiscale data, Dong *et al.*[180] analyzed the electron distributions in the inner region of the LLBL, during an active period of magnetic reconnection under southward interplanetary magnetic field. According to the measured electron energy anisotropy, they suggest that this inner LLBL can be divided into six sublayers corresponding to three types of magnetic field-line topologies: (i) open magnetic field line topology from magnetosheath to southern magnetosphere, (ii) open magnetic field line topology from magnetosheath to northern magnetosphere, and (iii) reclosed magnetic field line topology. These different scenarios indicate that magnetic reconnection occurs at both northern and southern locations of the spacecraft and thus suggest that magnetic reconnection was active simultaneously at high and low latitudes on the magnetopause, equatorward of the cusps. These results provide evidence within the LLBL for such multiple X-line formation.

The geospace inner magnetosphere, within about 10 Earth radii, contains various plasma populations with energy from a few electron volts to megaelectron volts and plays important roles in regulating the energy density of the magnetosphere, the magnetic field configuration, and wave dynamics. As an integrated part of the magnetosphere, the inner magnetosphere region also ties to other regions and can change the global geospace circulation. Therefore, understanding both internal and external cross-energy/population interactions can help further our knowledge of the inner magnetosphere dynamics and nonlinear feedback processes. In view of this, in the past 5 years (2014–2018), the Geospace Environment Modeling (GEM) Focus Group Inner Magnetosphere Cross-Energy/Population Interactions (IMCEPI) has gathered and boosted community-wide interactions among observation, simulation, and modeling studies. Yu *et al.*[181] commentary report some major accomplishments of the interactive inner magnetosphere community that were advanced by the IMCEPI Focus Group discussions and layouts remaining challenges that need to be carried on.

It is still unknown nowadays whether magnetic reconnection can intrinsically accelerate energetic electrons. Observations in the Earth's magnetotail usually indicate strong electron acceleration during magnetic reconnection, while observations at the Earth's magnetopause rarely show such features. With the recently launched Magnetospheric Multiscale (MMS) mission, Fu *et al.*[182] report the first evidence of energetic-electron acceleration at a reconnecting magnetopause. They find that the acceleration of electrons, with energy up to 70 times their thermal energy, occurs in the magnetosheath side of the ion diffusion region and is associated with strong whistler waves. Such acceleration, not contaminated by the magnetospheric population, is attributed to nonadiabatic wave-particle interactions, as supported by analyses of the resonance condition. It manifests that energetic-electron acceleration can happen at the reconnecting magnetopause, like that in the tail.

Energetic electrons exist widely in the turbulent magnetosheath, but how they are generated remains unclear. Liu *et al.*[183] report a new structure, at which electrons are efficiently accelerated in the direction parallel to the magnetic field. Such a structure, formed at the edge of a High-Speed Jet (HSJ), is a Tangential Discontinuity (TD) in the MHD regime, but exhibits impulsive fine structures in the kinetic-scale regime. The pulsation of the TD, caused by time-varying size of the HSJ, leads to the energization process: when the transverse section of the HSJ increases, a magnetic mirror is formed and subsequently electrons are trapped and accelerated via the Fermi mechanism; when the transverse section of the HSJ decreases, the magnetic mirror dis-

appears and subsequently electrons escape. Such parallel electron heating can lead to three times of parallel-temperature increase; it can shed light on the study of electron heating in the solar wind, where TDs exist extensively.

Magnetic nulls are believed to play important roles in the energy dissipation during reconnection. Such nulls have been observed in reconnection at the magnetopause, magnetosheath, and magnetotail but have never been observed in reconnection at the bow shock. Recently, four reconnection events were reported at the terrestrial bow shock, by utilizing Magnetospheric Multiscale (MMS) data. Chen *et al.*[184] examine whether the magnetic nulls exist in these events. They successfully find radial nulls in three of the events, meaning that spacecraft were close to x points in these events; we, however, cannot find radial nulls in another event, which was actually a crossing of the reconnection exhaust region. The minimum distance between radial nulls and spacecraft is 8 km, about 0.3 ion inertial length. They reconstruct topologies of these nulls and subsequently resolve the reconnection rates in these events. They find that the resolved reconnection rates are comparable with those at the magnetopause and magnetotail. Surprisingly, they do not find electron heating at the radial nulls. Their results are useful to understand the reconnection at bow shock.

8 Magnetotail

Dipolarization Fronts (DFs) are important for energy conversion, particle acceleration, and flux transport in the magnetotail. The partition of energy conversion between ions and electrons and the energy dissipation at DFs are not well understood. Zhong *et al.*[185] present a statistical study of energy conversion and dissipation of 122 DFs observed by Magnetospheric Multiscale mission in the magnetotail. Statistically, electromagnetic energy transfers to plasma at DF. The released energy is mainly transferred to ions rather than electrons. On average, ions gain energy across the whole DF, while electrons gain energy at the leading part but lose energy at the trailing part of DFs. Joule dissipation $\boldsymbol{J}\cdot(\boldsymbol{E}+\boldsymbol{v}_e\times\boldsymbol{B})$ can be either positive or negative at DFs, and its average value is very small. The kinetic energy dissipation parameter Pi-D does not exhibit clear signatures at the DFs; hence, it is not suitable for quantifying the energy dissipation at DF.

Magnetic reconnection in astronomical objects such as solar corona and the Earth's magnetotail theoretically produces a fast jet toward the object (known as a confined jet as it connects to the object through magnetic field lines) and a fast jet departing the object (known as an unconfined jet as it propagates freely in space). So far, energetic electron acceleration has been observed in the confined jet but never in the unconfined jet, arousing a controversy about whether or not reconnection jets can intrinsically accelerate electrons. By analyzing spacecraft measurements in the magnetotail, Chen *et al.*[186] report three events showing strong electron energization in unconfined reconnection jets. Such energization, occurring in the growing phase of the jet, is quasi-adiabatic; it leads to 30 times of flux enhancements and it is probably caused by the compression of the magnetic field (betatron effect) as well as the shrinking of magnetic field lines (Fermi effect). They quantitatively reproduce this energization process using a 2.5D particle-in-cell simulation. This finding implies that electron acceleration can happen in the solar wind and magnetosheath, where reconnection jets are usually unconfined.

Perpendicular anisotropy of suprathermal ions, observed inside some of the Dipolarizing Flux Bundles (DFBs) in the magnetotail plasma sheet, have been attributed to successive, betatron-type accelerations during the DFB entry of ambient ions. It has been unclear, however, where and how these ions enter the DFBs. The proposed locations include the DFB flanks where cross-tail drifting ions are picked up, and the DFB leading edge with a sharp magnetic field gradient (the Dipolarization Front, DF). Zhou *et al.*[187] examined the latter scenario, based on a simplistic, test particle approach, to predict the preferred conditions for the appearance of the DFB ion anisotropy. Their model predicts that the ion ani-

sotropy would be stronger at locations closer to the neutral sheet and would appear preferentially in the DFB dawnside and central sectors rather than the dusk side sector. They also predict that the ion anisotropy would more likely be observed in DFBs with higher propagation speeds. These properties can be understood in their model by the dawnward drift of ions during their DF penetration (attributed to the large magnetic gradient). To examine these predictions, they carry out a statistical survey based on observations from the THEMIS (Time History of Events and Macroscale Interactions during Substorms) mission, to show a clear dependence of the ion anisotropy on spacecraft location and the DFB propagation speed. These findings, therefore, are consistent with the scenario that the perpendicular ion anisotropy originates from the ion acceleration and penetration across sharp DFs.

Pitkänen *et al.*[188] use Geotail, Cluster, and Time History of Events and Macroscale Interactions during Substorms data over 15 years (1995–2009) to statistically investigate convective ion flows ($V_{\perp xy} < 200\ \mathrm{km \cdot s^{-1}}$) in the magnetotail plasma sheet under the influence of a clearly nonzero dawn-dusk interplanetary magnetic field (IMF B_y). They find that IMF B_y causes an interhemispheric asymmetry in the flows, which depends on the direction of IMF B_y. On the average, one magnetic hemisphere is dominated by a dawn-dusk flow component, which is oppositely directed compared to that in the other hemisphere. This asymmetry is observed for both earthward and tailward flows. A comparison to tail B_y reveals that the region where the asymmetry in the average flows appears agrees with the appearance of the tail B_y direction collinear to IMF B_y. The results imply that IMF B_y has a major influence on the direction of the magnetic flux transport in the magnetotail.

The Magnetospheric Multiscale spacecraft encountered an Electron Diffusion Region (EDR) in a symmetric reconnection in the Earth's magnetotail. The EDR contained a guide field of about 2 nT, which was 13% of the magnetic field in the inflow region, and its thickness was about 2 local electron inertial lengths. Intense energy dissipation, a super-Alfvénic electron jet, electron nongyrotropy, and crescent-shaped electron velocity distributions were observed in association with this EDR. These features are similar to those of the EDRs in asymmetric reconnection at the dayside magnetopause. Electrons gained about 50% of their energy from the immediate upstream to the EDR. Crescent electron distributions were seen at the boundary of the EDR, while highly curved magnetic field lines inside the EDR may have gyrotropized the electrons. The EDR was characterized by a parallel current that was carried by antiparallel drifting electrons that were probably accelerated by a parallel electric field along the guide field. These results of Zhou *et al.*[189] reveal the essential electron physics of the EDR and provide a significant example of an EDR in symmetric reconnection with a weak guide field.

Ren *et al.*[190] analyze Magnetospheric Multiscale Mission observations of whistler waves and associated electron field-aligned crescent distribution in the vicinity of the magnetotail near-Earth X-line. The whistler waves propagate outward from the X-line in the neutral sheet. The associated field- aligned streaming electrons exhibit a crescent-like shape, with an inverse slope ($\mathrm{d}f/\mathrm{d}|v_{||}|>0$) at 1~5 keV. The parallel phase velocity of the waves is in the range (1~5 keV) of the inverse slope of the field-aligned crescents in the velocity space. They demonstrate that the observed whistler waves are driven by the electron field-aligned crescents through Landau resonance. The cyclotron resonance is at the high-energy tail with negligible free energy of pitch angle anisotropy in these events.

Zhou *et al.*[191] report Magnetospheric Multiscale (MMS) observations of the sub-ion scale dynamics within the Ion Diffusion Region (IDR) in the Earth's magnetotail. MMS crossed the IDR from the southern to the northern hemisphere, at about two ion inertial length earthward of the X line with a small guide field. Electrons were anisotropic in the inflow region of the IDR and turned into isotropic within the IDR. The isotropization of the electrons was probably due to the pitch angle scattering in highly

curved magnetic field lines. They suggest that the thickness of the electron isotropic region strongly depends on the horizontal distance to the X line. The out-of-plane current bifurcated in the IDR. It peaked at the boundaries between the inflow and outflow electrons around the separatrices. Magnetic energy conversion and dissipation predominantly occurred at the peak of the out-of-plane current instead of at the neutral sheet center where BL=0. Both the energy dissipation and normal electric field E_N exhibited evident asymmetry with respect to the neutral sheet. The energy dissipation was larger around the northern separatrix than around the southern separatrix. The electric field E_N showed a tripolar variation across the neutral sheet, that is, a unipolar E_N around the southern separatrix and a bipolar E_N around the northern separatrix. The reasons and implications of these asymmetries are discussed.

ZHOU *et al.*[192] report Magnetospheric Multiscale observations of multiple vertical Current Sheets (CSs) in a bursty bulk flow in the near-Earth magnetotail. Two of the CSs were fine structures of a Dipolarization Front (DF) at the leading edge of the flow. The other CSs were a few Earth radii tailward of the DF; that is, in the wake of the DF. Some of these vertical CSs were a few electron inertial lengths thick and were converting energy from magnetic field to plasma. The currents of the CSs in the DF wake were carried by electrons that formed flow shear layers. These electron-scale CSs were probably formed during the turbulent evolution of the bursty bulk flow and are important for energy conversion associated with fast flows.

Previous studies suggest that Dipolarization Fronts (DFs) are 1 to 3 R_e (R_e is the Earth radius) wide in the dawn-dusk direction. Recent kinetic simulations have found that DFs may break up into small-scale structures after they are produced by reconnection. Motivated by this simulation, Huang *et al.*[193] revisit the scale size of DFs in the dawn-dusk direction by using Cluster observations during the years when the inter-distance among Cluster spacecraft was between 1000 and 2000 km. They selected the DFs that were detected by more than one spacecraft and estimated the radii of these DFs by a simple geometrical analysis, which is based on a comparison of DF normals observed by different spacecraft. They found a few DFs that were only a few ion inertial lengths in the dawn-dusk direction. These results point out the importance of multi-scale coupling during the evolution of DFs.

Ultra-low-frequency (ULF) waves are ubiquitous in the magnetosphere. Previous studies mostly focused on ULF waves in the dayside or near-Earth region (with radial distance R<12 R_e). In Ref.[194], by using the data of the Time History of Events and Macroscale Interactions during Substorms (THEMIS) mission during the period from 2008 to 2015, the Pc 5~6 ULF waves in the tail region with x'_{GSM}<0, $8R_e < R < 32R_e$ (mostly on the stretched magnetic field lines) are studied statistically. A total of 1089 azimuthal oscillating events and 566 radial oscillating events were found. The statistical results show that both the azimuthal and radial oscillating events in the magnetotail region ($12R_e < R < 32R_e$) are more frequently observed in the post-midnight region. The frequency decreases with increasing radial distance from Earth for both azimuthal oscillating events ($8R_e < R < 16R_e$) and radial oscillating events ($8R_e < R < 14R_e$), which is consistent with the field line resonances theory. About 52% of events (including the azimuthal and radial oscillating events) are standing waves in the region of 8~16 R_e, while only 2% are standing waves in the region of 16~32 R_e. There is no obvious dawn-dusk asymmetry of ULF wave frequency for events in $8R_e < R < 32R_e$, which contrasts with the obvious dawn-dusk asymmetry found by previous studies in the inner magnetosphere ($4R_e < R < 9R_e$). An examination for possible statistical relationships between the ULF wave parameters and substorm occurrences is carried out. They find that the wave frequency is higher after the substorm onset than before it, and the frequency differences are more obvious in the midnight region than in the flank region.

Curlometer analysis from four-point MMS satellites observations is applied by Zhang *et al.*[195] to study the vorticity (ω) in the Bursty Bulk Flow

(BBF) from tail reconnection. Increases of the vorticity are associated with enhancements of the high-energy ion flux (above 10 keV) and the flow speed during the BBF. Finger-like structure, consisting of the lower-energy ions below 10 keV, occurs mainly during intervals of small vorticity. The vorticity during BBF consistently shows a dominant $-z_{\mathrm{GSM}}$ component, indicating clock-wise vortexes in the flows. Combined with bipolar signals of V_{ij}-$_{\mathrm{GSM}}$, the MMS observations provide evidence for flow eddies in the BBF. Power spectral analysis suggests the existence of Kinetic Alfvénic Wave (KAW) emissions, in addition to the flow eddy, in the high frequency regime in the BBF turbulence.

Using high-resolution data of Magnetospheric Multiscale mission, Huang *et al.*[196] observed a gradual but periodical Dipolarization Process (DPs) in the Earth's magnetotail for the first time. These sub-DPs, characterized by increase of B_z component and magnetic magnitude Bt, have a period of about 16 s. The electrons have a cigar distribution in the first three sub-DPs but have a pancake distribution in the last sub-DP, which excites two oppositely propagating whistler waves. At the trailing boundary of the last sub-DP, B_z decreases sharply. Meanwhile, strong tailward and duskward plasma flow, intense current, ion and electron demagnetization, and positive energy conversion from the fields to the plasmas are observed at this boundary. By comparing the motion of this boundary with the plasma flow, they infer that the flow rebounds in longer period of the last DP and causes perpendicular electron acceleration. The periodical sub-DPs and kinetic effects on the DP could improve our understanding of substorm and the magnetotail dynamics.

An ion-scale Flux Rope (FR), embedded in a high-speed electron flow (possibly an electron vortex), is investigated in the magnetotail by Huang *et al.*[197] using observations from the Magnetospheric Multiscale (MMS) spacecraft. Intense electric field and current and abundant waves are observed in the exterior and interior regions of the FR. Comparable parallel and perpendicular currents in the interior region imply that the FR has a non-force-free configuration. Electron demagnetization occurs in some sub-regions of the FR. It is surprising that strong dissipation ($\boldsymbol{J}\times\boldsymbol{E}'$ up to 2000 pW·m^{-3}) occurs in the center of the FR without signatures of secondary reconnection or coalescence of two FRs, implying that FR may provide another important channel for energy dissipation in space plasmas. These features indicate that the observed FR is still highly dynamical, and hosts multiscale coupling processes, even though the FR has a very large scale and is far away from the reconnection site.

Kinetic-Size Magnetic Holes (KSMHs) in the terrestrial magnetotail plasma sheet are statistically investigated by Huang *et al.*[198] using the observations from the Magnetospheric Multiscale mission. The scales of KSMHs are found to be smaller than one ion gyroradius or tens of electron gyroradii. The occurrence distributions of KSMHs have dawn-dusk asymmetry (dusk side preference) in the magnetotail, which may be caused by the Hall effect. Most events of KSMHs (71.7%) are accompanied by a substorm, implying that substorms may provide favorable conditions for the excitation of KSMHs. However, there is a weak correlation between KSMHs and magnetic reconnection. The statistical results reveal that for most of the events, the electron total temperature and perpendicular temperature increase while the electron parallel temperature decreases inside the KSMHs. The electron temperature anisotropy ($T_{\mathrm{e}\perp}/T_{\mathrm{e}\parallel}>1$) is observed in 72% of KSMHs. Whistler-mode waves are frequently observed inside the KSMHs, and most (92%) KSMHs associated with whistler waves have enhancements of electron perpendicular distributions and satisfy the unstable condition of whistler instability. This suggests that the observed electron-scale whistler waves, locally generated by the electron temperature anisotropy, could couple with the electron-scale KSMHs. The observed features of KSMHs and their coupling to electron-scale whistlers are similar to the ones in the turbulent magnetosheath, implying that they are ubiquitous in the space plasmas. The generation of KSMHs in the plasma sheet could be explained by an electron vortex magnetic hole, magnetosonic solitons,

and/or ballooning/interchange instabilities.

The flapping motion of the current sheet, with the period from several minutes to tens of minutes, is one common dynamic phenomenon in the planetary magnetotail. Wei *et al.*[199] report on one current sheet flapping event with the short semi-period of about 6 s on 17 July 2017 in the Earth's magnetotail for the first time using the Magnetospheric Multiscale (MMS) mission. This short time period flapping event consists of five consecutive crossings of the current sheet. Based on a multipoint analysis of the MMS, it is found that the first four crossings propagated duskward and belong to kink-like flapping, and the fifth crossing belongs to steady flapping. The current sheet flapping was embedded in the diffusion region of magnetic reconnection, which was identified by the well-organized Hall electromagnetic field. The period of current sheet flapping was modulated by the reconnection electric field and perpendicular plasma flow, indicating that this flapping motion may be triggered by the periodical unsteady magnetic reconnection.

Heavy ions (O^+ and He^+) are an important constituent of plasma sheets. They are most significant during geomagnetic quiet periods when charge-exchange reactions result in a faster loss of H^+ ions than heavy ions. With inward injections of energetic particles from the plasma sheet into the inner magnetosphere, heavy ions play a key role in producing the ring current and radiation belt. Wang *et al.*[200] investigated the acceleration of heavy ions by Electromagnetic Ion Cyclotron (EMIC) waves, which has been recently observed in the near-Earth plasma sheet. Nonlinear motion of ions, including phase trapping and strong acceleration, can be induced by EMIC waves through cyclotron resonance. The frozen-in condition of the plasma is not satisfied in this process. The results of test particle simulations show that heavy ions following a wave-induced nonlinear motion from L=5~7 increase from 36% of the total test particles to 44%. The He^+ ions at L=5 can be accelerated to as much as ten times the initial energy of 30 keV. The attainable energy increase ΔE_k depends on the L value and the ion composition. An abundance of heavy ions in the background plasma lowers ΔE_k. This effect is more prominent farther out in the plasma sheet. Nonlinear phase trapping occurs when ions are accelerated, and stronger acceleration corresponds to a smaller trapping zone. Hence, wave-induced acceleration is closely associated with the redistribution of ions in their phase space. Heavy ions in the plasma sheet have an important impact on inner magnetosphere dynamics, and thus, EMIC waves should not be neglected in plasma sheet energization.

Flapping motion of the current sheets of planetary magnetotails is a common dynamic phenolmenon. Previous studies of the Earth's magnetotail suggest that its flapping motion has two forms, that is, kink-like flapping that can propagate as waves toward both flanks and steady flapping that moves up and down but does not propagate. Although some models have been proposed to explain the kink-like flapping, its mechanism remains unclear. Gao *et al.*[201] survey 87 flapping events statistically with respect to their flapping types, using the multipoint measurements of Cluster. The statistical results show that the up-down steady flapping events tend to occur around the midnight region, and the kink-like flapping events tend to occur near both flanks of the magnetotail. Thus, they propose that kink-like flapping motion is causally related to steady flapping motion; that is, the up and down motion of steady flapping around the midnight region induces kink-like flapping waves, which propagate toward both flanks of the magnetotail.

As reported by Rong *et al.*[202], a kink-like flapping event of Earth magnetotail current sheet, which consists of two frequency bands successively, is studied by the multipoint observations of Cluster. The multipoint analysis of Cluster observations demonstrates that the higher frequency band (period of 10 min) has faster propagation velocity (about 30 $km \cdot s^{-1}$), shorter wavelength (about $3R_e$), and smaller amplitude (1~1.5 R_e). In contrast, the lower frequency band (period of about 22 min) shows slower propagation velocity (about 21 $km \cdot s^{-1}$), longer wavelength (about $4.4R_e$), and larger amplitude (2~3R_e).

Comparison with the flapping models demonstrates that the dispersion of theoretical models does not show consistency with the results of this event, which suggests that new or more advanced kink-like flapping theories or models in the future have to consider the constraints of the dispersive properties demonstrated by this event.

Magnetic reconnection in the magnetotail accelerates plasma in short-duration bursts of fast flows, referred to as bursty bulk flows toward the Earth. These bursty bulk flows are typically accompanied by a sharp increase in the northward magnetic field component, the so-called Dipolarization Front (DF). This rapid increase in northward magnetic field is often preceded by a decrease, the so-called DF-dip, where the northward magnetic field component sometimes even changes sign and turns southward. Schmid *et al.*[203] present a statistical study of the DF-dip of 43 events, using observations from the Magnetospheric Multiscale (MMS) mission during summer 2017, when MMS's apogee was located in the magnetotail around 25 R_e. The 43 events are subdivided into two categories according to their DF-dip: 20 events where the DF-dip stays northward (positive DF-dip category) and 23 events where the DF-dip turns fully southward (negative DF-dip category). They find that (i) the magnetic field depression ahead of the DF of the positive DF-dip events correlates mainly with perpendicular currents and diamagnetic currents flowing ahead of the DF and (ii) the magnetic field depression ahead of the DF of the negative DF-dip events correlates mainly with field-aligned currents and that this type of events might be (a) earthward moving flux rope-like structures caused by multiple X-line reconnections and/or (b) are a result of localized, single X-line reconnection under a guide field.

Magnetotail Dipolarization Fronts (DFs) are referred to as the sharp increase of the northward magnetic field component, embedded in bursts of fast earthward moving plasma flows, so called bursty bulk flows. Earlier studies often considered DFs as Tangential Discontinuities (TDs), which can be understood as thin vertical current layers of earthward moving flux tubes, so called Dipolarzing Flux Bundles (DFBs), which separate the ambient plasma sheet plasma from the low entropy plasma within the DFB. Schmid *et al.*[204] present a statistical study of 23 DFs observed by the Magnetospheric Multiscale mission during 2017 and 2018 when the apogee was at 25 R_e in the magnetotail. They perform a test of the Walén relation to distinguish whether the observed DFs have rather a TD or rotational discontinuity character and evaluate the plasma flow across the DFs in detail. The results show that on MHD large scales, all 23 DFs can be considered as TD like, but sometimes may have a significant normal plasma flow across it: for 16 events (about 70%), the plasma flows mainly tangential to the DFs, while for seven events (about 30%), the plasma flows mainly across the DFs. Based on the findings present in this study, they further hypothesize that the DF structure becomes more distorted and unstable in a (locally) more dipolarized background magnetic field region, which may additionally facilitate the plasma flow across the front.

Wang *et al.*[205] report on a flapping motion event near the substorm onset on 17 June 2017 using Magnetospheric Multiscale (MMS) mission data. A strong current density with a maximum value of about 190 $\mathrm{nA{\cdot}m^{-2}}$ is observed during the flapping. The north-to-south (south-to-north) crossing of the neutral sheet corresponds to an increase (a decrease) of the Z_{GSM} component of the solar wind $V_{z,\mathrm{SW}}$. The periods (about 8 min) of the flapping and variations of $V_{z,\mathrm{SW}}$ are almost equal. In addition, $\mathrm{d}V_{z,\mathrm{SW}}/\mathrm{d}t$ and $\mathrm{d}B_x/\mathrm{d}t$ observed by MMS exhibit a strong negative correlation. These observations suggest that the flapping motions are triggered by the solar wind directional change *via* creating a motion of the current sheet in the north-south direction. The pressure difference between the northern and southern lobes caused by the solar wind is expected to be a possible contribution to the formation of the flapping.

With the in-situ observations from the Time History of Events and Macroscale Interactions during Substorms (THEMIS) probes, Wu *et al.*[206] report a wavy Dipolarization Front (DF) event, where the DF

has different magnetic structures and electron distributions at different y positions in the Geocentric Solar Magnetospheric (GSM) coordinates. At $y\approx 2.1R_e$, the DF has a relatively simple structure, which is similar to that of a conventional DF. At $y\approx 3.0\ R_e$, the DF is revealed to have a multiple DF structure, where the plasma exhibits a vortex flow. Such a wavy DF could be the result of the interchange instability. The different structure of such a wavy DF at different sites has a great effect on electron acceleration. Fermi acceleration can occur at the site of the DF with a simple or multiple DF structure, while betatron acceleration as a local process has the contribution to energetic electrons only at the site of the DF with a simple structure.

Electron scale magnetic cavities are electron vortex structures formed in turbulent plasma, while the evolution and electron dynamics of these structures have not been fully understood. Recently, high-energy, angular, and temporal electron measurements from Magnetospheric Multiscale have enabled the application of an energetic particle sounding technique to these structures. Liu *et al.*[207] analyzed an electron scale magnetic cavity observed by Magnetospheric Multiscale on 7 May 2015 in the plasma sheet. A comprehensive sounding technique is applied to obtain the geometry and propagation velocities of the boundaries. The result shows that the scale size of the structure is about 90 km, and the leading and trailing boundaries are moving in the same direction but with different speeds (about 11.5±2.2 km·s^{-1} and about 18.1±3.4 km·s^{-1}, respectively). The speed difference suggests a shrinking of the structure that may play a significant role in magnetic energy dissipation and electron energization of electron scale magnetic cavities.

Drifting Electron Holes (DEHs), manifesting as sudden but mild dropouts in electron flux, are a common phenomenon seen in the Earth's magnetosphere. It manifests the change of the state of the magnetosphere. However, previous studies primarily focus on DEHs during geomagnetically active time (*e.g.*, substorm). Not until recently have quiet time DEHs been reported. Liu *et al.*[208] presented a systematic study on the quiet time DEHs. BeiDa Imaging Electron Spectrometer (BD-IES) measurements from 2015 to 2017 are investigated. Twenty-two DEH events are identified. The DEHs cover the whole energy range of BD-IES (50~600 keV). Generally, the DEHs are positively dispersive with respect to energy. Time-of-flight analysis suggests the dispersion results from electron drift motion and gives the location where the DEHs originated from. Statistics reveal the DEHs primarily originated from the postmidnight magnetosphere. In addition, superposed epoch analysis applied to geomagnetic indices and solar wind parameters indicates these DEH events occurred during geomagnetically quiet time. No storm or substorm activity could be identified. However, an investigation into nightside midlatitude ground magnetic records suggests these quiet time DEHs were accompanied by Pi2 pulsations. The DEH-Pi2 connection indicates a possible DEH-Bursty Bulk Flow (BBF) connection, since nightside midlatitude Pi2 activity is generally attributed to magnetotail BBFs. This connection is also supported by a case study of coordinated magnetotail observations from Magnetospheric Multiscale spacecraft. Therefore, they suggest the quiet time DEHs could be caused by magnetotail BBFs, similar to the substorm time DEHs.

Dipolarizing Flux Bundles (DFBs), earthward propagating structures with enhanced northward magnetic field B_z, are usually believed to carry a distinctly different plasma population from that in the ambient magnetotail plasma sheet. The ion distribution functions within the DFB, however, have been recently found to be largely controlled by the ion adiabaticity parameter κ in the ambient plasma sheet outside the DFB. According to these observations, the ambient κ values of 2~3 usually correspond to a strong perpendicular anisotropy of suprathermal ions within the DFB, whereas for lower κ values the DFB ions become more isotropic. Zhou *et al.*[209] utilized a simple, test particle model to explore the nature of the anisotropy and its dependence on the ambient κ values. They find that the anisotropy originates from successive ion reflec-

tions and reentries to the DFB, during which the ions are consecutively accelerated in the perpendicular direction by the DFB-associated electric field. This consecutive acceleration may be interrupted, however, when magnetic field lines are highly curved in the ambient plasma sheet. In this case, the ion trajectories become stochastic outside the DFB, which makes the reflected ions less likely to return to the DFB for another cycle of acceleration; as a consequence, the perpendicular ion anisotropy does not appear. Given that the DFB ions are a free energy source for instabilities when they are injected toward Earth, their simple model (that reproduces most observational features on the anisotropic DFB ion distributions) may shed new lights on the coupling process between magnetotail and inner magnetosphere.

Pan *et al.*[210] use the Magnetospheric Multiscale mission to investigate electron-scale structures at a dipolarization front. The four spacecraft are separated by electron scales and observe large differences in plasma and field parameters within the dipolarization front, indicating strong deviation from typically assumed plane or slightly curved front surface. They attribute this to ripples generated by the lower hybrid drift instability (LHDI) with wave number of $kpe \simeq 0.4$ and maximum wave potential of $k_B T_e \approx 1$ kV. Power law-like spectra of $E_\perp$ with a slope of –3 indicates the turbulent cascade of LHDI. LHDI is observed together with bursty high-frequency parallel electric fields, suggesting coupling of LHDI to higher-frequency electrostatic waves.

Flapping motion of the Current Sheet (CS) is an important physical process in the Earth's magnetotail. The magnetic double gradient model, which includes both the instability and wave modes, offers a reasonable explanation for the exciting and propagation of the flapping wave. Duan *et al.*[211] applied an advanced numerical Magnetohydrodynamic scheme, Conservation Element and Solution Element (CESE)-MHD, to simulate the magnetic double-gradient instability in an idealized current sheet that mimics the magnetotail configuration. They initialize the simulations with a numerically relaxed magnetotail equilibrium, in which the normal component of the magnetic field has a tailward gradient. It is confirmed in their simulation that the instability develops in the current layer. The growth rate of the instability yielded from the simulation is very close to the prediction of theory, with a relative deviation of only ten percent. The results demonstrate that the CESE-MHD scheme is very powerful in numerical study of the double-gradient mechanism of the CS flapping mode, and can be used for further investigations of the flapping motion in more realistic CS configurations.

Dipolarization Front (DF), a sharp boundary separating hot tenuous plasmas from cold dense plasmas, is a key structure responsible for particle acceleration and energy transport in the magnetotail. How such a structure is formed has been unclear so far. Two possible mechanisms suggested in previous studies are magnetic reconnection and spontaneous formation. Both of them require current sheet thinning as a prerequisite. However, observational evidence of the DF formation associated with current sheet thinning has not been reported. Xu *et al.*[212] present such an observation, showing the DF formation after current sheet thinning. They estimate the half thickness of the current sheet to be about 1000 km and the rate of current sheet thinning as about 38 km·s^{-1}. They find that the DF is likely formed at $x_{GSM} \approx -20\ R_e$. During the current sheet thinning, the plasma becomes cold and dense; during DF formation, many magnetic islands are produced. Although current sheet thinning and DF formation have been individually analyzed in the previous studies, this study, for the first time, links the two transient processes in the magnetotail.

Dipolarization Front (DF), a sharp boundary with scale of ion inertial length (c/ω_{pi}) in the Earth's magnetotail, can also have fine structures at electron scale (c/ω_{pe}). Such electron-scale structures, determining the local energy conversion, have not been revealed by multispacecraft observations so far, due to the large separation of spacecraft in previous studies. Liu *et al.*[213] report the first electron-scale multispacecraft measurements of DF, using data from the recent Magnetospheric Multiscale mission.

They find strong parallel currents only in the high-density side of the DF but strong perpendicular currents across the whole DF. They find no parallel electric fields during the DF interval. Although DF is primarily an energy-load region ($\boldsymbol{E}\cdot\boldsymbol{J}>0$), the electron–scale currents could lead to a localized energy generation ($\boldsymbol{E}\cdot\boldsymbol{J}<0$). Such features are different from those reported in previous multispacecraft studies, where the currents, electric fields, and energy conversion are uniform across the DF; they also shed lights on the study of substorm current wedge, which is crucial in the magnetosphere-ionosphere coupling.

The cigar distribution of suprathermal electrons (40~200 keV), showing electron pitch angles primarily in the parallel and anti-parallel directions, has been frequently observed in the terrestrial magnetotail. The formation of such a distribution is typically attributed to Fermi acceleration, betatron cooling, or a combination of these. To date, Fermi acceleration has been well studied via both observations and simulations, while betatron cooling has not been verified directly. Liu *et al.*[214] focused on the betatron cooling of suprathermal electrons. By analyzing a unique case observed by the Cluster spacecraft in the Earth's magnetotail ($x_{\mathrm{GSM}}\approx -15R_{\mathrm{e}}$), they find a significant drop of electron flux in association with the decrease of magnetic field strength, *i.e.*, a magnetic dip. This magnetic dip is formed due to the expansion of flux tubes driven by two opposite flows. The drop in electron flux, primarily in the perpendicular direction, is therefore strong evidence of betatron cooling. They successfully reproduce these processes using an analytical model.

A two-dimensional extended MHD simulation, including Hall effect and Finite Larmor Radius (FRL) effect, is performed by Lu *et al.*[215] to study the kinetic nature of Dipolarization Fronts (DFs) in the scale of the ion inertial length/ion Larmor radius. The DF is self-consistently produced by the interchange instability, arising due to the force imbalance between the tailward gradient of thermal pressure and Earthward magnetic curvature force in the near-Earth region. Numerical investigations indicate that the DF is a tangential discontinuity, which means that the normal plasma velocity across the DF should be zero in the reference system that is static with the DF structure. Hall effect arising in the scale of ion inertial length determines the electric system, including electric field and current. Hall effect mainly contributes to the electric field normal to the tangent plane of the DF, increases the current along the tangent plane of the DF, but also makes the DF structure asymmetric. The drifting motion of the large-scale DF structure is determined by the FLR effect arising in the scale of ion Larmor radius. The ion magnetization velocity induced by the FLR effect is towards to duskward at the subsolar point of the DF, but the dawnward component of velocity in the region after the DF is increased, which dominantly results in the drifting motion of the whole mushroom structure towards the dawn.

Satellite observations indicate that multiple components often exist in the plasma sheet, particularly during impulsive fast flow events. Cao *et al.*[216] perform a kinetic analysis of the energy transport of plasma sheet ion flow using a model of two-component plasma sheet ion flows (Background convection flow represented by subscript "b" and Fast flow represented by subscript "f") and compare the energy transport calculated by kinetic approach Q_{k} with those obtained from Magnetohydrodynamic (MHD) approach QMHD. The ratio of $Q_{\mathrm{k}}/Q_{\mathrm{MHD}}$ is always larger than unity and is positively proportional to the ratios of $V_{\mathrm{f}}/V_{\mathrm{b}}$ and $T_{\mathrm{f}}/T_{\mathrm{b}}$. The maximum values of Q_{k}/QMHD occur in the low-speed ranges (*i.e.*, small density ratio N_{f}/N). When N_{f}/N exceeds 0.4, the ratio of $Q_{\mathrm{k}}/Q_{\mathrm{MHD}}$ is almost the same for a wide parameter range of V_{f}, T_{f}, and V_{b}. Heat flux is important in low-speed range and is neglectable in the high-speed range. The adiabatic polytropic index 5/3 cannot correctly describe energy transport rate. A density ratio N_{f}/N of 0.3% of high-speed ion flow can make the effective polytropic index obviously deviate from adiabatic polytropic index (5/3). The above theoretic results can well explain previously reported satellite in situ observations.

In Ref.[217], the particle acceleration processes

around magnetotail Dipolarization Fronts (DFs) are reviewed. They summarize the spacecraft observations (including Cluster, THEMIS, MMS) and numerical simulations (including MHD, test-particle, hybrid, LSK, PIC) of these processes. Specifically, they (i) introduce the properties of DFs at MHD scale, ion scale, and electron scale, (ii) review the properties of suprathermal electrons with particular focus on the pitch-angle distributions, (iii) define the particle-acceleration process and distinguish it from the particle-heating process, (iv) identify the particle-acceleration process from spacecraft measurements of energy fluxes, and (v) quantify the acceleration efficiency and compare it with other processes in the magnetosphere (*e.g.*, magnetic reconnection and radiation-belt acceleration processes). They focus on both the acceleration of electrons and ions (including light ions and heavy ions). Regarding electron acceleration, they introduce Fermi, betatron, and non-adiabatic acceleration mechanisms; regarding ion acceleration, they present Fermi, betatron, reflection, resonance, and non-adiabatic acceleration mechanisms. They also discuss the unsolved problems and open questions relevant to this topic, and suggest directions for future studies.

An anchor point, which is an energy threshold above which electrons are accelerated and below which electrons are decelerated, has recently been reported within the dipolarizing flux bundles behind Dipolarization Fronts (DFs) both in observations and simulations. However, what determines this point and how it is formed remain unclear. Liu and Fu[218] investigate for the first time the formation of this point and the relation between this point and the plasma properties by considering a large amount of DF events measured by Cluster. They find a good correlation between this anchor point and the plasma-sheet density and temperature. They notice that such a point appears primarily in the DF events associated with strong whistlers, suggesting that it is formed due to wave-particle interactions near DFs. Quantitatively, they establish a model for the anchor point, $E_{\mathrm{AP}} = 10^{2.2\pm0.3} \times (N/T)^{-0.6\pm0.1}$eV, where N and T are the normalized plasma-sheet density and temperature, respectively. With this model, they can predict the electron acceleration features behind DFs, by monitoring plasma properties in the plasma sheet. Such a model can be crucial for understanding electron acceleration regions elsewhere in space, such as reconnection diffusion region and collisionless shocks.

The electron rolling pin distribution, showing electron pitch angles primarily at 0°, 90°, and 180°, has recently been observed behind Dipolarization Fronts (DFs) and explained using an analytical model. However, the energy range of such distribution has been unknown so far, owing to the low-resolution data in previous spacecraft missions. Using the high-resolution measurements of Magnetospheric Multiscale, Zhao *et al.*[219] reveal the energy range of electron rolling pin distribution behind DFs for the first time. They find that such distribution appears only above 1.7 keV, falling well into the suprathermal energy range. Below 1.7 keV, electrons exhibit a Maxwell distribution, while above 1.7 keV, they exhibit a power law distribution. In addition, such distribution appears primarily in the growing phase of the flow and disappears quickly in the decaying phase. During the formation of the rolling pin distribution, electrons are gyrotropic. These findings have greatly improved our knowledge of electron dynamics around DFs.

Traditionally, the magnetotail flow burst outside the diffusion region is known to carry ions and electrons together ($V_{\mathrm{i}} = V_{\mathrm{e}}$), with the frozen-in condition well satisfied ($\boldsymbol{E} + V_{\mathrm{e}} \times \boldsymbol{B} = 0$). Such a picture, however, may not be true, based on their analyses of the high-resolution MMS (Magnetospheric Multiscale mission) data. Chen *et al.*[220] find that inside the flow burst the electrons and ions can be decoupled ($V_{\mathrm{e}} \neq V_{\mathrm{i}}$), with the electron speed 5 times larger than the ion speed. Such super-Alfvenic electron jet, having a scale of 10 d_{i} (ion inertial length) in x_{GSM} direction, is associated with electron demagnetization ($\boldsymbol{E} + V_{\mathrm{e}} \times \boldsymbol{B} \neq 0$), electron agyrotropy (crescent distribution), and O-line magnetic topology but not associated with the flow reversal and X-line topology; it can cause strong energy dissipation and electron heating. They quantitatively analyze the dissipation

and find that it is primarily attributed to lower hybrid drift waves. These results emphasize the non-MHD (magnetohydrodynamics) behaviors of magnetotail flow bursts and the role of lower hybrid drift waves in dissipating energies.

Traditionally, Dipolarization Front (DF) is a discontinuity at the leading edge of the high-speed plasma jets, separating hot tenuous plasma from the denser ambient plasma. The particles behind the DF are usually hot population resulting from various heating and acceleration processes therein. Using Magnetospheric Multiscale (MMS) observations, Xu *et al.*[221] report that cold ions of ionospheric origin can be found behind the DFs. These cold ions move along the reconnected magnetic field lines directly from the lobe during substorms, forming counter-streaming cold ion flows behind the DFs. They find that cold ionospheric ions, as an additional population behind the DF, could increase ion density by about 50%. This indicates that the cold ions can change the gradients in the plasma density, such as the density-driven instabilities near the DFs, and further affect the DF dynamics.

9 Planetary Magnetosphere

Yu *et al.*[222] examined the combined effects of equatorial chorus waves and high-latitude Z-mode waves on the energy and pitch angle distribution of Saturn's radiation belt electrons. Their simulation results show that these two types of waves at different latitudes jointly control the fluxes of Saturn's radiation belt electrons, which is very different from the individual effects of each kind of waves. The presence of Z-mode waves can efficiently inhibit the reversed energy spectrum of electrons driven by chorus waves, whereas the presence of chorus waves can further accelerate and scatter the relativistic electrons accelerated by Z-mode waves toward the larger and smaller pitch angles. Their findings provide new insight on how different types of waves at different latitudes jointly affect the radiation belt electron dynamics, including, but not limited to, Saturn.

The energetic electron spectra of Saturn's radiation belts are studied using Cassini's 13 years of measurements by the Magnetosphere Imaging Instrument/Low Energy Magnetospheric Measurement System detector. Sun *et al.*[223] find that between L-shells (L) of 10 and 4.5 the differential flux spectrum of 0.3 to 1.6 MeV electrons evolves from a single power-law to two power-law functions separated at an energy cutoff (E_c). They show that inside $L \approx 8$, E_c has an L shell dependence that tracks consistently the energy of corotation drift cancelation (or resonance) ECDR, that is, the energy at which magnetic electron drifts and azimuthal corotation cancel, and is not associated with the absorbing effects of Saturn's moons. E_c also deviates from what conservation of the first adiabatic invariant would dictate. Their results verify that electrons around ECDR can be transported radially very efficiently by variable convective flows, such as those related to the noon-midnight electric field in Saturn's magnetosphere.

Wang *et al.*[224] present preliminary results of a new global Magnetohydrodynamics (MHD) simulation model of the Jovian magnetosphere. The model incorporates mass loading from Jupiter's satellite Io, the planet's fast corotation, and electrostatic coupling between its magnetosphere and ionosphere (M-I coupling). The basic configuration of the Jovian magnetosphere including the equatorial plasma flow pattern, the corotation enforcement current system, and the Field Aligned Currents (FACs) in the ionosphere are presented under an antiparallel IMF condition. The simulation model results for equatorial density and pressure profiles are consistent with results from data-based empirical models. It is also found that there are similarities between the FACs distribution in the ionosphere and the observed aurora features, showing the potential application of the simple ionospheric model to the complicated M-I coupling. This model will help deepen our understanding of the global dynamics of the Jovian magnetosphere.

Martian crustal fields were considered too weak to have a distinctive effect on global escape rates of Martian heavy ions. However, new observations by

the MAVEN mission reveal a more precise result and show a notably lower atmospheric ion escape region above the area of strongest crustal fields. A comparison between the fluxes of high and low energy O^+ ions suggests that the strongest crustal fields may trap low energy ions and reduce the solar wind pick-up efficiency while high energy ions form a flux depletion above the crustal field. Statistical results of Fan *et al.*[225] indicate a maximum reduction of the global escape flux by nearly 35 percent when the strongest crustal field region is oriented sunward. This is the first time that the protective effect of the crustal fields on heavy planetary ions has been observed and it might indicate a more effective protection of atmospheres by stronger magnetic fields like at Earth.

The Martian ionopause is generally identified as a steep electron density gradient and the peak of photoelectrons near 27 eV. However, it is not clear whether these two criteria identify the same position in the Martian ionopause region. The Mars Atmosphere and Volatile Evolution Mission (MAVEN) provides a good chance to compare both criteria for the first time with electron density data taken from the Langmuir probe and electron energy spectra from the Solar Wind Electron Analyzer. Han *et al.*[226] identified 1121 steep electron density gradients and 4275 photoelectron boundary crossings within the first 2.7 years of MAVEN data. Observations show that two boundaries are nearly collocated when being observed simultaneously (about 15% of the available dataset). But when averaged over all observations, the photoelectron boundary locates higher than the steep electron density gradient. This may suggest a strong dependency of the Martian ionopause on magnetic field configuration in the Martian ionosphere. Results are generally consistent with previous observations made by Mars Express (MEX) and improve our understanding of the Martian ionosphere.

The internal mass source from the icy moon Enceladus in Saturn's rapidly rotating magnetosphere drives electromagnetic dynamics in multiple spatial and temporal scales. The distribution and circulation of the internal plasma and associated energy are thus crucial in understanding Saturn's magnetospheric environment. Magnetic reconnection is one of the key processes in driving plasma and energy transport in the magnetosphere, and also a fundamental plasma process in energizing charged particles. Recent works suggested that reconnection driven by Saturn's rapid rotation might appear as a chain of microscale structures, named drizzle-like reconnection. The drizzle-like reconnection could exist not only in the nightside magnetodisk, but also in the dayside magnetodisk. Using in situ measurements from the Cassini spacecraft, Guo *et al.*[227] report multiple reconnection sites that were successively detected during a time interval longer than one rotation period. The time separation between two adjacently detected reconnection sites can be much less than one rotation period, implying that the reconnection processes are likely small-scale, or frequently repetitive. The spatial distribution of the identified long-standing multiple small reconnection site sequences shows no significant preference on local times. They propose that the small reconnection sites discussed in this letter are rotationally driven and rotate with the magnetosphere. Since the reconnection process on Saturn can be long-durational, the rotational regime can cause these small scale reconnection sites to spread to all local times, resulting in global release of energy and mass from the magnetosphere.

Magnetic reconnection is a key process that explosively accelerates charged particles, generating phenomena such as nebular flares, solar flares, and stunning aurorae. In planetary magnetospheres, magnetic reconnection has often been identified on the dayside magnetopause and in the nightside magnetodisc, where thin-current-sheet conditions are conducive to reconnection. The dayside magnetodisc is usually considered thicker than the nightside due to the compression of solar wind, and is therefore not an ideal environment for reconnection. In contrast, a recent statistical study of magnetic flux circulation strongly suggests that magnetic reconnection must occur throughout Saturn's dayside magnetosphere. Additionally, the source of energetic plasma can be

present in the noon sector of giant planetary magnetospheres6. However, so far, dayside magnetic reconnection has only been identified at the magnetopause. Guo *et al.*[228] report direct evidence of near-noon reconnection within Saturn's magnetodisc using measurements from the Cassini spacecraft. The measured energetic electrons and ions (ranging from tens to hundreds of keV) and the estimated energy flux of about 2.6 $mW \cdot m^{-2}$ within the reconnection region are sufficient to power aurorae. They suggest that dayside magnetodisc reconnection can explain bursty phenomena in the dayside magnetospheres of giant planets, which can potentially advance our understanding of quasi-periodic injections of relativistic electrons and auroral pulsations.

Recently, rotationally driven magnetic reconnection was first discovered in Saturn's dayside magnetosphere. This newly confirmed process could potentially drive bursty phenomena at Saturn, *i.e.*, pulsating energetic particles and auroral emissions. Using Cassini's measurements of magnetic fields and charged particles, Guo *et al.*[229] investigated particle acceleration features during three magnetic reconnection events observed in Saturn's dayside magnetodisk. The results suggest that the rotationally driven reconnection process plays a key role in producing energetic electrons (up to 100 keV) and ions (several hundreds of kiloelectron volts). In particular, they find that energetic oxygen ions are locally accelerated at all three reconnection sites. Isolated, multiple reconnection sites were recorded in succession during an interval lasting for much less than one Saturn rotation period. Moreover, a secondary magnetic island is reported for the first time at the dayside, collectively suggesting that the reconnection process is not steady and could be "drizzle-like". This study demonstrates the fundamental importance of internally driven magnetic reconnection in accelerating particles in Saturn's dayside magnetosphere, and likewise in the rapidly rotating Jovian magnetosphere and beyond.

On 20–21 November 2003, when the most intense geomagnetic storm during Solar Cycle 23 was observed at Earth, XMM-Newton recorded the strongest Martian X-ray halo hitherto. The strongest Martian X-ray halo has been suggested to be caused by the unusual solar wind, but no direct evidence has been given in previous studies. Yan *et al.*[230] examined the Mars Global Surveyor (MGS) observations and found unambiguous evidence of unusual solar wind impact during that XMM-Newton observation: the whole induced magnetosphere of Mars was highly compressed. By comparing the solar wind dynamic pressure estimated at Mars from MGS observation and that predicted by different solar wind propagation models, it is further supported that the interplanetary condition during the XMM-Newton observation is not related to the quiet solar wind, but to solar wind disturbances with enhanced dynamic pressure, which is probably related to the interplanetary coronal mass ejection observed at Earth on 20 November 2003. A solar energetic particle event also impacted Mars during the XMM-Newton observation and lasted for several days. Its impact on the production of the X-ray emission from Mars may be worth investigating in the future.

Magnetic fields inconsistent with draped interplanetary magnetic fields and crustal fields have been observed on Mars. Considering the discovery of a global looping magnetic field around the Venusian magnetotail and the similarities in the solar wind interactions between Mars and Venus, Chai *et al.*[231] use Mars Atmosphere and Volatile Evolution observations to investigate the global looping field on Mars and its formation mechanism. It is found that a global looping field also exists on Mars; therefore, this type of global looping field is a common feature of unmagnetized planetary bodies with ionospheres, and therefore should also exist on Titan and near-Sun comets. The comparison of the looping fields on Mars and Venus shows that the looping field is stronger on Mars. Solar wind azimuthal flows around the magnetotail toward the $-E$ magnetotail polar region ($x_{MSE} < 0$, $y_{MSE} = 0$, $z_{MSE} < -1R_m$) are observed. They illustrate that the looping field can be formed by bending the draped field lines with these azimuthal flows, and that these azimuthal flows are associated with heavy ion plumes along the $+E$ direction that

are expected to be stronger on Mars than Venus. The current system associated with the looping field and its possible connection with the nightside ionosphere formations and ion escapes on Mars and Venus are discussed.

The location of Ultralow-Frequency (ULF) quasi-monochromatic wave onset upstream of Venus bow shock is explored using Venus Express magnetic field data. Shan *et al.*[232] report the existence of a spatial foreshock boundary behind which ULF waves are present. They have found that the ULF wave boundary at Venus is sensitive to the IMF direction like the terrestrial one and appears well defined for a cone angle larger than 30°. In the Venusian foreshock, the inclination angle of the wave boundary with respect to the Sun-Venus direction increases with the IMF cone angle. They also found that for the IMF nominal direction (θ_{BX}=36°) at Venus' orbit, the value of this inclination angle is 70°. Moreover, they have found that the inferred velocity of an ion traveling along the ULF boundary is in a qualitative agreement with a quasi-adiabatic reflection of a portion of the solar wind at the bow shock. For an IMF nominal direction at Venus, the inferred bulk speed of ions traveling along this boundary is 1.07 V_{SW}, sufficiently enough to overcome the solar wind convection. This strongly suggests that the back streaming ions upstream of the Venusian bow shock provide the main energy source for the ULF waves.

Rong *et al.*[233] use the magnetic field data measured by Mercury Surface, Space Environment, Geochemistry, and Ranging from 2011 to 2015 to investigate the average magnetic field morphology of Mercury's magnetotail in the down tail 0~3 R_m (R_m= 2440 km, Mercury's radius). It is found that Mercury has a terrestrial-like magnetotail; the magnetic field structure beyond 1.5 R_m down tail is stretched significantly with typical lobe field 50 nT. A cross-tail current sheet separating the antiparallel field lines of lobes is present in the equatorial plane. The magnetotail width in north-south direction is about 5 R_m, while the transverse width is about 4 R_m. Thus, the magnetotail shows elongation along the north-south direction. At the cross-tail current sheet center, the normal component of magnetic field (10~20 nT) is much larger than the cross-tail component. The lobe-field-aligned component of magnetic field over current sheet can be well fitted by Harris sheet model. The curvature radius of field lines at sheet center usually reaches a minimum around midnight (100~200 km) with stronger current density (40~50 nA·m^{-2}), while the curvature radius increases toward both flanks (400~600 km) with the decreased current density (about 20 nA·m^{-2}). The half-thickness of current sheet around midnight is about 0.25 R_m or 600 km, and the inner edge of current sheet is located at the down tail about 1.5 R_m. Their results about the field structure in the near Mercury's tail show an evident dawn-dusk asymmetry as that found in the Earth's magnetotail, but reasons should be different. Possible reasons are discussed.

Small-scale flux ropes, with estimated diameters of about 500 km and that pass over the MESSENGER spacecraft on timescales of seconds or less, are a common feature in Mercury's magnetosphere. These magnetic structures, sometimes referred to as plasmoids, are believed to form as a result of rapid transient reconnection in the cross-tail current sheet at Mercury and the other planets. Zhong *et al.*[234] reported the occurrence of unusually large plasmoids in Mercury's magnetotail observed, by the MESSENGER spacecraft. These plasmoids are remarkable for several reasons. Their spatial scales in the north-south direction exceed Mercury's radius of 2440 km, and their time durations are comparable to or longer than the average Dungey cycle time of about 200 s. They also have a more loop-like magnetic structure than the more common helical-like flux rope topology. These new MESSENGER observations suggest that Mercury's magnetosphere can dissipate large quantities of magnetic flux and energy not only through the formation of a large number of small flux ropes, but also occasionally by the formation and release of a single giant plasmoid.

The nature of magnetic reconnection in planetary magnetospheres may differ between various planets. Zhong *et al.*[235] report the first observations of a rapidly evolving magnetic reconnection process

in Mercury's magnetotail by the MESSENGER spacecraft. The reconnection process was initialized in the plasma sheet and then evolved into the lobe region during an about 35 s period. The tailward reconnection fronts of primary and secondary flux ropes with clear Hall signatures and energetic electron bursts were observed. The reconnection timescale of a few seconds is substantially shorter than that of terrestrial magnetospheric plasmas. The normalized reconnection rate during a brief quasi-steady period is estimated to be 0.2 on average. The observations show the rapid and impulsive nature of the exceedingly driven reconnection in Mercury's magnetospheric plasma that may be responsible for the much more dynamic magnetosphere of Mercury.

Although there is no intrinsic magnetic field at Venus, the convected interplanetary magnetic field piles up to form an induced magnetosphere around the planetary ionosphere. Previous investigations show that the magnetic barrier, the part of the induced magnetosphere in the dayside inner magnetosheath, can act as an effective obstacle to the solar wind during solar maximum, and the magnetic barrier can stop the solar wind even during solar minimum. Xiao and Zhang[236] performed a comprehensive statistical study of the magnetic barrier near the terminator during almost a complete solar cycle by using Venus Express magnetic data. The magnetic barrier configuration is located at the dayside even near the terminator and a hemispheric asymmetry exists during the whole solar cycle. They also demonstrate that the general magnetic barrier configuration is controlled by the interplanetary magnetic field orientation and solar cycle dependent. The magnetic barrier under IMF quasi-perpendicular to the solar wind flow is stronger than quasi-parallel to the solar wind flow during the solar cycle, and this difference becomes larger with the increase in solar activity.

Xiao *et al.*[237] statistically examined the characteristic scaling features of fluctuations in the dayside Venusian magnetosheath downstream of different types, quasi-parallel ($Q_{\parallel}$) and quasi-perpendicular ($Q_{\perp}$), of bow shock based on Venus Express data. They found that magnetic fluctuations have different characteristic scaling features downstream of $Q_{\parallel}$ and $Q_{\perp}$ bow shocks. Although the Venusian dayside magnetosheath is much thinner than the Earth magnetosheath, fully developed turbulence can be still observed downstream of the $Q_{\parallel}$ bow shock, while the turbulence is not dominant downstream of $Q_{\perp}$ bow shock. The type of bow shock plays an important role in the characteristic scaling features of downstream magnetic fluctuations. That means that the $Q_{\parallel}$ IMF might be a source of the turbulence in Venusian magnetosheath.

It has been demonstrated that Kelvin-Helmholtz (KH) instability is an essential large-scale mechanism to generate plasma waves along with the boundary layers of Venus. In Ref.[238], evolution of KH instability on the Venusian ionopause with the influence of the Hall effect was investigated under Hall Magnetohydrodynamic (MHD) simulations. Linear and nonlinear physical behaviors of KH instability with different wavelengths of perturbation, magnetic field configurations, and ion inertial lengths were studied. Numerical results indicate that, for perturbation with short wavelength, the circulation area of matter becomes small and the driving force is weakened. The combined effect of short wavelength and the antiparallel magnetic field leads to longer linear growth time, while the antiparallel magnetic field tends to enlarge the pressure gradient. As for the moderate wavelength of perturbation, the growth rate reaches its peak value, whereas the maximal y component of total kinetic energy increases significantly with the wavelength. Hall MHD simulations indicate that the Hall effect does not change the growth rates for different ion inertial lengths at all. However, the Hall effect has a depression effect on small structures at the nonlinear stage of KH instability.

10 Techniques

The energetic electron measurement is one of the most important issues to understand dynamics in space physics and the applications for Space Weather.

The principle and functional components of the Imaging Energetic Electron Spectrometer (IES) onboard a Chinese navigation satellite in the Inclined GeoSynchronous Orbit (IGSO) is introduced by Zou *et al.*[239]. The IES instrument is developed by the team in Peking University (BeiDa), thus it is named as BD-IES. Based on the pin-hole technique, the instrument can measure 50~600 keV electrons incident from 9 directions over a range of 180° in polar angle. With Pulse Height Analysis (PHA), the spectrum can be determined for each direction. The energy and angular calibrations were performed, which show the good energy and angular characteristics of BD-IES. Monte Carlo simulations show that the anti-proton design of BDIES can effectively decrease the proton contamination on the electron measurements in the IGSO. The primary results of BD-IES verify the successful design of this instrument.

An imaging energetic electron spectrometer built by the Peking University team (BD-IES) onboard a Chinese navigation satellite in an inclined GEO orbit has been launched successfully in September 2015, which measures the spectra of the energetic electrons with the energy range of 50~600 keV in nine directions. In Ref.[240], Monte Carlo simulations of the BD-IES sensor head were performed using Geant4 and the corresponding characteristic responses to the isotropic energetic particles were derived. The effective geometric factors were estimated using the typical electron and proton spectra in the GEO orbit and the corresponding simulated sensor head responses. It was found that the average effective geometric factors of nine directions are close to the nominal geometric factors calculated with the traditional method, but the effective geometric factor decreases as the central energy of the energy channel decreases. The BD-IES sensor head also responses to the energetic protons, but the average contamination rate of all 72 channels is about 2%, which means that the proton contamination is acceptable. The spectra of the energetic electrons measured by BD-IES are derived using the effective geometric factors of the sensor head and are comparable with the spectra measured by the magnetic electron-ion spectrometer (MagEIS) instrument onboard Van Allen Probes.

Zhang *et al.*[241] perform an L-shell dependent inter-satellite calibration of Fengyun-3 medium energy electron measurements with POES measurements based on rough orbital conjunctions within 5 min$\times$ 0.1$L\times$ 0.5 MLT. By comparing electron flux data between the U.S. Polar Orbiting Environmental Satellites (POES) and Chinese Sun-synchronous satellites including FY-3B and FY-3C for the whole year of 2014, they attempt to remove less reliable data and evaluate systematic uncertainties associated with the FY-3B and FY-3C datasets, expecting to quantify the inter-satellite calibration factors for the 150~350 keV energy channel at L=2~7. Compared to the POES data, the FY-3B and FY-3C data generally exhibit a similar trend of electron flux variations but more or less underestimate them within a factor of 5 for the medium electron energy 150~350 keV channel. Good consistency in the flux conjunctions after the inter-calibration procedures gives them certain confidence to generalize their method to calibrate electron flux measurements from various satellite instruments.

In the analysis of in-situ space plasma and field data, an establishment of the coordinate system and the frame of reference, helps us greatly simplify a given problem and provides the framework that enables a clear understanding of physical processes by ordering the experimental data. For example, one of the most important tasks of spatial data analysis is to compare the data with simulations and theory, which is facilitated by an appropriate choice of coordinate system and reference frame. While in simulations and theoretical work the establishment of the coordinate system (generally based on the dimensionality or dimension number of the field quantities being studied) and the reference frame (normally moving with the structure of interest) is often straightforward, in space data analysis these are not defined a priori, and need to be deduced from an analysis of the data itself. Although various ways of building a dimensionality-based (D-based) coordinate system (*i.e.*, one that takes account of the

dimensionality, *e.g.*, 1D, 2D, or 3D, of the observed system/field), and a reference frame moving along with the structure have been used in space plasma data analysis for several decades, in recent years some noteworthy approaches have been proposed. Shi *et al.*[242] reviewed the past and recent approaches in spatial data analysis for the determination of a structure's dimensionality and the building of D-based coordinate system and a proper moving frame, from which one can directly compare with simulations and theory. Along with the determination of such coordinate systems and proper frame, the variant axis/normal of 1D (or planar) structures, and the invariant axis of 2D structures are determined and the proper frame velocity for moving structures is found. These are found either directly or indirectly through the definition of dimensionality. They therefore emphasize that the determination of dimensionality of a structure is crucial for choosing the most appropriate analysis approach, and failure to do so might lead to misinterpretation of the data. Ways of building various kinds of coordinate systems and reference frames are summarized and compared here, to provide a comprehensive understanding of these analysis tools. In addition, the method of building these systems and frames is shown not only to be useful in spatial data analysis, but also may have the potential ability for simulation/laboratory data analysis and some practical applications.

It is important to determine the dimensionality and velocity information in the study of spatial magnetic structures. Many data analysis theories/techniques are based on the assumption of one or two dimensions. For example, the Grad-Shafranov (GS) reconstruction method assumes a dimensionality of two or less. The Minimum Direction Derivative (MDD) method provides an indication of the dimensionality. For the structure velocity, the components in each dimensionality can be calculated by Spatio-Temporal Difference analysis (STD). In order to improve the convenience of the use of MDD method, a new parameter Dm quantifying the dimensionality based on MDD eigenvalues is introduced by Ref.[243]. The influences of noise/turbulence, separation distance, and tetrahedron configuration on MDD and the evaluation of D_{m} are systematically tested using two analytical models for magnetic structures, representing a magnetic mirror and magnetic flux rope. They tested and gave the threshold values of three quality indicators for MDD results using the flux rope model. They also show that the error induced by turbulence is comparable to that of random noise when the turbulence scales are less than the spacecraft separation. Besides, the accuracy of STD velocity estimation will also be influenced by turbulence for cases with excessively high data time resolution. By using Dm, they show that an ideal model of a mirror-like structure can be divided into one dimension (1D) and three dimension (3D) regions. This restricts the applicability of the GS method in mirror-like structures. For example, in a given reconstruction range, the GS error increased from less than 7% to more than 15% by using the data along trajectories in 1D and 3D regions as predicated by Dm. Thus, it is important to estimate the structure dimensionality, which can be further used to estimate the reliability of the GS reconstruction map.

SMILE (Solar wind Magnetosphere Ionosphere Link Explorer) mission is a joint ESA-CAS space science project. The working orbit is a $19\,R_{\mathrm{e}}\times5000$ km HEO with 4 scientific instruments: Soft X-ray Imager (SXI), Ultra-Violet Imager (UVI), Magnetometer (MAG) and Light Ion Analyzer (LIA). SMILE aims to understand the interaction between the solar wind and the Earth's magnetosphere through the images of SXI and UVI and in-situ measurement from LIA and MAG. After the kick-off in 2016, the SMILE project went to Phase A study. The mission adoption is scheduled for November 2018, with a target launch date in 2022–2023. In Ref.[244], the background of the mission, scientific objectives, the design and characteristics of scientific instruments, and the mission outline are introduced in detail.

Soft X-Ray Imager (SXI) is a wide field lobster-eye telescope that equipped as a main payload on the SMILE satellite. Guo *et al.*[245] designed the prototype of SXI, including the Lobster eye optic

aperture frame, optical baffle, and radiation protection door, calculate the transmission character of the optical/UV filter. They also show simulations that demonstrate the performance of SXI, analysis of the effective area and sensitivity of SXI. SXI will provide the large spatial coverage and good energy resolution required to map the SWCX X-ray emission.

Solar Wind Magnetosphere Ionosphere Link Explorer (SMILE) scientific satellite is dedicated to observing solar wind-magnetosphere coupling. The key payload, Soft X-ray Imager (SXI), is designed to map the location, shape, and motion of dayside magnetospheric boundaries by Angel-type lobster-eye optical system. Contrast to traditional Wolter-type X-ray telescope with very narrow field-of-view, the lobster-eye-type optics has a unique capability of providing a wide field of view for panoramic imaging with moderate spatial resolution in soft X-ray band. Since the lobster-eye optics focus X-ray by reflecting on the inner walls of the micro-channel array shaped in a spherical surface, traditional optical design tools can't well match to the requirements of simulation for SXI. In Ref.[246], a 3D Angel type lobster-eye model is designed for simulation of lobster-eye optics and its capability is demonstrated for the applying scenarios including the imaging of point light source, a surface light source with uniform and non-uniform intensity distribution. The simulation results are well consistent with those of theoretical estimates.

Fast Magnetosonic (MS) waves can play an important role in the evolution of the inner magnetosphere. However, there is still not an effective method to quantitatively identify such waves for observations of the Van Allen Probes reasonably. Yuan *et al.*[247] used Van Allen Probes data from 18 September 2012 to 30 September 2014 to find a more comprehensive automatic detection algorithm for fast MS waves through statistical analysis of the major properties, including the planarity, ellipticity, and wave normal angle of whole fluctuations using the singular value decomposition method. According to a control variate method, they find an obvious difference between fast MS waves and other waves in the statistical distribution of their major properties. After eliminating the influence of background noises, by excluding fluctuations at $L<1.8$, they set up an automatic detection algorithm applied to fast MS waves, that is, smaller than 0.2 for the absolute value of wave ellipticity, larger than 70° for the wave normal angle, with a frequency range of 2 Hz to 1.5 f_{LHR} (f_{LHR} is the local lower hybrid resonance frequency). Finally, they have checked the planarity to verify availability of this method and tested this completely automatic method on the Van Allen Probes data and found some results consistent with previous studies. Inside the plasmapause, they found that there is a more obviously favorable occurrence of MS waves at dusk sector with increasing magnetic latitudes.

The seismic activities on the Earth can produce a disturbance of the electromagnetic field and particles in the ionosphere. The Search Coil Magnetometer (SCM) mounted on China Seismo-Electromagnetic Satellite (CSES) is designed by the team of Cao *et al.*[248] to measure the magnetic field fluctuation of low frequency electromagnetic waves in the frequency range of 0.01~20 kHz. The SCM comprises a three-axis search coil sensor mounted on a 4.5 m boom and an electronic box inside satellite module. The sampling rate of the SCM is 51.2 kHz and the time resolution of the Power Spectrum Density (PSD) is 2 s. The frequency resolution is 12.5 Hz. There are three operation modes: survey, detailed survey, and calibration. In the survey mode, the SCM can provide a PSD in the whole frequency range of 0.01~20 kHz and wave forms in the low frequency range below 2 kHz while in the detailed survey mode the SCM can provide both PSD and wave forms in the whole frequency range of 0.01~20 kHz. The sensitivity of the SCM instrument is 5.0×10^{-4} nT·Hz$^{-1/2}$ at 10 Hz, 5.0×10^{-5} nT·Hz$^{-1/2}$ at 200 Hz, 3.4×10^{-5} nT·Hz$^{-1/2}$ at 2 kHz and 1.1×10^{-4} nT·Hz$^{-1/2}$ at 20 kHz. The telemetry rate is about 0.85 Mbit·s^{-1} in the survey mode and about 3.0 Mbit·s^{-1} in the detailed survey mode. The phase difference between three axes can be made generally with a precision of less than 1.0°. The dynamic range of the SCM instrument is over 100 dB. The orthogonality of three mechanical axes

of search coil senor is better than 0.13°. The performance of SCM can satisfy the requirement of the scientific objectives of CSES mission.

Acknowledgements The authors thank the community of magnetospheric physics in China for providing relevant material.

References

[1] CHEN S, CHAI L, XU K, WEI Y, *et al.*Estimation of the occurrence probability of extreme geomagnetic storms by applying extreme value theory to an index [J]. *J. Geophysi. Res.: Space Phys.*, 2019, **124**(12):9943-9952

[2] LIU B, ZHANG *X*, HE F. Tilt of the ring current during the main phases of intense geomagnetic storms [J]. *Sci. China Technol. Sci.*, 2019, **62**(5):820-828

[3] WANG H, HE Y, LÜHR H, *et al.* Storm time EMIC waves observed by Swarm and Van Allen Probe satellites [J]. *J. Geophys. Res.: Space Phys.*, 2019, **124**(1):293-312

[4] DEGELING A W, RAE I J, WATT C E J, *et al.* Control of ULF wave accessibility to the inner magnetosphere by the convection of plasma density [J]. *J. Geophys.l Res.: Space Phys.*, 2018, **123**(2):1086-1099

[5] QIAO Z, YUAN Z, TU J. A simulation of the field-aligned plasma transport in the plasmaspheric plume during the 2015 St. Patrick's day storm [J]. *J. Geophys. Res.: Space Phys.*, 2019, **124**(11):8617-8628

[6] TULASI RAM S, NILAM B, BALAN N, *et al.* Three different episodes of prompt equatorial electric field perturbations under steady southward IMF B_z during St. Patrick's day storm [J]. *J. Geophys. Res.: Space Phys.*, 2019, **124**(12):10428-10443

[7] BALAN N, ZHANG Q H, XING Z, *et al.* Capability of geomagnetic storm parameters to identify severe *Space Weather* [J]. *Astrophys. J.*, 2019, **887**(1):51

[8] BALAN N, ZHANG Q H, SHIOKAWA K, *et al.* Ips*Dst* of *Dst* storms applied to ionosphere-thermosphere storms and low-latitude aurora [J]. *J. Geophys. Res.: Space Phys.*, 2019, **124**(11):9552-9565

[9] HE F, ZHANG X X, WANG W, *et al.* Evolution of the subauroral polarization stream oscillations during the severe geomagnetic storm on 20 November 2003 [J]. *Geophys. Res. Lett.*, 2019, **46**(2):599-607

[10] LIU B J, ZHANG X X, HE F, *et al.* The magnetic local time distribution of storm geomagnetic field disturbance under different conditions of solar wind and interplanetary magnetic field [J]. *J. Geophys. Res.: Space Phys.*, 2019, **124**(4): 2656-2667

[11] CHENG L B, LE GM, ZHAO M X. Sun-Earth connection event of super geomagnetic storm on March 31, 2001: the importance of solar wind density [J]. *Res. Astron. Astrophys.*, 2019, **20**(3):28-43

[12] HE F, ZHANG X X, WANG W, *et al.* Large–scale structure of subauroral polarization streams during the main phase of a severe geomagnetic storm [J]. *J. Geophys. Res.: Space Phys.*, 2018, **123**(4):2964-2973

[13] YU Y, RASTÄTTER L, JORDANOVA V K, *et al.* Initial results from the GEM challenge on the spacecraft surface charging environment [J]. *Space Weather*, 2019, **17**(2):299-312

[14] ZONG Q, WANG Y, ZOU H, *et al.* New magnetospheric substorm injection monitor: image electron spectrometer on board a Chinese navigation IGSO satellite [J]. *Space Weather*, 2018, **16**(2):121-125

[15] MA X H, ZONG Q G, LIU Y. The intense substorm incidence in response to interplanetary shock impacts and influence on energetic electron fluxes at geosynchronous orbit [J]. *J. Geophys. Res.: Space Phys.*, 2019, **124**(5):3210-3221

[16] GAO Z, SU Z, XIAO F, *et al.* Exohiss wave enhancement following substorm electron injection in the dayside magnetosphere [J]. *Earth Planet. Phys.*, 2018, **2**(5):359-370

[17] TANG B, WANG C. Large scale current systems developed from substorm onset: global MHD results [J]. *Sci. China Technol. Sci.*, 2018, **61**(3):389-396

[18] WANG C, WANG J, LOPEZ R, *et al.* Determination of polar cap boundary for the substorm event of 8 March 2008 [J]. *Front. Phys.*, 2018, **6**:50

[19] SUN X, LIU W W, DUAN S. Magnetic dipolarizations inside geosynchronous orbit with tailward ion flows [J]. *Ann. Geophys.*, 2019, **37**(3):289-297

[20] LIU Z, ZONG Q G, HAO Y, *et al.* The radial propagation characteristics of the injection front: a statistical study based on BD-IES and Van Allen Probes Observations [J]. *J. Geophys. Res.: Space Phys.*, 2018, **123**(3):1927-1937

[21] LI L, WANG Z. The effects of solar wind dynamic pressure changes on the substorm auroras and energetic electron injections on 24 August 2005 [J]. *J. Geophys. Res.: Space Phys.*, 2018, **123**(1):385-399

[22] YU Y, JORDANOVA V K, MCGRANAGHAN R M, *et al.* Self-consistent modeling of electron precipitation and responses in the ionosphere: application to low-altitude energization during substorms [J]. *Geophys. Res. Lett.*, 2018, **45**(13):6371-6381

[23] GUO R, PU Z, YAO Z, *et al.* A three-dimensional model of spiral null pair to form ion-scale flux ropes in magnetic reconnection region observed by Cluster [J]. *Phys. Plasmas*, 2019, **26**(11):112901

[24] JIANG K, HUANG S, YUAN Z, *et al.* The role of upper hybrid waves in the magnetotail reconnection electron diffusion region [J]. *Astrophys. J. Lett.*, 2019, **881**(2):L28

[25] HUANG S Y, JIANG K, YUAN Z G, *et al.* Observations of the electron jet generated by secondary reconnection in the magnetotail [J]. *Astrophys. J.*, 2018, **862**(2):144

[26] BAI S C, SHI Q, ZONG Q G, *et al.* Electron dispersion and parallel electron beam observed near the separatrix [J]. *J. Geophys. Res.: Space Phys.*, 2019, **124**(9):7494-7504

[27] DAI L. Structures of Hall fields in asymmetric magnetic reconnection [J]. *J. Geophys. Res.: Space Phys.*, 2018, **123**(9):7332-7341

[28] ZHONG Z, TANG R, ZHOU M, *et al.* Evidence for secon-

dary flux rope generated by the electron Kelvin-Helmholtz instability in a magnetic reconnection diffusion region [J]. *Phys. Rev. Lett.,* 2018, **120**(7):075101

[29] MAN H, ZHOU M, DENG *x*, *et al.* In situ observation of magnetic reconnection between an earthward propagating flux rope and the geomagnetic field [J]. *Geophys. Res. Lett.*, 2018, **45**(17):8729-8737

[30] YI Y, ZHOU M, SONG L, *et al.* On the energy conversion rate during collisionless magnetic reconnection [J]. *Astrophys. J. Lett.*, 2019, **883**(1):L22

[31] SONG L, ZHOU M, YI Y, *et al.* Reconnection front associated with asymmetric magnetic reconnection: particle-in-cell simulations [J]. *Astrophys. J. Lett.*, 2019, **881**(1):L22

[32] ZHONG Z, ZHOU M, HUANG S, *et al.* Observations of a kinetic-scale magnetic hole in a reconnection diffusion region [J]. *Geophys. Res. Lett.*, 2019, **46**(12):6248-6257

[33] FU S, HUANG S, ZHOU M, *et al.* Tripolar electric field Structure in guide field magnetic reconnection [J]. *Ann. Geophys.*, 2018, **36**(2):373-379

[34] ZHANG Q, LOCKWOOD M, FOSTER J C, *et al.* Observations of the step-like accelerating processes of cold ions in the reconnection layer at the dayside magnetopause [J]. *Sci. Bull.*, 2018, **63**(1):31-37

[35] ZONG Q G, ZHANG H. In situ detection of the electron diffusion region of collisionless magnetic reconnection at the high-latitude magnetopause [J]. *Earth Planet. Phys.*, 2018, **2**(3):231-237

[36] GUO Z, LIN Y, WANG *x*, *et al.* Magnetosheath reconnection before magnetopause reconnection driven by interplanetary tangential discontinuity: a Three-Dimensional global hybrid simulation with oblique interplanetary magnetic field [J]. *J. Geophys. Res.: Space Phys.*, 2018, **123**(11):9169-9186

[37] FUJIMOTO K. Multi-scale kinetic simulation of magnetic reconnection with dynamically adaptive meshes [J]. *Front. Phys.*, 2018, **6**:119

[38] XU Y, FU H, LIU C, *et al.* Electron acceleration by dipolarization fronts and magnetic reconnection: a quantitative comparison [J]. *Astrophys. J.*, 2018, **853**(1):11

[39] LIU C, FU H, CAO D, *et al.* Detection of magnetic nulls around reconnection fronts [J]. *Astrophys. J.*, 2018, **860**(2):128

[40] LIU C, FU H, VAIVADS A, *et al.* Electron jet detected by MMS at dipolarization front [J]. *Geophys. Res. Lett.*, 2018, **45**(2):556-564

[41] HUANG H, YU Y, DAI L, *et al.* Kinetic Alfvén waves excited in two-dimensional magnetic reconnection [J]. *J. Geophys. Res.: Space Phys.*, 2018, **123**(8):6655-6669

[42] FU H S, CAO J B, CAO D, *et al.* Evidence of magnetic nulls in electron diffusion region [J]. *Geophys. Res. Lett.*, 2019, **46**(1):48-54

[43] FU H S, XU Y, VAIVADS A, *et al.* Super-efficient electron acceleration by an isolated magnetic reconnection [J]. *Astrophys. J.*, 2019, **870**(2):L22

[44] WANG Z, FU H S, LIU C M, *et al.* Electron distribution functions around a reconnection *x*-line resolved by the FOTE method [J]. *Geophys. Res. Lett.*, 2019, **46**(3):1195-1204

[45] LIU Y Y, FU H S, OLSHEVSKY V, *et al.* SOTE: a nonlinear method for magnetic topology reconstruction in space plasmas [J]. *Astrophys. J.(Suppl. Series),* 2019, **244**(2):31

[46] CHEN Z, FU H, WANG T, *et al.* Reconstructing the flux-rope topology using the FOTE method [J]. *Sci. China Technol. Sci.*, 2019, **62**(1):144-150

[47] LIU C M, VAIVADS A, GRAHAM D B, *et al.* Ion-Beam-Driven intense electrostatic solitary waves in reconnection jet [J]. *Geophys. Res. Lett.*, 2019, **46**(22):12702-12710

[48] LIU C M, CHEN Z Z, WANG Z, *et al.* Evidence of radial nulls near reconnection fronts [J]. *Astrophys. J.*, 2019, **871**(2):209

[49] WANG H, LüHR H, ZHENG Z, *et al.* Dependence of the equatorial electrojet on auroral activity and in situ solar insulation [J]. *J. Geophys. Res.: Space Phys.*, 2019, **124**(12): 10659-10673

[50] WANG J, HUANG C, YASONG S G, *et al.* Asymmetric transport of the Earth's polar outflows by the interplanetary magnetic field [J]. *Astrophys. J. Lett.*, 2019, **881**(2):L34

[51] LU J, ZHANG H, WANG M, *et al.* Magnetosphere response to the IMF turning from north to south [J]. *Earth Planet. Phys.*, 2019, **3**(1):8-16

[52] ZHANG L, WANG C, WANG J, *et al.* Statistical properties of the IMF clock angle in the solar wind with northward and southward interplanetary magnetic field based on ACE observation from 1998 to 2009: dependence on the temporal scale of the solar wind [J]. *Adv. Space Res.*, 2019, **63**(10): 3077-3087

[53] NOWADA M, FEAR R C, GROCOTT A, *et al.* Subsidence of ionospheric flows triggered by magnetotail magnetic reconnection during transpolar arc brightening [J]. *J. Geophys. Res.: Space Phys.*, 2018, **123**(5):3398-3420

[54] PITKäNEN T, KULLEN A, SHI Q Q, *et al.* Convection electric field and plasma convection in a twisted magnetotail: a THEMIS case study 1–2 January 2009 [J]. *J. Geophys. Res.: Space Phys.*, 2018, **123**(9):7486-7497

[55] SHI R, NI B, SUMMERS D, *et al.* Generation of electron acoustic waves in the topside ionosphere from coupling with kinetic alfven waves: a new electron energization mechanism [J]. *Geophys. Res. Lett.*, 2018, **45**(11):5299-5304

[56] JIN Y, XING Z, ZHANG Q, *et al.* Polar cap patches observed by the EISCAT Svalbard Radar: a statistical study of its dependence on the solar wind and IMF conditions [J]. *J. Atmos. Sol.:Terr. Phys.*, 2019, **192**:104768

[57] LEI Zhu, XING Zanyang, ZHANG Qinghe, *et al.* The global characteristic of a magnetic crochet and some statistic results [J]. *Chin. J. Geophys.*, 2018, **61**(2):437-448

[58] PRIYADARSHI Shishir, ZHANG Qinghe, MA Yuzhang, *et al.* The behaviors of ionospheric scintillations around different types of nightside auroral boundaries seen at the Chinese Yellow River Station, Svalbard [J]. *Front. Astron. Space Sci.*, 2018. DOI:10.3389/fspas.2018.00026

[59] XING Z, ZHANG Q, HAN D, *et al.* Conjugate observations of the evolution of polar cap arcs in both hemispheres [J]. *J. Geophys. Res.: Space Phys.*, 2018, **123**(3):1794-1805

[60] MA Y Z, ZHANG Q H, XING Z Y, *et al.* The ion/electron temperature characteristics of polar cap classical and hot patches and their influence on ion upflow [J]. *Geophys. Res.*

Lett., 2018, **45**(16):8072-8080
[61] MA Y Z, ZHANG Q H, XING Z Y, *et al.* Combined contribution of solar illumination, solar activity, and convection to ion upflow above the polar cap [J]. *J. Geophys. Res.: Space Phys.*, 2018, **123**(5):4317-4328
[62] WANG Y, ZHANG Q H, JAYACHANDRAN P T, *et al.* Experimental evidence on the dependence of the standard GPS phase scintillation index on the ionospheric plasma drift around noon sector of the polar ionosphere [J]. *J. Geophys. Res.: Space Phys.*, 2018, **123**(3):2370-2378
[63] XU J, LU J, WANG M, *et al.* Cusp location dependence on IMF: cluster statistical study [J]. *Chin. J. Geophys. Chin. Ed.*, 2018, **61**(9):3526-3535
[64] BAI S, SHI Q, TIAN A, *et al.* Spatial distribution and semiannual variation of Cold-Dense plasma sheet [J]. *J. Geophys. Res.: Space Phys.*, 2018, **123**(1):464-472
[65] LI H, WANG C, HE S, *et al.* Plausible modulation of solar wind energy flux input on global tropical cyclone activity [J]. *J. Atmos. Sol.: Terr. Phys.*, 2019, **192**:104775
[66] WU Q, LI H, WANG C. Lightning response during Forbush Decrease in the tropics and subtropics [J]. *J. Atmos. Sol.: Terr. Phys.,* 2019, **195**:105134
[67] LI K, WEI Y, HAALAND S, *et al.* Estimating the kinetic energy budget of the polar wind outflow [J]. *J. Geophys. Res.: Space Phys.*, 2018, **123**(9):7917-7929
[68] ZHANG K, LIU J, WANG W, *et al.* The effects of IMF Bz periodic oscillations on thermospheric meridional winds [J]. *J. Geophys. Res.: Space Phys.,* 2019, **124**(7):5800-5815
[69] WANG H, ZHANG K, ZHENG Z, *et al.* The effect of subauroral polarization streams on the mid-latitude thermospheric disturbance neutral winds: a universal time effect [J]. *Ann. Geophys.*, 2018, **36**(2):509-525
[70] WAN X, XIONG C, WANG H, *et al.* A statistical study on the climatology of the Equatorial Plasma Depletions occurrence at topside ionosphere during geomagnetic disturbed periods [J]. *J. Geophys. Res.: Space Phys.,* 2019, **124**(10): 8023-8038
[71] WANG H, LUEHR H. SWARM dual satellite observation of longitudinal variation of field-aligned currents. in 42nd COSPAR Scientific Assembly [J]. *Chin. J. Geophys.*,2018, **62**(2):447-461
[72] CHEN Y, WU M, WANG G, *et al.* Carriers of the field-aligned currents in the plasma sheet boundary layer: an MMS multicase study [J]. *J. Geophys.Res.: Space Phys.*, 2019, **124**(4):2873-2886
[73] CHEN Y, ZHANG T, WU M, *et al.* Small spatial-scale field-aligned currents in the plasma sheet boundary layer surveyed by magnetosphere multiscale spacecraft [J]. *J. Geophys. Res.: Space Phys.*, 2019, **124**(12):9976-9985
[74] LIU M, ZHANG X X, HE F, *et al.* A Long-Term data set of vertical ion drift velocity at high latitudes constructed from DMSP measurements [J]. *J. Geophys. Res.: Space Phys.,* 2018, **123**(7):6090-6102
[75] OUYANG X, ZONG Q, BORTNIK J, *et al.* Nightside ULF waves observed in the topside ionosphere by the DEMETER satellite [J]. *J. Geophys. Res.: Space Phys.*, 2018, **123**(9):7726-7739
[76] LIU Z Y, ZONG Q G, ZHOU X Z, *et al.* ULF waves modulating and acting as mass spectrometer for dayside ionospheric outflow ions [J]. *Geophys. Res. Lett.*, 2019, **46**(15):8633-8642
[77] ZHAO H, ZHOU *x* Z, LIU Y, *et al.* Poleward-moving recurrent auroral arcs associated with impulse-excited standing hydromagnetic waves [J]. *Earth Planet. Phys.*, 2019, **3**(4):305-313
[78] YIN Z, ZOU H, YE Y, *et al.* Superposed epoch analysis of the energetic electron flux variations during CIRs measured by BD-IES [J]. *Space Weather*, 2019, **17**(12):1765-1782
[79] YU J, LI L, CUI J, *et al.* Ultrawideband rising-tone chorus waves observed inside the oscillating plasmapause [J]. *J. Geophys. Res.: Space Phys.*, 2018, **123**(8):6670-6678
[80] SAMANES J, RAULIN J P, CAO J, *et al.* Nighttime lower ionosphere height estimation from the VLF modal interference distance [J]. *J. Atmos. Sol.: Terr. Phys.*, 2018, **167**:39-47
[81] WEI D, YU Y, RIDLEY A J, *et al.* Multi-point observations and modeling of Subauroral Polarization Streams (SAPS) and Double-Peak Subauroral Ion Drifts (DSAIDs): a case study [J]. *Adv. Space Res.*, 2019, **63**(11):3522-3535
[82] WEI D, YU Y, HE F. The magnetospheric driving source of double-peak subauroral ion drifts: double ring current pressure peaks [J]. *Geophys. Res. Lett.*, 2019, **46**(13):7079-7087
[83] YANG J Y, DUNLOP M, LüHR H, *et al.* Statistical correlation analysis of field-aligned currents measured by Swarm [J]. *J. Geophys. Res.: Space Phys.*, 2018, **123**(10):8170-8184
[84] LIU S, ZHANG J, CHEN L, *et al.* Examining wave vector and minimum cyclotron resonant electron energy of emic waves with magnetospheric multiscale mission [J]. *Geophys. Res. Lett.*, 2018. **45**(19):10138-10149
[85] ZHAO H, ZHOU X Z, ZONG Q G, *et al.* Small-Scale aurora associated with magnetospheric flow vortices after a solar wind dynamic pressure decrease [J]. *J. Geophys. Res.: Space Phys.*, 2019, **124**(5):3303-3311
[86] LIU Y, ZONG Q G, ZHOU X Z, *et al.* Understanding electron dropout echoes induced by interplanetary shocks: test particle simulations [J]. *J. Geophys. Res.: Space Phys.*, 2019, **124**(8):6759-6775
[87] XU J, HE Z, BAKER D, *et al.* Characteristics of high-energy proton responses to geomagnetic activities in the inner radiation belt observed by the RBSP satellite [J]. *J. Geophys. Res.: Space Phys.,* 2019, **124**(9):7581-7591
[88] TANG R, SUMMERS D. Dependence of whistler mode chorus wave generation on the maximum linear growth rate [J]. *J. Geophys. Res.: Space Phys.*, 2019, **124**(6):4114-4124
[89] LOU Y, GU X, SUMMERS D, *et al.* Statistical distributions of dayside ECH waves observed by MMS [J]. *Geophys. Res. Lett.*, 2018, **45**(23):12730-12738
[90] YI JUAN G X, LI Zhipeng, LIN Rentong, *et al.* Modeling and analysis of NWC signal propagation amplitude based on LWPC and IRI models [J]. *Chin. J. Geophys.*, 2019, **62**(9): 3223-3234
[91] FU S, HE F, GU X, *et al.* Occurrence features of simultaneous H^+- and He^+-band EMIC emissions in the outer radiation belt [J]. *Adv. Space Res.*, 2018, **61**(8):2091-2098
[92] WANG Q, FU S, NI B, *et al.* Bounce resonance scattering of

ring current electrons by H^+ band EMIC waves [J]. *Phys. Plasmas*, 2018, **25**(8):082903

[93] XIANG Z, TU W, NI B, *et al.* A statistical survey of radiation belt dropouts observed by Van Allen Probes [J]. *Geophys. Res. Lett.*, 2018, **45**(16):8035-8043

[94] HUA M, LI W, MA Q, *et al.* Modeling the electron flux enhancement and butterfly pitch angle distributions on L Shells <2.5 [J]. *Geophys. Res. Lett.*, 2019, **46**(20): 10967-10976

[95] XIANG Z, LI X, SELESNICK R, *et al.* Modeling the quasi-trapped electron fluxes from Cosmic Ray Albedo Neutron Decay (CRAND) [J]. *Geophys. Res. Lett.*, 2019, **46**(4): 1919-1928

[96] WEI C, DAI L, DUAN S, *et al.* Multiple satellites observation evidence: high-m poloidal ULF waves with time-varying polarization states [J]. *Earth Planet. Phys.*, 2019, **3**(3):190-203

[97] FU S, NI B, LOU Y, *et al.* Resonant scattering of near-equatorially mirroring electrons by landau resonance with H^+ band EMIC waves [J]. *Geophys. Res. Lett.*, 2018, **45**(20):10866-10873

[98] HUA M, NI B, LI W, *et al.* Evolution of radiation belt electron pitch angle distribution due to combined scattering by plasmaspheric hiss and magnetosonic waves [J]. *Geophys. Res. Lett.*, 2019, **46**(6):3033-3042

[99] CAO X, NI B, SUMMERS D, *et al.* Sensitivity of EMIC wave-driven scattering loss of ring current protons to wave normal angle distribution [J]. *Geophys. Res. Lett.*, 2019, **46**(2):590-598

[100] FU S, NI B, TAO X, *et al.* Interactions between H^+ band EMIC waves and radiation belt relativistic electrons: comparisons of test particle simulations with quasi-linear calculations [J]. *Phys. Plasmas*, 2019, **26**(3):032901

[101] HUANG JING N B, FU SONG, *et al.* Analysis of whistler waves in the Jovian magnetosphere based on data from JUNO waves Instrument [J]. *Chin. J. Geophys.*, 2019, **62**(3):817-824

[102] HUA M, NI B, FU S, *et al.* Combined scattering of outer radiation belt electrons by simultaneously occurring chorus, exohiss, and magnetosonic waves [J]. *Geophys. Res. Lett.*, 2018, **45**(19):10057-10067

[103] FU S, NI B, ZHOU R, *et al.* Combined scattering of radiation belt electrons caused by landau and bounce resonant interactions with magnetosonic waves [J]. *Geophys. Res. Lett.*, 2019, **46**(17-18):10313-10321

[104] NI B, ZOU Z, FU S, *et al.* Resonant scattering of radiation belt electrons by off-equatorial magnetosonic waves [J]. *Geophys. Res. Lett.,* 2018, **45**(3):1228-1236

[105] NI B, CAO X, SHPRITS Y Y, *et al.* Hot plasma effects on the cyclotron-resonant pitch-angle scattering rates of radiation belt electrons due to EMIC waves [J]. *Geophys. Res. Lett.*, 2018, **45**(1):21-30

[106] HE Y, XIAO F, SU Z, *et al.* Generation of lower l shell dayside chorus by energetic electrons from the plasma sheet [J]. *J. Geophys. Res.: Space Phys.,* 2018, **123**(10):8109-8121

[107] JIN Y, YANG C, HE Y, *et al.* Butterfly distribution of Earth's radiation belt relativistic electrons induced by dayside chorus [J]. *Sci. China Technol. Sci.*, 2018, **61**(2):212-218

[108] DEGELING A W, RANKIN R, WANG Y, *et al.* Alteration of particle drift resonance dynamics near poloidal mode field line resonance structures [J]. *J. Geophys. Res.: Space Phys.,* 2019, **124**(9):7385-7401

[109] TANG C L, XIE X J, NI B, *et al.* Rapid enhancements of the seed populations in the heart of the Earth's outer radiation belt: a multicase study [J]. *J. Geophys. Res.: Space Phys.*, 2018, **123**(6):4895-4907

[110] ZHOU Q, YANG C, HE Y, *et al.* Excitation of highly oblique lower band and upper band chorus by a loss cone feature and temperature anisotropy distribution [J]. *Geophys. Res. Lett.*, 2019, **46**(4):1929-1936

[111] CHEN Y, ZHOU Q, HE Y, *et al.* Global occurrences of electrostatic electron cyclotron harmonic waves associated with radiation belt electron distributions [J]. *Geophys. Res. Lett.,* 2019, **46**(10):5028-5033

[112] ZHAO W, LIU S, ZHANG S, *et al.* Global occurrences of auroral kilometric radiation related to suprathermal electrons in radiation belts [J]. *Geophys. Res. Lett.*, 2019, **46**(13):7230-7236

[113] LIU S, XIA Z, CHEN L, *et al.* Magnetospheric multiscale observation of quasiperiodic EMIC waves associated with enhanced solar wind pressure [J]. *Geophys. Res. Lett.*, 2019, **46**(13):7096-7104

[114] GAO Z, ZOU Z, ZUO P, *et al.* Low-frequency hiss-like whistler-mode waves generated by nonlinear three-wave interactions outside the plasmasphere [J]. *Phys. Plasmas*, 2019, **26**(12):122901

[115] YANG C, XIAO F, HE Y, *et al.* Storm time evolution of outer radiation belt relativistic electrons by a nearly continuous distribution of chorus [J]. *Geophys. Res. Lett.*, 2018, **45**(5):2159-2167

[116] LIU S, YAN Q, YANG C, *et al.* Quantifying extremely rapid flux enhancements of radiation belt relativistic electrons associated with radial diffusion [J]. *Geophys. Res. Lett.*, 2018, **45**(3):1262-1270

[117] GAO Z, SU Z, XIAO F, *et al.* Nonlinear coupling between whistler-mode chorus and electron cyclotron harmonic waves in the Magnetosphere [J]. *Geophys. Res. Lett.*, 2018, **45**(23):12685-12693

[118] YU X, YUAN Z. Saturation characteristics of parallel EMIC waves in the inner magnetosphere [J]. *Geophys. Res. Lett.*, 2019, **46**(14):7902-7910

[119] YUAN Z, YU X, OUYANG Z, *et al.* Simultaneous trapping of electromagnetic ion cyclotron and magnetosonic waves by background plasmas [J]. *J. Geophys.Res.: Space Phys.*, 2019, **124**(3):1635-1643

[120] YU X, YUAN Z, HUANG S, *et al.* Excitation of extremely low-frequency chorus emissions: the role of background plasma density [J]. *Earth Planet. Phys.*, 2019, **3**(1):1-7

[121] YUAN Z, LIU K, YU X, *et al.* Precipitation of radiation belt electrons by EMIC waves with conjugated observations of NOAA and Van Allen satellites [J]. *Geophys. Res. Lett.*, 2018, **45**(23):12694-12702

[122] YU X, YUAN Z, LI H, *et al.* Response of banded whistler mode waves to the enhancement of solar wind dynamic

pressure in the inner Earth's Magnetosphere [J]. *Geophys. Res. Lett.,* 2018, **45**(17):8755-8763

[123] YU X, YUAN Z, HUANG S, *et al.* Excitation of O^+ band EMIC waves through H^+ ring velocity distributions: Van Allen Probe observations [J]. *Geophys. Res. Lett.*, 2018, **45**(3):1271-1276

[124] YUAN C J, ZONG Q G. The efficiency of coronal mass ejection with different IMF preconditions on the production of megaelectronvolt electron content in the outer radiation belt [J]. *J. Geophys. Res.: Space Phys.*, 2019, **124**(5):3222-3235

[125] WANG G, ZHANG T, GAO Z, *et al.* Propagation of EMIC waves inside the plasmasphere: a two-event study [J]. *J. Geophys. Res.: Space Phys.*, 2019, **124**(11):8396-8415

[126] HAO Y, ZONG Q G, ZHOU X Z, *et al.* Global-Scale ULF waves associated with SSC accelerate magnetospheric ultrarelativistic electrons [J]. *J. Geophys. Res.: Space Phys.*, 2019, **124**(3):1525-1538

[127] REN J, ZONG Q, ZHOU X, *et al.* Cold plasmaspheric electrons affected by ULF waves in the inner magnetosphere: a Van Allen Probes statistical study [J]. *J. Geophys. Res.: Space Phys.*, 2019, **124**(10):7954-7965

[128] CHEN X, ZONG Q, ZOU H, *et al.* BD-IES Observation of multi-period electron flux modulation caused by localized Ultra-Low frequency waves [J]. *Ann. Geophys.*, 2019, **38**(4):801-813

[129] YUE C, BORTNIK J, LI W, *et al.* Oxygen ion dynamics in the Earth's ring current: Van Allen Probes observations [J]. *J. Geophys. Res.: Space Phys.*, 2019, **124**(10):7786-7798

[130] LI L, ZHOU X Z, OMURA Y, *et al.* Nonlinear drift resonance between charged particles and ultralow frequency waves: theory and observations [J]. *Geophys. Res. Lett.*, 2018, **45**(17):8773-8782

[131] YANG M, ZHOU X Z, ZONG Q G, *et al.* Traveling ultralow-frequency waves and their influences over low-energy, charged particles [J]. *J. Geophys. Res.: Space Phys.,* 2018, **123**(5):3848-3858

[132] YU J, LI L, CUI J, *et al.* Effect of hot He^+ Ions on the electron pitch angle scattering driven by H^+, He^+, and O^+ band EMIC waves [J]. *Geophys. Res. Lett.*, 2019, **46**(12):6306

[133] YU J, WANG J, CUI J. Ring current proton scattering by low-frequency magnetosonic waves [J]. *Earth Planet. Phys.*, 2019, **3**(4):365-372

[134] TAO D, LIU W, MA Y. Plasma perturbations in the coexisting environment of VLF transmitter emission, lightning strokes and seismic activity [J]. *Sci. China Technol. Sci.*, 2018, **61**(5):678-686

[135] ZHANG D, LIU W, LI X, *et al.* Observations of impulsive electric fields induced by interplanetary shock [J]. *Geophys. Res. Lett.*, 2018, **45**(15):7287-7296

[136] LV X, LIU W. Measurements of convection electric field in the inner magnetosphere [J]. *Sci. China Technol. Sci.*, 2018, **61**(12):1866-1871

[137] YU Y, DELZANNO G L, JORDANOVA V, *et al.* PIC simulations of wave-particle interactions with an initial electron velocity distribution from a kinetic ring current model [J]. *J. Atmos. Sol.:Terr. Phys.*, 2018, **177**:169-178

[138] LI L Y, YANG S S, CAO J B, *et al.* Effects of solar wind plasma flow and interplanetary magnetic field on the spatial structure of earth's radiation belts [J]. *J. Geophys. Res.: Space Phys.*, 2019, **124**(12):10332-10344

[139] YU J, LI L Y, CUI J, *et al.* Effect of low-harmonic magnetosonic waves on the radiation belt electrons inside the plasmasphere [J]. *J. Geophys. Res.: Space Phys.,* 2019, **124**(5):3390-3401

[140] ZHANG S, TIAN A, DEGELING A W, *et al.* Pc4-5 Poloidal ULF wave observed in the dawnside plasmaspheric plume [J]. *J. Geophys. Res.: Space Phys.*, 2019, **124**(12):9986-9998

[141] YUAN Z, YU X, HUANG S, *et al.* Cold ion heating by magnetosonic waves in a density cavity of the plasmasphere [J]. *J. Geophys. Res.: Space Phys.,* 2018, **123**(2):1242-1250

[142] ZHANG W, FU S, GU X, *et al.* Electron scattering by plasmaspheric hiss in a nightside plume [J]. *Geophys. Res. Lett.*, 2018, **45**(10):4618-4627

[143] ZHANG W, NI B, HUANG H, *et al.* Statistical properties of hiss in plasmaspheric plumes and associated scattering losses of radiation belt electrons [J]. *Geophys. Res. Lett.*, 2019, **46**(11):5670-5680

[144] HE Z, CHEN L, LIU X, *et al.* Local generation of high-frequency plasmaspheric hiss observed by Van Allen Probes [J]. *Geophys. Res. Lett.*, 2019, **46**(3):1141-1148

[145] HE Z, YAN Q, MA Y, *et al.* Precipitation loss of Van Allen radiation belt electrons by hiss waves outside the plasmasphere [J]. *Astrophys. Space Sci.*, 2018, **363**(4):66

[146] NI B, HUANG H, ZHANG W, *et al.* Parametric sensitivity of the formation of reversed electron energy spectrum caused by plasmaspheric hiss [J]. *Geophys. Res. Lett.*, 2019, **46**(8):4134-4143

[147] YUAN Z, OUYANG Z, YU X, *et al.* Global distribution of proton rings and associated magnetosonic wave instability in the inner magnetosphere [J]. *Geophys. Res. Lett.*, 2018, **45**(19):10160-10166

[148] REN J, ZONG Q, MIYOSHI Y, *et al.* A comparative study of ULF waves' role in the dynamics of charged particles in the plasmasphere: Van Allen probes observation [J]. *J. Geophys. Res.: Space Phys.*, 2018, **123**(7):5334-5343

[149] ZONG Q G, LEONOVICH A, KOZLOV D. Resonant alfven waves excited by plasma tube/shock front interaction [J]. *Phys. Plasmas*, 2018, **25**(12):122904

[150] LIU B, LI L, YU J, *et al.* The effect of hot protons on magnetosonic waves inside and outside the plasmapause: new observations and theoretic results [J]. *J. Geophys. Res.: Space Phys.*, 2018, **123**(1):653-664

[151] ZHANG H, FU S, PU Z, *et al.* Statistics on the magnetosheath properties related to magnetopause magnetic reconnection [J]. *Astrophys. J.*, 2019, **880**(2):122

[152] KLIMUSHKIN D Y, MAGER P N, ZONG Q, *et al.* Alfvén wave generation by a compact source moving on the magnetopause: asymptotic solution [J]. *J. Geophys. Res.: Space Phys.*, 2019, **124**(4):2720-2735

[153] LIU H, ZONG Q G, ZHANG H, *et al.* MMS observations of electron scale magnetic cavity embedded in proton scale magnetic cavity [J]. *Nat. Commun.*, 2019, **10**(1):1-11

[154] SHEN X C, SHI Q, WANG B, *et al.* Dayside magnetospheric and ionospheric responses to a foreshock transient on 25 June 2008: 1. FLR observed by satellite and ground-based magnetometers [J]. *J. Geophys. Res.: Space Phys.*, 2018, **123**(8):6335-6346

[155] HUANG S, SAHRAOUI F, YUAN Z, *et al.* Observations of whistler waves correlated with electron-scale coherent structures in the magnetosheath turbulent plasma [J]. *Astrophys. J.*, 2018, **861**(1):29

[156] HUANG S, ZHAO P, HE J, *et al.* A new method to identify flux ropes in space plasmas [J]. *Ann. Geophys.*, 2018, **36**(5):1275-1283

[157] DUAN S, DAI L, WANG C, *et al.* Conjunction observations of energetic oxygen ions O^+ accumulated in the sequential flux ropes in the high-altitude cusp [J]. *J. Geophys. Res.: Space Phys.*, 2019, **124**(10):7912-7922

[158] WANG M, LU J, KABIN K, *et al.* The influence of IMF by on the bow shock: observation result. [J]. *J. Geophys. Res.: Space Phys.*, 2018, **123**(3):1915-1926

[159] YAO S T, SHI Q Q, YAO Z H, *et al.* Electron mirror-mode structure: magnetospheric multiscale observations [J]. *Astrophys. J.*, 2019, **881**(2):L31

[160] LU J, ZHOU Y, MA X, *et al.* Earth's bow shock: a new Three-Dimensional asymmetric model with dipole tilt effects [J]. *J. Geophys. Res.: Space Phys.*, 2019, **124**(7):5396-5407

[161] TANG B, LI W, WANG C, *et al.* Magnetic depression and electron transport in an ion-scale flux rope associated with Kelvin-Helmholtz waves [J]. *Ann. Geophys.*, 2018, **36**(3):879-889

[162] TANG B B, LI W Y, WANG C, *et al.* Effect of kinetic alfvén waves on electron transport in an ion-scale flux rope [J]. *Chin. Phys. Lett.*, 2018, **35**(11):119401

[163] YAO S T, SHI Q Q, YAO Z H, *et al.* Waves in kinetic-scale magnetic dips: MMS observations in the magnetosheath [J]. *Geophys. Res. Lett.*, 2019, **46**(2):523-533

[164] YAO S T, SHI Q Q, LIU J, *et al.* Electron dynamics in magnetosheath mirror-mode structures [J]. *J. Geophys. Res.: Space Phys.*, 2018, **123**(7):5561-5570

[165] LING Y, SHI Q, SHEN X C, *et al.* Observations of kelvin-helmholtz waves in the Earth's magnetotail near the lunar orbit [J]. *J. Geophys. Res.: Space Phys.*, 2018, **123**(5): 3836-3847

[166] YAO S T, SHI Q Q, GUO R L, *et al.* Magnetospheric multiscale observations of electron scale magnetic peak [J]. *Geophys. Res. Lett.*, 2018, **45**(2):527-537

[167] TANG B B, LI W, GRAHAM D B, *et al.* Crescent-shaped electron distributions at the nonreconnecting magnetopause: magnetospheric multiscale observations [J]. *Geophys. Res. Lett.*, 2019, **46**(6):3024-3032

[168] CHEN Chen, SUN Tianran, TANG Binbin, *et al.* Global MHD results of flux transfer events at the dayside magnetopause under high solar wind spee [J]. *Chin. J. Space Sci.*, 2019, **39**(2):149-157

[169] LU S, WANG C, LI W Y, *et al.* Prolonged kelvin–helmholtz waves at dawn and dusk flank magnetopause: simultaneous observations by MMS and THEMIS [J]. *Astrophys. J.*, 2019, **875**(1):57

[170] CHEN C, SUN T, WANG C, *et al.* The effect of solar wind mach numbers on the occurrence rate of flux transfer events at the dayside magnetopause [J]. *Geophys. Res. Lett.*, 2019, **46**(8):4106-4113

[171] SUN T, TANG B, WANG C, *et al.* Large-scale characteristics of flux transfer events on the dayside magnetopause [J]. *J. Geophys. Res.: Space Phys.*, 2019, **124**(4):2425-2434

[172] SUN T, WANG C, SEMBAY S, *et al.* Soft X-ray imaging of the magnetosheath and cusps under different solar wind conditions: MHD simulations [J]. *J. Geophys. Res.: Space Phys.*, 2019, **124**(4):2435-2450

[173] JIANG K, HUANG S, YUAN Z, *et al.* Observations of whistler waves in two sequential flux ropes at the magnetopause [J]. *Astrophys. Space Sci.*, 2019, **364**(10):168

[174] WANG J, GUO Z, YASONG S G, *et al.* The responses of the earth's magnetopause and bow shock to the IMF B_z and the solar wind dynamic pressure: a parametric study using the AMR-CESE-MHD model [J]. *J. Space Weather Space Climate*, 2018, **8**:A41

[175] PANG X, CAO J, DENG Z, *et al.* Spatial distribution of ion polytropic index joint-modulated by temperature anisotropy and MHD disturbances in the southern high latitude magnetosheath [J]. *Sci. China Technol. Sci.*, 2018, **61**(3):381-388

[176] ZHU C, ZHANG H, FU S, *et al.* Trapped and accelerated electrons within a magnetic mirror behind a flux rope on the magnetopause [J]. *J. Geophys. Res.: Space Phys.*, 2019, **124**(6):3993-4008

[177] HAO Y, LI Q, ZHANG D, *et al.* Using GNSS TEC technique to observe compression of the plasmasphere by an interplanetary shock [J]. *Sci. Sin. Technol.*, 2018, **48**(8):853-862

[178] DONG X C, DUNLOP M, WANG T Y, *et al.* Carriers and sources of magnetopause current: MMS case study [J]. *J. Geophys. Res.: Space Phys.*, 2018, **123**(7):5464-5475

[179] XIAO C, LIU W, SHEN C, *et al.* Study on the curvature and gradient of the magnetic field in earth's cusp region based on the magnetic curvature analysis method [J]. *J. Geophys. Res.: Space Phys.*, 2018, **123**(5):3794-3805

[180] DONG X C, DUNLOP M W, TRATTNER K J, *et al.* Electron sublayers and the associated magnetic topologies in the inner low-latitude boundary layer [J]. *Geophys. Res. Lett.*, 2019, **46**(11):5746-5753

[181] YU Y, LIEMOHN M W, JORDANOVA V K, *et al.* Recent advancements and remaining challenges associated with Inner Magnetosphere Cross-Energy/Population Interactions (IMCEPI) [J]. *J. Geophys. Res.: Space Phys.*, 2019, **124**(2):886-897

[182] FU H S, PENG F Z, LIU C M, *et al.* Evidence of electron acceleration at a reconnecting magnetopause [J]. *Geophys. Res. Lett.*, 2019, **46**(11):5645-5652

[183] LIU Y Y, FU H S, LIU C M, *et al.* Parallel electron heating by tangential discontinuity in the turbulent magnetosheath [J]. *Astrophys. J.*, 2019, **877**(2):L16

[184] CHEN Z Z, FU H S, WANG Z, *et al.* Evidence of magnetic nulls in the reconnection at bow shock [J]. *Geophys. Res. Lett.*, 2019, **46**(17/18):10209-10218

[185] ZHONG Z, DENG X, ZHOU M, *et al.* Energy conversion

and dissipation at dipolarization fronts: a statistical overview [J]. *Geophys. Res. Lett.*, 2019, **46**(22):12693-12701

[186] CHEN G, FU H S, ZHANG Y, *et al.* Energetic electron acceleration in unconfined reconnection jets [J]. *Astrophys. J.*, 2019, **881**(1):L8

[187] ZHOU X Z, XU Y, RUNOV A, *et al.* On the origin of perpendicular ion anisotropy inside dipolarizing flux bundles [J]. *J. Geophys. Res.: Space Phys.*, 2019, **124**(6):4009-4021

[188] PITKÄNEN T, KULLEN A, LAUNDAL K M, *et al.* IMF by influence on magnetospheric convection in Earth's magnetotail plasma sheet [J]. *Geophys. Res. Lett.*, 2019, **46**(21): 11698-11708

[189] ZHOU M, DENG X, ZHONG Z, *et al.* Observations of an electron diffusion region in symmetric reconnection with weak guide field [J]. *Astrophys. J.*, 2019, **870**(1):34

[190] REN Y, DAI L, LI W, *et al.* Whistler waves driven by field-aligned streaming electrons in the near-earth magnetotail reconnection [J]. *Geophys. Res. Lett.*, 2019, **46**(10): 5045-5054

[191] ZHOU M, MAN H, ZHONG Z, *et al.* Sub-ion-scale dynamics of the ion diffusion region in the magnetotail: MMS observations [J]. *J. Geophys. Res.: Space Phys.*, 2019, **124**(10): 7898-7911

[192] ZHOU M, HUANG J, MAN H, *et al.* Electron-scale vertical current sheets in a bursty bulk flow in the terrestrial magnetotail [J]. *Astrophys. J. Lett.*, 2019. **872**(2):L26

[193] HUANG J, ZHOU M, LI H, *et al.* Small-scale dipolarization fronts in the Earth's magnetotail [J]. *Earth Planet. Phys.,* 2019, **3**(4):358-364

[194] ZHANG S, TIAN A, SHI Q, *et al.* Statistical study of ULF waves in the magnetotail by THEMIS observations [J]. *Ann. Geophys.*, 2018, **36**(5):1335-1346

[195] ZHANG L, BAUMJOHANN W, DAI L, *et al.* Measurements of the vorticity in the bursty bulk flows [J]. *Geophys. Res. Lett.,* 2019, **46**(17-18):10322-10329

[196] HUANG S Y, JIANG K, FU H S, *et al.* Periodical dipolarization processes in earth's magnetotail [J]. *Geophys. Res. Lett.*, 2019, **46**(23):13640-13648

[197] HUANG S Y, JIANG K, YUAN Z G, *et al.* Observations of flux ropes with strong energy dissipation in the magnetotail [J]. *Geophys. Res. Lett.*, 2019, **46**(2):580-589

[198] HUANG S Y, HE L H, YUAN Z G, *et al.* MMS observations of kinetic-size magnetic holes in the terrestrial magnetotail plasma sheet [J]. *Astrophys. J.*, 2019, **875**(2):113

[199] WEI Y, HUANG S, RONG Z, *et al.* Observations of short-period current sheet flapping events in the Earth's magnetotail [J]. *Astrophys. J. Lett.*, 2019. **874**(2):L18

[200] WANG Z Q, SUN K, ZHANG Y S, *et al.* Heavy ion acceleration by EMIC waves in the near-Earth plasma sheet [J]. *Phys. Plasmas,* 2019, **26**(2):022903

[201] GAO J, RONG Z, CAI Y, *et al.* The distribution of two flapping types of magnetotail current sheet: implication for the flapping mechanism [J]. *J. Geophys. Res.: Space Phys.*, 2018, **123**(9):7413-7423

[202] RONG Z, CAI Y, GAO J, *et al.* Cluster observations of a dispersive flapping event of magnetotail current sheet [J]. *J. Geophys. Res.: Space Phys.*, 2018, **123**(7):5571-5579

[203] SCHMID D, VOLWERK M, PLASCHKE F, *et al.* A statistical study on the properties of dips ahead of dipolarization fronts observed by MMS [J]. *J. Geophys. Res.: Space Phys.,* 2019, **124**(1):139-150

[204] SCHMID D, VOLWERK M, PLASCHKE F, *et al.* Dipolarization fronts: tangential discontinuities on the spatial range of validity of the MHD jump conditions [J]. *J. Geophys. Res.: Space Phys.,* 2019, **124**(12), 9963-9975

[205] WANG G, ZHANG T, WU M, *et al.* Solar wind directional change triggering flapping motions of the current sheet: MMS observations [J]. *Geophys. Res. Lett.*, 2019, **46**(1):64-70

[206] WU M, LU Q, VOLWERK M, *et al.* Electron acceleration behind a wavy dipolarization front [J]. *Astrophys. Space Sci.*, 2018, **363**(2):22

[207] LIU H, ZONG Q G, ZHANG H, *et al.* The geometry of an electron scale magnetic cavity in the plasma sheet [J]. *Geophys. Res. Lett.*, 2019, **46**(16):9308-9317

[208] LIU Z Y, ZONG Q G, ZOU H, *et al.* Drifting electron holes occurring during geomagnetically quiet times: BD-IES observations [J]. *J. Geophys. Res.: Space Phys.*, 2019, **124**(11): 8695-8706

[209] ZHOU X Z, RUNOV A, ANGELOPOULOS V, *et al.* On the acceleration and anisotropy of ions within magnetotail dipolarizing flux bundles [J]. *J. Geophys. Res.: Space Phys.,* 2018, **123**(1):429-442

[210] PAN D X, KHOTYAINTSEV Y V, GRAHAM D B, *et al.* Rippled electron-scale structure of a dipolarization front [J]. *Geophys. Res. Lett.*, 2018, **45**(22):12116-12124

[211] DUAN A, ZHANG H, LU H. 3D MHD simulation of the double-gradient instability of the magnetotail current sheet [J]. *Sci. China Technol. Sci.*, 2018, **61**(9):1364-1371

[212] XU Y, FU H, NORGREN C, *et al.* Formation of dipolarization fronts after current sheet thinning [J]. *Phys. Plasmas*, 2018, **25**(7):072123

[213] LIU C, FU H, XU Y, *et al.* Electron-scale measurements of dipolarization front. *Geophys. Res. Lett.*, 2018. **45**(10): 4628-4638.

[214] LIU C, LIU Y, XU Y, *et al.* Betatron cooling of suprathermal electrons in the terrestrial Magnetotail [J]. *Astrophys. J.*, 2018, **866**(2):93

[215] LU H Y, LI Y, GE Y S. On the kinetic nature of dipolarization fronts produced by interchange instability in the magnetotail [J]. *Chin. J. Geophys.: Chin. Ed.*, 2018, **61**(2):403-410

[216] CAO J B, REN G, MA Y. Kinetic analysis of the energy transport of two-flow components in the plasma sheet [J]. *J. Geophys. Res.: Space Phys.*, 2019, **124**(8):6730-6739

[217] FU H, GRIGORENKO E E, GABRIELSE C, *et al.* Magnetotail dipolarization fronts and particle acceleration: a review [J]. *Sci. China Earth Sci.*, 2019, **63**(2):235-256

[218] LIU C M, FU H S. Anchor point of electron acceleration around dipolarization fronts in space plasmas [J]. *Astrophys. J.*, 2019, **873**(1):L2

[219] ZHAO M J, FU H S, LIU C M, *et al.* Energy range of electron rolling pin distribution behind dipolarization front [J]. *Geophys. Res. Lett.*, 2019, **46**(5):2390-2398

[220] CHEN Z Z, FU H S, LIU C M, *et al.* Electron-Driven dissipation in a tailward flow burst [J]. *Geophys. Res. Lett.*, 2019, **46**(11):5698-5706

[221] XU Y, FU H S, NORGREN C, *et al.* Ionospheric Cold Ions Detected by MMS Behind Dipolarization Fronts [J]. *Geophys. Res. Lett.*, 2019. **46**(14):7883-7892.

[222] YU J, LI L Y, CUI J, *et al.* Combined effects of equatorial chorus waves and high-latitude z-mode waves on Saturn's radiation belt electrons [J]. *Geophys. Res. Lett.*, 2019, **46**(15): 8624-8632

[223] SUN Y, ROUSSOS E, KRUPP N, *et al.* Spectral signatures of adiabatic electron acceleration at saturn through corotation drift cancelation [J]. *Geophys. Res. Lett.*, 2019, **46**(17-18): 10240-10249

[224] WANG Y, GUO X, TANG B, *et al.* Modeling the Jovian magnetosphere under an antiparallel interplanetary magnetic field from a global MHD simulation [J]. *Earth Planet. Phys.*, 2018, **2**(4):303-309

[225] FAN K, FRAENZ M, WEI Y, *et al.* Reduced atmospheric ion escape above martian crustal magnetic fields [J]. *Geophys. Res. Lett.*, 2019, **46**(21):11764-11772

[226] HAN Q, FAN K, CUI J, *et al.* The relationship between photoelectron boundary and steep electron density gradient on Mars: MAVEN observations [J]. *J. Geophys. Res.h: Space Phys.,* 2019, **124**(10):8015-8022

[227] GUO R, YAO Z, SERGIS N, *et al.* Long-standing small-scale reconnection processes at saturn revealed by cassini [J]. *Astrophys. J. Lett.*, 2019, **884**(1):L14

[228] GUO R, YAO Z, WEI Y, *et al.* Rotationally driven magnetic reconnection in Saturn's dayside [J]. *Nat. Astron.*, 2018, **2**(8):640-645

[229] GUO R, YAO Z, SERGIS N, *et al.* Reconnection acceleration in Saturn's dayside magnetodisk: a multicase study with cassini [J]. *Astrophys. J. Lett.*, 2018, **868**(2):L23

[230] YAN L, GAO J, CHAI L, *et al.* Revisiting the strongest martian X-ray halo observed by XMM-Newton on 2003 November 19–21 [J]. *Astrophys. J. Lett.,* 2019, **883**(2):L38

[231] CHAI L, WAN W, WEI Y, *et al.* The induced global looping magnetic field on Mars [J]. *Astrophys. J. Lett.*, 2019, **871**(2):L27

[232] SHAN L, MAZELLE C, MEZIANE K, *et al.* The Quasi-monochromatic ULF wave boundary in the venusian foreshock: Venus express observations [J]. *J. Geophys. Res.: Space Phys.*, 2018, **123**(1):374-384

[233] RONG Z, DING Y, SLAVIN J, *et al.* The magnetic field structure of Mercury's magnetotail [J]. *J. Geophys. Res.: Space Phys.*, 2018, **123**(1):548-566

[234] ZHONG J, ZONG Q, WEI Y, *et al.* MESSENGER observations of giant plasmoids in mercury's magnetotail [J]. *Astrophys. J. Lett.*, 2019, **886**(2):L32

[235] ZHONG J, WEI Y, PU Z, *et al.* MESSENGER observations of rapid and impulsive magnetic reconnection in Mercury's magnetotail [J]. *Astrophys. J. Lett.*, 2018, **860**(2):L20

[236] XIAO S, ZHANG T. Solar cycle variation of the venus magnetic barrier [J]. *Planet. Space Sci.*, 2018, **158**:53-62

[237] XIAO S, ZHANG T, VÖRÖS Z. Magnetic fluctuations and turbulence in the venusian magnetosheath downstream of different types of bow shock [J]. *J. Geophys. Res.: Space Phys.*, 2018, **123**(10):8219-8226

[238] LI Y, LU H. Evolution of kelvin–helmholtz instability on the venusian ionopause with the influence of hall effect [J]. *Astrophys. J.,* 2019, **875**(1):47

[239] ZOU H, YE Y, ZONG Q, *et al.* Imaging energetic electron spectrometer onboard a Chinese navigation satellite in the inclined GEO orbit [J]. *Sci. China Technol. Sci.*, 2018, **61**(12):1845-1865

[240] ZOU H, YE Y, ZONG Q, *et al.* Monte carlo simulations of the sensor head of imaging energetic electron spectrometer onboard a Chinese IGSO navigation satellite [J]. *Sci. China Technol. Sci.*, 2019, **62**(7):1169-1181

[241] ZHANG Y, NI B, XIANG Z, *et al.* Inter-satellite calibration of Fengyun-3 medium energy electron fluxes with POES electron measurements [J]. *Adv. Space Res.*, 2018, **61**(9): 2290-2300

[242] SHI Q Q, TIAN A M, BAI S C, *et al.* Dimensionality, coordinate system and reference frame for analysis of in-situ space plasma and field data [J]. *Space Sci. Rev.*, 2019, **215**(4):35

[243] TIAN A, SHI Q, DEGELING A W, *et al.* Analytical model test of methods to find the geometry and velocity of magnetic structures [J]. *Sci. China Technol. Sci.,* 2019, **62**(6):1003-1014

[244] WANG C, BRANDUARDI RAYMOND G. Progress of solar wind magnetosphere ionosphere link explorer (SMILE) mission [J]. *Chin. J. Space Sci.,* 2018, **38**(5):657-661

[245] GUO Y H, PENG S W, FEI W, *et al.* Design and simulation of Soft X-Ray imager on SMILE satellite [J]. *Chin. J. Geophys.:Chin. Ed.*, 2018, **61**(11):4348-4355

[246] PENG S, YE Y, WEI F, *et al.* Numerical model built for the simulation of the earth magnetopause by lobster-eye-type soft X-ray imager onboard SMILE satellite [J]. *Opt. Express*, 2018, **26**(12):15138-15152

[247] YUAN Z, YAO F, YU X, *et al.* An automatic detection algorithm applied to fast magnetosonic waves with observations of the Van Allen Probes [J]. *J. Geophys. Res.: Space Phys.*, 2019, **124**(5):3501-3511

[248] CAO J, ZENG L, ZHAN F, *et al.* The electromagnetic wave experiment for CSES mission: search coil magnetometer [J]. *Sci. China Technol. Sci.*, 2018, **61**(5):653-658

LIU Libo, WAN Weixing. Chinese Ionospheric Investigations in 2018–2019. *Chin. J. Space Sci.*, 2020, **40**(5): 269-303. DOI:10.11728/cjss2020.05.269

Chinese Ionospheric Investigations in 2018–2019*

LIU Libo WAN Weixing

(*Key Laboratory of Earth and Planetary Physics, Institute of Geology and Geophysics, Chinese Academy of Sciences, Beijing* 100029)

(*Innovation Academy for Earth Science, Chinese Academy of Sciences, Beijing* 100029)

(*Beijing National Observatory of Space Environment, Institute of Geology and Geophysics, Chinese Academy of Sciences, Beijing* 100029)

(*College of Earth and Planetary Sciences, University of the Chinese Academy of Sciences, Beijing* 100049)

Abstract Scientists from Mainland China have made fruitful investigations on various ionosphere related issues after the release of 2018 National Report of China on ionospheric researches in Ref.[1] to the Committee on Space Research (COSPAR). In this report, we briefly introduce more than 130 works in recent two years (2018–2019). The current report covers the topics as follows: ionospheric space weather, ionospheric structures and climatology, ionospheric dynamics and couplings, ionospheric irregularity and scintillation, modeling and data assimilation, and radio wave propagation in the ionosphere and sounding techniques.

Key words Ionosphere, Ionospheric storm, Dynamics, Data assimilation, Space weather

Classified index P 352

1 Ionospheric Space Weather

Solar flare effects on the ionosphere were continuously investigated. Previous studies have revealed the solar flare effects on the ionosphere having a negative relationship with the Solar Zenith Angle (SZA). The largest enhancement in electron density always occurs around the subsolar point. However, Le *et al.*[2] found that the enhancements in the Total Electron Content (TEC) during six solar flare events in 2001–2014 are not strongly dependent on the SZA, with enhancement peaks rather far away from the subsolar point. The regions with the largest TEC enhancements seem to be in a zonal belt with similar latitude. Spatial analysis of the TEC enhancements showed that such an anomaly distribution was not due to traveling ionospheric disturbances, and the anomaly distribution was not related to the background neutral density. The anomaly distribution of TEC enhancements may therefore be possibly due to the combined effect of enhancement in solar Extreme Ultraviolet (EUV) rays and transport processes induced by significant geomagnetic disturbances during the six solar flares.

Zhao *et al.*[3] investigated the ionospheric response to the 13–14 March 1989 great magnetic storm by using ground-based and satellite measurements and model simulations as well. They found that the mid - low latitude ionosphere in East Asia was characterized by strong westward electron density gradients persisting over a day at both the bottom side and topside ionosphere during the main and recovery phases of the storm. Their study shows that the ionospheric responses at nearby stations could be different strongly during the superstorm event.

Liu *et al.*[4] explored the responses of the ionosphere inside the disturbance composition zone to the

* Supported by National Natural Science Foundation of China (41774161)
Received March 2, 2020
E-mail: liul@mail.iggcas.ac.cn

October 2002 geomagnetic storms by using the long-duration continuous experiments of the Millstone Hill Incoherent Scatter Radar (ISR). At Millstone Hill, the electron density often responds considerably differently at lower and higher altitudes to geomagnetic disturbances. A decrease change in electron density is prevailing at low altitudes, whereas at topside altitudes it may sometimes enhance or do not deviate remarkably from the quiet-time values. During geomagnetic disturbances, the values of h_mF_2 and the topside vertical scale height around 600 km become larger. Although the electron density having altitudinal different responses, N_mF_2 and TEC still generally follow a similar pattern of depletions or enhancements. There are time-varying zonal differences in midlatitude TEC between Millstone Hill and a nearby location 28.5° west (Figure 1). The zonal difference of TEC becomes stronger during storm times. The fine structure of the ionospheric storm responses at middle and low latitudes[3,4] brings a great challenge to the capability of the models in the space weather predictions.

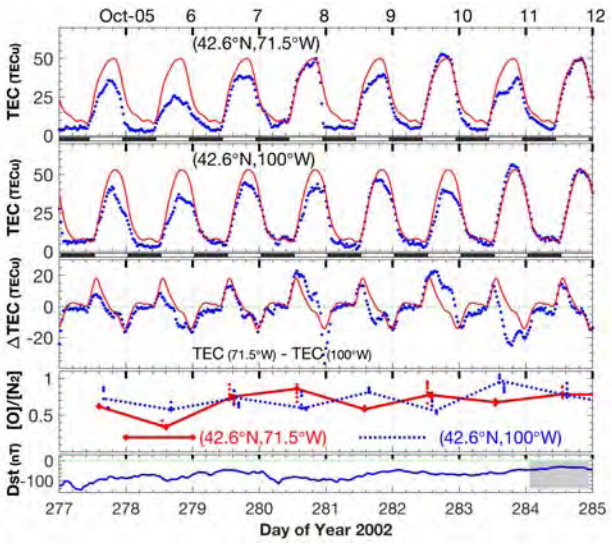

Fig. 1 Top two-panel plot Total Electron Content (TEC) at Millstone Hill (42.6°N, 71.5°W) and at (42.6°N, 100°W). The blue points mark individual observations, and the red curve plots the daily medians of observations. Followed is the differences of TEC between the two points. The fourth displays the $[O]/[N_2]$ ratio observations of TIMED/GUVI passing over Millstone Hill (42.6°N, 71.5°W) and a west location (42.6°N, 100°W), within in a window of (latitude ±2°) × (longitude ±2°). The bottom gives the *Dst* index

Zhang *et al.*[5] investigated the response of the ionospheric electric field and currents to the solar flares and geomagnetic storm on 6–11 September 2017 using the ISR and magnetometer observations over the Jicamarca sector. Significant differences are found in the response of ionospheric currents to the flare events. The increase and decrease of the ionospheric current are attributed to the enhanced conductivity in the initial stage of solar flare and by the weakened electric field in the later stage, respectively. The disturbance plasma drifts persist for three days with westward polarities at about 10:00 LT–16:00 LT and eastward at post-midnight and early morning. A downward disturbance plasma drift firstly occurs at high altitudes around 10:00 LT and the disturbance amplitude increases with altitude from 200 to 500 km. The latitudinal structure of the disturbance winds is thought to be the possible source for the observed altitudinal variations of the disturbance plasma drift. The Jicamarca ISR observations show the distinct altitudinal differences in the responses of the F region electron density to the disturbance electric field.

Zhang *et al.*[6] investigated the disturbance field-aligned plasma drift in the equatorial topside ionosphere during selected eight geomagnetic storms in 2011–2015 using the Communication/Navigation Outage Forecasting System (C/NOFS) data. The disturbance field-aligned plasma drifts during the six solstice storms are found to flow from the winter to the summer hemisphere during morning-midnight hours and indiscernible in the midnight-morning hours. There are little effects on the field-aligned plasma drift during the two equinoctial storms. In terms of the GPS-TEC and the plasma temperature data from Defense Meteorological Satellite Program (DMSP), the conjugate difference of storm-time disturbance plasma density gradient seems most likely caused the disturbance winter-to-summer plasma drift, while the disturbance plasma temperature gradient shows a signature opposite to that of the disturbance plasma drift (Figure 2).

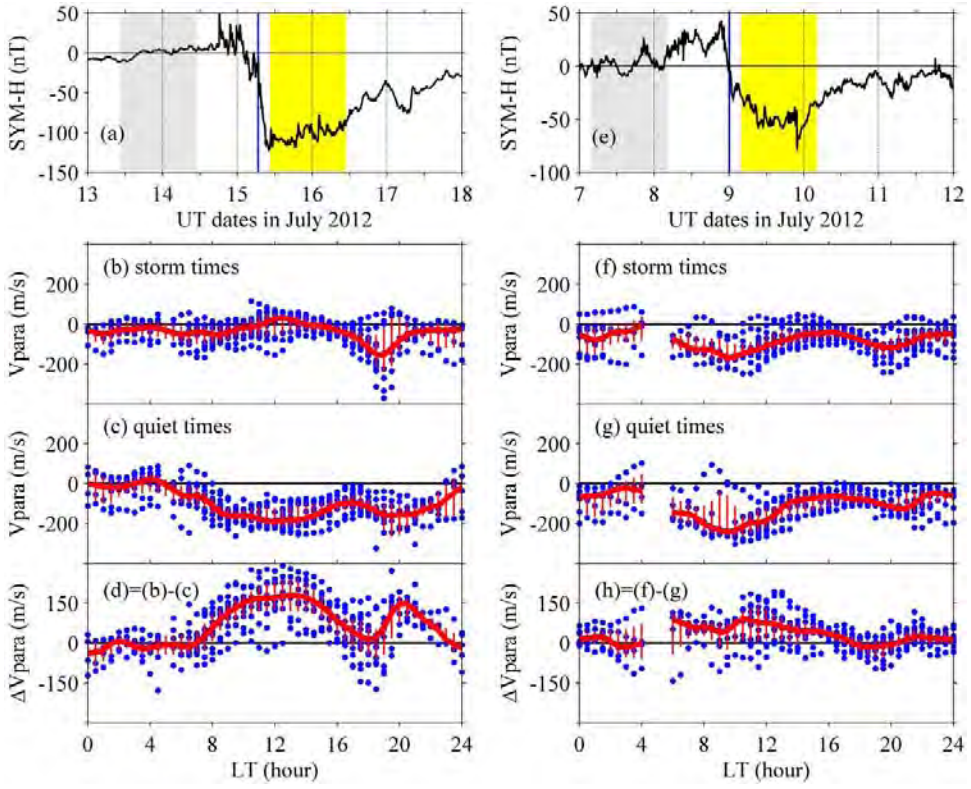

Fig. 2 (a) Sym-*H* index on 13–17 July 2012. The blue line marks the storm onset (at 06:42 UT on 15 July), and yellow and gray areas indicate the 24 h storm-time and 24 h quiet-time intervals. (b) The blue dots denote the storm-time equatorial field-aligned plasma drifts observed by C/NOFS with a red curve representing median and red lines denoting upper and lower quartile values. (c) Same as panel b, but for the 24-hour quiet time interval. (d) The difference between (b) and (c). (e)~(h) Same as panels (a)~(d), but for the case on 7–11 July 2012 where the 24 h quiet and storm intervals start at 04:12 UT on 7 and 9 July, respectively.

Jimoh *et al.*[7] investigated the topside ionospheric conditions during the September 2017 geomagnetic storm using up-looking TEC from GRACE, SWARM-A, TerraSAR-X, and MetOp-A satellites. Significant enhancements in TEC were present during the main phase of the storm, whereas no unusual enhancement was observed at the local morning and evening hours in the Asian-Australian sector during the recovery phase of the storm as observed by Lei *et al.*[8]. The ionospheric electric field disturbances were proposed to play an important role in triggering ionospheric irregularities under a relatively weak geomagnetic condition on 7 September 2017.

Balan *et al.*[9] investigated ionosphere-thermosphere storms and low-latitude (630 nm) aurora by using some derived parameters (Ips*Dst*, Ips*Kp*, and Ips*AE*). The derived parameters representing the impulsive strength of geomagnetic storms seem to have more systematic dependence among themselves than among the intensities ($Dst_{\min}$, $Kp_{\max}$, and $AE_{\max}$). The ionosphere-thermosphere storms observed by the Challenging Minisatellite Payload (CHAMP) satellite and low-latitude auroras observed by optical imagers are much more intense during high impulsive storms than high intensity storms. In a statistical sense, over 175 positive ionospheric storms ($\Delta N_m F_2 > 0$) observed in 1985–2005 and the intensity of 20 red auroras observed in 1989–2004 at midlatitudes correlate better with the impulsive parameters than the intensity parameters, with the best correlation being with Ips*Dst*. The mechanism of the impulsive action (high-energy input over a short duration) leading to large Ips*Dst* arises from the impact of fast solar

storms (interplanetary coronal mass ejections) with large IMF B_z southward at their front (or shock). The impulsive action results in bright low-latitude auroras and strong ionosphere-thermosphere storms.

Zhang *et al.*[10] investigated the ionospheric and thermospheric responses to oscillated Interplanetary Magnetic Field (IMF) B_z with 10, 30 and 60 min periods. The magnetosphere-ionosphere-thermosphere coupling system acts as a low-pass filter. There are two different thermospheric wind responses, almost simultaneous responses at different latitudes, and a typical traveling atmospheric disturbances signature with a time delay with respect to latitude.

Liu *et al.*[11] comprehensively observed the Large-Scale Traveling Ionospheric Disturbances (LSTIDs) in the eastern Asian sector during the 2015 St. Patrick's Day (17 March 2015) geomagnetic storm (Figure 3). An LSTID spanning in longitude (80°–140°E) occurs as a result of possible Atmospheric Gravity Waves (AGWs) propagated equatorward, and the crest of this LSTID shows a tendency of dissipation starting from the eastern side. The propagation parameters are of longitudinal dependence, probably related to the regional geomagnetic declination.

Li *et al.*[12] investigated the ionospheric response of the D region to solar flares. The results show that a sharp decrease of the effective reflection height H' can be detected clearly from 76 km to 80 km during the non-flare period to nearly 58 km with flares, and a sudden increase of electron density (N_e) during 13 M-level flares. The changes of N_e are strongly correlated with the variation of X-ray flux, while the changes of H' exhibit a negative correlation with that of X-ray flux

2 Ionospheric Structures and Climatology

Using Constellation Observing System for Meteorology, Ionosphere, and Climate (COSMIC) ionospheric radio occultation data, Huang *et al.*[13] explored the longitudinal and altitudinal patterns of the transition of interhemispheric asymmetry of Equatorial Ionization Anomaly (EIA) during solstices (Figure 4). During the June solstice, the stronger EIA peak transits from the winter to the summer hemisphere earlier in the sectors where the geomagnetic equator is further away from the subsolar point

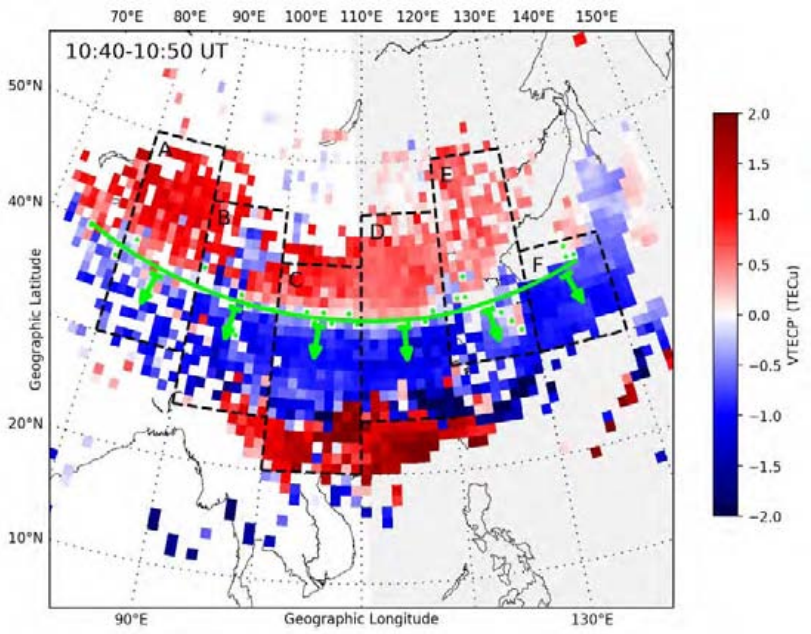

Fig. 3 Map of TEC disturbances during 10:40 UT–10:50 UT on 17 March 2015[11]

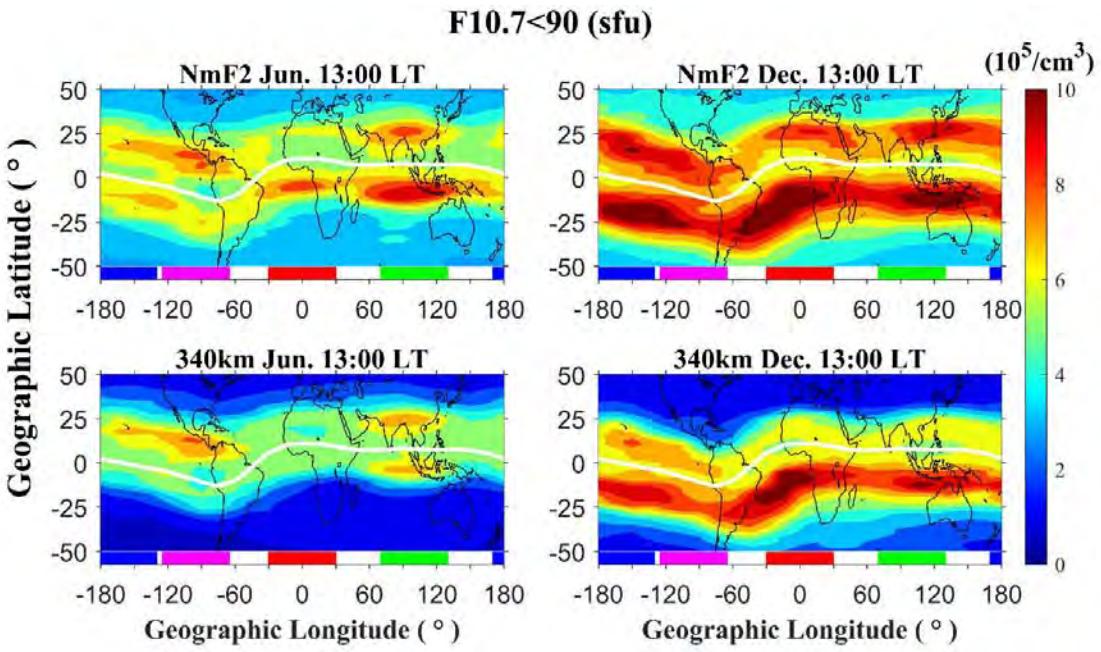

Fig. 4 Electron density maps at h_mF_2 and 340 km at 13:00 LT during the June solstice (a) and December solstice (b) for $F_{10.7}$<90 sfu. The white line stands for the geomagnetic dip equator[13]

and the geomagnetic field declination is larger, while during the December solstice the longitudinal variations generally show the opposite compared with that in the June solstice. The distance between the geomagnetic equator and subsolar point and the geomagnetic field configuration control the upward/downward plasma movements in the summer/winter hemisphere, leading to the different transition times in different longitudinal sectors. For both solstices, transition times emerge earlier as height increases, which is mainly caused by the larger effective scale height in the summer hemisphere than in the winter hemisphere, resulting in a smaller electron density difference at higher altitudes with a fast transition.

Mo *et al.*[14] studied the features of EIA crests by using the ionospheric TEC data observed at Nanning (22.84°N, 108.33°E) from 2006 to 2015. Both the value of TEC and the location of the northern EIA crest have positive solar activity dependence and show a semi-annual variation, larger in equinoctial months than in solstitial months. Their local time, seasonal and solar cycle variations are consistent with that of the strength of Equatorial Electrojet (EEJ) (Figure 5). Particularly, the EEJ strength has

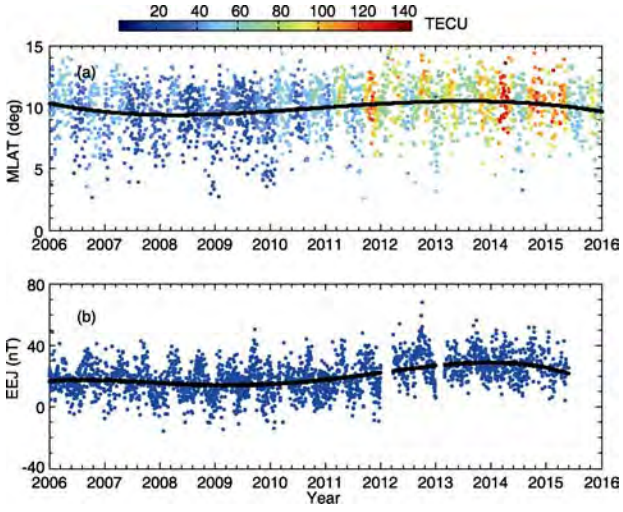

Fig. 5 Day-to-day variations of the location of the northern EIA crest and the strength of EEJ from 2006 to 2015[14]

a stronger correlation with the EIA crest location than with the TEC value of the EIA crest.

Tian *et al.*[15] studied the asymmetric EIA structure, especially a single peak in the latitudinal structure of electron density. The single crest phenomenon occurs frequently at longitudes where the double crests structure is weak. The longitudinal

dependence is clearly observed at 10:00 LT–18:00 LT, with zonal wavenumber 4 around equinox and 3 around winter solstice. This leads to the conclusion that, the single crest phenomenon can be an indicator of the diurnal eastward wave number 2 DE2 and wave number 3 DE3 components of nonmigrating tides, which modulate the wind field and thus the atmospheric dynamo electric field to cause the single or double crest structure.

Li *et al.*[16] presented a comprehensive picture of the longitudinal variation of mid-latitude (40°–50° mag. lat.) ionosphere under magnetically quiet and low solar activity by using 2006–2011 COSMIC electron density (N_e) profiles. The zonal difference of N_e mainly exists above 220 km, caused by combined effects of vertical drift driven by zonal and meridional winds. The longitudinal difference of vertical drift driven by zonal winds mainly caused by the zonal difference of the magnetic declination. The longitudinal difference of vertical drift driven by meridional winds mainly caused by the zonal difference of the wind itself.

Scale height is a key parameter to measure the electron density profile and the ionospheric chemistry and dynamics. The longitudinal variation of scale height has not been investigated in both analyses and empirical modeling. Li *et al.*[17] collected the 11-year electron density profiles from COSMIC radio occultations to retrieve the α -Chapman scale height from the lower topside ionospheric electron density profile. The midlatitude α -Chapman scale height shows evident longitudinal variations and its zonal structure shows consistency with that of h_mF_2 during daytime. They built an empirical model of the scale height, which well captures the key temporal-spatial variations of the scale height.

Solar Rotation (SR) variation dominates solar Extremely Ultraviolet (EUV) changes and significantly affects ionospheric variability on the timescale of days. The $F_{10.7}$ index is usually used as an indicator for solar EUV. $F_{10.7}$ significantly enhanced during the 2008 to 2009 Carrington Rotations (CRs) owing to a very intense active region, causing the most prominent SR variation of F10.7 during solar cycle 23 (Figure 6). Chen *et al.*[18] found that the responses of $F_{10.7}$ and EUV to that intense active region are very discrepant. $F_{10.7}$ response was much stronger than EUV response so that the EUV–$F_{10.7}$ slope significantly decreases during the 2008th–2009th CRs. That results in large errors when estimating EUV and ionospheric electron density using $F_{10.7}$. And they also found that the time lag of EUV to $F_{10.7}$ exaggerates ionospheric time lag effect to EUV when using $F_{10.7}$. Moreover, they further presented that EUV–$F_{10.7}$ slope statistically tends to decrease when the SR variation of $F_{10.7}$ significantly enhances.

The ionosphere closely couples with the overlying plasmasphere at both sides of magnetic flux tubes. It is difficult to confirm interhemispheric coupling between the northern and southern mid-latitude ionosphere through the plasmasphere directly from observations. A possible result induced by this coupling is interhemispheric conjugacy of the mid-latitude ionosphere (Figure 7). Chen *et al.*[19]

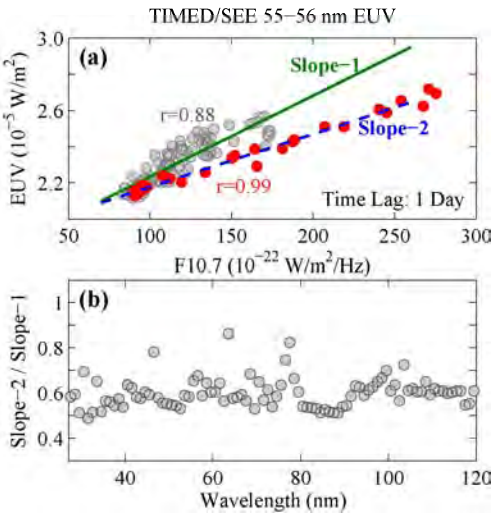

Fig. 6 (a) Scatter plots of 55~56 nm EUV flux versus $F_{10.7}$. Red dots are the measurements during the 2008 to 2009 CRs and gray dots present the measurements during adjacent CRs for reference; the 1-day time lag effect of EUV to $F_{10.7}$ has been considered. Green solid line and blue dashed line are the linear fittings for the grey dots and the red dots (Slope-1 and Slope-2 indicate their slopes), respectively; the parameter r is the correlation coefficient between EUV and $F_{10.7}$. (b) The ratios of Slope-2 to Slope-1 for different wavelengths (after Chen *et al.*[18])

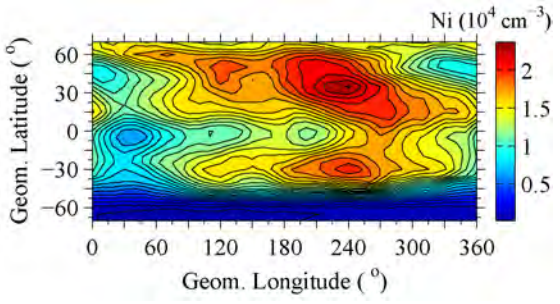

Fig. 7 Geomagnetic longitude and latitude variations of the ion density at 840 km measured by the DMSP F12 satellite at nightside 21:30 LT around the June solstice of 1996 (after Chen *et al.*[19])

reported interhemispheric conjugate effect in longitude variations of mid-latitude ion density (N_i) using the Defense Meteorological Satellite Program (DMSP) measurements; northern and southern N_i longitude variations at dusk side are similar between magnetically conjugate mid-latitudes around solar minimum June Solstice. The conjugate effect occurs only inside the plasmapause where magnetic flux tubes are closed and the plasma in these tubes can stably corotate with the Earth. Neutral wind induced ionospheric transport causes topside longitude variations *via* upward diffusion at summer mid-latitudes; this further induces similar longitude variations of topside ion density N_i at winter mid-latitudes via the summer to winter interhemispheric coupling. The conjugate effect not only proves mid-latitude interhemispheric coupling through the plasmasphere, but also implies that neutral wind induced transport can affect ionospheric coupling to the plasmasphere at mid-latitudes.

Li *et al.*[20] identified the enhancements in nighttime ionization in the midlatitude ionosphere by using in situ electron density measurements from the Challenging Challenging Minisatellite Payload (CHAMP) and the DMSP satellites. The enhancements are found to be potentially connected to the plasmasphere with the magnetic flux tubes of L= 1.3~2.4. It implies that the nighttime ionization enhancements are possibly formed under the coupling between the plasmasphere and the midlatitude ionosphere through a downward plasma influx.

Global Navigation Satellite Systems (GNSS) and COSMIC radio occultation observations are widely used in ionospheric monitoring. Zhong *et al.*[21] revealed that the nighttime N_e at about ±40° geomagnetic latitudes is generally greater, especially in the topside ionosphere, during the solstices, at later local times at night and under lower solar activity, as referring to the middle-latitudinal bands (Figure 8). At this bands, the downward plasma diffusion from the plasmasphere provides stable plasma source to

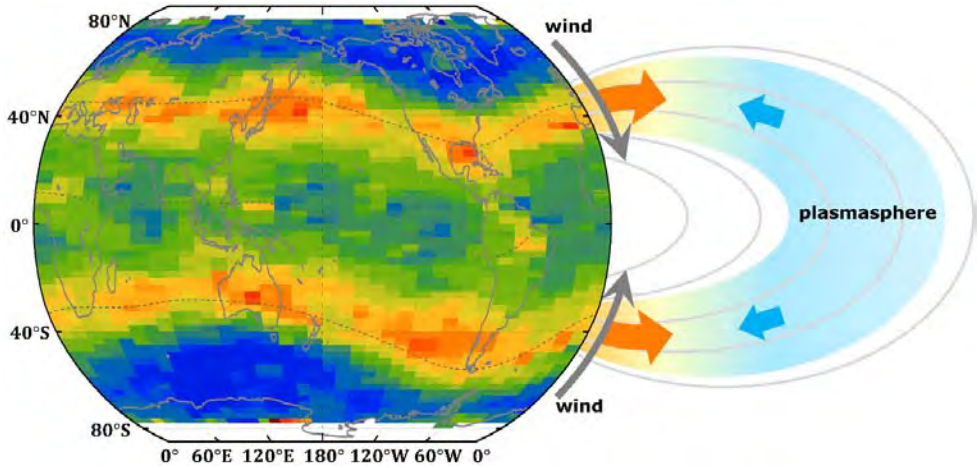

Fig. 8 New discovery of the middle-latitudinal band structure in the nighttime topside ionosphere. The middle-latitudinal band structure at around ±40° geomagnetic latitudes is clearly shown in the electron densities at 800 km and 03:00 LT, which can be caused by the plasma maintenance associated with equatorward neutral winds and downward ambipolar diffusion from the plasmasphere (after Zhong *et al.*[21])

the topside ionosphere, while the upward plasma motion due to the neutral winds is the primary source for the F_2 peak region.

Li *et al.*[22] revealed the longitudinal variation characteristics of the ionospheric F_1 layer occurrence at middle- and high-latitudes in the daytime summer under low solar activity conditions using the COSMIC observations. Combined with the TIMED/GUVI observations and TIEGCM simulations, the results show that the higher F_1 layer occurrence can be significantly affected by longitudinal variations of the $[O]/[N_2]$ ratios. The low $[O]/[N_2]$ ratios deplete the ionospheric electron density above the F_1 layer at middle and high latitudes and thus make the F_1 layer stand out.

The state of topside ionosphere has attracted more and more attention. Zhong *et al.*[23] used the topside TECs observed by the MetOp-A and TerraSAR-X satellites for multiple local times to develop global topside ionospheric and plasmaspheric TEC models, based on Empirical Orthogonal Function (EOF) analysis. The first five EOFs, which can account for more than 98.8% of the total variance, are applied in model construction. The comparisons indicate that the EOF TEC models can well reproduce the observations, including TEC magnitudes and longitudinal variations.

Yang *et al.*[24] statistically analyzed the mid-latitude trough position in the Northern and Southern hemispheres based on the ion density data from the Defense Meteorological Satellite Program (DMSP) satellites in 1996–2016. The longitudinal variation of the trough position has a significant season, solar activity, and geomagnetic activity dependences. There are significant differences in the longitudinal variation of the trough position between the Northern and Southern Hemispheres.

Yang *et al.*[25] investigated the features of the high latitude trough in the Southern Hemisphere based on the electron density, Field-Aligned Currents (FACs), and ion drift velocity data from the Swarm-A satellite during 2013–2018. In the Southern Hemisphere, the high latitude trough is a persistent post-midnight feature in winter, observed mainly in the eastern longitudes. There is a longitude dependence of features of FACs and ion drift velocity distribution in the high latitude trough region.

Zhang *et al.*[26] reported in situ observations from a partial crossing of a reconnection layer near the subsolar magnetopause. During this crossing, step-like accelerating processes of the cold ions were clearly observed, suggesting that the inflow cold ions may be separately accelerated by the rotation discontinuity and slow shock inside the reconnection layer (Figure 9). Cold ions of plasmaspheric origin have been observed to abundantly appear in the magnetospheric side of the Earth's magnetopause. These cold ions could affect the magnetic reconnection processes at the magnetopause by changing the Alfvén velocity and the reconnection rate, while they could also be heated in the reconnection layer during the ongoing reconnections.

Ding *et al.*[27] presented some examples of the Qujing Incoherent Scatter Radar (QJISR). The spectra shape changes from a single hump to double humps with increasing of altitude. They showed the diurnal variations of ionospheric electron density, electron temperature, and ion temperature. The electron temperature at 200 km varies slowly during daytime and decreases quickly at sunset. The electron temperature near the peak height of F_2 layer shows two peaks near sunrise and sunset. The ion temperature has no obvious diurnal characteristics.

Ding *et al.*[28] further investigated the electron temperature (T_e) of ionospheric F layer by using the Qujing Incoherent Scatter Radar (QJISR) measurements in 2017 and 2018. T_e increases from about 150 km, reaches the maximum at about 220 km, then decreases and reaches the minimum at 300~350 km. T_e above the F_2 peak height has the morning and sunset enhancements with the maximum value of about 3000 K. The sunset rise of T_e occurs earlier at higher altitudes. T_e and electron density (N_e) have a positive correlation below 200 km and a negative relationship between 200 and 450 km.

Yang *et al.*[29] investigated two cases of F_2-lacuna and their simultaneous ionospheric convection and TEC variations at Zhongshan Station (69.4°S, 76.4°E,

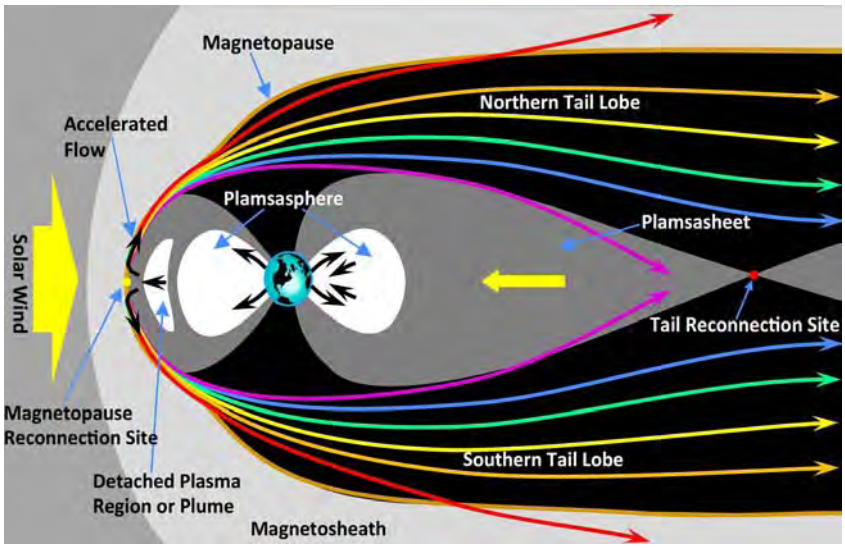

Fig. 9 Schematics of ionospheric ion outflow. The brown line is the outer boundary of the magnetosphere, the magnetopause, inside which are three distinct regions: the tail lobes (black) contain "open" magnetic field lines that thread the magnetopause which are generated in the Dungey cycle during periods of southward IMF by magnetic reconnection at the dayside magnetopause (at the yellow dot) and re-closed by reconnection in the tail (at the red dot). The plasma sheet (dark grey) contains closed field lines which connect the ionospheres in the two hemispheres and never thread the magnetopause. Closed field lines convect sunward in the Dungey cycle. The plasmasphere (in white) is also on closed field lines and has higher plasma densities than the plasma sheet because magnetic flux tube volumes are smaller and can be filled by outflows from the ionosphere. The colored lines show trajectories for ions of plasmaspheric origin from reconnection acceleration region. Note that all ions are moving along the magnetic field lines but trajectories are not field-aligned because the field lines move as part of the Dungey convection cycle. Higher energy ion trajectories (red arrows) are closer to field-aligned than lower energy ones (in mauve) because they have higher field parallel velocity (after Zhang *et al.*[26]).

corrected geomagnetic latitude 74.5°S). The two cases of F_2-lacuna are accompanied by a decrease of electron density and an increase in plasma flow. They proposed that the strengthened electric field brings Joule heating and frictional heating, which enhances the electron and ion temperature. Subsequently, the enhancement of the recombination rate and the O^+ upflow results in the decrease of O^+ density in F_2 region.

Zhang *et al.*[30] investigated the longitudinal patterns of middle and low latitude zonal thermospheric winds from CHAMP observations and TIEGCM modeling. Their results show that there are large longitudinal variations in zonal thermospheric winds, having no significant solar activity dependence. The geomagnetic configuration is the main agent of the longitudinal changes in the zonal wind. Further, the zonal wind shows great hemispheric asymmetry, local time, and seasonal variations.

3 Ionospheric Dynamics and Couplings

The dense oblique-incidence ionosonde network in North China makes it possible to monitor the ionospheric regional variations with a high spatial resolution. Chen *et al.*[31] used the network to investigate the ionospheric nighttime oscillations in January and February 2011. Opposite latitudinal dependencies are present in the premidnight and postmidnight enhancements in electron density. The premidnight enhancements appeared earlier at higher latitudes and then moved to lower latitudes, as a part of the Large-Scale Travelling Ionospheric Disturbance (LSTID) being produced by gravity waves. The LSTIDs is considered to form the positive latitudinal dependence of the wave peaks and troughs. The postmidnight oscillation was present with a peak and

a trough. The most likely agent is the westward electric field-induced $E\times B$ drift, which pushed the F layer to lower altitudes.

The solar eclipse provides a great opportunity to explore the basic physics of the Ionosphere-Thermosphere (I-T) system. Dang *et al.*[32] and Lei *et al.*[33] investigated the global dynamic and electrodynamic responses of the ionosphere and thermosphere to the 2017 solar eclipse, using a high-resolution global coupled ionosphere-thermosphere-electrodynamics model. They found that the I-T response to the eclipse is global and long-lasting, not local as previously expected. The ionosphere and thermosphere showed significant global changes (Figure 10), even after the eclipse had been over for more than a half-day. Furthermore, an evident suppression of the TOI was reported by Dang *et al.*[34] when the eclipse occurs in the afternoon sector at middle latitudes, due to the electron density reduction in the middle latitude source region.

Sun *et al.*[35] analyzed the massive Total Electron Content (TEC) observations from 2255 ground-based Global Navigation Satellite System (GNSS) receivers on the Continent of United States (CONUS) during the total solar eclipse on 21 August 2017. The results show that the moon shadow (about 80% obscuration) generates a great ionospheric bow wave (period< 10 min) which extends about 1500 km away from the totality path. The bow wave consists of the acoustic shock wave due to the supersonic/near-supersonic moon shadow ship and the significant plasma recombination due to the reduction in solar irradiation within the shadow area. The bow-wave crest in front of the totality is most intense as the moon shadow over the northwest coast of the CONUS where the shadow is supersonic (about 1000 $m\cdot s^{-1}$). The crest decreases by 80% when the boat velocity reduces to sound speed (about 650 $m\cdot s^{-1}$) on the eastern coast.

Since the greenhouse gas was proposed to have effects on the ionosphere, huge efforts have been implemented on ionospheric climate study. Recently, the Wuhan ionosonde observations were digitized and standardized through a unified method back to 1947. Yue *et al.*[36] used the Artificial Neural Network

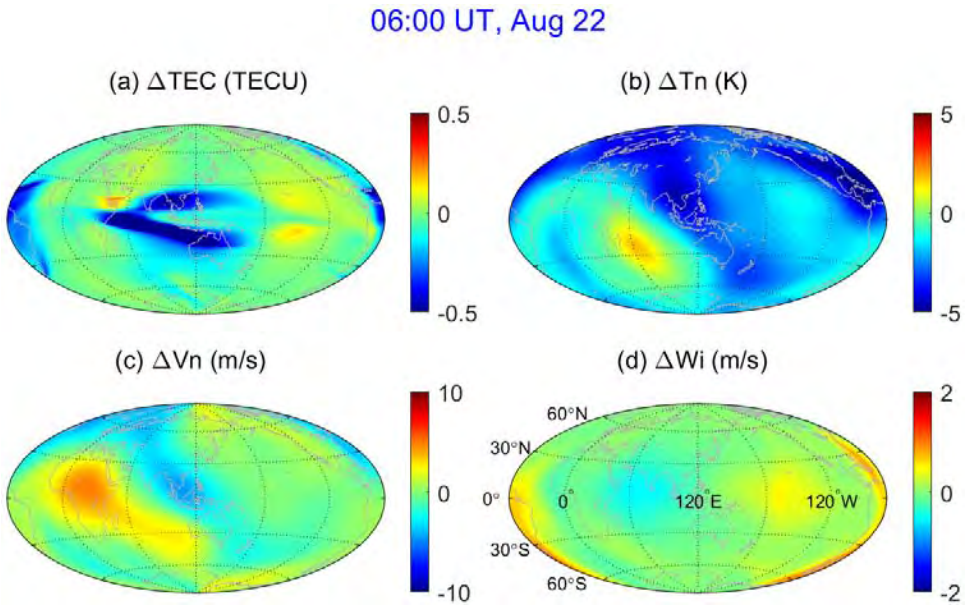

Fig. 10 Global maps of differential TEC, neutral temperature, meridional winds (northward positive), and $E\times B$ vertical plasma drifts (upward positive) at pressure level 2 (about 300 km) between the model simulations with and without eclipseat 06:00 UT on 22 August 2017, 9 h after the final contact of an eclipse. The solar eclipse is a transient local event, but its impact on the ionosphere and thermosphere can persist for a long time over the entire globe, rather than just being an impulse event with a localized response as was previously expected (after Lei *et al.*[33])

(ANN) to analyze the long term trend of Wuhan by applying these data and found a mean f_0F_2 and h_mF_2 trend –0.0021 MHz per year and –0.106 km per year, respectively. They further used the NCAR-TIEGCM driven by Mauna Loa Observatory observed CO_2 level and International Geomagnetic Reference Field (IGRF) geomagnetic field to simulate their effects on ionospheric long-term trend over Wuhan. Simulation results show that the CO_2 and geomagnetic field have a comparable effect on h_mF_2 trend, while geomagnetic field effect is stronger than CO_2 on f_0F_2 trend over Wuhan. Both factors result in obvious but different diurnal variations of f_0F_2/h_mF_2 long-term trends. The geomagnetic field effect is nonlinear versus years since the long-term variation of geomagnetic field intensity and orientation is complex. Regarding the diurnal variation of the trend, the simulation accords well with that of observation except for N_mF_2 results around 12:00 UT. Overall, good agreement between observation and simulation illustrates the good quality of Wuhan ionosonde long-term data. Furthermore, little attention has been paid to the topside ionosphere. Cai *et al.*[37] used the series Defense Meteorological Satellite Program (DMSP) satellites since 1987 to derive the long - term trend of the topside ionosphere for the first time. The electron density (N_e) trend in the middle and low latitudes at about 860 km around 18 MLT was derived using the ANN method from 1995–2017. The trend from DMSP observations has a mean magnitude ranging from about –2% to about 2% per decade, with clear seasonal, latitude, and longitude variations. The derived trend was evaluated by directly comparing with the simulated trend at 500 km from the NCAR-TIEGCM driven by realistic changes of CO_2 level and geomagnetic field. The observed and simulated trends have similar geographic distribution patterns at 18 MLT. The good agreement between the observed trend around 860 km and the simulated trend near 500 km implies that the physical processes controlling the N_e trends above the peak height might be identical. Further control simulations show that the geomagnetic field secular variation is the dominant factor of the electron density trend at around 500 km, rather than the CO_2 long-term enhancement.

Chen *et al.*[38] developed a new method to interpret the atmospheric contribution to the ionospheric Wave Number-4 (WN4) structure according to their coherences in annual variations based on IGS TEC and TIMED wind data. They confirmed former suggestions that symmetric zonal DE3 is the primary source for ionospheric WN4, and the contributions due to antisymmetric wind components are relatively small in TEC WN4.

Mo and Zhang[39] investigated the longitudinal dependence of periodic meridional movement of EIA crest during sudden stratospheric warming events in 2003, 2006, and 2009 by using the GPS TEC observations in China and Brazilian sectors. There are in-phase 14-day to 15-day periodic oscillations of the locations of EIA crests in the two sectors, coinciding with half of the lunar revolution period (29.53 days) and the lunar phase. Its temporal feature is consistent with that of stratospheric zonal wind.

Liu *et al.*[40] further studied the longitudinal differences of the low-latitudinal TEC responses in the winters between the East Asian and American sectors. The analysis suggests that the M2 effects on the low-latitudinal ionosphere during SSWs are likely to be more prominent in the American sector than in the East Asian sector. These differences probably result from a combined effect of the longitudinal variety in atmospheric (especially tidal) and electrodynamic processes.

The physical mechanism of the ionospheric electric field has not been well understood. CHE-Nand Lei[41] found that the altitudinal and latitudinal variations of zonal electric fields are associated with the latitudinal variations of meridional winds, the longitudinal gradients of zonal winds, and global nature of dynamo process. Moreover, when neutral winds affect electric fields by wind dynamo, the $E\times B$ drifts caused by electric fields can drag thermospheric winds as well. The interaction of electric fields and neutral winds will result in the relationship between field-aligned and field-perpendicular plasma velocities in the ionospheric F region[41].

The polar ionosphere/thermosphere system di-

rectly connects the solar wind/magnetosphere and lower atmosphere, and is a crucial part of space weather. Based on the high-resolution Thermosphere Ionosphere Electrodynamics General Circulation Model (TIEGCM) simulations as well as DMSP satellite observations, Dang *et al.*[42] have reported the occurrence of double Tongues of Ionization (TOIs) (Figure 11) and carried out a comprehensive study on the dynamic evolution and formation mechanism of double TOIs. Predicting the cusp electron precipitation is important in investigating the dayside solar wind-magnetosphere-ionosphere coupling process and in forecasting space weather phenomena. Dang *et al.*[43] used the global MHD simulation to investigate the correlation between the fluxes of precipitating electrons in the cusp and the upstream solar wind conditions. The statistical results indicated that both hemispheric precipitation rate and hemispheric power of precipitating soft electrons closely correlated with the solar wind dynamic pressure.

Wu *et al.*[44] analyzed the Universal Time (UT) variations of the polar ionosphere (Figure 12) in terms of the mean polar electron content based on COSMIC observations. It is found that the UT variation has a stronger intensity in the Antarctic than in the Arctic, and their phases have a difference

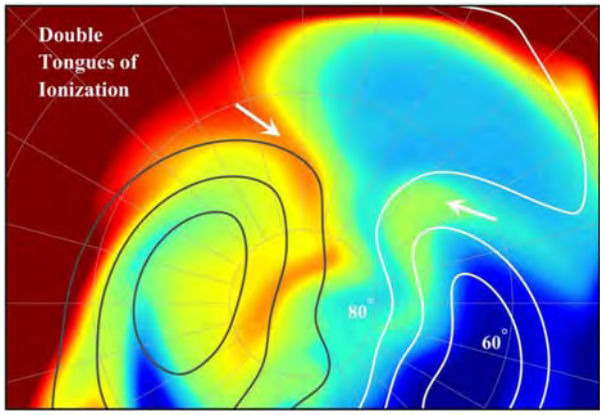

Fig. 11 Polar map of the simulated electron densities as a function of local time and geographic latitude at 10:00 UT during 17 March 2013 geomagnetic storm. The results clearly show that two TOIs existed within dawn and dusk convection cells (after Dang *et al.*[42])

of 12 h. The main driver of the UT variation of polar ionosphere is the varying convection pattern in geographic coordinates.

Guo *et al.*[45] simulated the isolated density cell in the high-latitude thermosphere by the Global Ionosphere-Thermosphere Model (GITM). They suggested that the downward wind and ion drag-driven force should lead to the density depletion or low density cell. Further, Weng *et al.*[46] invested the

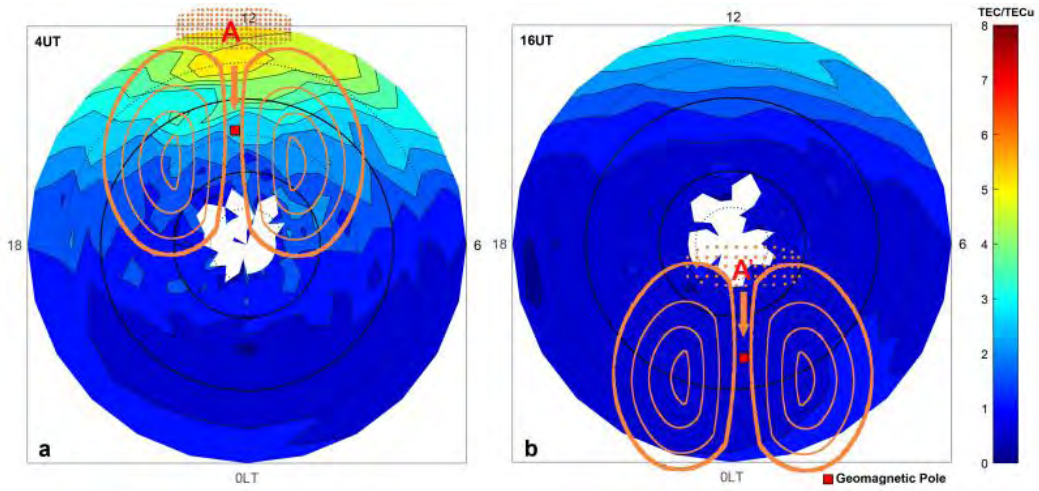

Fig. 12 TEC maps at (a) 04:00 UT and (b) 16:00 UT in winter in the Antarctic in geographic coordinates. The red square gives the location of the magnetic pole in the southern hemisphere. The orange circles and the dots are schematic diagrams, standing for the convection electric fields and the electron densities, respectively (after Wu *et al.*[44])

climatological view of density cell structures at high latitudes in the lower thermosphere, using neutral mass density at 270 km derived from GOCE (Gravity Field and Steady-State Ocean Circulation Explorer) satellite. They found that the density cell structures in the lower thermosphere tend to occur in the local summer and the northern hemisphere, and the local time distributions, horizontal scales, and relative magnitudes depend on the type of the density cell structure. Weng *et al.*[47] further discussed the seasonal variations of lower thermospheric density by using GOCE satellite data and the Empirical Orthogonal Function method. They found that the seasonal density variations show obvious hemispheric asymmetry, with large amplitudes in the southern hemisphere, and the annual asymmetry and effect of the Sun-Earth distance vary with latitude and solar activity.

The thermospheric temperature is an important parameter for both physics understanding and space weather prediction. Ruan *et al.*[48] revealed and quantified the potential impact of satellite sampling on dynamical modeling of thermosphere. They found a significant reduction of the relative deviation via blending one more satellite. Based on observations and numerical simulations, RUAN and Lei[49] developed an empirical temperature model via data-driving technology, for a purpose of dynamical correction in thermospheric determination. Ren *et al.*[50] investigated the thermospheric responses to the 27-day variation of solar EUV flux. They found that the 1-day peak response time of the thermospheric temperature to the periodicity of solar EUV flux corresponds to the balance between the heating and cooling processes, and the circulation modulates this delay.

Owolabi *et al.*[51] studied the driving forces of the EEJ current, tidal variability in EEJ current, Counter equatorial Electrojet (CEJ) current, and ionospheric electric current system during two major SSW events (2006 and 2009) at three different longitude sectors. They found that the tidal components are responsible for modulating ionospheric currents during SSW events. The tidal component in EEJ strength is associated with significant reduction and enhancement in EEJ strength during SSW event.

The enhancement in EEJ could modulate directly the variations of the ionosphere. Liu *et al.*[52] analyzed the characteristics of the TEC (Figure 13) recorded at middle- and low-latitude stations over the Chinese sector during the 2018 SSW event. The deviation of TEC from its mean exhibits strong semi-diurnal and diurnal oscillations, and the EEJ shows a significant correlation with peak TEC in the low latitude region, illustrating the energy transmission and coupling between the lower atmosphere and the ionosphere.

Sun[53] summarized the recent studies of the effect of solar (geomagnetic storm and total solar eclipse), tropospheric (typhoon, walker circulation, and El Niño-Southern Oscillation), and earthquake/tsunami activities on the ionosphere utilizing the global ground- and space-based GNSS observations. Both solar activities from above and perturbations of Earth's surface and troposphere from below disturb ionospheric structure and its dynamics. Numerous ionospheric phenomena remain unexplained due to the complicated nature of the solar-terrestrial environment. The ground- and space-based Global Navigation Satellite System (GNSS) techniques being around and providing global observations with high resolutions will help us to resolve unexplained phenomena.

To better understand the ionospheric morphology response to the possible lithospheric activities, Sun *et al.*[54] examined the global location preference of the positive and negative TEC anomalies persisting continuously longer than 24 h at middle and low latitudes (within $\pm 60^{\circ}$N geomagnetic latitudes). There are a few (less than 4%) TEC anomalies that can persist over 24 h. The conjugate phenomenon of the TEC persistence is the most significant in eastern Asia to Australia longitudinal sector. Their result shows the persistence of the positive TEC anomaly along the ring of fire on the western edge of the Pacific Ocean. The high persistence of the TEC anomalies at midlatitudes suggests that thermospheric neutral wind contributes to the anomaly formation.

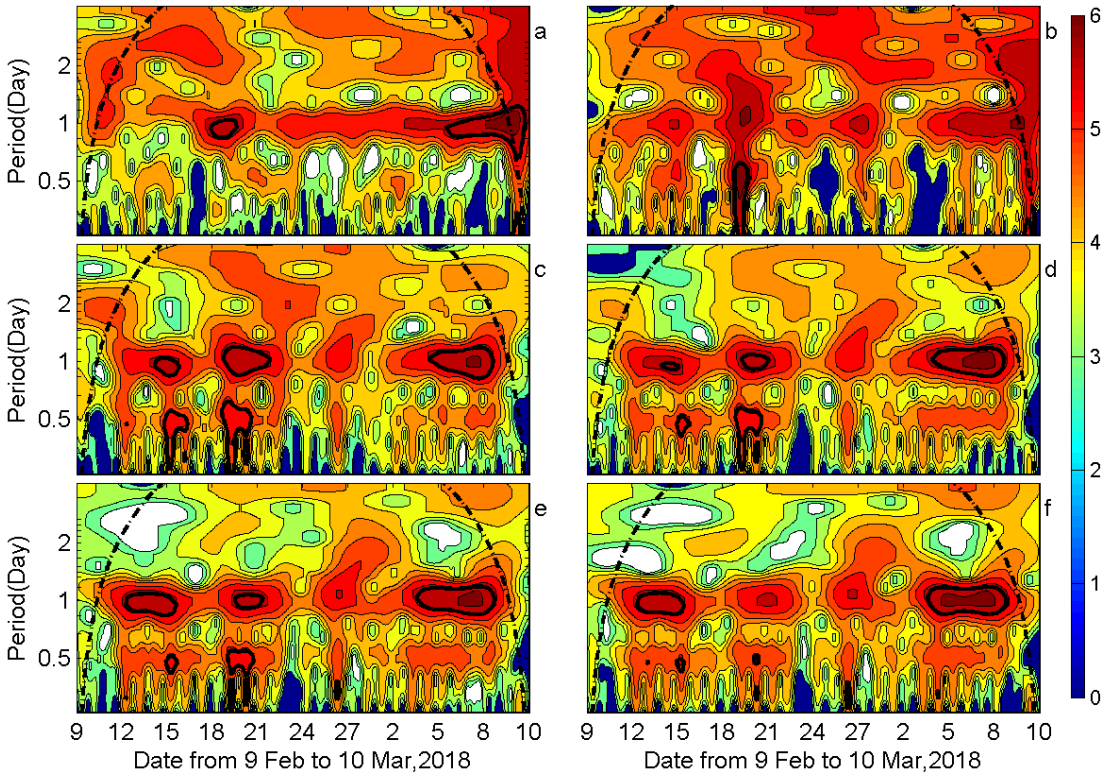

Fig. 13 Continuous wavelet power spectra of the deviation of TEC from its mean for (a) Mohe, (b) Beijing, (c) Xiamen, (d) Guangzhou, (e) Nanning, and (f) Kunming. The solid black curves designate the 5% significant level. The dashed lines are the cone of influence[52]

Sun *et al.*[55] examined the influence of the El Niño-Southern Oscillation (ENSO) on the ionospheric TEC DE3 (Diurnal Eastward wavenumber 3) and SPW4 (Stationary Planetary Wavenumber 4) which are the major components of the ionospheric wave-4 longitudinal structure. The TEC is the integration of electron density from 200 km to 800 km sounded by the GPS Radio Occultation (RO) experiment onboard the FORMOSAT-3/COSMIC satellites during the period of January 2007 to December 2015. Their results show that the TEC DE3 and SPW4 amplitudes respond to the ENSO signature in the thermospheric wind DE3 in the Northern Hemisphere during the lower solar activity period. The 2010/2011 strong ENSO cold phase significantly enhances the TEC DE3 and SPW4 amplitudes with periods from 1 year to quasi-biennial periodicity at low latitude of the Northern Hemisphere. The QBO crests of the TEC DE3/SPW4 and the wind DE3 at lower thermosphere are almost in phase during the 2010/2011 ENSO cold phase.

Sun *et al.*[56] studied the El Niño - Southern Oscillation (ENSO) signals in the two dominant temperature diurnal tides, DW1 (Diurnal Westward wavenumber 1) and DE3 (Diurnal Eastward wavenumber 3) on the Quasi-Biennial Oscillation (QBO) scale (18 to 34 months) from 50 km to 100 km altitudes. The tides are derived from the 21-year (January 1996 to February 2017) GAIA (Ground-to-topside model of Atmosphere and Ionosphere for Aeronomy) temperature simulations and 15-year (February 2002 to February 2017) TIMED (Thermosphere Ionosphere Mesosphere Energetics and Dynamics)/SABER (Sounding of the Atmosphere using Broadband Emission Radiometry) temperature observations. The GAIA simulations and SABER observations show that the ENSO controls the QBO in the stratosphere, mesosphere, and lower thermosphere. ENSO warm phases shorten the period (about 2 years) of the QBO in DW1 amplitude near

the equator and DE3 amplitude at low latitudes of the Northern Hemisphere. In contrast, the QBO period lengthens (about 2.5 years) during the ENSO neutral and cold phases. Correlation analysis revealed that the ENSO effect on the tidal QBO can last more than one year in the mesosphere and lower thermosphere.

Wang *et al.*[57] investigated the temporal and spatial variations of thermospheric neutral winds at 400 km altitude under the influence of Subauroral Polarization Streams (SAPS) based on the simulations of the Global Ionosphere and Thermosphere Model (GITM). During SAPS periods under southward IMF conditions, the westward neutral winds are greatly strengthened at dusk at subauroral latitudes. The strongest westward neutral winds exhibit large variations in amplitudes when SAPS commence at different universal times.

Wang *et al.*[58] investigated how the Counter Equatorial Electrojet (CEJ) depends on the Interplanetary Magnetic Field (IMF) conditions by using 10 years of CHAMP observations. The longitudinal distribution of the Equatorial Electrojet (EEJ) is closely modulated by the solar zenith angle. The correlation between the EEJ intensity and the square root of the average value of $\cos(\theta_{\mathrm{SZA}})$ during CEJ events becomes stronger around June solstice (Here θ_{SZA} represents the mathematical symbol of solar zenith angle). Compared to the normal conditions, the occurrence of CEJ has doubled during subauroral polarization stream periods.

The Radio Occultation (RO) technique is a useful tool for detecting the atmospheric waves induced by earthquake/tsunami. Yan *et al.*[59] examined the FORMOSAT-3/COSMIC RO soundings of TEC in the ionosphere (from 150 to 550 km) and refractivity index in the lower atmosphere (from 0 to 60 km) after/during the 2011 Mw9.0 Tohoku earthquake/tsunami. Their results showed that the atmospheric oscillations with vertical wavelength ranging from 0.5 to 8 km and 10 to 40 km, respectively, appear in the stratosphere and ionosphere after the earthquake onset. These atmospheric oscillations were also identified after the 2008 Mw7.9 Wenchuan earthquake. The interesting point is that these atmospheric oscillations can also excite secondary oscillations in the solid Earth as examined by ground seismic data[60].

Liu *et al.*[61] investigated the effects of Underground Nuclear Explosion (UNE) on the ionosphere in the nuclear test of North Korea in 2017 by using IGS stations and Swarm satellites. Geomagnetic conjugate ionospheric TEC disturbances were simultaneously observed during the nuclear test. Their results proposed that the UNE-generated ionospheric TEC disturbances are results of electrodynamic process caused by LAIC (Lithosphere-Atmosphere-Ionosphere Coupling) electric field or electric current penetration.

4 Ionospheric Irregularity and Scintillation

The polar region opens a natural window to space. There are various irregularities including patches in the polar ionosphere. The plasma patches are usually linking to the ion upflow. The applications of Global Navigation Satellite System (GNSS) are often degraded during the formation and evolution of the multiple-scale plasma irregularities, especially combined with simultaneous particle precipitation. Jin *et al.*[62] performed a statistical analysis of 345 dayside patches observed by the EISCAT Svalbard Radar from 2010 to 2013. The polar cap patches are preferentially formed under southward IMF conditions. There is a clear IMF By-related asymmetry in their Magnetic Local Time (MLT) dependence. The pulsed dayside magnetic reconnection is proposed to possibly be a significant formation mechanism of polar cap patches.

Xing *et al.*[63] reported a case of conjugate polar cap arcs on 5 February 2006 (Figure 14) observed by the ground-based all-sky imager at Yellow River Station (Svalbard) and by the space-based DMSP/SSUSI and TIMED/GUVI instruments. The movement of the polar cap arc shows a clear dependence on the Interplanetary Magnetic Field (IMF) By

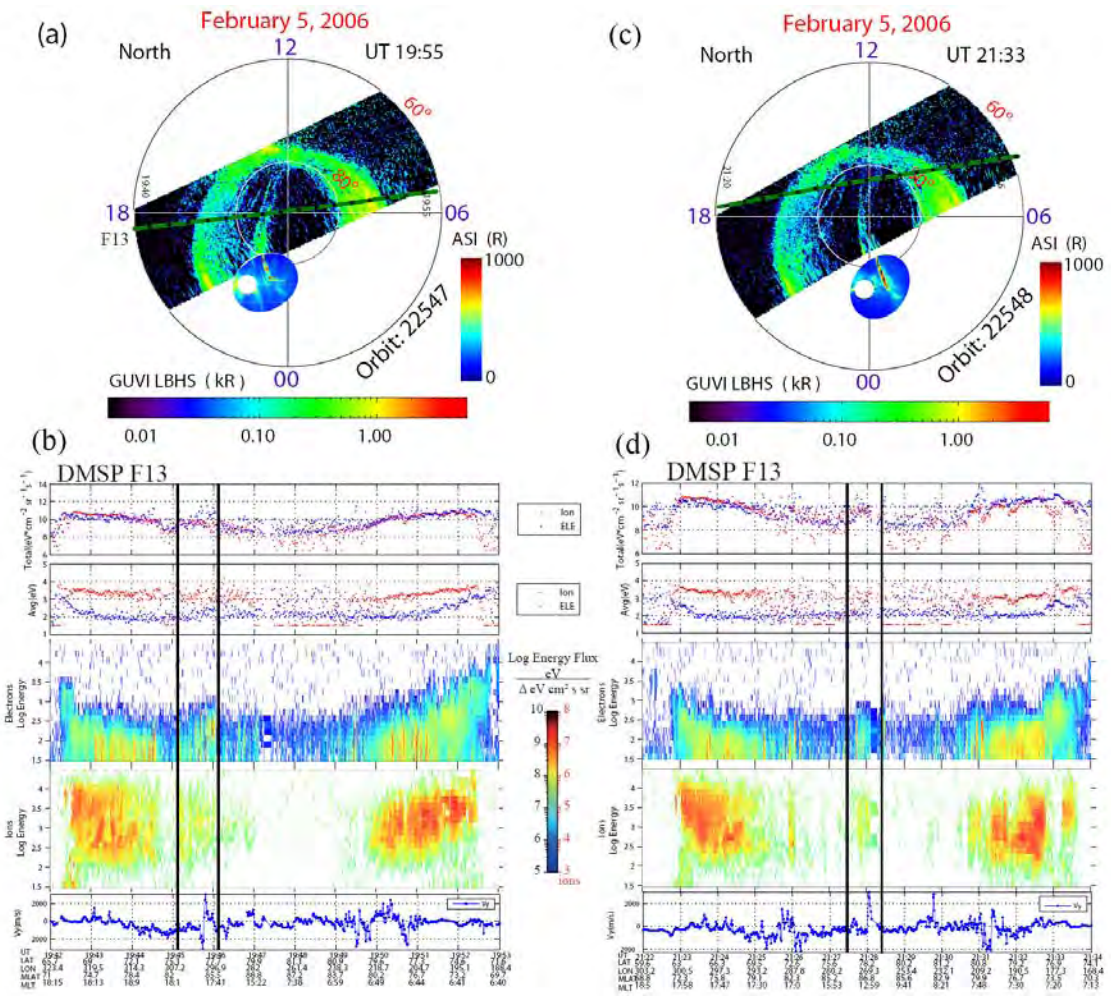

Fig. 14 (a) and (c) TIMED/GUVI data superimposed on the 557.7 nm ASI data at 19:55 UT and 21:33 UT and the overpass of DMSP F13 crossed the PCA superimposed on the image shown in MLAT/MLT coordinates. The white spots dusk side of the PCA on the ASI image are used to cover the moonlight. (b) and (d) Data from a DMSP F13 pass during the interval from 19:39 UT to 19:56 UT and 21:00 UT to 21:37 UT. The spectrogram includes (top to bottom) integral energy flux, average energy, spectra of precipitating electron and ion, and velocity of cross-track horizontal plasma drift. The vertical black lines mark the times when DMSP F13 passed over the PCA[63]

component, moving from dusk to dawn in the northern hemisphere and vice versa in the southern hemisphere. Strong flow shears are observed around the polar cap arc in both hemispheres. It is reasonably expected that the topological changes in the magnetotail can produce a strip of closed field lines. Local processes would set up conditions for the formation and evolution of polar cap arcs.

Wang *et al.*[64] presented a clear and strong dependence of the phase scintillation index derived using GPS measurements on the ionospheric plasma flow measured by the SuperDARN radars around the noon sector of the polar ionosphere. The phase scintillation index shows a strong linear dependence on the plasma drift speed, whereas the amplitude scintillation index does not have such dependence, implying the phase scintillation index is much more sensitive to the plasma flow. It was explained as a consequence of Fresnel frequency dependence on the relative drift and they used constant cutoff frequency (0.1 Hz) to detrend the data for obtaining the standard phase scintillation index. Care must be taken when identifying phase scintillation (diffractive phase variations) from refractive (deterministic)

phase variations especially in the polar region where the ionospheric plasma drift is much larger than in equatorial and midlatitude regions.

Priyadarshi *et al.*[65] identified the orientation of the ionospheric irregularities over Weihai with the local geomagnetic field by using the phase screen model and the wave propagation theory in random media. Amplitude and phase scintillation data observed using GNSS receiver deployed at the mid-latitude observation station Weihai, have been used along with *K*-index derived from the horizontal magnetic field component of the local magnetometer. They proposed a model that uses the scintillation indices relationship with the local *K*-index. There is a scintillation dependence on the local K-index under the geomagnetic quiet and disturbed condition.

Ma *et al.*[66] investigated ion upflow occurrence, speed, density, and flux above the polar cap in the northern hemisphere under different solar zenith angle, solar activity ($F_{10.7}$), and convection speed by analyzing a five-year period (2010–2014) of DMSP plasma data. High upflow occurrence rates in the dawn sector are associated with regions of higher convection speed, while higher upflow flux in the dusk sector is associated with higher density. The upflow occurrence increases with convection speed and solar activity but decreases with SZA. Upflow occurrence is the lowest when the SZA$>$100° and the convection speeds are low. While the upflow velocity and flux show a clear seasonal dependence with higher speed in the winter and higher flux in the summer during low convection conditions. However, they are detected to be both higher in summer during high convection conditions. The ion upflow in the polar cap is suggested to be controlled by the combination of convection, solar activity, and solar illumination.

Ma *et al.*[67] investigated the characteristics of hot patches versus classical patches by using five years' in situ database of plasma observations from DMSP satellites. The vertical ion flux is generally downward in classical patches (T_i/T_e>0.8 or T_e<T_i + 600 K), and generally upward. in hot patches (T_i/T_e <0.8 or T_e>T_i+600 K). Thus, the ion/electron temperature ratio can be used as a parameter to identify classical and hot patches. The highest upflow occurrence was found near the polar cap boundary, associated with hot patches, particle precipitation, strong convection speed, and localized field-aligned currents. The polar cap hot patches may play a very important role in solar wind-magnetosphere-ionosphere coupling processes.

The storm-time variation of ionospheric Equatorial Plasma Bubbles (EPBs) and the associated driven mechanisms can be highly complicated. Aa *et al.*[68] first reported a unique observation of post sunset super EPBs over China and adjacent areas during the second main phase of the geomagnetic storm on 7–8 September 2017. Moreover, Aa *et al.*[69] also observed similar post sunset super EPBs over the American sector during the first main phase of the same geomagnetic storm on 7–8 September 2017. In both cases, the signatures of EPBs can be observed from the following measurements: (i) prominent stream-like structures of depletion (about 5~15 TECU) in GNSS TEC and irregularities in ROTI maps, (ii) severe plasma bite-out of 2~3 orders from the Swarm/DMSP N_e profiles, and (iii) significant enhancement of F-layer height and vertical drifts. The ionospheric irregularities were registered for about 5 h and even reached 45° Magnetic Latitude in both Asian and American sectors.

Furthermore, Aa *et al.*[70] presented coordinated and fortuitous ground-based and spaceborne observations of EPBs, combining the Global-scale Observations of Limb and Disk (GOLD) far-ultraviolet emission images, GNSS TEC data, and Swarm in situ plasma density measurements. This multi-instrument measurements (Figure 15 and 16) provides an effective way to illustrate an integrated and comprehensive image for specifying both large-scale and mesoscale features of EPBs.

In recent years, an international space weather meridian circle program has been launched with an aim to unfold a global picture of space weather events by using diverse instruments along the meridian approximate 120°E/60°W, that is, the Asian and American longitude sectors. Li *et al.*[71] reported a

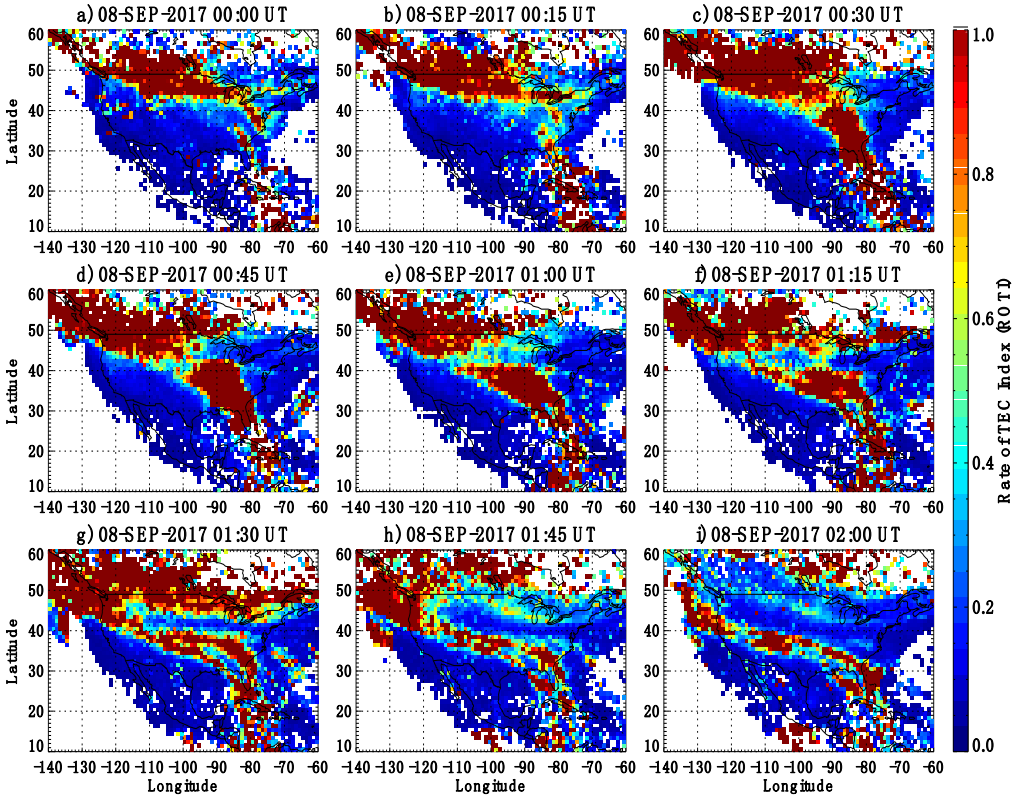

Fig. 15 TEC Rate of Change Index (ROTI) maps of ionospheric irregularities over East Asian sectors, respectively (Adapted from Aa *et al.*[70])

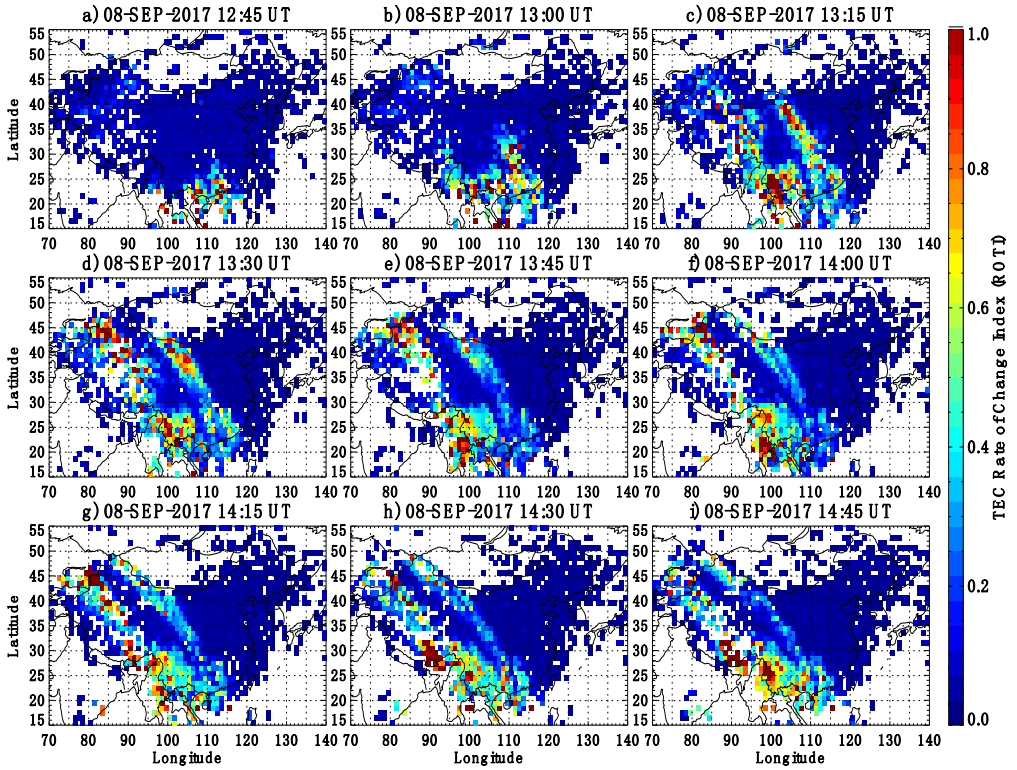

Fig. 16 TEC Rate of Change Index (ROTI) maps of ionospheric irregularities over North American sectors, respectively (Adapted from Aa *et al.*[70])

unique case of significantly enhanced post sunset EPBs developments by prompt Penetration Electric Field (PPEF) in both the American and Asian sectors, but their total absence by disturbance dynamo electric fields in the Pacific sector during the September 2017 geomagnetic storm sequence. The PPEF induced EPBs along the meridian showed different characteristics, with an apparent west-tilted structure in the Asian sector but unapparent in the American sector. This sort of study based on the international space weather meridian circle program observations would strengthen the understanding of the generation and evolution characteristics of EPBs during geomagnetic storms.

The fresh generation of Equatorial Plasma Bubbles (EPBs) is usually a nighttime phenomenon. Li *et al.*[72] reported an unexpected case of daytime F-region irregularities freshly generated following the appearance of an ionospheric hole over low latitude on 30 May 2016. The irregularities developed initially above the F-region peak height (about 360 km) with a thickness of about 30 km and an east-west extension of more than 200 km around 10:57 LT and then expanded upward to 500 km altitude behaving like the EPB irregularities of the nighttime ionosphere (Figure 17). Based on the coincidence, both in space

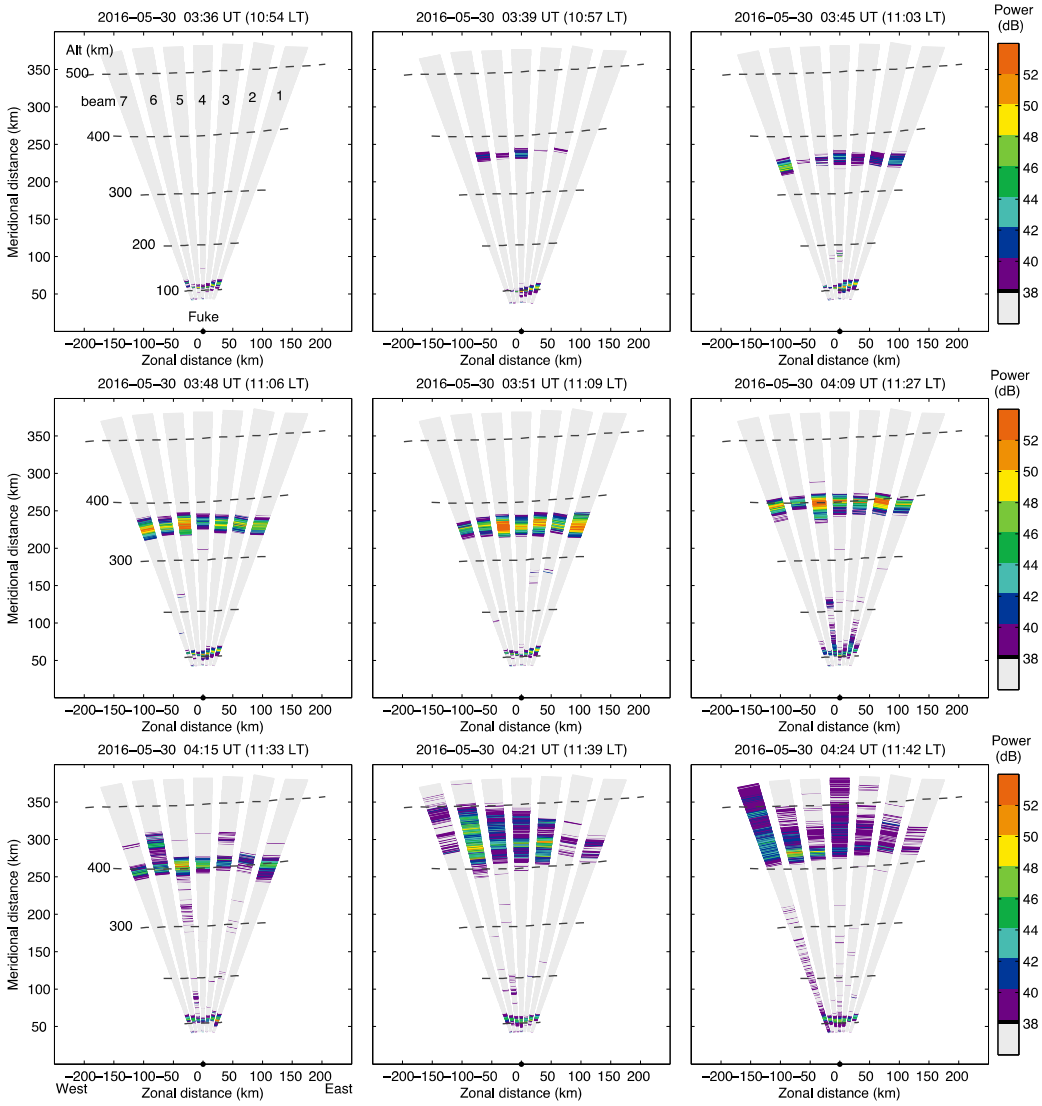

Fig. 17 Fan sector maps of echo power (in dB) taken from 10:54 LT (03:36 UT) to 11:42 LT (04:24 UT) on 30 May 2016 showing the onset and growth of F-region irregularities[72]

and time, with the appearance of an ionospheric hole, which was generated after the passage of a rocket, they concluded that the daytime F-region irregularities must have been artificially generated locally through a manifestation of plasma instability triggered by the rocket exhaust-induced ionospheric hole over low latitude. Their results provide solid evidence on the possibility of the artificial triggering of EPB irregularities.

The coupling of equatorial and low-latitude ionosphere has been an active area of research for many years. By using the Sanya (18.4°N, 109.6°E, dip latitude 12.8°N) VHF radar and ionosonde observations during equinoctial months of 2012–2016, Xie *et al.*[73] statistically investigated the occurrences of post-sunset ionospheric E, valley, and F region irregularities, the post sunset rise of F layer, and their correlations. Their results showed that there was a statistically significant correlation between the presence of Valley Region Irregularities (VRIs) and initial development of EPBs. They suggested that the electrodynamic processes associated with EPB development and ionospheric background electric field contribute significantly to the generation of E Region Irregularities (ERIs) and VRIs over Sanya. The mapping of Polarization Electric Fields (PEFs) generated within the fresh EPB structure could enhance (inhibit) the generation of VRI (ERI) over Sanya. The occurrence peak of ERI around 11:00 UT, however, could be due to the mapping of downward electric field above the equatorial plasma vortex shear node.

The Small-Scale Wave-like Structure (SSWS) of plasma density in the bottomside F region was proposed to be an important seeding for Equatorial Plasma Bubble (EPB) generation. Although the seeding role of SSWS has reproduced in theoretical simulations of EPBs in recent years, the observation fact is not identified. Liu *et al.* [74] reported two Large-Scale Wave-like Structures (LSWSs) were closely situated in longitude by using the Fuke all-sky airglow imager (19.3°N, 109.1°E; dip latitude 14.3°N) observations. The LSWSs were amplified and drifted eastward during the sunset pre-reversal enhancement of zonal electric field. Two SSWSs appeared later in the western LSWS and subsequently developed into an EPB. For the eastern LSWS, no SSWS and EPB were observed. Their results could provide supporting evidence for SSWS seeding of EPBs.

Based on multi-instruments observations, Luo *et al.*[75] studied the possible physical processes of controlling low-latitude plasma density enhancements, which also referred to as plasma blobs. Their results indicated that the meridional wind plays an important role in the formation of plasma blob in low-latitude regions, besides the polarized electric field due to the generation of plasma density depletions.

Yu *et al.*[76] studied the solar activity variation of global Equatorial F region Irregularities (EFIs) using the data of the COSMIC S_4 index profiles. The occurrence rates of EFIs at higher altitudes (greater than 500 km) show a clear solar activity dependence, while at entire altitudes (from 150 to 800 km) do not have a clear relationship with solar activity. The solar activity sensitivity of the occurrence rates of EFIs is the strongest in equinoxes and weakest in summer.

Yu *et al.*[77] developed a new method for estimating the Equatorial Plasma Bubble (EPBs) motions from airglow emission all-sky images. The method can determine the velocity of different parts in EPBs, after considering the EPBs deformation.

Wu *et al.*[78] showed a feature related with the equatorial plasma depletions by using four years' (2012–2015) observations of the all - sky imager and C/NOFS satellite. The Edge Plasma Enhancements of Equatorial Plasma Depletions (EPEEPDs) is a high-incidence phenomenon, with a rate of up to 82%. The zonal extension of EPEEPDs has scale characteristics varying with altitude. The generation mechanism of EPEEPDs is possibly related to the polarized electric field of EPDs.

Wang *et al.*[79] reported three cases of concurrent plasma blobs and bubbles around 22:30 LT in the same magnetic meridian in Asian-Oceanian sector during solar maximum, in terms of simultaneous observations from in-situ satellite and ground ionosonde/GPS scintillations at Vanimo station (geog. 2.7°S, 141.3°E; geom. 11.2°S, 146.2°W) and at

Hainan station (geog. 19.5°N, 109.1°E; geom. 9.1°N, 179.1°W). Magnetic field line mapping shows that the blobs in two cases were at equatorward and above bubbles, providing direct observational evidence for blob formation in the intermediate stage of plasma bubble evolution.

Zhang *et al.*[80] studied the temporal and spatial distribution of the amplitude scintillation at Shenzhen. It is found that the amplitude scintillation mainly occurs after sunset and lasts to midnight in equinox months. The Loss of Lock (LoL) of GPS signals at HKSL, a nearby GPS station has a very similar temporal variation as the amplitude scintillation. The scintillation and LoL occur more frequently in the southern part of Shenzhen. The strong amplitude scintillation mainly occurs at the azimuth angle of 180°~200°, and the LoL of GPS at azimuth of 170°~180° (Figure 18).

Xu *et al.*[81] proposed to use the standard deviation of the TEC fluctuation as a characteristic parameter serving as an indicator of the strength of the phase scintillation. It avoids the influence of the ionospheric projection of the satellite velocity and the ionospheric irregularity drift. This TEC fluctuation index is equivalent to the phase scintillation index, with the advantage for batch processing of large data without human intervention.

Wang *et al.*[82] reported the global observations of the S_4 amplitude scintillation index by the GPS Occultation Sounder (GNOS) on Fengyun-3C (FY-3C) satellite. The observations reveal global dynamic patterns of strong pre-midnight scintillations in ionospheric F region during the St. Patrick's Day geomagnetic superstorm of 17–19 March 2015. During the main storm phase on 17 March, the scintillations were first triggered at 160°E longitude in the New Zealand sector, extending beyond 40°S dip latitude. The scintillations were also enhanced in the Indian sector, but significantly suppressed in East Asia near 120°E longitude and in Africa around 30°E longitude. The feature is consistent with the density depletion structures by the C/NOFS satellite and ground-based instruments.

Wang *et al.*[83] investigated the spread-F at four ionosondes located at Haikou (20°N, 110.34°E), Guangzhou (23.14°N, 113.36°E), Beijing (40.11°N, 116.28°E), and Changchun (43.84°N, 125.28°E). The Frequency Spread-F (FSF) occurrences show a negative correlation with solar activity at all four sites, and the Range Spread-F (RSF) has a positive occurrence with solar activity at Haikou. The frequency spread-F appears more often after midnight with higher occurrence at mid-latitudes and summer months. The range spread-F occurs mostly in the

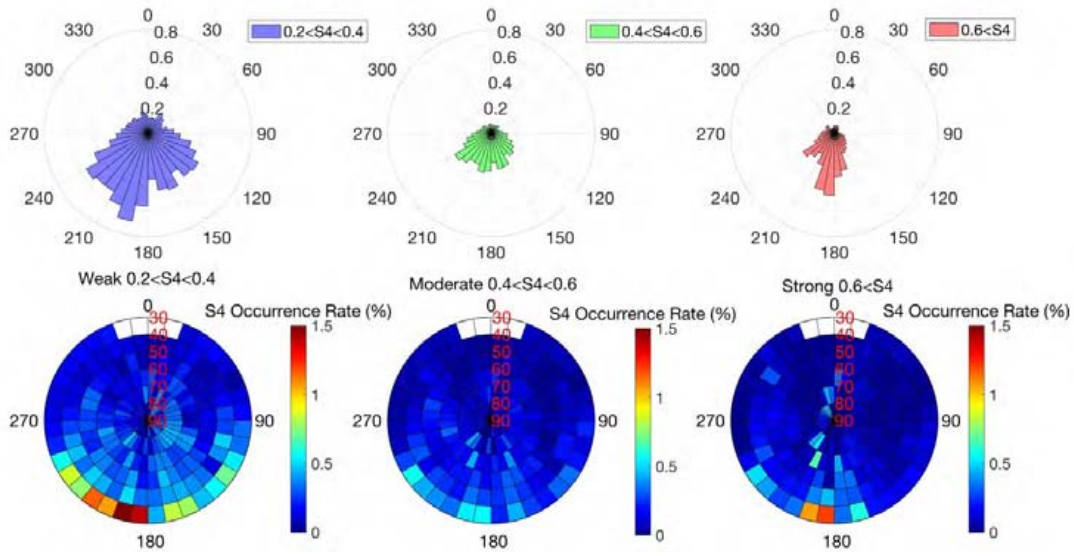

Fig. 18 Spatial distribution of six years averaged amplitude scintillation occurrence with different S_4 intervals in Shenzhen[80]

equinoctial months of 2000–2002 at Haikou and Guangzhou. The favorable virtual height of F layer for the RSF occurrence ranges between 240 and 290 km.

Wang *et al.*[84] and Wang *et al.*[85] investigated the spread-F and made a comparative study of spread-F and scintillation occurrence rates in East Asia. The occurrence of FSF is oppositely correlated with solar or geomagnetic activities. The occurrence of FSF is higher than that of RSF. The FSF occurs more frequently in summer, and there is a higher RSF occurrence in winter at latitude near 45°N. The spread-F occurrence is higher in the coastal areas than in the continental region between 35°N and 45°N latitudes and no remarkable difference at lower latitudes.

Liu *et al.*[86] investigated the statistical characteristics of global sporadic E (Es) occurrence and its relation with wind shear by using GNSS radio occultation measurements and TIMED/TIDI dataset during 2002–2016. Their results presented that Es occurrence had distinct temporal and spatial variations, which reached a maximum at local daytime and post-sunset period in summer (winter) season in the Northern (Southern) hemisphere. The wind shear is found to play a significant role in the formation of E_S, especially in the mid-latitude region.

Zhou *et al.*[87] showed the morphology of E region Field-Aligned Irregularity (FAI) at Wuhan by using Wuhan VHF radar observations during 2015–2016. Quasi-period echoes were frequently observed at summer post-sunset period in the height range of 100~120 km. The Doppler spectra reveal that type 2 irregularity is dominant during the observational period. Wuhan ionosonde during 2015–2016 revealed a strong linkage between E region FAI and Es. Several mechanisms, such as Kelvin-Helmholtz Instability (KHI) or ES instability, could be considered as the possible mechanism for the generation of E region FAI in the mid-latitude region.

By using Wuhan VHF radar, Wuhan GNSS network, and Wuhan ionosonde, Liu *et al.*[88] investigated mid- and low-latitude nighttime ionospheric E-F coupling. Results show that E- and F-region irregularities, nighttime MSTIDs, strong ES, and Spread F were simultaneously observed on 25 May 2016. Our results firstly provide the observational evidence of the full electrodynamic and links among different ionospheric irregularities in the mid- and low-latitude nighttime region of China.

Chen *et al.*[89] investigated Medium-Scale Traveling Ionospheric Disturbances (MSTIDs) by using the Hong Kong Continuously Operating Reference Stations network with a short baseline length of 10~15 km. The occurrence rate of MSTIDs has a strong dependence on local time and season. They categorized the MSTIDs during 2014–2017 can be into three types. There is no distinguishable difference in the MSTID parameters between the cyclone period and non-cyclone period.

Jiang *et al.*[90] carried out a modeling study of the F_2 layer stratification on ionograms using a ray-tracing method based on a simple model of TIDs. Results show that gravity waves/TIDs might play a significant role in formation of the F_2 layer stratification. TIDs induced gradients could cause different features on ionograms. The F_2 layer stratification is mainly due to the vertical gradient in the ionosphere, and the horizontal gradient could lead to spread F on ionograms. Jiang *et al.*[91] further conducted a statistical study on the F_2 layer stratification at Puer station (22.7°N, 101.05°E, Dip Latitude 12.9°N) in 2015 and 2016. The F_2 layer stratification occurs at daytime and nighttime, moving upward and downward. The new cusp could originate from different positions on ionograms. Statistical studies show that the daytime F_2 layer stratification occurred later in winter. The post-midnight F_2 layer stratification could be observed frequently in the spring days.

Yang *et al.*[92] studied the daytime spread F at Zhangye station (39.4°N, 100.0°E, dip Lat. 29.6°N). The ionosonde recorded daytime spread F three times on 6 January 2017. The daytime spread F observed might be attributed to Traveling Ionospheric Disturbances (TIDs)/atmospheric gravity waves induced by a geomagnetic storm.

Spread F frequently occurred at Puer station. Lan *et al.*[93] developed a method for automatic

identification of Spread F using decision trees. Lan *et al.*[94] further carried out a statistical study of spread F at Puer station in the years of 2015 and 2016. FSF and MSF were dominant at Puer. Most types of SF appeared mostly in summer, and the maximum occurrence of SSF in equinox. They suggested that Medium-Scale Traveling Ionospheric Disturbances (MSTIDs) may play a key role in the formation of SF.

Zhou *et al.*[95] investigated the coupling between ionosphere E and F regions at Wuhan by using Wuhan ionosonde and VHF coherent scatter radar, and Mengcheng airglow imager. Diffuse Es layers and E region irregularities are related to the F region medium-scale traveling ionospheric disturbances or spread F through polarized electric field mapping along the field lines. The Wuhan ionosonde and VHF radar data from 2015 to 2016 show that the coincidence of diffuse Es layers, E region FAIs, and spread F is much high at nighttime. Their work indicates that polarized electric field generated in the E region irregularity could map to F region and excite electrodynamic process, such as Perkins instability, which is important for nighttime midlatitude ionospheric E and F region coupling.

Meng *et al.*[96] reported the band - like irregularity structures with a short lifetime. The structures initially appeared at altitudes higher than 400 km and moved to higher altitudes but without zonal propagation. The band-like irregularities were accompanied by spread echoes.

Low frequency plasma instabilities are considered as a dominant generation mechanism of the ionospheric irregularities. Laboratory experiments can provide a complementary approach to investigate the ionospheric plasma instabilities, waves, and irregularities. Compared to a satellite mission or rocket campaign, the laboratory experiments (Figure 19) have many benefits such as reproducibility, controllability, diagonality, and reconfigurability. Liu *et al.*[97, 98] designed controlled experiments to simulate the ionospheric collisional plasma environment, which provides evidences that the low frequency plasma instabilities such as the Kelvin-Helmholtz Instability

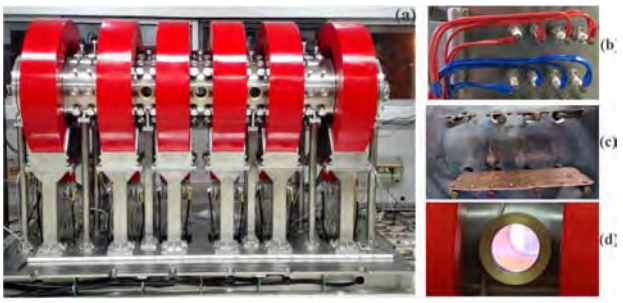

Fig. 19 (a) Front view of the Keda Space Plasma EXperiment (KSPEX), (b) the Kovar electrodes used for heating filaments, (c) arrangement of the filaments in the primary chamber, and (d) a picture of the double layer plasmas (Picture is provided by LIU Y)

(KHI) can be generated in the ionospheric-like plasma. Through the experimental work, the theoretical mechanism can be more confidently applied to explain the excitation of ionospheric irregularities.

5 Modeling and Data Assimilation

Aa *et al.*[99] presented a data ingestion technique to incorporate the Madrigal TEC data into the NeQuick 2 model. The method is based on retrieving an appropriate global distribution of effective ionization parameter (A_z), which can be implemented through minimizing the difference between the measured and modeled TEC at each grid in the local time-modified dip latitude coordinates. The NeQuick 2 model could be driven by an Az map to reproduce ionospheric parameters, such as N_e, TEC, N_mF_2, h_mF_2, and so forth. Their validations show that a general accuracy improvement of 30%~50% can be achieved after data ingestion. In addition, the Empirical Orthogonal Function (EOF) analysis technique is used to construct a parameterized time-varying global A_z model. The NeQuick TEC driven by EOF-modeled A_z shows 10%~15% improvement in accuracy over the standard ionosphere correction algorithm in the Galileo navigation system.

The widely used data source of ionospheric data assimilation is the global ground-based GNSS slant TEC. Given that more ground GNSS receivers have the capability to track multiple navigation signals,

She *et al.*[100] proposed a new method to estimate the receiver's Differential Code Bias (DCB) based on local spherical symmetry assumption of ionosphere, which could calibrate the slant TEC self-consistently without aiding by other data source or model. He *et al.*[101] constructed an Ensemble Kalman Filter (EnKF) ionosphere and thermosphere data assimilation system using the National Center for Atmospheric Research Thermosphere Ionosphere Electrodynamics General Circulation Model (NCAR-TIEGCM) as the background model. They use a sparse matrix method to avoid significant matrix related calculation and storage. A series of observing system simulation experiments have been conducted to assess the performance of the system. The results show that the system optimizes ionosphere drivers efficiently by assimilating electron densities through their covariance. The short - term forecast capability is enhanced significantly, and the effect of initial condition correction lasts for longer than 24 h. Their study demonstrates that the EnKF based global ionosphere and thermosphere data assimilation can be conducted without using a supercomputer. The ionosphere and thermosphere data assimilation system benefits both scientific studies and near real-time operation.

Liu *et al.*[102] made validation of the predictions of IRI-2016 model by using the ionosonde measurements from 4 Chinese stations. They found that the daily minimum value of f_0F_2 occurs earlier in the IRI-2016 prediction than the observations. Around the sunrise, the IRI-2016 prediction shows a very sharp rise and much faster than the observed f_0F_2. The CCIR option of IRI is found to perform better than the URSI option during post sunset under low solar activity or in EIA region over China.

Wang *et al.*[103] developed a dual-parameter regularization algorithm to reconstruct the three-dimensional ionospheric electron density under the assumption that the ionospheric spatial variations can be separable in the horizontal and vertical directions. Wang *et al.*[104] adopted the Tikhonov regularization method to reconstruct the 3D ionospheric electron density by incorporating the electron density profiles data from COSMIC radio occultation technique and ground ionosondes. A regularization parameter was introduced to balance the weights between the prior (or background) information and measurements. The model function in the modified *L*-curve method is used to determine the optimal regularization parameter.

Zhao *et al.*[105] developed an algorithm to determine the wave turbopause based on numerical differentiation. Tikhonov regularization is used to reasonably solve the numerical differential ill posed problem, which laid a foundation for quantitatively determining the wave turbopause in the lower ionosphere through using the vertical gradient profile of temperature standard deviation.

6 Radio Wave Propagation in the Ionosphere and Sounding Techniques

A number of ionosondes have been operated in China to detect ionospheric disturbances for many years. The ionosondes, however, are not very suitable for the short-period (<15 min) disturbances due to the limited time resolutions (>5 min). In recent years, the Institute of Geology and Geophysics, Chinese Academy of Sciences, together with the South Central University for Nationalities has been developing a Portable Digital Ionosonde (PDI) equipped with the improved capability to detect and characterize small-scale/short-period ionospheric disturbances and to be quickly assembled and set up at temporary field stations for campaign coordinated observations. Lan *et al.*[106] performed a preliminary analysis of the observations by employing a PDI at Sanya (18.3°N, 109.6°E). Their results showed the presence of ionospheric disturbances with periods ranging from several to tens of minutes. Interestingly, the disturbances (with different periods) were found to occur simultaneously at different F region altitudes, for example, with periods of 5 min and 20 min below and above about 180 km, respectively (Figure 20). The absence of shorter-period disturbance at higher

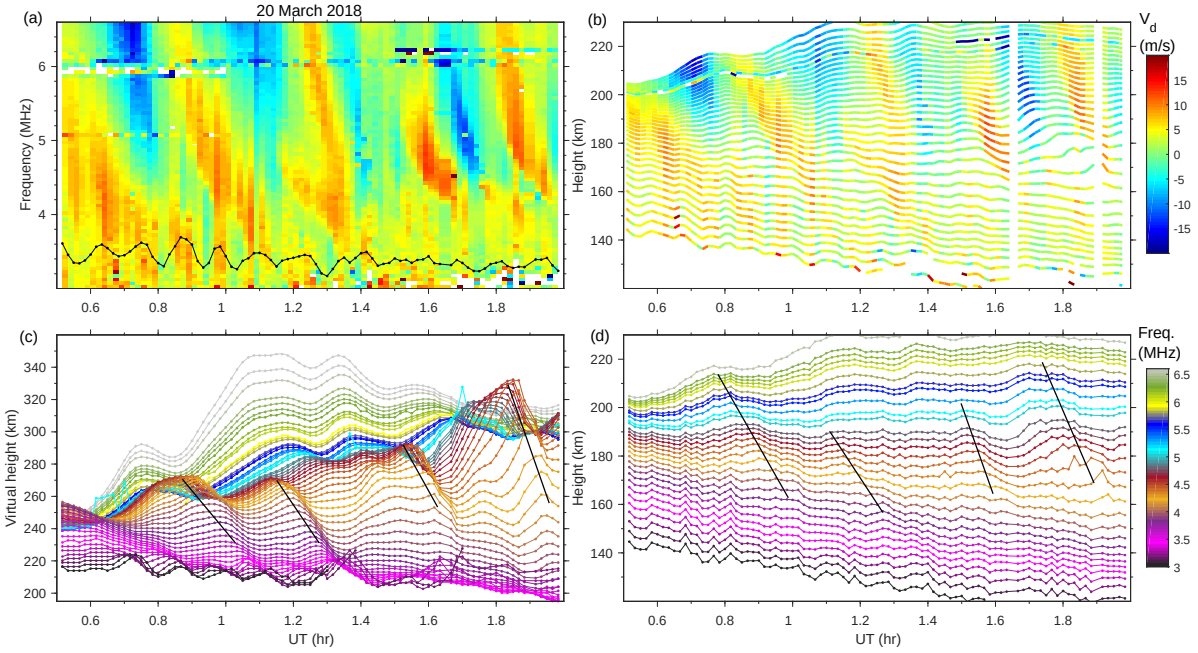

Fig. 20 Doppler velocity as functions of (a) sounding frequency and time, and (b) true height and time, and temporal variations of (c) virtual height and (d) true height for the plasma frequencies of 3~11 MHz indicated by different colors during 00:30 UT–02:00 UT on 20 March 2018[106]

altitudes is consistent with the fact of acoustic gravity waves through the region with intrinsic periods above the Brunt-Väisälä period. Their results demonstrated the capability of PDI in routine ionogram mode to detect ionospheric disturbances with temporal scales down to a few minutes.

An ionogram contains important information of the ionosphere. Therefore, it is essential to automatic scaling and inversion of the ionograms with accuracy as high as possible in real-time monitoring the ionosphere. Chen *et al.*[107] developed a method to scale the ionograms automatically. The method is based on the pattern recognition technology, mathematical morphology, and the echo characteristics of each layer of the ionosphere, having low computational complexity, strong universality, and high accuracy over 90% when it was applied to scale the observations of Chinese Academy of Sciences Digital Ionosonde (CAS-DIS). The method can deal with ionograms in the routine situations and the ionograms with irregularities too.

An Ionospheric Observation Network for Irregularity and Scintillation in East/Southeast Asia (IONISE*) was recently deployed by Beijing National Observatory of Space Environment (Figure 21). Using ionospheric Total Electron Content (TEC) from the two crossed Beidou geostationary satellite receiver chains of the network along 110°E and 23°N and Doppler velocity measurements from the Sanya (18.3°N, 109.6°E) portable digital ionosonde, Li *et al.*[108] reported observations of low latitude TEC oscillations synchronized over a wide longitude range in East/Southeast Asia, which occur at nighttime, after the main phase of the 20 April 2018 geomagnetic storm. Their results showed that the periodic TEC enhancements correlate with F region downward plasma drifts and IMF B_z southward turnings. It was suggested that the quasiperiodic southward turnings of IMF B_z could produce multiple short-lived westward prompt penetration electric fields, which contribute to driving the nighttime low latitude TEC oscillations simultaneously over the wide longitude range. Compared with the TEC measurements by GPS receiver network that are affected

* http://ionise.geophys.ac.cn/

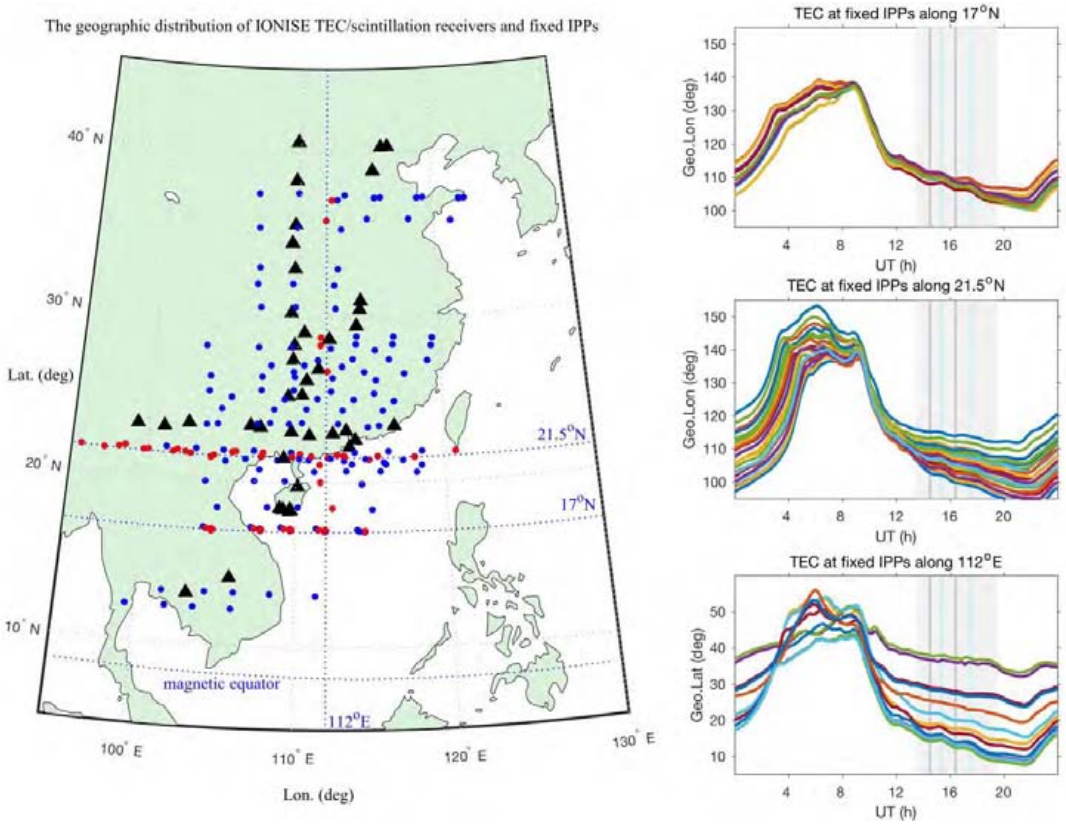

Fig. 21 Map of the IONISE TEC/scintillation receivers (marked with triangles) and fixed ionospheric pierce points (marked with dots)[108]. For the near real-time IONISE plots please visit http://ionise.geophys.ac.cn/. Samples of TEC are also given in the right panels

by satellite motion, the IONISE, which measures TEC at fixed ionospheric pierce points along the same longitude/latitude by receiving Beidou geostationary satellite signals, provides a unique means for fine-scale observations of ionospheric perturbations.

The Chinese Beidou navigation satellite System (BDS) now provides a great chance to promote the investigation of the ionospheric structures. Huang *et al.*[109] used the Beidou GEO TEC to detect the characteristics of nighttime Medium-Scale Traveling Ionospheric Disturbances (MSTIDs) at middle latitudes, which further compared with those from the airglow images and GPS TEC observations. Three peaks in a year for the seasonal variations of the nighttime MSTID occurrence rate in 2016 are found. Meanwhile, the results show that the features of nighttime MSTIDs from the Beidou GEO TEC are in better agreement with those from the airglow images than those from the GPS TEC, given that the GPS TEC results are affected by Doppler shift and ionospheric background TEC due to movement of GPS satellites. Huang *et al.*[110] firstly analyzed daytime ionospheric periodic wave-like structures in the low-latitude ionosphere over the Asian-Australian sector using TEC from Beidou GEO observations. They found that these structures have the periods of about 18~28 min and show obvious seasonal, local time, and latitudinal variations. No clear correlation between the two Hemispheres is found. They argued that daytime ionospheric periodic wave-like structures in the low-latitude ionosphere could be triggered by GWs from the lower atmosphere, and generated in the low-latitude ionosphere rather than propagating from the other latitudes.

Zhao and Zhou[111] proposed the concept of optimal ionospheric shell height to minimize the absolute values of DCB. Based on the data from five IGS stations at different latitudes during 2003–2013,

their results show that the optimal ionospheric shell height performs much better than the fixed ionospheric shell height. The optimal ionospheric shell heights show 11-year and 1-year periods and latitudinal dependence.

Zhao and Zhou[112] examined whether the optimal ionospheric shell height derived from IGS station can be applied to non-IGS stations or isolated GNSS receivers. Their study shows that the optimal ionospheric shell height calculated by reference IGS stations can be applied to its nearby non-IGS stations or isolated GNSS receivers for accurate TEC estimation, and the error of DCB estimation nearby non-IGS station or isolated GNSS receiver is generally linear with the distance away from the reference IGS station.

The existence of GNSS Differential Code Biases (DCBs) provides a challenge for estimating the ionospheric TEC. Li *et al.*[113] comprehensively assessed the intra-day stability of receiver DCBs over a period of 1 month in terms of hour-to-hour estimating of multi-GNSS receiver DCBs. Their extracted receiver DCBs may not change abruptly in two consecutive days, but with a gradual shift over short-term intervals instead. They also verified that in case there are significant short-term variations in the derived receiver DCBs, the assumption of constant receiver DCBs will partially account for the errors in ionospheric TEC extraction (with the RMS of 12.96 TECU).

Dual-frequency GNSS receivers are widely used for sensing the earth's ionosphere. Zhao *et al.*[114] proposed a Multi-GNSS Single-Frequency (MSF) precise point positioning approach enabling the simultaneous retrieval of VTEC with low-cost MSF receivers. The ionospheric VTEC being estimated with their MSF approach reaches the accuracy at the same level as that of the dual-frequency approach.

The ionospheric sporadic E (Es) layer has a significant impact on radio wave propagation. The traditional techniques employed for Es layer observation, for example, ionosondes, are not dense enough to resolve the morphology and dynamics of Es layer in spatial distribution. Based on the Chinese ground-based GNSS networks, including the Crustal Movement Observation Network of China and the Beidou Ionospheric Observation Network, Sun *et al.*[115] observed a large-scale strong Es event in the middle latitude of China. The strong Es shown as a band-like structure in the southwest-northeast direction extended more than 1000 km. By making a comparative analysis of Es occurrences identified from the simultaneous observations by ionosondes and GNSS TEC receivers over China middle latitude statistically, they found that GNSS TEC can be well employed to observe strong Es occurrence with a threshold value of f_0E_s.

Using Total Electron Content (TEC) data from 902 global navigation satellite system stations over China, Liu *et al.*[116] analyzed the ionospheric responses following two similar launches of the Long March 4B from Taiyuan, China, that is, China-Brazil Earth Resources Satellite 3 launched on 9 December 2013 and China-Brazil Earth Resources Satellite 4 launched on 7 December 2014. They found that the ionospheric disturbances of these two launches were almost the same and identified three types of disturbances following both launches: depletions, shock wave-related Traveling Ionospheric Disturbances (TIDs), and acoustic wave-related circle TIDs. The buildup time of depletion was influenced by the amount of exhaust expelled into the ionosphere. After the electron depletion was formed, it drifted westward for approximately 300 km. The shock wave-related TIDs can only be observed near the trajectory and reflect the acceleration of the rockets. The acoustic wave-related circle TIDs were observed at the southeast of the launch site.

The rapidly developing GNSS constellations give us unprecedented abilities to monitor and study the near-Earth space. Hao *et al.*[117] recently used GNSS beacons to investigate the prompt response of the plasmasphere to an interplanetary shock. The Beidou Navigation Satellite System and GPS receivers are used to examine sudden TEC variations when the shock impinged on the dayside magnetosphere. The dense GNSS constellations and globally distributed ground receivers enable us to possibly

estimate the propagation velocity of the shock induced pulse in the magnetosphere.

Ding *et al.*[118] introduced the configuration and implementation of the Qujing Incoherent Scatter Radar (QJISR), including the antenna, transmitter, receiver, signal processing, and data analysis. They reported some preliminary observations of the raw echoes and power spectra, and the derived ionospheric parameters (electron density, electron temperature, and ion temperature).

Wu *et al.*[119] reported a remarkable extension of observing altitudes of the High Frequency pumping enhanced Plasma Line (HFPL) and the Ion Line (HFIL) in the observations of the Ultrahigh Frequency Incoherent Scatter Radar (UHF-ISR) of European Incoherent Scatter scientific Association (EISCAT), implying that the enhanced ion acoustic wave and Langmuir wave should satisfy the Bragg condition within the extending altitude range. The dependence of the wave-number of the traveling ion acoustic wave on the profile of enhanced electron temperature and ion mass leads to the extension of observing altitudes of the enhanced ion line. The altitude extension of the enhanced plasma line is dependent on the profile of the electron density, the enhanced electron temperature, and the thermal conduction along the magnetic field.

Wu *et al.*[120] further reported that the enhanced electron temperature plays a significant role in determining the intensities of the enhanced Langmuir and ion acoustic waves by the parametric decay instability and the oscillation two-stream instability. The intensities of the enhanced plasma and ion lines depend on the Bragg condition being satisfied by the enhanced Langmuir and ion acoustic waves. The overshoots in the enhanced plasma and ion lines may be attributed to the anomalous absorption of the pump and the modifications of the plasma on the propagating path of the enhanced Langmuir and ion acoustic waves.

Lv *et al.*[121] derived the scattering equations of electron density fluctuations generated by HF heating based on the scattering theory of anisotropic irregularities with assumptions of a Gaussian auto-correlation function. The variances of scattering coefficients with the geomagnetic field, Effective Radiated Power (ERP), and frequency were studied by numerical simulations. The scattering coefficients are larger at high latitudes than at mid and low latitudes under the same conditions. According to the simulations, the scattering coefficients with an HF pumping ERP exceeds 250 MW at Wuhan or 650 MW at Guangzhou can have magnitude comparable with those at Platteville to support VHF transmission on long-distance circuits.

Xu *et al.*[122] performed a polarization analysis of Beat-Wave (BW) generated Extremely Low Frequency (ELF)/Very Low Frequency (VLF) waves using EISCAT heating facility near Tromsø. The ELF/VLF waves can be decomposed into right- (R) and left- (L) handed circularly polarized waves with comparable strengths, and the polarization ellipse tends to be parallel to the well-known dominant background electric field, consistent with the recognized features of ELF/VLF waves generated by PEJ modulation. Hence, their result demonstrates that the BW generated current is located in the D/E region, not in the F region.

Yang *et al.*[123] examined the effect of the duty cycle and heating frequency on the radiation efficiency of VLF/ELF in amplitude modulated ionospheric heating experiments by using simulations of the lower-ionosphere modulated heating model. The numerical simulation shows that the intensity of the VLF/ELF equivalent radiation changes from increase to decrease with increasing of the modulated duty cycle and heating frequency.

Yang *et al.*[124] investigated the modulated ionospheric heating by using the EISCAT facility in Tromso, Norway. The experiments show that, in the Amplitude Modulated (AM) mode, the amplitude of the ELF/VLF signal decreases as the radiation frequency increases when the amplitude of the ELF/VLF signal reaches the maximum at 2017 Hz. In the Beat-Wave (BW) mode, the maximum appears at 2017 Hz, but the overall amplitude of the ELF/VLF signal increases with the radiation frequency. When the frequency is low, the ELF/VLF

signal excited has a larger amplitude in the AM mode than in the BW mode. In contrast, the BW mode performs better than the AM mode at a higher frequency. The AM mode tends to produce circularly polarized waves, and the BW mode produces linearly polarized waves.

Yang *et al.*[125] reported the experiments of the ELF/VLF radiation from the ionosphere by AM mode and dual-beam Beat-Wave (BW) mode modulation heating using the EISCAT heating facility. In the AM mode, the intensity of the ELF/VLF radiation source depends on the intensity of geomagnetic disturbance and on the magnitude of natural currents in the ionosphere. In the BW mode, the intensity of the ELF/VLF radiation source is less dependent on the intensity of geomagnetic disturbance.

Yu *et al.*[126] constructed an empirical model of GUVI neutral density aiming to solve the difficulty of the direct comparison of GUVI and CHAMP observations due to their different local times at a given location in a given day. The GUVI model is in good agreement with CHAMP observations with the small standard deviations of their ratios (less than 10%) except at low solar flux levels. The correlation coefficients are greater than 0.9, and the relative standard errors are less than 20%. Comparison between the GUVI model and CHAMP observations during solar minimum shows a large bias (about 30%). Their results demonstrate the validity and accuracy of the model based on GUVI data against the density data from the CHAMP satellite.

Meteoroids entering the Earth's atmosphere can create meteor trail irregularity seriously disturbing the background ionosphere. By installing multiple video cameras near the Sanya VHF radar site, Li *et al.*[127] conducted an observational campaign during the period from November 2016 to February 2017. Their results showed a good agreement between the angular positions of non-specular echoes and those of optical meteors, which verified the interferometry capability of Sanya radar for meteor trail irregularity observation. The non-specular echo duration was found to have a general linear relationship with its corresponding meteor visual magnitude. Further, In some cases optical meteors were detected, while there are no simultaneous radar non-specular echoes, indicating some optical meteors could appear at extremely low altitudes.

Bai *et al.*[128] made a comparison of GNSS Occultation Sounder (GNOS) results from a radio occultation sounding payload onboard the Fengyun-3C (FY-3C) satellite with ground-based ionosonde observations. They verified the reliability of radio occultation data products with an event investigation of the March 2015 magnetic storm and a correlation analysis of peak electron density (N_mF_2) derived from data products of GNOS Global Position System (GPS) and Beidou navigation System (BDS) with ionosonde data.

Sui and Fu[129] investigated the ionospheric effects on phase and Faraday rotation of interferometry for TwinSAR-L synthetic aperture radar SAR mission (Terrain Wide-swath Interferometric L-band mission) for global earth remote sensing, which will be launched by China in future.

Fu *et al.*[130] investigated the asymmetry in stimulated emission polarization and irregularity evolution during ionospheric electron gyroharmonic heating. The high-frequency radar echoes and Stimulated Electromagnetic Emission (SEE) polarimetry appear asymmetric for pumping above $3f_{ce}$ (f_{ce}, the electron cyclotron frequency), implying that the broad upshifted maximum spectral line formation involves plasma irregularities scattered by high-frequency radar echoes. Fu and Scales[131] established a two-dimensional kinetic model of stimulated electromagnetic emissions to investigate this SEE asymmetry near electron gyro harmonic.

Incoherent Scatter Radar (ISR) is the most powerful ground-based measurement facility to study the ionosphere. The plasma lines are not routinely detected by the incoherent scatter radar and fall below the measured spectral noise level. The plasma lines are occasionally enhanced by suprathermal electrons through the Landau damping process and detectable to the incoherent scatter radar. Wang and Zhou[132] derived the electron density from plasma

lines induced by a suprathermal electron in the ionospheric modification experiment. The European Incoherent Scatter Association (EISCAT) UHF incoherent scatter radar observed the enhanced plasma lines, considering as a manifest of the suprathermal electrons generated by the high-frequency heating wave during the ionospheric modification.

Wang *et al.*[133] conducted a theoretical investigation on the threshold of parametric instability in the ionospheric heating experiments. A general dispersion relation and the threshold of the parametric instability excitation in the heating experiment are derived by considering the inhomogeneous spatial distribution of pump wave field. They showed that the threshold of parametric instability is influenced by the effective electron and ion collision frequencies and the pump wave frequency. Both collision and Landau damping should be considered in the parametric instability calculation.

Wang *et al.*[134] investigated the generation of the small-scale field aligned irregularities in the ionosphere heating experiments. A theoretical model is used to describe the small-scale irregularities excited by powerful high frequency (3~30 MHz) electromagnetic waves in ionosphere heating. The model is based on the transport equation in magnetic plasma and mode conversion from electromagnetic waves to electrostatic waves in ionospheric modification. The calculations indicate that background electron density and geomagnetic field play an important role in the threshold electric field and the spatial scale of the electron density irregularities. The electric field threshold is found to increase with the decrease of the spatial scale of the irregularities.

Wang *et al.*[135] investigated the Stimulated Electromagnetic Emissions (SEEs) spectrum observed during an X-mode heating experiment at the EISCAT (European Incoherent Scatter Scientific Association). SEEs spectra were observed by the high-power high-frequency transmitter facility located at Tromsø belongs to the EISCAT in the experiment. A narrow continuum occurred under cold-start conditions and showed an overshoot effect lasting several seconds. Cascading peaks occurred on both sides of the heating frequency only in the preconditioned ionosphere and also showed an overshoot effect.

Liu *et al.*[136] investigated the ionospheric heating by the oblique incidence of powerful HF radio waves using three-dimensional numerical simulations. They established a model to simulate three-dimensional ionospheric heating by oblique incidence of powerful HF radio waves. A plane wave spectral integral method is used to calculate the electric field in the caustic region. The simulation results indicate that the ionospheric electron density and temperature can be disturbed by the oblique incidence of powerful radio waves, especially in the caustic region. They compared the effects of heating with wave incidence in parallel and perpendicular directions to the geomagnetic field. The ionospheric modulation is found to be more effective when the heating wave propagates longitudinally.

Acknowledgments LIU Libo would like to express his gratitude to the colleagues for kindly providing their articles and pictures in the course of the preparation for this national report. The contributors are AA E, CHEN Gang, CHEN Yiding, CHEN Ziwei, DANG Tong, DING Feng, DING Zonghua, FANG Hanxian, FU Haiyang, HAO Yongqiang, HUANG Fuqing, HUANG He, HUO Xingliang, LE Huijun, LEI Jiuhou, LI Guozhu, LIU Guoqi, SUN Y Y, WANG Hui, WANG Zheng, WU Yewen, YAN Xiangxiang, YANG Na, YU Tao, YUE Xinan, ZHANG Beichen, ZHANG Dengke, ZHANG Donghe, ZHANG Qinghe, ZHANG Ruilong, ZHAO Biqiang, ZHOU Chen, ZHU Zhenping.

References

[1] LIU L, WAN W. Chinese ionospheric investigations in 2016--2017 [J]. *Earth Planet. Phys.*, 2018, **2**:89-111

[2] LE H J, LOU L, CHEN Y, *et al.* Anomaly distribution of ionospheric total electron content responses to some solar flares [J]. *Earth Planet. Phys.*, 2019, **3**(6):481-488

[3] ZHAO B, YANG C, CAI Y, *et al.* East-west difference in the ionospheric response of the March 1989 great magnetic storm throughout East Asian region [J]. *J. Geophys. Res.: Space Phys.*, 2019, **124**:9364-9380

[4] LIU Libo, LE Huijun, CHEN Yiding, *et al.* New aspects of the ionospheric behavior over Millstone Hill during the

30-day incoherent scatter radar experiment in October 2002 [J]. *J. Geophys. Res.: Space Physics*, 2019, **124**:6288-6295

[5] ZHANG Ruilong, LIU Libo, LE Huijun, *et al.* Equatorial ionospheric electrodynamics over Jicamarca during the 6-11 September 2017 space weather event [J]. *J. Geophys. Res.: Space Phys.*, 2019, **124**:1292-1306

[6] ZHANG R, LIU L, BALAN N, *et al.* Equatorial ionospheric disturbance field-aligned plasma drifts observed by C/NOFS [J]. *J. Geophys. Res.: Space Phys.,* 2018, **123**:4192-4201

[7] JIMOH O, LEI J, ZHONG J, *et al.* Topside ionospheric conditions during the 7--8 September 2017 geomagnetic storm [J]. *J. Geophys. Res.: Space Phys.*, 2019, **124**:9381-9404

[8] LEI J, HUANG F, CHEN X, *et al.* Was magnetic storm the only driver of the long-duration enhancements of daytime total electron content in the Asian-Australian sector between 7 and 12 September 2017 [J]. *J. Geophys. Res.: Space Phys.*, 2018, **123**:3217-3232

[9] BALAN N, ZHANG Q H, SHIOKAWA K, *et al.* Ips*Dst* of *Dst* storms applied to ionosphere-thermosphere storms and low latitude aurora [J]. *J. Geophys. Res.: Space Phys.*, 2019, **124**:9552-9565

[10] ZHANG K, LIU J, WANG W, *et al.* The effects of IMF Bz periodic oscillations on thermospheric meridional winds [J]. *J. Geophys. Res.: Space Phys.*, 2019, **124**:5800-5815

[11] LIU Jing, ZHANG Donghe, COSTER A J, *et al.* A case study of the large-scale traveling ionospheric disturbances in the eastern Asian sector during the 2015 St. Patrick's Day geomagnetic storm [J]. *Ann. Geophys.*, 2019, **37**:673-687

[12] LI N, LEI Jiuhou, LUAN Xiaoli, *et al.* Responses of the D region ionosphere to solar flares revealed by MF radar measurements [J]. *J. Atmos. Sol.:Terr. Phys.*, 2019, **182**:211-216

[13] HUANG H, LU X, LIU L, *et al.* Transition of interhemispheric asymmetry of equatorial ionization anomaly during solstices [J]. *J. Geophys. Res.: Space Phys.*, 2018, **123**(12): 10283-10300

[14] MO X H, ZHANG D H, LIU J, *et al.* Morphological characteristics of equatorial ionization anomaly crest over Nanning region [J]. *Radio Sci.*, 2018, **53**: 37-47

[15] TIAN Y, HAO Y, ZHANG D, *et al.* Single crest phenomenon in the equatorial ionospheric anomaly region and its longitudinal distribution caused by nonmigrating tides [J]. *Chin. J. Geophys.*, 2019, **62**(11):4067-4081

[16] LI Qiaoling, LIU Libo, BALAN N, *et al.* Longitudinal structure of the mid-latitude ionosphere using COSMIC electron density profiles [J]. *J. Geophys. Res.: Space Phys.*, 2018, **123**:8766-8777

[17] LI Qiaoling, LIU Libo, JIANG Jinzhe, *et al.* α-Chapman scale height: longitudinal variation and global modeling [J]. *J. Geophys. Res.: Space Phys.*, 2019, **124**:2083-2098

[18] CHEN Y, LIU L, LE H, *et al.* Responses of solar irradiance and the ionosphere to an intense activity region [J]. *J. Geophys. Res.: Space Phys.,* 2018, **123**:2116-2126

[19] CHEN Y, LIU L, LE H, *et al.* Interhemispheric conjugate effect in longitude variations of mid-latitude ion density [J]. *J. Space Weather Space Clim.,* 2019, **9**:A40

[20] LI Q, HAO Y, ZHANG D, *et al.* Nighttime enhancements in the midlatitude ionosphere and their relation to the plasmasphere [J]. *J. Geophys. Res.: Space Phys.*, 2018, **123**:7686-7696

[21] ZHONG J, LEI J, YUE X, *et al.* Middle-latitudinal band structure observed in the nighttime ionosphere [J]. *J. Geophys. Res.: Space Phys.*, 2019, **124**:5857-5873

[22] LI Z, LUAN X, REN D. Longitudinal variations of the occurrence probability of the ionospheric F1 layer peak at middle and high latitudes [J]. *J. Geophys. Res.: Space Phys.*, 2019, **124**: 9592-9609

[23] ZHONG J, LEI J, YUE X, *et al.* Empirical orthogonal function analysis and modeling of the topside ionospheric and plasmaspheric TECs [J]. *J. Geophys. Res.: Space Phys.*, 2019, **124**:3681-3698

[24] YANG N, LE H, LIU L, *et al.* Statistical behavior of the longitudinal variations of the evening topside midlatitude trough position in both Northern and Southern Hemispheres [J]. *J. Geophys. Res.: Space Phys.*, 2018, **123**:3983-3997

[25] YANG N, YU T, LE H, *et al.* The high-latitude trough in the Southern Hemisphere observed by Swarm-A satellite [J]. *J. Geophys. Res.: Space Phys.*, 2019, **124**:9475-9485

[26] ZHANG Qinghe, LOCKWOOD Michael, FOSTER John C, *et al.* Observation of the step-like accelerating processes of cold ions in the reconnection layer at the dayside magnetopause [J]. *Sci. Bull.*, 2018, **63**:31-37

[27] DING Z H, DAI L D, YANG S, *et al.* Preliminary measurement and analysis of the power spectra by the Qujing incoherent scatter radar [J]. *Prog. Geophys.*, 2018, **33**(6): 2204-2210

[28] DING Z H, DAI L D, YANG S, *et al.* Preliminary analysis of the ionospheric electron temperature variations of F layer in daytime using the Qujing incoherent scatter radar measurements [J]. *Chin. J. Geophys.*, 2020, **63**(2). DOI: 10.6038/cjg2020N091

[29] YANG Shenggao, ZHANG Beichen, LIU Yang, *et al.* Case studies: a possible mechanism for F_2-lacuna formation [J]. *Adv. Space Res.*, 2019, **64**:2290-2304

[30] ZHANG K, WANG W, WANG H, *et al.* The longitudinal variations of upper thermospheric zonal winds observed by CHAMP satellite at low and midlatitudes [J]. *J. Geophys. Res.: Space Phys.*, 2018, **123**(11):9625-9668

[31] CHEN G, WANG J, ZHANG S, *et al.* Opposite latitudinal dependence of the premidnight and postmidnight oscillations in the electron density of midlatitude F layer [J]. *J. Geophys. Res.: Space Phys.*, 2018, **123**:796-807

[32] DANG T, LEI J, WANG W, *et al.* Global responses of the coupled thermosphere and ionosphere system to the August 2017 great American solar eclipse [J]. *J. Geophys. Res.: Space Phys.*, 2018, **123**:7040-7050

[33] LEI J, DANG T, WANG W, *et al.* Long-lasting response of the global thermosphere and ionosphere to the 21 August 2017 solar eclipse [J]. *J. Geophys. Res.: Space Phys.,* 2018, **123**:4309-4316

[34] DANG T, LEI J, WANG W, *et al.* Suppression of the polar tongue of ionization during the 21 August 2017 solar eclipse [J]. *Geophys. Res. Lett.*, 2018, **45**:2918-2925

[35] SUN Y Y, LIU J Y, LIN C H, *et al.* Ionospheric bow wave induced by the moon shadow ship over the continent of United States on 21 August 2017 [J]. *Geophys. Res. Lett.*, 2018, **45**(2):538-544

[36] YUE X, HU L, WEI Y, *et al.* Ionospheric trend over Wuhan during 1947-2017: comparison between simulation and observation [J]. *J. Geophys. Res.: Space Phys.*, 2018, **123**:1396-1409

[37] CAI Y, YUE X, WANG W, *et al.* Long-term trend of topside ionospheric electron density derived from DMSP data during 1995-2017 [J]. *J. Geophys. Res.: Space Phys.*, 2019, **124**. DOI:10.1029/2019JA027522

[38] CHEN T, WAN W, XIONG J, *et al.* A statistical approach to quantify atmospheric contributions to the ITEC WN4 structure over low latitudes [J]. *J. Geophys. Res.: Space Phys.*, 2019, **124**:2178-2197

[39] MO X H, ZHANG D H. Lunar tidal modulation of periodic meridional movement of equatorial ionization anomaly crest during sudden stratospheric warming [J]. *J. Geophys. Res.: Space Phys.*, 2018, **123**:1488-1499

[40] LIU J, ZHANG D H, HAO Y Q, *et al.* The comparison of lunar tidal characteristics in the low-latitudinal ionosphere between East Asian and American sectors during stratospheric sudden warming events: 2009--2018 [J]. *J. Geophys. Res.: Space Phys.*, 2019, **124**:7013-7033

[41] CHEN J, LEI J. A simulation study on the latitudinal variations of ionospheric zonal electric fields under geomagnetically quiet conditions [J]. *J. Geophys. Res.: Space Phys.*, 2019, **124**:1444-1453

[42] DANG T, LEI J, WANG W, *et al.* Formation of double tongues of ionization during the 17 March 2013 geomagnetic storm [J]. *J. Geophys. Res.: Space Phys.*, 2019, **124**. DOI:10.1029/2019JA027268

[43] DANG T, ZHANG B, WILTBERGE M, *et al.* On the relation between soft electron precipitations in the cusp region and solar wind coupling functions [J]. *J. Geophys. Res.: Space Phys.*, 2018, **123**:211-226

[44] WU Y W, LIU R Y, ZHANG B C, *et al.* The UT variation of the polar ionosphere based on COSMIC observations [J]. *J. Geophys. Res.: Space Phys.*, 2019, **124**:3139-3148

[45] GUO D, LEI J, RIDLEY A, *et al.* Low-density cell of the thermosphere at high latitudes revisited [J]. *J. Geophys. Res.: Space Phys.*, 2019, **124**:521-533

[46] WENG L, LEI J, LIU H, *et al.* Thermospheric density cells at high latitudes as observed by GOCE satellite: Preliminary results [J]. *Geophys. Res. Lett.*, 2019, **46**:11615-11621

[47] WENG L, LEI J, DOORNBOS E, *et al.* Seasonal variations of thermospheric mass density at dawn/dusk from GOCE observations [J]. *Ann. Geophys.*, 2018, **36**:489-496

[48] RUAN H, LEI J, DOU X, *et al.* An exospheric temperature model based on CHAMP observations and TIEGCM simulations [J]. *Space Weather*, 2018, **16**:147-156

[49] RUAN H, LEI J. Quantifying the impact of satellite sampling on the dynamic modeling of the upper thermosphere [J]. *Space Weather*, 2019, **17**:757-766

[50] REN D, LEI J, WANG W, *et al.* A simulation study on the time delay of daytime thermospheric temperature response to the 27-day solar EUV flux variation [J]. *J. Geophys. Res.: Space Phys.*, 2019, **124**:9184-9193

[51] OWOLABI C, LEI J, BOLAJI O S, *et al.* Investigation on the variability of the geomagnetic daily current during sudden stratospheric warmings [J]. *J. Geophys. Res.: Space Phys.*, 2019, **124**: 6156-6172

[52] LIU G, HUANG W, SHEN H, *et al.* Ionospheric response to the 2018 sudden stratospheric warming event at middle-and low-latitude stations over China sector [J]. *Space Weather*, 2019, **17**:1230-1240

[53] SUN Y Y. GNSS brings us back on the ground from ionosphere [J]. *Geosci. Lett.*, 2019, **6**. DOI:10.1186/s40562-019-0144-0

[54] SUN Y Y, LIU J Y, WU T Y, *et al.* Global distribution of persistence of total electron content anomaly [J]. *Atmosphere*, 2019, **10**:297

[55] SUN Y Y, LIU H, MIYOSHI Y, *et al.* El Niño-Southern Oscillation effect on ionospheric tidal/SPW amplitude in 2007--2015 FORMOSAT-3/COSMIC observations [J]. *Earth Planet Space*, 2019, **71**:35

[56] SUN Y Y, LIU H, MIYOSHI Y, *et al.* El Niño - Southern Oscillation effect on quasi-biennial oscillations of temperature diurnal tides in the mesosphere and lower thermosphere [J]. *Earth Planet Space*, 2018, **70**:85

[57] WANG H, ZHANG K, ZHENG Z, *et al.* The effect of subauroral polarization streams on the mid-latitude thermospheric disturbance neutral winds: a universal time effect [J]. *Ann. Geophys.*, 2018, **36**(2):509-525

[58] WANG H, LÜHR H, ZHENG Z, *et al.* Dependence of the equatorial electrojet on auroral activity and in situ solar insulation [J]. *J. Geophys. Res.: Space Phys.*, 2019, **124**. DOI:10.1029/2019JA027320

[59] YAN X, SUN Y, YU T, *et al.* Stratosphere perturbed by the 2011 Mw9.0 Tohoku earthquake [J]. *Geophys. Res. Lett.*, 2018, **45**(19):10050-10056

[60] YAN X, YU T, SUN Y, *et al.* Vertical structure of the ionospheric response following the Mw 7.9 Wenchuan earthquake on 12 May 2008 [J]. *Pure Appl. Geophys.*, 2019. DOI:10.1007/s00024-019-02175-7

[61] LIU Y, ZHOU C, TANG Q, *et al.* Geomagnetic conjugate observations of ionospheric disturbances in response to a North Korean underground nuclear explosion on 3 September 2017 [J]. *Ann. Geophys.*, 2019, **37**:337-345

[62] JIN Y Y, XING Z Y, ZHANG Q H, *et al.* Polar cap patches observed by the EISCAT Svalbard Radar: a statistical study of its dependence on the solar wind and IMF conditions [J]. *J. Atmos. Sol.: Terr. Phys.*, 2019, **192**:104768

[63] XING Z, ZHANG Q, HAN D, *et al.* Conjugate observations of the evolution of polar cap arcs in both hemispheres [J]. *J. Geophys. Res.: Space Phys.*, 2018, **123**:1794-1805

[64] WANG Y, ZHANG Q H, JAYACHANDRAN P T, *et al.* Experimental evidence on the dependence of the standard GPS phase scintillation index on the ionospheric plasma drift around noon sector of the polar ionosphere [J]. *J. Geophys. Res.: Space Phys.*, 2018, **123**:2370-2378

[65] PRIYADARSHI Shishir, ZHANG Qinghe, WANG Yong. An empirical L-band scintillation model for a mid-latitude station, Weihai, China during the low solar activity period [J]. *Sci. China: Technol. Sci.*, 2019, **62**:1182

[66] MA Y Z, ZHANG Q H, XING Z Y, *et al.* Combined contribution of solar illumination, solar activity, and convection to ion upflow above the polar cap [J]. *J. Geophys. Res.: Space Phys.*, 2018, **123**:4317-4328

[67] MA Y Z, ZHANG Q H, XING Z Y, *et al.* The ion/electron temperature characteristics of polar cap classical and hot patches and their influence on ion upflow [J]. *Geophys. Res. Lett.*, 2018, **45**:8072-8080

[68] AA E, HUANG W, LIU S, *et al.* Midlatitude plasma bubbles over China and adjacent areas during a magnetic storm on 8 September 2017 [J]. *Space Weather*, 2018, **16**:321-331

[69] AA E, ZOU S, RIDLEY A J, *et al.* Merging of storm time midlatitude traveling ionospheric disturbances and equatorial plasma bubbles [J]. *Space Weather*, 2019, **17**:285-298

[70] AA E, ZOU S, EASTES R, *et al.* Coordinated ground-based and space-based observations of equatorial plasma bubbles [J]. *J. Geophys. Res.: Space Phys.*, 2020, **125**:285-298

[71] LI G, NING B, WANG C, *et al.* Storm-enhanced development of postsunset equatorial plasma bubbles around the meridian 120°E/60°W on 7-8 September 2017 [J]. *J. Geophys. Res.: Space Phys.*, 2018, **123**:7985-7998

[72] LI G, NING B, ABDU M A, *et al.* Daytime F-region irregularity triggered by rocket-induced ionospheric hole over low latitude [J]. *Prog. Earth Planet. Sci.*, 2018, **5**:11

[73] XIE H, LI G, ZHAO X, *et al.* Statistical study on the occurrences of postsunset ionospheric E, valley, and F region irregularities and their correlations over low-latitude Sanya [J]. *J. Geophys. Res.: Space Phys.*, 2018, **123**:9873-9880

[74] LIU K, LI G, NING B. Possible evidence for small-scale wave seeding of equatorial plasma bubbles [J]. *Adv. Space Res.*, 2019, **63**(11):3612-3620

[75] LUO W, XIONG C, ZHU Z, *et al.* Onset condition of plasma density enhancements: a case study for the effects of meridional wind during 17-18 August 2003 [J]. *J. Geophys. Res.: Space Phys.*, 2018, **123**:6714-6726

[76] YU T, MIYOSHI Y, XIA C, *et al.* Solar dependence of equatorial F region irregularities observed by COSMIC radio occultations [J]. *J. Geophys. Res.: Space Phys.*, 2018, **123**:9775-9787

[77] YU T, LI M, XIA C, *et al.* A new method for deriving equatorial plasma bubble velocity by tracing OI 630 nm all-sky images [J]. *J. Geophys. Res.: Space Phys.*, 2018, **123**:9619-9633

[78] WU Kun, XU Jiyao, XIONG Chao, *et al.* Edge plasma enhancements of equatorial plasma depletions observed by All-Sky imager and the C/NOFS satellite [J]. *J. Geophys. Res.: Space Phys.*, 2018, **123**:8835-8849

[79] WANG Z, LIU H, SHI J, *et al.* Plasma blobs concurrently observed with bubbles in the Asian-Oceanian sector during solar maximum [J]. *J. Geophys. Res.: Space Phys.*, 2019, **124**:7062-7071

[80] ZHANG M, ZHANG D H, HAO Y Q, *et al.* A statistical study on L-band ionospheric amplitude scintillation in Shenzhen during 2011--2016 (in Chinese) [J]. *Sci. Sin. Tech.*, 2019, **49**:1570-1582

[81] XU L, CHENG J, XU J S. Statistical features of TEC and ionospheric scintillation over the low latitude of China [J]. *Adv. Space Res.*, 2019, **64**:2164-2175

[82] WANG Guojun, SHI Jiankui, BAI Weihua, *et al.* Global ionospheric scintillations revealed by GPS radio occultation data with FY3C satellite before midnight during the March 2015 storm [J]. *Adv. Space Res.*, 2019, **63**:3119-3130

[83] WANG Ning, GUO Lixin, ZHAO Zhenwei, *et al.* Spread-F occurrences and relationships with f_0F_2 and h'F at low- and mid-latitudes in China [J]. *Earth Planet. Space*, 2018, **70**:59

[84] WANG Ning, GUO Lixin, DING Zonghua, *et al.* Longitudinal differences in the statistical characteristics of ionospheric spread-F occurrences at mid-latitude in Eastern Asia [J]. *Earth Planet. Space*, 2019, **71**:47

[85] WANG Ning, GUO Lixin, ZHAO Zhenwei, *et al.* A comparative study of ionospheric spread-F and scintillation at low- and mid-latitudes in China during the 24th solar cycle [J]. *Adv. Space Res.*, 2019, **63**(2):986-998

[86] LIU Y, ZHOU C., TANG Q, *et al.* The seasonal distribution of sporadic E layers observed from radio occultation measurements and its relation with wind shear measured by TIMED/TIDI [J]. *Adv. Space Res.*, 2018, **62**(2):426-439

[87] ZHOU C, LIU Y, TANG Q, *et al.* Investigation on the occurrence of Mid-Latitude E-Region irregularity by Wuhan VHF radar and its relationship with sporadic E layer [J]. *IEEE Trans. Geosci. Remote Sens.*, 2018, **56**(12):7207-7216

[88] LIU Y, ZHOU C, TANG Q, *et al.* Evidence of mid- and low-latitude nighttime ionospheric E–F coupling: coordinated observations of sporadic E layers, F -Region Field-Aligned irregularities, and medium-scale traveling ionospheric disturbances [J]. *IEEE Trans. Geosci. Remote Sens.*, 2019, **57**:7547-7557

[89] CHEN G Y, ZHOU C, LIU Y, *et al.* A statistical analysis of medium-scale traveling ionospheric disturbances during 2014--2017 using the Hong Kong CORS network [J]. *Earth Planet. Space*, 2019, **71**:52

[90] JIANG C, YANG G, LIU J, *et al.* A study of the F_2 layer stratification on ionograms using a simple model of TIDs [J]. *J. Geophys. Res.: Space Phys.*, 2019, 124:1317-1327

[91] JIANG C, HU H, YANG G, *et al.* A statistical study of the F_2 layer stratification at the northern equatorial ionization anomaly [J]. *Adv. Space Res.*, 2019, **63**(10):3167-3176

[92] YANG G, JIANG C, LAN T, *et al.* Ionosonde observations of daytime spread F at middle latitudes during a geomagnetic storm [J]. *J. Atmos. Sol.: Terr. Phys.*, 2018, **179**:174-180

[93] LAN T, ZHANG Y, JIANG C, *et al.* Automatic identification of Spread F using decision trees [J]. *J. Atmos. Sol.: Terr. Phys.,* 2018, **179**:389-395

[94] LAN T, JIANG C, YANG G, *et al.* Statistical analysis of low-latitude spread F observed over Puer, China, during 2015-2016 [J]. *Earth Planets Space*, 2019, **71**:138

[95] ZHOU C, TANG Q, HUANG F, *et al.* The simultaneous observations of nighttime ionospheric E region irregularities and F region medium-scale traveling ionospheric disturbances in midlatitude China [J]. *J. Geophys. Res.: Space Phys.,* 2018, **123**:5195-5209

[96] MENG X, FANG H, LI G, *et al.* Observations of evolution-type band - like structures of F region irregularities [J]. *J. Geophys. Res.: Space Phys.*, 2019, **124**:1426-1443

[97] LIU Y, LEI J, YU P, *et al.* Spontaneous emission of alfvénic branch oscillations from a strong inhomogeneous plasma flow [J]. *Geophys. Res. Lett.*, 2018, **45**(2):64-70

[98] LIU Y, LEI J, YU P, *et al.* Laboratory excitation of the Kelvin-Helmholtz instability in an ionospheric-like plasma [J]. *Geophys. Res. Lett.*, 2018, **45**(9):3846-3853

[99] AA E, RIDLEY A J, HUANG W, *et al.* An ionosphere specification technique based on data ingestion algorithm and empirical orthogonal function analysis method [J]. *Space Weather*, 2018, **16**:1410-1423

[100] SHE C, YUE X, HU L, *et al.* Estimation of ionospheric total electron content from a Multi-GNSS station in China [J]. *IEEE Trans. Geosci. Remote Sens.*, 2019. DOI: 10.1109/TGRS.2019.2941049

[101] HE J, YUE X, WANG W, *et al.* EnKF ionosphere and thermosphere data assimilation algorithm through a sparse matrix method [J]. *J. Geophys. Res.: Space Phys.*, 2019, **124**:7356-7365

[102] LIU Z, FANG H, WENG L, *et al.* A comparison of ionosonde measured f_0F_2 and IRI-2016 predictions over China [J]. *Adv. Space Res.*, 2019, **63**(6):1926-1936

[103] WANG Sicheng, HUANG Sixun, FANG Hanxian. Dual-parameter regularization method in three-dimensional ionospheric reconstruction [J]. *Ann. Geophys.*, 2018, **36**:1255-1266

[104] WANG Sicheng, HUANG Sixun, LU Shuai, *et al.* Three-dimensional ionospheric tomography using model function in the modified L-curve method [J]. *IEEE Trans. Geosci. Remote Sens.,* 2019, **57**(6):3135-3147

[105] ZHAO X R, SHENG Z, LI J W, *et al.* Determination of the "wave turbopause" using a numerical differentiation method [J]. *J. Geophys. Res.: Atmos.*, 2019, **124**:10592-10607

[106] LAN J, NING B, LI G, *et al.* Observations of short-period ionospheric disturbances using a portable digital ionosonde at Sanya [J]. *Radio Sci.*, 2018, **53**:1521-1532

[107] CHEN Z, GONG Z, ZHANG F, *et al.* A new ionogram automatic scaling method [J]. *Radio Sci.*, 2018, **53**(9):1149-1164

[108] LI G, NING B, ZHAO X, *et al.* Low latitude ionospheric TEC oscillations associated with periodic changes in IMF Bz polarity [J]. *Geophys. Res. Lett.*, 2019, **46**:9379-9387

[109] HUANG F, LEI J, DOU X, *et al.* Nighttime medium-scale traveling ionospheric disturbances from airglow imager and Global Navigation Satellite Systems observations [J]. *Geophys. Res. Lett.*, 2018, **45**:31-38

[110] HUANG F, OTSUKA Y, LEI J, *et al.* Daytime periodic wave-like structures in the ionosphere observed at low latitudes over the Asian-Australian sector using total electron content from Beidou geostationary satellites [J]. *J. Geophys. Res.: Space Phys.*, 2019, **124**:2312-2322

[111] ZHAO J, ZHOU C. On the optimal height of ionospheric shell for single-site TEC estimation [J]. *GPS Solut.*, 2018, **22**(2):48

[112] ZHAO J, ZHOU C. Validation and application of optimal ionospheric shell height model for single-site estimation of total electron content [J]. Ann. Geophys. 2019, **37**(2):263-271

[113] LI M, YUAN Y, WANG N, *et al.* Estimation and analysis of the short-term variations of multi-GNSS receiver differential code biases using global ionosphere maps [J]. *J. Geod.*, 2018, **92**:889-903

[114] ZHAO C, YUAN Y, ZHANG B, *et al.* Ionosphere sensing with a low-cost, single-frequency, multi-GNSS receiver [J]. *IEEE Trans. Geosci. Remote Sens.*, 2018, **57**(2):881-892

[115] SUN W, NING B, YUE X, *et al.* Strong sporadic E occurrence detected by ground-based GNSS [J]. *J. Geophys. Res.: Space Phys.*, 2018, **123**:3050-3062

[116] LIU H, DING F, YUE X, *et al.* Depletion and traveling ionospheric disturbances generated by two launches of China's Long March 4B rocket [J]. *J. Geophys. Res.: Space Phys.,* 2018, **123**:10319-10330

[117] HAO Y, LI Q, ZHANG D, *et al.* Using GNSS TEC technique to observe compression of the plasmasphere by an interplanetary shock [J]. *Sci. Sin. Tech.*, 2018, **48**:853-862

[118] DING Zonghua, WU Jian, XU Bin, *et al.* The Qujing incoherent scatter radar: system description and preliminary measurements [J]. *Earth Planet. Space*, 2018, **70**:87

[119] WU Jun, WU Jian, RIETVELD M T, *et al.* The extending of observing altitudes of plasma and ion lines during ionospheric heating [J]. *J. Geophys. Res.: Space Phys.,* 2018, **123**:918-930

[120] WU Jun, WU Jian, RIETVELD M T, *et al.* The intensities of high frequency-enhanced plasma and ion lines during ionospheric heating [J]. *J. Geophys. Res.: Space Phys.*, 2019, **124**(1):603-615

[121] LV Libin, LI Qingliang, HAO Shuji, *et al.* Study on scattering characteristic of AFAI in ionospheric heating by powerful high frequency waves [J]. *Chin. J. Geophys.*, 2018, **61**(6):2177-2185

[122] XU Tong, RIETVELD Michael, WU Jian, *et al.* Polarization analysis of ELF/VLF waves generated by beating of two HF waves in the polar ionosphere [J]. *J. Atmos. Sol.: Terr. Phys.,* 2019, **195**:105-133

[123] YANG Jutao, LI Qingliang, HAO ShuJi, *et al.* Theoretical analysis of parameter optimization for lower-ionosphere modulated excitation VLF/ELF waves [J]. *Chin. J. Geophys.*, 2018, **61**(2):477-483

[124] YANG Jutao, LI Qingliang, WANG Jianguo, *et al.* The polarization characteristics of ELF/VLF waves generated via HF heating experiments of the ionosphere by EISCAT [J]. *Phys. Plasmas*, 2018, **25**:92902

[125] YANG Jutao, WANG Jianguo, LI Qingliang, *et al.* Experimental comparisons between AM and BW modulation heating excitation of ELF/VLF waves at EISCAT [J]. *Phys. Plasmas*, 2019, **26**(8):82901

[126] YU T, REN Z, YUE X, *et al.* Comparison of thermospheric density between GUVI dayside limb data and CHAMP satellite observations: based on empirical model [J]. *J. Geophys. Res.: Space Phys.*, 2019, **124**:2165-2177

[127] LI G, NING B, LI A, *et al.* First results of optical meteor and meteor trail irregularity from simultaneous Sanya radar and video observations [J]. *Earth Planet. Phys*, 2018, **2**:15-21

[128] BAI Weihua, WANG Guojun, SUN Yueqiang, *et al.* Application of the Fengyun 3 C GNSS occultation sounder for assessing the global ionospheric response to a magnetic storm event [J]. *Atmos. Meas. Tech.*, 2019, **12**:1483-1493

[129] SUI Y, FU H, XU F, *et al.* Estimation of ionospheric effects on spacebore twinsar-L SAR Interferograms [C]. IGARSS 2019-2019 IEEE International Geoscience and Remote Sensing Symposium.IEEE Geoscience and Remote Sensing Symposium, 2019:2081-2084

[130] FU H Y, SCALES W A, BERNHARDT P A, *et al.* Asymmetry in stimulated emission polarization and irregularity evolution during ionospheric electron gyroharmonic heating [J]. *Geophys. Res. Lett.*, 2018, **45**:9363-9371

[131] FU H Y, SCALES W A. Kinetic modeling of stimulated electromagnetic emissions during ionospheric heating experiment [C]//12th International Symposium on Antennas, Propagation and EM Theory (ISAPE). IEEE, 2018:1-3

[132] WANG X, ZHOU C. Electron density inversed by plasma lines induced by suprathermal electron in the ionospheric modification experiment [J]. *Adv. Space Res.*, 2018, **61**(9):2252-2258

[133] WANG X, ZHOU C, LIU M, *et al.* Threshold of parametric instability in the ionospheric heating experiments [J]. *Plasma Sci. Technol.*, 2018, **20**(11):115301-115301

[134] WANG X, ZHOU C, LIU M, *et al.* Density disturbance of small-scale field aligned irregularities in the ionosphere heating experiments [J]. *Plasma Sci. Technol.*, 2018, **20**(12):125001-125010

[135] WANG X, ZHOU C, XU T, *et al.* Stimulated electromagnetic emissions spectrum observed during an X-mode heating experiment at the European Incoherent Scatter Scientific Association [J]. *Earth Planet. Phys.*, 2019, **3**(5):391-399

[136] LIU M, ZHOU C, WANG X, *et al.* Numerical simulation of oblique ionospheric heating by powerful radio waves [J]. *Ann. Geophys.*, 2018, **36**(3):855-866

CHEN Zeyu, CHEN Hongbin, XU Jiyao, HUANG Kaiming, XUE Xianghui, HU Dingzhu, CHEN Wen, YANG Guotao, TIAN Wenshou, HU Yongyun, XIA Yan. Advances in the Researches of the Middle and Upper Atmosphere in China. *Chin. J. Space Sci.*, 2020, **40**(5): 304-322. DOI:10.11728/cjss2020.05.304

Advances in the Researches of the Middle and Upper Atmosphere in China

CHEN Zeyu[1,6] CHEN Hongbin[1,6] XU Jiyao[2,6] HUANG Kaiming[3]

XUE Xianghui[4] HU Dingzhu[5] CHEN Wen[1,6] YANG Guotao[2]

TIAN Wenshou[7] HU Yongyun[8] XIA Yan[8]

1 (*LAGEO, Institute of atmospheric physics, Chinese Academy of Sciences, Beijing* 100029)

2 (*National Space Science Center, Chinese Academy of Sciences, Beijing* 100190)

3 (*School of Electronic Information, Wuhan University, Wuhan* 430072)

4 (*School of Earth and Space Sciences, University Science and Technology of China, Hefei* 230026)

5 (*School of Physics, Nanjing University of Information Science and Technology, Nanjing* 210044)

6 (*School of Earth Science, University of Chinese Academy of Sciences, Beijing* 100049)

7 (*College of Atmospheric Science, Lanzhou University, Lanzhou* 730000)

8 (*School of Physics, Peking University, Beijing* 100871)

Abstract In this report we summarize the research results by Chinese scientists in 2018–2020. The focuses are placed on the researches of the middle and upper atmosphere, specifically the researches on atmospheric structure and composition, climate and chemistry-climate coupling and climate modelling, dynamics in particular those inducing the coupling of the atmospheric layers.

Key words Middle and upper atmosphere, Structure and composition, Climate, Layer coupling

Classified index P 351

1 Structure and Composition in the Middle Atmosphere

Xia *et al.*[1] investigated the impact of tropical tropopause warming on the stratospheric water vapor using the Specified-Dynamics version of the NCAR Whole Atmosphere Community Climate Model. It is found that the tropical tropopause warming results in a strengthening of the Brewer-Dobson Circulation (BDC). The strengthening of BDC induced by a narrow warming of tropical tropopause within 12° latitude, which is much stronger in boreal winter than that in boreal summer, propagates more dry air from the tropical tropopause into the stratosphere and thus causes a reduction of water vapor in the middle stratosphere. On the contrary, the seasonal difference of the BDC strengthening is weaker in the experiment with a broader tropical tropopause warming within 25° latitude. The drying effect of the BDC is counteracted by the moistening effects of the tropical tropopause warming and methane oxidation. This leads to the moistening in both the lower and upper stratosphere. The results suggest the control of the stratospheric humidity by the tropical tropopause temperature could be significantly offset by the associated BDC changes.

Xia *et al.*[2] showed that stratospheric ozone-induced cloud radiative effects also play important roles in causing changes in Antarctic sea ice. Their simulations demonstrate that the recovery of the

Received June 23, 2020

E-mail: chb@mail.iap.ac.cn

Antarctic Ozone Hole causes decreases in clouds over Southern Hemisphere (SH) high latitudes and increases in clouds over the SH extratropics. The decrease in clouds leads to a reduction in downward infrared radiation, especially in austral autumn. This results in the cooling of the Southern Ocean surface and increasing Antarctic sea ice. Surface cooling also involves ice-albedo feedback. Increasing sea ice reflects solar radiation and causes further cooling and more increases in Antarctic sea ice.

Liu and Fu[3] constructed an approximate month-to-month temperature change equation and extended it to a new form for decade-to-decade changes. Their result showed that at 100 hPa, the month-to-month Arctic temperature increment is a small term compared to the dynamical heating and diabatic heating, which are largely canceling terms with maximum magnitudes in November to April and October to March, respectively. However, it is not the case for their decadal changes and the decadal change of the Arctic current-month temperature compared to those of the regressed dynamical heating and radiative heating, where the current-month decadal changes and the corresponding trends are approached except in March and a rough agreement exists between these trends and those reported in other studies. The dynamical plus diabatic heating term and the temperature increment, as well as their decadal changes, are roughly balanced during the annual oscillation. However, some departures exist in both cases because of the large deviations or uncertainties of relevant terms and also probably due to the quasi-geostrophic approximation and the eddy heat flux approximation of the dynamical heating, and a restricted condition of the eddy heat flux approximation is given at the end.

Based on measurements of the solar cycle by the Spectral Irradiance Monitor onboard the SORCE satellite, monthly ERA-Interim Reanalysis data, the radiative transfer scheme of the Beijing Climate Center (BCC-RAD) and a multiple linear regression model, Shi *et al.*[4] showed that during periods of strong solar activity, the solar shortwave heating anomaly from the climatology in the tropical upper stratosphere triggers a local warm anomaly and strong westerly winds in mid-latitudes, which strengthens the upward propagation of planetary Wave 1 but prevents that of Wave 2. The enhanced westerly jet makes a slight adjustment to the propagation path of Wave 1, but prevents Wave 2 from propagating upward, decreases the dissipation of Wave 2 in the extratropical upper stratosphere and hence weakens the Brewer-Dobson circulation. The adiabatic heating term in relation to the Brewer-Dobson circulation shows anomalous warming in the tropical lower stratosphere and anomalous cooling in the mid-latitude upper stratosphere.

Hu *et al.*[5] found an out-of-phase relationship between the northern Hadley Circulation (HC) Extent (HCE) and Arctic Stratospheric Ozone (ASO) during boreal spring on interannual timescales during 1979–2014. Decreased (increased) ASO tends to result in a poleward (equatorward) shift of HCE by +0.67° (– 0.45°) latitude per standard deviation of decreased (increased) ASO year. Observational analysis and model simulations showed that increased ASO leads to an equatorward shift of HCE and subtropical moistening *via* weakened eddy momentum flux and decreased subtropical static stability, accompanied with negative eddy momentum flux divergence anomalies and northward meridional wind anomalies over the subtropics. Their results may help to understand the linkage between the Arctic and mid-latitudes, especially important for the subtropical precipitation and hydrological cycle.

Ma *et al.*[6] reported a Rayleigh and sodium lidar system, which was recently upgraded at the University of Science and Technology of China (USTC) in Hefei, China (31.5°N, 117°E). The lidar system has features of high temporal and vertical resolutions, a high Signal-to-Noise Ratio (SNR), and mobility. Using the time-division and wavelength-division multiplexing methods, only one piece of the photomultiplier tube is used in the optical receiver, which makes the system compact and robust. Wideband filtering and narrowband filtering are both used in the lidar system to obtain high SNR data under city lights. The lidar system was established on 24 September

2016 and has run stably for 2 years. Meteor trail events that lasted for only a few seconds were extracted from the high resolution, high SNR observational data. The sodium observational data in 2017 were fitted annually and semiannually, and the results were similar to those obtained in previous studies. The monthly average atmospheric temperature showed semiannual variations. Stratospheric aerosols were observed for two consecutive days during the observations.

Zou *et al.*[7] presented a general response of the high latitude mesospheric HO_2 and O_3 to several extremely large SPEs, using the Microwave Limb Sounder (MLS) observations onboard the Aura satellite. Through complicate ion chemistry, energetic protons that deposited in the atmosphere lead to the HO_2 enhancement of more than 0.2 ppbv (part per billion volume) above 0.2 hPa for 2 days. In a similar height range, the catalytic decomposition of O_3 is more than about 10% and the peak values of about >20% can last 1~3 days. The superposition analysis found that the O_3 depletion was delayed by 1 day relative to the HO_2 increment, which further indicates that HO_2 catalyzes the decomposition of O_3.

Xun *et al.*[8] reported the first concurrent observations of thermospheric Na layers from two nearby lidar stations located at Yanqing (40.5°N, 116.0°E) and Pingquan (41.0°N, 118.7°E). From one year data set, they found four such layers, including an unprecedented one reaching 200 km with the highest density of 35 cm^{-3} and fastest descending rate. While the main Na layers were comparable, in three nights, these thermospheric layers were observed only in one station (Yanqing), suggesting that these layers often occur locally with a horizontal scale less than about 250 km. They tabulate, compare, and discuss the principle characteristics of all the reported thermospheric layers.

Jiao *et al.*[9] presented the first simultaneous observation of mesopause sodium (Na) and potassium (K) layer by a Na-K lidar at the South Hemisphere site, São José dos Campos (23.1°S, 45.9°W). On 21 November 2016, sporadic layers in both Na and K layer occurred in main layer height with obvious descending variations with time, which seems like tidal induced. Notably, the peak K/Na ratio slowly increased with time. And Na layer and K layer showed different processes along with time with K density reaching its maximum 1 h later than that of Na.

Wang *et al.*[10] found a special behavior of the potassium layer in the mesopause region, by analyzing Yanqing lidar data. They called it as lower-triangle potassium layer, which appeared frequently in January. The frequent appearance of the lower-triangle potassium layer has made the average column density and peak density increase by 15.7% and 12.9%. It can be speculated that the increasing potassium atoms in the lower-triangle potassium layer were mainly converted from KO_2, and partly from KOH.

Yang *et al.*[11] found a prominent Sporadic Sodium Layer (SSL), which is the largest one in 222 SSL events found from Haikou lidar data. The peak density of this large SSL was as high as 37087 cm^{-3}. By comparing the corresponding data of the nearest ionosonde and VHF radar at Danzhou (19.5°N, 109.1°E), it was found that SSL is closely related to Es.

Based on the FPI observations and HWM14 and TIEGCM model results, Jiang *et al.*[12] studied the thermospheric horizontal winds at three FPI stations: Xinglong (40.2°N, 117.4°E), Kelan (38.7°N, 111.6°E) and Millstone Hill (42.6°N, 71.5°W). The results showed that the winds at Millstone Hill were more southward and more westward in four seasons compared to the other two stations; the directional reversal time of zonal winds at Millstone Hill was earlier than the other two stations. TIEGCM model was more consistent with FPI observations in the winter months compared to summer. Furthermore, TIEGCM model could in general replicate the observations at Millstone Hill. HWM14 model-data discrepancies mainly appeared in the winter zonal winds. Overall, among three stations, HWM14 predicted MH FPI observations best.

Liu *et al.*[13] studied the responses of neutral temperature in the lower thermosphere to the 2013 St. Patrick's Day geomagnetic storm based on

TIMED/SABER and AIM/SOFIE satellites observations. The results indicated that the temperature in the two hemispheres varied drastically due to the storm. The variation of the temperature depended on latitude, altitude, and the phase of the storm, and the maximum variation of the temperature could exceed 15 K. The temperature increase reached its peak 0.5~1.5 d (depending on latitude and height) after that the *AE* index reached its peak.

Liu *et al.*[14] studied the responses of the multi-day oscillations in thermospheric temperature to oscillations in $F_{10.7}$ and *Ap* index by using the nighttime thermospheric temperature (about 250 km) measured by FPI at Xinglong (40.2°N, 117.4°E) station between 2010 and 2018. The results showed that the 27, 13.5, 9, and 7-day oscillations depended on solar phases. The 27-day oscillation was predominant during solar maximum and highly correlated with the $F_{10.7}$ and *Ap* index. The 13.5, 9, and 7-day oscillations were important and highly correlated with *Ap* index during solar ascending phase.

In addition, Yang *et al.*[15] compared three methods (radius method, complete Fourier series description method and nonlinear regression fitting method) to derive neutral winds from ground-based FPI observation. The results showed that the nonlinear regression fitting method was the best because more comprehensive fringe information was taken into account to derive the neutral winds by this method.

Xu *et al.*[16] simulated the impacts of super volcanoes on ozone depletion by using a transport model and a coupled chemistry-climate model, since strong volcanic activity can cause ozone depletion that might be severe enough to threaten the existence of life on Earth. In their experiments, the volcanic eruptions were the 1991 Mount Pinatubo eruption and a 100× Pinatubo size eruption. The results indicated that the percentage of global mean total column ozone depletion in the 2050 RCP8.5 100× Pinatubo scenario could reach approximately 6% compared to two years before the eruption and 6.4% in tropics. Another identical simulation, 100 × Pinatubo eruption only with natural source Ozone Depleting Substances (ODSs), produced an ozone depletion of 2.5% compared to two years before the eruption, and with 4.4% loss in the tropics. Their model results suggested that the reduced ODSs and stratospheric cooling could lighten the ozone depletion after super volcanic eruption.

2 Climate and Modeling

Xia *et al.*[17] revisited the problem of the SH stratospheric warming in the recent decade. It is found that the SH high-latitude stratosphere continued warming in September and October over 2007–2017, but with very different spatial patterns. Multiple linear regression demonstrates that ozone increases play an important role in the SH high-latitude stratospheric warming in September and November, while the changes in the Brewer-Dobson circulation contributes little to the warming. This is different from the situation over 1979–2006 when the SH high-latitude stratospheric warming was mainly caused by the strengthening of the Brewer-Dobson circulation and the eastward shift of the warming center. Simulations forced with observed ozone changes over 2007–2017 shows warming trends, suggesting that the observed warming trends over 2007–2017 are at least partly due to ozone recovery. The warming trends due to ozone recovery have important implications for stratospheric, tropospheric, and surface climates on SH.

Li *et al.*[18] investigated the independent and joint impacts of ENSO Modoki and QBO on stratospheric ozone in the Northern Hemisphere (NH) in winter. Their results showed that stratospheric ozone in the NH in winter increases during El Nino Modoki events but increases during La Nina Modoki, whereas increases during the easterly phase of QBO and decreases in the westerly phase of QBO. Further, they found that the EQBO enhances the effect of El Nino Modoki events on stratospheric ozone, but weakens the effect of La Nina Modoki, and vice versa for the WQBO.

Xie *et al.*[19] found that replacing the original specified Arctic Stratospheric Ozone (ASO) forcing

with more accurate stratospheric ozone variations improves the simulated variations of global surface temperature in a climate model. The decreasing trend of stratospheric ozone may have enhanced the warming trend at high latitudes in the second half of the 20th century. Xie *et al.*[20, 21] and Ma *et al.*[22] further found that ASO changes have significant regional impacts.

Xie *et al.*[23] found that a warmer Indo-Pacific Warm Pool (IPWP) significantly dries the stratospheric water vapor by causing a broad cooling of the tropopause, and vice versa for a colder IPWP. They further found the frequency of ENSO Modoki events was higher from 1984 to 2000 than after 2000, the BD circulation anomalies related to central ENSO were stronger during 1984–2000, which caused ENSO Modoki events to have a greater effect on lower stratospheric ozone before 2000 than eastern ENSO[24].

Zhang *et al.*[25] identified a Eurasia-North America dipole mode in the Total Column Ozone (TCO) over the Northern Hemisphere, showing negative and positive TCO anomaly centers over Eurasia and North America, respectively. The positive trend of this mode explains an enhanced TCO decline over the Eurasian continent in the past three decades, which is closely related to the polar vortex shift towards Eurasia. Moreover, they found that the positive Eurasia-North America dipole trend in late winter is likely to continue in the near future.

Zhang *et al.*[26] found that there are significant negative total column ozone (TCO) trends over the North Pacific and positive TCO trends over northwestern North America in winter during 1979–2015. The zonally asymmetric TCO trends are mainly contributed by dynamical processes related to the teleconnection pattern changes of the Cold Ocean - Warm Land (COWL) and the North Pacific (NP). By contrast, chemical processes make a relatively smaller contribution to the zonally asymmetric TCO trends.

Shangguan *et al.*[27] analyzed the variability and trends of temperature and ozone in the UTLS for the period of 2002–2017. A significant warming of 0.2~0.3 K per decade is found in most areas of the troposphere while the stratospheric temperature decreases at a rate of 0.1~0.3 K per decade. They also found the temperature increase in the troposphere, as well as ozone decrease in the NH stratosphere, is mainly connected to the increase of SST and subsequent changes of atmospheric circulations.

Xiao *et al.*[28] investigated the impact of increasing surface emissions of Nitrogen Oxide (NO_x) in East Asia on ozone and temperature in the UTLS region. Their results showed that in summer the south Asia anticyclone can transport the NO_x in the East Asian UTLS region to the low latitudes and result in an increase in the low-latitude ozone concentration, leading to warming in the UTLS region in winter, while the intensified cyclic ozone depleting in the mid-latitudes results in the mid-latitude ozone concentration decreasing, leading to cooling in the UTLS region in winter.

Yi *et al.*[29] estimated neutral mesospheric densities at low latitude have been derived from April 2011 to December 2014 using data from the Kunming meteor radar in China (25.6°N, 103.8°E). The daily mean density at 90 km was estimated using the ambipolar diffusion coefficients from the meteor radar and temperature from the Sounding of the Atmosphere using Broadband Emission Radiometry (SABER) instrument. The seasonal variations of the meteor radar derived density are consistent with the density from the Mass Spectrometer and Incoherent Scatter (MSIS) model, show a dominant annual variation, with a maximum during winter, and a minimum during summer. In addition, a comparison of the ambipolar diffusion coefficient and peak height observed simultaneously by two co-located meteor radars indicates that the relative errors of the daily mean ambipolar diffusion coefficient and peak height should be less than 5% and 6%, respectively; the absolute error of the peak height is less than 0.2 km.

Wu *et al.*[30] analyzed a long-term simulation of the Whole Atmosphere Community Climate Model with the chemistry of three metals (Na, K, and Fe) to investigate the response of the meteoric metal layers in the mesosphere and lower thermosphere regions to the 27-day solar rotational cycle. This is the first

time that the solar-driven 27-day variation of the metal layers in the MLT region has been identified. The correlation between variability in the metal layers and solar 27-day forcing during different phases of the solar 11-year cycle reveals that the response in the metal layers is much stronger during solar maximum. The altitude-dependent correlation and sensitivity of the metal layers to the solar spectral irradiance demonstrate that there is a significant increase in sensitivity to solar rotational cycle with increasing altitude. Above 100 km, the sensitivity of the metals to changes of 10% in the solar spectral irradiance at Lyman-alpha is estimated to be −5%. A similar response is seen in Na layer measurements made by the Optical Spectrograph and InfraRed Imaging System instrument on the Odin satellite.

Yi *et al.*[31] presented observations of a quasi-90-day oscillation in the Mesosphere and Lower Thermosphere (MLT) region from April 2011 to December 2014. There is clear evidence of a quasi-90-day oscillation in temperatures obtained from the Kunming meteor radar (25.6°N, 103.8°E) and the SABER, as well as in wind observed by the Kunming meteor radar. The amplitudes and phases of the quasi-90-day oscillation in the SABER temperature show a feature similar to that of upward-propagated diurnal tides, which have a vertical wavelength of about 20 km above 70 km. Similar to the quasi-90-day oscillation in temperature, a 90-day variability of ozone (O_3) is also present in the MLT region and is considered to be driven by a similar variability in the upwardly-propagated diurnal tides generated in the lower atmosphere. Moreover, the 90-day variability in the absorption of Ultraviolet (UV) radiation by daytime O_3 in the MLT region is an in situ source of the quasi-90-day oscillation in the MLT temperature.

Yi *et al.*[32] reported a climatology of the global mesopause relative density estimated using multiyear observations from meteor radars located from high to low-latitude regions. The seasonal variations of the southern polar mesopause relative density are mainly dominated by an Annual Oscillation (AO). The mesopause relative densities at high latitudes and high mid-latitudes in the Northern Hemisphere show mainly an AO and a relatively weak Semiannual Oscillation (SAO). The SAO is evident in the Northern Hemisphere, especially at high latitudes, which is comparable to the AO amplitudes. The mesopause relative densities at lower mid-latitudes and low latitudes show mainly an AO. These observations indicate that the mesopause relative densities over the southern and northern high latitudes exhibit a clear seasonal asymmetry. The maxima of the yearly variations in the mesopause relative densities display a clear latitudinal variation across the spring equinox as the latitude decreases; these latitudinal variation characteristics may be related to latitudinal changes influenced by gravity wave forcing.

Rao *et al.*[33] revealed that the ratio of the ensemble members that forecast the zonal wind reversal with a 5-day delay allowed (hit ratio) is higher for SSW events with a small decrease in the zonal mean zonal winds (moderate SSWs) than for events with a large decrease in the zonal mean zonal winds (radical SSWs) in hindcasts initialized around 1 (7 day) and 2 (14 day) weeks in advance. The underestimated cumulative eddy heat flux associated with weak wave activities accounts for the weaker-than-observed deceleration of westerlies. The preexisting extratropical wave patterns are satisfactorily forecast in 14 day for most (9/12) cases, and the wave phase bias is reasonably small for those cases. After the climatology bias is deducted from the hindcasts, an increase in the hit ratio can be identified for moderate SSW events as the evolutions of zonal winds are improved. Following the error correction by remapping the zonal wind probability distribution function in the forecast system to the reanalysis, the SSW hit ratios increase in the 7 day (43% to 57%) and/or 14 day (11% to 21%) initializations. Rao *et al.*[34] also found when the hindcasts are initiated less than two weeks before SSW onset, BCC_CSM and ECMWF show comparable predictive skill in terms of the temporal evolution of the stratospheric circumpolar westerlies and polar temperature up to 30 days after SSW onset. However, with earlier hindcast initialization, the predictive skill of BCC_CSM gradually decreases, and the reproduced maximum circulation

anomalies in the hindcasts initiated four weeks before SSW onset replicate only 10% of the circulation anomaly intensities in observations. The earliest successful prediction of the breakdown of the stratospheric polar vortex accompanying SSW onset for BCC_CSM (ECMWF) is the hindcast initiated two (three) weeks earlier.

Yu *et al.*[35] evaluated the prediction skill for the stratospheric mass circulation variability in winter (November to March) in the Climate Forecast System, version 2 (CFSv2), from 2011 to 2018. Three stratospheric mass circulation indices measuring meridional mass transport into the polar stratosphere by the total flow (ST60N), wavenumber-1 (ST60N_W1), and wavenumber-2 waves (ST60N_W2) are considered. Systematic forecast bias is found in both the 7-year averaged winter mean and seasonal cycle, which is tied to the overestimation of damping in amplitude and westward tilting variations of total waves and difficulties in forecasting the exact contributions from different spatial scales of waves. The intra-seasonal variations of stratospheric mass circulation indices, with the systematic forecast bias corrected, can be modestly predicted at a forecast lead time of about 20 days, in terms of both the anomaly value and timing of negative and positive peak events. The 20-day prediction limit of the stratospheric mass circulation indices is mainly due to the 2-week limit of the CFSv2 model in predicting the variability of anomalous wave tilt angle, whereas the prediction limit of the wave amplitude anomaly can exceed 50 days.

3 Dynamics in the Middle Atmosphere

3.1 Meteorological Process

Hu and Ren[36] reported a significant linkage between the seasonal timing of boreal spring Stratospheric Final Warming (SFW) events and the onset of the Indian Summer Monsoon (ISM). The leading singular vector decomposition pattern reveals a significant, coupled interannual variation between the SFW-related circulation in the lower stratosphere and the ISM-related circulation in the lower troposphere, objectively confirming the intimate relationship between SFWs and the ISM. Associated with a late SFW, the stratospheric polar vortex and the polar jet are anomalously stronger in April to early May, which is coupled with positive anomalies of the Northern Annular Mode (NAM) and the Arctic Oscillation (AO) in the troposphere. These tropospheric NAM/AO anomalies act to pass the extratropical anomaly signals to western central Asia *via* a NAM-/AO-related Rossby wave train in the upper troposphere, which is initiated over the North Atlantic jet exit region and extends across Eurasia. This results in an anomalous upper tropospheric anticyclone accompanied by anomalous descent over western central Asia that in turn warms the in situ air column and results in an enhanced meridional gradient of tropospheric temperature over the land to the north of the Arabian Sea and the Indian Ocean and therefore an early onset of the ISM.

Yu *et al.*[37] revealed that SSW events correspond to a large-amplitude or long-lasting subset of pulse-like, anomalously strong, stratospheric mass circulation events. The anomalously strong, stratospheric mass circulation events (referred to as PULSE events) occur more than nine times in an average winter. The displacement versus split types of SSWs tend to correspond to the Wavenumber 1 versus Wavenumber 2 types of PULSEs, though the relationship between split-type SSWs and Wavenumber-2-type PULSEs is weaker. Like SSW events, PULSEs also have a close relationship with CAOs. The robust relationship with CAOs still holds for the PULSE events not accompanied by SSW events. More than 70% of CAOs in the 37 winters occur in the week before and after a PULSE event, with a false alarm rate of CAO occurrence of about 25.7%. SSW events, however, are associated with only about 5.7% of CAOs, with a false alarm rate of 21.7%. Therefore, the linkage between individual continental-scale CAOs and PULSE events represents a more generalized relationship between the stratospheric circulation anomalies and surface weather.

Hu *et al.*[38] reported a statistically significant relationship between the North Pacific Gyre Oscillation (NPGO) and Stratospheric Final Warming (SFWOD) in the Northern Hemisphere in two subperiods (1951–1978 and 1979–2015), *i.e.*, in the first (second) sub-period, the NPGO is negatively (positively) linked with SFWOD. During 1951–1978, positive NPGO years tend to strengthen the Pacific-North America (PNA) pattern in the mid-troposphere in boreal winter. The strengthened PNA pattern in February leads to strong planetary wave activity in the extratropical stratosphere from late February to March and causes the early onset of SFW in early April. By contrast, a strengthened Western Pacific pattern from January to early February in negative NPGO years causes a burst of planetary waves in both the troposphere and extratropical stratosphere from late January to mid-February and results in more winter stratospheric sudden warming events, which, in turn, leads to a dormant spring and a late onset of SFW in late April. During 1979–2015, positive (negative) NPGO years strongly strengthen (weaken) the mid-tropospheric Aleutian low and the Western Pacific pattern from January to mid-March, leading to increased (decreased) planetary Wavenumber-1 activity in the stratosphere from mid- to late winter and thus more (less) winter stratospheric sudden warming events and late (early) onsets of SFW in early May (mid-April).

Rao *et al.*[39] analyzed a major Stratospheric Sudden Warming (SSW) event in February 2018 after a 4-year absence since the winter of 2013/2014. Based on the reanalysis data, the polar night jet changed from a very strong state to a moderate state during 12–19 January, and the moderate westerlies directly reversed to easterlies during 5–15 February. The intensified East Asian trough, Alaskan blocking, and East U.S. trough amplified the extratropical climatological Wave 2, which propagated upward into the stratosphere, leading to a vortex-splitting SSW event. Predictions of the February 2018 SSW event are explored in hindcasts initialized 0~4 weeks in advance by the BCC_CSM. Less than 20% of the 28 ensemble members predict the reversal of $\bar{U}$ at 60°N, 10 hPa in hindcasts initialized 3 or 4 weeks in advance if a 5-day error is allowed, while this ratio increases to 43% in hindcasts initialized 1 week in advance. Based on the climatological occurrence of SSW events in the forecast system, the maximum deterministic predictable limit of this event is 1~2 weeks in this forecast system. The eddy heat flux and its domination by Wave 2 can only be predicted within the predictable time limit. The predictable limit of the stratospheric circulation pattern for the February 2018 SSW, 1~2 weeks, also generalizes to other vortex split SSW events such as the January 2009 and February 1999 cases.

3.2 Influence of Lower Atmospheric Perturbation on Thermosphere/Ionosphere

Yu *et al.*[40] presented a multi-instrument experiment analysis of the intensification of metallic layered phenomena above thunderstorms. An enhanced ionospheric sporadic E layer with a downward tidal phase was observed followed by a subsequent intensification of neutral Na layer. The Na chemistry model simulation reproduced a consistent result of an enhanced Na layer by using the ionospheric observation as input. They found the enhancement of metallic layered phenomena above thunderstorms is associated with the atmospheric tides owing to the troposphere-mesosphere-ionosphere coupling.

Sun *et al.*[41] analyzed a special mid-latitudinal Medium-scale Traveling Ionospheric Disturbance (MSTID) event using OI (630.0 nm) all-sky airglow imager observations. The event was accompanied by a poleward surge of airglow depletion/enhancement and a bifurcation of depletion during the magnetically quiet period. The special structures were generated at a decreasing height of ionosphere with the enhancement of nighttime plasma density and the increase of airglow intensity. They suggested that the poleward surge and bifurcation of airglow depletion were the result of the interaction between the passing-by MSTID and nighttime plasma density enhancement.

Based on four-year observations (2012–2015) from both all-sky airglow imager and the C/NOFS satellite, Wu *et al.*[42] studied the Edge Plasma Enhan-

cements of Equatorial Plasma Depletions (EPEEPDs). The results showed that the EPEEPDs occurred only in the east and west edges of EPDs but not at the poleward edge. This was different from the earlier in-situ measurements obtained by low Earth orbit satellites. Both the all-sky airglow image observation and C/NOFS observation showed that the plasma enhancement was a high-incidence phenomenon, and the average incidence reached about 82% during days with EPDs observed. The zonal extension of EPEEPDs at different altitudes showed different scale characteristics. They suggested that the generation mechanism of EPEEPDs was possibly related to the polarized electric field of EPDs.

By combining observations from three meteor radars and an MST radar established by the Chinese Meridian Project with reanalysis data, Yu *et al.*[43] studied the SFW in 2015 spring and PW activities from the troposphere to the MLT at different latitudes. By means of the two warming events separated by only several days, the polar mean temperature increases by nearly 20 K at 10 hPa level, and the mean zonal wind decreases from more than 30 $m \cdot s^{-1}$ to about –10 $m \cdot s^{-1}$, thus seasonal transition of the polar circulation is completed. The investigation shows that the Q10DW and Q16DW occur around the SFW. In the troposphere, their amplitudes are close to 10 $m \cdot s^{-1}$ in the wind field. At 10 hPa level of the stratosphere, the strong wave activities arise before the SFW, while in the MLT, the waves are amplified following the SFW with the amplitude peaks about 10 days after the SFW onset. The wave amplitude in the MLT tends to increase in the zonal wind but decrease in the meridional wind with decreasing latitude, which is roughly consistent with the Hough modes. Hence, the Q10DW and Q16DW in the MLT are distinct from those in the stratosphere, and they are likely to be generated and strengthened in situ in the upper stratosphere and MLT.

Using measurements of meteor radar and MST radar established by the Chinese Meridian Project and reanalysis data, Huang *et al.*[44] report an ISO with about 30-day period at mid and high latitudes. Radar observations indicate that in the troposphere, the oscillation attains an amplitude peak in zonal wind at about 9 km, and propagates downward below 9 km. At about 9~16 km, the oscillation gradually decays with height, and then strengthens again as it propagates upward in the stratosphere. In the mesosphere, the oscillation obviously appears at 78~86 km with an maximum amplitude at 80 km. Reanalysis data show that in the troposphere, the oscillation propagates southward. At about 100 to 10 hPa levels, the oscillation is gradually reflected back to propagate northward, and then propagates poleward at higher altitude. Refractive index can explain its complex propagation characteristics very well. Consistency and coherence of its phase progression indicate that in the lower atmosphere, the oscillation comes from the polar region. Hence, ISOs can not only originate from but also propagate in the atmosphere at mid and high latitudes.

3.3 Gravity-wave Processes

Chen *et al.*[45] found that the time series of Gravity Wave Square Temperature Amplitude (GWSTA) and absolute Gravity Wave (GW) Momentum Flux (GWMF) at a certain altitude and latitude results from the complex interplay of GW sources, propagation through and filtering in lower altitudes, oblique propagation superposing GWs from different source locations, and, finally, the modulation of the GW spectrum by the winds at a considered altitude and latitude. The strongest component is the annual variation, dominated in the summer hemisphere by subtropical convective sources and in the winter hemisphere by polar vortex dynamics. At heights of the wind reversal, a 180° phase shift also occurs, which is at different altitudes for GWSTA and GWMF. In the intermediate latitudes, a Semiannual Variation (SAV) is found. Dedicated GW modeling is used to investigate the nature of this SAV, which is a different phenomenon from the tropical SAO also seen in the data. In the tropics, a stratospheric and a mesospheric QBO are found, which are, as expected, in antiphase.

Hu *et al.*[46] showed that the Stratospheric Wave Intensity (SWI) in December during 2001–2015

weakens, which is opposite to that during 1979–2000, implying a shift around the 2000s. The weakened SWI is dominated by its Wave Number-1 component, which is related to the wave propagation impeded by the decreased refractive index at high latitudes and the weakened wave activity in the troposphere. Changes in refractive index are mainly contributed by changes in the meridional potential vorticity gradient *via* the barotropic term. This shift in the wave number-1 waves leads to a shift in the stratospheric Arctic temperature, that is, warming (cooling) during 1979–2000 (2001–2015), implying that similar shifting phenomena may appear regardless of the continued greenhouse gas emissions.

Wu *et al.*[47] performed the Weather Research and Forecasting (WRF) simulations with five different spatial resolutions (25, 20, 15, 10, and 4 km) to examine the scale interactions between the GWs resolved by high-resolution Whole Atmosphere Community Climate Model (WACCM) and those with smaller scales, its potential impact on the resolved waves, and the dependence of wave characteristics on spatial resolution. The sensitivity of GW structure to the choice of model horizontal resolutions is examined, the simulation reveals more power at shorter horizontal wavelengths of GWs at finer resolutions. The magnitude of the zonal momentum flux calculated from the high-resolution WACCM is greater than the WRF-25 simulation, in addition, the magnitude is comparable to the results from the WRF-15 and WRF-10 simulations.

Relative to many investigations IGWs in the Antarctic, IGW activity in the Arctic region was paid less attention to. Huang *et al.*[48] use radiosonde observations at the Ny-Alesund station to investigate the IGW characteristics in the lower stratosphere over the Arctic. The observation reveals a prevailing eastward zonal wind below 20 km and an obvious annual cycle of the temperature from the troposphere to the lower stratosphere. By combining Lomb-Scargle spectrum and hodograph technique, the case study demonstrates that the lower stratospheric IGWs exhibit a feature of freely propagating waves. Statistical analysis indicates that the IGWs have a dominant horizontal (vertical) wavelength of 50~1050 km (1~4 km), and ratio (1~2.5) of the intrinsic to inertia frequencies. Wave energy exhibits an annual oscillation with the maximum in winter and the minimum in summer. In winter, the downward propagating waves increase to about 20% due to polar stratospheric vortex. Because of the lower atmospheric filtering, the IGWs display a dominant direction of westward propagation, thus have a mean vertical flux of –0.647 mPa for the zonal momentum, which indicates that the IGWs can put a westward drag on the atmospheric wind field over the Arctic as they dissipate. All the vertical wavenumber spectra have spectral slopes from –2.23 to –2.99 close to the universal spectrum index of –3.

Gong *et al.*[49] studied a low-frequency inertial Atmospheric Gravity Wave (AGW) event with the data from three deferent detection tools, which are lidar, meteor radar, and TIMED/SABER. Observations from these three different instruments were compared, and it was found that signatures in the temperature perturbations and horizontal winds were induced by identical AGWs. According to these coordinated observation results, the horizontal wavelength and intrinsic phase speed were inferred to be about 560 km and about 21 $m \cdot s^{-1}$, respectively. Analyses of the Brunt-Väisälä frequency and potential energy illustrated that this persistent wave propagation had good static stability.

Based on the OH all-sky airglow imager observation over Kazan (55.8°N, 49.2°E), Russia, between August 2015 and July 2016, Li *et al.*[50] studied the mesospheric Gravity Waves (GWs) in the latitude band of 45°–75°N. The observed GWs showed a strong preference of propagation toward northeast in the whole year. This was significantly different from the results for other latitudes, where the propagation directions depended on season. It was reported that deep tropospheric convections were the dominant source of the GWs in spring, summer, and autumn. The results indicated that convection might also be an important source of GWs in the higher latitudes. Jet stream systems were considered as the generation mechanism of the GWs in winter.

Li *et al.*[51] studied a mesospheric bore event occurring on the night of 16–17 December 2014 by using the observations from both OH and OI (557.7 nm) all-sky airglow imagers in Lhasa (29.66°N, 90.98°E), the NPP and TIMED satellites, and a Doppler meteor radar. The results indicated that the winds in the height range of the OH layer were almost orthogonal to the propagation direction of the mesospheric bore. Both hydraulic jump theory and observations indicated that the duct initially shrank and followed by an expansion. The duct was strong in the OH layer but weak in the OI layer. The horizontal wavelengths and phase speeds of the bore packet decreased as the duct shrank and increased as the duct expanded. The intensity amplitude of the bore packet decreased slowly and then decreased sharply after dissipation. The bore might have leaked out of the duct with the variation of the depth of the duct.

Based on the OH all-sky airglow imager and the TIMED/SABER satellite observations and the ECMWF data, Wang *et al.*[52] studied the sources of two gravity wave events, which occurred on the night of 15–16 September 2013, using a method of reverse ray tracing. The results indicated that the wave source location of one event was highly related with intensity convective activity; the other might be related to dynamic instability due to vertical motion of air masses or convection activity.

Liu *et al.*[53] studied the seasonal and height dependencies of the orographic primary and larger-scale secondary Gravity Waves (GWs) by using the temperature profiles observed by the TIMED/SABER satellite from 2002 to 2017. The results indicated that at about 40°S and during Southern Hemisphere winter, there was a strong GW peak over the Andes Mountains which could extend to an altitude of about 55 km. The orographic GWs breaking occurred above the peak height of the stratospheric jet. At the altitude of 55~65 km, the body forces produced by GW breaking and momentum deposition generated larger-scale secondary GWs. At middle latitudes during summer, orographic GW breaking also generated larger-scale secondary GWs which could propagate to higher altitudes.

In addition, Lai *et al.*[54] developed a program to automatically extract gravity wave patterns from the all-sky airglow imager observation. The auto-extraction program included a classification model based on a convolutional neural network and an object detection model based on a faster region-based convolutional neural network. In addition, the program can remove the interference of the wavelike mist near the imager.

4 Coupling between Stratosphere and Troposphere

Huang *et al.*[55] examined the preconditioning of events in which the Arctic stratospheric polar vortex shifts toward Eurasia, North America, and the Atlantic. They found that certain patterns of anomalous tropospheric blocking over northern Europe, the Bering Strait, and the eastern North Atlantic can be taken as the potential blocking precursors of the stratospheric polar vortex shifting toward Eurasia, North America, and the Atlantic.

Huang and Tian[56] analyzed the differences and similarities of Eurasian cold air outbreaks under the weak, strong, and neutral stratospheric polar vortex states. They found that the preexisting negative North Atlantic Oscillation pattern, the considerably negative stratospheric Arctic Oscillation signals entering the troposphere and positive sensible heat flux anomalies in the later stages of cold air outbreaks play important roles in the differences and similarities of these three types of cold air outbreaks.

Li *et al.*[57] investigated the connections between the first two Principle Components (PCs) of the SST anomalies over the North Pacific and the SSWs in the Northern Hemisphere winter. Their results showed that the SSW event occurs more frequently and is longer during the positive phases of PC2 than the negative phases of PC2. Moreover, they found that the positive phases of PC2 are marked by more positive Pacific–North America (PNA) and Western Pacific (WP) teleconnections in the upper tropo-

sphere.

Liang *et al.*[58] analyzed the upper tropospheric and stratospheric signals before the "June 5th" heavy rainfall event in South China in 2005. Their results showed that before the heavy rainfall there is a lower-lift-lower trend of tropopause over the rainfall region, stronger and more northward easterly winds in the UTLS over the subtropical region and the eastward shifted center of the South Asian High.

Luo *et al.*[59] investigated seasonal features of the tropopause fold events over TP and found that shallow tropopause folds occur mostly in spring while medium and deep folds occur mostly in winter. The relatively high-frequency areas of medium and shallow folds are located over the southern edge of TP. The region of high-frequency tropopause folds is located in the southern portion of the plateau in spring and moves northward in summer, controlled by the westerly jet movement.

Wang *et al.*[60] investigated the influence of the occurrence frequency of the MJO phases on the interannual variability of stratospheric wave activity in the mid-high latitudes of the Northern Hemisphere during boreal winter. The occurrence frequency of MJO Phase 4 in winter is significantly positively correlated with the interannual variability of the EP flux divergence anomalies in the northern extratropical stratosphere, while the occurrence frequency of MJO Phase 7 has an opposite and weaker effect on wave activities in the northern extratropical stratosphere.

Zhang *et al.*[61] found that the weakened/enhanced Arctic polar vortex in the lower stratosphere during Easterly/Westerly QBO (EQBO/WQBO) phases is more noticeable in January and February than in November and December. The Arctic polar vortex shows a shift toward the Eurasian continent and away from North America in winter during EQBO phases compared with that during WQBO phases, with a greater shift in January and February than in November and December.

Zhang *et al.*[62] found that there is a dipole-like structure of geopotential height anomalies over the North Pacific Ocean during weak stratospheric polar vortex events. When the stratospheric polar westerly is decelerated, the high-latitude eastward waves slow down and equatorward propagation of eddy momentum flux at 60°N enhances. Hence the tropospheric eddy-driven jet over the North Pacific Ocean weakens and shows a southward displacement, leading to the dipole in geopotential height via geostrophic equilibrium.

Zhang *et al.*[63] found that the upward wave fluxes entering the stratosphere are stronger and more persistent during the downward-extending negative NAM events than during the non-downward-extending negative NAM events. And the tropospheric wave intensity plays a more important role than the tropospheric conditions of planetary wave propagation in modulating the upward wave fluxes into the stratosphere.

Han *et al.*[64] found that the tropical tropopause temperature is uncorrelated with stratospheric water vapor in 1996. They showed that the instantaneous intensity of four short periods of deep convective activity, caused by strong surface cyclones and high sea surface temperatures can, on the one hand, transport water vapor in the troposphere directly into the lower stratosphere, and on the other hand, lift the tropopause and cool its temperature.

Li *et al.*[65] investigated the changing trend of ozone and its influence factors over Beijing during 2003–2013. Their results showed that the tropospheric ozone over Beijing increased significantly during 2003–2013. Further, they found that surface emission contributed to around 60% of the increase of tropospheric ozone over Beijing, while downward transmission from stratosphere and horizontal transport contribute to about 20% and 10% of the increase of tropospheric ozone, respectively.

Luo *et al.*[66] found that the day-to-day changes in carbon monoxide (CO) and ozone (O_3) tracer distributions in the UTLS are consistent with the dynamical variability during the Asian Summer Monsoon (ASM) season. The CO vertical cross sections from the Infrared Atmospheric Sounding Interferometer (IASI) combined with the daily maps provide the first observational evidence for a model

analyses-based hypothesis on the preferred ASM vertical transport location and the subsequent horizontal redistribution *via* east-west eddy shedding.

Sang *et al.*[67] investigated how overshooting convection affects the water vapor content in the lower stratosphere. Their results showed that the net effect of overshooting convection on the lower stratospheric water content is moistening. Also they found that convective intensity is directly related to the effect of overshooting convection on the lower stratospheric humidity. They discovered that changes in vertical wind shear near the tropopause have no significant impact on the extent of overshooting but have important impacts on cross-tropopause water vapor exchange.

Han *et al.*[68] confirmed that the significant hemispheric asymmetries in the trends of N_2O, CH_4 and HCl existed in the mid-latitude middle and lower stratosphere during the period of 2004–2012. They showed that changes in the vertical and meridional transport due to the residual circulation contribute to the observed asymmetric hemispheric trends of stratospheric trace gases. Southward shift of the upwelling branch of the residual circulation in recent decades partly explains the trends of these trace gases in the middle stratosphere while the eddy mixing has a small effect.

Wang *et al.*[69] investigated solar signals in the atmosphere and the ocean. Results indicate that the 11-year solar cycle is related to anomalous positive SST anomalies in the central Pacific which resemble an El Niño Modoki event. Such SST anomalies are amplified by a positive feedback through oceanic subsurface currents and heat transport in the equatorial Pacific and in turn modify the circulation and convection in the troposphere, resulting in lagged solar signals in tropical tropopause heights and temperatures as well as lower stratospheric water vapor.

Wang *et al.*[70] highlighted the importance of the vertical resolution in model development and climate change assessment. They found that a model with High Vertical-Resolution (HV-Res) gives a better representation of tropical Tropopause Temperature (TPT) in absolute values and seasonal variations. The corresponding changes in TPTs associated with SST anomalies are 30% stronger and more realistic in the HV-Res model.

Wang *et al.*[71] reported a severe surface ozone pollution episode over the YRD in 2018 spring associated with a deep SI event. This SI event is caused by a strong horizontal-trough, which brought ozone-rich air from stratosphere to troposphere. They demonstrated that deep SIs contribute about 15 ppbv in spring to surface ozone variations in eastern China.

In recent years, several studies have documented the impact of stratospheric dynamic processes on tropospheric climate variability in the extra-tropics. Wei *et al.*[72] investigated the effect of a well-resolved stratosphere on East Asian winter climate by using the model outputs from the Coupled Model Intercomparison Project phase 5 (CMIP5). A comparison between models with and without a well-resolved stratosphere revealed that the models with model top above the stratopause had a better simulation of the distribution of surface air temperature, sea level pressure, and precipitation than the models with a low-top below the stratopause. The difference of the East Asian winter climate between High-Top (HT) and Low-Top (LT) CMIP5 models is also evident in the future projection under higher (RCP85) and midrange (RCP45) emission scenarios. The HT models present about 1.3 and 1.7°C higher surface air temperature in East Asian region under RCP45 and RCP 85 scenarios by the end of this century than that of the LT models, respectively. As climate models have now become one of the primary tools in climate change assessment and projection, which was used as the base for mitigation measure and adaption policy. The results suggested that insufficient representation of the stratosphere might lead to underestimation of the anthropogenic global warming in a regional scale and hence had the potential to lead to insufficient response action and mitigation measures.

The Arctic Oscillation (AO) is the most dominant low-frequency mode of atmospheric variability in the extratropical Northern Hemisphere, which can strongly influence the global and regional climate through its teleconnections. Gong *et al.*[73] investi-

gated the patterns and teleconnections of the winter mean AO based on observational and reanalysis datasets. They found that the Atlantic center of the AO pattern remains unchanged throughout the period of 1920–2010, whereas the Pacific center of the AO is strong during 1920–1959 and 1986–2010 and weak during 1960–1985. Gong *et al.*[74] further evaluated the CMIP5 model performance in simulating the wintertime AO pattern. The magnitude of the North Pacific center of the AO pattern is shown to vary largely among the models, which is primarily modulated by the strength of the stratospheric polar vortex. A stronger stratospheric polar vortex can induce more planetary waves to reflect from the North Pacific to the North Atlantic and more wave activity fluxes to propagate from the North Pacific to the North Atlantic in the Strong Polar Vortex (SPV) models than in the Weak Polar Vortex (WPV) models. Hence, the coupling of atmospheric circulation between the North Pacific and North Atlantic is stronger in the SPV models, which may induce a stronger North Pacific center in the AO pattern. The increase in vertical resolution may improve the simulation of the stratospheric polar vortex, and thereby reduces the model biases in the North Pacific–North Atlantic coupling and the amplitude of the North Pacific center of the AO pattern in models.

Previous studies have found that the AO may also influence the atmosphere-ocean systems over the tropics. For instance, boreal spring AO may contribute to the occurrence of an El Niño event during the following winter through inducing westerly wind anomalies over the western tropical Pacific[75]. A recent study of Chen *et al.*[76] revealed a pronounced enhancement of the linkage between autumn Arctic Sea Ice Concentration (ASIC) changes and following spring AO since the mid-1990s. After the mid-1990s, there exists a significant connection between interannual variation of the autumn ASIC and subsequent spring AO. During this period, autumn ASIC decrease results in pronounced tropospheric warming over the high latitudes and a reduction of the meridional temperature gradient. This leads to a decrease in circumpolar westerly winds and an increase in the upward propagation of quasi-stationary planetary waves, which weakens stratospheric polar vortex. Hence, a negative spring AO phase is generated via the downward propagation of the easterly wind anomalies. The results suggest that the interannual variability of autumn ASIC is much larger after the mid-1990s, which contributes to stronger stratospheric response and ASIC-spring AO connection.

The tropical convection anomaly, for example, associated with El Niño-Southern Oscillation (ENSO), plays an important role in the formation of extratropical teleconnections. Ding *et al.*[77] investigated the distinct patterns of boreal winter convection anomalies over the tropical Pacific and associated wave trains in the extratropics, and identified five major categories of tropical convection anomalies. Mechanisms for the formation of quasi-stationary extratropical wave trains associated with distinct winter patterns of seasonal mean tropical Pacific convection anomalies were further studied by utilizing observational and six Atmospheric Model Inter-comparison Project Phase 5 (AMIP5) high-skilled models datasets[78]. They found that the stratosphere-troposphere interaction plays an important role for extratropical atmospheric circulation anomalies. The stratospheric polar vortex not only modulates the underlying wave train, especially for the North Atlantic/Europe sector, but is also affected by the upper-tropospheric disturbance in high-latitudes through the upward propagating quasi-stationary planetary waves.

Huang *et al.*[79] demonstrated that the cross tropopause wind shear associated with stratospheric Quasi-biennial Oscillation (QBO) could impact the convection over the Western North Pacific (WNP) and the resultant Tropical Cyclone (TC) genesis in May. The results indicate that the strong cross-tropopause shear over the key region (0°–5°N, 160°–180°E) may suppress convection over the tropical WNP, especially over the South China Sea and the Philippines. This cross-tropopause wind shear is negatively correlated with TC genesis in May, with a decreased (increased) number of TCs corresponding

to strong (weak) cross-tropopause wind shear. They suggested that this cross-tropopause wind shear can be treated as the combined impacts of the ENSO events and the QBO. The energy analysis indicates that the combined impacts of the decaying El Niño events and the QBO easterly phase might suppress the barotropic eddy kinetic energy conversion in May, whereas the decaying La Niña events and the QBO west phase act in an opposite manner.

Huang *et al.*[80] synthesized recent progress in researches on the atmospheric dynamics in the stratosphere and its dynamical interaction with the tropospheric processes. They focused on the dynamics of quasi-stationary planetary waves, the wave-basic flow interaction in the tropical stratosphere, the impact of atmospheric circulation variability in the stratosphere on circulation variability and climate in the troposphere, the numerical simulation of stratospheric atmosphere and climate projection in the stratosphere under the background of global warming. The importance of variability of planetary wave activity and its association with the northern annular mode, a wider spectrum of gravity waves in forcing a realistic QBO and global meridional circulation, the cooling trend in the stratosphere and stratospheric processes for weather and climate anomalies near the surface was highlighted. More in-depth studies on the atmospheric dynamics in the stratosphere and improvements of the model performance in the stratosphere were suggested in the future.

The Stratospheric Arctic Vortex (SAV) plays a critical role in forecasting cold winters in northern mid-latitudes. Its influence on the tropospheric mid- and high-latitudes has attracted growing attention in recent years. However, the trend in the SAV during the recent two decades is still unknown. Here, using three reanalysis datasets, Hu *et al.*[81] found that the SAV intensity during 1998–2016 has a strengthening trend, in contrast to the weakening trend before that period. Approximately 25% of this strengthening is contributed by the warming of Sea-Surface Temperature (SST) over the Central North Pacific (CNP). Observational analysis and model experiments show that the warmed CNP SST tends to weaken the Aleutian low, subsequently weakening the upward propagation of wavenumber-1 planetary wave flux, further strengthening the SAV. This strengthened SAV suggests important implications in understanding the Arctic warming amplification and in predicting the surface temperature changes over the northern continents.

Hu *et al.*[82] examined the decadal relationship between the Stratospheric Arctic Vortex (SAV) and Sea Surface Temperature Anomalies (SSTAs) in the North Atlantic and the dynamic mechanisms involved in the linkage between the two. Their results showed that there is a significant decadal linkage between SSTAs over the North Atlantic and the SAV, where warmed (cooled) SSTAs over the North Atlantic in association with its principal mode correspond to a weakened (strengthened) SAV. The warmed North Atlantic SSTAs tend to result in a weakened SAV *via* two dynamic processes: (i) constructive interference at high latitudes with a ridge in the Atlantic sector and a trough in the Pacific accompanied by a negative North Atlantic Oscillation-like pattern over the North Atlantic and a weakened Aleutian low over the North Pacific; and (ii) more wavenumber-1 waves propagated into the Arctic stratosphere by modifying the baroclinic term of the zonal mean background state and altering the propagating conditions around the tropopause over the Arctic. Results from reanalysis and model simulations both suggest that a strengthening wave intensity in the high-latitude troposphere and more upward propagation of the planetary wavenumber-1 wave in response to the warmed North Atlantic SSTAs conjunctly contribute to the increased planetary wave flux in the Arctic stratosphere, facilitating a weakened SAV.

Hu and Guan[83] reported a significant in-phase relationship between the PDO and Stratospheric Arctic Vortex (SAV) on decadal time scales during 1950–2014, that is, the North Pacific Sea Surface Temperature (SST) cooling (warming) associated with the positive (negative) PDO phases is closely related to the strengthening (weakening) of the SAV. This decadal relationship between the North Pacific

SST and SAV is different from their relationship on sub-decadal time scales. Observational and modeling results both demonstrated that the decadal variation in the SAV is strongly affected by the North Pacific SSTs related to the PDO via modifying the upward propagation of planetary Wavenumber-1 waves from the troposphere to the stratosphere. The decreased SSTs over the North Pacific tend to result in a deepened Aleutian low along with a strengthened jet stream over the North Pacific, which excites a weakened western Pacific pattern and a strengthened Pacific–North American pattern. These tropospheric circulation anomalies are in accordance with the decreased Refractive Index (RI) at middle and high latitudes in the northern stratosphere during the positive PDO phase. The increased RI at high latitudes in the upper troposphere impedes the planetary Wavenumber-1 wave from propagating into the stratosphere, and in turn strengthens the SAV. The responses of the RI to the PDO are mainly contributions of the changes in the meridional gradient of the zonal-mean potential vorticity *via* alteration of the baroclinic term.

Using the CMIP5 Multimodel Ensemble (MME) historical experiments, the modulation of the stratospheric El Niño–Southern Oscillation (ENSO) teleconnection by the Pacific Decadal Oscillation (PDO) is investigated by Rao *et al.*[84]. El Niño (La Niña) significantly impacts the extratropical stratosphere mainly during the positive (negative) PDO in the MME. Although the composite tropical ENSO SST intensities are similar during the positive and negative PDO in models, the Pacific–North America (PNA) responses are only significant when the PDO and ENSO are in phase. The local SST anomalies in the North Pacific can constructively (destructively) interfere with the tropical ENSO forcing to influence the extratropical eddy height anomalies when the PDO and ENSO are in (out of) phase. The difference between the positive and negative PDO in El Niño or La Niña winters filters out the tropical SST forcing, permitting the deduction of the extratropical SST contribution to the atmospheric response. The composite shows that the cold (warm) SST anomalies in the central North Pacific associated with the positive (negative) PDO have a similar impact to that of the warm (cold) SST anomalies in the tropical Pacific, exhibiting a positive (negative) PNA-like response, enhancing (weakening) the upward propagation of waves over the western coast of North America. The composite difference between the positive and negative PDO in El Niño or La Niña winters, as well as in eastern Pacific ENSO or central Pacific ENSO winters, presents a highly consistent atmospheric response pattern, which may imply a linear interference of the PDO's impact with ENSO's.

To show the typical spatiotemporal evolution of circulation anomalies during the NAM's life cycle, Yu *et al.*[85] revisited the various stratosphere-troposphere coupling relation from the perspective of the meridional mass circulation, and indicated that there is a large case-to-case difference in the temporal evolution and vertical profile of polar temperature anomalies during NAM events, which shows no strong dependence on the intensity and duration of NAM events, but agrees well with the variations of the three branches of mass circulation at 60°N: the stratospheric poleward warm air branch (ST), the poleward warm air branch in the upper troposphere (WB), and the equatorward cold air branch in the lower troposphere (CB). The various relationships among the three mass circulation branches are attributed to anomalous wave activities. The amplitude and westward tilt of waves are always stronger (weaker) throughout the stratosphere before (after) the peak time of negative NAM events, leading to a stronger (weaker) ST before (after) the peak time. Variations in WB and CB are mostly dependent on wave variabilities in the mid- to lower-troposphere, leading to variations in the timing of in or out-of-phase coupling of the ST with the WB and CB, and thus various thermal structures during NAM events.

References

[1] XIA Y, HUANG Y, HU Y, *et al.* Impacts of tropical tropopause warming on the stratospheric water vapor [J]. *Climate Dyn.*, 2019, **53**:3409-3418

[2] XIA Y, HU Y, LIU J, *et al.* Stratospheric ozone-induced

cloud radiative effects on Antarctic sea ice [J]. *Adv. Atmos. Sci.*, 2020, **37**:1-10

[3] LIU R, FU Y. Verification of an approximate thermodynamic equation with application to study on Arctic stratospheric temperature changes [J]. *J. Atmos. Sci.*, 2019, **76**:3-9

[4] SHI C, GAO Y, CAI J, *et al.* Response of the dynamic and thermodynamic structure of the stratosphere to the solar cycle in the boreal winter [J]. *J. Atmos. Sol-Terr. Phys.*, 2018, **169**:122-129

[5] HU D, GUAN Z, TIAN W. Signatures of the arctic stratospheric ozone in northern hadley circulation extent and subtropical precipitation [J]. *Geophys. Res. Lett.*, 2019, **46**:12340-12349

[6] MA J, SHANGGUAN M, XIA H, *et al.* Rayleigh and sodium lidar system incorporating time-division and wavelength-division multiplexing [J], *Opt. Commun.*, 2019, **448**:116-123

[7] ZOU Z, XUE X, SHEN C, *et al.* Response of mesospheric HO_2 and O_3 to large Solar proton events [J]. *J. Geophys. Res.: Space Phys.*, 2018, **123**:5738-5746

[8] XUN Y, YANG G, SHE C Y, *et al.* The first concurrent observations of thermospheric Na layers from two nearby central mid-latitude lidar stations [J]. *Geophys. Res. Lett.*, 2019, **46**(4):1892-1899

[9] JIAO J, YANG G, CHENG X, *et al.* Simultaneous lidar observation of peculiar sporadic K and Na layers at São José dos Campos (23.1° S, 45.9° W), Brazil [J]. *Adv. Space Res.*, 2018, **61**(7):1942-1951

[10] WANG Z, YANG G, WANG J, *et al.* Lidar observations and studies of the lower-triangle potassium layer over Beijing [J]. *Chin. J. Space Sci.*, 2018, **38**(1):65-72

[11] YANG D, ZHANG T, WANG J, YAN C, PENG H. Observations of the prominent sporadic sodium layer over Haikou (in Chinese) [J]. *Chin. J. Space Sci.*, 2018, **38**(6):886-890

[12] JIANG G, XU J, WANG W, *et al.* A comparison of quiet time thermospheric winds between FPI observations and model calculations [J]. *J. Geophys. Res.: Space Phys.*, 2018, 123. DOI.org/10.1029/2018JA025424

[13] LIU X, YUE J, WANG W, *et al.* Responses of lower thermospheric temperature to the 2013 St. Patrick's Day geomagnetic storm [J]. *Geophys. Res. Lett.*, 2018, **45**:4656-4664

[14] LIU Y, XU J, LIU X, *et al.* Responses of multiday oscillations in the nighttime thermospheric temperature to solar and geomagnetic activities measured by Fabry-Perot interferometer in China [J]. *J. Geophys. Res.: Space Phys.*, 2019, 124. DOI.org/10.1029/2019JA027237

[15] YANG R, XU J, ZHU Y, YUAN W. Comparison of Retrieval Methods for Neutral Wind Based on Airglow Measurements by a Ground-based Fabry-Perot Interferometer [J]. *Chin. J. Space Sci.*, 2019, **39**(1):76-83

[16] XU L Y, WEI K, WU X, *et al.* The effect of super volcanic eruptions on ozone depletion in a chemistry-climate model [J]. *Adv. Atmos. Sci.*, 2019, **36**(8):823-836

[17] XIA Y, XU W, HU Y, *et al.* Southern-hemisphere high-latitude stratospheric warming revisit [J]. *Climate Dyn.*, 2020, **54**:1671-1682

[18] LI Xiaoting, TIAN Wenshou, XIE Fei, *et al.* Joint impacts of ENSO Modoki and QBO on stratospheric ozone in winter in the Northern Hemisphere [J]. *Acta Meteor. Sin.*, 2019, **77**(3): 456-474

[19] XIE Fei, LI Jianping, SUN Cheng, *et al.* Improved global surface temperature simulation using stratospheric ozone forcing with more accurate variability [J]. *Sci. Rep.*, 2018, **8**(1):1-10

[20] XIE Fei, MA Xuan, LI Jianping, *et al.* An advanced impact of Arctic stratospheric ozone changes on spring precipitation in China [J]. *Clim. Dyn.*, 2018b, **51**(11/12):4029-4041

[21] XIE Fei, MA Xuan, LI Jianping, *et al.* Using observed signals from the arctic stratosphere and indian ocean to predict April–May precipitation in central China [J]. *J. Clim.*, 2020, **33**(1):131-143

[22] MA Xuan, XIE Fei, LI Jianping, *et al.* Effects of Arctic stratospheric ozone changes on spring precipitation in the northwestern United States [J]. *Atmos. Chem. Phys.*, 2019, **19**(2):861-875

[23] XIE Fei, ZHOU Xin, LI Jianping, *et al.* Effect of the indo-pacific warm pool on lower-stratospheric water vapor and comparison with the effect of ENSO [J]. *J. Clim.*, 2018, **31**(3):929-943

[24] LU Jinpeng, XIE Fei, TIAN Wenshou, *et al.* Interannual variations in lower stratospheric ozone during the period 1984–2016 [J]. *J. Geophys. Res.: Atmos.*, 2019, **124**(14): 8225-8241

[25] ZHANG Jiankai, TIAN Wenshou, XIE Fei, *et al.* Stratospheric ozone loss over the Eurasian continent induced by the polar vortex shift [J]. *Nat. Commun.*, 2018, **9**(1):1-8

[26] ZHANG Jiankai, TIAN Wenshou, XIE Fei, *et al.* Zonally asymmetric trends of winter total column ozone in the northern middle latitudes [J]. *Clim. Dyn.*, 2019, **52**(7/8):4483-4500

[27] SHANGGUAN Ming, WANG Wuke, JIN Shuanggen. Variability of temperature and ozone in the upper troposphere and lower stratosphere from multi-satellite observations and reanalysis data [J]. *Atmos. Chem. Phys.*, 2019, **19**(10):6659-6679

[28] XIAO Na, ZHANG Jiankai, TIAN Wenshou, *et al.* Effects of nitrogen oxide emissions over East Asia on ozone and temperature in UTLS region of the Northern Hemisphere [J]. *Plat. Meteor.*, **39**(3):1-14

[29] YI W, XUE X, REID I, *et al.* Estimation of mesospheric densities at low latitudes using the Kunming meteor radar together with SABER temperatures [J]. *J. Geophys. Res.: Space Phys.*, **123**: 3183-3195

[30] WU J, FENG W, XUE X, *et al.* The 27-day solar rotational cycle response in the mesospheric metal layers at low latitudes [J]. *Geophys. Res. Lett.*, 2019, **46**:7199-7206

[31] YI W, XUE X, CHEN J, *et al.* Quasi-90-day oscillation observed in the MLT region at low latitudes from the Kunming meteor radar and SABER [J]. *Earth Planet. Phys.*, **3**:136-146

[32] YI W, XUE X, REID I M, *et al.* Climatology of the mesopause relative density using a global distribution of meteor radars [J]. *Atmos. Chem. Phys.*, **19**:7567-7581

[33] RAO J, REN R, CHEN H, *et al.* Predictability of stratospheric sudden warmings in Beijing climate center forecast system with statistical error corrections [J]. *J. Geophys. Res.: Atmos.*, 2019, **124**:8385-8400

[34] RAO J, REN R, CHEN H, *et al.* Sub-seasonal to seasonal hindcasts of stratospheric sudden warming by BCC–CSM1.1 (m): a comparison with ECMWF [J]. *Adv. Atmos. Sci.*, 2019, **36**(5):479-494

[35] YU Y, CAI M, SHI C, *et al.* Sub-seasonal prediction skill for the stratospheric meridional mass circulation variability in CFSv2 [J]. *Clim. Dyn.*, 2019, **52**:631-650

[36] HU J, REN R. Stratospheric control of the Indian summer monsoon onset [J]. *Dyn. Atmos. Ocean.*, 2018, **83**:135-147

[37] YU Y, CAI M, SHI C. On the linkage among strong stratospheric mass circulation, stratospheric sudden warming, and cold weather events [J]. *Mon. Weather Rew.*, 2018, **146**: 2717-2739

[38] HU J, LI T, XU H. Relationship between the North Pacific Gyre Oscillation and the onset of stratospheric final warming in the northern hemisphere [J]. *Clim. Dyn.*, 2018, **51**:3061-3075

[39] RAO J, REN R, CHEN H, *et al.* The stratospheric sudden warming event in February 2018 and its prediction by a climate system model [J]. *J. Geophys. Res.: Atmos.*, 2018, **123**:13332-13345

[40] YU B, XUE X, KUO C, *et al.* The intensification of metallic layered phenomena above thunderstorms through the modulation of atmospheric tides [J]. *Sci. Rep.*, 2019, **9**(1):1-13

[41] SUN L, XU J, XIONG C, *et al.* Midlatitudinal special airglow structures generated by the interaction between propagating medium-scale traveling ionospheric disturbance and nighttime plasma density enhancement at magnetically quiet time [J]. *Geophys. Res. Lett.*, 2019, **46**. DOI.org/10.1029/2018GL080926

[42] Wu K, Xu J, Xiong C, Yuan W. Edge plasma enhancements of equatorial plasma depletions observed by all-sky imager and the C/NOFS satellite [J]. *J. Geophys. Res.: Space Phys.*, 2018, **123**:8835-8849

[43] YU F R, HUANG K M, ZHANG S D, *et al.* Quasi 10- and 16-day wave activities observed through meteor radar and MST radar during stratospheric final warming in 2015 spring [J]. *J. Geophys. Res.: Atmos.*, 2019, **124**. DOI.org/10.1029/2019JD030630

[44] HUANG K M, XI Y, WANG R, *et al.* Signature of a quasi 30-day oscillation at midlatitude based on wind observations from MST radar and meteor radar [J]. *J. Geophys. Res.: Atmos.*, 2019, **124.** DOI.org/10.1029/2019JD031170

[45] CHEN D, STRUBE C, ERN M, *et al.* Global analysis for periodic variations in gravity wave squared amplitudes and momentum fluxes in the middle atmosphere [J]. *Ann. Geophys.*, 2019, **37**:487-506

[46] HU D, GUO Y, GUAN Z. Recent weakening in the stratospheric planetary wave intensity in early winter [J]. *Geophys. Res. Lett.*, 2019, **46**:3953-3962

[47] WU J F, XUE X H, LIU H L, *et al.* Assessment of the simulation of gravity waves generation by a tropical cyclone in the high-resolution WACCM and the WRF [J]. *J. Adv. Model. Earth Syst.*, 2018, **10**:2214-2227

[48] HUANG K M, YANG Z X, WANG R, *et al.* A statistical study of inertia gravity waves in the lower stratosphere over the Arctic region based on radiosonde observations [J]. *J. Geophys. Res.: Atmos.*, 2018, **123**. DOI.org/10.1029/2017JD027998

[49] GONG S, YANG G, XU J, *et al.* Gravity wave propagation from the stratosphere into the mesosphere studied with lidar, meteor radar, and TIMED/SABER [J]. *Atmosphere*, 2019, **10**(2):81

[50] LI Q, YUSUPOV K, AKCHURIN A, *et al.* First OH airglow observation of mesospheric gravity waves over European Russia region [J]. *J. Geophys. Res.: Space Phys.*, 2018, **123**:2168-2180

[51] LI Q, XU J, YUE J, *et al.* Evolution of a mesospheric bore in a duct observed by ground-based double-layer imagers and satellite observations over the Tibetan Plateau region [J]. *J. Geophys. Res.: Space Phys.*, 2019, **124**: 1377-1388

[52] WANG C M, LI Q Z, XU J Y, *et al.* A study of wave sources of gravity wave events observer by OH airglow imager located at Donggang station [J]. *Chin. J. Geophys.*, 2018, **61**(6):2198-2206

[53] LIU X, XU J, YUE J, *et al.* Orographic primary and secondary gravity waves in the middle atmosphere from 16-year SABER observations [J]. *Geophys. Res. Lett.*, 2019, **46**:4512-4522

[54] LAI C, XU J, YUE J, *et al.* Automatic extraction of gravity waves from all-sky airglow image based on machine learning [J]. *Remote Sens.*, 2019, **11**:1516

[55] HUANG Jinlong, TIAN Wenshou, GRAY L J, *et al.* Preconditioning of Arctic stratospheric polar vortex shift events [J]. *J. Clim.*, 2018, **31**(14):5417-5436

[56] HUANG Jinlong, TIAN Wenshou. Eurasian cold air outbreaks under different arctic stratospheric polar vortex strengths [J]. *J. Atmos. Sci.*, 2019, **76**(5):1245-1264

[57] LI Yuanpu, TIAN Wenshou, XIE Fei, *et al.* The connection between the second leading mode of the winter North Pacific sea surface temperature anomalies and stratospheric sudden warming events [J]. *Clim. Dyn.*, 2018, **51**(1/2):581-595

[58] LIANG Jinglin, LUO Jiali, TIAN Hongying, *et al.* Analysis of abnormal signals in the upper troposphere and stratosphere before the persistent heavy rainfall event in South China in June 2005 [J]. *Clim. Environ. Res.*, **24**(2):237-250

[59] LUO Jiali, LIANG Wenjun, XU Pingping, *et al.* Seasonal features and a case study of tropopause folds over the Tibetan Plateau [J]. *Adv. Meteor.*, 2019. DOI: 10.1155/2019/4375123

[60] WANG Feiyang, TIAN Wenshou, XIE Fei, *et al.* Effect of Madden–Julian oscillation occurrence frequency on the interannual variability of Northern Hemisphere stratospheric

wave activity in winter [J]. *J. Clim.*, 2018, **31**(13):5031-5049

[61] ZHANG Jiankai, XIE Fei, MA Zhichao, *et al.* Seasonal evolution of the quasi-biennial oscillation impact on the Northern Hemisphere polar vortex in winter [J]. *J. Geophys. Res.: Atmos.*, 2019, **124**(23):12568-12586

[62] ZHANG Kequan, WANG Tao, XU Mian, *et al.* Influence of wintertime polar vortex variation on the climate over the North Pacific during late winter and spring [J]. *Atmosphere*, 2019, **10**(11):670

[63] ZHANG Ruhua, TIAN Wenshou, ZHANG Jiankai, *et al.* The corresponding tropospheric environments during downward-extending and nondownward-extending events of stratospheric northern annular mode anomalies [J]. *J. Clim.*, 2019, **32**(6):1857-1873

[64] HAN Yuanyuan, TIAN Wenshou, ZHANG Jiankai, *et al.* A case study of the uncorrelated relationship between tropical tropopause temperature anomalies and stratospheric water vapor anomalies [J]. *J. Trop. Meteor.*, 2018, **24**(3):356-368

[65] LI Yang, ZHANG Jiankai, TIAN Wenshou, *et al.* Impact of dynamical transmission and surface emission on ozone change in troposphere over Beijing [J]. *Arid Meteor.*, 2018, **36**(2):157-166

[66] LUO Jiali, PAN L L, HONOMICHL S B, *et al.* Space-time variability in UTLS chemical distribution in the Asian summer monsoon viewed by limb and nadir satellite sensors [J]. *Atmos. Chem. Phys.*, 2018, **18**(16):12511-12530

[67] SANG Wenjun, HUANG Qian, TIAN Wenshou, *et al.* A large eddy model study on the effect of overshooting convection on lower stratospheric water vapor [J]. *J. Geophys. Res.: Atmos.*, 2018, **123**(18):10023-10036

[68] HAN Yuanyuan, TIAN Wenshou, CHIPPERFIELD M P, *et al.* Attribution of the hemispheric asymmetries in trends of stratospheric trace gases inferred from Microwave Limb Sounder (MLS) Measurements [J]. *J. Geophys. Res.: Atmos.*, 2019, **124**(12):6283-6293

[69] WANG Wuke, SHANGGUAN Ming, TIAN Wenshou, *et al.* Large uncertainties in estimation of tropical tropopause temperature variabilities due to model vertical resolution [J]. *J. Geophys. Res.*, 2019, **46**(16):10043-10052

[70] WANG Wuke, MATTHES K, TIAN Wenshou, *et al.* Solar impacts on decadal variability of tropopause temperature and Lower Stratospheric (LS) water vapour: a mechanism through ocean-atmosphere coupling [J]. *Clim. Dyn.*, 2019, **52**(9/10):5585-5604

[71] WANG Yiping, WANG Hongyue, WANG Wuke. A stratospheric intrusion-influenced ozone pollution episode associated with an intense horizontal-trough event [J]. *Atmosphere*, 2020, **11**(2):164

[72] WEI K, CAI Z, CHEN W, XU L. The effect of a well-resolved stratosphere on East Asian winter climate [J]. *Climate Dyn.*, 2018, **51**:4015-4028

[73] GONG H, WANG L, CHEN W, NATH D. Multidecadal fluctuation of the wintertime Arctic Oscillation pattern and its implication [J]. *J. Climate*, 2018, **31**:5595-5608

[74] GONG H, WANG L, CHEN W, *et al.* Diversity of the wintertime Arctic oscillation pattern among CMIP5 models: role of stratospheric polar vortex [J]. *J. Climate*, 2019, **32**:5235-5250

[75] CHEN S, YU B, CHEN W, WU R. A review of atmosphere-ocean forcings outside the tropical Pacific on the El Niño-Southern Oscillation occurrence [J]. *Atmosphere*, 2019, **9**:439

[76] CHEN S, WU R, CHEN W. Enhanced impact of Arctic sea ice change during boreal autumn on the following spring Arctic oscillation since the mid-1990s [J]. *Climate Dyn.*, 2019, **53**:5607-5621

[77] DING S, CHEN W, GRAF H F, *et al.* Distinct winter patterns of tropical Pacific convection anomaly and the associated extratropical wave trains in the Northern Hemisphere [J]. *Climate Dyn.*, 2018, **51**:2003-2022

[78] DING S, CHEN W, GRAF H F, *et al.* Quasi-stationary extratropical wave trains associated with distinct tropical Pacific seasonal mean convection patterns: observational and AMIP model results [J]. *Climate Dyn.*, 2019, **53**:2451-2476

[79] HUANGFU J, CHEN W, JIAN M, HUANG R H. Impact of the cross-tropopause wind shear on tropical cyclone genesis over the Western North Pacific in May [J]. *Climate Dyn.*, 2019, **52**:3845-3855

[80] HUANG R H, CHEN W, WEI K, *et al.* Atmospheric dynamics in the stratosphere and its interaction with tropospheric processes: progress and problems [J]. *Chin. J. Atmos. Sci.*, 2018, **42**(3):463-487

[81] HU D, GUAN Z, TIAN W, *et al.* Recent strengthening of the stratospheric Arctic vortex response to warming in the central North Pacific [J]. *Nature Commun.*, 2018, **9**:1697

[82] HU D, GUAN Z, GUO Y, *et al.* Dynamical connection between the stratospheric Arctic vortex and sea surface temperatures in the North Atlantic [J]. *Clim. Dyn.*, 2019, **32**:6979-6993

[83] HU D, GUAN Z. Decadal relationship between the stratospheric Arctic vortex and Pacific Decadal oscillation [J]. *J. Climate*, 2018, **31**:3371-3386

[84] RAO J, GARFINKEL C, REN R. Modulation of the northern winter stratospheric El Niño–Southern Oscillation teleconnection by the PDO [J]. *J. Climate*, 2019, **32**:5761-5783

[85] YU Y, REN R. Understanding the variation of stratosphere-troposphere coupling during stratospheric northern annular mode events from a mass circulation perspective [J]. *Clim. Dyn.*, 2019, **53**:5141-5164

LIU Siqing, CHEN Yanhong, LUO Bingxian, CUI Yanmei, ZHONG Qiuzhen, WANG Jingjing, YUAN Tianjiao, HU Qinghua, HUANG Xin, CHEN Hong. Development of New Capabilities Using Machine Learning for Space Weather Prediction. *Chin. J. Space Sci.*, 2020, **40**(5): 323-331. DOI:10.11728/cjss2020.05.323

Development of New Capabilities Using Machine Learning for Space Weather Prediction*

LIU Siqing[1,2,3] CHEN Yanhong[1,2] LUO Bingxian[1,2,3] CUI Yanmei[1,2]

ZHONG Qiuzhen[1,2,3] WANG Jingjing[1,2] YUAN Tianjiao[1,2]

HU Qinghua[3,4] HUANG Xin[4,5] CHEN Hong[5,6]

1 (*National Space Science Center, Chinese Academy of Sciences, Beijing* 100190)

2 (*Key Laboratory of Science and Technology on Environmental Space Situation Awareness, Chinese Academy of Sciences, Beijing* 100190)

3 (*University of Chinese Academy of Sciences, Beijing* 100049)

4 (*School of Computer Science and Technology, Tianjin University, Tianjin* 300072)

5 (*Key Laboratory of Solar Activity, National Astronomical Observatories of Chinese Academy of Sciences, Beijing* 100101)

6 (*College of Science, Huazhong Agricultural University, Wuhan* 430070)

Abstract With the development of space exploration and space environment measurements, the numerous observations of solar, solar wind, and near Earth space environment have been obtained in last 20 years. The accumulation of multiple data makes it possible to better use machine learning technique, which has achieved unforeseen results in industrial applications in last decades, for developing new approaches and models in space weather investigation and prediction. In this paper, the efforts on the forecasting methods for space weather indices, events, and parameters using machine learning are briefly introduced based on the study works in recent years. These investigations indicate that machine learning, especially deep learning technique can be used in automatic characteristic identification, solar eruption prediction, space weather forecasting for solar and geomagnetic indices, and modeling of space environment parameters.

Key words Space weather forecasting, Machine learning, Deep learning

Classified index P353

1 Automatic Characteristic Identification

In last decades, machine learning, especially deep learning pushed a big success in image and voice recognition. In space weather field, there are numerous solar images observations which provide abundant information about solar active region, magnitude, emission, *etc.* Sunspots are darker areas on the solar photosphere and most of solar eruptions occur in complex sunspot groups. The morphological or magnetic features of sunspot groups are mainly predictors of solar eruption forecasting. Currently, both identification and classification of sunspots are mainly carried out manually by experts, which is a subjective, time-consuming, and labor-intensive process. With the rapid accumulation of solar observation data, applying the machine learning method into solar active feature automatic recognition and solar eruption forecasting is explored.

* Supported by National Natural Science Foundation of China (41574181)
Received March 15, 2020
E-mail: chenyh@nssc.ac.cn

The Mount Wilson classification scheme describes the spatial distribution of magnetic polarities in sunspot groups, which plays an important role in forecasting solar flares. This scheme considers bipolar sunspot groups as a basic type, and other types are regarded as deformations of the bipolar sunspot group. Statistically, large flares are more likely to occur in ARs with complex magnetic types, while the ARs of Alpha type have a lower probability of flare eruption. Using a Convolutional Neural Network (CNN) method, Fang *et al.*[1] developed an automatic procedure for the recognition of the predefined magnetic types in sunspot groups, which is based on the SDO/HMI SHARP data taken during the time interval 2010–2017 (Figure 1). In the study, the sunspot magnetic type falls into three categories, the unipolar group α, the bipolar group β, and other complex multipolar groups, called β-x. There are three different models (A, B, and C) built, which take magnetograms, continuum images, and the two-channel pictures as input, respectively.

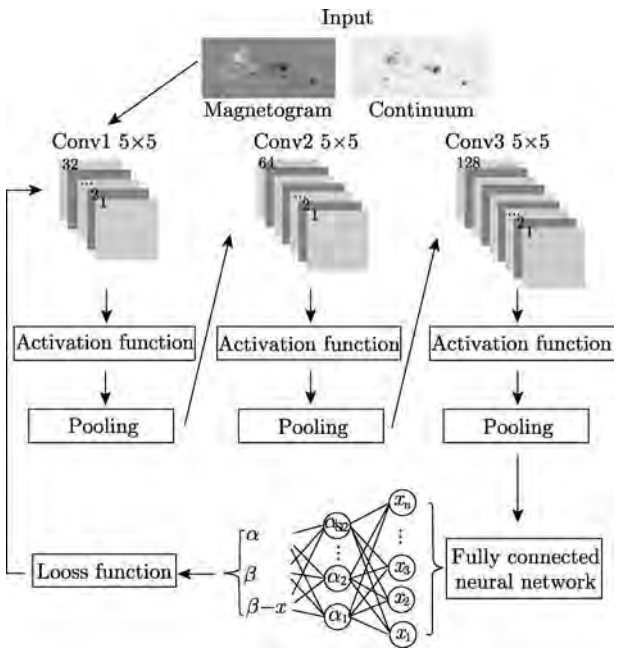

Fig. 1 Schematic of the CNN structure for automatic recognition of magnetic type in sunspot groups[1]

The model results show that CNN has a productive performance in identification of the magnetic types in solar active regions (Table 1). The best recognition result emerges when continuum images are used as input data solely, and the total accuracy exceeds 95%, for which the recognition accuracy of Alpha type reaches 98% while the accuracy for β type is slightly lower but maintains above 88%.

2 Machine Learning for Solar Eruption Forecasting

Solar eruptions, such as solar flare, Coronal Mass Ejections (CMEs), Solar Proton Event (SPE) can significantly affect near-Earth space environment and lead the subsequent effects on space assets, navigation and communication, and ground based electric power system. Therefore, it is very important to predict when solar eruption occurs. However, the current capability is still very limited.

The conventional solar flare forecasting models mainly rely on morphological or physical parameters extracted from active regions, but these parameters have limited forecasting capability. Instead of extracting the man-made physical parameters from the active region, Huang *et al.*[2] firstly try to apply the deep learning method to automatically dig out the forecasting patterns hidden in the data. In this manuscript, all active regions within ±30° of the central meridian for line-of-sight magnetograms observed by the SOHO/MDI and the SDO/HMI from 1996 April to 2015 October are collected, and the HMI data is fused with the MDI data to generate a

Table 1 Performance of the three models (A, B, and C), which take magnetograms, continuum images, and the two- channel pictures as input, respectively[1]

Model	Data source	Number of convolutions	Size of the convolution kernel	Total accuracy	α	β	β-x
A	magnetogram	4	3×3	0.935	0.990	0.880	0.928
B	continuum	3	5×5	0.954	0.985	0.885	0.958
C	magnetogram+continuum	A+B	–	0.953	0.980	0.895	0.960

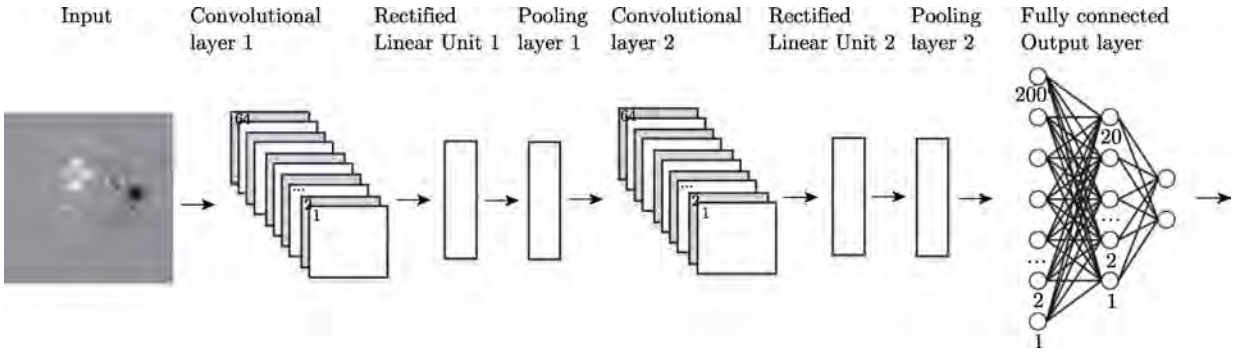

Fig. 2 Structure of the convolutional neural network for solar flare forecasting[2]

big data set. Supported by this data set, a solar flare forecasting model by using the convolutional neural network (Figure 2) is developed. The network consists of the convolutional layer, the nonlinear layer, the pooling layer, and the fully connected layer. The convolutional layer is used to extract forecasting patterns from input magnetograms. The nonlinear layer adds the nonlinear transform into the forecasting model. The pooling layer reduces the dimensionality of parameters in the network. And finally, the fully connected layer can provide high-level reasoning for the solar flare forecasting. This forecasting model can be used to forecast solar flares with the threshold of C, M, or X levels within the forecasting period of 6, 12, 24, or 48 h. The testing results of the forecasting model show that the performance of the proposed forecasting model is comparable to the state-of-the-art flare forecasting models.

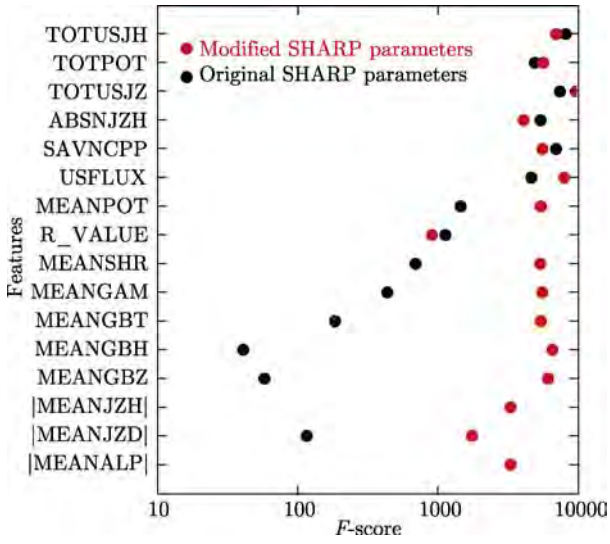

Fig. 3 Fisher ranking score (F-score) for each parameter. Black dots refer to the F-scores for the original SHARP parameters; red for the modified SHARP parameters. Names of the parameters are on the Y-axis[3]

It is well established that solar flares and Coronal Mass Ejections (CMEs) are powered by the free magnetic energy stored in volumetric electric currents in the corona, predominantly in Active Regions (ARs).The parameters in the Space-weather HMI Active Region Patches (SHARP) data from the Solar Dynamics Observatory/HMI observation of vector magnetic field are designed and generated to search for eruption-related signatures that can be further employed for predicting flares and CMEs. Wang *et al.*[3] reported research done on the modification of these SHARP parameters with an attempt to improve flare prediction. The newly modified parameters are weighed heavily by magnetic Polarity In version Lines (PIL) with a high magnetic gradient, as suggested by Schrijver, by multiplying the parameters with a PIL mask. It is demonstrated that the number of the parameters that can well discriminate erupted and non-erupted ARs increases significantly by a factor of two, in comparison with the original parameters (as shown in Figure 3). This improvement suggests that the high-gradient PILs are tightly related with solar eruption that agrees with previous studies. This also provides new data that possess potential to improve the machine-learning based solar flare prediction models.

It is known that the properties of the Polarity Inversion Line (PIL) in solar Active Regions (ARs)

are strongly correlated to flare occurrences. Wang *et al.*[3] suggested that the PIL mask, enclosing the PIL areas, had significant potential for improving machine learning based flare prediction models. Wang *et al.*[4] adopted an unsupervised machine learning algorithm, Kernel Principle Component Analysis (KPCA), to directly derive features from the PIL mask and difference PIL mask (as shown in Figure 4), and use those features to classify ARs into two categories, non-strong flaring ARs and strong-flaring (M-class and above flares) ARs, for time-in-advance from one hour to 72 h at a 1 hour cadence. The two best features are selected from the KPCA results to develop random forest classifiers for predicting flares, and the models are then evaluated and compared to similar models based on the *R*-value (as suggested by Schrijver) and difference *R*-value. The results show that the features derived from the PIL masks by KPCA are effective in predicting flare occurrence, with overall better Fisher ranking scores and similar predictive statistics as the *R*-value characteristics.

3 Forecasting of Solar and Geomagnetic Indices with Machine Learning

The forecasting of solar activity index, represented by Solar 10.7 cm radio flux ($F_{10.7}$), and geomagnetic activity, represented by *Ap*, *Kp*, *Dst*, *etc.*, is very

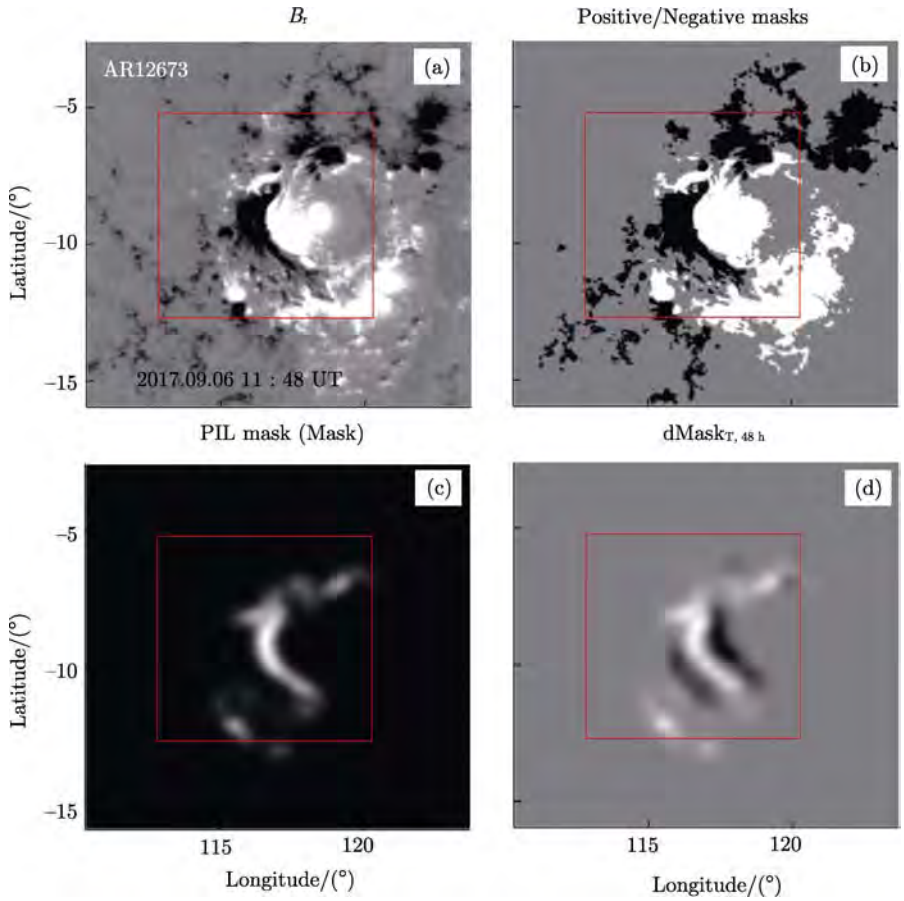

Fig. 4 Radial magnetic field, B_r, in the active region AR 12673 taken at 11:48 UT, 6 September 2017, and minimum and maximum of the image are –1000 Gs and 1000 Gs, respectively (a). Positive/negative magnetic polarity mask derived from the B_r image (b). PIL mask derived from the B_r polarity mask. The red squares enclose the sub-images with a size of 250×250 Pixel centered at the centroid of the PIL mask used in this study (c). Bottom right: the corresponding difference PIL mask at $Y = 48$ h (d)[4]

important in space weather as they are widely used to describe the level of solar activity and geomagnetic fields. These indices are also the necessary inputs for many empirical and theoretical models in space environment research and application.

Traditional methods for $F_{10.7}$ medium-term forecasting mainly include linear regression and empirical model based on the periodic variation. Wang *et al.*[5] discovered that forecasting errors of $F_{10.7}$ are heteroscedastic, something that is not often considered in previous models. In addition, task correlation between different forecasting steps is ignored in current multistep-ahead forecast models. Wang *et al.*[5] proposed a linear multistep forecasting model based on the correlation between different forecasting steps and the characteristic of heteroscedasticity (CH-MF model). Further, a variational Bayesian procedure was introduced to optimize the model. The performance of the proposed model is tested using $F_{10.7}$ historical data. Figure 5 shows the forecasting results in 2001, which indicates that the model is more effective and reliable than the linear regression model for $F_{10.7}$ multistep forecasting task. Thus, it is reasonable to consider task correlation and to embed heteroscedasticity in $F_{10.7}$ medium-term forecasting task.

For geomagnetic index, there are various studies related to *Kp* forecasting. The artificial Neural Network (NN) is the most popular algorithm for short-time *Kp* forecasting. For example, Liu *et al.*[6] developed a model forecasting *Kp* 1~3.5 h in advance using traditional NN, which is used in practical operations, and its forecast results are on the website of Space Environment Prediction Center (SEPC), Chinese Academy of Science. Tan *et al.*[7] proposed a *Kp* forecasting model 1-hour in advance based on Long Short-Term Memory (LSTM). LSTM is developed from Recurrent Neural Networks (RNNs)[8]. LSTM can hold long-term memory and is helpful for learning sequential data. It can find complex nonlinear relationships in the data set. The input of the LSTM model for *Kp* forecasting is made up of a time series of *BI*, *Kp* and *Dp*, with 6 h of time lag. *BI* is the Boyle Index[9] which is related to solar wind, while *Dp*

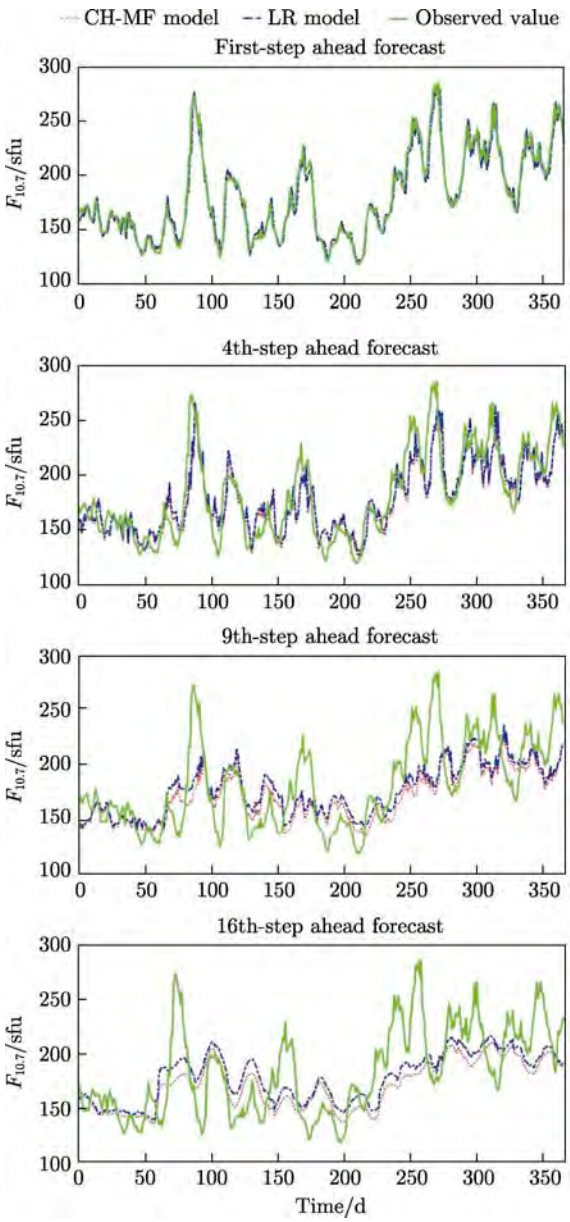

Fig. 5 Comparison between $F_{10.7}$ observations and forecast values in 2001[5]

is the solar wind dynamic pressure. Considering the data imbalance between storm and no-storm time, the three sub-model structure is designed (Figure 6), which includes a classification model and two regression sub-models to improve the performance of geomagnetic storm forecasting.

The effectiveness of deep learning in *Kp* forecasting was compared with another five *Kp* forecasting models dealing with the performance for *Kp* forecasting and geomagnetic storm forecasting. Table 2 shows that the RMSE and MAE of the LSTM model

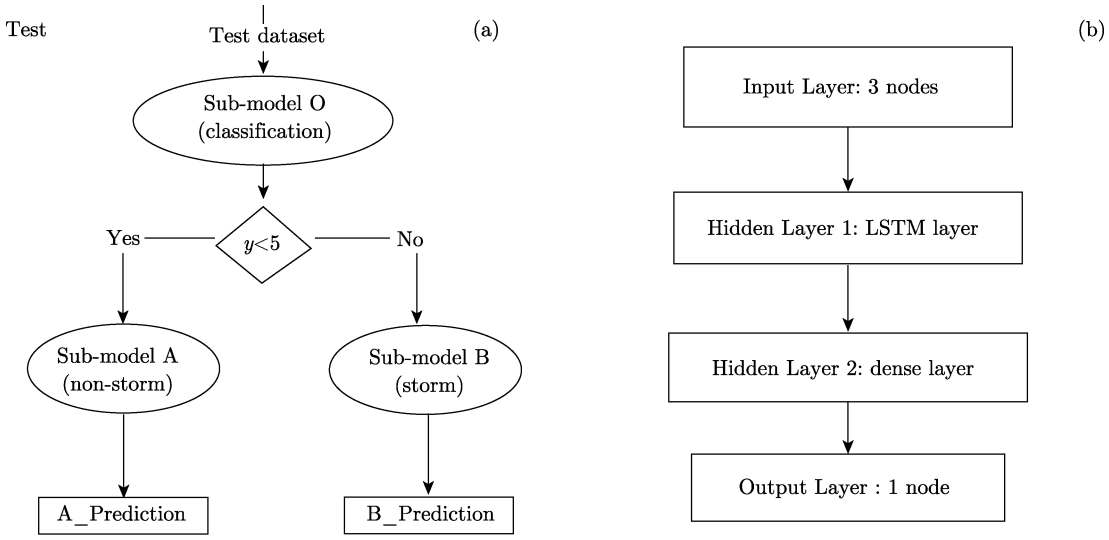

Fig. 6 *Kp* forecasting model structure (a) and the structure of the submodels A and O (b)[7]

Table 2 Comparison on Root Mean Square Error (RMSE), Mean Absolute Error (MAE) and Correlation Coefficient (CC) of *Kp* forecasting among six models[7]

Model	MAE	RMSE	CC
AR model	0.5641	0.7593	0.7334
Linear regression	0.4969	0.6591	0.7997
Lasso regression	0.5091	0.6665	0.7968
SVR	0.4835	0.6522	0.8050
BP neural network	0.4946	0.6596	0.7990
Our model	0.4765	0.6382	0.8147

are the smallest among the six models which are 0.4765 and 0.6382, respectively. In addition, CC is the largest among the six models which is 0.8147. The verification for geomagnetic storm forecasting also indicates the LSTM model can improve the prediction ability of the occurrence of geomagnetic storms ($Kp \geqslant 5$). It is helpful using LSTM for deep learning to build the *Kp* forecasting model.

4 Modeling Space Environment Parameters Using Deep Learning

The ultimate purpose of space weather prediction is to give the accurate description of all kinds of space environment parameters, such as high energetic particle flux, magnetic field, electron density, plasma density, neutral density, *etc.* Many research and modeling works were performed considering the physical process and mechanism of space environment. They can give a relatively objective description of the long-term behavior of the system, while most of them are not appropriately used in space weather operation.

Therefore, empirical model is still a useful method to give the prediction of space weather parameters. Traditional NN method is also tried to make some parameters prediction. For ionosphere, the f_0F_2 (The critical frequency of ionospheric F_2-layer) prediction model for 24 h in advance was established using traditional Back-Propagation (BP) network[10,11]. With more and more ionospheric measurements obtained, new skills in machine learning should be developed to give a more accurate forecast of ionosphere in global range, especially to improve the prediction during geomagnetic storms. Using IGS TEC products, solar 10.7 cm flux index, geomagnetic index *ap*, solar wind speed and the southward components of interplanetary magnetic field, Yuan *et al.*[12] built a forecast model for Beijing station (40°N, 115°E) based on the deep learning Recurrent Neural Network (RNN). The Root Mean Square Error (RMSE) of the disturbed ionosphere TEC predicted by RNN model is lower than that of BPNN (Back Propagation Neural Network) model by 0.49~1.46 TECU

Fig. 7 Forecasting RMSE of TEC during magnetic disturbed time (a) and magnetic quite time (b) in Beijing. Inputs are $F_{10.7}$, TEC and Ap for sample set 1, $F_{10.7}$, TEC, Ap, solar wind speed and IMF B_z for sample set 2 and $F_{10.7}$, TEC, solar wind speed and IMF B_z for sample set 3[12]

(Figure 7). The forecasting accuracy of ionospheric positive storm by RNN model is increased by 16.8% with solar wind parameters. Furthermore, the RMSE of RNN model on 31 strong TEC storm in 2001 and 2015 are less than that of BPNN model by 0.2 TECU, and the RMSE of RNN model is decreased by 0.36~0.47 TECU as solar wind parameters are added. The results indicate that RNN model is more reliable than BP model for short-term forecasting of TEC. Moreover, the adding of interplanetary solar wind parameters is helpful for predicting TEC positive storm.

Based on deep learning, a regional TEC prediction model 24 h in advance for Chinese region is also developed. The RMSE is 4.84 TECU during the quiet time, and 6.86 TECU during the geomagnetic disturbed time. The spatial distribution of the RMSE during geomagnetic quiet time and geomagnetic storm time are shown in Figure 8.

High-energy electron at GEO is regarded as a killed electron as it can penetrate the components of satellites and result in an accumulated charge within the material, causing a deep dielectric charging and discharging process which can cause abnormal behavior in satellite systems[13]. Based on a deep learning method of Long Short-Term Memory (LSTM),

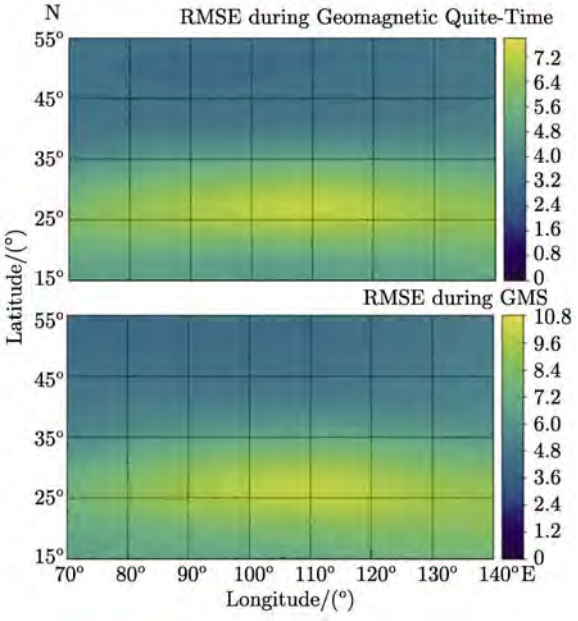

Fig. 8 RMSE of TEC regional prediction model during quiet time and geomagnetic storm time

Wei *et al.*[14] developed a model to predict the daily >2 MeV electron integral flux 1-day ahead at geostationary orbit. The experiment included different input combinations among geomagnetic indices and solar wind parameters. It showed that when the model takes daily >2 MeV electron integral flux, daily averaged magnetopause subsolar distance, and

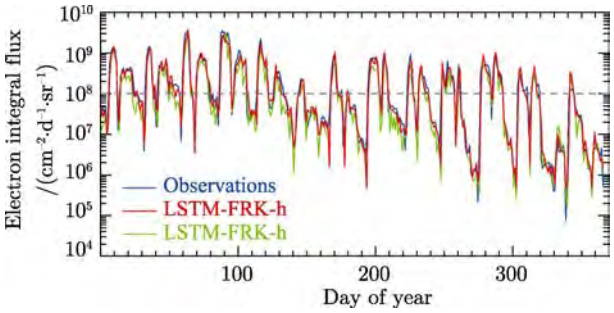

Fig. 9 Comparison among forecasting results of two categories of forecasting models and observations in 2008. The daily >2 MeV electron integral flux of 10^8 cm^{-2}·d^{-1}·sr^{-1} over the entire time of each year is shown as a dark gray dashed curve. LSTM represents Long Short-Term Memory[14]

daily summed *Kp* index as inputs, the prediction efficiencies in 2008, 2009, and 2010 are 0.833, 0.896 and 0.911, respectively. This value reaches 0.900 for 2008, when hourly >2 MeV electron integral flux, hourly magnetopause subsolar distance, and daily summed *Kp* index are taken as inputs. Figure 9 shows the comparisons among the results of two categories of forecasting models and observations in 2008. The prediction efficiencies of the Persistence model and the 27-order Autoregressive model for the same tested time are 0.679 and 0.743, respectively. Therefore, the model developed based on the LSTM method can improve the prediction efficiency significantly for daily >2 MeV electron integral flux 1-day ahead at geostationary orbit.

5 Other Potential Applications for Machine Learning

Currently, some new applications are developing under the cooperation of experts on space weather, computer science, statistics. For example, a sparse robust additive machine (called pin-SAM) model was proposed to investigate whether CME can reach Earth space or not. Pin-SAM can achieve robust classification and variable selection simultaneously, which is formulated by integrating the empirical risk with the pinball loss and the ℓ_q-regularizer $(q \geqslant 1)$ with data dependent hypothesis spaces. This method can explore and utilize the structure information among the input variables, and give interpretability in high dimensional data analysis. A list of CMEs that includes 115 positive-examples (ICMEs) and 11212 negative-examples (CMEs except ICMEs) was used to train and test in pin-SAM. Twenty features in total are considered which includes the parameters of corresponding CMEs, such as the Central PA (CPA), Angular Width, three approximated speeds, Mass, Kinetic Energy and MPA, and the solar wind parameters. For the hyperparameters of pin-SAM, $q = 2$ and $\tau = 0.2, 0.4, 0.6$ are set. Each evaluation is repeated for 100 times and the average results on accuracy and the recall of positive-examples are calculated. The selected variables in the process of estimation are shown in Figure 10. The result shows that the CME angular width plays the most important role in determining CMEs propagation under varying hyperparameters. This provides the data-driven support for the statement that the angular width contains the key information of CME propagating direction. More such kind of knowledge discovery experiments are developing now in space weather filed.

Another aspect of application is the similarity model for a recommendation in operational space weather prediction. If a similar event was dug out from historical data and recommended to forecasters, the forecasters can reference the event's process and give a more reliable forecast for current event. A CME event similarity model for the recommendation was now developing in Space Environment Prediction Center (SEPC) for better predicting the effect of the observed CME on Earth space.

Machine learning is not new to space weather. Traditional Neural Network has been used since1990 s. However, machine learning has never been as successful as it is now, which necessarily leads to new success and progress in space weather. The efforts introduced in this paper are just the beginning of the innovation. It is expectable that more helpful methods will be developed and used in automatically identifying events/features, space weather forecasting, modeling, and knowledge discovery in the future.

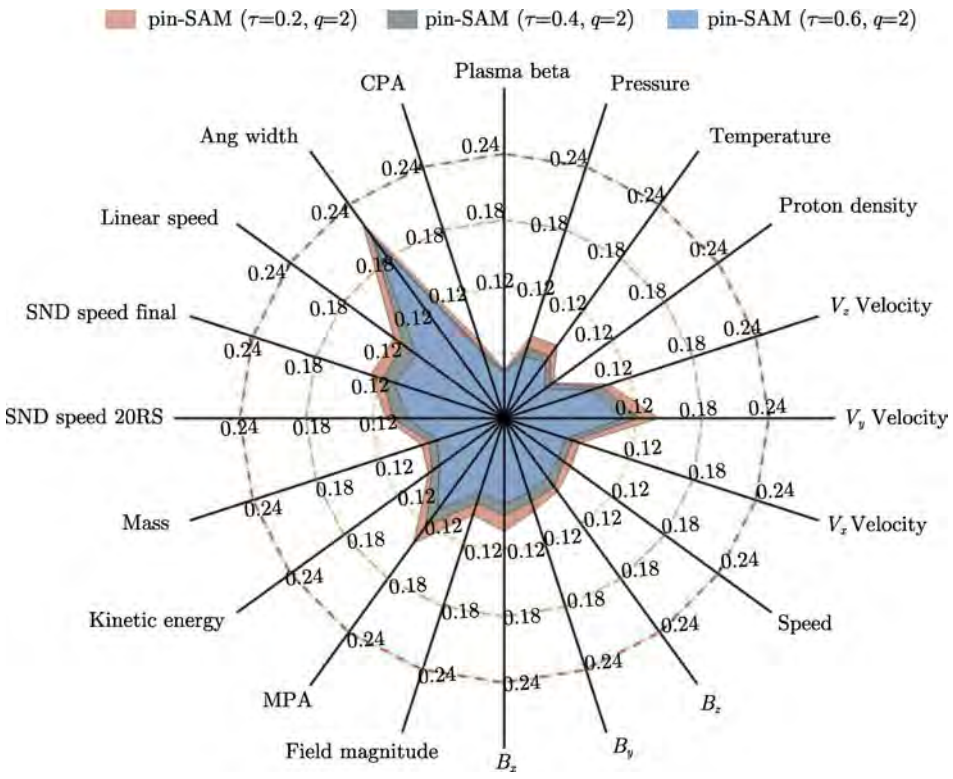

Fig. 10 Radar map of variable weights for CME parameters from additive models

References

[1] FANG Y, CUI Y, AO X, Deep learning for automatic recognition of magnetic type in sunspot groups [J]. *Adv. Astron.*, 2019:9196234

[2] HUANG X, WANG H, XU L, *et al.* Deep learning based solar flare forecasting model. I. Results for line-of-sight magnetograms [J]. *Astrophys. J.*, 2019, **856**:7

[3] WANG J, LIU S, AO X, *et al.* Parameters derived from the SDO/HMI vector magnetic field data: potential to improve machine-learning-based solar flare prediction models [J]. *Astrophys. J.*, 2019, **884**:175

[4] WANG J, LIU S, AO X, *et al.* Solar flare predictive features derived from polarity inversion line masks in active regions using an unsupervised machine learning algorithm [J]. *Astrophys. J.*, 2020, **92**:140

[5] WANG Z, HU Q, ZHONG Q, WANG Y. Linear multistep $F_{10.7}$ forecasting based on task correlation and heteroscedasticity [J]. *Earth Space Sci.*, 2018, **5**:863-874

[6] LIU Y, LUO B, LIU S, GONG J. *Kp* Forecast models based on neural networks [J]. *Manned Spaceflight*, 2013, **19**(2):70-80

[7] TAN Y, HU Q, WANG Z, ZHONG Q. Geomagnetic index *Kp* forecasting with LSTM [J]. *Space Weather*, 2018, **16**:406-416

[8] GRAVES A. Supervised Sequence Labelling with Recurrent Neural Networks [M]. Heidelberg: Springer, 2012

[9] BOYLE C, REIFF P, HAIRSTON M. Empirical polar cap potentials [J]. *J. Geophys. Res.*, 1997, 102(A1):111-125

[10] CHEN Y, XUE B, LI L. Forecasting of ionospheric critical frequency using neural networks [J]. *Chin. J. Space Sci.*, 2005, **25**(2):99-103

[11] CHEN C, WU Z, SUN S, *et al.* Forecasting of ionospheric f_0F_2 in china using neural network [J]. *Chin. J. Space Sci.*, 2011, **31**(3):304-310

[12] YUAN T, CHEN Y, LIU S, GONG J. Prediction model for Ionospheric total electron content based on deep learning recurrent neural network [J]. *Chin. J. Space Sci.*, 2018, **38**(1):48-57

[13] LANZEROTTI L J, LAFLEUR K, MACLENNAN C G, MAURER D W. Studies of spacecraft charging on a geosynchronous telecommunications satellite [J]. *Adv. Space Res.*, 1998, **22**(1):79-82

[14] WEI L, ZHONG Q, LIN R *et al.* Quantitative prediction of high-energy electron integral flux at geostationary orbit based on deep learning [J]. *Space Weather*, 2018, **16**:903-916

ZHANG Peng, CHEN Lin, XIAN Di, XU Zhe, GUAN Min. Update on Fengyun Meteorological Satellite Program and Development. *Chin. J. Space Sci.*, 2020, **40**(5): 332-345. DOI:10.11728/cjss2020.05.332

Update on Fengyun Meteorological Satellite Program and Development*

ZHANG Peng CHEN Lin XIAN Di XU Zhe GUAN Min

(*National Satellite Meteorological Center/National Center for Space Weather, China Meteorological Administration, Beijing* 100081)

Abstract China began to develop its meteorological satellite program since 1969. With 50-years' growing, there are 17 Fengyun (FY) meteorological satellites launched successfully. At present, seven of them are in orbit to provide the operational service, including three polar orbiting meteorological satellites and four geostationary meteorological satellites. Since last COSPAR report, no new Fengyun satellite has been launched. The information of the on-orbit FY-2 series, FY-3 series, and FY-4 series has been updated. FY-3D and FY-2H satellites accomplished the commission test and transitioned into operation in 2018. FY-2E satellite completed its service to decommission in 2019. The web-based users and Direct Broadcasting (DB) users keep growing worldwide to require the Fengyun satellite data and products. A new Mobile Application Service has been launched to Fengyun users based on the cloud technology in 2018. In this report, the international and regional co-operations to facilitate the Fengyun user community have been addressed especially. To strengthen the data service in the Belt and Road countries, the Emergency Support Mechanism of Fengyun satellite (FY_ESM) has been established since 2018. Meanwhile, a Recalibrating 30-years' archived Fengyun satellite data project has been founded since 2018. This project targets to generate the Fundamental Climate Data Record (FCDR) as a space agency response to the Global Climate Observation System (GCOS). At last, the future Fengyun program up to 2025 has been introduced as well.

Key words Fengyun meteorological satellite, Product and data service, International co-operation and supporting, Historical Chinese Fengyun satellite data recalibrating, Future program

Classified index P 351

1 Introduction

The CMA Fengyun (FY) Meteorological Satellite Program includes both geostationary and polar orbit satellite missions. Fengyun satellites take place in series. The odd number series is the polar-orbiting series, while the even number series is the geostationary. The capital letter in the serial number refers to the seat of a particular satellite in the launching sequence.

Currently, 7 Fengyun satellites are running operationally in space, including 3 polar orbit and 4 geostationary satellites. Figure 1 shows the present operational Fengyun satellite flying in space. In the past two years, no new Fengyun meteorological satellite has been launched. FY-2E was decommissioned on 11 January 2019, while FY-2H took its position on 1 January 2019[1,2].

In this report, the status of current polar orbiting, or Low Earth Observation (LEO), and Geostationary (GEO) meteorological satellites are updated in Chapter 2 and Chapter 3. The data service is introduced in Chapter 4. Especially, two useful mobile applications on WeChat platform are released to public to strengthen the data service of Fengyun satellites in 2018. With the continuous development

* Supported by the National Key Research and Development Program of China (2018YFB0504900, 2018YFB0504905)
Received March 20, 2020
E-mail: zhangp@cma.gov.cn

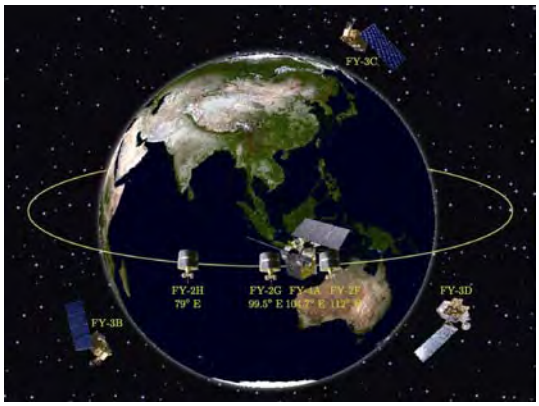

Fig. 1 Operational Fengyun satellites in space

of Fengyun satellite, there are increasing international users. Chapter 5 introduces the progress of international and regional cooperation, especially the Emergency Support Mechanism of Fengyun Satellite (FY_ESM) and its application in the Belt and Road countries. In Chapter 6, some recent progress of retrospective calibration of historical Chinese Fengyun satellite data is introduced. Finally, in Chapter 7, we look forward to the future planning of Fengyun satellite[3,4].

2 Status of Current LEO

The current operating LEO satellite system of CMA is the FY-3 series satellites flying on AM and PM orbits. Most of the sensors on-board satellites work well. Considered FY-3B on orbit for almost 10 years, there are some instruments out of work due to aging. Some instruments on-board FY-3C have been forced to shut down for the energy failure on the satellite platform. Some updated information of FY-3 is listed in the Table 1.

The FY-3 polar-orbiting satellite series is developed for LEO service from 2008 to 2025 beyond. Basically, the FY-3 series are capable of global atmospheric sounding, IR/VIS/Microwave imaging, radiation budget measurement and atmospheric composition measurement, including O_3 amount, CO_2 amount, *etc*. The capability of precipitation sounding with radar has been developed for the coming rainfall mission in 2022.

The detailed descriptions for main instruments are as follows.

VIRR (Visible and Infra-Red Radiometer), flying on FY-3A/B/C, 10-channel VIS/IR radiometer for multi-purpose imagery, resolution 1.1 km, swath 2800 km.

MERSI (Medium Resolution Spectral Imager), flying on FY-3A/B/C, 20-channel radiometer (19 in VIS/NIR/SWIR and one in TIR at 10.0~12.5 μm) for ocean color and vegetation indexes. Resolution 250 m for 4 VIS/NIR and one TIR channel, 1 km for other channels; swath 2800 km. Since FY-3D, the MERSI is evolved to MERSI-2, which has 25 channels (19 in VIS/NIR/SWIR and 6 in TIR from 3.7~12.5 μm).

MWRI (Micro-Wave Radiation Imager), flying on FY-3A/B/C/D, 5-frequencies/10 channels (all frequencies in double polarization) for multi-purpose MW imagery. Conical-scanning radiometer, resolution 9.5 km×15 km at 90 GHz, 30 km×50 km at 19 GHz, swath 1400 km.

IRAS (Infra-Red Atmospheric Sounder), flying on FY-3A/B/C, 26-channel IR radiometer (including one VIS) for temperature/humidity sounding, resolution 17 km, swathe 2250 km.

MWTS (Micro-Wave Temperature Sounder), flying on FY-3A/B, 4-channel MW radiometer for nearly-all-weather temperature sounding, 54 GHz band, resolution 70 km, cross-track scanning, swath 2200 km.

MWTS-2 (Micro-Wave Temperature Sounder), flying on FY-3C/D, 13-channel MW radiometer for nearly-all-weather temperature sounding, 54 GHz band, resolution 70 km, cross-track scanning, swath 2200 km.

MWHS (Micro-Wave Humidity Sounder), flying on FY-3A/B, 4-frequency/5-channel (one frequency in double polarization) MW radiometer for nearly-all-weather humidity sounding. 183 GHz band, resolution 15 km, cross-track scanning, swath 2700 km.

MWHS-2 (Micro-Wave Humidity Sounder), flying on FY-3C/D, 15-channel MW radiometer for nearly-all-weather humidity sounding. 183 GHz band, resolution 15 km, cross-track scanning, swath 2700 km.

Table 1 Current Fengyun polar-orbiting satellites (as of 1 March 2020)

Orbit type (Local time of descending node/ascending node)	Satellites currently in orbit	Equatorial crossing time (design specifications)	Equatorial crossing time (present)	Launch date	Status	Main instruments
Morning orbit (07:00 LT–12:00 LT)/ (19:00 LT–24:00 LT)	FY-3C	10:00 LT	09:07 LT	23 Sept. 2013	Primary operation	VIRR(O) MERSI(S) IRAS(S) MWRI(S) MWTS-2(S) MWHS-2(O) TOU(O) SIM(S) ERM(O) GNOS(O) SEM(S)
Afternoon orbit (12:00 LT–17:00 LT)/ (00:00 LT–05:00 LT)	FY-3B	14:00 LT	16:06 LT	5 Nov. 2010	Secondary operation	VIRR(O) MERSI (O) IRAS(O) MWRI(S) MWTS(S) MWHS(O) TOU(O) SBUS(S) ERM(O) SIM(S) SEM(S)
	FY-3D	14:00 LT	13:29 LT	15 Nov. 2017	Primary operation	MERSI-II(O) HIRAS(O) MWTS-II(O) MWHS-II(O) MWRI(O) GAS(O) GNOS(O) WAI(O) IPM(O) SEM(O)

Note (O) means the instruments working operationally, (S) means the instruments are shutdown.

TOU/SBUS (Total Ozone Unit and Solar Backscatter Ultraviolet Sounder), flying on FY-3A/B/C, a suite of two UV spectro-radiometers, one (TOU) with 6 channels in the 308~360 nm range, resolution 50 km, swath 3000 km, for total ozone; the other one (SBUS) with 12 channels in the range 252~340 nm, resolution 200 km, nadir viewing, for ozone profile.

ERM (Earth Radiation Measurement), flying on FY-3A/B/C, 2 broad-band channels radiometer for Earth reflected solar flux and Earth emitted thermal

flux over total (0.2~50 μm) and short (0.2~4.3 μm) waveband; resolution 28 km, cross-track scanning with 2° NFOV, swath 2300 km, nadir viewing with 120° WFOV.

SIM (Solar Irradiance Monitor), flying on FY-3A/B/C, 3-channel radiometer over 0.2~50 μm waveband for the total incident solar flux; viewing the Sun near the north pole area.

GNOS (GNSS Occultation Sounder), flying on FY-3C/D, receives the signal from GPS or China Beidou satellites; observing over 1000 occultation events per day.

GAS (Greenhouse gases Absorption Spectrometer), flying on FY-3D, has four narrow bands with center wavelength located at 0.76 μm, 1.6 μm, 2.1 μm and 2.3 μm, which observes infrared light reflected from the Earth's surface and the atmosphere. Column abundances of CO_2 and CH_4 are calculated from the observational data.

SEM (Space Environment Monitor), flying on FY-3A/B/C/D, for in-situ observation of charged particles in the proximity of satellite.

WAI (Wide-field Auroral Imager), flying on FY-3D, for remote sensing imaging the N_2 Lyman-Birge-Hopfield (LBH) auroral bands.

IPM (Ionospheric PhotoMeter), flying on FY-3D, for nadir remote sensing the airglow intensity of the OI 135.6 nm and N_2 Lyman-Birge-Hopfield (LBH) bands.

3 Status of Current GEO

The first generation of GEO satellites of CMA is FY-2s, a series of spacecraft containing 8 models. The FY-2 spacecraft is spin-stabilized that rotates at speed of 100 r·min^{-1}. The primary payload is a 5-channel Visible and Infrared Spin Scan Radiometer (VISSR), which takes hourly full-disk imagery of the Earth in VIS, IR, and water vapor spectral bands.

The primary operational observation position of FY-2 satellites is 105°E, the secondary position is 86.5°E. The current FY-2 constellation consists of 5 satellites, namely FY-2H/G/F/E/D. FY-2D was retired and stand by at 123.5°E. FY-2H was the latest one, which is positioned at 79° especially for Indian ocean observation.

The second generation of GEO satellite of CMA is FY-4 series. Unlike FY-2, FY-4 is three-axis stabilized; and apart from inherited and much enhanced capability in imaging, it's also designed to have sounding, lightning mapping, and space weather monitoring capabilities. On 11 December 2016, the first FY-4 model FY-4A was launched from the Xichang satellite launch center. It was positioned at 99.5°E for in-orbit check out and moved to 104.7°E for primary operation. The first imagery obtained by ground station was released 27 February 2017, implying that both space and ground segments are functioning well[5, 6].

Table 2 Current Fengyun geostationary satellites (as of 1 March 2020)

Sector	Satellites currently in orbit	Location	Launch date	Status	Instrument capacity
West-Pacific (108°–180°E)	FY-2F	112°E	13 Jan. 2012	Primary operation for rapid scan	VISSR SEM
Indian Ocean (36°–108°E)	FY-2G	99.5°E	31 Dec. 2014	Primary operation for full disk scan	VISSR SEM
	FY-4A	104.7°E	11 Dec. 2016	Primary operation for full disk scan	AGRI GIIRS LMI SEP
	FY-2H	79°E	5 Jun. 2018	Primary operation for full disk scan since 1, Jan. 2019	VISSR SEM

3.1 FY-2 Program

The primary objectives of FY-2 program are as follows: (i) continuously observing to obtain the Earth imagery in visible, infrared, and water vapor spectral bands, from which sea surface temperature, cloud parameters, and wind vectors can be derived; (ii) operating the Data Collection System (DCS) to collect and transmit data from domestic and overseas data collection platforms (DCPs); (iii) broadcasting data in HRIT/LRIT format, and (iv) Monitoring space environment.

There are two main payloads carried on FY-2. The detailed descriptions for each payload are as follows.

VISSR (Visible and Infrared Spin Scan Radiometer): The version for FY-2A/B had three VIS/IR channels (05~1.05 μm, 6.3~7.6 μm, and 10.5~12.5 μm), the improved version for FY-2C/D/E/F/G/H splits the IR channels into two and adds a 3.5~4.0 μm channels. The resolution is slightly improved from 5.76 km (IR) and 1.44 km (VIS), to 5.0 km (IR) and 1.25 (VIS). The image cycle is 30 min.

SEM (Space Environment Monitor): A space particle monitor and an X-ray monitor are mounted on FY-2 to detect the space environment in proximity of the satellite, the solar activities, and relevant space phenomena. The SEM is transmitted *via* telemetry to the ground system.

Data Collection System of FY-2 has two uplink bands, whose frequencies are 402.0~402.1 MHz for international DCPs (33 channels of bandwidth 3 kHz, bit rate 100 bit·s^{-1}, modulation BPSK/PCM) and frequencies 401.1~401.4 MHz for domestic DCPs (400 channels of 750 Hz spacing, bit rate 600 bit·s^{-1}, modulation QBSK), with right-hand circular polarization.

3.2 FY-4 Program

FY-4 program is the successor of FY-2 program. The primary objectives of FY-4 program are as follows: (i) to take multiple spectral channel imagery of the Earth with high temporal resolution; (ii) to measure atmospheric vertical profile of temperature and humidity with improved vertical resolution and detection accuracy; (iii) to detect and map positions of lightning events; (iv) to monitor solar activities and space environments for space weather forecast service; (v) to collect data from data platforms and transmit to users; (vi) to broadcast observational images, data, and derived products with aboard transponder.

There are four main payloads carried on FY-4. The detailed descriptions for each payload are as follows.

AGRI (Advanced Geosynchronous Radiation Imager): to fly on FY-4A/B/C, multispectral imager with two independent mirrors scanning north-south and east-west directions respectively; 216 sensors in 14 bands from visible to long-wave infrared (0.55~13.8 μm); on-board calibration for all bands, full optic length of radiation considered in calibration; resolutions: 1 channel in 500 m, 2 channels in 1 km, 4 channels in 2 km, 7 channels in 4 km; S/N 90~200, NE ΔT 0.2~0.7 K at 300 K; full-disk scanning time <15 min.

GIIRS (Geo. Interferometric Infrared Sounder): to fly on FY-4A/B/C, two independent mirrors scanning north-south and east-west directions respectively; 32×4 plane arrays for mid-wave (375 S/MIR channels) and long-wave infrared bands (538 LWIR channels); resolution 16 km; active and radiant coolers; radiometric calibration accuracy 1 K; spectral calibration accuracy 10 ppm; Mesoscale 35 min (1000 km×1000 km), China area 67 min (5000 km×5000 km).

LMI (Lightning Mapping Imager): to fly on FY-4A/B/C, two tubes for observation to achieve more spatial coverage; central frequency: 777.4 nm; $S/N \geqslant 6$; spatial resolution: 7.8 km temporal resolution 2 ms.

SEP (Space Environment Package): to fly on FY-4A/B/C, a suite that contains a Magnetometer for magnetic field vector, an Energetic Particle Detector detecting high-energy electron storms (1~165 MeV, and >165 MeV) and proton events (0.4~4 MeV), and Space Weather Effect Detectors for the impact of space weather on the spacecraft.

DCS of FY-4 has two uplink bands, with frequencies from 402.0 to 402.1 MHz for international DCPs (33 channels of 3 kHz bandwidth, bit rate

100 bit·s^{-1}, modulation BPSK/PCM) and frequencies 401.1~401.4 MHz for domestic DCPs (400 channels of 750 Hz spacing, bit rate 600 bit·s^{-1}, modulation QBSK), and right-hand circular polarized

4 Product and Data Service

4.1 Archive Data Service

NSMC preserves data to the domestic and international user communities since 1983. The daily archive data volume is increasing rapidly at 0.5 GByte in 1987 and 8000 GByte in 2019. By the end of 2019, NSMC has stored data volume up to 15 PB from 25 satellites. Fengyun series meteorological satellites data catalog statistics which are shared by the global community shown in the table 3.

NSMC Data Center is responsible for Fengyun series satellite and the third party satellite data management and long term preservation, allows data download and assists domestic and international users with as much convenience as possible in their search for meteorological and environmental satellite products.

Table 3 Fengyun satellite data catalog statistic

Satellite series	Instruments (Groups)	Data level	Data catalog
FY-2	1	L1	3
		L2+Atmosphere	13
		L2+Radiation	4
		L2+Ocean	1
		L2+Land	2
		L2+Imagery	8
FY-3	17	L1	14
		L2+Atmosphere	26
		L2+Radiation	3
		L2+Ocean	4
		L2+Land	8
		L2+Imagery	1
FY-4	3	L1	3
		L2+Atmosphere	17
		L2+Radiation	5
		L2+Ocean	1
		L2+Land	2
		L2+Lighting	2
		L2+Imagery	9

The full Fengyun satellite archive dataset will be available on NSMC satellite data service website in English version (http://data.nsmc.org.cn). Users can search and download Fengyun satellite data after registration.

Over the past 12 years, more than 80 thousands users registered on the Fengyun satellite data service website by the end of 2019. More than 5.4 PB satellites' data have been delivered to domestic and international users in 2019.

4.2 Rear Time Data Service

NSMC/CMA distributes real-time Fengyun meteorological satellite data for the high timeliness requirement users through Fengyun satellite direct broadcast and CMACast. Users in Fengyun satellites direct broadcast service area with appropriate receiving equipment can directly receive real-time data.

FY-2 DB: Stretched VISSR (S-VISSR) Data Transmission, compatible with MDUS acquisition stations. Main features: frequency 1687.5 MHz; bandwidth 2.0 MHz; polarization linear; antenna diameter about 3 m, G/T about 12 dB·K^{-1}, data rate 660 kbit·s^{-1}.

FY-4 DB: FY-4 provides 1675~1687 MHz HRIT (High Rate Image Transmission), 1696~1698 MHz LRIT (Low Rate Image Transmission).

FY-3 DB: MPT (Medium-resolution Picture Transmission), for full information transmission of MERSI measurement on FY-3A/B/C. Main features: frequency: 7775 MHz; bandwidth: 45 MHz; polarization: right-hand circular; antenna diameter about 3 m, G/T about 21.48 dB·K^{-1}, data rate 18.7 Mbit·s^{-1}; AHRPT (Advanced High Resolution Picture Transmission) for full information transmission of the instruments exclusive of the MERSI on FY-3A/B/C. Main features: frequency: in the range of 1704.5 MHz; bandwidth: 6.8 MHz; polarization: right -hand circular; Antenna diameter about 3 m, G/T about 6.8 dB·K^{-1}, data rate: 4.2 Mbit·s^{-1}.

To support DB users to receive and process FY-3 transmission data, NSMC/CMA provides the Satellite to Ground Interface Control Document, pre-processing software packages for 5 instruments,

namely MERSI, VIRR, MWTS, MWHS, and MWRI on http://satellite.nsmc.org.cn. Processing software for GNOS is also provided since FY-3D.

The CMACast users can receive Fengyun satellite data and product with DVB-S equipment in near real-time. There are 2525 deployed CMACast receiving terminals, in which 22 overseas. Additional information of CMACast can be found on CMA WIS Portal (http://gisc.wis.cma.cn/wis/portal.pub).

4.3 Mobile Application Service Launched in 2018

To increase the impact of Fengyun series satellites and help users obtain Fengyun satellite imagery, NSMC has launched 2 mobile applications on WeChat platform in 2018, *i.e.*, FY Earth View for LEO satellites and FY Live for GEO satellites.

WeChat is one of the most popular instant messaging services in China and some overseas countries. By the end of 2019, WeChat had over 1.15 billion monthly active users from a wide range of age groups worldwide. WeChat Applet (mini-App, little program) is a special framework designed by Tencent that provides a light solution for using mobile application within the WeChat eco-system. It allows users to launch new Apps without download.

Fengyun Earth View WeChat Applet releases the latest 7 days global true color Earth image captured by the MERSI-II instrument onboard FY-3D. The functions include: (i) dragging and zooming in/out to view the full resolution global image; (ii) switching to the previous or next date; (iii) choosing interface between 3D mode and 2D mode; (iv) showing the location of current user.

Fengyun Live WeChat Applet shows the time-series live cloud images taken by AGRI onboard FY-4A. Its functions include: (i) the most recent image of China region and full disk; (ii) the videos of different regions in the latest 3/6/12/24/48/72 hours. This WeChat Applet can provide a convenient way for users to have a timely view of the live cloud imagery of FY-4A by using mobile phones. By the end of 2019, Fengyun Live has accumulated 95375 users. Its daily active user count reached its peak at nearly four thousand on 10 August, as typhoon LEKIMA (201909) was approaching eastern China.

The interfaces of Fengyun Earth View and Fengyun Live are shown in Figure 2.

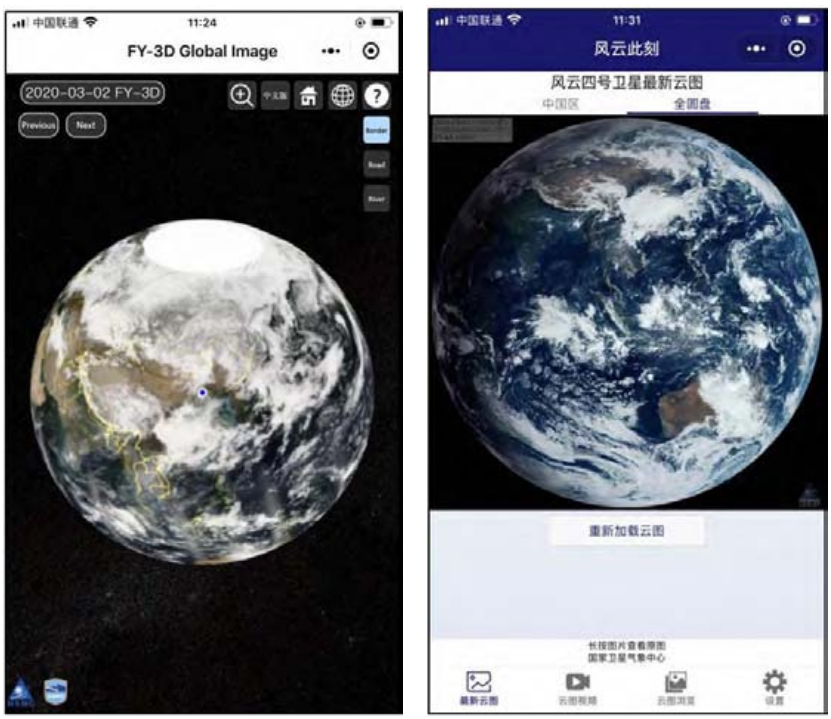

Fengyun Earth View Fengyun Live

Fig. 2 Interface of Fengyun Earth View and Fengyun Live

5 International Co-operation and Supporting

5.1 International and Regional Co-operations

With the capability of multi-spectral global monitoring, and timeliness full disk quick observation, Fengyun satellites were ready to serve global users, especially to Belt and Road. Figure 3 illustrates Fengyun user distribution map on Belt and Road region. By the year of 2019, many countries along Belt and Road received Fengyun satellite data by various means. Real-time data users established different kinds of satellite data direct broadcasting systems, including 19 CMACast stations, 6 FY-2 DB stations, and 2 FY-3 DB stations. FY-3 preprocessing software packages have been freely shared and installed in 25 countries. 27 countries registered as members of FY_ESM. The Fengyun satellite data center website users have expended to 106 counties. Fengyun satellites have been incorporated into the global operational application meteorological satellite series by the World Meteorological Organization (WMO). NSMC is also cooperating with EUMETSAT, NOAA, CGMS, CEOS, CSPP, and other foreign satellite agencies and organizations. Besides, CMA strengthened cooperation with regional and Belt and Road countries by enhance Fengyun satellites service capabilities. CMA signed an agreement with the National Institute of Meteorology of Mozambique (INAM), the Ministry of Emergency Situations of the Kyrgyz Republic (MES KR), and the Civil Aviation of the Sultanate of Oman represented by the Directorate General of Meteorology (DGMet) in 2019. Those agreements aimed to improve the application of Fengyun meteorological satellite data and enhance the capacity in weather forecasting, disaster warning, and disaster prevention and mitigation service, which are of great significance to protecting the safety and well-being of the peoples of the two countries and the national economic development as well as to promoting regional cooperation.

5.2 Disaster Support

In April 2018, the China Meteorological Administration (CMA), the China National Space Administration (CNSA), and Asia-Pacific Cooperation Organization (APSCO) jointly signed the Letter of Intention for Cooperation in the Application of Fengyun meteorological satellite. This will improve international cooperation related with Fengyun satellite. At the same time, CMA introduced the Emergency Support Mechanism of Fengyun satellite (FY_ESM), open to international users who made a request once visited by such extreme events as typhoon, heavy rain, severe convection, forest or grassland fire, and sand storm. By 2019, twenty-eight countries registered as a member of FY_ESM. According to FY_ESM user's requirements, CMA initiated several times of FY_ESM, provided FY-2, FY-3, and FY-4 data, products and application tools, supported disaster prevention and mitigation in those countries. Besides, Fengyun satellites were important members of the Global Earth Observation (GEO), as well as the duty satellite of International Charter Mechanism for Disaster Reduction (CHARTER), CDDR mechanism (China GEOSS Disaster Data Response), and United Nations Platform for Space-Based Information for Disaster Management and Emergency Response (UN-SPIDER). Table 4 lists the Fengyun satellite disaster support cases between 2018 and 2019.

5.3 Belt and Road Supporting Action and Plan

To support Belt and Road countries, a series of action plans in three parts have been put on the agenda. Some actions have been implemented by NSMC and related organizations in CMA.

The first part of this plan is to enhance data receiving capabilities on Belt and Road. CMA is planning to help regional countries receiving Fengyun satellite data by building or updating Direct Broadcasting system (DB), CMA Data Broadcasting System (CMACast), cloud services, and other means. In December 2019, Mozambique has built a FY-2H DB antenna and operationally received images. More DB antennas planned to build in other 8 counties were decided and supported by CMA and APSCO. More than thirty countries were downloading Fengyun data *via* NSMC FTP server. Forty-four users from

Table 4 List of Fengyun satellite disaster support cases between 2018 and 2019

Request date	Country	Disaster	Request source
17 Jan. 2018	Philippines	Volcano eruption	CHARTER
12 Feb. 2018	Pacific island countries	Tropical cyclone	CDDR
29 Jul. 2018	Indonesia	Earthquake	CDDR
16 Aug. 2018	Venezuela	Wildfire	CHARTER
12 Sept. 2018	Vietnam	Tropical cyclone	FY_ESM
12 Sept. 2018	Vietnam	Tropical cyclone	UN-SPIDER
30 Sept. 2018	Indonesia	Earthquake	CDDR
30 Oct. 2018	Philippines	Tropical cyclone	FY_ESM
23 Dec. 2018	Indonesia	Tsunami	CHARTER
30 Jan. 2019	Brazil	Dam break	CDDR
28 Mar. 2019	Iran	Flash flood	CDDR
6 Apr. 2019	The Republic of Korea	Wildfire	CHARTER
25 Apr. 2019	Mozambique	Tropical cyclone	FY_ESM
28 Jun. 2019	Russia	Flash flood	CHARTER
21 Aug. 2019	Bolivia	Wildfire	CHARTER
19 Sept. 2019	Mozambique	Weather early warning	FY_ESM
10 Oct. 2019	India	Flash flood	CHARTER
14 Nov. 2019	Australia	Wildfire	CHARTER
28 Nov. 2019	Mozambique	Tropical cyclone	FY_ESM
22 Dec. 2019	Sri Lanka	Flash flood	FY_ESM

twenty-five countries installed FY-3 pre-processing software packages which can help those users generate level 1 data from level 0 which they received from MERSI, VIRR, MWRI, MWTS, MWHS and IRAS on FY-3 satellites by their own antennas.

The second part is to enhance user's capability of applications by using Fengyun satellite data. NSMC developed two application tools which can help users to process Fengyun satellite data in their work. Satellite Weather Application Platform 2.0 (SWAP 2.0) focused on weather analysis, and weather forecast which mainly adopted GEO Fengyun satellites. SWAP 2.0 has two versions, web-based version, and stand-alone version. Web-based SWAP 2.0 (http://rsapp.nsmc.org.cn) displays FY-2H, FY-4A full disk and regional images, 28 products, and multi-language supported, such as English, Russia, and Chinese. Satellite Monitoring and Remote-sensing Toolkit (SMART 2.0) focused on environment and biological monitoring on land surface, ocean surface, water body, and ice surface based on medium and high-resolution Earth observation satellites, including FY-3, GAOFEN, NOAA and so on. Besides those application tools, NSMC planned to generate customized products according to international users' requirements.

The last part is to strengthen international scientific exchange and communications with Belt and Road countries, including holding international user conference and training courses, financing scientist exchange, and organizing training materials. NSMC planned to hold an international user conference every two years from 2019. The First Fengyun satellite international user conference took place on 15–17 November 2019 in Haikou, Hainan province, China[7]. Experts from over 30 countries and regions, WMO, APSCO, NOAA, EUMETSAT, and the Sixth International Strategic Consultative Committee on Chinese Meteorological Satellite Programs (ISCC) attended this conference. In 2019, CMA held two international training courses on Fengyun satellite applications. CMA delegations visited Thailand,

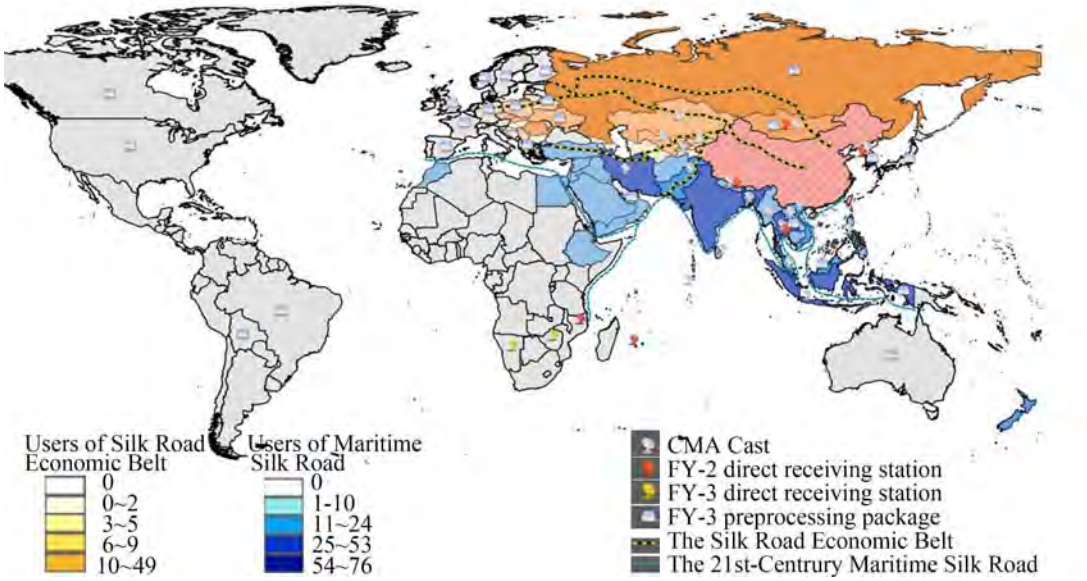

Fig. 3 Fengyun user distribution map in Belt and Road region

Kyrgyzstan, Kazakhstan, and other five countries on Fengyun satellite cooperation and held on-site training and facility maintenance during the visit.

The Belt and Road supporting project on Fengyun satellite will last until 2023. NSMC will make a special effort on this project, improve remote sensing application level of international users, and strengthen Fengyun satellite socio-economic benefits for those countries.

6 Progress of Retrospective Calibration of Historical Chinese Fengyun Satellite Data

The first Chinese meteorological satellite was launched in 1988. So far, the Chinese meteorological satellites have been continuously observing for nearly 30 years. Satellite replacement and on-board sensors upgrade make the old and new observation data non-harmonized in terms of accuracy, stability, and consistency, which cannot meet the basic needs of long-term sequence climate and environmental change research.

To enhance the capability on the space-based Essential Climate Variable (ECV), a new National Key Research & Development Program of China was funded since 2018 to re-calibrate the historical Chinese Earth Observation satellite data including the Chinese Fengyun meteorological satellites, the Chinese Haiyang Oceanic Satellites (HY), and the Chinese Ziyuan Resource Satellites (ZY).

The historical Chinese Fengyun satellites include thirteen meteorological satellites (FY-1A, FY-1B, FY-1C, FY-1D, FY-2A, FY-2B, FY-2C, FY-2D, FY-2E, FY-2G, FY-3A, FY-3B, and FY-3C) and seven types of on-boarded instruments (VIRR, VISSR, MERSI, IRAS, MWTS, MWHS, and MWRI). The vicarious China Radiance Calibration Site (CRCS) calibration, the Pseudo-Invariant Calibration Sites (PICS) calibration, the Deep Convective Clouds (DCC) calibration, and the lunar calibration have been considered in the procedure of the re-calibration for solar reflectance bands. New on-board calibrate models will be built for infrared and microwave bands re-calibration.

To construct Fundamental Climate Data Record (FCDR) of Fengyun meteorological satellites for FY-1/2/3 series optical and microwave remote sensing instruments, some of the key technologies need to break through, including the historical data backtrack and diagnosis, high-precision positioning with lack of attitude and orbit information. Key

technologies such as radiometric information restoration and inter-generational satellite radiometric homogenization, and rapid processing of satellite big data are used to support platform for PB-level Fengyun historical data re-processing. Based on the common and individual requirements, four climate product data sets, including sea surface temperature, outgoing longwave radiation at the top of the atmosphere, surface temperature, and vegetation index, have been preliminarily established after repositioning and recalibration of the nearly 30 years' historic data. A unified and standardized data set is expected to be released in 2021.

Mining the multi-source calibration information, establishing the historical radiometric benchmark for the optical instrument, constructing the accurate physical calibration model of the similar instruments, the radiometric response and attenuation behaviour model within the life cycle, and the inter-generational radiometric reference transfer model, which are the key technologies for long series of historical data of the optical instruments.

A long-range radiometric reference for microwave payloads is established, and the physical mechanism of radiometric response of the microwave radiometer calibration system is revealed, breaking through the key technologies of full-link radiometric transfer and characteristic evolution analysis during the lifetime and inter-generational period of the instruments. Reprocessing based on re-analyzed data verifies that the microwave historical data re-calibration model is constructed successfully.

Other key technologies include historical data backtracking and defect diagnosis, track information location and backtracking deficiency, and radiometric information recovery in a non-ideal calibration state. It is realized to transfer inter-generation satellite radiometric reference, and to construct a big data and rapid intensive processing platform for LEO and GEO Fengyun satellites. The primary climate data sets and more than three Thematic Climate Data Record (TCDR) data-sets for 30 years will be established and released. The research scheme is shown in Figure 4.

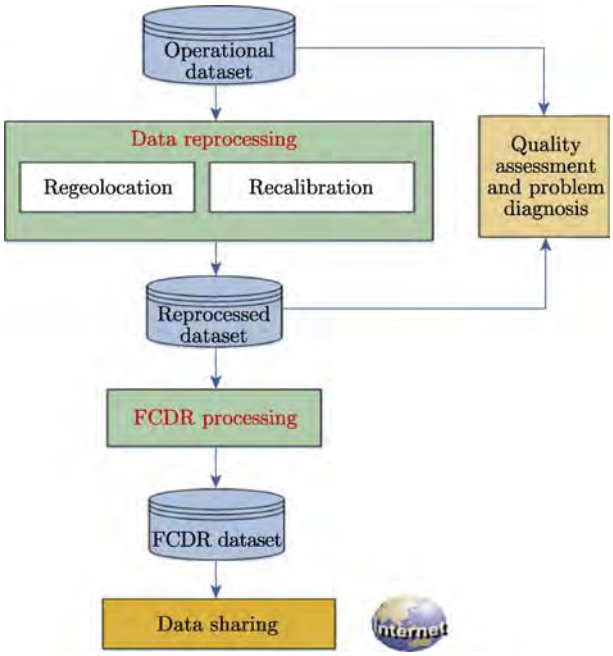

Fig. 4 Research scheme for retrospective calibration of historical Chinese Fengyun satellite data

7 Future Program

According to the approved plan for China's meteorological satellites and its application[8,9], by 2020, a stable operational system of FY-3 polar-orbiting meteorological satellites will be established, which can form a network observation capability of morning, afternoon and inclined orbit constellation. Meanwhile, the operational pattern of the FY-4 geostationary meteorological satellites "dual-satellite operation and in-orbit backup" will be established. Up to now, there are four FY-3 polar-orbiting satellites to be launched, which will be arranged by the layout of three solar synchronous polar-orbiting satellites in early-morning, mid-morning and afternoon, and one precipitation measurement satellite in an inclined orbit. There are two more FY-4 geostationary satellites to be launched.

7.1 Future FY-3 Polar-orbit Satellites

The third batch of FY-3 satellite program, which includes four satellites FY-3E/F/G/H, has been approved and scheduled to be launched in the next three years.

FY-3E, which is the first early-morning orbit

satellite in China's polar-orbiting meteorological satellite family, is scheduled to be launched in 2020. Its local time at descending node is 05:30. It is equipped with 11 advanced remote sensing instruments. There are the MERSI for low-light level, the HIRAS, the GNOS, the MWTS, the MWHS, the SIM, the Solar Spectral Irradiance Monitor (SSIM), the Wind Radar, the SEM, the Multi-angle Ionospheric Photometer (MIPM) and the Solar X-ray and Extreme Ultraviolet Imager (XEUVI). FY-3E will focus on the application of Numerical Weather Prediction (NWP), while ensuring the global imaging observation and atmospheric vertical sounding measurement.

FY-3F is a mid-morning orbit satellite with descending equatorial crossing time at 10:00 LT. It's scheduled to be launched in 2022. There are 9 remote sensing instruments on it, which are MERSI, MWTS, MWHS, MWRI, GNOS, HIRAS, Ozone Measurement Suite (OMS), the ERM, and SIM. FY-3F will focus on the observation of the Earth's surface imagery, which is mainly applied to weather forecasting, ecological environment monitoring, meteorological disaster monitoring, and research.

FY-3G, which is an inclined low Earth orbit satellite mainly used for precipitation measurement, is scheduled to be launched in 2022. There are 4 remote sensing instruments on it, which are MERSI (simplified type), MWRI (precipitation type), GNOS, and the Precipitation Measurement Radar (PMR). FY-3G is mainly used for monitoring heavy rainfall in severe weather system, providing three-dimensional structure information of precipitation in the middle and low latitudes of the world, and supporting for improving the accuracy of precipitation meteorological forecast.

FY-3H, which is the last one in the third batch of FY-3 satellite program, is an afternoon orbit satellite, scheduled to be launched in 2023. Its local time at ascending node is 14:00 LT. There are 9 remote sensing instruments on FY-3H, which are MERSI, MWTS, MWHS, MWRI, GNOS, HIRAS, GAS, WAI, and IPM. The main objectives of FY-3H are the quantitative detection of atmospheric composition and the monitoring of climate change. Its data can be used for weather forecasting, atmospheric chemistry, and climate change monitoring and research. Table 5 shows the information of the future FY-3 polar-orbiting satellites and their instruments.

The fully networked FY-3 operational satellites will have integrated observation capabilities, such as high temporal and spatial resolution global optical imaging observation capability, high precision optical and microwave combined atmospheric temperature and humidity vertical distribution detection capability, GHG measurement capability, wind field and precipitation measurement capabilities with active remote sensing instruments, and the solar and space environment monitoring capabilities.

7.2 Future FY-4 Geostationary Satellites

According to China's meteorological satellite development plan, two operational meteorological satellites in geostationary orbit, named the FY-4B and FY-4C in the second batch of FY-4, will be launched around 2020 to ensure the continuity, reliability, and stability of the observation service of geostationary meteorological satellites.

FY-4B, which is the first operational geostationary satellite in FY-4 series, is scheduled to be launched in 2020. The main observation capabilities are similar to those of FY-4A, with some significant performance improvements. It will be probably positioned at a 105°E to continue operations as a main operational geostationary meteorological satellite. The remote sensing instruments on FY-4B are the AGRI, the GIIRS, the Geostationary Fast-scan Imager (GFI), and the SEP.

Compared with the previous two satellites FY-4A and FY-4B, the capability of FY-4C will reach and exceed the international advanced level. The space weather monitoring capability of FY-4C has been further enhanced with the addition of some space weather observation instruments. It is scheduled to be launched in 2022. The position will be determined according to the technical status and other factors at that time. The remote sensing instruments include AGRI, GIIRS, LMI, SEP, the Multiband Ionospheric Ultra-Violet Spectrum Imager

Table 5 Future Fengyun polar-orbiting satellites

Orbit type (Local Time of descending node/ascending node)	Satellites currently in orbit	Equatorial crossing time	Scheduled launch year	Instruments
Early morning orbit (05:00 LT–07:00 LT)/ (17:00 LT–19:00 LT)	FY-3E	05:30 LT	2020	MERSI MWTS MWHS GNOS WindRad HIRAS SIM SSIM SEM IPM XEUVI
Morning orbit (07:00 LT–12:00 LT)/ (19:00 LT–24:00 LT)	FY-3F	10:00 LT	2022	MERSI MWTS MWHS MWRI GNOS HIRAS OMS ERM SIM
Afternoon orbit (12:00 LT–17:00 LT)/ (00:00 LT–05:00 LT)	FY-3H	14:00 LT	2023	MERSI MWTS MWHS MWRI GNOS HIRAS GAS WAI IPM
Low inclination satellite	FY-3G	–	2022	MERSI MWRI GNOS PMR

(MUSI), the Solar Extreme-Ultraviolet Imager (SUVI), and the Solar X-EUV Irradiance Sensor (SXUS). The information of future FY-4 geostationary satellites and their instruments are showed in Table 6.

FY-4 series satellites represent an improved and new capability of the Chinese geostationary weather satellite system. With advanced imaging and sounding instruments on FY-4 series, providing high temporal, spatial, and spectral resolution measurements, the benefit is expected to be large for severe

Table 6 Future Fengyun geostationary satellites

Future additional satellite	Scheduled launch	Planned location	Instruments
FY-4B	2020	105°E	AGRI
			GIIRS
			GFI
			SEP
FY-4C	2022	TBD	AGRI
			GIIRS
			LMI
			SEP
			MUSI
			SUVI
			SXUS

weather monitoring, warning, and forecasting. The lightning information is expected to significantly improve warnings of severe storm hazards, convection precipitation, and lightning strikes. Assimilation of data and derived products from the AGRI, GIIRS, and LMI in both global and regional NWP models are expected to show valuable improvement in forecast capabilities. FY-4 series will also enhance the capabilities of space weather monitoring and warning.

8 Conclusions

Tremendous efforts have been made for the establishment and improvement of Fengyun GEO and LEO systems. The Fengyun Program is of long term, application-oriented, continuously being developed for the benefit of user community in pursuit of quality Earth Observation data and products for weather, climate, and environmental services.

As the FY-1 C/D polar orbit operational meteorological satellite triumphantly launched and run in 1999 and 2002, the impact of meteorological satellite of China increasingly grows, playing a more and more important role.

Comparing with the achievement in the space segment, great efforts still need to be endeavored for instrument calibration, product generation, and scientific applications. For the instrument calibration, limited by the insufficient capability of the on-board calibrator of Fengyun satellites, the vicarious calibration, such as Simultaneous Nadir Overpasses (SNO), Pseudo-Invariant Calibration Sites (PICS), Deep Convective Clouds (DCC), the lunar calibration, etc. which recommended by the CEOS WGCV and the Global Space-based Inter-Calibration System (GSICS), should be implemented to monitor and validate the Fengyun satellite radiometric data performance for the whole lifetime. For the product generation, responding to the requirements of global climate observation, the long-term Climate Data Records (CDRs) should be considered to process and re-process on a regular basis. With the concrete improvements from the data pre-processing, the product processing and re-processing of the Fengyun satellites, the consolidated and enlarged applications will be expected.

References

[1] ZHANG P, LU Q F, HU X Q, *et al.* Latest progress of the Chinese meteorological satellite program and core data processing technologies [J]. *Adv. Atmos. Sci.*, 2019, **36**(9):1027-1045

[2] YANG Z D, ZHANG P, GU S Y, *et al.* Capability of FY-3D satellite in Earth system observation [J]. *J. Meteor. Res.*, 2019, **33**(6):1113-1130

[3] ZHANG Peng, CHEN Lin, XIAN Di, XU Zhe. Recent progress of Fengyun meteorology satellites [J]. *Chin. J. Space Sci.*, 2018, **38**(5):788-796

[4] WANG T, GAO T, ZHANG H, *et al.* Atmospheric science study in China in recent 70 years: Atmospheric physics and atmospheric environment [J]. *Sci. China Earth Sci.*, 2019, **62**

[5] YANG Jun, ZHANG Zhiqing, WEI Caiying, *et al.* Introducing the new generation of Chinese geostationary weather satellites Fengyun-4 (FY-4) [J]. *Bull. Am. Meteor. Soc.*, 2017, **98**(8):1636-1658

[6] ZHANG P, ZHU L, TANG S L, *et al.* General comparison of FY-4A/AGRI with other GEO/LEO Instruments and its potential and challenges in non-meteorological applications [J]. *Front. Earth Sci.*, 2019, **6**:224

[7] XIAN D, ZHANG P, FANG M, *et al.* The first Fengyun satellite international user conference [J]. *Adv. Atmos. Sci.*, 2020 (in press)

[8] National Satellite Meteorological Center. Fengyun3-03 User Requirement Specification [R]. Beijing: National Satellite Meteorological Center, 2015

[9] National Satellite Meteorological Center. Fengyun4-02 Requirement Specification [R]. Beijing: National Satellite Meteorological Center, 2019

LIN Mingsen, JIANG Xingwei. Ocean Observation from Haiyang Satellites. *Chin. J. Space Sci.*, 2020, **40**(5): 346-355.
DOI:10.11728/cjss2020.05.346

Ocean Observation from Haiyang Satellites

LIN Mingsen JIANG Xingwei

(*National Satellite Ocean Application Service, Beijing* 100081)

Abstract In 2018, China successfully launched three new Haiyang (which means ocean in Chinese, referred to as HY) satellites which are an ocean color observation satellite HY-1C (operational), an ocean dynamics environment satellite HY-2B (operational) and the China-France ocean satellite CFOSAT (experimental). In 2019, all the three satellites had finished their commissioning phases and were declared operational. HY-2A satellite continues to operate in-orbit, and its operational status is basically normal. So in 2020, China has 4 Haiyang satellites in-orbit, China's ocean satellites enter into a new operational application phase. The operation of the ground application system of Chinese ocean satellites is stable. In 2019, Beijing, Hainan, Mudanjiang, and Hangzhou ocean satellite ground stations had received the data of HY-1C, HY-2A, HY-2B, and CFOSAT 5012 orbits and 26.46 TB data had been distributed to both domestic and international users. Chinese ocean satellite data has played an important role in marine disaster prevention and mitigation, development and management of marine resources, maintenance of marine rights and interests, marine environment protection, scientific researches, and blue economy development.

Key words HY-1C, HY-2B, CFOSAT, Ocean observation satellite, Ocean remote sensing, Satellite ocean applications

Classified index P 731

1 Development of Haiyang Satellites

In 2018, China successfully launched three new Haiyang (which means ocean in Chinese, referred to as HY) satellites which are the ocean color observation satellite HY-1C (operational), the ocean dynamics environment satellite HY-2B (operational) and the China-France ocean satellite CFOSAT (experimental). In 2019, all the three satellites finished their in-orbit tests, respectively. The test results show that the three satellites satisfy the design requirements. Then they were officially delivered to the Ministry of Natural Resources of People's Republic of China (MNR) for the operational usage. All relevant Research and Development (R&D) tasks of HY-1D and HY-2C are almost done. The two operational satellites are planned to be launched in 2020. The missions of the other three operational satellites, *i.e.*, HY-2D and the two 1-meter C-SAR satellites, progress as expected. In terms of the experimental satellites, the R&D of the new generation ocean color satellite goes well, and the project of the ocean salinity observation satellite is under approval. They are planned to be launched during 2021 and 2022. The high orbit ocean and coastal zone environment monitoring satellite, the next generation ocean dynamics satellite and the geostationary microwave satellite are in the preliminary study phase.

HY-2A, the first ocean dynamic environment satellite of China, has been operated normally in-orbit for more than 8 years. Its operation status is basically stable, and its ground segment including receiving, processing, archiving, distribution and application systems works well, too. The ground segments of the other Chinese ocean satellites are designed and will be constructed as a whole mission including two phases according to the 12th National Five-Year Plan and 13th National Five-Year Plan of

Received March 21, 2020
E-mail: mslin@mail.nsoas.org.cn

China. The first phase of the Chinese ocean satellite ground segment construction is to serve five satellites which are HY-1C, HY-1D, HY-2B, HY-2C, and CFOSAT. In 2019, the first phase of construction was almost done. The second phase construction is to serve the other 9 Chinese ocean satellites including 7 operational satellites and 2 experimental satellites. Some tasks of the second phase construction have already started in 2019 such as the data processing system of the two 1-meter C-SAR satellites. The calibration and authenticity inspection system of all Chinese ocean satellites is designed as an independent mission which has already been approved by the state.

In 2019, ocean applications of satellite data had been further improved. The operational monitoring of SST, sea ice, green tide, and typhoon are applied to ocean fishery, polar navigation support, marine environment and ecology protection, marine disaster mitigation, and island management. All the applications are carried out with not only Chinese ocean satellite data but also other domestic and international satellite data. In 2019, National Satellite Ocean Application Service (NSOAS) produced the daily, weekly, monthly and annual mean sea surface temperature fusion products of China's adjacent sea areas and global oceans, respectively; issued 90 reports of sea ice monitoring, 129 reports of green tide monitoring and 121 reports of red tide monitoring of Chinese seas. NSOAS monitored 27 typhoons in 2019 and 384 thematic maps of typhoon remote sensing monitoring in the northwest Pacific region were produced and released. 407 reports of near real-time sea state analysis and fishery forecast information were issued to the ocean fishery enterprises. Satellite remote sensing images and thematic products were provided for the navigation support of China's 36th Antarctic Scientific Expedition. The monitoring of suspicious illegal sea reclamation areas was carried out every 15 days. In general, the ocean application of satellite data had been further strengthened and expanded. It has played an important role in China's marine disaster mitigation, comprehensive management of sea areas, marine environment and ecology protection, marine resource development, marine scientific research, regional marine applications, and international cooperations.

2 Data Acquisition and Distribution

National Satellite Ocean Application Service (NSOAS), which is a commonweal organization of MNR, is responsible for receiving, processing, archiving, managing, and distributing all collected products of Haiyang satellites. NSOAS owns four ground stations which are located at Beijing, Mudanjiang, Sanya, and Hangzhou respectively.

The operation of the Haiyang satellite ground system is stable. In 2019, it received the data of Chinese ocean series satellites (HY-1C, HY-2A, HY-2B, and CFOSAT) 5012 orbits and distributed 26.46 TB data to the domestic and international users.

2.1 Main Products

2.1.1 Ocean Color and Sea Surface Temperature

In 2019, based on the data of HY-1C, NSOAS operationally produced marine color products of China's adjacent sea areas, such as the averaged chlorophyll-a concentration products of ten days, every month, quarter, and the whole year (Figure 1). NSOAS also produced global land normalized difference vegetation index and ocean chlorophyll-a concentration product monthly and annually (Figure 2). All the aforementioned products were provided to relevant uses of marine environment monitoring, marine fishery, and so on. The users commented that the products had become an important information source to support their operational works.

In 2019, the sea surface temperature fusion products with a spatial resolution of 5 km were made daily, weekly, monthly, quarterly, and annually for China's adjacent sea areas and global oceans based on the data of HY-2A, HY-2B, and HY-1C. Sea surface temperature fusion products have played an important role in both sea surface temperature prediction and marine fishery environment monitoring.

2.1.2 Ocean Reanalysis Products

Based on HY-2 satellites, POMgcs and MITgcm ocean models, the Northwest Pacific Ocean and global

ocean reanalysis products were developed with the sea surface temperature data of radiometers, sea surface height data of altimeters and wind field data of scatterometers, combining the 0.25° resolution OISST sea surface temperature data and the 0.125° resolution CLS sea surface height data provided by NOAA and other foreign fusion data (Figure 3). The multi-grid three-dimensional variation method is used to assimilate the on-site temperature and salt observations, satellite remote sensing sea surface temperature, and sea surface height data. The Northwest Pacific Ocean and global ocean reanalysis products are released through the national marine science data sharing service platform. The accuracy of the mode field is effectively improved.

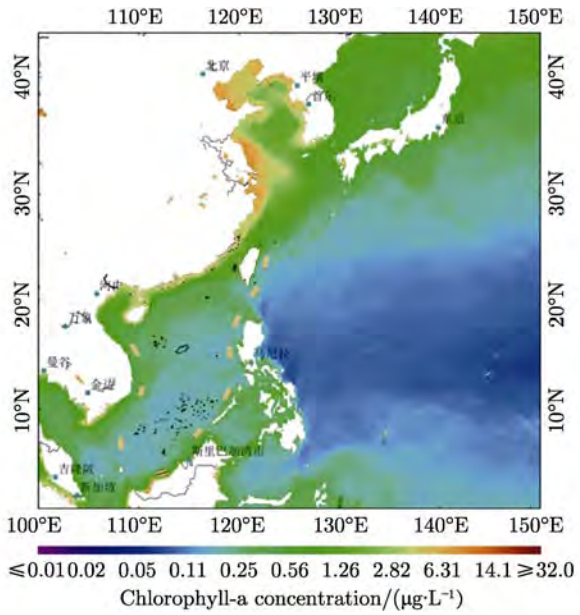

Fig. 1 Averaged chlorophyll-a concentration product of China's adjacent sea areas in 2019 (© NSOAS/MNR, 2019 - All Rights Reserved)

2.1.3 Ocean Three-dimensional Products

Based on the independently developed Northwest Pacific real-time analysis system, the three-dimensional real-time analysis products of temperature, salt, density, and sound velocity for the Northwest Pacific ocean were produced in 2019 (Figure 4). The data of daily remote sensing sea surface temperature and sea surface height are fused. The products provide the initial field conditions for the ocean numerical models and the underwater dynamic environment data for the real-time support of the marine environment.

2.1.4 Ocean Surface Laminar Flow Fusion Products

Based on the data of sea surface dynamic height and scatterometer wind field, the inversion of geostrophic current and Ekman current is calculated, and the comprehensive flow field of sea surface is constructed by integrating sea surface current. On this basis, the multi-scale surface current assimilation model is used to assimilate the observation data of the surface current field, such as ground wave radar, so as to form the integrated surface current products.

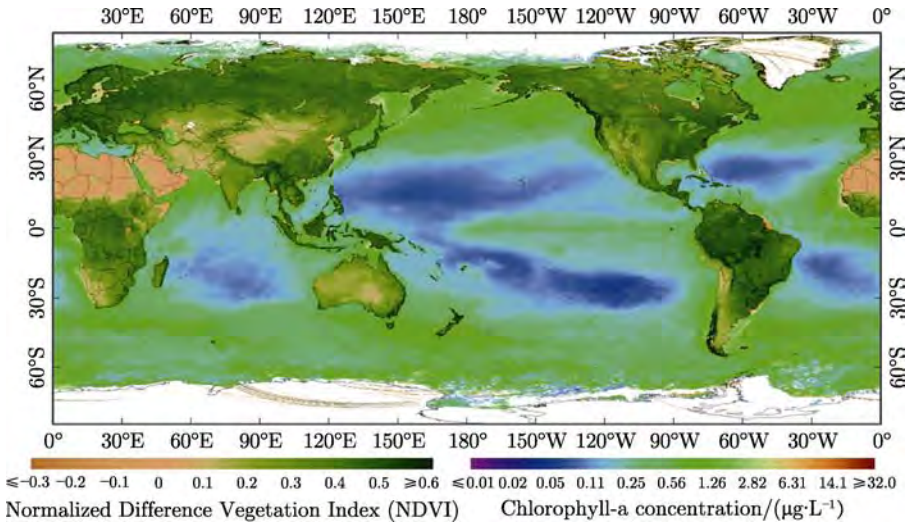

Fig. 2 Global averaged land normalized difference vegetation index and ocean chlorophyll-a concentration product of 2019 (© NSOAS/MNR, 2019 - All Rights Reserved)

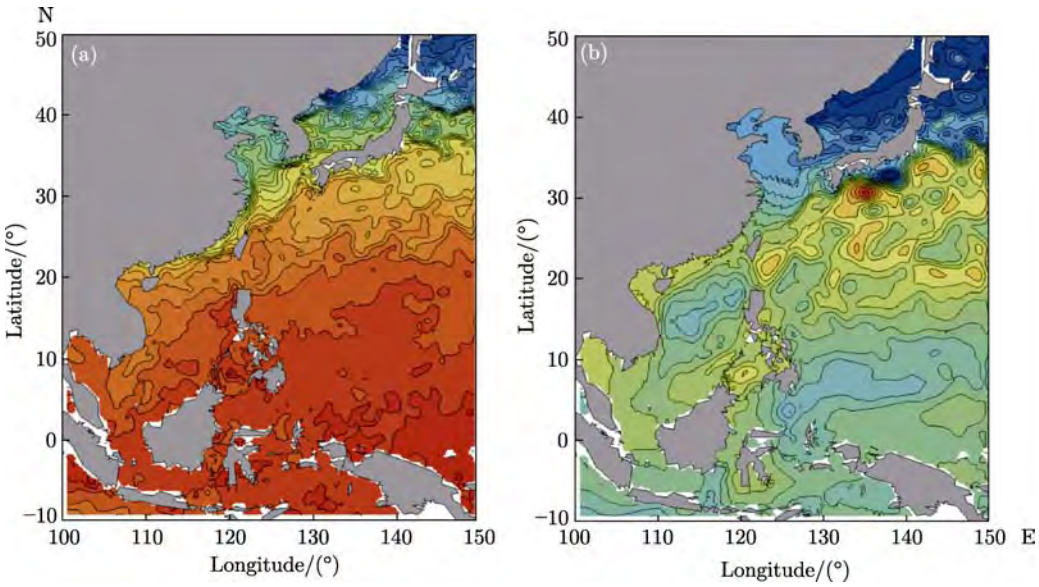

Fig. 3 Northwest Pacific sea surface temperature (a) and sea surface height (b) reanalysis products on 1 December 2017

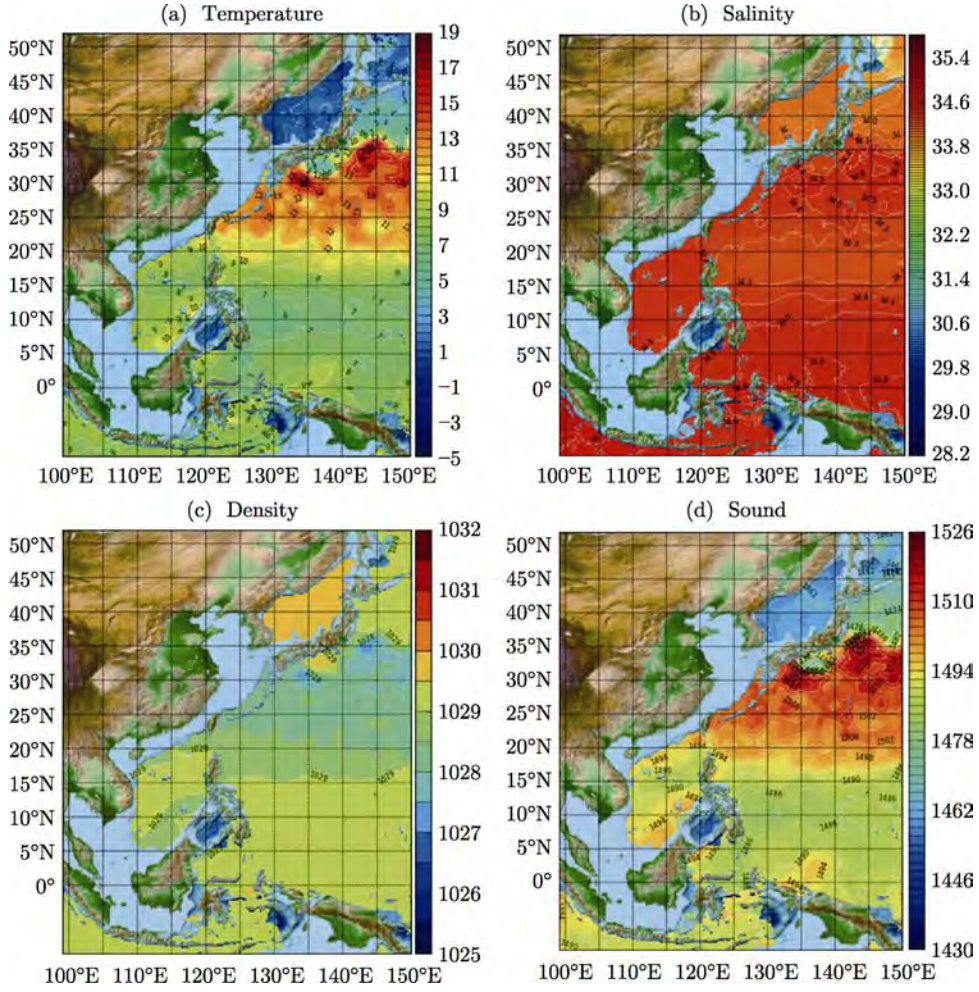

Fig. 4 Products of temperature, salinity, density and sound velocity for the Northwest Pacific Ocean (taking 500 m depth as an example) on 18 December 2019

2.2 Product Distribution

In 2019, through Chinese ocean satellite application services, 49611 GB of HY-1C satellite data, 14123 GB of HY-2A satellite data, 6546 GB of HY-2B satellite data and 3509 GB of CFOSAT data were distributed to 275 users from 131 organizations, institutes, universities, *etc.* 230622 scenes and 304.16 TB data of Gaofen (which means high resolution in Chinese, referred to as GF) satellites were distributed to 72 departments, including 3156 scenes and 1.27 TB data of GF-1, 5456 scenes and 1.93 TB data of GF-2, 211370 scenes and 299.00 TB data of GF-3, 10640 scenes and 1.96 TB data of GF-4.

3 Application Achievements

3.1 Ocean Disaster Surveillance

3.1.1 Spilled Oil Monitoring

In 2019, oil spill remote sensing monitoring was carried out over Bohai Sea, the East China Sea and the South China Sea mainly using the satellite data of GF-3 and Radarsat-2. Particularly for the oil spill incident of the sea area near Sanya, Hainan Province, the GF-3 SAR data, HY-1C CZI, UVI data, and other sensors data were used to implement the oil spill monitoring. The products provided important information to support decision makings of rapid response, emergency treatment, marine ecological environment protection, and restoration caused by the oil spill incident (Figure 5).

3.1.2 Ice Monitoring

In 2019, the operational monitoring of winter sea ice in the Bohai Sea and the northern Yellow Sea was carried out as usually with the data of HY-1C, Gaofen satellite, EOS/MODIS, Radarsat-2, and other satellites. It realized one ice period per day and 90 ice periods in total. The products were distributed to sea area management departments, provincial and municipal departments providing indispensable information support for sea ice monitoring, disaster assessment and emergency response (Figure 6).

3.1.3 Green Tide Monitoring

In 2019, the operational monitoring of green tide in China's offshore sea areas was carried out normally particularly for the joint prevention and control of green tide in the Yellow Sea cross region (Figure 7). GF-1, GF-2, GF-3, GF-4, EOS/MODIS, and other satellite data were used. 129 reports of green tide satellite remote sensing monitoring were issued. The early detection of green tide disaster and the whole process tracking monitoring were realized which made the path prediction of green tide drift possible. The products provided accurate and timely information services for disaster prevention and mitigation.

3.1.4 Red Tide Monitoring

In 2019, the red tide monitoring was carried out in the North Sea and South China Sea with the data of GF-4, EOS/MODIS, and NOAA/AVHRR. Seven red tide satellite remote sensing monitoring information express reports of Liaodong bay, and 46 red tide satellite remote sensing monitoring information express reports of Beidaihe and its adjacent waters were produced. Twelve monthly reports and 52 weekly reports of red tide remote sensing monitoring in the South China Sea were produced and an emergency phase 4 alert was issued. All the products are provided to relevant departments of coastal provinces and cities through leased lines, E-mail, *etc.*

3.1.5 Tropical Cyclones Monitoring

In 2019, using microwave scatterometer data such as HY-2A, HY-2B, CFOSAT and METOP-A/B satellites, NSOAS carried out typhoon monitoring in the Northwest Pacific Ocean area. A total of 27 typhoon processes were monitored throughout the year, and 384 thematic maps of typhoon remote sensing monitoring were made, which were timely provided to the marine forecasting departments at the national, regional and provincial levels for consultation of Typhoon Forecasting in flood season. It provides near real-time information supporting typhoon treatments.

3.2 Costal Zone and Sea Management

3.2.1 Suspicious Illegal Sea Reclamation Monitoring

In 2019, with the data of GF-1A/B/C/D, GF-2, GF-3, GF-6, Resource-3/01~02, and Resource-1/02C, suspicious illegal sea reclamation area monitoring was carried out to entire China's coastal zone areas every 15 days. The operational products and reports provided efficient and powerful information support for the state to strictly manage the reclamation.

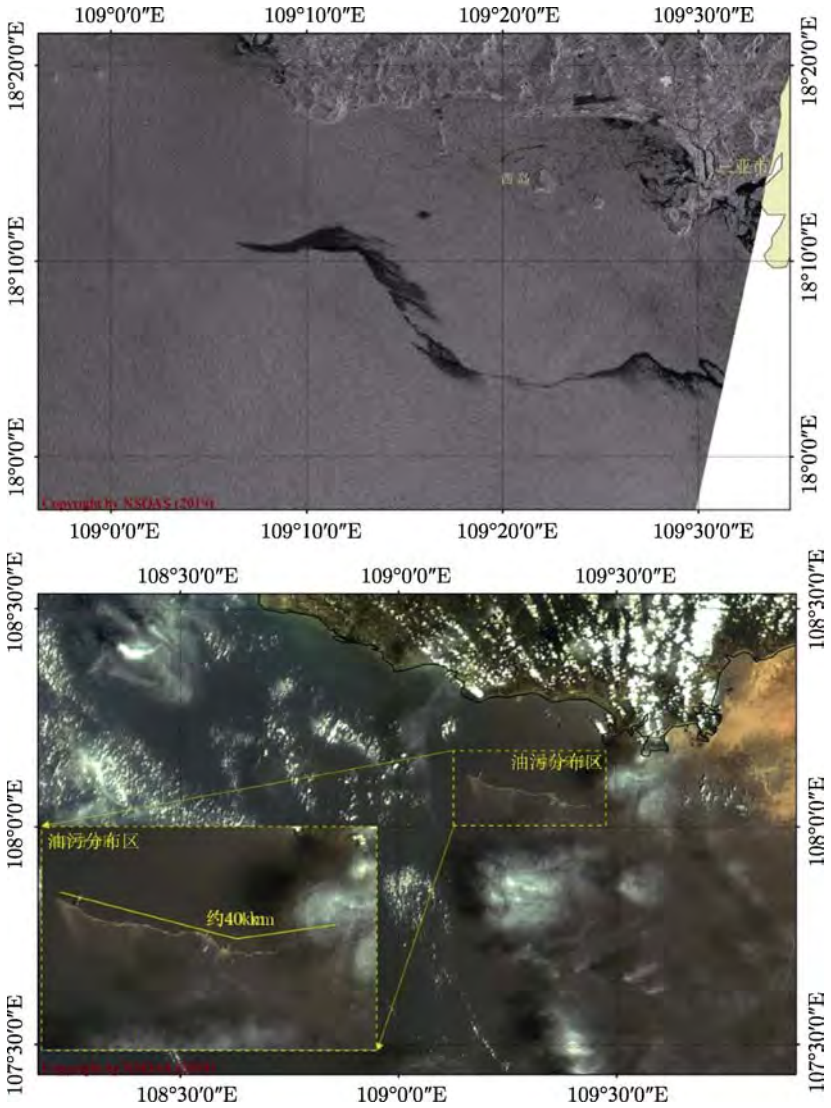

Fig. 5 Sanya oil spill monitoring products respectively derived with GF-3 and HY-1C data (8–9 April 2019)

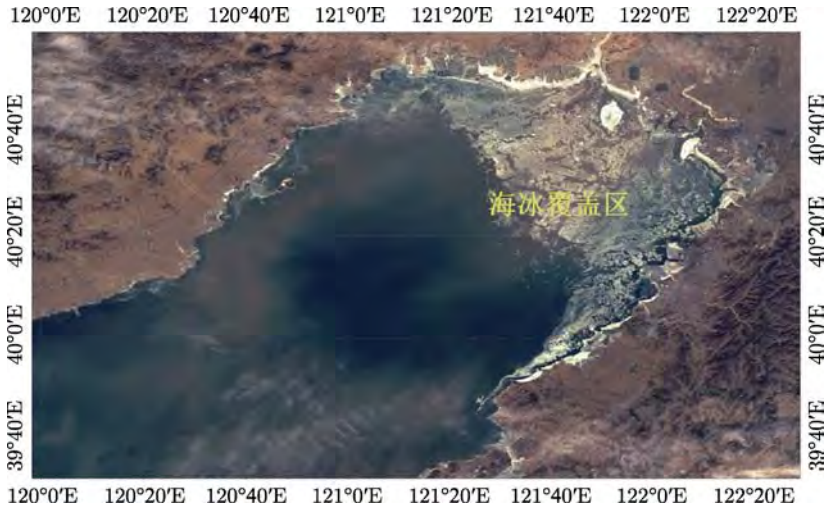

Fig. 6 Sea ice situation image of Bohai Sea derived by HY-1C satellite (9 January 2019)

3.2.2 Continuously Monitoring of Reclamation Projects

The reclamation projects approved by national and local governments were quarterly monitored with high-resolution time-series satellite images. Combining with the on-site survey data, the reclamation beyond the approved scope was identified. The products were operationally distributed to relevant government departments for the supervision usage.

3.2.3 Ecological Red Line Verification

In 2019, with the data of GF-1 and GF-2 satellites, Beihai Bureau of MNR verified human development activities according to the marine ecological protection red line. Remote sensing images were interpreted and analyzed to detect the human development activities in the red line protection areas (Figure 8). The detected areas were continuously monitored; the dynamic changes of human development and utilization activities in the red line protection areas were issued to relevant government departments for the supervision and management of the marine ecological protection red line.

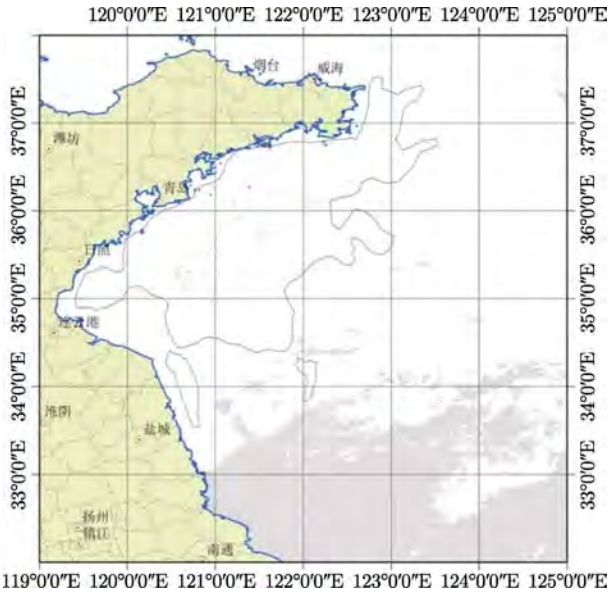

Fig. 7 Thematic map of green tide monitoring in Yellow Sea with the data of HY-1C (6 July 2019)

3.2.4 Mariculture Area Monitoring

In 2019, the mariculture area monitoring was carried out with the data of GF-1, GF-2, GF-3, GF-6, and other satellites. For Rongcheng city of Shandong province, Lianyungang city of Jiangsu province and Ningde city of Fujian province, monthly monitoring was carried out to derive the dynamic changes of mariculture areas. A floating raft mariculture area thematic map of Changhai county, Dalian city, Liaoning province is presented as follows (Figure 9). This kind of product is provided to continuously monitor sea areas and to support island management for Liaoning province. The monitoring report has become an important basic map for sea area management of Liaoning province.

3.3 Ocean and Polar Applications

3.3.1 Ocean Fisheries Services

In 2019, based on the data of HY-2A, HY-2B, and HY-1C satellites, combined with the GF satellite data, the weekly operational analysis, and forecast of fishery situation in 10 sea areas of the three oceans

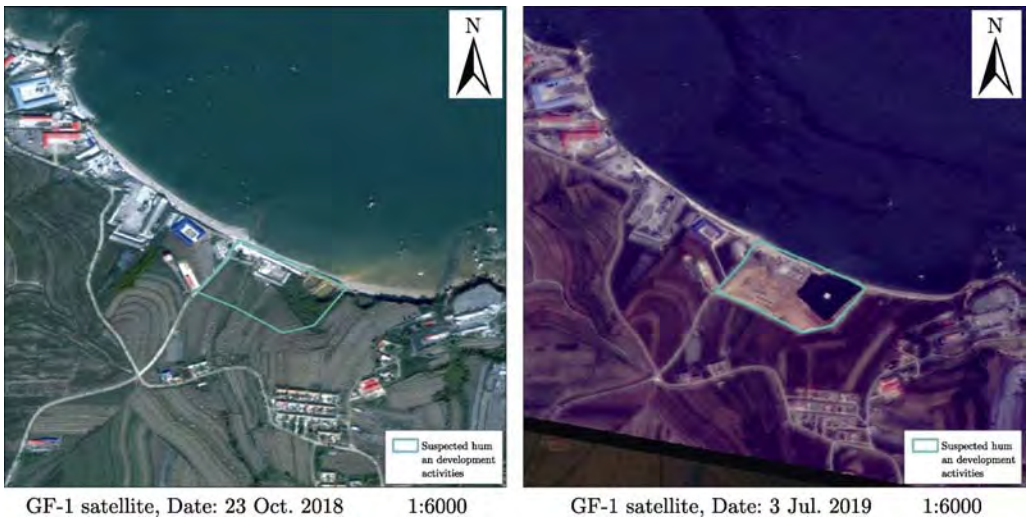

Fig. 8 Detected human development activities in the restricted development zone

Fig. 9 Mariculture area monitoring product of Changhai county, Dalian city, Liaoning province

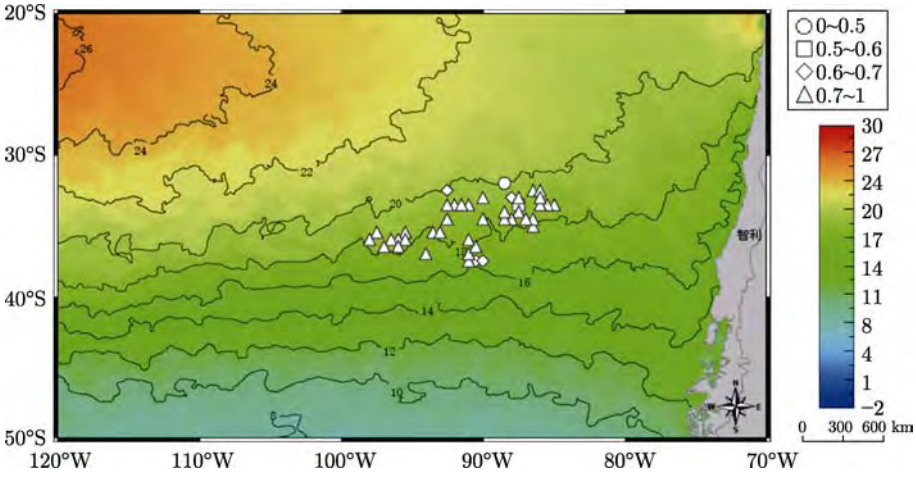

Fig. 10 Prediction results of sea surface temperature and fishing situation of Trachurus murphyi fishing grounds in the Southeast Pacific on 11 February 2019

all over the world were carried out. 407 reports of near real-time sea situation analysis and forecast information were issued to the national ocean fishery enterprises. The reports were helpful to the scientific ocean fishery management of China to gain significant economic benefits (Figure 10).

3.3.2 Polar Navigation Safeguard

In 2019, the ship-borne mobile receiving and data processing system on the Xuelong (which means snow dragon) ship provided satellite remote sensing images and thematic products for the navigation safeguard of China's 36th Antarctic Scientific Expedition. With the data of HY-1C and GF-3, the floating ice dynamic change monitoring products were provided for the icebreaker navigation to guarantee it travels safely and rapidly in the floating ice areas. To guarantee the unloading procedure of Zhongshan station, HY-1C, GF-3, and other satellites had continuously

monitored the fixed ice around Zhongshan station. Key information such as ice disorder areas, ice crack distributions, and selected suitable landing points for Xuelong ship had obtained to help the investigation team to reasonably plan the ice transportation routes of snowmobiles. With the guarantee of the products, the sea ice unloading of Zhongshan Station was completed safely and smoothly (Figure 11, 12).

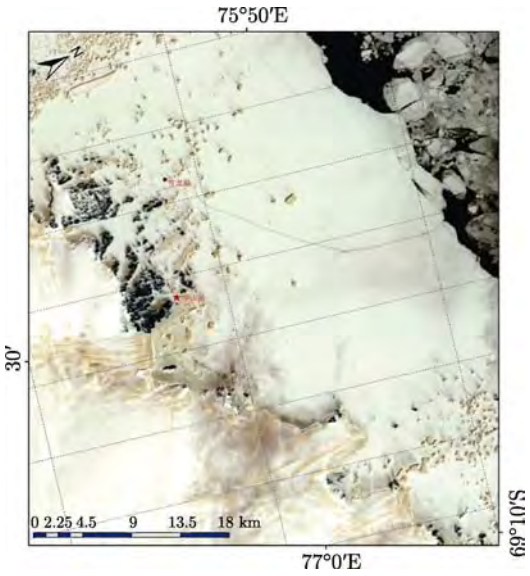

Fig. 11 50 m resolution image of the ice area near Zhongshan Station derived by HY-1C satellite on 24 November 2019

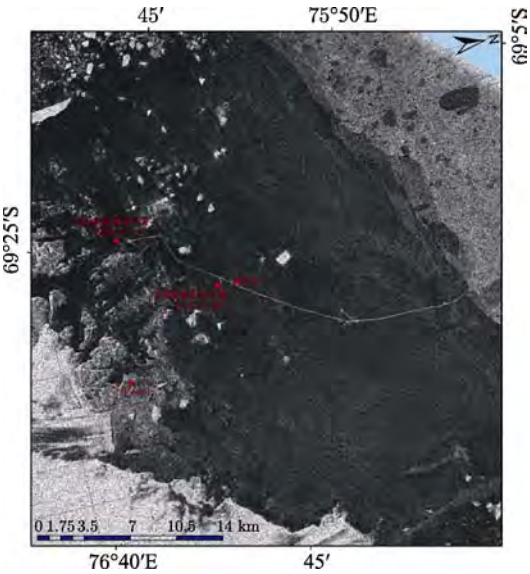

Fig. 12 10-meter resolution image of fixed ice areas around Zhongshan Station derived by GF-3 satellite on 27 November 2019

3.4 Marine Ecology Protection and Restoration

3.4.1 Coastal Wetland Investigation

In 2019, based on the 16-meter resolution satellite remote sensing images of GF-1, a coastal wetland inventory investigation was carried out around the North Sea, focusing on the information of wetland type, distribution, and area elements. Based on the satellite remote sensing images of GF-2, a refined monitoring was carried out in the typical ecological monitoring areas of the Yellow River Estuary and Jiaozhou Bay. The wetland resources and ecological changes in these typical ecological monitoring areas were completely derived and had supported the coastal wetland ecological protection.

3.4.2 Invasive Plant Alterniflora in the Coastal Zone

Based on the data of GF-1 satellite derived in 2019, the remote sensing investigation of the invasive plant Spartina alterniflora in Shandong coastal zone was carried out, and the invasion status of Spartina alterniflora in different regions was analyzed. The thematic map of the spatial distribution of Spartina alterniflora in Shandong coastal zone was made. It provided important information support to the control and management of Spartina alterniflora in Shandong Province.

3.4.3 Biomass Distribution of Typical Vegetation

Based on the WFV sensor data derived by GF-1 in September 2019 and the on-site survey data, the typical vegetation biomass estimation of Jiaozhou Bay coastal wetland was carried out. The thematic map of typical vegetation biomass distribution of Jiaozhou Bay coastal wetland was made (Figure 13). It provided basic information support for the marine and coastal zone management departments of Qingdao city to formulate the protection and management policies of Jiaozhou Bay coastal wetland.

3.4.4 Mangrove Ecosystem in China

Based on the GF-1 data of 2019, the national mangrove spatial distribution information extraction was carried out, and the thematic map of mangrove spatial distribution in China was made. In 2019, the national mangrove area is about 216.1 km^2. The results provided basic information support for mangrove management and protection in China.

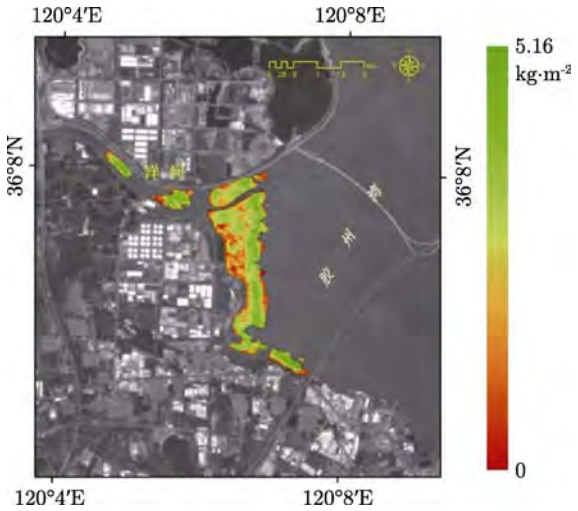

Fig. 13 Thematic map of biomass spatial distribution of Spartina alterniflora around Jiaozhou Bay

3.4.5 Coral Reef Ecosystem Investigation

With the GF-1/GF-2 satellite remote sensing data obtained from 2016 to 2018, an investigation of the distribution of coral reef geomorphic units in Xisha Islands was carried out for reef building and reef coverage usages. The first thematic map of coral coverage of Xisha Islands was made, which provided basic information support for the management of coral islands and reefs in the South China Sea of Sansha city.

4 Future Plans

Seven Chinese ocean satellites have been successfully launched. In 2020, five of them operate normally in-orbit (including GF-3). Five operational Haiyang satellites are under development. Two experimental Haiyang satellites will be approved soon. More than three other new Haiyang satellites are under preliminary study.

Chinese ocean satellites have achieved the parallel operations of three series Haiyang satellites which carry optical sensors, microwave sensors, and synthetic aperture radars, respectively. Haiyang satellites take the wide swath advantage of medium and low resolution remote sensing techniques to repeatedly observe the global oceans with high time-resolution. The data of Haiyang satellites have been widely used in marine disaster mitigation, marine environment, and ecology protection, marine resource development, coastal zone and island management, etc. Their products have become an indispensable information source for the comprehensive management of the seas and oceans.

Acknowledgements Thanks for the technical cooperations provided by Centre National d'Etudes Spatiales, France (CNES) on the precise orbit determination, and the radar altimeter data processing of HY-2. Thanks to EUMESAT, the exchanged European Centre for Medium-Range Weather Forecasts (ECMWF) data have provided significant helps to the data processing and the measurement error correction of HY satellite sensors. Thanks for the cooperation of Royal Netherlands Meteorological Institute (KNMI) for the data processing and the performance evaluation of scatterometers.

References

[1] Ministry of Natural Resources of the People's Republic of China. Chinese Ocean Development Report in 2019 [R]. Beijing: Ministry of Natural Resources of the People's Republic of China, 2019

[2] Ministry of Natural Resources of the People's Republic of China. Chinese Ocean satellite Application Report in 2018 [R]. Beijing: Ministry of Natural Resources of the People's Republic of China, 2019

[3] Ministry of Natural Resources of the People's Republic of China. Chinese Ocean satellite Application Report in 2019 [R]. Beijing: Ministry of Natural Resources of the People's Republic of China, 2020

[4] LIN Mingsen, HE Xianqiang, JIA Yongjun, *et al.* Advances in marine satellite remote sensing technology in China [J]. *Haiyang Xuebao*, 2019, **41**(10):99-112

[5] JIANG Xingwei, HE Xianqiang, LIN Mingsen, *et al.* Progresses on ocean satellite remote sensing application in China [J]. *Haiyang Xuebao*, 2019, **41**(10):113-124

[6] Ministry of Natural Resources of the People's Republic of China (MNR)& China Aerospace Science and Technology Corporation (CASC). General Requirements of HY-1C Satellite Engineering Research [R]. Beijing: MNR and CASC, 2010

[7] Ministry of Natural Resources of the People's Republic of China (MNR)& China Aerospace Science and Technology Corporation (CASC). General Requirements of HY-1B Satellite Engineering Research [R]. Beijing: MNR and CASC, 2011

[8] Ministry of Natural Resources of the People's Republic of China (MNR)& China Aerospace Science and Technology Corporation (CASC). General Requirements of CFOSAT Satellite Engineering Research [R]. Beijing: MNR and CASC, 2012

GUO Huadong, LIANG Dong, LIU Guang. Progress of Earth Observation in China. *Chin. J. Space Sci.*, 2020, **40**(5): 356-367.
DOI:10.11728/cjss2020.05.356

Progress of Earth Observation in China*

GUO Huadong[1,2] LIANG Dong[1,2] LIU Guang[1]

1 (*Key Laboratory of Digital Earth Science, Aerospace Information Research Institute, Chinese Academy of Sciences, Beijing* 100094)

2 (*University of Chinese Academy of Sciences, Beijing* 100049)

Abstract China is expanding and sharing its capacity for Earth observation by developing sensors, platforms, and launch capabilities in tandem with growing lunar and deep space exploration. China is considering the Moon as a viable Earth observation platform to provide high-quality, planetary-scale data. The platform would produce consistent spatiotemporal data because of its long operational life and the geological stability of the Moon. China is also quickly improving its capabilities in processing and transforming Earth observation data into useful and practical information. Programs such as the Big Earth Data Science Engineering Program (CASEarth) provide opportunities to integrate data and develop "Big Earth Data" platforms to add value to data through analysis and integration. Such programs can offer products and services independently and in collaboration with international partners for data-driven decision support and policy development. With the rapid digital transformation of societies, and consequently increasing demand for big data and associated products, Digital Earth and the Digital Belt and Road Program (DBAR) allow Chinese experts to collaborate with international partners to integrate valuable Earth observation data in regional and global sustainable development.

Key words Earth observation, Big Earth Data, Digital Earth, Moon-based Earth observation

Classified index P 35

1 Introduction

The emergence of the concept of a "Digital China", and subsequently its adoption as a national strategy, has boosted the development of the digital economy in the country. Enabling technologies such as cloud computing, 5G, and block chain complemented by big data analytics and artificial intelligence are accelerating the pace of our digital transformation[1]. Data, the key component of any digital infrastructure, is increasingly being collected and exploited in new and innovative ways, providing new opportunities to generate insight and information about our behaviors, society, natural and anthropogenic patterns, and our environment. With the systematic collection of Earth observation data over the past several decades and our rapidly improving capabilities to collect this data from various platforms in space, the atmosphere, and on the ground, we have an invaluable resource that has still not been fully utilized[2].

Due to its synoptic coverage, Earth observation provides valuable data to resolve global and regional challenges as growing global economic integration and interdependence are linking and complicating risks. For example, crop failure in one country may have consequences well beyond its borders and, similarly, destruction and disruptions from a disaster event, exacerbated by climate change, may have far reaching consequences both in time and space. China is one of the few nations that has been successful in developing a strong Earth observation system both on the ground and in space. As of 2019, China has

* Supported by the Chinese Academy of Sciences Strategic Priority Research Program of the Big Earth Data Science Engineering Program (XDA19090000, XDA19030000)
Received March 16, 2020
E-mail: liangdong@radi.ac.cn

Table 1 China's Earth observation satellites launched in 2018

Satellite	Launch date	Rocket model
Gaojing-1 03/04	9 Jan. 2018	CZ-2D Y40
LKW-3	13 Jan. 2018	CZ-2D Y49
Jilin-1 Video-07/08	19 Jan. 2018	CZ-11
LKW-4	17 Mar. 2018	CZ-2D Y51
GF-1 02/03/04	31 Mar. 2018	CZ-4C Y26
Zhuhai-1 OHS 2A/2B/2C/2D	26 Apr. 2018	CZ-11
GF-5	9 May 2018	CZ-4C Y20
GF-6	2 Jun. 2018	CZ-2D Y52
Luojia-1 01	2 Jun. 2018	CZ-2D Y52
FY-2H	5 Jun. 2018	CZ-3A
PRSS-1	9 Jul. 2018	CZ-2C/SMA Y3
HY-1C	7 Sept. 2018	CZ-2C
HY-2B	25 Oct. 2018	CZ-4B
China-France Oceanography Satellite (CFOSat)	29 Oct. 2018	CZ-2C Y22
Saudi-5A/5B	7 Dec. 2018	CZ-2D
Yunhai-2 01/02/03/04/05/06	29 Dec. 2018	CZ-2D

Table 2 China's Earth observation satellites launched in 2019

Satellite	Launch date	Rocket model
Jilin-1 Spectrum-01/02	21 Jan. 2019	CZ-11
Tianhui-2 01A/B	30 Apr. 2019	CZ-4B
Bufeng 1A/1B	5 Jun. 2019	CZ-11
Jilin-1 High Resolution-03A	5 Jun. 2019	CZ-11
Qiancheng 01 (QS1-01)	17 Aug. 2019	SD-1
Xingshidai-5	17 Aug. 2019	SD-1
ZY-1 02D	12 Sept. 2019	CZ-4B Y39
BNU-1	12 Sept. 2019	CZ-4B Y39
Zhuhai-1 OHS 3A/3B/3C/3D	19 Sept. 2019	CZ-11 Y7
Zhuhai-1 OVS 3A	19 Sept. 2019	CZ-11 Y7
Yunhai-1 02	25 Sept. 2019	CZ-2D Y43
GF-7	3 Nov. 2019	CZ-4B
SRSS-1	3 Nov. 2019	CZ-4B
Jilin-1 High Resolution-02A	13 Nov. 2019	KZ-1A Y11
Ningxia-1 01/02/03/04/05 (Zhongzi 01/02/03/04/05)	13 Nov. 2019	CZ-6 Y4
Jilin-1 High Resolution-02B	7 Dec. 2019	KZ-1A Y2
TY-16/17	7 Dec. 2019	KZ-1A Y12
CBERS-04A (ZY-1 04A)	20 Dec. 2019	CZ-4B Y44
ETRSS-1	20 Dec. 2019	CZ-4B Y44
Tianyan-01/02	20 Dec. 2019	CZ-4B Y44

successfully launched about 280 satellites, 200 of which host specialized equipment and sensors for meteorological, oceanographic, resource mapping, environmental monitoring, and disaster risk reduction applications. Apart from these, around 80 communication, navigation, and positioning satellites have been launched. The concept of Moon-based Earth observation is also progressing steadily[3].

The Chinese government has policies to facilitate integrating Earth observation resources for social and economic development, such as infrastructure, logistics, agriculture, and urban and rural planning. Meanwhile, technological concepts such as Digital Earth and Big Earth Data highlight multi-disciplinary and complex data use scenarios. China's Earth observation satellites launched in 2018 and 2019 are listed in Table 1 and Table 2.

2 Land Observation Satellites

2.1 Resource Satellite: ZY

In 1986, the launch of the first optical remote sensing satellite of the CBERS-1 project marked the beginning of China's resource satellite program, which has led to the successful deployment of multiple satellite constellations, including CBERS-1, ZY-2, and ZY-3. Within the CBERS-1 constellation, jointly developed by China and Brazil, CBERS-02D was successfully launched in September 2019 to replace the CBERS-02C satellite. It is equipped with a 9-band visible near-infrared camera and a 166-band hyperspectral camera that helps to fill the medium-resolution remote sensing data gap and reduce the costs of purchasing foreign data.

The ZY-3 satellites, independently developed by China, are China's first autonomous, high-resolution, three-dimensional mapping satellites for civilian use. Through stereo observations, they can measure topographic maps at a scale of 1:50000, providing services for land, resources, agriculture, forestry, and other fields. The ZY-3 01 satellite, equipped with a three-line array camera and a multi-spectral camera, can obtain stable high-resolution stereo images and

multi-spectral images and auxiliary data covering the whole of China. The ZY-3 02 satellite is a remote sensing commercial satellite, and the main payloads are three-line array cameras, multispectral cameras, and laser rangefinders. The ZY-3 02 satellite has high stereo image resolution and elevation measurement accuracy. Double-satellite networking can shorten the revisit time to 3 days and improve stereo mapping to ensure long-term, stable acquisition of high-resolution stereo mapping data.

The number of China's resource satellites continues to increase, and the technology is continuously being upgraded. China's resource satellites play an important role in the monitoring, planning, and management of land resources, agriculture, forestry, water conservancy, environmental protection, and disaster mitigation.

2.2 Environmental Protection and Disaster Monitoring Constellation: HJ

The HJ satellites are a small constellation for environmental and disaster monitoring and forecasting. The system has optical, infrared, hyperspectral, and microwave detection methods. It is mainly used for large-scale, 24 h dynamic monitoring of ecological environments and disasters, and estimating their trends for rapid assessment to coordinate informed and timely emergency response, post-disaster rescue, and reconstruction.

The HJ system, consisting of two optical satellites (HJ-1A and HJ-1B) and a radar satellite (HJ-1C), is used for environmental and disaster monitoring. The HJ-1A/1B satellites, which were launched on 6 September 2008, are both equipped with a CCD camera, and there is a Hyperspectral Imager (HSI) onboard HJ-1A and an infrared camera (IRS) onboard HJ-1B. The CCD cameras on the two platforms are placed symmetrically under the star point, with the field of view equally divided, making parallel observations in four spectral bands at a ground pixel resolution of 30 m. The push-broom hyperspectral imager onboard the HJ-1A satellite provides a ground pixel resolution of 100 m within 110 to 128 spectral bands and also has an onboard calibration function and provides 30° side-look capability. The infrared camera onboard the HJ-1B satellite has four spectral bands with a ground pixel resolution of 150/300 m. The two satellites collectively provide a two-day revisit time, capturing macro-scale, multi-scale characteristics useful for weather, environmental, and disaster monitoring. The HJ-1C satellite, launched in November 2012, is China's first S-band Synthetic Aperture Radar (SAR) satellite. The S-band SAR has two working modes: stripe mode and scan mode. The imaging bandwidths are 40 km and 100 km. The HJ-1C SAR has a single-view mode with a spatial resolution of 5 m and a four-view mode with a spatial resolution of 20 m, and the SAR images provided are mainly on multi-view mode.

2.3 High-resolution Earth Observation System: GF Series

The China High-resolution Earth Observation System (in short referred to as CHEOS) is one of 16 major science and technology projects identified in the Guidelines for The National Mid-term and Long-term Science and Technology Development Plan (2006–2020). Following the successful launches of the GF-1 to GF-4 and GF-8 and GF-9 optical satellites between 2013 and 2015, China successfully launched the GF-5 to GF-7 and GF-10 to GF-12 satellites between 2018 and 2019, putting a total of 12 satellites in orbit for the GF series[4]. The launch dates and payloads from GF-1 to GF-7 are listed in Table 3.

The GF-5 satellite is the only land and environmental hyperspectral observation satellite of CHEOS, and the world's first atmosphere and land hyperspectral observation satellite. The GF-5 satellite can detect the specific components of substances by high-precision spectral analysis of the whole spectrum from ultraviolet to longwave infrared. The GF-6 satellite is the first low-orbit optical satellite for precision agriculture and the first satellite with a red edge band in China. The GF-6 satellite forms a "2 m/8 m optical imaging satellite system" with the GF-1 satellite, and provides valuable data for agriculture, forestry, and disaster reduction, as well as environmental protection, national security, and residential construction. It is the first submeter-level

Table 3 China's high-resolution Earth observation satellites

Satellite	Launch date	Payload
GF-1 (Optical satellite)	4 Apr. 2013	2×2 m panchromatic/8 m multispectral camera (Combined width: 70 km) 4×16 m multispectral wide imaging camera (Combined width: 830 km)
GF-2 (Optical satellite)	19 Aug. 2014	2×0.8 m panchromatic/3.2 m multispectral camera (Combined width: 45 km)
GF-3 (Microwave satellite)	10 Aug. 2016	C-band multi-polarization Synthetic Aperture Radar (Resolution: 1~500 m. Width: 10~650 km)
GF-4 (Optical satellite)	29 Dec. 2015	50 m visible light/multispectral camera 400 m infrared camera (Width: 400 km)
GF-5 (Hyperspectral satellite)	9 May 2018	Atmospheric Infrared Ultraspectral (AIUS) (Spectral wavelength: 2.4~13.3 μm. Spectral resolution: 0.03 cm) Environment Monitoring Instrument (EMI) (Spectral resolution: 0.3~0.5 nm. Spatial resolution: 48 km/13 km) Advanced Hyperspectral Imager (AHSI) (Spatial resolution: 20 m/40 m. Width: 60 km) Greenhouse-gases Monitoring Instrument (GMI) (Spectral resolution: 0.6 cm/0.27 cm) Directional Polarization Camera (DPC) (Spatial resolution: >3.5 km at nadir) Visual and Infrared Multispectral Sensor (VIMS) (Spectral resolution: 5 nm/10 nm, Spectral wavelength: 0.4~2.5 μm. Spatial resolution: 30 m, width: 60 km)
GF-6 (Optical satellite)	2 Jun. 2018	2 m panchromatic/8 m multispectral camera (Width: >90 km) 16 m multispectral wide imaging camera (Width: >800 km)
GF-7 (Stereo mapping satellite)	3 Nov. 2019	0.8 m panchromatic/3.2 m multispectral camera (Width: 20 km) laser altimeter (2-beam 1064 nm laser)

high-resolution stereo mapping satellite in China. The GF-7 satellite is equipped with a two-line array camera and a laser altimeter. The two-line array camera can continuously obtain overlapping ground images and stereo mapping at 1:10000 scale. The laser altimeter can map areas with complicated terrain conditions and further improve the elevation positioning accuracy with fewer control points. The GF-7 satellite is mainly used in the acquisition of high-resolution three-dimensional mapping imagery for construction and remote sensing statistical surveys.

The GF-10 satellite is a microwave remote sensing satellite of CHEOS. Due to its high, sub-meter resolution, GF-10 is mainly used for land surveys, urban planning, land approval, road network design, and disaster prevention, as well as information support for the Silk Road Economic Belt and the 21st-century Maritime Silk Road (Belt and Road)

initiative and other national strategies. GF-11, like GF-10, has a submeter resolution. However, operating in the optical spectrum, it is mainly used in crop estimation, land surveys, and disaster prevention. The GF-11 satellite also has a massive on-orbit data processing and high-speed data transmission subsystem that enables, for the first time in space, high-speed two-way data transmission between GF-11 and the relay satellite. The GF-12 satellite, the latest to have been launched, is a microwave remote sensing satellite. With a submeter spatial resolution, it is mainly designed for land surveys, urban planning, land approval, and disaster prevention.

2.4 Commercial Satellites

In recent years, China's national policies have facilitated the development and deployment of commercial remote sensing satellites. These policies stimulated investment from private commercial enterprises, attracted talent, and spurred technological innovation in this sector. With the improving quality and quantity of commercial satellites, there have been several launched in the past two years. A number of these commercial satellites are equipped with high spatial resolution sensors. For example, the Luojia-1 satellite records night-time light imagery at 130 m resolution, which is higher than most of the existing night-time light images to date. Similarly, the Jilin-1 High Resolution-02A and Jilin-1 High Resolution-02B satellites feature an imaging system with a resolution of 0.75 m in panchromatic mode and better than 3 m in multispectral mode. Also, the commercial optical remote sensing satellite Jilin-1 Wideband-01 features a high-resolution (submeter) wide-field-of-view telephoto range imager. The push-broom imager also has a multi-spectral resolution better than 4 m and features high-speed storage and high-speed digital transmission systems. Another satellite, Qiancheng, with Earth observation and narrow-band communication capabilities, has an imaging payload with a resolution of more than two meters. With a mass of 65 kg, Qiancheng is the largest satellite in orbit independently developed by a private satellite start-up company in China. Commercial satellites launched from June 2018 to February 2020 are listed in Table 4.

Commercial entities are being allowed to develop and deploy constellations of satellites. In China, Zhuhai-1 OHS 3A/3B/3C/3D was launched in September 2019. This constellation of four satellites with a ground resolution of 10 m, spectral resolution of 2.5 nm, and a swath width of 150 km can cover the entire globe in 5 days and provide multiple revisits a day to monitor a specific site. Another constellation, the Ningxia-1 01/02/03/04/05 satellites, was successfully launched on 13 November 2019. They are a commercially operated global EM spectrum signal monitoring satellite system (SIGINT).

A couple of experimental commercial satellites have also been launched. Jingshi-1 or BNU1, a small 16 kg experimental satellite by Beijing Normal University (BNU), conducts all-weather polar climate and environmental observations. Weilai-1 (Future 1) is a small satellite for space-based science experiments and remote sensing by CCTV (China Central Television). Also, Bufeng 1A/1B, which marks China's first maritime launch mission, measures the velocity of the wind by measuring the signals of navigation satellites reflected on the ocean's surface (GNSS-R). With the continuous development of the domestic remote sensing market, commercial satellite remote sensing will continue to grow.

Table 4 Commercial satellites launched from June 2018 to February 2020

Satellite	Launch date	Rocket model
Luojia-1 01	1 Jun. 2018	CZ-2D
Jilin-1 Spectrum-01/02	21 Jan. 2019	CZ-11
Lingque 1A	21 Jan. 2019	CZ-11
Jilin-1 High Resolution-03A	5 Jun. 2019	CZ-11H
Bufeng 1A/1B	5 Jun. 2019	CZ-11H
Qiancheng 01	17 Aug. 2019	Jielong-1
Xingshidai-5	17 Aug. 2019	Jielong-1
Jingshi 1	12 Sept. 2019	CZ-4B
Zhuhai-1 OHS 3A/3B/3C/3D OVS 3A	19 Sept. 2019	CZ-11
Jilin-1 High Resolution-02A	13 Nov. 2019	Kuaizhou-1A
Ningxia-1 01/02/03/04/05	13 Nov. 2019	CZ-6
Jilin-1 High Resolution-02B	7 Dec. 2019	Kuaizhou-1A
Weilai 1R	20 Dec. 2019	CZ-4B
Jilin-1 Wideband-01	15 Jun. 2020	CZ-2D

3 Scientific Satellites

3.1 Satellite Platforms

China has successfully developed and launched several specialized scientific satellites since 2018. The first was the Sino-French ocean satellite, adopting the CAST2000 satellite platform, which was successfully launched on 29 October 2018, with a design life of 3 years. It is the first satellite jointly developed by China and France, and simultaneously observes sea wind and waves, utilizing information from a microwave radiometer (SCAT) and radar spectrometer (SWIM). SCAT uses a wide fan beam direction map of the scanning antenna at a speed of 35 revolutions every 10 min to measure the wind, improving the number of observations per direction and thereby improving the sea surface wind speed and wind direction inversion accuracy. Both SCAT and SWIM are unique achievements, as the SCAT scanning system is the first of its kind, and SWIM is the world's first satellite-borne sea wave spectrometer. SWIM can obtain wave direction spectrum data and obtain marine dynamics information such as wavelength and propagation direction through further data processing.

China also launched Taiji-1 on 31 August 2019. It is China's first experimental space gravitational wave detection satellite. At present, Taiji-1 has successfully completed the first phase of on-orbit testing tasks. It has laid a solid foundation for China's space gravity wave detection. On 12 September 2019, China also launched Jingshi-1, which is the first satellite of China's Weijing constellation, and also China's first satellite dedicated to polar climate and environmental monitoring. Aboard the CAST5 micro-nano satellite platform, Jingshi-1 has a revisit period of 5 days, and an observation range between 60° to 80° north-south latitude. It is equipped with three kinds of payloads, including a wide-angle camera with a resolution of 73.69 m and a swath of 744 km and a medium-resolution camera with a nadir resolution of 8 m and a swath of 25 km. It has a high dynamic push scan for glaciers and terrestrial water bodies and is also equipped with an AIS receiver, which can receive AIS signals from ships in global waters. Jingshi-1 is a significant achievement as it makes up for the lack of polar observation data in China.

The China Seismo-Electromagnetic Satellite Zhangheng-1 (ZH-1), launched on 2 February 2018, is the first space-based platform for China's stereoscopic seismic observation system, with a dynamic, wide viewing angle and all-weather space-to-Earth observation. The satellite can provide data on the global electromagnetic field, ionospheric plasma, and high-energy particles using several instruments: a search coil magnetometer, high-precision magnetometer, electric field detector, GNSS occult receiver, plasma analyzer, high-energy particle detector, Langmuir probe, and three-frequency beacon transmitter. The satellite is used to study the interaction and effects of the Earth system, especially the ionosphere, with Earth's other spheres. Real-time monitoring of ionospheric dynamics and seismic precursor tracking in China and its surrounding areas can make up for the lack of ground observation. It is expected that by 2022, China will have three electromagnetic monitoring satellites in orbit including Zhangheng-1 and 2, Macao's first scientific satellite. The three satellites in orbit will effectively support the scientific exploration of seismic monitoring and prediction, as well as the early warning of space weather, for years to come.

China's Global Carbon Dioxide Monitoring Science Experiment Satellite, known as TANSAT or CarbonSat, is the first experimental satellite for observing global atmospheric carbon dioxide and the third satellite with the capability to detect greenhouse gases with high precision. Launched on 22 December 2016, the satellite can provide basic data for research in the fields of greenhouse gas emissions and carbon verification, provide data support for macro-decision-making such as energy conservation and emission reduction, and increase China's voice in international carbon emissions. The satellite is equipped with two scientific payloads in an integrated design, the Atmospheric Carbon-dioxide Grating Spectroradiometer (ACGS) and the Cloud Aerosol Polarization Imager (CAPI). Using TANSAT's data, scientists have successfully developed two products: a global chlorophyll fluorescence product in 2017,

found to be highly consistent in terms of value, distribution, and change when compared with Japan's Orbital Carbon Observation 2 (OCO-2) satellite products and relevant data from NASA; and the first map of the global distribution of atmospheric carbon dioxide at the beginning of 2018. These demonstrate China's achievements in developing a world-class global carbon monitoring system.

The Big Earth Data Science Engineering Program (CASEarth), is preparing the first Earth science satellite in China and the first human trace satellite in the world. The CASEarth satellite will provide necessary information about national urban growth, monitor the quality of coastal and offshore environments, and give insights into the status, patterns, and regional gaps in socioeconomic development in China at a very fine scale. The acquired Earth observation data will be released to the world through CASEarth, which will contribute to the Sustainable Development Goals (SDGs) and the Community of a Shared Future for Mankind. The CASEarth satellite, still in the prototype phase, will be carrying multiple sensors onboard including a Thermal Infrared Imager, the world's first high-resolution noctilucent Urban Low-light Imager, and an Offshore Multispectral Imager. Tests were successfully conducted in early 2020, and on-orbit deployment is targeted for 2021.

3.2 Moon-based Earth Observation

Aside from traditional satellites, Chinese scientists have proposed a radically different approach: establish a long-term Earth observation system on the Moon to collect high-quality, planetary-scale Earth observation data that is spatiotemporally consistent because of the Moon's stability and the platform's long operational life. Sensors installed on the Moon will be able to simultaneously observe Earth's whole Moon-facing surface, thus providing the opportunity to integrate data from these sensors. Moon-based Earth observation can provide key insights to solve a series of key scientific problems related to multi-sphere interaction on Earth, enhancing our understanding of the dynamic Earth system[5]. The possibility of establishing an Earth observation system on the lunar surface has become quite possible with China's growth in lunar and deep space exploration and continued improvements in sensor and spacecraft design, especially after gaining experience and confidence from the successful Chang'E-1~4 missions. Several studies have been completed and are also underway in Chinese institutions to establish the principles and feasibility of Moon-based Earth observation systems.

A Moon-based Earth observation system presents new challenges to sensor design and function due to its distance from Earth. Research has been conducted on the operation and imaging mechanisms of Moon-based sensors, such as multispectral imagers, cavity radiometers, and SAR, using rigorous geometric models to simulate the conditions on the Moon. In addition, the effects of the traveling time of light, light aberration, and bending due to gravity have been assessed. Possible errors due to signal propagation have been evaluated by a geometric error estimation method, which is an automatic geometric correction approach for cross-platform imagery. A geometric expression method for sub-lunar points in polar coordinate systems is currently being tested to ensure the integrity and authenticity of imagery[6-8].

Similarly, studies on sensors and observation strategies have proposed phase scanning control for lunar SAR, which can aid in centering radar beams to improve the pointing accuracy in the direction of the zero Doppler surface on Earth. Studying beam pointing errors revealed that look-angle pointing errors and azimuth pointing errors in lunar Doppler radar would lead to the emergence of residual error. For estimating the global energy balance, the radiative transfer model and the surface bi-directional reflection distribution function are used to calculate the correlation between the shortwave reflected radiation from the top of Earth's atmosphere and the surface. These models are also applied to simulations of observation geometry that calculate the emission energy distribution characteristics of the space between the Moon and Earth[9,10].

To make better use of the lunar surface as a

natural platform, research on the lunar environment and observation site are being conducted, which is critical to ensuring maximum benefit from a relatively permanent Earth observation station. These studies have considered topographic features such as relief, roughness, slope, and slope direction at three lunar sites. The Chang'E-2 Digital Elevation Model (DEM), SLDEM2015, and LOLA DEM products were used to calculate and develop a database of long-term evolution of the illumination characteristics of the lunar surface. A preliminary site selection framework for a Moon-based Earth observation system has been established based on a number of characteristics such as Sun-Earth-Moon motion, the lunar surface environment, long-term illumination, visibility, the ionosphere, and the structural morphology of the lunar surface[11].

This is an area of active and promising research. The successful launch of the Changzheng-5 vehicle furthered China's lunar and deep space exploration capabilities. With close collaboration with other countries, and continued improvements in technology, the vision for a Moon-based Earth observation system will begin to take shape in the next decade or two, providing valuable global-scale data for understanding our planet and supporting sustainable human development.

4 Key Contributions in Global Applications

China's ongoing digital transformation, resulting from fast-paced scientific research, technological development, and innovation in utilizing digital space technologies, is fueling rapid development of digital infrastructure, value-added services, and data-driven decision making, not only in China but also in other countries. China is supporting, participating in, contributing to, and leading international research programs and collaborations in management of the environment, resources, disaster risk reduction, marine ecosystems, coastal areas, and cities.

4.1 Towards a Digital Earth

China's Digital Earth scientific research and technological applications have achieved fruitful results in establishing technical platforms that provide strong support to China's response to global climate change, disaster mitigation, urban management, heritage protection, sustainable development, and other fields[12]. With data-driven technology as the engine, Digital Earth will enable deep integration of spatial data in the digital economy and enhance China's core competitiveness in the field[13]. The efforts towards a Digital Earth system would benefit from our experiences in developing the Digital China infrastructure and would help to improve our understanding of natural processes and consequently help decision making.

Due to this potential, the Digital Earth community in China is actively engaging both national and international experts by holding conferences and publishing journals and books, such as the recent "Manual of Digital Earth" [14].

4.2 Facilitating Sustainable Development along the Belt and Road Region

Many countries along the Belt and Road are facing developmental challenges such as water shortages, frequent occurrences of disasters, and huge ecosystem changes. In the Belt and Road region, the speed of data processing and analysis is much lower than the speed of data acquisition, leaving massive amounts of scientific data and information unprocessed and underutilized. The Digital Belt and Road Program (DBAR), an international collaborative research program, is committed to developing a platform for sharing advanced Earth observation technologies among the Belt and Road regions. DBAR has five priority areas [15]: (i) enhance infrastructure with an open platform for shared data, code, and algorithms to analyze vast amounts of data; (ii) promote data sharing and interoperability for open exchange of data between users in the region towards the collective benefit; (iii) extend applications to more people, and diversify users and disciplines that can utilize Earth observation and Big Earth Data towards development across the region; (iv) identify research opportunities and discover knowledge within huge multidisciplinary datasets; and (v) strengthen in-

ternational collaboration to set up bilateral or multilateral arrangements and stronger links with international scientific programs and organizations.

To work on these five priority areas, DBAR has established nine working groups focused on Big Earth Data, agriculture and food security, coastal zones, environmental change, natural and cultural heritage, disaster risk reduction, water, high-mountain and cold regions, and urban environments. DBAR has also launched eight International Centers of Excellence (ICoEs), located in Thailand, Pakistan, Finland, Italy, Russia, Morocco, Zambia, and the United States.

Since starting in 2018, DBAR members have developed the DBAR Big Earth Data System, a spatial information repository and decision-making tool for the Belt and Road region. It aims to develop a cloud-based scalable platform for handling Big Earth Data, giving access to vast amounts of satellite imagery and socioeconomic data. Currently, the system provides real-time hardware and software monitoring, online data sharing for more than 100000 images, and online viewing and analysis for public users. For the next three years, the system will serve the countries along the Belt and Road, providing Big Earth Data sharing and cloud-based online analysis features at the regional, sub-regional, and national levels.

4.3 Data-driven Services Towards Solutions for Global Challenges

At present, the United Nations as well as governments and international organizations are conducting research on constructing SDG indexes that can be monitored and evaluated. This needs to be done in three broad aspects: (i) fill in missing data and develop technologies to generate data for SDG evaluation; (ii) develop Big Earth Data methods and models to evaluate SDGs; and (iii) provide decision support to SDGs by monitoring and identifying progress.

CASEarth and DBAR selected 20 indicators of 6 SDGs for analysis and carried out 27 case studies to demonstrate the benefits of using Earth observation within the Big Earth Data framework. These cases were presented in the report titled "Big Earth Data in Support of the Sustainable Development Goals (2019)", which was selected as one of four official documents that the Chinese government submitted during the 74th UN General Assembly and one of two documents officially submitted to the UN Sustainable Development Summit[16].

4.4 Disaster Risk Reduction

Deepening disaster system theory and the rapid development of Earth observation technology has benefited China's research in disaster risk reduction. After more than 40 years of development, China has established satellite programs such as the FY meteorological satellites, the ZY Earth resources series, and the HJ-1A/B/C small satellite constellation. The GF satellites launched in the past seven years have considerably improved China's disaster monitoring and management capabilities in monitoring risk, loss, and post-disaster reconstruction[17].

Monitoring seismic activity has been an important focus in Chinese disaster research since the 1970s. An important recent achievement in this field is the launch of China's first seismic-electromagnetic satellite, Zhangheng-1, under the National Geophysical Field Exploration Satellite Program. Since entering its present orbit on 2 February 2018[18], it has significantly facilitated the development of China's first global geomagnetic map by filling in data gaps in the global geophysical field. With a growing collection of post-disaster Earth observation images, Chinese scientists have proposed a multi-source heterogeneous Earth observation image change detection method using multi-temporal remote sensing imagery before and after an earthquake[19]. The method overcomes requirements for data types and temporal consistency, assimilates multi-sensor data, and allows collaborative information processing. Among the Earth observation data, SAR has become an invaluable data source for earthquake damage assessment.

For example, following the Jiuzhaigou earthquake, high-resolution optical and SAR imagery were used to investigate the consequences from different perspectives including road damage analysis, extraction of secondary disasters (*e.g.*, landslides), and calculation of the co-seismic displacement field[20, 21].

Additionally, to evaluate the earthquake recovery progress in Wenchuan, the Chinese Academy of Sciences integrated multi-temporal, massive satellite and aerial observation data over the past 10 years, and found valuable information about disaster chain effects and potential future disasters, long-term recovery processes of the natural ecology, and the progress of post-disaster reconstruction in cities and towns[22].

Forest fires are another important application for Earth observation data. On 2 June 2018, after the onset of forest fires in the Greater Khingan Mountains in Inner Mongolia, the Chinese government swiftly moved to acquire satellite data to monitor the situation. Using FY meteorological satellites, GF-4 satellites, and multiple polar-orbit optical and SAR satellites, forest fires and burned areas were actively monitored to coordinate relief and emergency response activities[23]. Similarly, ZY-3, GF-1, and Landsat-TM data combined with LiDAR point clouds and CCD images also enable dynamic monitoring of forest fires. Important components of improving the quality of forests are the study of forest fire intensity and the restoration of vegetation. Multi-modal Earth observation can help improve the efficiency of regional-scale forest structure monitoring by providing horizontal and vertical forest structure information, Fractional Vegetation Cover (FVC), Above-Ground Biomass (AGB), and canopy height. The parameters allow for quantitative analysis of the effects of fire on forests[23].

4.5 Environmental Change Monitoring

Since May 2018, China has launched over 20 Earth observation satellites including but not limited to: GF-5, the world's first full-spectrum hyperspectral satellite, which can capture comprehensive observations of both the atmosphere and land surface; HY-1C, which can obtain 24 h water color, sea surface temperature, coastal zone and inland water information with 50 m resolution globally; and BNU-1, which is the first Chinese polar observation minisatellite. These missions have improved our observation capabilities in the Arctic and Antarctic. Civil and commercial satellites such as Jilin-1, OVS-1 03, Yunhai-1, Ningxia-1, and ZY-1 02D also consider environmental observations as an important part of their operations.

Chinese scientists have released numerous environmental observation products, which include the first global CO_2 map measured by China's carbon satellite[24]; global chlorophyll fluorescence products, which can support the distribution analysis of CO_2 concentration[25]; the first global fire mask and forest cover product with 30 m resolution[26]; comprehensive surface reflectance products over China; and the first global map of fine-mode Aerosol Optical Depth (AODf) at a spatial scale of 3.3 km, which achieves the highest spatial resolution among similar products[27]. Moreover, primary products such as global sea surface wind field, wave spectrum, and other dynamic marine environmental parameters have been obtained with CFOSAT[28].

Earth observation technologies have also facilitated monitoring programs on key ecological and environmental problems. China's annual dynamic monitoring of soil erosion conducted by the Ministry of Water Resources also incorporates Earth observation data in their analysis. The national key research and development program "Marine Environmental Security" and "Cooperation Platform for Arctic Environmental Satellite Remote Sensing and Numerical Prediction" have been launched to promote three-dimensional ocean observation in polar regions. Earth observing technology is also an important component of special actions of the Ministry of Ecology and Environment, such as the "Green Shield", "Clairvoyance Plan", "Waste Removal Action", and blue-green algae bloom prevention in key lakes and reservoirs.

Earth observation data has enabled important breakthroughs in environmental change studies. Multi-source satellite data being used to monitor the environment and resources in the Belt and Road region revealed that solar energy is affected by latitude and the spatial distribution of the water budget is uneven[29]. The global internal thermal structure of oceans in different seasons has been inverted based on data on ocean surface height, temperature, sa-

linity, and wind field. This has shown that the spatial heterogeneity of marine internal temperature anomalies in shallow water varies with different seasons, while that in deep water (>300 m) is basically invariant. Earth observation has also been used to study the effects of climate change on the Arctic ecosystem[30]. The relationships between surface temperature and radiation change under clouds detected by thermal infrared remote sensing have shown that the radiation change has a linear relationship with the magnitude of surface temperature[31].

China is also cooperating with other countries to improve their Earth observation capability; for example, under the framework of South-South Cooperation on Climate Action, the Ministry of Ecology and Environment gifted the Ethiopian Ministry of Science and Technology a wide-range, multi-spectral Earth observation mini-satellite, which has enhanced Ethiopia's capacity to cope with climate change and promoted Chinese aerospace technology in the global market.

5 Perspective on Trends in Earth Observation

The global acquisition, analysis, distribution, and use of Earth observation data is increasingly becoming viable, in particular due to cloud computing infrastructure, data analysis capabilities, improved connectivity, e-commerce, and other associated technologies. This creates the potential for commercial exploitation of data in online services and data analytics. This has resulted in attracting investments in, and acquisitions of, companies specializing in a wide variety of Earth observation-related services.

In the last two decades, investment in the Earth observation sector in China and the rest of the world has largely gone towards technological development – improving Earth observation systems, sensors, platforms, and the viability of data. This includes algorithms and methodologies to process raw data to quantify different parameters. The increasing demand for big data as societies digitally transform has also increased the demand for Earth observation data, creating an industry that provides global data services to big businesses and government organizations.

Agriculture, disaster risk reduction, urban planning, and other large-scale planning, monitoring, and data processing sectors are already utilizing Earth observation data. The integration and utilization of Earth observation data will continue to be improved and simplified through advancements such as 5G network integrations, economically viable cloud computing infrastructure and services, increasing online data analysis services, and growing competitive products. Innovative commercial applications and services for Earth observation data and products will increasingly be the focus in the coming years. Commercial enterprises can adopt the use cases of Earth observation from large-scale operations and transform them for adoption by more local-scale operations. For example, large agricultural setups are already using Earth observation products, but in the future, new online services powered by cloud technology and 5G would be able to simplify interfaces and information that would facilitate their adoption by local farmers.

China is successfully developing its capacity in all aspects of the Earth observation industry. Growing numbers of satellites, high-tech sensors, research into ambitious Moon-based Earth observation systems, and increasing support to commercial satellite programs will drive China's data acquisition capabilities and establish a viable data acquisition, processing, and analysis industry. Based on these gains in infrastructure, programs such as CASEarth will facilitate research and development of platforms for data integration and Big Earth Data analysis to create value-added products and facilitate data-driven policy development and decision support systems. Digital Earth and DBAR will provide collaborative platforms to China towards regional and global sustainable development, collaborative research, and human resources[32,33].

Acknowledgements The authors are grateful for helpful comments from many researchers and colleagues. Thanks go to CHEN Fang, YAN Dongmei, LI Xiaoming,

LI Xinwu, CHEN Liangfu, SUN Zhongchang, LIU Zhen, and Zeeshan SHIRAZI for feedback, as well as the editor and anonymous referees. All views and errors are the responsibility of the authors.

References

[1] GUO H D, LIU Z, JIANG H, *et al.* Big Earth Data: a new challenge and opportunity for Digital Earth's development [J]. *Int. J. Digit. Earth*, 2017, **10**(1):1-12

[2] GUO H D. Big data drives the development of Earth science [J]. *Big Earth Data*, 2017, **1**(1/2):1-3

[3] GUO H D, LIU G, DING Y X. Moon-based Earth observation: scientific concept and potential applications [J]. *Int. J. Digit. Earth*, 2018, **11**(6):546-557

[4] CHEN L, JIA J, WANG H Q. An overview of applying high resolution remote sensing to natural resources survey [J]. *Remote Sens. Land Resources*, 2019, **31**(1):1-7

[5] YE H L, GUO H D, LIU G, *et al.* Observation scope and spatial coverage analysis for earth observation from a Moon-based platform [J]. *Int. J. Remote Sens.*, 2017:1-25

[6] GUO H D, REN Y Z, LIU G, *et al.* The angular characteristics of Moon-based Earth observations [J]. *Int. J. Digit. Earth*, 2020, **13**(3):339-354

[7] YE H L, GUO H D, LIU G, *et al.* Impacts of platform's position errors on geolocation for a Moon-based sensor [J]. *IEEE Geos. Remote Sens. Lett.*, 2020, **17**(1):112-116

[8] ZHANG L, GUO H D, JIAO H, *et al.* A polar coordinate system based on a projection surface for Moon-based Earth observation images [J]. *Adv. Space Res.*, 2019, **64**(11):2209-2220

[9] XU Zhen, CHEN Kunshan. Effects of the Earth's curvature and lunar revolution on the imaging performance of the Moon-based synthetic aperture radar [J]. *IEEE Trans. Geosci. Remote Sen.*, 2019, **57**(8):5868-5882

[10] NIE Chenwei, LIAO Jingjuan, SHEN Guozhuang, DUAN Wentao. Simulation of the land surface temperature from Moon-based Earth observations [J]. *Adv. Space Res.*, 2019, **63**(2):826-839

[11] GUO H D, FU W X, LIU G. Scientific Satellite and Moon-based Earth Observation for Global Change [M]. Singapore: Springer, 2019

[12] GUO H D, WANG L Z, LIANG D. Big Earth data from space: a new engine for Earth science [J]. *Sci. Bull.*, 2016, **61**(7):505-513

[13] GUO H D. Scientific big data: a footstone of national strategy for big data [J]. *Bull. Chin. Acad. Sci.*, 2018, **33**(8):768-773

[14] GUO H D, GOODCHILD M F, ANNONI A. Manual of Digital Earth [M]. Singapore: Springer, 2020

[15] GUO H D. Steps to the digital silk road [J]. *Nature*, 2018, **554**(7690):25-27

[16] GUO H D. Big Earth Data in Support of the Sustainable Development Goals [M]. Beijing: Science Press and EDP Sciences, 2019

[17] YANG S Q. Development and prospect of disaster remote sensing monitoring system [J]. *City Disaster Reduction*, 2018, **6**:12-19

[18] SHEN Xuhui, ZHANG Xueming, CUI Jing, *et al.* Remote sensing application in earthquake science research and geophysical fields exploration satellite mission in China [J]. *J. Remote Sens.*, 2018, **22**(S1):5-20

[19] LI Qiang. Study on Key Technology of Earthquake Emergency using Multi-Mode Remote Sensing Data [D]. Harbin: Institute of Engineering Mechanics, China Earthquake Administration, 2018

[20] WANG Zhiyi, XU Suning, WANG Na, *et al.* Application of the high resolution optical and SAR remote sensing data images induced by the Jiuzhaigou M7.0 earthquake geological hazards survey [J]. *Chin. J. Geolog. Hazard Control*, 2018, **29**(5):81-88

[21] DONG Xiujun, XU Qiang, SHE Jinxing, *et al.* Preliminary study on the interpretation of geological hazards in jiuzhaigou based on multi-source remote sensing data [J]. *Geomat. Inf. Sci.Wuhan Univ.*, 2020, **45**(3):432-441

[22] DING Jia. Chinese Academy of Sciences launches remote sensing dynamic monitoring for the tenth anniversary of the Wenchuan earthquake[OL] [2018-04-17]. Beijing: China Science Daily, 2018. http://www.cas.cn/cm/201804/t20180417_4642260.shtml

[23] LIU Ming, JIA Dan. Application of satellite remote sensing technology in forest fire fighting [J]. *City Disaster Reduction,* 2018, **6**:66-70

[24] YANG D, LIU Y, CAI Z, *et* al. First global carbon dioxide maps produced from TanSat measurements [J]. *Adv. Atmos. Sci.*, 2018, **35**(6):621-623

[25] LI X, XIAO J. A global, 0.05-degree product of solar-induced chlorophyll fluorescence derived from OCO-2, MODIS, and reanalysis data [J]. *Remote Sens.*, 2019, **11**(5):517

[26] LONG T, ZHANG Z, HE G, *et al.* 30 m resolution global annual burned area mapping based on landsat images and Google Earth engine [J]. *Remote Sens.*, 2019, **11**(5). arXiv:1805.02579

[27] ZHANG Shuang, WU Jian, WEN xuanfan, *et al.* Review of aerosol optical depth retrieval using visibility data [J]. *Earth Sci. Rev.*, 2020, **200**:102986

[28] XU Y, LIU J, XIE L, *et al.* China-France Oceanography Satellite (CFOSAT) simultaneously observes the typhoon-induced wind and wave fields [J]. *Acta Ocean. Sin.*, 2019, **38**(11):158-161

[29] LIU Q H, WU J J, LI L, *et al.* Ecological environment monitoring for sustainable development goals in the Belt and Road region [J]. *J. Remote Sens.*, 2018, **22**(4):686-708

[30] WU Wenjin, SUN Xiaohui, EPSTEIN H, *et al.* Spatial heterogeneity of climate variation and vegetation response for Arctic and high-elevation regions from 2001–2018 [J]. *Environ. Res. Commun.*, 2020, **2** (1). DOI: 10.1088/2515-7620/ab6369

[31] LIANG D, GUO H D, ZHANG L, *et al.* Analyzing Antarctic ice sheet snowmelt with dynamic Big Earth Data [J]. *Int. J. Digit. Earth*, 2020. DOI: 10.1080/17538947.2020.1798522

[32] GUO H D. A project on Big Earth data science engineering [J]. *Bull. Chin. Acad. Sci.*, 2018, **33**(8):818-824

[33] GUO H D, NATIVI Stefano, LIANG D, *et al.* Big Earth data science: an information framework for a sustainable planet [J]. *Int. J. Digit. Earth*, 2020, 13:7, 743-767

HU Wenrei, KANG Qi. Advanced Research in Microgravity Science. *Chin. J. Space Sci.*, 2020, 40(5): 368-371. DOI:10.11728/cjss 2020.05.368

Advanced Research in Microgravity Science

HU Wenrei KANG Qi

(*Institute of Mechanics, Chinese Academy of Sciences, Beijing* 100190)

(*University of Chinese Academy of Sciences, Beijing* 100490)

Abstract Microgravity science is an important branch of space science. Its advanced subjects, to some extent, reflect the ability of human beings to understand nature and the research level in this field in various countries. Under the extreme condition of microgravity, there exist potential possibilities to discover new phenomena and laws in physical and chemical processes and material fabrication, and to test and verify some fundamental laws of physics with higher precision. In this paper, the most important research progresses in microgravity science in recent years are summarized.

Key words Microgravity science, Space science, Microgravity fluid physics, Microgravity combustion science, Space materials science, Space fundamental physics, Space station, Recoverable satellite

Classified index V 524

Manned Space Flight is the advanced field of space activities of human beings, and it represents the comprehensive national strength. The space station in the near-earth orbit, the lunar space station, and the mars space station are all operated under microgravity, which needs support by microgravity science and technology; on the other hand, space exploration provides conditions for developing research and application on microgravity science. Microgravity is an extreme condition in physics. In this environment, there are potential possibilities to discover new phenomena and new laws in physical and chemical processes as well as material fabrication and biological processes, and to test and verify some fundamental laws of physics with higher precision. Studies on microgravity science and technology not only have scientific significance for people to understand nature, but also have great application values in activities of space exploration.

Fluid motion, combustion, and material fabrication process, etc. are all directly related to the fluid medium. The microgravity environment provides an approximately isotropic physical condition for fluids. Buoyancy convection, gravity settlement and stratification, and static pressure gradient of liquid decrease significantly in this environment, and some minor effects (such as interface action) which are neglected due to gravity effect on the ground will be highlighted, affecting or changing mechanisms of fluid convection and combustion and influencing material fabrication and biological processes.

Since 2011, Nayangam *et al.* have published results of a series of experiments on droplet burning carried out on the international space station (FLEX)[1]. They observed that burning reactions of the droplet continued under low temperature (600~800℃) after the 'hot flames' extinguished, that is, the 'cool flames' burning. It could be seen that the vaporization of the droplet was supported by chemical reactions under low temperature (*i.e.*, cool flames) after the flame died out. This kind of 'cool flames' was unknown in the past, and traditional theories of droplet burning could not explain this new phenomenon discovered in the combustion experiments under microgravity conditions. In fact, a similar phenomenon of the second order combustion was also found in the experiments on octane and decane later on, which means that the happening and existence of cool flames burning do

Received June 12, 2020

E-mail: wrhu@imech.ac.cn, kq@imech.ac.cn

not depend on the type of liquid fuel. The quasi-steady cool flames caused by visible flames found in the diffusion system in the FLEX experiments of NASA was a brand new discovery, and it would not only improve the refinement of combustion theories but also inspire the development of fire safety of space crafts. The discovery of "cool flames" was selected by NASA as one of the top ten achievements on the International Space Station.

Since 2012, the space science innovation project of Chinese Academy of Sciences has been carrying out the mission of SJ-10 recoverable scientific satellite that was dedicated to studies on microgravity science and life science, including 28 projects of scientific researches[2]. The satellite was launched on 6 April 2016. Space experiments that lasted for 20 days have been accomplished successfully, abundant scientific results have been obtained, and nearly 200 SCI papers have been published. In November 2019, the Springer Nature Press together with the Science Press of China published the monograph of research achievements "Physical Science under Microgravity: Experiments on Board the SJ-10 Recoverable Satellite"[3]. Some typical researches are as follows.

(1) In the experiments on gas-liquid separation of granular fluids, the phenomenon of segregated aggregation--Maxwell demon of granular gases under microgravity was firstly observed; phase diagrams of bulk and clusters of granular gases were obtained from microgravity experiments; the granular gas-liquid separation theory was verified; the diffusion equation and theoretical model of nucleation based on the first principles were established[4].

(2) The space experiments on the annular liquid pool with a large curvature surface were carried out for the first time internationally; innovative approaches were attempted based on original studies on the volume effect of a liquid bridge; space experimental results verified the forming mechanism of volume effect and extended the general applicability of volume effect theories[5,6].

(3) Scientific breakthrough has been achieved on some key scientific issues in the forming processes of particle assembly and dry pattern; the management and control of a complex system of colloid in space have been technically realized; the key dynamic process that dominates the pattern of gas-liquid interface has been further clarified[7,8].

(4) Complete diagrams of flame propagation modes in low-speed flows were revealed for the first time; flame propagation and extinction laws of hot-thick materials in low-speed flows (under microgravity) were obtained; the dynamic response characteristics of flame to air flow as well as mechanisms of flame stability and extinction were understood; this is significantly meaningful and valuable in developing theories and models of solid material burning and improving the evaluation method of flammability of spacecraft material[9].

(5) The high-quality ternary crystal InxGa1-xSb has been successfully obtained in space crystal growth with a high concentration of the content ln (x= 0.11) for more than 60 h; the crystal growth process and solute transport phenomenon have been studied in depth. The ternary photoelectric crystal InxGa1-xSb is one of the best semiconductor materials for high-efficiency thermophotovoltaic cells, however, crystals grown on the ground can only contain 3% indium[10].

For more than a decade, the International Space Station (ISS) has always been the main platform for microgravity study internationally. The manned space mission of China also arranged researches on microgravity science. In the Tiangong-2 space laboratory and the rendezvous and docking cargo spacecraft Tianzhou-1 launched in 2016 and 2017, studies on microgravity fluid science (scientific experiments on liquid bridges, technical verification experiments on two-phase systems), microgravity materials science (multifunctional crystal growing furnace), and key technologies of fundamental physics in space (electrostatic suspension accelerometer) have also been carried out. And on the future space station, it has been arranged with some special experimental platforms such as the experiment racks for studies on microgravity fluid science, combustion, space materials, and fundamental physics, respectively, and some general experimental platforms such as the experi-

ment rack with variable gravity, experiment rack with advanced microgravity, and experiment rack of a glove box, *etc.* Among those, the racks that are related to microgravity experiments are more than ten in total[11]. In addition, various microgravity platforms such as new-type recoverable satellites have been gradually built, which provides a good environment for studies and applications on microgravity science in our country.

The constraints on macro-objects and microparticles caused by gravity are changed in the microgravity environment. Knowledge on the laws of theories of relativity and gravitation, cold atom physics, low temperature condensed matter physics, and so on, which have been explored in fundamental physics, has become the focus of study on space fundamental physics. Under microgravity in space, the effect of the gravitational background, degree of atomic thermal motion, etc. are reduced significantly, the scale of free fall is amplified, and the action of the non-conservative force is greatly weakened, so it is possible to test and verify the theory of relativity and the equivalence principle of gravitational physics with higher precision, and to reach the extreme low temperature for the studies on cold atom physics (cold atom clock) and (low temperature) condensed matter physics.

In recent years, some programs such as the Cold Atom Laboratory (CAL) and Primary Atomic Reference Clock in Space (PARCS) by NASA, and Atomic Clock Ensemble in Space (ACES) by Europe are all in progress; the Space Optical Clocks (SOC) project co-funded by ESA and Deutsches Zentrum für Luft- und Raumfahrt e.V. (DLR) has been in operation on the ISS; the MICROSCOPE satellite launched by Centre National d'Études Spatiales (CNES) together with ESA is running in space, planning to test the equivalence principle in the accuracy of 10^{-15}.

Since 2008, Shanghai Institute of Optics and Fine Mechanics has started to develop a ground principle prototype for the laser-cooled atom clock in space, the Rubidium fountain clock. The space experiments on the cold atom clock carried out on Tiangong-2 in 2019 were based on this clock directly. It was the first time in the world to carry out experiments on the cold atom clock in space. The key results are listed[13]: (i) the atomic temperature was about 3.3 μK, and the laser-cooled efficiency under microgravity was about 3 times higher than that on the ground; (ii) the changing rule of the linewidth of Ramsey fringes with ejection velocity under microgravity was obtained; the daily stability of the cold atom clock was calculated to be 7.2×10^{-16} based on in-orbit data, and it was at the top level in the world. This was a milestone event. The success of this project built a technical foundation for the importantly required ultrahigh-precision time and frequency standard in space, and provided enlightenment for the study on space fundamental physics in the future. The research tasks including the optical clock have also been planned on the ultrahigh-precision time and frequency system on the future space station of China.

The detection of gravitational waves is a cutting edge research field in space astronomy and also an important subject in studies on the theory of gravitation in space fundamental physics. On 11 February 2016, the Laser Interferometer Gravitational-wave Observatory (LIGO) Scientific Collaboration (LSC) of USA announced that signals of high-frequency gravitational waves were detected for the first time[14]. Medium- and low-frequency gravitational waves corresponding to large-scale mass fluctuations can only be detected in space. ESA and NASA collaborate on the Laser Interferometer Space Antenna (LISA) mission which has been in operation for the detection of gravitational waves in space, and a probe satellite is expected to launch around 2030[15-17]. China is also in an effort to carry out relevant researches[18,19]. That low-frequency gravitational waves in space directly detected phenomena such as supermassive black hole mergers and original gravitational waves will help to make a breakthrough in astronomy of gravitational waves in space.

Microgravity science has great importance in fundamental studies, affects directly mans' understanding of physical laws of nature, and has great

application values in the development of space exploration and new ground-based technologies. China has long-term plans for the study of microgravity science, and various microgravity space experiment platforms are under construction, with a good prospect of development. However, support and funding to the earlier stage of fundamental studies are extremely limited, and the capacity for sustainable development needs to be raised. We would like to see balanced distribution and coordinated development in different disciplinal systems in our country. We hope a large number of young scientists would like to devote themselves to aggressive innovations, dedicate to the long-term development of microgravity science, and make important and landmark contributions for man's exploration of nature and understanding of the universe.

References

[1] NAYANGAM V, UIETRICH D L, FERKUL P V, *et al.* Can cool flames support quasi-steady alkane droplet burning [J]. *Combust. Flame*, 2012, **159**(12):3583-3588

[2] KANG Qi, HU Wenrui. Microgravity scientific experimental satellite -- SJ-10 [J]. *Bull. Chin. Acad. Sci.*, 2016, **31**(5):574-580

[3] HU Wenrui, KANG Qi. Physical Science under Microgravity: Experiments on Board the SJ-10 Recoverable Satellite [M]. Singapore: Springer Nature, 2019

[4] WANG Wenguang, HOU Meiying, CHEN Ke, *et al.* Experimental and numerical study on energy dissipation in freely cooling granular gases under microgravity[J]. *Chin. Phys.: B*, 2018, **27**(8):084501

[5] KANG Q, WANG J, DUAN L, *et al.* The volume ratio effect on flow patterns and transition processes of thermocapillary convection [J]. *J Fluid Mech.*, 2019, **868**:560-583

[6] KANG Qi, WU Di, DUAN Li, *et al.* Surface configurations and wave patterns of thermocapillary convection onboard the SJ-10 satellite [J]. *Phys. Fluids*, 2019, **31**(4):20

[7] LI Weibin, JI Wenjie, LAN Ding, *et al.* Self-assembly of ordered microparticle monolayers from drying a droplet on a liquid substrate [J]. *J. Phys. Chem. Lett.,* 2019, **10**(20):6184-6188

[8] LI Weibin, JI Wenjie, SUN Honghui, *et al.* Patterns formation in drying sessile and pendant droplet: interactions of gravity settling, interface shrinkage and capillary flow [J]. *Langmuir,* 2019, **35**:113-119

[9] ZHU Feng, LU Zhanbin, WANG Shuangfeng, *et al.* Microgravity diffusion flame spread over a thick solid in step-changed low-velocity opposed flows [J]. *Combust. Flame*, 2019, **205**:55-67

[10] YU Jianding, INATOMI Y, KUMAR V N, *et al.* Homogeneous InGaSb crystal grown under microgravity using Chinese recovery satellite SJ-10 [J]. *NJP Microg.*, 2019, **5**:8-6

[11] National Natural Science Foundation of China/Chinese Academy of Sciences, National Science Think Tank: China's Discipline Development Strategy-- Space Science [M]. Beijing: Science Press, 2019

[12] TOUBOUL P, M´ETRIS G, RODRIGUES M, *et al.* MICROSCOPE mission: first results of a space test of the equivalence principle [J]. ***P**hys. Rev. Lett.* 2017, **119**:231101

[13] LIU Liang, LÜ Desheng, CHEN Weibiao. In-orbit operation of an atomic clock based on laser-cooled ^{87}Rb atoms [J]. *Nat. Commun.*, 2018, **9**(1):2760

[14] The LIGO Scientific Collaboration and the Virgo Collaboration. Observation of gravitational waves from a binary black hole [J]. *Phys. Rev. Lett.*, 2016, **116**:061102

[15] MCNAMARA P. LISA Pathfinder: First step to observing gravitational waves from space [J]. *J. Phys. Conf. Ser.*, 2017, **840**:012001

[16] DANZMANN K, PRINCE T A, BINETRUY P, *et al.* LISA-Unveiling a hidden Universe [R]. Paris: European Space Agency, 2011

[17] AMARO-SEOANE P, SOFIANE A, BABAK S, *et al.* Low-frequency gravitational-wave science with eLISA/NGO [J]. *Class. Quant. Gravity,* 2012, **29**(12):124016

[18] HU W R, WU Y L. The Taiji program in space for gravitational wave physics and the nature of gravity [J]. *Natl. Sci. Rev.,* 2017, **4**(5):685-686

[19] HU Wenrui. Discussion on detection plan of gravitational waves in space [J]. *Sci. Technol. Rev.*, 2018, **36**(12):1

DING Bai, LIU Zhaoxia, LÜ Ke, LING Shukuan, LIU Yue, XU Zi, LI Yinghui. Progress of Space Medicine Research in China. *Chin. J. Space Sci.*, 2020, **40**(5): 372-379. DOI:10.11728/cjss2020.05.372

Progress of Space Medicine Research in China

DING Bai LIU Zhaoxia LÜ Ke LING Shukuan

LIU Yue XU Zi LI Yinghui

(*Astronaut Center of China, Beijing* 100094)

Abstract With the approaching of the Chinese Space Station (CSS) era, the focus of space medicine applications and related research has shifted to addressing the astronauts' health support in long-duration spaceflights, including nutrition, countermeasure against the physiological effects of weightlessness, medical monitoring and support, psychology status, *etc.*, and accordingly the human experiments to simulate long-duration weightlessness have been carried out. Increasingly, basic research has been put forward in the key areas, such as space bone loss, cardiovascular dysfunction and the molecular mechanisms underlying radiobiological effects. Moreover, specific novel research fields, such as hypometabolism technology, were explored. The research projects in the field of space medicine experiment, as an important aspect of the Chinese Space Station's application, have been officially approved and launched.

Key words Space medicine, Chinese Space Station, Health risk

Classified index V 524

1 Introduction

On 19 July 2019, the Tiangong-2 space laboratory was de-orbited in a controlled demolition, a milestone marking the successful completion of all missions of the space laboratory mission phase of China's manned space project and officially ushering the era of the space station in China.

Aiming at the completion of China's space station, the construction of the national space laboratory and the long-term in-orbit stay of astronauts, a slew of health measures has been developed to ensure the health of astronauts and their safety during a long-term stay in orbit. A bunch of space medical experiments research projects have been systematically laid out, achieving a number of ground-based research results in space medicine and laying solid theoretical and technical foundations for the sustainable development of China's manned space project.

This report provides a brief introduction to the recent progress of space medicine research in China from 2018 to 2020.

2 Application and Research in Space Medicine for Long-term Spaceflights

2.1 Astronaut Health Support

The Chinese astronauts' stay in orbit will be gradually extended to 180 days during the upcoming routine flight missions, posing greater challenges to their health support as follows. The physiological effects of weightlessness will become more prominent, such as bone loss, muscular atrophy, decreased muscular strength and cardiovascular dysfunction. The systematic and comprehensive accommodation is increasingly required for the nutritional supply of space food during long-term spaceflight. Furthermore, the health risks become greater, such as clinical disorders/illness, accidental injury and psychological

Received September 8, 2020

E-mail: yinghuidd@vip.sina.com

problems. Focusing on the goal of ensuring astronauts' health and their efficient work in orbit, the Astronaut Center of China established the astronauts' health support technology system for long-term spaceflight, including four aspects: the countermeasure against physiological effects of weightlessness, nutritional supply, medical monitoring and support, and psychological support.

2.1.1 Countermeasure Against Physiological Effects of Weightlessness

To tackle the adverse physiological effects of long-term weightlessness on human body and consequently effectively protect against the decline in aerobic exercise capacity, muscular atrophy and bone loss, a number of experimental studies on human body have been carried out. These studies include the vertical treadmill exercise and long-term Head-down Bed Rest (HDBR) weightlessness simulation experiments. Other in-orbit countermeasure technologies have been developed, *e.g.* space bicycle, space treadmill, resistance exercise device, gradient compression garments, respiratory muscle exercisers, *etc.* In addition, targeted exercise prescriptions/recommendations have been developed and, based on different flight duration, different episodes and in-orbit tasks, a comprehensive countermeasure protocol has been accomplished, which integrates exercise, physics and medicine, and also combines duration-specificity, mission-orientation and individualization. The protocol has been verified by ground-based experiments and is expected to effectively play important roles in the aerobic exercise capacity, muscle dimension and strength, bone density, and orthostatic tolerance.

2.1.2 Nutritional Supply

Research has been conducted to form the nutrition supply standards for long-term in-orbit flights, and to establish a dietary structure framework and flight menu. Safe and reliable, comprehensively nutritional and sensory acceptable space food products have been developed. To tackle the potential problems during the long-term flight, such as decreased immune function, fatigue, oxidative damage and intestinal dysbacteriosis, special functional food products have been developed to ensure that astronauts are in good nutritional condition and to reduce their body mass loss, consequently to maintain astronauts' normal physical work capability. Additionally, multiple protocols are coordinated to maintain the homeostasis of the astronauts.

To address the risk of a possible decline in food sensory acceptability, which is prominent in long-term missions, the food diversity has been further enriched in staple and subsidiary-foods, fast foods, beverages and condiments. The menu cycle has been extended to no less than 7 days, achieving both the reasonable combination of long-term and short-term expiration period and cold and hot foods, and the consideration for the individualized requirements.

2.1.3 Medical Monitoring and Support

Integrated medical monitoring and support technology has been established, which contains diagnosis, prevention, treatment and recovery, for the astronauts during long-term spaceflight.

In health condition assessment and disorder diagnosis, the spectrum of spaceflight disorders has been established, and an integrated diagnosis system of traditional and western medicine has been constructed. It combines physiological functions, biochemical indicators, medical imaging and the "Four Diagnostic methods" of Traditional Chinese Medicine. Integrated mode of both regular and individualized durations for medical monitoring and support has been established, which makes it precisely to assess the major physiological functions and the health status of "core" tissues and organs in human body.

In terms of disorder prevention and treatment, based on the core concept of "preventive treatment of disease" from Traditional Chinese Medicine, electrical stimulation and regulation technology in neuromuscular tissues has been developed to solve the problems that commonly happen during long-term spaceflights, such as muscle tension, back pain, sleep disturbances, *etc.* In addition, the research and development of the Chinese patent medicines for bone-strengthening and anti-atrophy are supportive in enhancing the countermeasure against muscular atrophy and bone loss. Integration of the methods from both physical interference and Chinese-western

medicines could regulate and maintain astronauts' health in multi-dimensional ways.

In order to ensure sound body recovery after long-term spaceflight, integrated recovery measures, including exercise, physiotherapy, medication and traditional medicine, have been formulated. Accordingly, the comprehensive recovery protocol has been formed, which adopts the principle of "dynamic assessment, gradual progress, continuous rehabilitation and individualization".

2.1.4 Psychological Support

With regard to the mental health risks during long-term spaceflights in space station missions, the astronauts' mental health support program has been developed, *via* the utilization of the 4-person 180-day Controlled Ecological Life Support System (CELSS) experiment, astronauts' in field training, science experiment during Antarctic expedition and long-term integrated manned simulation and verification experiment. The psychological evaluation protocols and technical standards suitable for long-term spaceflight have been set up, and a combination of both social and professional psychological support has been established. Effective measures for self-adjustment and self-relaxation has been developed. All these measures are expected to reduce and control the negative psychological factors during long-term flights and consequently maintain the well psychological state of astronauts.

2.2 Space Experiments in Space Medicine and Biology

Venturing into the "deep blue" to expand the space for human survival is the goal of human space exploration. To tackle the major medical problems and the human factor-related engineering problems that restrict long-term space flight, and to provide theoretical and technical support for the enhancement of astronauts' ability to remain healthy in orbit, the space medicine experiment research focuses on the "human-system-risks" during long-term spaceflight, and the space medicine experiments during the construction and operation phases of the Chinese Space Station have been evaluated and planned. In addition, aiming at the future manned lunar exploration, considerations have also been taken into the future research program.

The Phase I research platform for space medical experiments has been constructed which has developed human systems research cabinets and medical sample analysis payloads and boasts in-orbit human research capabilities, *e.g.* brain function research, vascular function research, muscle structure function research, medical sample preparation and observation, metabolomics research, biomechanics testing of human movement, basic cognitive testing, biological rhythm testing, and visual function testing, *etc.*

The project guidance of space medicine experiments has been drafted and announced. The first batch of research projects have been selected and 81 research institutes involved in the projects will conduct research in five directions, including the impact of long-term weightlessness on astronauts' health and related countermeasure technology, the impact of space radiation on astronauts' health and related countermeasure technology, astronauts' behavior and ability, advanced in-orbit monitoring and medical treatment technology, and space application technology of traditional medicine. These research will systematically analyze the dynamic evolution of the effect of weightlessness on human body, explore the mechanism of multi-system mutual adjustment network, and develop new protection technology and methods; it will also study the main hazards of space radiation on human body and establish space radiation assessment model; it will study the changes of the human's basic ability during long-term weightlessness, human adaptiveness in the space station, the influence of space environment on biological rhythm and the effective entrainment technology, and human-computer interaction; it will aim at the R&D of advanced in-orbit monitoring and medical treatment technologies, such as microchip laboratory and wearable biosensors. In addition, the research projects will develop diagnostic technologies featuring Traditional Chinese Medicine (TCM), and health support and adjustment technologies based on the TCM and traditional medical therapies.

In the Tianzhou-1 cargo spacecraft mission, an application project, Professor Shang Peng in Northwestern Polytechnical University and Professor Chen

Guoqiang of Tsinghua University conducted a 7–21 day space flight study of bone tissue cells using an in-orbit system of automated cell cultivation and real-time microscopic recording, which revealed that morphological changes in murine osteocyte -MLO-Y4 and the reduced cell mineralization capacity are caused by space microgravity, and 3-Hydroxybutyric (3-HB) plays an antagonistic effect against microgravity-induced slowing of osteoblast MC3T3-E1 proliferation. The research also found that in microgravity environment Casein Kinase 2 Interacting Protein 1 (CKIP-1) is involved in regulating osteoblast differentiation process.

2.3 Basic Research in Space Medicine

The basic theory with regard to the effects of weightlessness has been enriched by the research advances in cellular and molecular mechanisms underlying bone loss in space, degradation of cardiovascular function, muscular atrophy, neurocognition, and the frontier explorations in the fields of space pathogenic microbes, and radiation biology effects. Furthermore, hypometabolism regulation techniques have provided new perspectives and new approaches to long-term in-orbit health support.

2.3.1 Bone Loss and Muscular Atrophy in Space

Bone dynamic homeostasis under force stimulation involves a very complex regulatory network. Using tail-suspended transgenic rats, Shang Peng *et al.* showed that blocking glucocortical signaling pathways in osteoblasts and osteocytes can prevent cortical bone loss due to weightlessness, suggesting an important role of stress response and elevated glucocorticoid levels in the process of bone loss induced by space flight[1]. Li Yingxian *et al.* found that the endoplasmic reticulum protein TMCO1-mediated Ca^{2+} leak provides local Ca^{2+} signals to activate the CaMKII-HDAC4-RUNX2 signaling axis. The establishment of TMCO1 as a pivotal player in osteogenesis uncovers a novel potential therapeutic target for ameliorating osteoporosis and bone loss[2]. Sun Weijia *et al.* revealed that the mechanosensitive channel-Piezo1 functions as a key mechanotransducer for conferring mechanosensitivity to osteoblasts and determining mechanical load-dependent bone formation, and represents a novel therapeutic target for treating osteoporosis or mechanical unloading-induced severe bone loss[3]. Sun Lianwen *et al.* showed that the simulated weightlessness may inhibit and restrain early osteogenic differentiation of bone marrow-derived mesenchymal stem cells through negative regulating Transcriptional co-Activator (TAZ)[4]. Qian Airong *et al.* found that the cytoskeletal key regulator-microtubule Microfilament Crosslinking Factor (MACF1), affects osteoblast differentiation through the β-catenin signaling pathway[5]. Chen Xiaoping *et al.* found that Hemojuvelin is a novel suppressor for Duchenne muscular dystrophy and age-related muscle wasting[6]. Wang Linjie *et al.* found that 2~4 weeks' high-intensity intermittent exercise can rapidly increase oxygen uptake and maintain lower limb muscle strength, and that continuous endurance exercise can steadily increase aerobic endurance and improve bone density through 8-week-1 *g* -weight-loss endurance exercise[7].

2.3.2 Cardiovascular Function in Space

Cardiac remodeling is closely related to hemodynamic loading. Li Yingxian *et al.* demonstrated that CKIP-1 protein exerts an inhibitory effect on pressure overload-induced cardiac remodeling by regulating the dephosphorylation process of HDAC4. Moreover, myocardial CKIP-1 overexpression inhibited cardiac remodeling and functional decline induced by simulated weightlessness[8]. Peng Tianqing *et al.* suggested that blocking angiotensin II receptor can inhibit myocardial atrophy and cardiac dysfunction induced by Hindlimb Unloading, which may be related to Reactive Oxygen Species (ROS) production, Calpain activation and ERK1/2 inhibition[9]. Sun Xiqing *et al.* elucidated that under the effect of simulated weightlessness, autophagy of human umbilical vein endothelial cells is enhanced, and that phagocytosis of ubiquitinated proteins further inhibits unfolded protein responses so as to inhibit apoptosis. Furthermore, the differential analysis of microRNA expression suggests that, under simulated weightlessness, miR-27b-5p may affect apoptosis of vascular endothelial cells by regulating ZHX1[10].

2.3.3 Neuro-immuno-endocrine Functions and Sleep Medicine

Qu Lina *et al.* investigated the mechanism of neu-

rocognitive decline due to simulated weightlessness which found that the MGF-NRF2-HO-1 signaling pathway and the hypoxia-inducible factor HIF-1a correlated with the regulation of learning and memory function, revealing the important regulatory role of oxygen stress triggered by oxygen metabolic imbalance in spatial cognitive dysfunction[11, 12]. Adopting combined analysis of cycle RNA sequencing and serum metabolomics, Dai Zhongquan and Zhang Hongyu found that simulated microgravity enhances circulating miR-383-5p expression which is involved in the process of weightlessness headward distribution of body fluids on learning and memory through the brain tissue water channel protein APQ4[13]. By analyzing changes in the proportions and functions of HSC differentiated immune cells, hematopoietic cells, and HSC in a simulated weightlessness mouse model, the research shows that weightlessness can alter the proportions of B cells, T cells, and NK cells and that weightlessness leads to an increase in the number of HSC while a decrease in HSC function, and these changes can be restored after the removal of weightlessness[14]. The Cooperative research by Wang Liping and Li Yinghui found that the neural circuit of the Nucleus Stria Terminalis (BNST)-Ventromedial Hypothalamus (VMH)-Nucleus Tractus Solitarius (NTS) regulates the bone loss induced by chronic pressure stress by regulating the activity of the peripheral sympathetic nervous system process[15]. Wu Bin *et al.* reviewed the on-orbit sleep problems, which is crucial to health and performance and is commonly caused by the space risk factors (*e.g.* microgravity, isolation, insufficient light exposure, *etc.*), could be interfered with or regulated by seven kinds of potentially efficacious countermeasures, including pharmacologic interventions, light treatment, crew selection and training, and so on[16]. Wu Xiaorui *et al.* testified the negative effects of 72 h Isolation and Confinement (IC) and sleep deprivation on the attention of network functions and operational performance via fMRI and manual controlled rendezvous and docking simulation task, respectively[17].

2.3.4 Space Microbes

Changes in the characteristics of microorganisms in the space environment, including pathogenic changes, are important risk factors for long-term spaceflight activities. Onboard Shenzhou-8, Shenzhou-10, and Tiangong-2, a series studies on space microbes were conducted, and some of the results are as follows: the changes in the biological phenotype, genome and transcriptome of Klebsiella Pneumoniae Carbapenemase (KPC-2) after space flight mainly concentrate on the transport and metabolism of inorganic ions, amino acids and carbohydrates; the second space flight changed the biological traits such as growth rate and biofilm-forming ability of Immobilis shenensis; the cell wall of *Staphylococcus warneri* showed prominent changes such as increased physical resistance, increased sensitivity to antibiotics and biofilm thickening after the space flight; the biofilm-forming ability of Immobilis baumanensis was enhanced after 64 days of flight. Systematic ground-based studies were performed by Li Yongzhi *et al.* about the effects of simulated weightlessness on Fungi, Staphylocollcu aureus, E. col, Candida albicans and so on[18]. Wang Jiaping *et al.* revealed the accumulation of cysteine and methionine in *Candida albicans* after 12-day spaceflight on the SJ-10 satellite and provides an important basis for the assessment of the risk that the opportunistic pathogenic yeast could cause[19].

2.3.5 Radiobiological Effects

Space radiation may induce tumors, cause neurological damage and cognitive ability decline, degenerative lesions, and immunosuppression *etc.* Zhou Guangming and his team establish a quantitative relationship for radiation-induced carcinogenesis and obtained lung cancer cell models at different developmental stages by irradiating human lung epithelial cells with long-term low-dose-rate alpha particles. The afore-mentioned research found that the risk of low-dose-rate radiation-induced carcinogenesis was positively correlated with radiation dose without any dose threshold, and there is no difference in tumor formation between long-term low-dose rate irradiation and equal-dose single irradiation, but long-term irradiation leads to increased malignancy of tumors; there is a synergistic effect between microgravity and radiation to reinforce radiation-induced epithelial mesenchymal transformation. The study suggests

that non-coding RNAs play an important regulatory role in the space radiation effect, and that high LET ions can specifically induce the expression of the long-non-coding RNA-LNC-CRYBG3, which directly binds G-actin to inhibit microfilament skeleton assembly and constrict loop formation, leading to M-phase cell block[20]; LNC-CRYBG3 can also bind the LDHA, which alters cellular metabolism and promotes glycolysis[21]. The research also reveals that the low dose rate and high LET radiation environment in space makes the paracrine effect more prominent[22]. It is noteworthy that resting cells are more radiation resistant than dividing cells, and data from studies on cells that are at the phase of exponentially growing tend to overestimate the risk of space radiation. The expression level of the NADPH oxidase subunit RAC2 is significantly lower in resting cells than in dividing cells, resulting in lower radiation-induced endogenous Reactive Oxygen Species (ROS) than in dividing cells; In addition, radiation-generated ROS tends to lead to Dephosphorylation of P38 MAPK, which can mutually regulate with RAC2 through feedback and negative feedback, resulting in increased radiation resistance of G0 cells[23].

2.3.6 Hypometabolic Technology

Technologies and methods for long-term manned spaceflight health support remain to be the frontier of space exploration and Li Yinghui and her team have conducted research to explore hypometabolism regulation technology. In 2018, a 12-person 24-day human hypometabolism regulation technology experiment was performed and successfully completed, which was designed to analyze the tendency of psychological and cognitive changes in hypometabolism conditions and their correlation with energy metabolism substrates. A hibernation model of chipmunk was established and researchers completed the samples collection at consecutive time points of chipmunk hibernation and the analysis of the transcriptome data of brain tissue, as well as sorted out the possible molecular mechanisms underlying the rhythmic changes in the formation of hibernation bouts. Researchers also investigated the hypometabolic state induction techniques on non-hibernating rats, such as fasting, hypothermia, and drugs, and successfully induced golden gophers and rats into a hypometabolic state in spring and summer, respectively.

3 Large-scale Experiments and Major Projects

3.1 Long-term Head-down Bed Rest Weightlessness Simulation Experiment

The 90-day long-term Head-down Bed Rest experiment (HDBR) is China's first large-scale long-term mission simulation experiment to study the effects of weightlessness and the countermeasures on human body. In 2019, the experiment was led by Li Yinghui, Wang Linjie, Qu Lina *et al.* from Astronaut Center of China with more than 20 domestic scientific research institutes involved. 36 male volunteers were recruited to participate in the experiment, who were divided into the bed rest control group, the comprehensive countermeasure-I group, the comprehensive countermeasure-II group, space treadmill exercise group and the resistance exercise group.

During the 90-day head-down bed rest experiment, temporal change data of 9830 times were obtained regarding the participants' basic physiology. It includes the indicators from cardiovascular system, musculoskeletal system, psychological assessment, nutritional status and other systems. It is the first time in China that the experiment accumulated the objective data on the physiological and psychological changes and adaptive characteristics of the human body under long-term simulation conditions of weightlessness. It improves the understanding of the main physiological characteristics of the human body changes in long-term simulated weightlessness. The experiment promotes China's capability of mastering the countermeasure efficacy of the single resistance exercise and space treadmill exercise, which verifies the rationality and effectiveness of the two comprehensive countermeasure protocols against weightlessness, the weightlessness countermeasure evaluation index system and evaluation protocol, and the post-flight recovery protocol that is mainly based on exercise therapy, therefore, providing important data support for countermeasure against physiological effects

of weightlessness in long-term spaceflight missions and other astronauts' health counter-measure technology development.

3.2 Long-term Confinement and Isolation Environment Experiment ("Space-180" Experiment)

The 4-person 180-day controlled ecological life support system ("Space-180" experiment) based medical research projects continue to yield scientific findings and publications. Analysis of blood cell DNA methylation, metabolic and biochemical group data revealed the correlation between human DNA methylation and biochemical and psych-physiological phenotypes, including perturbations in glucose metabolism and emotional states. Feng Qiang *et al.* showed that in the simulated space environment, human microecology is affected by circadian rhythm and other factors under the overall stable state, the correlation analysis between microecology and plasma metabonomics shows that the ratio of Phosphatidylcholine (PC): Phosphatidylamide (PE) plays an important role in the regulation of intestinal inflammation[24]. Dong Haisheng *et al.* showed that the unique isolation process could lead to a loss of alpha diversity and a transition of enterotypes between Bacteroides and Prevotella[25]. The study from Yuan Ming and the colleagues in ACC and CNES suggests the need for countermeasures to prevent increased carotid Intima-Media Thickness (IMT) and endothelial deconditioning[26]. Chen Hailong *et al.* found that serum protein levels were changed, *e.g.* total protein, globulin and bilirubin exhibited chronic acclimatization[27]. Psychological study by Wu Ruilin *et al.* and the colleagues in ACC identified that leadership had a positive effect on the group climate by clarifying tasks and reducing aggression and the various functions of perceived leadership roles could be explained by crew composition and occupational features[28, 29].

3.3 National Instrumentation Program of China

The real-time, dynamic, comprehensive and in-orbit analysis of space medical body fluid sample is of crucial importance to the in-flight monitoring and assessment of health risks and the acquirement of new knowledge in space medicine. The project "development and application of space medical body fluid research equipment" in the framework of the national instrumentation program of China was successfully completed by Li Yinghui and her colleagues. The project integrated microfluidics, MEMS, nano technology and other advanced technologies to overcome a series of key technologies for space-based application, and a body fluid sample pre-processing and multi-indicator real-time testing equipment has been developed to further accommodate the space environment application. The equipment integrates six independent functional modules, including sample pre-processing module, protein detection module, semi-antigen detection module, virus nucleic acid detection module, nucleic acid epigenetic information detection module and blood cell characterization analysis module. It can automatically, in a fully enclosed way, achieving the multi-target cell typing tests of the protein, small molecule semi-antigen, virus nucleic acid, microRNA, DNA methylation and so on, in blood, urine, saliva and other body fluid samples, which will provide core equipment support for the Chinese Space Station.

4 Conclusion

The Chinese Space Station provides a broader platform for space medicine research and its discipline development. The implementation of research projects in the field of space medical experiments and the increasing advancement of ground-based basic research will continue to improve the understanding of the impact of the space environment on human health. Noteworthily, the progress of relevant theories and related technologies will not only pave the way for mankind to march into deep space, but also facilitate the development of medicine to serve the public health, make contributions to the economy and society, and be beneficial to the future.

References

[1] YANG J, LI J, CUI X, *et al.* Blocking glucocorticoid signaling in osteoblasts and osteocytes prevents mechanical unloading-induced cortical bone loss [J]. *Bone*, 2020, **130**:115108

[2] LI J, LIU C, LI Y, *et al.* TMCO1-mediated Ca(2$^+$) leak

underlies osteoblast functions via CaMKII signaling [J]. *Nat. Commun.*, 2019, **10**(1):1589

[3] SUN W, CHI S, LI Y, *et al.* The mechanosensitive Piezo1 channel is required for bone formation [J]. *eLife*, 2019, **8**:e47454

[4] HUANG Y, SUN L, YANG X, *et al.* The effect of TAZ on osteogenic differentiation of bone marrow mesenchymal stem cells under simulated weightlessness on-line shearing [C]//Proceedings of the 22th symposium of Space Life Professional Committee of China Space Science Society and the 6th symposium of Space Medico-Engineering and Space Biology Committee of Chinese society of Astronautics. Suzhou: China Space Science Society and Chinese society of Astronautics, 2018

[5] HU L, YIN CH, WU Z, *et al.* Mechanically sensitive molecule MACF1 promotes osteoblast differentiation[C]//Proceedings of the 22th symposium of Space Life Professional Committee of China Space Science Society and the 6th symposium of Space Medico-Engineering and Space Biology Committee of Chinese society of Astronautics. Suzhou: China Space Science Society and Chinese society of Astronautics, 2018

[6] ZHANG P, HE J, WANG F, *et al.* Hemojuvelin is a novel suppressor for Duchenne muscular dystrophy and age-related muscle wasting [J]. *J. Cach. Sarcop. Muscle.,* 2019, **10**(3):557-73

[7] WANG L, LI Z, TAN C, *et al.* Physiological effects of weightlessness: countermeasure system development for a long-term Chinese manned spaceflight [J]. *Front. Med.*, 2019, **13**(2):202-12

[8] LING S, LI Y, ZHONG G, *et al.* Myocardial CKIP-1 Overexpression Protects from Simulated Microgravity-Induced Cardiac Remodeling [J]. *Front. Physiol.*, 2018, **9**:40

[9] YUAN W, LIANG L, QU L, *et al.* The effect of blocking angiotensin II receptor signal on preventing myocardial atrophy and cardiac dysfunction induced by weightlessness [C]//Proceedings of the 22th symposium of Space Life Professional Committee of China Space Science Society and the 6th symposium of Space Medico-Engineering and Space Biology Committee of Chinese society of Astronautics. Suzhou: China Space Science Society and Chinese society of Astronautics, 2018

[10] LI C H, PAN Y, WANG Y, *et al.* The relationship between autophagy and apoptosis of venous endothelial cells under simulated weightlessness [C]//Proceedings of the 22th symposium of Space Life Professional Committee of China Space Science Society and the 6th symposium of Space Medico-Engineering and Space Biology Committee of Chinese society of Astronautics. Suzhou: China Space Science Society and Chinese society of Astronautics, 2018

[11] WANG T, CHEN H, LV K, *et al.* Activation of HIF-1alpha and its downstream targets in rat hippocampus after long-term simulated microgravity exposure [J]. *Biochem. Biophys. Res. Commun.*, 2017, **485**(3):591-7

[12] WANG T, CHEN H, LV K, *et al.* iTRAQ-based proteomics analysis of hippocampus in spatial memory deficiency rats induced by simulated microgravity [J]. *J. Proteomics.* 2017, **160**:64-73

[13] ZHANG H, CHEN J, WANG H, *et al.* Serum metabolomics associating with circulating microrna profiles reveal the role of miR-383-5p in rat hippocampus under simulated microgravity [J]. *Frontiers Physiology.*, 2020, **11**:939

[14] CAO D, SONG J, LING S, *et al.* Hematopoietic stem cells and lineage cells undergo dynamic alterations under microgravity and recovery conditions [J]. *FASEB J.*, 2019, 33(6): 6904-18

[15] YANG F, LIU Y H, CHEN S P, *et al.* A GABAergic Neural Circuit in the Ventromedial Hypothalamus Mediates Chronic Stress induced bone loss [J]. *J. Clinical Invest.*, 2020 (in press)

[16] WU B, WANG Y, WU X, *et al.* On-orbit sleep problems of astronauts and countermeasures [J]. *Mil. Med. Res.*, 2018, **5**(1):17

[17] WU X, LIN G, XU D, *et al.* Effects of 72h isolation and confinement with sleep deprivation on astronaut's attention on network functions and operation performance of manual controlled simulated rendezvous and docking task [J]. *Chin. J. Aerospace Med.*, 2019, **30**(1):1

[18] ZHAO G,WANG J,GAO J, *et al.* Research progress of effects of wightlessness/simulated weightlessness on Fungi [J]. *Space Med. Med. Eng.*, 2018, **31**(5):571-576

[19] WANG J, LIU Y, ZHAO G, *et al.* Integrated proteomic and metabolomic analysis to study the effects of spaceflight on Candida albicans [J]. *BMC Genomics.,* 2020, **21**(1):57

[20] PEI H, HU W, GUO Z, *et al.* Long noncoding RNA CRYBG3 blocks cytokinesis by directly binding G-Actin [J]. *Cancer Res.*, 2018, **78**(16):4563-72

[21] CHEN H, PEI H, HU W, *et al.* Long non-coding RNA CRYBG3 regulates glycolysis of lung cancer cells by interacting with lactate dehydrogenase A [J]. *J. Cancer.,* 2018, **9**(14):2580-8

[22] HU W, PEI W, ZHU L, *et al.* Microarray profiling of TGF- β 1-Induced long non-coding RNA expression patterns in human lung bronchial epithelial BEAS-2B cells [J]. *Cell. Phys. Biochem.*, 2018, **50**(6):2071-85

[23] PEI H, ZHANG J, NIE J, *et al.* RAC2-P38 MAPK- dependent NADPH oxidase activity is associated with the resistance of quiescent cells to ionizing radiation [J]. *Cell Cycle.*, 2017, **16**(1):113-122

[24] FENG Q, LAN X, JI X, *et al.* Time series analysis of microbe and metabolome at multiple body sites in steady long-term isolation confinement [J]. *GUT,* 2020. DOI: 10.1136/gutjnl-2020-320666

[25] DONG HS, CHEN P, YU YB, *et al.* Simulated manned Mars exploration: effects of dietary and diurnal cycle variations on the gut microbiome of crew members in a controlled ecological life support system [J]. *Peer. J.*, 2019, **7**:7762

[26] YUAN M, CUSTAUD MA, XU Z, *et al.* Multi-system adaptation to confinement during the 180-day Controlled Ecological Life Support System (CELSS) experiment [J]. *Front Physiol.*, 2019, **10**:575

[27] CHEN H, LV K, JI G, YUAN Y, *et al.* Physiological acclimatization of the liver to 180-Day isolation and the mars solar day [J]. *Biomed. Re.s Int.,* 2020. DOI: 10.1155/2020/2796510

[28] WU R, MA Q, XIONG J, *et al.* Leadership roles and group climate in isolation: a case study of 4-subject 180-day mission [J]. *Acta Astron.*, 2020, 166:554-9

[29] MA Q, SANDAL GM, WU R, *et al.* Personal value diversity in confinement and isolation: pilot study results from the 180-day CELSS integration experiment [J]. *Acta Astron.*, 2019, **164**:84-91

MA Hong, CHEN Yu, REN Hao, LI Xiaoqiong, YANG Chunhua, LI Bo, HAN Chu, ZHANG Ying, LONG Mian, ZHUANG Fengyuan, DENG Yulin. Space Life Science of China. *Chin. J. Space Sci.*, 2020, **40**(5): 380-386. DOI:10.11728/cjss2020.05.380

Space Life Science of China*

MA Hong[1] CHEN Yu[1] REN Hao[1] LI Xiaoqiong[1]
YANG Chunhua[1] LI Bo[1,2] HAN Chu[1,2] ZHANG Ying[1] LI Yujuan[1]
LONG Mian[3] ZHUANG Fengyuan[1,4] DENG Yulin[1]

1 (*School of Life Science, Beijing Institute of Technology, Beijing* 100081)
2 (*Advanced Research Institute of Multidisciplinary Science, Beijing Institute of Technology, Beijing* 100081)
3 (*National Microgravity Laboratory, Institute of Mechanics, Chinese Academy of Sciences, Beijing* 100190)
4 (*School of Biological Science and Medical Engineering, Beihang University, Beijing* 100191)

Abstract In the past two years, China's space life science has made great progress. Space biomedical and life science programs have carried out ground-based research for the first batch of projects, and are preparing to carry out space-based experiments along with the construction of China's space station. And space life science payload of the space station completed the development of positive samples. Thus, with the development of lunar exploration and Mars exploration projects, astrobiology research has also made a lot of basic achievements. On the basis of summarizing the development of space life science in China, this paper mainly introduces the important progress of payload technology and life science research.

Key words Space life sciences, Space payload, Simulated microgravity, Ionizing radiation
Classified index V 419

Space life science is a discipline that studies the life phenomena and their laws under the action of special environmental factors of space (such as vacuum, high or low temperature, microgravity, and cosmic radiation, *etc.*). Broadly speaking, it includes space biology, space physiology, space medicine, and space bioengineering. It belongs to the edge discipline of space science and life science, and is also a newly formed branch of space science. If human beings want to live in the space for a long time and develop the space, we need to study and solve a series of space life problems induced by cosmic environmental factors on the life process. Here, we review and summarize the researches on space life sciences which were contributed by Chinese scientists in the last two years.

1 Payloads Technology in Space Life Science

1.1 Automatic Device for Cell Culture in Space Based on Microfluidic Chip

Mammalian cell culture is one of the commonest methods in life science research. In space, cell culture was commonly carried out in T-flask, coverslips, Teflon culture bag or other traditional tools. These tools are lowly integrated and disable to precisely control the environment around the cells. In recent decades, microfluidic chip was applied to research in space biology. Microfluidic chip offers promising solutions for mammalian cell culture and precise control of the extracellular microenvironment in vitro.

* Supported by Space Medical Experiment Project of China Manned Space Program (HYZHXM02003)
Received June 28, 2020
E-mail: deng@bit.edu.cn

Therefore, a device for mammalian cell culture in microfluidic chip was developed for space biology research[1]. The device consists of a cell culture unit based on microfluidic chip, microscope imaging system, injection pump, reagents control unit, waste storage unit, central control unit. Mammalian cells were cultured in a single-chamber microfluidic chip placed in a cell culture unit that can control the temperature of chip, commonly at 37℃. Injection pump was connected with the microfluidic chip to perfuse the fresh cell culture medium. Using valve and pump group in reagents control unit, the reagents can be injected into microfluidic chip, such as Phosphate Buffer Saline (PBS) buffer solution, trypsine solution, dye solution, *etc.* Thus, cells in the chip can be trypsinized, dyed or lysed. Then the cells or cell lysates can be collected for further analysis. During the experiment, cells can be observed constantly by microscope imaging system, capable of recording the cell morphology change during the whole experiment.

Some experiments were carried out to test the performance of the device. Firstly, the thermal control ability was analyzed. The results show that the temperature of cell culture unit was 37±0.5℃. Then the analysis of resolution of the microscope imaging system was carried out. The results showed that the resolution was higher than 2 μm. Finally, U87-MG cells were cultured then dyed by eosin and imaged by a microscope imaging system. In summary, this device, integrated cell culture, microscope imaging, and cell sample collecting, is highly integrated and flexible. In addition, more function is developing by designing new microfluidic chips or adding some new components to the device. Therefore, this device can be a valuable tool for cell research in space.

1.2 Lab-on-a-chip and its Application in Spaceflight Experiment

Astronauts face serious health threats during spaceflight. The two major factors that may lead to an astronauts' physiological dysfunction are space radiation and microgravity[2]. Heavy ion radiation, one of the important components of charged particles in orbit, can cause Deoxyribonucleic Acid (DNA) damage and gene mutations. Microgravity can also affect a series of cell physiology functions, including cytoskeleton remodeling, DNA modification, interactions between molecules, *etc.* Several ionizing radiation experiments performed in many previous studies suggested the variation in the mutation across different selected immune genes. Scientists performed a further experiment (Immune Gene Mutation-Beijing Institute of Technology-1, IGM-BIT-1) on board the International Space Station (ISS) to explore the molecule evolution rules of the selected DNA. To conduct the on-orbit amplification of the DNA fragments from the antibody encoding genes in the ISS, a self-developed portable and programmable PCR device was designed and produced[3]. They developed a novel PCR chip that consisted of a multi-channel optical adhesive reaction chamber and a miniature thermal cycler. The reaction chamber was cost effective and disposable. The thermal cycler was used to achieve both rapid heating and cooling. As the DNA amplification yield of IGM-BIT-1 PCR device was much similar or even higher than the commercial devices, the IGM-BIT-1 payload has been proven to be suitable for space life science research.

1.3 Design and Surface Modification of a Microfluidic Chip for Intercellular Interactions Research during Spaceflight

Intercellular interactions widely exist in multicellular organisms. The exposure of astronaut's body to space environment results in a series of biological effects including intercellular interactions. However, these interactions have not been studied extensively in space because of the difficulties faced in performing such experiments in the space. To solve this problem, a co-culture microfluidic chip was designed for studying intercellular interactions and provides an effectively dynamic co-culture method to both adherent cells and suspension cells. Its structure consists of two cell chambers which are divided by polycarbonate semipermeable membrane. The membrane is permeable to signal molecules which are secreted by cells but it is impermeable to the cells itself. Each cell chamber is divided by bolting silk.

This results in a control of flow shear stress exerted on the cells and it also results in trapping the suspended cells. As the surface property of the base of any microfluidic chip is important, therefore, they optimized a surface modification strategy using MTS assays and water contact angle test. The results showed that the optimum surface modification strategy is using air plasma treated polystyrene surface for 90 s. Moreover, the contact angle recovery after plasma treatment indicated that the co-culture microfluidic chip should be seeded within 6 days after surface modification. This co-culture microfluidic chip can be a valuable tool for investigating intercellular interactions in space as it can be operated automatically during a spaceflight[1].

2 Biological Study in the Ground-based Simulated Microgravity

2.1 Microbe Research in Simulated Microgravity Condition

2.1.1 Microbiomes of China's Space Station during Assembly, Integration and Test Operations

Sufficient evidence indicates that orbiting space stations contain diverse microbial populations, which may threaten astronaut health and equipment reliability. Understanding the composition of microbial communities in space stations will facilitate further development of targeted biological safety prevention and maintenance practices. Therefore, this study systematically investigated the microbial community of China's Space Station (CSS)[4]. Air and surface samples from 46 sites on the CSS and Assembly Integration and Test (AIT) center were collected, from which 40 bacteria strains were isolated and identified. Most isolates were cold and desiccation-resistant and adapted to oligotrophic conditions. Bacillus was the dominant bacterial genus detected by both cultivation-based and Illumina MiSeq amplicon sequencing methods. Microbial contamination on the CSS was correlated with encapsulation staff activities. Analysis by spread plate and qPCR revealed that the CSS surface contained 22.4~54.7 CFU·cm^{-2} culturable bacteria and 9.32×10^{3}~ 5.64×10^{4} 16S rRNA gene copies cm^{-2}; BacLight™ analysis revealed that the viable/total bacterial cell ratio was 1.98%~13.28%. This is the first study to provide important systematic insights into the microbiome of the CSS during assembly that describes the pre-launch microbial diversity of the space station. Our findings revealed the following results: (i) bacillus strains and staff activities should be considered major concerns for future biological safety; (ii) autotrophic and multi-resistant microbial communities were widespread in the AIT environment. Although harsh cleaning methods reduced the number of microorganisms, stress-resistant strains were not completely removed; (iii) sampling, storage, and analytical methods for the space station were thoroughly optimized, and are expected to be applicable to low-biomass environments in general. Microbiology-related future works will follow up to comprehensively understand the changing characteristics of microbial communities in CSS.

2.1.2 Fungi from Low-biomass Spacecraft Assembly Clean Room Aerosols

Highly sensitive and rapid detection of airborne fungi in space stations is essential to ensure disease prevention and equipment safety. In this study, quantitative Loop-Mediated Isothermal Amplification (qLAMP) was used to detect fungi in the aerosol of the low-biomass environment of China's Space Station Assembly Clean room (CSSAC)[5]. A qLAMP primer set for detecting a wide range of aerosol fungi was developed by aligning 34 sequences of isolated fungal species and 17 space station aerosol-related fungal species. Optimization of sample pretreatment conditions of the LAMP reaction increased the quantitative results by 1.29~1.96 times. The results showed that our qLAMP system had high amplification specificity for fungi, with a quantifiable detection limit as low as 10^{2}. The detected fungal biomass in the aerosol of CSSAC was 9.59×10^{2}~ 2.20×10^{5} 28S rRNA gene copy numbers m^{-3}. This qLAMP assay may therefore replace the traditional colony-forming unit and quantitative PCR methods

as an effective strategy for detecting fungi in space stations.

2.2 Biological Effects in Simulated Microgravity Conditions

To explore the dynamic impacts of Simulated Microgravity (SM) on different vital brain regions of rats, microgravity was simulated for 7 and 21-day, respectively, using the tail-suspension rat model[6,7]. Histomorphology, oxidative stress, inflammatory cytokines, and the expression of some key proteins were determined in hippocampus, cerebral cortex, and striatum. The results showed that 21-day SM decreased brain derived neurotrophic factor and induced neuron atrophy in the cerebral cortex. Strong oxidative stress was triggered at Day 7 and the oxidative status returned to the physiological level at Day 21. Inflammatory cytokines were gradually suppressed and in striatum, the suppression was regulated partially through c-Jun/c-Fos. All of these data revealed that the significant impacts of SM on rat brain tissue depended on durations and regions, which might help to understand the health risk and to prevent brain damage for astronauts in space travel.

Moreover, a proteomic approach was used to investigate rat intestinal homeostasis alterations induced by 7-day simulated microgravity effect[8]. Tail-suspension model was used to simulate microgravity effect and a label-free quantitative proteomic strategy was employed to determine proteins in rat intestine. As a result, 717 differently expressed proteins were identified and 29 proteins were down-regulated while 688 proteins were up-regulated. The three highest enrichment scores were annotation cluster I about cell-cell adhesion, annotation cluster II about carbohydrate metabolism, and annotation cluster III about the activity of peptidase. Results of rat intestine proteomics indicate that SMG might disrupt intestinal homeostasis, which possibly resulted in the opening of Intestinal Epithelial Barrier (IEB), potentially leading to the risk of Systemic Inflammatory Response (SIR) and Inflammatory Bowel Diseases (IBD). The present results also provide some useful information for mechanisms and countermeasures of intestine injuries induced by microgravity.

3 Basic Research for Underlying Mechanisms of Radiation Injury

3.1 Biology Effect of Irradiation on Neuron Cell or Tissue

3.1.1 Autophagy Protects Neural Cells from Carbon-ion Beam Irradiation Injury

The present study investigated autophagy changes and the expression of HMGB1 in human glioblastoma cells[9], responding to carbon-ion beam irradiation (35 keV·μm^{-1}, 80.55 MeV per unit nucleon). U251 cells were irradiated with carbon ion beams and cell proliferation was measured by counting the number of living cells. The expression of Light Chain 3 Beta (LC3B), Beclin 1, High-Mobility-Group Box 1 (HMGB1), pro-form caspase-3, and Cellular FLICE-like Inhibitory Protein (c-FLIP) was analyzed by western blotting. Caspase enzyme activity was determined *via* a caspase cleavage based florescent substrate commercial Kit. Living cell counting demonstrated a time and dose dependent cell death in U251 cells. The expression of LC3B and Beclin 1 revealed that, a high level of autophagy was induced 24 h after irradiation with 1 Gy carbon ions and then decreased in a time- and dose-dependent manner. The expression of the whole HMGB1 showed a good correlation with the dynamic autophagic level. Cytoplasmic HMGB1 maintained autophagy was concluded. Enzyme-Linked Immuno Sorbent Assay (ELISA) measurement found that HMGB1 was released into the extracellular space in a time- and dose-dependent manner. Lower intracellular HMGB1 levels correlated with decreased autophagy as measured by the expression of LC3B. Decreased expression of pro-form caspase-3 and c-FLIP as well as the increased caspase enzyme activity indicated that apoptosis was induced by carbon-ion beam irradiation. Inhibition of HMGB1 release from the area of intracellular to that of extracellular significantly increased cell survival. In summary, carbon-

ion beam irradiation could elevate autophagy and HMGB1 expression efficiently, which would protect the cells from programmed cell death via inducing autophagy. Apoptosis as measured by expression of caspase activities increased as the dose increased, which was accompanied with decreased levels of LC3B and HMGB1.

3.1.2 Autophagy Can Promote Apoptosis after Irradiation

As a cancer treatment strategy, irradiation therapy is widely used that can cause DNA breakage and increase free radicals, which leads to different types of cell death. Among them, apoptosis and autophagy are the most important and the most studied cell death processes. Although the exploration of the relationship between apoptosis and autophagy has been a major area of focus, still the molecular mechanisms of autophagy on apoptosis remain unclear. The recent results have revealed that apoptosis was enhanced by the Death Receptor 5 (DR5) pathway, and the effect of autophagy on apoptosis was promoted by DR5 interacting with LC3B as well as Caspase8 in gliomas after irradiation[10]. Interestingly, they observed that the addition of four different autophagy inducers, Rapamycin (RAP), CCI779, ABT737, and Temozolomide (TMZ), induced the differences of DR5 expression and cell apoptosis after irradiation. Unlike RAP and CCI779, ABT737 and TMZ were able to increase DR5 expression and further induce cell death. Therefore, they have concluded that DR5 plays a novel and indispensable role in promoting cell apoptosis under irradiation.

3.2 Carbon Ion Radiation Induced Lipid Disturbance in Brain

The concentration of lipids in the Central Nervous System (CNS) was second only to adipose tissue. Phospholipids (PLs) accounted for 45% of the total brain dry weight and nearly 60% of myelin. The structural unit of lipids was ketoethyl and isoprene, which had both hydrophilic and lipophilic properties and played an important role in cellular structure and function. Lipids also provided energy for the metabolic processes of life, form biofilms, and established an appropriate hydrophobic environment, forming ion channels together with proteins. On the other hand, lipids can also serve as second messengers for signal transduction. Although some studies had shown that space particle radiation causes metabolic disorders of the brain tissue metabolites including 4-butylamic acid, glutamic acid, lactic acid, and other important neurotransmitters[11-15], there was still a lack of in-depth research on the molecular mechanism of brain lipid damage and its relationship with nerve function damage under spatial radiation environment.

In these recent studies, they used UPLC-MS untargeted and targeted lipidomics to screen potential lipid biomarkers in the rat brain induced by simulated space radiation environment from the perspective of lipid molecule changes and to reveal the molecular mechanism of carbon ion radiation-induced brain damage. The 7 weeks male Wistar wild-type rats were exposed to a single high dose of 15 Gy $12C^{6+}$ radiation vertically on the back of the head at Wuwei Heavy Ion Hospital in Gansu province, China. The control group was consistent with the irradiated group except for not receiving irradiation. UPLC-MS untargeted and targeted lipidomics were performed on the brain tissue and plasma of rats on the seventh-day post-irradiation. Statistical methods such as unsupervised Principal Component Analysis (PCA), supervised Partial Least Squares Discriminant Analysis (PLS-DA) and Orthogonal Partial Least Squares Discriminant Analysis (OPLS-DA) showed that there was a difference in the lipid metabolism in the brain tissue of the irradiated and control groups. In untargeted lipidomics, we screened out 29 differential lipids between the control group and the irradiated group using a multiple test Fold Change (FC)>1.5, PLS-DA model with a VIP>1 and a T test with a $p<0.1$ by volcano plot model. These 29 differential lipids included Diacylglycerol (DAG), Triacylglycerol (TAG), Lysophosphatidylethanolamine (LPE), Lysophosphatidylcholine (LPC), Phosphatidylcholine (PC), Phosphatidylethanolamine (PE), Sphingomyelin (SM) and branched Fatty Acid

esters of Hydroxy Fatty Acids (FAHFAs). The results after classification showed that DAGs were significantly different lipids upon $12C^{6+}$ radiation. Targeted quantitative analysis of DAGs that had significant changes in the brain tissue and plasma of the irradiated and control rats were also performed to screen out the differential lipids. Based on the quantitative analysis results, they finally screened out three DAG lipids as potential biomarkers for brain damage induced by $12C^{6+}$ ion irradiation. Interestingly, the contents of these three DAGs in the rat brain tissue and plasma were negatively correlated. The mechanism through which differential lipids induced CNS damage are under explored in our group.

3.3 Bystander Effect Induced by Different Irradiation

3.3.1 Mechanism of Bystander Effect Induced by Different Irradiation

Cells exposed with irradiation can induce different biological effects in non-irradiated cells due to the cell-cell interactions. Herein, they investigated the bystander effect of different types of irradiation including Gamma Irradiation (GR) and lithium heavy ion irradiation (LR) on the model human neuroblastoma cell line (SH-SY5Y). The gamma and lithium ion irradiation induced different bystander effects on the SH-SY5Y cell line[16]. The bystander effect induced by gamma irradiation promoted cell proliferation through activating the ERK and AKT signaling pathways, but it could slightly influence the cell cycle of non-irradiated SH-SY5Y cells. Whereas, the bystander effect induced by lithium heavy ion irradiation inhibited the cell proliferation, arrested the cell cycle, and activated the process of pro-apoptosis. The findings of this study confirm the diversified bystander effects of various irradiation on the non-irradiated cells, therefore it highlights the importance of a revised strategy for radioprotection to reduce the damages caused by bystander effects. Further, the in-depth mechanism research on cell proliferation influenced by the bystander effect of radiation will also be useful to understand the biological effects of radiation.

3.3.2 Effect of γ-ray-induced Central Nervous System Injury on Peripheral Immune Response

Radiotherapy of the brain can be harmful to the Central Nervous System (CNS) and it stimulates a series of immune responses in both the CNS as well as the peripheral immune system. The present studies have mostly focused on the changes occurring in the immune response within the CNS[17]. In this study, they have investigated the effect of γ-ray- induced CNS injury on the peripheral immune response by using a cell co-culture model and Whole Brain Irradiation (WBI) rat model. Analyses were performed based on the response of immune cells in conditional medium. WBI of SD rats was performed with different doses and rats were fed for one week to one month. Then spleen and peripheral blood were isolated and analyzed. The results showed that the number of monocytes in peripheral blood, the level of NK cells, and NKT cells in spleen increased after CNS injury. However, the level of T cells in spleen did not change and the level of B cells in the spleen decreased after inducing CNS injury by γ-ray.

3.4 DNA Mismatching during PCR Reaction Exposed to Space Environment

Mutation is the most important driving force of genome evolution. The pattern of mutation is the key to many questions in evolutional biology. Mutation could be induced by space radiation and microgravity, which are the two major factors leading to astronauts' physiological dysfunction. Especially the heavy ion radiation, which is one of the important components of charged particles in orbit, can cause DNA damages and gene mutation. Several ionizing radiation experiments performed in our previous study suggest the variation in the mutation across different selected immune genes. Here, we performed a further experiment to explore the molecule evolution of the DNA on the International Space Station (ISS) utilizing the space environment, providing basic research for life science theory for universe evolution and deep space exploration life science research. This project is the first time an ISS experiment has been inde-

pendently designed and fabricated in China. It has broken through the bottleneck of Sino-US cooperation in the 30 years, with the meaning of ice- breaking.

To investigate the radiation cumulative effect, two batches of DNA amplification experiments were performed respectively during the spaceflight. The first run was started at the beginning of the on-orbit flight (7–8 June 2017) and the second run was started 10 days after the first one (19–20 June 2017). On 3 July, after the payload returned to earth, the process data and bio-samples are both checked to be good. All samples were analyzed by Agilent 2100 bioanalyzer and the results showed that all the genes were amplified successfully in the space environment.

Some samples were also analyzed by deep sequencing on the HiSeq2500. Sequencing reads were processed for quality control and aligning. We achieved high quality data, and the times of the median depth for all samples was over 8000. For the gene which was composed of the Homosapien immunoglobulin heavy chain variable region germline gene fragments V7~18, D3~10, J2, sequencing data showed there were heteroplasmy both in the ground and space. For the space samples, the average mismatch rate is 1.51% (1st batch) and 1.53% (2nd batch). For the ground samples, the average mismatch rate is 2.67% (1st batch) and 2.74% (2nd batch). However, as there were inevitable errors in the sample preparation and sequencing for the next generation sequencing, ranging from 0.1% to 1%. Ultrasensitive detection of rare mutation and computational analysis of the mismatching information should be further applied in this space experiment samples.

References

[1] CHEN Y, PEI S Z, YAN L B, *et al.* Design and surface modification of a microfluidic chip for intercellular interactions research during space flight [J]. *Acta Astron.*, 2020, **166**(1):619-627

[2] SONG C, GAO X, SONG W, *et al.* Simulated spatial radiation impacts learning and memory ability with alterations of neuromorphology and gut microbiota in mice [J]. *RSC Adv.*, 2020, **10**:16196-16208

[3] YANG C H, DENG Y L, REN H, *et al.* A multi-channel polymerase chain reaction lab-on-a-chip and its application in spaceflight experiment for the study of gene mutation. *Acta Astron.*, 2020, **166**(1):590-598

[4] ZHANG Y, ZHANG L T, LI Z D, *et al.* Microbiomes of China's space station during assembly, integration, and test operations [J]. *Microb. Ecol.*, 2019, **78**(3):631-650

[5] ZHANG Y, XIN CX, ZHANG L T, *et al.* Detection of fungi from low-biomass spacecraft assembly clean room aerosols [J]. *Astrobiology*, 2018, **18**(12):1585-1593

[6] CHEN B, ZHANG Y S, LI G, *et al.* The impacts of simulated microgravity on rat brain depended on durations and regions [J]. *Biomed. Environ. Sci.*, 2019, **32**(7):496-507

[7] HUANG B, LI D G, HUANG Y, *et al.* Effects of spaceflight and simulated microgravity on microbial growth and secondary metabolism [J]. *Mil. Med. Res.*, 2018, **5**(1):18

[8] WANG S B, ZHANG Y S, GUO J J, *et al.* Investigation on rat intestinal homeostasis alterations induced by 7-day simulated microgravity effect based on a proteomic approach [J]. *Acta Astron.*, 2020, **166**(1):560-566

[9] LEI R H, YAN L B, DENG Y L, *et al.* HMGB1 mediated autophagy protects glioblastoma cells from carbon-ion beam irradiation injury [J]. *Acta Astron.*, 2020, **166**(1):628-634

[10] ZHANG P, WANG HL, CHEN Y, *et al.* DR5 related autophagy can promote apoptosis in gliomas after irradiation [J]. *Biochem. Biophys. Res. Commun.*, 2020, **522**(2020):910-916

[11] LUCHYMAN D W, SONG C. Cognitive enhancement by omega-3 fatty acids from child-hood to old age: findings from animal and clinical studies [J]. *Neuropharmacology*, 2013, **64**:550-565

[12] FAHY E, COTTER D, SUD M, *et al.* Lipid classification, structures and tools [J]. *Biochim. Biophys. Acta Molec. Cell Biol. Lipids.*, 2011, **1811**(11):637-647

[13] DART C. Lipid microdomains and the regulation of ion channel function [J]. *J. Physiol.*, 2010, **588**:3169-3178

[14] MARTELLI A M, BILLI A M, FALA F, *et al.* Metabolism and signaling activities of nuclear lipids [J]. *Cell. Molec. life Sci.: CMLS.*, 2004, **61**(10):1143-1156

[15] BELOV O V, BELOKOPYTOVA K V, KUDRIN V S, *et al.* Neurochemical insights into the radiation protection of astronauts: distinction between low- and moderate-LET radiation components [J]. *Phys. Med.*, 2019, **57**:7-16

[16] CHEN B, ZHANG P, SUN F, *et al.* The mechanism of bystander effect induced by different irradiation in human neuroblastoma cells [J]. *Acta Astron.*, 2020, **166**(1):599-606

[17] ZHANG P, CHEN Y, ZHU H, *et al.* The effect of gamma-ray-induced central nervous system injury on peripheral immune response: an in vitro and in vivo study [J]. *Radiat. Res.*, 2019, **192**(4):440-450

LONG Mian, SUN Shujin, LI Ning, LÜ Dongyuan, GAO Yuxin. Progress Update in Space Cell Mechano-biological Coupling. *Chin. J. Space Sci.*, 2020, **40**(5): 387-388. DOI:10.11728/cjss2020.05.387

Progress Update in Space Cell Mechano-biological Coupling*

LONG Mian SUN Shujin LI Ning LÜ Dongyuan GAO Yuxin

(*National Microgravity Laboratory, Institute of Mechanics, Chinese Academy of Sciences, Beijing* 100190)

Abstract Recent progresses in 2018–2019 from space experiments onboard SJ-10 recoverable satellite and on parabolic flight were summarized, mainly focusing on cell mechano-biological coupling under microgravity. In the meantime, technical pre-research and experimental system design for the biomechanics research platform on China Space Station was carried out and updated.

Key words Microgravity, SJ-10 satellite, Parabolic flight, Endothelial cells, Mesenchymal stem cells, Hepatocytes, Mechanotransduction, China Space Station

Classified index V 524

In 2018 and 2019, we focused on elucidating the mechano-biological coupling mechanisms of mammalian cells under microgravity and developing the novel techniques for the biomechanics experimental platform on China space station. The progress is updated briefly as follows.

1 Data Analysis and Technical Summary of the Space Experiment Onboard SJ-10 Recoverable Satellite

Data collected from a space experiment on SJ-10 recoverable satellite in 2016 and ground-based control experiments were analyzed, and the performance of the hardware developed for the space experiment was summarized. The results indicated that space microgravity improved the hepatocyte differentiating capability of rat mesenchymal stem cells by up-regulating hepatocyte-specific albumin and cytokeratin 18[1]. Meanwhile, space microgravity suppressed the glucose metabolism, modulated the expression of cellular adhesive molecules such as ICAM-1, VCAM- 1, and CD44, and depressed the pro-angiogenesis and pro-inflammation cytokine secretion in EA.hy926 Endothelial Cells (ECs). Cytoskeletal remodeling, such as depolymerization of actin filaments and microtubules were found in space samples. Three-dimensional cell growth or enhanced nitric oxide production, which was documented in clinostat experiments, was not observed in ECs cultured in space[2]. Experimental techniques used in the space experiment were reviewed, and the performance of an integration design including gas exchange, bubble separation, and flow control was verified, providing a valuable platform for establishing space experimental technical standard[3].

2 Data Analysis of the Experiment on Parabolic Flight in 2017

This study was proposed to characterize how immune cell function is affected by altered gravity produced by Parabolic Flight (PF, 30th DLR parabolic flight,

* Supported by Strategic Priority Research Program and Frontier Science Key Project of Chinese Academy of Sciences (XDA04020202-17, XDA04020416, XDA15014100 and QYZDJSSW-JSC018), National Natural Science Foundation of China (U1738115)
Received March 13, 2020
E-mail: mlong@imech.ac.cn

a 4-day mission in September 2017). It applied an integrated biomechanical and biomedical approach with forced fluid flow and on-line cell imaging, allowing to elucidate the rolling and adhering features of Jurkat cells and Peripheral Blood Mononuclear Cells (PBMC) on flow chamber substrate coated with different adhesion molecules. The results indicate that, in contrast to hyper-g (1.8 g) and control conditions (1 g), the rolling speed of PBMCs was moderately accelerated during μg -periods which were accompanied by a clear reduction in rolling rate. Whole blood analyses revealed a primed state of monocytes after PF with potentiated antigen-induced pro-inflammatory cytokine responses. At the same time, the concentrations of anti-inflammatory cytokines were increased and monocytes displayed a surface molecule pattern that indicated immunosuppression. The results suggested an immunologic counterbalance to avoid disproportionate immune responses[4].

3 Technical Pre-research and Experimental System Design for the Biomechanics Research Platform on China Space Station

A space biomechanics experimental platform on China Space Station is under development for a series of biomechanics studies. This work aimed at quantitatively controlling different mechanical conditions for cell and tissue samples that mimic the mechanical environment in *vivo* under microgravity. Techniques for loading modulation of flow shear stress, substrate tension, substrate physical property, and mass transport were tested. In order to obtain data with reliable control design and adequate repeatability, the factors that could affect experimental results were analyzed. The fast handling techniques for sample modules and the on-line automatic operations of medium supply, chemical fixing, and microscopic observation are under optimization. The designed experimental system is expected to provide a normalized platform for elucidating mechano-biological coupling mechanisms during gravity-varied processes.

References

[1] LÜ Dongyuan, SUN Shujin, ZHANG Fan, *et al.* Microgravity-induced hepatogenic differentiation of rBMSCs on board SJ-10 satellite [J]. *FASEB J.*, 2019, **33**(3):4273-4286

[2] LI Ning, WANG Chengzhi, SUN Shujin, *et al.* Microgravity-induced alterations of inflammation-related mechanotransduction in endothelial cells on board SJ-10 satellite [J]. *Front. Physiol.* 2018, **9**:1025

[3] SUN Shujin, WANG Chengzhi, BI Yuzhen, *et al.* An integration design of gas exchange, bubble separation and flow control in a space cell culture system on board the SJ-10 satellite [J]. *Rev. Sci. Instrum.,* 2019, **90**(7):075114

[4] MOSER D, SUN Shujin, LI Ning, *et al.* Cells flow and immune cell priming under alternating g-forces in parabolic flight [J]. *Sci. Rep.*, 2019, **9**:11276

ZHAO Yufen, HUA Yuejin, ZHANG Hongyu, HE Yujian, ZHU Ting, LIU Yan, WU Li. Progress of Research on Origins of life in China. *Chin. J. Space Sci.*, 2020, **40**(5): 389-397. DOI:10.11728/cjss2020.05.389

Progress of Research on Origins of Life in China

ZHAO Yufen[1,2,3] HUA Yuejin[4] ZHANG Hongyu[5]

HE Yujian[6] ZHU Ting[7] LIU Yan[1] WU Li[6]

1 (*Department of Chemical Biology, College of Chemistry and Chemical Engineering, Xiamen University, Xiamen* 361005)

2 (*Institute of Drug Discovery Technology, Ningbo University, Ningbo* 315221)

3 (*Key Laboratory of Bioorganic Phosphorus Chemistry and Chemical Biology of Ministry of Education, Department of Chemistry, Tsinghua University, Beijing* 100084)

4 (*Institute of biophysics, College of Life Sciences, Zhejiang University, Hangzhou* 310029)

5 (*Hubei Key Laboratory of Agricultural Bioinformatics, College of Informatics, Huazhong Agricultural University, Wuhan* 430070)

6 (*School of Chemical Sciences, University of Chinese Academy of Sciences, Beijing* 101408)

7 (*School of Life Sciences, Tsinghua-Peking Center for Life Sciences, Tsinghua University, Beijing* 100084)

Abstract The development of Chinese space science and technology plays a great role in promoting the researches in the field of the origin of life. With the multidisciplinary cooperation, there are fruitful achievements in this research field obtained over the past two years. This report summarizes the major progress of the basic researches about the origin of life in China during 2018–2020.

Key words Origin of genetic code, Origin of metabolism, Evolution prototype of modern enzyme, Mirror-image biological system, Extremophiles

Classified index P 149

1 Introduction

Where did life come from? The origin and evolution of life are one of the fundamental science problems, which is always fascinating and widely concerned in the world today. So far there are two main theories. One is "meteoritic origin", that means life on Earth must have originated in outer space and come to Earth through meteorites with organic matters, especially prebiotic materials as life seeds. Another is "the origin of living systems on the Earth" that life arose from lifeless matters under some extreme conditions on the Earth. However, no matter which theoretical system is, both follow the basic concept of the origin of life. That means modern biological functional macromolecules are originated from the original, simple inorganic or organic small molecules which go through the evolution of structure and function. It is the origin of chemical stage in the process of the origin of life.

Investigation of the internal nature of the origin of life involves in the multidisciplinary cooperation covers a wide range of researches. As one of the frontiers of science, related researches inevitably promote the development and innovation of the scientific and technological level in China. With the development of national economy and the construction of the Chinese manned space station and recoverable satellite science experimental platform, there are more and more opportunities to be created for exploring the origin of life in space with a broader perspective. In 2007, the Professional Committee of

Received March 21, 2020

E-mail: stacyliu@xmu.edu.cn

the Chinese Space Science Society on Space Life Origin and Evolution was established at Xiamen University. Since then, the researchers with the common interest in exploring the origin of life have a platform to realize the extensive discussion and cooperation. Herein, we review and summarize the researches on the origin of life contributed by Chinese scientists in the past two years.

2 Regulation and Catalysis of Phosphorus in Prebiotic Chemistry Conditions

As the significant element for life, phosphorus inevitably plays a vital role in the process of the origin of life. In 2019, in view of phosphorus chemistry, Zhao *et al.*[1] collected their previous and systematic researches focusing on the origin of life in a book named as "Phosphorus Chemistry: The role of phosphorus in prebiotic chemistry". The book mainly contents are as these follows: (i) penta-coordinate phosphorus activated intermediates have a vital regulation role in biological system; (ii) phosphorus selects the α-amino acids to be the structural unit of proteins; (iii) *N*-phosphoryl amino acid is a delicate Co-evolution Model of Nucleic acids and Proteins; (iv) the discovery of Ser-His, the smallest functional dipeptide; (v) the chemical models for the investigation of the origin of chirality and the genetic code. The correlative researches will trigger people's consideration about the effects of phosphorus in the origin of life. It will provide some novel clues and pivotal experiment supports to explain the eternal enigma during the evolution process of life.

3 Discovery of Analogs of 5'-aa-AMPs (aa-*N*-NMPs) in Prebiotic Chemistry System

The genetic code undoubtedly plays an essential role in life sciences; thus its origin, which remains ambiguous, is the most fundamental issue. Aminoacyladenylates (5'-aa-AMPs) are key intermediates in peptide synthesis of life system. In 2018, Zhao *et al.*[2] reported analogs of 5'-aa-AMPs, namely nucleotide amidates (aa-*N*-NMPs), could be obtained under Hadean conditions (Figure 1). Significantly, dipeptides were detected from the above reactions and their yields varied with different nucleosides through the formation of different aa-*N*-NMPs. That means the nucleoside could regulate peptide formation through the intermediate aa-*N*-NMP. In addition, aa-*N*-NMP further reacts with the *N*-terminal of peptide (D_p=n) to form nucleotide-peptide (NMP-peptide, D_p=n+1). Then, the peptide (D_p=n+1) was formed by NMP-peptide hydrolysis (Figure 1). The related mechanism for producing the intermediate aa-*N*-NMP was double checked in the organic phase

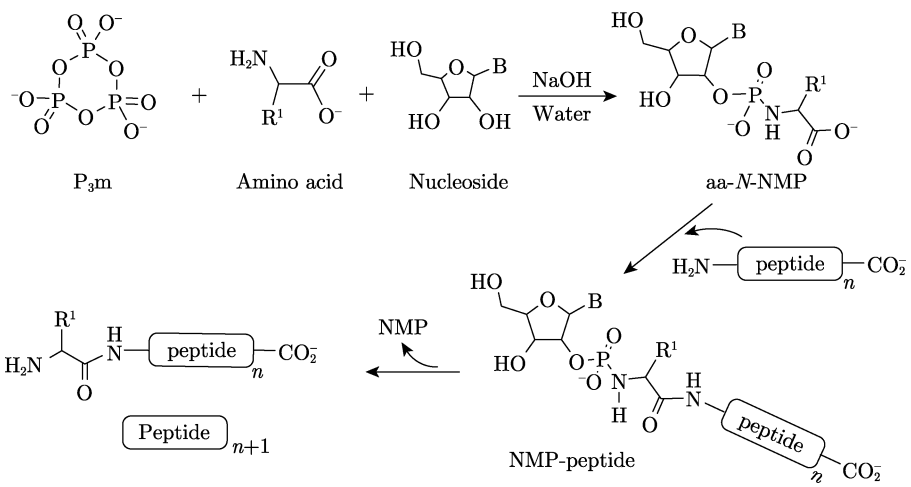

Fig. 1 Mechanism influencing the yield of peptide by nucleosides

reaction system[3]. This chemical model provides the primordial version of the genetic code and reasonably explained the possible mechanism of prebiotic peptides synthesis.

4 Seryl-histidine Dipeptide: Potential Evolution Prototype of Modern Enzyme

Seryl-histidine dipeptide (Ser-His) has been identified as the shortest functional peptide with multifarious hydrolysis cleavage activity, such as the hydrolysis of protein, DNA, and carboxyl ester. Ser-His (Figure 2) has the two critical functional amino acid residues of the Ser-His-Asp catalytic triad of serine proteases. Therefore, it is worth exploring if there are some evolutionary relationships between Ser-His and modern serine proteases.

To this end, four differently folded proteins were treated with Ser-His, such as bovine serum albumen, green fluorescent protein, cyclophilin A and myoglobin. The resulting digestion products were evaluated with high-resolution mass spectrometry. The cleavage efficiency and cleavage propensity of Ser-His against these protein substrates were calculated at both the primary and secondary sequence levels. It was found that Ser-His cleaves a broad spectrum of substrate proteins of varying secondary structures. Ser-His has the original digestion function of serine proteases to cleave at all 20 amino acids with different efficiencies according to the protein. Besides, through comparing the catalytic sites and cleavage sites of 340 extant serine proteases derived from 17 representative organisms, a consensus motif Ser-[X]-His was identified as the major pattern at the catalytic sites of serine proteases from all of the organisms represented except *Danio rerio*, which uses

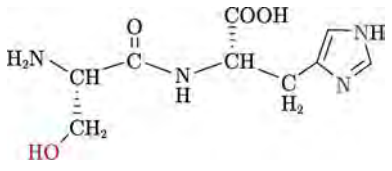

Fig. 2 Molecular structure of Ser-His dipeptide

Ser-Lys instead. This finding indicates that Ser-His is the core component of the serine protease catalytic site. Moreover, the above analysis revealed that the cleavage sites of modern serine proteases have become more specific over the evolutionary history of this family[4].

Furthermore, it's well known that protease can also catalyze the formation of peptide bonds based on the microscopic reversibility theory. Exhilaratingly, Ser-His can catalyze the formation of peptides and phosphodiester bonds as the modern hydrolase, which was proved by Pier Luigi Luisi, Wieczorek R. and Jack W. Szostak in succession. In addition, it was reported that Ser-His could be obtained under prebiotic chemistry conditions[5]. Therefore, it is reasonable to believe that Ser-His is likely the candidate of evolution prototype for serine protease.

5 Contributions of Phosphates to the Metabolism Origin

As mentioned before, phosphates are basic components of many biomolecules and essential for modern biochemical reactions. However, most of the phosphates are either insoluble in water or have low reactivity, which is considered to be problematic for primordial biological use. To avoid this phosphorus problem, Goldford *et al.* constructed a phosphate-free metabolic network starting from a set of prebiotically abundant compounds excluding phosphates and proposed an unconventional new view: a phosphorus-independent metabolism could exist before the emergence of the phosphate-based genetic coding system. This new opinion stimulated researchers' interest in the systematical exploration of the role that phosphorus played in the origin of metabolism.

In Zhang's laboratory, first, phosphorus-dependent protometabolic networks were constructed using the method of Goldford *et al.* with seed sets containing different prebiotically available phosphates. The obtained phosphorus-dependent metabolic networks were composed of the same reactions, implying

that the network was robust to different phosphorus sources (Figure 3). The following bioinformatics and chemical informatics analysis showed that the phosphorus-dependent metabolic network exhibits several ancient features. The enrichment of the Last Universal Common Ancestor (LUCA)-related features observed in the phosphorus-dependent network implied that a great portion of the reactions in this network also existed in the earliest life. The origins of the enzymes participating in the networks were traced by the protein-domain structure-based molecular clocks.

This analysis showed that phosphorus-dependent and independent metabolic networks originated at the same evolutionary stage. By analyzing the chemical characteristics, it was found that the metabolites in both kinds of networks have higher water solubility, stronger molecular polarity, and smaller molecular weight than modern metabolites. These findings showed that the phosphorus-dependent metabolic network exhibits critical ancient characters, thus both phosphorus-dependent and -independent networks have an ancient origin.

Subsequently, the influence of phosphates on the protometabolic network was studied by the KEGG pathway enrichment analysis. It was found that phosphates promote carbon metabolism as well as carbohydrate metabolism. These metabolic pathways are extremely important for sustaining energy flow in modern life and for the formation of the RNA world. In addition, the presence of phosphorus also promotes the production of complex metabolites and

Fig. 3 Construction of phosphorus-dependent metabolic network. Network expansion simulation was executed using a set of defined seed compounds and all balanced reactions in the background metabolism pool derived from the updated KEGG reactions. The figure displays the obtained phosphorus-dependent network in which metabolites are linked if they have a reactant-product relationship during the expansion. The metabolites generated at different iteration steps during the network expansion process are represented by nodes in different colors. The size of node represents the degree of the node, *i.e.*, the number of reactions added in the subsequent iteration

enhanced the diversity of metabolites.

To explore the influence of phosphorus on the thermodynamic feasibility of ancient metabolic system, the thermodynamically constrained network expansion with various forms of phosphates was simulated. This study found that some phosphorous intermediates of the glycolytic pathway could dramatically alleviate the thermodynamic bottlenecks and promote the expansion of the network. Further study of scale-limiting reactions during the thermodynamically constrained network expansion showed that the expansion of ancient metabolic network might be feasible with the presence of phosphorous intermediates such as glucose 6-phosphate and glyceraldehyde 3-phosphate.

In summary, the phosphorous-dependent metabolism could originate in very early stage of biochemical processes. Phosphorus can promote reactions which are essential for life and some high-energy phosphates can ensure the prebiotic metabolism under feasible energetic constraints. Taken together, phosphorus is indispensable for metabolism origin, as material and energy sources, which provides deeper insights into the origin of life[6].

6 Origin of Homochirality and Mirror-image Biological System

The essence of life is chirality. It is well known that the protein-helix is a right-handed helix, and the structural unit amino acids of protein are all in the L-configuration. DNA is a right-handed helix in which the ribose is in the D-configuration. Therefore, the origin of life is the origin of homochirality. Up to now, the origin of homochirality in life on the Earth is still a puzzle.

It is interesting to know what happens to the mirror-image molecular system containing L-nucleosides during their replication and transcription and whether it would bring about deleterious effects during the evolution of nucleic acids. He *et al.*[7] previously investigated that several general DNA polymerases and T7 RNA polymerase catalyze polymerization reactions of nucleotides directed by the DNA template containing an L-Thymidine (L-T). It was found that mirror-image thymidine discriminates against incorporation of deoxyribonucleotide triphosphate into DNA and repairs itself by normal DNA polymerases.

As we have known, protein, which consists of L-amino acid, is the direct performer of vital movement, and weed-out of D-amino acids within living cells or organism that are necessary for the maintenance of life. A small but moderate amount of D-amino acids is also essential for life. Excess D-amino acids cause DNA oxidative damage. Some diseases of the human body are positively correlated with the content of D-amino acids in the body. D-amino acid toxicology is very important for studying certain diseases and aging mechanisms. Stereospecific enzyme plays an important role in the metabolism, which controls the balance of L or D-amino acids. D-amino Acid Oxidase (DAAO) catalyzes the oxidative deamination of a majority of D-amino acids rather than L-amino acids. Once the enantioselectivity of DAAO is disturbed, the metabolic systems might be disordered, which might be found as precipitating factors of chiral disease. Enzymatic enantioselectivity of amino acids with DAAO could be controlled by adjusting the pH of aqueous solution and adding ionic liquid, which means that the external chemical environments are likely to affect the enzyme specificity[8]. Additionally, D-amino acids occur widely in food. The related reactive oxygen species accumulation and biochemical damage caused by D-amino acids are evaluated by using *Saccharomyces cerevisiae* as a model[9] or in beer[10].

The racemization of amino acids is liable to happen under extreme conditions, such as space radiation and strong acid or alkalinity, microbial fermentation. Therefore, the space response of chiral molecules, such as amino acids, chiral medicine and so on, is worth obtaining more attention, which is of great importance for space medicine and astronaut's health.

The chiral selection rules above-mentioned are for the life system on the Earth. How about extraterrestrial life? Does the extraterrestrial life have the

same rules with terrestrial life? The search for mirror-image biology systems in the universe may open the next frontier for biomedical technology development and discovery. Zhu's group at Tsinghua University first demonstrated that two key steps in the central dogma of molecular biology, the template-directed polymerization of DNA and transcription into RNA, can be catalyzed by a chemically synthesized D-amino acid polymerase on an L-DNA template[11]. The two chirally mirrored polymerase systems can operate in a racemic mixture without obvious enantiomeric cross-inhibition to the activity of each other. Additionally, a mutant version of the thermostable *Sulfolobus solfataricus* P2 DNA polymerase IV (Dpo4) consisting of D-amino acids was designed and chemically synthesized, and used for realizing mirror-image PCR[12]. More recently, they further demonstrated the transcription of a mirror-image gene into L-RNA, and reverse transcription into L-DNA by synthetic D-polymerases based on designed mutants of the mirror-image Dpo4[13].

Furthermore, a practical method for sequencing mirror-image DNA by adopting the Maxam-Gilbert sequencing approach was developed through nucleobase-specific cleavage by achiral chemicals. The technique may facilitate the therapeutic application of nuclease-resistant L-aptamer drugs, and bring the vision of building an alternative, mirror-image self-replicating system closer to reality[14].

After the realization of mirror-image genetic replication, transcription, and reverse transcription, the big remaining challenge in establishing a mirror-image version of the central dogma of molecular biology is to build a mirror-image ribosomal translation apparatus. Zhu's group reported the chemical synthesis of three ribosomal proteins (L5, L18, and L25) in the large subunit of the *E. coli* ribosome with post-translational modifications, which can fold properly in vitro and assemble with enzymatically transcribed mirror-image 5S ribosomal RNA into stable ribonucleoprotein complexes through chiral-specific binding[15].

In summary, a mirror-image form of life based on D-amino acids and L-nucleic acids, is conceivable and is possible to exist on other planets. The above-mentioned ground-based research may provide experimental support for the exploration of extraterrestrial life.

7 Progress of Survival and Evolution of Earth-originating Extremophiles in Space Environment

How does the Earth life deal with and adapt to the extreme environment such as cosmic ray, anoxia and dryness of space is not only a key scientific problem to understand the origin and evolution of life on the Earth, but also a technical problem to be solved for human beings to realize "livable" in the extraterrestrial space such as Mars. Deep space exploration driven by the research on the origin, evolution, and livable environment of life has become the consensus of the international scientific community. At present, the research on the survival ability and stress response of related organisms in the space environment is mainly ground-based experiments. With the initiation of a series of National Science and Technology Major Projects, including the China Manned Space Station Project and Deep Space Exploration mission, *etc.*, an unprecedented opportunity for space life sciences has been provided. Because of the stress-tolerance of various extremophiles on the Earth, it is of great scientific value using the extremophiles as model organisms to explore the survival and evolution of life in extraterrestrial space and even Mars. These researches will greatly help to develop the knowledge and techniques to enable life on the Earth to be livable in space.

Extremophiles refer to the microorganisms that can live in various extreme environments of the Earth, including irradiation and desiccation. They are unique biological resources and precious research materials left to human beings by this planet. For example, *Deinococcus radiodurans* is one of the most radioresistant organisms on the Earth. It is not only tolerant of strong ionizing radiation and ultraviolet

radiation, but also endure extreme environment such as oxidative stress and desiccation, and its radioresistant ability of ionizing radiation is 200 times of that of *Escherichia coli* and more than 1000 times of that of human beings. *Methanogenic archaea* is a kind of strictly anaerobic archaea emerging in the early stage of life evolution on the Earth, which can withstand extreme environments such as hypoxia and low temperature. For example, *Methanococcoides burtonii* isolated from Antarctica has a unique cold adaptation mechanism.

For many years, Hua *et al.*[16,17] have been engaged in the research on the stress-resistant mechanism of *Deinococcus radiodurans*. It was found that the extraordinary resistance of *D. radiodurans* was attributed to its efficient DNA damage response and repair system. The global regulatory factor PprI (Inducer of Pleiotropic Proteins Promoting DNA Repair) and its DNA damage response regulatory pathway were identified. A series of important findings are as follows: PprI is a new type of protease, which can specifically cleave the substrate protein DdrO (DNA damage response protein O). The novel DNA damage response regulatory pathway mediated by PprI-DdrO regulates the transcription of more than 20 genes involved in DNA damage response and repair related, and the pathway is different from the classical SOS pathway[18, 19]; the research on the new pathway has found many functional genes, and expanded a number of new functions of genes[20]. The connection of multiple functional modules in the cell was completed, and a new idea that the stress response of cells is closely related to DNA damage repair was proposed. In addition, a new technology was developed using the PprI as a regulatory element to enhance the resistance of some microorganisms and plants to various stresses[21]. PprI can improve the resistance of microorganisms (*E. coli*, *etc.*) or plants (corn, *etc.*) to stresses such as osmotic pressure, oxidation, or high temperature, demonstrating a good application prospect. These findings and techniques laid a solid theoretical and application foundation for exploring the origin and evolution of life and the utilization of extreme microorganism resources.

8 Planned Experiments On-orbit and on Manned Space Experiment Platform

In 2019, we have planned to carry out projects including the experiment of returning space payload carrying the Earth's extremophile and an application mission project in China's manned space station. These projects take extremophiles of the Earth as the model organisms, and investigate the survival ability and the changing pattern of genome, transcriptome and proteome in the extreme environment of the space through space flight or space station in-situ experiments, so as to reveal the survival ability, stress response, evolution and diversity formation mechanism of organisms in the space environment. The implementation of the project will greatly promote the research on the survival and evolution of life on the Earth in the extraterrestrial space. Meanwhile, it will provide key technologies for the Earth's life and ecosystems suitable for survival in the Mars environment.

The experiment of returning space payload carrying the Earth's extremophiles has cooperated with China Academy of Space Technology (CAST). The stress response mechanism of radiation-resistant *D. radiodurans* in space environment will be studied by using unmanned spacecraft. The objective is to reveal the changing pattern and regulatory network of genetic material and proteins in the radioresistant bacterium under the extreme environment of space. The results are of great scientific significance to evaluate the living ability and stress response of organisms to the space environment, and understand the evolution and diversity formation of organisms in the early extreme environment of the Earth. The project is in the stage of launch preparation, and the samples have been sent to the launch site. It is expected to launch and complete the experiment in 2020.

The application mission project in China's manned space station "The survival and evolution of the Earth or man-made anaerobic life in the Martian

environment" is in the application stage. The project objective is to research the survival and evolution of the Earth life in the simulated Martian environment in China's manned space station. The manned space experiment platform's instruments support two working modes: in-place operation experiment and remote control experiment. During the on orbit operation of the space station, the microorganism analysis payload, life ecology experiment payload, space biology exposure experiment device, and the radiation effect analysis platform will be used to carry out the radiation biology and omics analysis of microorganisms. We planned to investigate on the extreme environmental adaptation mechanism and re-construction of a variety of extreme microorganisms (*D. radiodurans*, *cyanobacteria*, *anaerobic methanogenic archaea* and *Lactobacillus*), including the following aspects.

(1) To explore the stress-response, adaptation and change of life phenotype at different levels of components (cells, organelle, biological macromolecules) after entering space, and explore the survival and evolution of life in extraterrestrial space and even Mars environment. Through interdisciplinary research and comprehensive research, the expected results will reveal the survival of life in the extreme environment of space, the evolution of its genome, transcriptome and proteome, and clarify the stress response mechanism of DNA repair, regulatory factors, metabolic synthase and other important proteins in space.

(2) To investigate the adaptability of artificial modified anaerobic life in space. Through the fusion and transformation of the genome, new species that can survive in the space environment similar to Mars are selected and constructed, which provides the basis for the subsequent improvement of the soil ecosystem of Mars and the establishment of Mars agricultural base.

These studies are planned to set up ground-based experiments simulating the space environment, such as hypoxia and radiation, and carry out the parallel experimental study of biological samples.

9 Future Expectations

With the construction of Chinese manned space station and recoverable satellite science experimental platform, more and more space-based experiments focusing on the origin of life have opportunities to be carried out. In the future, at the molecular level, there are some key issues that should be further explored to well-understand the origin of homochirality and genetic code. For examples, which are critical factors to induce the chiral symmetry breaking? Is there the common genetic code between extraterrestrial and terrestrial life? What will be the potential biomarker for extraterrestrial life exploration besides water? How about oxygen isotope ratios of PO_4^3? Additionally, the photochemical response behavior of chiral molecules, such as amino acids, chiral medicines, and so on, under space extreme environments should further get more attention.

To take extremophiles as the model organism, through the research on extremophiles in space environment including space on-orbit flight and China's manned space station in-situ experiments, the expected results will reveal the survival of organisms in the extreme environment of space, the changes and evolution of their genomes, transcriptome and proteome, *etc.* The results will shed light on the stress response mechanism and key factors in the interaction between stresses such as cosmic rays and organisms. At the same time, by using synthetic biology and other technologies, through genome fusion, modification, and transformation, the starting species will be constructed to adapt to the Martian environment. The important role of man-made organisms in the synthesis of energy sources, carbon sources and ecosystem construction will be investigated further, so as to provide technical support for the research and improvement of the space adaptability of the Earth's organisms.

The relative researches on the origin and evolution of life should execute more sufficient and extensive interdisciplinary cooperation, involving astrobiology, chemistry, biology, geology, space science and technology, and so on. If the special fund will be

established to support these relevant studies, it will be better to promote the development in this research field.

References

[1] ZHAO Y F, LIY Y, GAO X, XU P X. Phosphorus Chemistry: The Role of Phosphorus in Prebiotic Chemistry [M]. Berlin: De Gruyter, 2019

[2] YING J X, FU S S, LI X, *et al.* A plausible model correlates prebiotic peptide synthesis with the primordial genetic code [J]. *Chem. Commun.*, 2018, **54**:8598-8601

[3] WANG T, ZHANG P B, HU G B, *et al.* Mixed anhydrides of nucleotides and amino acids give dipeptides: a model system for studying the origin of the genetic code [J] *Chemistryselect*, 2018, **3**:7849-7855

[4] LIU Y, LI Y B, GAO X, *et al.* Evolutionary relationships between seryl-histidine dipeptide and modern serine proteases from the analysis based on mass spectrometry and bioinformatics [J]. *Amino Acids*, 2018, **50**:69-77

[5] SHU W Y, YU Y F, CHEN S, *et al.* Selective formation of ser-his dipeptide via phosphorus activation [J]. *Origins Life Evol.: B*, 2018, **48**:213-222

[6] TIAN T, CHU X Y, YANG Y, *et al.* Phosphates as energy sources to expand metabolic networks [J]. *Basel Life,* 2019, **9**:43

[7] XIAO Y, LIU Q, TANG X, *et al.* Mirror-image thymidine discriminates against incorporation of deoxyribonucleotide triphosphate into DNA and repairs itself by DNA polymerases [J]. *Bioconjug. Chem.*, 2017, **28**:2125-2134

[8] LIU Q, CHEN L, ZHANG Z, *et al.* pH-dependent enantioselectivity of D-amino acid oxidase in aqueous solution [J]. *Sci. Reports*, 2017, **7**:2994

[9] LIU Q J, HE Y J, WU L, *et al.* Reactive oxygen species accumulation induced by D-amino acid in *Saccharomyces cerevisiae* [J]. *J. Univ. Chin. Acad. Sci.*, 2018, **35**:473-480

[10] KAN Y, ZHANG Z K, YANG, K H, *et al.* Influence of D-amino acids in beer on formation of uric acid [J]. *Food Technol. Biotech.*, 2019, **57**:418-425

[11] WANG Z M, XU W L, LIU L, *et al.* A synthetic molecular system capable of mirror-image genetic replication and transcription [J]. *Nat. Chem.,* 2016, **8**:698-704

[12] JIANG W J, ZHANG B C, FAN C Y, *et al.* Mirror-image polymerase chain reaction [J]. *Cell Discov.,* **2017**, **3**:17037

[13] WANG M, JIANG W J, LIU X Y, *et al.* Mirror-image gene transcription and reverse transcription [J]. *Chem-US,* 2019, **5**:848-857

[14] LIU X Y, ZHU T F. Sequencing mirror-image DNA chemically [J]. *Cell Chem. Biol.*, 2018, **25**:1151-1156

[15] LING J J, FAN C Y, QIN H, *et al.* Mirror-image 5S ribonucleoprotein complexes [J]. *Angew. Chem. Int. Edit.*, 2020, **59**:3724-3731

[16] HUA Y J, NARUMI I, GAN G J, *et al.* PprI: a general switch responsible for extreme radioresistance of deinococcus radiodurans [J]. *Biochem. Bioph. Res. Co.*, 2003, **306**:354-360

[17] LU H M, GAO G J, XU G Z, *et al.* Deinococcus radiodurans PprI switches on DNA damage response and cellular survival networks after radiation damage [J]. *Mol. Cell Proteom.,* 2009, **8**:481-494

[18] LU H Z, WANG L Y, LI S J, *et al.* Structure and DNA damage-dependent derepression mechanism for the XRE family member DG-DdrO [J]. *Nucl. Acids Res.*, 2019, **47**:9925-9933

[19] ZHAO Y, LU M H, ZHANG H, *et al.* Structural insights into catalysis and dimerization enhanced exonuclease activity of RNase J [J]. *Nucl. Acids Res.,* 2015, **43**:5550-5559

[20] LI S J, CAI J L, LU H Z, *et al.* N-4-Cytosine DNA Methylation Is Involved in the Maintenance of Genomic Stability in *Deinococcus radiodurans* [J]. *Front. Microbiol.,* 2019, **10:**1905

[21] HUA Y W, WANG Y G, WANG L Y. Polypeptide Having Protease Activity and Methods for Increasing Its Activity Thereof: US 10, 316, 310 B2 [P]. 2019-06-11

ZHANG Xingwang, YIN Zhigang, YU Jianding, YUAN Zhangfu, ZHAO Jiuzhou, LUO Xinghong, PAN Mingxiang. Space Materials Science in China: I. Experiment Studies under Microgravity. *Chin. J. Space Sci.*, 2020, **40**(5): 398–401. DOI:10.11728/cjss2020.05.398

Space Materials Science in China: I. Experiment Studies under Microgravity*

ZHANG Xingwang[1,2] YIN Zhigang[1,2] YU Jianding[2,3] YUAN Zhangfu[4]

ZHAO Jiuzhou[5,6] LUO Xinghong[5] PAN Mingxiang[7,8,9]

1 (*Institute of Semiconductors, Chinese Academy of Sciences, Beijing* 100083)

2 (*Centre of Materials Science and Optoelectronics Engineering, University of Chinese Academy of Sciences, Beijing* 100049)

3 (*Shanghai Institute of Ceramics, Chinese Academy of Sciences, Shanghai* 200050)

4 (*Collaborative Innovation Center for Steel Technology, University of Science and Technology Beijing, Beijing* 100083)

5 (*Institute of Metal Research, Chinese Academy of Sciences, Shenyang* 110016)

6 (*School of Materials Science and Engineering, University of Science and Technology of China, Shenyang* 110016)

7 (*Institute of Physics, Chinese Academy of Sciences, Beijing* 100191)

8 (*School of Physical Sciences, University of Chinese Academy of Sciences, Beijing* 100049)

9 (*Songshan Lake Materials Laboratory, Dongguan* 523808)

Abstract The virtual absence of gravity-dependent phenomena in microgravity allows an in-depth understanding of fundamental events that are normally obscured and therefore are difficult to study quantitatively on Earth. Of particular interest is that the low-gravity environment aboard space provides a unique platform to synthesize alloys of semiconductors with homogeneous composition distributions, on both the macroscopic and microscopic scales, due to the much reduced buoyancy-driven convection. On the other hand, the easy realization of detached solidification in microgravity suppresses the formation of defects such as dislocations and twins, and thereby the crystallographic perfection is greatly increased. Moreover, the microgravity condition offers the possibilities to elucidate the liquid/solid interfacial structures, as well as clarify the microstructure evolution path of the metal alloys (or composites) during the solidification process. Motivated by these facts, growths of compound semiconductors and metal alloys were carried out under microgravity by using the drop tube, or on the scientific platforms of Tiangong-2 and SJ-10. The following illustrates the main results.

Key words Space materials, Microgravity, Bubble behavior, Microstructural evolution

Classified index V 45

1 Marangoni-convection-driven Bubble Behavior and Microstructural Evolution of Sn-based Alloy

The Marangoni convective effect gives rise to convection during the alloy solidification process. It plays a key role in the heat and mass transfers, and significantly affects the microstructure and elemental distribution of the alloys[1]. Microgravity condition provides a platform that favors a better understanding of this effect, due to the alleviation of gravity-

* Supports by the National Natural Science Foundation of China (U1738114), the Strategic Priority Research Program on Space Science, the Chinese Academy of Sciences (XDA15051200), the China's Manned Space Station Project (TGJZ800-2-RW024), and the Chinese manned space flight pre-research project (030302)

Received March 26, 2020

E-mail: xwzhang@semi.ac.cn, panmx@iphy.ac.cn

induced buoyancy convection. Here we choose Sn-3.5Ag/Sn-17Bi-0.5Cu as a model system to study the effects of Marangoni convection on the microstructures of metal alloys under space microgravity condition. Cylindrical alloy bars of Sn-3.5Ag and Sn-17Bi-0.5Cu with diameters of 5 mm were prepared using a Cu mold and were cast in a vacuum induction furnace. They were cut into cylindrical samples with a height of 5 mm and fixed to the Cu ring, and then the samples were packaged into a quartz tube under vacuum condition. A multi-function materials synthesis furnace was used as the heating device and the solidification was carried out on the recoverable satellite SJ-10. The total time from heating to cooling was 1664 min, with durations at 773 K for 52 min and 930 K for 165 min. For comparison, the Sn-3.5Ag/Sn-17Bi-0.5Cu (wt. pct) alloy was also solidified under normal gravity conditions.

The comparative studies revealed that Marangoni convection significantly affects the solidification structure as it controls the bubble behavior and mass transfer in the melt under microgravity. The surface tension gradient induced by the Bi concentration difference leads to the formation of Marangoni convection from the right to left of the melt. And in the left (Bi-scarce) part of the melt, Marangoni convection induced by the Cu concentration difference flows from the outside to the inside. Due to the bubble-agitation convection, Cu mainly migrates from the substrate to the right part of the melt. Therefore, a gradient distribution of dendrite-like Cu_xSn_y is observed. While under the normal gravity condition, gravity-induced convection gives rise to an even distribution of Bi and Cu, which reduces the contact angle and the surface tension, thereby promoting the nucleation of the alloy. Therefore, fine dendrite-like Cu_xSn_y with high density is uniformly distributed in the melt.

2 Solidification of TC8 Alloy

Titanium alloy has amazing properties including high specific strength, good machining performance and strong corrosion resistance, and is widely used in the aerospace field[2]. Different from the commonly observed columnar structure, the solidification of duplex titanium alloy usually yields an equiaxed polycrystalline structure. However, few works have yet been reported on the solidification behavior of titanium alloy in the microgravity environment. For better understanding, the effect of microgravity on the structure of titanium alloy, the solidification of TC8 alloy was carried out under a microgravity environment with a drop tube. Rod samples with a diameter of 6 mm and a length of 28 mm were used in this study. The 50-m-high drop tube can supply a microgravity environment at an acceleration level down to 10^{-6} g_0 for about 3.2 s.

The solidification microstructure of TC8 alloy is composed of fine equiaxed grains that appeared at an early stage and bigger elongated grains formed at later stage. Between these two kinds of grains, a flat transition interface was observed in the μg sample, while a curved one appeared in the $1g$ sample. Generally, the amounts and aspect ratios of the grains are smaller, and the grain sizes are larger in the μg sample. Moreover, no visible element macro-segregation occurred in both the μg and $1g$ samples. These observations indicate that the solidification velocities of the samples are rather rapid, and therefore the convection and solute transport driven by gravity only has limited influence on the solidification microstructure. To sum up, the solidification process is mainly controlled by the thermal diffusion, in which the hydrostatic pressure and wall effect plays a key role.

3 Solidification of Al-Bi-Sn Immiscible Alloy in Space

Immiscible alloys are characterized by the occurrence of a miscibility gap in the liquid state, and have a strong industry application background. These alloys transform into two liquids enriched with different components when cooling into the miscibility gap on the ground, generating a phase-segregated micro-

structure. Microgravity is an excellent environment to inhibit the gravity-related convection, which is helpful for elucidating the roles of nucleation, growth, Ostwald ripening and motions of the minority phase droplets. Herein, the directional solidification experiment was performed with Al-Bi-Sn immiscible alloy under microgravity environment onboard the Tiangong-2 space laboratory. During the solidification, the hold temperature and the withdrawn velocity are about 950 K and 28 $\mu m \cdot s^{-1}$, respectively[3].

A well-dispersed microstructure was achieved by properly optimizing the experimental scheme, and the matrix exhibits equiaxed morphology with no visible gas cavity. By contrast, the reference samples solidified under $1g$ contain gas cavities and show a phase-segregated structure. The microgravity conditions effectively diminish the convective flow of the melt and the Stokes motions of the minority phase droplets and gas bubbles, which are favorable for suppressing the appearance of macro-segregation and the formation of porosity. Our results also reveal that the microgravity condition favors the detachment between the melt and the crucible wall, and prevents the heterogeneous nucleation of the α-Al nuclei on the crucible wall. The increase of the nucleation undercooling of α-Al nuclei promotes the formation of equiaxed grains.

4 Detached Growth of InSb

Bridgman method is one of the mainstream techniques to grow semiconductor crystals. However, considerable thermal mismatch appears when the crystal adheres to the container, due to the difference in their thermal expansion coefficients. Calculations show that, this mismatch can result in thermal stress orders of magnitude larger than that caused by the temperature gradient. Experimentally, such large thermal stress usually leads to an increased dislocation density or even worse, macroscopic cracks, when cooling the crystals from the growth temperature. Detached growth, under which the crystal grows without contacting the container, is a possible way to alleviate the thermal stress and therefore improve the crystal quality. Herein, detached Bridgman growth of InSb, a typical narrow bandgap III~V semiconductor, was achieved onboard the Tiangong-2 space laboratory[4].

It was found that in the region adjacent to the seed most of the space-based InSb crystal grew without touching the crucible wall. By contrast, the ground-grown InSb crystal has a uniform diameter and its outer-surface replicates the inner-surface of the crucible. As a result, the space-grown InSb crystal has a largely reduced defect density, as compared with its terrestrial counterpart. Moreover, room temperature electrical characterizations of the space InSb crystal within the detached region yield considerably improved electron mobility. The space-based InSb crystal was utilized to fabricate Corbino disk, a two-terminal magnetic sensor, and a considerably enhanced sensitivity was achieved. The observed magnetoresistance increases by about 50% as compared with that of the terrestrial device. Our results have significant implications for the high-quality growth of InSb-related materials and their future applications.

5 Space-grown Homogeneous $In_xGa_{1-x}Sb$ Crystal

The growth of high-quality homogeneous $In_xGa_{1-x}Sb$ bulk crystals is a challenging task by conventional methods such as Czochralski and Bridgman techniques, since there exists a large separation between the solidus and liquidus lines in the InSb-GaSb binary phase diagram. The Vertical Gradient Freezing (VGF) method is very promising for addressing this issue. Herein, $In_xGa_{1-x}Sb$ crystal growth was performed on the recoverable satellite SJ-10 by using the VGF method. A $GaSb(111)_A$/InSb/$GaSb(111)_A$ sandwich sample was used as the starting material, and the lengths of GaSb and InSb crystals were 23 mm and 4 mm, respectively. After holding for 3 h at the growth temperature of about 933 K, the temperature was decreased at a rate of 0.5 $K \cdot h^{-1}$ to grow homogeneous crystals for 49 h. An experiment was also

conducted on the ground using a 3-zone vertical gradient furnace to replicate the microgravity experiment[5].

$In_{0.11}Ga_{0.89}Sb$ with uniform composition was obtained under microgravity environment on board the platform of SJ-10. The shapes of the initial and final growth interfaces, the dissolution tendency of the seed and feed crystals, and the growth kinetics of this experiment are similar to the long duration microgravity experiments performed at the international space station, suggesting the high repeatability and reproducibility of the microgravity experimental results. As compared with the composition uniformity of space-grown $In_xGa_{1-x}Sb$, crystal growth under normal gravity only yields an indium composition that is gradually increased along the growth direction. Our results show that normal gravity is helpful for achieving a steady state of equilibrium in the melt composition. However, the non-steady state equilibrium in the melt composition under microgravity favors for a higher growth rate and compositional homogeneity at higher indium composition of $In_xGa_{1-x}Sb$ solid solution.

References

[1] YUAN Zhangfu, WANG Rongyue, XIE Shanshan, *et al.* Wettability of high-temperature melts under microgravity and ground gravity conditions [J]. *Sci. Sin. Phys. Mech. Astron.*, 2020, **50**:047004

[2] LUO X H, WANG Y Y, LI Y. Role of hydrostatic pressure and wall effect in solidification of TC8 alloy [J]. *NPJ Microgravity*, 2019, **5**:23

[3] LI Wang, JIANG Hongxiang, ZHANG Lili, *et al.* Solidification of Al-Bi-Sn immiscible alloy under microgravity conditions of space [J]. *Scr. Mater.*, 2019, **162**:426-431

[4] YIN Zhigang, ZHANG Xingwang, WU Jinliang. Growth of III-V semiconductor crystals under microgravity [J]. *Sci. Sin. Phys. Mech. Astron.*, 2020, **50**:047003

[5] YU J, INATOMI Y, KUMAR V N, *et al.* Homogeneous InGaSb crystal grown under microgravity using Chinese recovery satellite SJ-10 [J]. *NPJ Microgravity*, 2019, **5**(1):8

PAN Mingxiang, WANG Weihua, FAN Shuqian, ZHANG Qi, PAN Xiuhong, DENG Weijie, HU Liang, WEI Bingbo, WANG Haipeng, YIN Zhigang, FANG Jinghong, YU Jianding, ZHANG Xingwang, YUAN Zhangfu, JIANG Hongxiang, ZHAO Jiuzhou, WANG Gong. Space Materials Science in China: II. Ground-based Researches and Academic Activities. *Chin. J. Space Sci.*, 2020, **40**(5): 402-407. DOI:10.11728/cjss2020.05.402

Space Materials Science in China: II. Ground-based Researches and Academic Activities*

PAN Mingxiang[1,2,3] WANG Weihua[1,2,3] FAN Shuqian[4] ZHANG Qi[4] PAN Xiuhong[5]
DENG Weijie[5] HU Liang[6] WEI Bingbo[6] WANG Haipeng[6] YIN Zhigang[2,7]
FANG Jinghong[2,5] YU Jianding[2,5] ZHANG Xingwang[2,7] YUAN Zhangfu[8,9]
JIANG Hongxiang[10] ZHAO Jiuzhou[10] WANG Gong[2,11]

1 (*Institute of Physics, Chinese Academy of Sciences, Beijing* 100191)
2 (*School of Physical Sciences, University of Chinese Academy of Sciences, Beijing* 100049)
3 (*Songshan Lake Materials Lab., Dongguan* 523808)
4 (*Chongqing Institute of Green and Intelligent Technology, Chinese Academy of Sciences, Chongqing* 400714)
5 (*Shanghai Institute of Ceramics, Chinese Academy of Sciences, Shanghai* 201899)
6 (*Laboratory of Space Materials Science and Technology, Northwestern Polytechnical University, Xi'an* 710072)
7 (*Key Laboratory of Semiconductor Materials Science, Institute of Semiconductors, Chinese Academy of Sciences, Beijing* 100083)
8 (*Collaborative Innovation Center of steel technology, University of Science and Technology Beijing, Beijing* 100083)
9 (*College of Engineering, Peking University, Beijing* 100871)
10 (*Institute of Metal Research, Chinese Academy of Sciences, Shenyang* 110016)
11 (*CAS Key Laboratory of Space Manufacturing Technology, Technology and Engineering Center for Space Utilization, Chinese Academy of Sciences, Beijing* 100094)

Abstract Activities of space materials science research in China have been continuously supported by two main national programs. One is the China Space Station (CSS) program since 1992, and the other is the Strategic Priority Program (SPP) on Space Science since 2011. In CSS plan in 2019, eleven space materials science experimental projects were officially approved for execution during the construction of the space station. In the SPP Phase II launched in 2018, seven pre-research projects are deployed as the first batch in 2018, and one concept study project in 2019. These pre-research projects will be cultivated as candidates for future selection as space experiment projects on the recovery of scientific experimental satellites in the future. A new apparatus of electrostatic levitation system for ground-based research of space materials science and rapid solidification research has been developed under the support of the National Natural Science Foundation of China. In order to promote domestic academic activities and to enhance the advancement of space materials science in China, the Space Materials Science and Technology Division belong to the Chinese Materials Research Society was established in 2019. We also organized scientists to write five review papers on space materials science as a special topic published in the journal *Scientia Sinica* to

* Supports by the Strategic Priority Research Program on Space Science, the Chinese Academy of Sciences (XDA15013200, XDA15013700, XDA15013800, XDA15051200), the China's Manned Space Station Project (TGJZS00-2-RW024), and the National Natural Science Foundation of China (51327901)
Received March 26, 2020
E-mail: panmx@iphy.ac.cn

provide valuable scientific and technical references for Chinese researchers.

Key words Additive manufacturing, Aerogel preparation, Electrostatic levitation system, Crystal growth, Solidification, Academic activities of space materials science

Classified index V 45

1 Introduction

Chinese planned space materials science experiments began in 1992 with the launch of China's manned spaceflight program. Space materials science as a branch of space science in China has been continuously supported by two main national programs: one is the China Space Station (CSS) program that started in 1992, and the other is the Strategic Priority Program (SPP) on Space Science since 2011. Most of the space materials science experiments conducted in the past, including those performed on board the Tiangong-2 space laboratory and the SJ-10 recovery satellite in China, are mainly exploratory, due to the limitation on space resource conditions and experimental opportunities and the considerations of developing the space technologies first. In the era of China's own space station, space materials science will focus on systemic and quantitative research. In the CSS plan in 2019, 11 space materials science experimental projects were finally reviewed and officially approved for implementation during the construction of the space station. By launching scientific experiment satellites the SPP will primarily support those space materials science experiments that are not suitable for the space station, such as with the requirement of high microgravity level or long-time microgravity environment with small gravity disturbances, or safety considerations for astronauts. In the SPP phase II launched in 2018, the Qingyang program (alias for space materials science in SPP) deployed 7 pre-research projects on the ground as the first batch in 2018, and 1 concept study project for the necessity of integrating a materials science experiment satellite in 2019. These pre-research projects will be cultivated as candidates for future selection as space experiment projects on recovery scientific experimental satellites in the future.

In recent years the National Natural Science Foundation of China (NSFC) has also increased funding for related researches including space materials science, and a new apparatus of electrostatic levitation system for ground-based research of space materials science and rapid solidification research has been developed under the support of the NSFC[1-3].

In order to promote domestic academic exchange activities and to enhance the advancement of space materials science in China, the Space Materials Science and Technology Division belonging to the Chinese Materials Research Society (CMRS) was established in 2019. We also organized scientists to write review papers on space materials science as special topic published in the journal *Scientia Sinica Physica, Mechanica & Astronomica*) to provide valuable scientific and technical references for Chinese researchers or scholars who are interested in joining the team of space materials science research in the future in the planning and design of materials science experiments in related directions[4-8].

2 Ground-based Researches

2.1 Fundamental Science Problems during the Rapid Solidification of Metallic Materials in Microgravity

There may be significant differences in the material manufacturing process between space and ground, due to the special environment in space such as micro-gravity, high vacuum, and ultra-low temperature. To study the special phenomenon and the mechanism for additive manufacturing in space, including the microstructure, the mechanical properties, and the correlation among them, the Chongqing Institute of Green and Intelligent Technology of CAS has started an advanced research program titled "Fundamental science problems during the rapid solidification of

metallic materials in microgravity", and following preliminary results have been achieved.

(1) Design of prototype machine for space experiments (suitable for both the space environments and the resource constraints), and the verification of key components.

(2) Finite element simulation of the rapid solidification process for metallic materials under microgravity, including the heat and mass transportation, the phase transition, and the instability of liquid bridge caused by the environmental disturbance such as equipment vibration and gravity fluctuation.

(3) Design and early-stage verification of space experiments, including on ground experiments and the optimization of manufacturing parameters.

(4) Suggestions for an experiment payload and accompanying program that will be run in the recovery experiment satellite.

(5) Progress of circular multi-laser melting wire additive manufacturing experiment in parabolic flight test to simulate microgravity environment.

The achievements above would be very helpful for the science experiments in space, especially for the discovering of new phenomena, effects, and new rules in the additive manufacturing process in space.

2.2 Facility for Aerogel Preparation in Space

A prototype of the facility to be served under microgravity for aerogels preparation was developed. This facility has the functions of both the sol-gel process and the sample drying process. It consists of three main parts: one synthesis part for the sol-gel process, one heating part for sample drying, and a controller. The core of synthesis part is three cylindrical chambers made of stainless steel. The inner diameter of each chamber is 25 mm and the height is 80 mm. The sol-gel process is performed by injecting the solvent and the catalytic agent into one synthesis chamber simultaneously from two individual smaller tubes through plastic pipes by a motor. In order to avoid the backflow under microgravity, one-way electromagnetic valves are used. The chamber is sealed by one cover, on which a vacuum pump adapter is designed besides two plastic pipe connectors. Thus, the gas pressure in the chamber can be adjusted according to experimental requirements. The mixture of solvent and catalysis agent in the synthesis chamber can be stirred by the rotation of one magnetic rotor near the inside wall of the chamber, which is driven by a rotating magnet outside.

Totally three types of gelatum can be achieved by this facility in space. The synthesis chamber can be heated up to 400°C by the heating unit which is a tubular heating furnace. By this way, the gel can be dried and xerogel is obtained. The heating furnace is composed of helical resistance coils which are enclosed by some inorganic ceramic fibers. One S-type thermocouple is used for temperature control.

All the operations such as solvent injection, magnet rotation, furnace heating are controlled by the controller. The present prototype is designed aiming to prepare inorganic aerogels in space, especially for the preparation of heat insulating materials. Some synthesis experiments have been done on the ground for the preparation of SiO_2 aerogel as well as SiO_2-Al_2O_3 aerogel.

3 Electrostatic levitation System for Rapid Solidification of Metallic Materials

A large scale new apparatus for rapid solidification research and space materials science has been developed under the support of NSFC National Special Fund for Major Research Instruments. It was designed and manufactured by a research team directed by Prof. Wei from the Laboratory of Space Materials Science and Technology in Northwestern Polytechnical University.

The extraordinary solidification of metallic materials and the ground simulation of microgravity environment are essential subjects for both materials science and space science. According to the national strategy for medium and long-term scientific development, China is about to embrace a space station era in the year of 2020–2030. This experimental system has been developed on the basis of electrostatic levitation technique, which can simulate outer-space

environments like microgravity, containerless state, and ultrahigh vacuum, to accomplish the extraordinary solidification of metallic materials. A series of scientific and technological problems such as intrinsic physicochemical properties and rapid solidification mechanisms of liquid alloys are effectively solved by utilizing these extraordinary conditions[1-3].

This system occupies an area of 110 m^2 and exceeds 2 m in height. The original design ideas, blue prints, and kernel control programs are all fulfilled by the research team independently. Several progresses have been made at least in three key techniques and important scientific issues, which are levitation capability, containerless rapid solidification, and thermophysical properties. Firstly, the electrostatic levitation ability has been improved to set a new record of 15 mm diameter metallic sample, which almost triples the previously published international record. Secondly, the liquid supercooling and containerless solidification of tungsten, which is the most refractory metal in nature with a melting point up to 3695 K, have been achieved under electrostatic levitation conditions. And the in-situ observation and measurement on its solidification rate have been accomplished for the first time to reveal the dendritic growth mechanism within liquid tungsten. Thirdly, the ultrafast solidification of metallic materials has been realized, where liquid titanium displays a dendritic growth velocity as high as 122 $m \cdot s^{-1}$ on account of the ultrahigh vacuum condition (about 10^{-8} Pa) and precisely active control performance in the system. Moreover, it integrates the five experimental functions including electrostatic levitation, thermophysical property measurement, rapid solidification, material preparation, and real-time data processing. The relevant investigations are being conducted on thermophysical properties, rapid solidification mechanism, and novel material synthesis of refractory alloys, titanium alloys, and nickel-based superalloys.

On the basis of this innovative instrument, the research on solidification science and space science in China will be facilitated to a desirable extent. It helps to update the preparation technique of traditional materials and push forward the research and development on new materials. Meanwhile, it may also promote the research on fluid science under stimulated space environments[9]. Besides, this system is even capable of evolving into a platform mounted on China's space station after a miniaturization design.

4 Establishment of a Space Materials Science and Technology Division

The Space Materials Science and Technology Division, affiliated with the CMRS, was established in Beijing in 2019.

The scope of academic activities of the space materials science and technology division covers: (i) The physical characteristics of outer space environment and its ground simulation; (ii) materials preparation, research, and development for manufacturing rockets and outer spacecraft; (iii) preparation and processing of metals and non-metallic materials in space environment (including ground-based simulation, the same below); (iv) the physical and chemical properties, application performance, and service behavior of the materials in space environment; (v) the solidification, heat treatment, plastic processing, and jointing, *etc.* of various spacecraft materials; (vi) the mathematical modeling and computational simulation relating to space materials science and technology.

As part of the CMRS's annual conference, the division has hosted three symposia. The 2018's symposium was held in Xiamen, Fujian Province, and the 2019's one was held in Chengdu, Sichuan Province. This year will be held in Qingdao, Shandong Province, China.

5 Publications of Special Topic: Space Material Science

5.1 Study on Crystal Growth of $In_xGa_{1-x}Sb$ under Microgravity[4,10]

$In_xGa_{1-x}Sb$ is a ternary alloy that has tunable pro-

perties. The wavelength of $In_xGa_{1-x}Sb$ can be varied in the range 1.7~6.8 μm, which is in the Infrared (IR) region and makes that $In_xGa_{1-x}Sb$ can be used as a substrate for IR detector and Thermophotovoltaic (TPV). The phase diagram reveals that there is a large temperature gap between liquidus and solidus lines, which leads to constitutional supercooling and the formation of crystal defects during the solidification process of InGaSb crystal. Moreover, convection caused by gravity will increase the inhomogeneity of transport in the liquid region near the crystal growth interface, making it difficult to grow $In_xGa_{1-x}Sb$ crystal. The convection will be restrained in microgravity environment, and thus, it is very beneficial for crystal growth. This article introduces the effect of microgravity on the growth of $In_xGa_{1-x}Sb$ crystal and the results of the space growth experiment of $In_xGa_{1-x}Sb$ ternary crystal with a high In concentration in SJ-10 Recoverable scientific experiment satellite.

5.2 Growth of III-V Semiconductor Crystals under Microgravity

The low-gravity environment aboard the space provides a unique platform for both understanding the crystal-growth-related phenomena that are masked by gravity on the Earth and exploring new crystal growth techniques. III~V semiconductor crystal growths were carried out under microgravity and the main results include: (i) device-grade semi-insulating GaAs single crystal with improved stoichiometry was grown under microgravity condition, and low noise field-effect transistors and analog switch integrated circuits were fabricated and the performances were better than their terrestrial counterparts; (ii) detached Bridgman growth was realized in two model systems of GaSb and InSb by suppressing the hydrostatic pressure of melt, and largely reduced dislocation densities in the materials were observed; (iii) the contributions of buoyancy-driven convection, Marangoni convection, and rotation magnetic field forced convection on the microscopic segregation were carefully studied; (iv) the vertical gradient freezing method was employed to grow semiconductor alloys and chemically homogeneous GaInSb crystal was obtained. In this review, the main progress in these aspects are summarized and future challenges are discussed[5].

5.3 Wettability of High-temperature Melts under Microgravity and Ground Gravity Conditions

The physical characteristics of the material could not be accurately observed due to the effect of gravity which hides some experimental phenomena of the material surface and interface. So, it is greatly significant to study the influence mechanism of microgravity on the melt wetting behavior and solid/liquid interface reaction. In this paper, the wetting behavior of high-temperature melts, especially of Sn-based alloys, and the reaction properties on the melt/substrate interface were summarized. Comparing with related research and experimental results under normal gravity and microgravity conditions, the high-temperature melt wetting characteristics in both satellite microgravity environment and ground environment are summarized. This paper provides a theoretical reference for future space microgravity experiments and analysis[6].

5.4 Progress in the Solidification of Monotectic Alloys under the Microgravity Condition of Space

Monotectic alloys or alloys with a miscibility gap in the liquid state are a broad kind of materials. They are especially suitable for the manufacturing of either the in-situ particle composite materials or the composite materials with a core/shell structure and, thus, have a strong industry application background. These alloys, however, have an essential drawback that just the miscibility gap poses problems during solidification. When a single-phase melt of these alloys is cooled into the miscibility gap, it decomposes into two liquids enriched with different components. Generally, the convection flow caused by the gravity and the liquid-liquid phase transformation causes the formation of a phase segregated microstructure when these alloys are solidified under the normal gravitational conditions. Under microgravity condition, the convection flow caused by the gravity and the sediment or floating of the second phase due to the density difference between the components are

obviously weakened, it is beneficial for the study of solidification theory of monotectic alloy and the preparation of monotectic alloys composited with a well dispersed microstructure. In recent decades, plenty of efforts have been made to investigate the solidification of monotectic alloys under microgravity conditions, this article will review the research work in this field during the last few decades[7,11,12].

5.5 Review of Space Manufacturing Technique and Development

Since the first additive manufacturing equipment was sent to the international space station in 2014, space manufacturing technology has become one of the most active scientific and application frontiers of the world's major space powers. Space manufacturing technology is a key strategic technology to enhance the capability of human space activities and deep space exploration. By investigating the development status of space manufacturing technology and combining the development status of advanced manufacturing technology at home and abroad. We introduce the space manufacturing materials (including polymer, composite, biological materials, metals, and ceramics) and the development trend of space manufacturing in the future, which provides a theoretical reference for the deployment of space manufacturing technology in China[8].

References

[1] ZOU P F, WANG H P, YANG S J, *et al.* Density measurement and atomic structure simulation of metastable liquid Ti-Ni alloys [J]. *Metal. Mater. Trans.: A*, 2018, **49A**:5488-5496

[2] LU P, WANG H P, ZOU P F, *et al.* Local atomic structure correlating to phase selection in undercooled liquid Ni-Zr peritectic alloy [J]. *J. Appl. Phys.*, 2018, **124**:025103

[3] ZOU P F, WANG H P, YANG S J, HU L, WEI B. Anomalous temperature dependence of liquid state density for $Ni_{50}Ti_{50}$ alloy investigated under electrostatic levitation state [J]. *Chem. Phys. Lett.*, 2017, **681**:101-104

[4] FANG Jinghon, XIA Zhaoyang, WANG Hui, *et al.* Study on crystal growth of $In_xGa_{1-x}Sb$ under microgravity [J]. *Sci. Sin. Phys. Mech. Astron.*, 2020, **50**:047002

[5] YIN Zhigang, ZHANG Xingwang, WU Jinliang. Growth of III-V semiconductor crystals under microgravity [J]. *Sci. Sin. Phys. Mech. Astron.*, 2020, **50**:047003

[6] YUAN Zhangfu, WANG Rongyue, XIE Shanshan, *et al.* Wettability of high-temperature melts under microgravity and ground gravity conditions [J]. *Sci. Sin. Phys. Mech. Astron.*, 2020, **50**:047004

[7] JIANG Hongxiang, LI Wang, ZHANG Lili, *et al.* Progress in the solidification of monotectic alloys under the microgravity condition of space [J]. *Sci. Sin. Phys. Mech. Astron.*, 2020, **50**:047005

[8] WANG Gong, ZHAO Wei, CHENG Tianjin, LIU Yifei. Review of space manufacturing technique and developments [J]. *Sci. Sin. Phys. Mech. Astron.*, 2020, **50**:047006

[9] WANG H P, LI M X, ZOU P F, *et al.* Experimental modulation and theoretical simulation of zonal oscillation for electrostatically levitated metallic droplets at high temperatures [J]. *Phys. Rev.: E*, 2018, **98**:063106

[10] YU J, INATOMI Y, KUMAR V N, *et al.* Homogeneous InGaSb crystal grown under microgravity using Chinese recovery satellite SJ-10 [J]. *NPJ Microgravity*, 2019, **5**(1):8

[11] LI Wang, JIANG Hongxiang, ZHANG Lili, *et al.* Solidification of Al-Bi-Sn immiscible alloy under microgravity conditions of space [J]. *Scr. Mater.*, 2019, **162**:426-431

[12] JIANG Hongxiang, LI Shixin, ZHANG Lili, *et al.* Effect of microgravity on the solidification of aluminum–bismuth–tin immiscible alloys [J]. *NPJ Microgravity*, 2019, **5**:26

LIU Jing, JIANG Hai, YANG Xu, LI Fen, ZHAO Nanying. Space Debris Research Progress of China. *Chin. J. Space Sci.*, 2020, **40**(5): 408-413. DOI:10.11728/cjss2020.05.408

Space Debris Research Progress of China

LIU Jing[1,2,3] JIANG Hai[1,2] YANG Xu[1,2,3] LI Fen[1,2] ZHAO Nanying[1,2]

1 (*National Astronomical Observatories, Chinese Academy of Sciences, Beijing* 100101)

2 (*Space Debris Observation and Data Application Center, China National Space Administration, Beijing* 100101)

3 (*University of Chinese Academy of Sciences, Beijing* 100049)

Abstract The rapid increase of space debris population has posed serious threaten to the safety of human space activities and became a global issue. How to enhance the technical capabilities of space debris threat coping ability is of great significance to the sustainable development of space activities, the further development, and utilization of outer space. In this paper, we describe space debris research progress of China on observation, collision avoidance, protection, mitigation, regulation, and standard during the last twenty years, and look forward to the future development direction of space debris.

Key words Space debris, Observation, Collision avoidance, Protection, Mitigation

Classified index V 520.7

1 Introduction

Since the first space launch in 1957, a total of 7985 space launch activities has been conducted by the end of July 2020, 9900 spacecraft and 6121 rockets have been successfully launched into Earth orbit. As a result of these space activities, the Earth orbit space has been filled with space objects. Most of them are space debris except for some operational spacecraft. So far, there have been more than 500 on-orbit breakup events, which are the main source of space debris, and the defunct spacecraft are another important source of space debris, the other sources of debris include the wreckage of launch vehicle, mission related debris, tiny paint spots on the exterior of spacecraft, and rocket components, *etc.*

According to the European Space Agency, the number of space debris larger than 10 cm has exceeded 34000, larger than 1 cm has exceeded 900000, and larger than 1 mm is hundreds of millions (https://www.esa.int/Safety_Security/Space_Debris/Space_debris_by_the_numbers). Because of the high speed of space debris up to 8 km·s^{-1}, a collision with even a 1 cm space debris can damage or even destroy a spacecraft. In addition, according to statistic data published by the United States, there are about 400 debris reentered into the atmosphere each year, the maximum exceeds 1000. The reentry of large space objects also poses serious threat to the safety of human beings and ground properties (https://www.space-track.org/#decay)

2 Current Research Status

Space debris poses serious threat to the on-orbit space activities and has become an international focus and hot issue. To ensure the long-term sustainability of outer space activities, space debris research has been carried out by the major spacefaring nations in observation, collision avoidance, protection, mitigation, and regulation and standard to improve technical capabilities over the past few years. United States has established a global Space Surveillance Network, which can fully catalog space debris larger than 10 cm. Russia also has its own network, and plays a leading role in high-earth-orbit object observation.

Received August 25, 2020

E-mail: liujing@bao.ac.cn

ESA proposed its space situation awareness program in 2009 and formed an observation network composed of several radars and telescopes, which can observe space debris larger than 5 cm in Low-Earth-Orbit (LEO) and 50 cm in high-Earth-orbit. In addition, Surrey Space Center of United Kingdom and many European research institutions successfully launched a test satellite from International Space Station to implement the RemoveDEBRIS project in 2018.

Since 1995, China National Space Administration officially joined Inter-Agency Space Debris Coordination Committee (IADC), continuously conducted space debris research work and actively participated in international cooperation, has achieved a series of important and influential results, laid a solid technical foundation to effectively respond to space emergent events and support international cooperation. Based on the above mentioned, this paper summarizes the main progress of space debris research in China during the last twenty years on observation, collision avoidance, protection, mitigation, and regulation and standard, and looks forward to the future works.

3 Space Debris Research Achievements

Since China National Space Administration (CNSA) launched the Space Debris Research Project in 2000, China has achieved a series of important results in five aspects, observation, collision avoidance, protection, mitigation, regulation, and standard, respectively.

3.1 Observation

China draws lessons from the international advanced experience and actively promotes the research and development of observation architecture, infrastructure, and technology. We have finished the demonstration of space and ground-based observation network, studied the key technologies for small-size debris observation, high-precision detection and imaging, developed prototypes, preliminarily established the space debris emergency observation network, as shown in Figure 1. Based on the above mentioned, we have developed a reliable space debris observation facility performance evaluation model,

Fig. 1 Space debris emergency observation network of China

which can accurately evaluate the performance of space debris facilities of the network, and optimize scheduling the network timely. We have broken through key technologies on telescope remote operation, optimal scheduling of joint observation network, and cooperative emergency observation network, which can efficiently improve the response to space debris emergency events.

3.2 Collision Avoidance

Space Debris Observation and Data Application Center (SDOAC) of CNSA was established in the Chinese Academy of Sciences in June 2015. SDOAC is responsible for the operation and management of space debris and near-Earth object observation facilities, space debris observation database maintenance, as well as on-orbit conjunction analysis and collision avoidance, space debris mitigation policy, standard and regulation research, and international cooperation activities on space debris and near-Earth object research.

The center established a collision avoidance model based on independent data, conducted in-depth research on risk assessment methods, formed an autonomous collision avoidance procedure (Figure 2), and established a space debris application and service system (Figure 3), which can be used to evaluate space debris impact of spacecraft's entire lifetime, support space events observation and response, and conduct mission planning and performance evaluation for the joint space and ground-based observation facilities and network, and can provide launch collision avoidance, on-orbit collision avoidance maneuver design, mission design and performance evaluation for post mission disposal, reentry safety analysis, and space debris events identification. SDOAC independently developed China's first space debris long-term evolution model-SOLEM[1], continuously participates in IADC cooperative research, has reached an advanced international level, can provide analysis support for mitigation measures, and plan and design missions to actively remove debris. The key technologies have been broken through during the development and application of the system, laying the foundation for the formulation of technical standards for space debris collision avoidance.

SDOAC has provided services for many space events, successfully eliminated two times of false alarm of Venezuelan 1 remote sensing satellite based on our analysis results, efficiently coordinated the SJ-11 satellite to avoid the threat of collision, achieved excellent results in IADC joint reentry campaigns, such as TG-1 reentry campaign, provided de-orbits mission design and post evaluation service to CHINASAT 5A. In addition, SDOAC provides consulting services for satellite and constellation mission design, evaluates space debris mitigation measures, and supports space emergency event analysis and satellite failure analysis.

3.3 Protection

China Academy of Space Technology has researched the method of Meteoroid/Orbital Debris (M/OD) risk assessment and developed the Meteoroid and

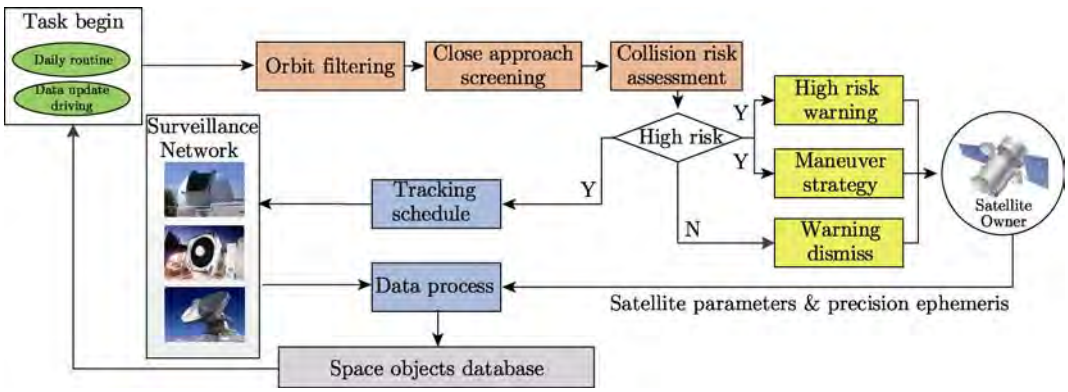

Fig. 2 Workflow of joint collision avoidance

Fig. 3 Typical scenarios of the space debris application and service system

Fig. 4 Resistance sail of BP-1B

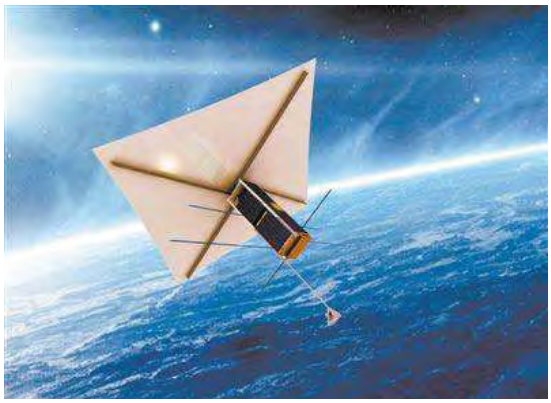

Fig. 5 Deorbit sail of Taurus

Orbital Debris Assessment and Optimization System Tools (MODAOST), which has been successfully applied in China's Manned Spacecraft and accepted by international counterparts. The results have been published in the Protection Manual of IADC[2].

Harbin Institute of Technology (HIT) has led the development of the spacecraft survivability assessment system S^3DE[3], which is compatible with data formats of typical space debris engineering models (ORDEM, MASTER, and SDEEM), and has the preliminary capability to evaluate and calculate the spacecraft survivability. Besides, HIT has analyzed the generation, evolution, and spatial-temporal distribution of space debris, developed the LEO-to-GTO space debris environment engineering model, built the LEO-to-GTO spacecraft environment analysis system on space debris and meteoroids[4].

3.4 Mitigation

In 2016, China Academy of Launch Vehicle Technology conducted the first on-orbit active debris removal experiment with AL-1 spacecraft (https://www.guancha.cn/Science/2016_06_26_365454.shtml). HIT has studied the folding and unfolding active control technology for the inflation resistance increase device, verified the compatibility of the device to the space environment, and provided a reliable deorbit method for LEO micro-satellites and satellite constellations which may out of control[5].

In order to meet the requirements of IADC Space Debris Mitigation Guidelines, Beijing Institute

of Technology (http://www.bit.edu.cn/xww/zhxw/173330.htm) and Shanghai Institute of Aerospace Technology (http://www.chinanews.com/gn/2019/09-12/8954806.shtml) added drag sail and deorbit sail devices to spacecraft as shown in Figure 4 and Figure 5, and successfully verified the reliability of the LEO fast deorbit technology and the deorbit device, which provides practical experience for the small satellites and satellite constellations to efficiently conduct post- mission disposal.

3.5 Regulation and Standard

China has also actively participated in the compilation of the IADC Space Debris Mitigation Guidelines, and issued the Chinese Space Debris Mitigation and Protection Management Measures[6]. The Measures stipulate the subjects and requirements involved in the entire process of spacecraft development, design, development and production, on-orbit operations, and post-mission disposal, detailed the seven requirements of the United Nations Space Debris Mitigation Guidelines, and presented the implementation requirements. Now, the Measures is a national regulation of China's space development and operational departments, which is a critical element to pass the review of the spacecraft launch license.

China's space debris standard system has been preliminarily established with the support of China's space debris research projects, which includes standards for management, protection, mitigation, observation, and collision avoidance as shown in Figure 6, and nearly 50 draft standards have been formed. In 2020, the Subcommittee 5 on Space debris of National Technical Committee 425 on Space Technology and Operation of Standardization Administration of China has been established, with members from government, industries, academies, universities, and commercial entities, including space activity managers, spacecraft producers, satellite operators, scientific researchers and space data users, *etc.* The extensive coverage of the Subcommittee members

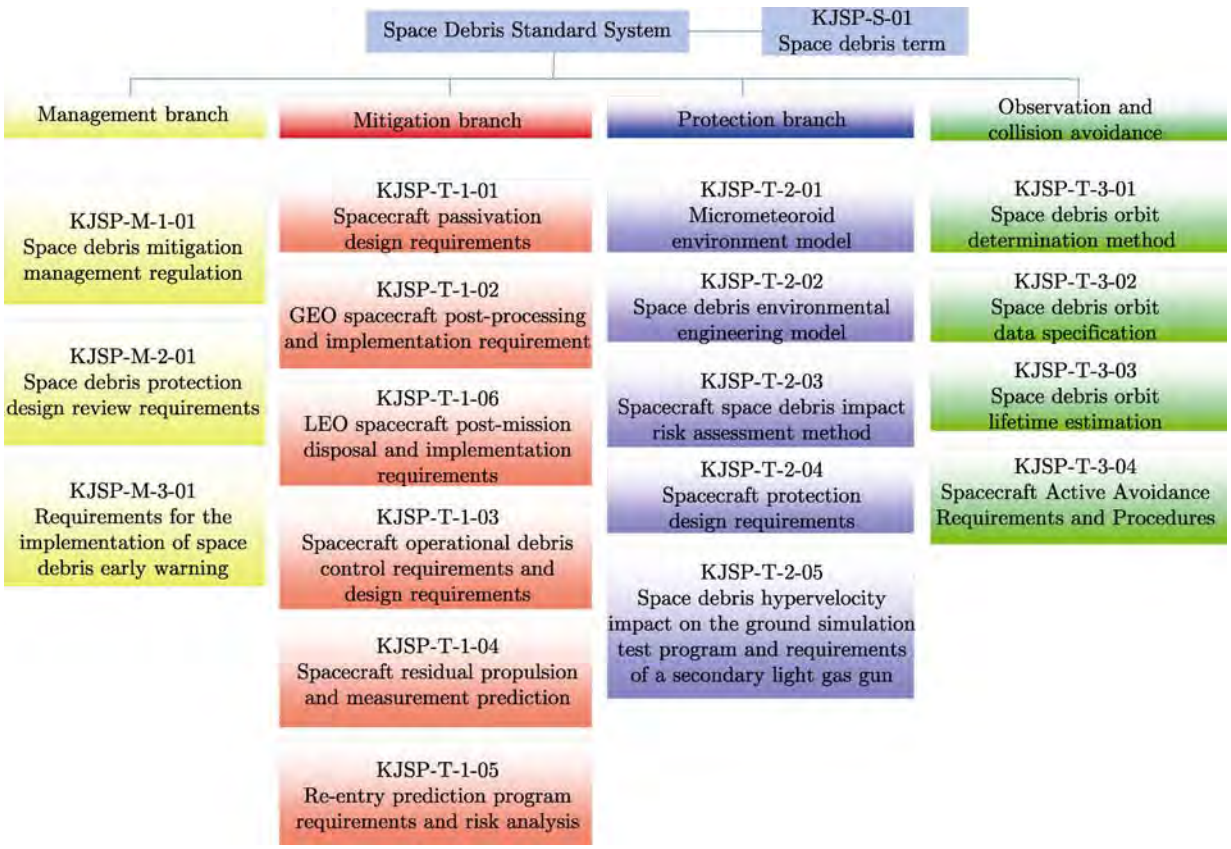

Fig. 6 Diagram of China's space debris standard system

also lays a personnel foundation for the integrity of the space debris standard system and the feasibility of standard specification formulation. As the National Space Debris Standardization Technical Organization, the Subcommittee will carry out the formulation and revision of national standards in the aspects of space debris observation, collision avoidance, protection and mitigation, and will connect with the ISO/TC20/SC14, meet the international space debris mitigation requirements, and facilitate the long-term sustainability of outer space activities.

4 Future Works

In recent years, with the continuously development of space technology, various giant constellation plans have been proposed. In the future, more spacecraft will enter space and the collision probability will greatly increase. The safety of space assets will face more severe challenges. Therefore, in response to the increasingly complex requirements of the space environment, the development of space debris observation should take our current status into consideration, develop a space-ground coordinated observation system, and develop miniaturized, low-cost space-based observation facility to gradually improve the small debris observation capability. At the same time, we will coordinate existing technical foundation in the aspects of observation, collision avoidance, protection, and mitigation, strengthen research on new technologies related space debris, and establish a reliable dynamic database of space debris environment to support the safe, rapid and sustainable development of space activities, and support China's deep participation in the international cooperation on space debris.

References

[1] WANG X W, LIU J. An introduction to a new space debris evolution model SOLEM [J]. *Adv. Astron.*, 2019. DOI:10.1155/2019/2738276

[2] ZHENG Shigui, HAN Zengyao, YAN Jun, *et al.* Calibration of M/OD failure probability assessment software [J]. *Spacecraft Env. Eng.*, 2005, **22**(1):57-62

[3] MA Zhenkai, CHI Runqiang, PANG Baojun. Design and implementation of S^3DE software for spacecraft survivability evaluation in space debris environment[C]//The Ninth National Symposium on Space Debris. Pingtang: Space Debris Monitoring and Application Center, 2017

[4] PANG B J, WANG D F, XIAO W K, *et al.* Characterizing space debris longitude-dependent distribution based on RAAN perturbation rate [J]. *Adv. Space Res.*, 2020, **65**(7):1714-1722

[5] ZHANG Yi, WEI Jianzheng, TAN Huifeng. The design and analysis of inflatable drag balloon [C]//The 3rd International Conference on Advanced Lightweight Structures and Reflector Antennas. Tbilisi, Georgia, 2018

[6] LI Yufei, SHEN Lin. An introduction of space debris mitigation and protection regulation [J]. *Space Debris Res.*, 2017, **17**(1):41-45

FALANGA Maurizio, DONG Xiaolong. Progresses and Activities of the International Space Science Institute in Beijing (ISSI-BJ). *Chin. J. Space Sci.*, 2020, **40**(5): 414-419. DOI:10.11728/cjss2020.05.414

Progresses and Activities of the International Space Science Institute in Beijing (ISSI-BJ)*

FALANGA Maurizio[1,3] DONG Xiaolong[1,2,4]

1 (*International Space Science Institute – Beijing* 100190 *Beijing*)

2 (*National Space Science Center, Chinese Academy of Sciences* 100190 *Beijing*)

3 (*International Space Science Institute* 3012 *Bern*)

4 (*School of Astronomy and Space Science, University of Chinese Academy of Sciences* 100049 *Beijing*)

1 Introduction

The International Space Science Institute - Beijing (ISSI-BJ. http://www.issibj.ac.cn) was jointly established by the National Space Science Center of Chinese Academy of Sciences (NSSC, CAS) in Beijing, China, and the International Space Science Institute (ISSI) in Bern, Switzerland, with the support of the Chinese Academy of Sciences (CAS). ISSI-BJ is a close cooperation partner of ISSI, as they share the same Science Committee, the same study tools, the connections with international space science communities, and other information of mutual relevance and interest. However, the two institutes have independent operational fund resources and operating models.

ISSI-BJ is an institute of advanced studies where scientists from all over the world meet in a multi- and interdisciplinary setting to reach out for new scientific horizons. Its main mission is to contribute to the achievement of a deeper scientific and technological understanding of future space missions as well as of the scientific results yielded from current and past missions through multidisciplinary research, eventually resorting to the use of ground-based observations and laboratory experiments. ISSI-BJ uses the same tools as ISSI, i.e. International Teams, Forums, Workshops, Working Groups, or individual Visiting Scientists (see details at http://www.issibj.ac.cn/Program/), as well as outreach activities such as the Understanding Science seminars and the biennial Space Science School. ISSI-BJ Program covers a wide spectrum of space science disciplines, including astronomy and astrophysics, solar and space physics, planetary science, astrobiology and microgravity science, and Earth science from space-based observations. It offers a complement to the ISSI program with some special emphasis on future scientific opportunities, by its forums on the science and international cooperation for future space science missions and programs. ISSI-BJ was officially inaugurated on 16 July 2013, and during these seven years, ISSI-BJ has become a platform for the exchange of scientific and technological ideas in the field of space research. ISSI-BJ is also a window for the Chinese space science community to get more familiar with the frontiers of space research, as well as for the international space science community to learn about the most recent developments in Chinese space science research and development.

During the two-year period from 2018 to 2019, ISSI-BJ had selected and supported 13 international teams for the advanced studies of space science data processing and research; it has organized nine forums for the discussion of the science, technology, and international cooperation and the future of the development of ISSI-BJ itself. In this time span, ISSI-BJ has also organized two workshops on "Tropical and Subtropical Cyclones with Improved Satellite Observations" and "Oscillatory Processes in

Solar and Stellar Coronae". As part of the Understanding Science seminar series, five public talks were held from 2018 to 2019, and jointly with the Asia-Pacific Space Cooperation Organization (APSCO) the second Space Science School on "Study Space Weather Effects – From the Sun to the Ground" has successfully taken place in 2018.

In the years of 2018--2019, ISSI-BJ has attracted almost 400 international visitors to participate in different activities, and thus, it has managed to establish its reputation as an important platform for the exchange and collaboration in in space science research.

2 International Teams

Every year in January, ISSI-BJ and ISSI jointly release the Call for International Teams in Space and Earth Sciences to invite proposals for study projects from international teams of scientists from different institutions. In 2018 and 2019, after the review by the Science Committee, ISSI-BJ selected 13 teams for independent or joint activities. The teams cover a wide range of fields of space sciences, as illustrated below.

International Teams Approved in 2018

(1) Chemical abundances in the ISM: the litmus test of stellar IMF variations in galaxies across cosmic time – D Romano (INAF, Italy); Z Y Zhang (PMO, China).

(2) Weak Gravitational Lensing Studies from Space Missions - Z Fan (PKU & YNU, China).

(3) Cross-calibration of Laser-Induced Breakdown Spectroscopy (LIBS) instruments for planetary exploration – J Lasue (IRAP, France); R Wiens (LANL, US).

(4) Understanding and unifying the gamma rays emitting scenarios in high mass and low mass X-ray binaries – J Li (Deutsches Elektronen-Synchrotron, Germany).

(5) Relativistic electron precipitation and its atmospheric effect – I Mironova (St. Petersburg State University, Russia).

(6) The eruption of solar filaments and the associated mass and energy transport J C Vial (IAU, France); P F Chen (Nanjing University, China).

International Teams Approved in 2019

(1) Dynamical signatures of energetic particle precipitation in atmospheric re-analyses – Y Orsolini (NILU, Norway); S He (NILU, Norway).

(2) The electromagnetic data validation and scientific application research based on CSES satellite – X Shen (China Earthquake Administration, China); X Zhang (China Earthquake Administration, China); G Hulot (IPGP, France).

(3) Searching for Subglacial Water on Mars with Orbiting Ground Penetrating Radars – R. Orosei (INAF/University of Bologna, Italy).

(4) Using Energetic Electron and Ion Observations to Investigate Solar Wind Structures and Infer Solar Wind Magnetic Field Configurations – G Li (University of Alabama in Huntsville, US); L Wang (Peking University, China).

(5) Modeling Space Weather and Total Solar Irradiance over the Past Century – A Pevtsov (National Solar Observatory, US).

(6) The morphology of aurora at Earth and giant planets: characteristics and their magnetospheric implications – Z Yao (STAR, Belgium); Q Shi (Shandong University at Weihai, China).

(7) Active Galaxies in Crisis: A Statistical Study of Ultra-Violet Variability – M. Ward (Durham University, UK).

The International Team on "Understanding and unifying Gamma Rays emitting Scenarios in High Mass and Low Mass X-Ray Binaries" at ISSI-BJ in March 2019

By the end of 2019, these teams have met in ISSI-BJ for one-week long meetings, and as a result of their research, they have published 81 papers in peer-reviewed journals.

3 Forums

Forums are informal and free debates on open questions of scientific nature or science policy matters among 20 to 25 high-level participants. Forums may lead to formal recommendations or decisions depending upon the topic or issues addressed during the activity. At ISSI-BJ, forums are also organized to discuss the science, technology, and international cooperation of future space science missions.

The outputs of ISSI-BJ forums are published in the ISSI-BJ's TAIKONG magazine series, which reports on the contents of the Forums and reflects in a neutral way the Forum discussions and advises from all the participants.

In the period from 2018 to 2019, ISSI-BJ has organized nine forums dedicated to discussions of different topics related to space science.

(1) Roads towards Sample Return from Comets and Asteroids in January 2018.

(2) Variability and Predictability of Solar-Terrestrial Coupling: The Next Scientific Program of SCOSTEP in November 2018.

(3) Discover the Sky by Longest Wavelength with Small Satellite Constellation in January 2019.

(4) Science Missions using CubeSats in June 2019.

(5) Exploring greenhouse gases, water and climate changes by LEO-LEO occultation in July 2019.

(6) 2nd Strategic Forum on Space Science in September 2019.

(7) Cross-scale Measurements of Space Plasmas to Explore Magnetic Reconnection in September 2019.

(8) Science Objectives and Observation System for the International Meridian Circle in September 2019.

(9) Exploration of Outer Heliosphere and Nearby Interstellar Medium in November 2019.

Group photo of the participants of the forum on "Roads towards Sample Return from Comets and Asteroids"

During the two-three days of each forum, the international participants discussed the key science questions, payload configurations, technologies, and the international cooperation opportunities for space missions and research projects. After each gathering, a forum-related issue of the ISSI-BJ *TAIKONG* magazine was published, in which participants summarize their discussions and reflections on the topics addressed and provided the international community with a thorough introduction to these missions and projects. Two more *TAIKONG* issues are scheduled for 2020. The summaries of the forums can also be published in the peer-reviewed Chinese Journal of Space Science, based on the authors' intentions.

4 Workshops

Workshops are study projects on specific scientific themes, selected in consultation with the Science Committee. The duration of Workshops is typically one week. Workshops are organized by a group of conveners who define the theme, set up the program, and list the group of participants. Participation is by invitation only. The size of any Workshop is usually limited to a maximum of 45 researchers, including a few young scientists. The results of the activity are published as refereed papers in issues of Space Science Reviews and in parallel as volumes of the Space Science Series of ISSI/ISSI-BJ (SSSI). In 2018 and 2019, two workshops were organized by ISSI-BJ, and one book will be published by Springer.

Workshop on Tropical and Subtropical Cyclones with Improved Satellite Observation (7--11 May

2018)

This workshop aimed to review the key science questions on tropical cyclones and the related extreme weather events, and discuss new developments and contributions of satellite observations to these important scientific questions and applications. The list of contributors included atmospheric and meteorological researchers, and satellite remote sensing communities' members.

Oscillatory Processes in Solar and Stellar Coronae (14--18 October 2019)

The workshop covered a wide range of fields related to coronal physics: (i) Seismology of coronal plasma structures; (ii) Novel data analysis techniques, addressing the intrinsically non-stationary nature of the observed oscillatory patterns; (iii) Nonlinear effects: manifestation in observations and theoretical modelling; (iv) Complementarity and exploitation of multi-instrumental and multi-wavelength observations; (v) The similarity of quasi-periodic pulsations detected in solar and stellar flares, and its importance for revealing the mechanisms for those pulsations and the energy releases.

5 Outreach Activities

Understanding Science

In addition to the research projects, ISSI-BJ regularly organizes popularization talks to reduce the gap between science and the public as part of the Understanding Science, which is a series of outreach activities organized by the UK Royal Society of Chemistry (RSC), the Beijing University of Chemical Technology (BUCT), and ISSI-BJ. A collaboration with SELF was recently started.

Its goal is to make a broader public aware of today's accomplishments in science research through short scientific lectures in English (popularization talks) as well as to have an opportunity to talk with either international or Chinese scientists in a friendly environment.

From 2018 to 2019, five Understanding Science seminars were organized.

(1) The Galactic Adventure of the First Interstellar Asteroid - A/2017 U1 Oumuamua – by Prof. Wing Ip (National Central University, Taiwan) on 16 January 2018.

(2) Gravitational Lenses: Mirages in the Universe – by Prof. Georges Meylan (Ecole Polytechnique Fédérale de Lausanne, Switzerland) on 8 June 2018.

(3) How does Nature beat the Large Hadron Collider? Cosmic Rays, the most Energetic Particles in the Universe – by Dr. Luke Drury (Dublin Institute for Advanced Studies, Ireland) on 10 September 2018.

(4) Traveling to the Black Hole – by Dr. Pavel Bakala (Silesian University in Opava, Czech Republic) on 22 January 2019.

(5) Life in the Universe – by Prof. Alvaro Giménez (Spanish National Research Council, Spain) on 5 December 2019.

Picture of the workshop "Oscillatory Processes in Solar and Stellar Coronae" held at ISSI-BJ on October 14-18, 2019

Prof. Alvaro Giménez (CSIC, Spain) giving his lecture on Life in the Universe

Space Science School

ISSI-BJ/APSCO Space Science School, which is a joint biennial project of ISSI-BJ and APSCO, the Asia-Pacific Space Cooperation Organization. This space science school provide training courses on the topics of space sciences and space science missions for international students. The students are provided with the required scientific background relevant to producing a report.

On 10--19 October 2018, the 2nd ISSI-BJ/APSCO Space Science School with EISCAT on "Study Space Weather Effects: From the Sun to the Ground" was held at Sanya Institute of Remote Sensing (RADI) in Sanya, Hainan Province, China. Throughout the school, 10 lecturers and 14 tutors from Asia and beyond shared their knowledge and experience with 57 students from 10 countries.

The School started with a short introduction school given by the organizers, Prof. Maurizio Falanga, Executive Director of the International Space Science Institute – Beijing (ISSI-BJ), Dr. Ebrahimi Mohammad Seyedabadi, Director General of the Asia-Pacific Space Cooperation Organization (APSCO), and Dr. Craig J. Heinselman, Director of the EISCAT Scientific Association.

The first two and a half days were dedicated to introductory lectures given by the invited speakers on various elements of Space Weather. The opening talks revolved around the Sun and its connection to the Space Weather, and the first day was concluded with a Welcome Reception sponsored the Embassy of Switzerland.

On the following days, experts gave an overview of the Space Weather history, forecasting, and SW Science Program of ESA. After a seminar on the interplanetary coronal mass ejections, and a talk on solar energy particles, the following lectures brought the Space Weather topics closer to the Ground. The third day finished with the introduction to students group work, and a social dinner sponsored by ISSI-BJ and APSCO to help the students of each group do some networking. On 13 October, the participants seized the chance to learn more about the Sanya Institute of Remote Sensing during the technical tour around the campus facilities.

Group Picture of the 2018 Space Science School participants

During the following days, students were divided into four working groups, depending on their expertise and preferences: Sun/Heliosphere, Impact and Magnetosphere-Ionosphere-Thermosphere Coupling, Ionosphere/EISCAT Incoherent Scatter Radars, and Effects on Satellites and Ground-based Infrastructures. The groups have analyzed in parallel several extreme Space Weather events, such as the ones detected in September 2017.

The School provided young space researchers and engineers with the opportunity to gain the in-depth knowledge on the science of Space Weather, observational methods, and its relevance to applications from the Sun to the ground. The final report including the reports written by all the working groups, have been published jointly with APSCO and EISCAT in the TAIKONG ISSI-BJ magazine.

6 Publications

Taikong Magazine

The Taikong magazine series constitutes the output of the Forums organized at ISSI-BJ. The magazine reports on the content of the forums and reflects in a neutral way the Forum discussions and advices from all participants.

Nine issues were published between 2018 and 2019(1) TAIKONG No. 10: Lunar and Planetary Seismology

(2) TAIKONG No. 11: Roads towards Sample Return from Comets and Asteroids.

(3) TAIKONG No. 12: Study Space Weather

Effects: From the Sun to the Ground.

(4) TAIKONG No. 13: PRESTO: Predictability of the Variable Solar-Terrestrial Coupling.

(5) TAIKONG No. 14: Discover the Sky by Longest Wavelength.

(6) TAIKONG No. 15: Exploring Greenhouse Gases, Water, and Climate Changes by LEO-LEO Occultation.

(7) TAIKONG No. 16: Frontiers and Opportunities of Space Science: NSSC/ISSI-BJ 2nd Strategic Forum on Space Science.

(8) TAIKONG No. 17: Cross-scale Measurements of Space Plasmas to explore Magnetic Reconnection.

(9) TAIKONG No. 18: Science Missions using CubeSats.

Space Sciences Series of ISSI (SSSI)

The Space Sciences Series of ISSI books are coherent reports of the findings, discussions, and ideas that result from Workshops regularly held at ISSI Bern and ISSI-BJ.

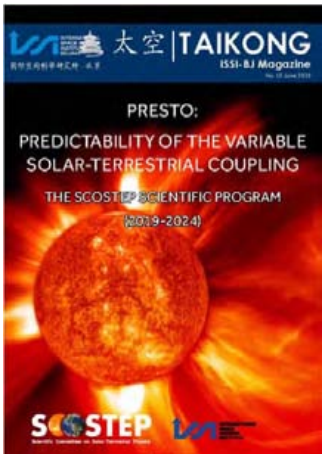

Cover of the TAIKONG No. 13 on "PRESTO: Predictability of the Variable Solar-Terrestrial Coupling"

From 2018 to 2019, one topical volume was edited and issued first in Space Science Reviews, to be then published in 2019 as part of the SSSI: Astronomical Distance Determination in the Space Age – R. de Grijs and M. Falanga (Eds.), Volume 66, Springer 2019.

Cover of the ISSI-BJ TAIKONG No. 14 on "Discover the Sky by Longest Wavelength"

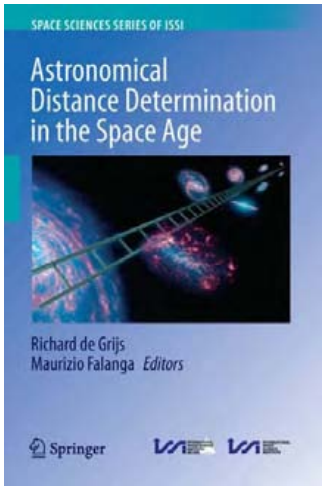

Volume No. 66 of the Space Science Series of ISSI on "Astronomical Distance Determination in the Space Age"